Observations and modelling of exoplanet atmospheres : from the top of hot-Jupiters to the bottom of temperate terrestrial planets, investigating the transition from Super-Earth to Sub-Neptune with a Hubble survey

Amélie Gressier

université
PARIS-SACLAY

Observations and modelling of exoplanet atmospheres: from the top of hot-Jupiters to the bottom of temperate terrestrial planets, investigating the transition from Super-Earth to Sub-Neptune with a Hubble survey

Observations et modélisations de l'atmosphère des exoplanètes: de la haute atmosphère des Jupiter-chauds à la surface des planètes terrestres tempérées, étude de la transition des Super-Terre aux Sub-Neptune avec un relevé Hubble

Thèse de doctorat de l'université Paris-Saclay

École doctorale n° 127 Astronomie et Astrophysique d'Ile de France (AAIF)
Spécialité de doctorat: Astronomie et Astrophysique
Graduate School : Physique Référent : Université de Versailles-Saint-Quentin-en-Yvelines

Thèse préparée dans les unités de recherche **LATMOS** (Université Paris-Saclay, UVSQ, CNRS) et **IAP** (Sorbonne Universités, CNRS) sous la direction de **Emmanuel MARCQ**, Maître de conférences, la co-direction de **Jean-Philippe BEAULIEU**, Directeur de recherche et le co-encadrement de **Benjamin CHARNAY**, chargé de recherche

Thèse soutenue à Paris, le 09 décembre 2022, par

Amélie Gressier

Composition du jury

Membres du jury avec voix délibérative

Hélène Brogniez Professeure des Universités, UVSQ	Présidente
Néstor Espinoza Assistant Astronomer, Space Telescope Science Institute (STScI)	Rapporteur et Examinateur
Michaël Gillon Directeur de Recherches FNRS, Université de Liège	Rapporteur et Examinateur
Claire Moutou Directrice de Recherche CNRS, IRAP	Examinatrice

THESE DE DOCTORAT

NNT : 2022UPASP155

université PARIS-SACLAY

ÉCOLE DOCTORALE
Astronomie
et Astrophysique
d'Île-de-France (AAIF)

Titre: Observations et modélisations de l'atmosphère des exoplanètes: de la haute atmosphère des Jupiter-chaud à la surface des planètes terrestres tempérées, étude de la transition des Super-Terre aux Sub-Neptune avec un relevé Hubble

Mots clés: exoplanètes, atmosphères, transfert radiatif, Télescope Spatial Hubble, Sub-Neptune, Super-Terre

Résumé:
En août 2022, le JWST Transiting Exoplanet Community Early Release Science Team a révélé la détection de dioxyde de carbone dans l'atmosphère de la géante gazeuse WASP-39 b, démontrant les capacités exceptionnelles du Télescope spatial James Webb (JWST) pour la caractérisation de l'atmosphère des planètes extrasolaires. Alors que de nombreuses nouvelles données seront disponibles dans les années à venir, cette thèse propose d'utiliser les observations du télescope spatial Hubble (HST) en spectroscopie de transit dans le but de préparer les futures analyses mais aussi de développer des méthodes pour passer de la caractérisation d'une seule cible à l'étude statistique d'une population de planètes. Nous commençons par l'étude de la haute atmosphère des Jupiter-chauds avec les observations en proche ultra-violet du Space Telescope Imaging Spectrograph (STIS), avant de nous pencher sur les régions plus profondes de l'atmosphère à l'aide du Wide Field Camera 3 (WFC3). Vingt-six spectres en transmission sont analysés de manière cohérente afin d'explorer la transition entre Super-Terre et Sub-Neptune. Nous mettons en évidence des dégénérescences dans l'analyse de ces spectres et nous proposons des stratégies d'observations pour les résoudre avec le JWST et ARIEL. Nous étudions l'origine de ces solutions dégénérées avec Exo-REM, un modèle radiatif convectif. En particulier, nous nous intéressons à l'impact de la sédimentation des nuages sur le spectre en transmission, la nature des espèces carbonées et la différence entre l'absorption de l'eau et du méthane.

Title: Observations and modelling of exoplanet atmospheres: from the top of Hot-Jupiters to the bottom of temperate terrestrial planets, investigating the transition from Super-Earth to Sub-Neptune with a Hubble survey

Keywords: exoplanets, atmosphere, radiative transfer, Hubble Space Telescope, Sub-Neptune, Super-Earth

Abstract: In August 2022, the JWST Transiting Exoplanet Community Early Release Science Team revealed the carbon dioxide detection in the atmosphere of the gas giant WASP-39 b, proving the outstanding capabilities of the James Webb Space Telescope (JWST) in characterising exoplanets' atmosphere. As we explore this new range of possibilities with JWST and as many new data will be available in the coming years, this thesis uses Hubble observations in transit spectroscopy and develop methods to move from the study of a single dataset to the statistical study of a population of planets. We start by studying the upper atmosphere of hot Jupiter with near-ultraviolet observations from the Space Telescope Imaging Spectrograph (STIS) before looking at the deeper regions of the atmosphere with the Wide Field Camera 3 (WFC3). Twenty-six transmission spectra are consistently analysed to explore the transition from Super-Earth to Sub-Neptune. We highlight degeneracies in analysing these spectra and propose observing strategies to resolve them with the JWST and ARIEL. We study the origin of these degenerate solutions with Exo-REM, a convective radiative model. In particular, we focus on the impact of cloud sedimentation on the transmission spectrum, the nature of carbon-bearing species and the difference between the absorption of water and methane.

To Manon,

But you know happiness can be found even in the darkest of times, when one only remembers to turn on the light
Spoken by Albus Dumbledore in *Harry Potter and the Prisoner of Azkaban*'s screenplay by Alfonso Cuaròn and Steve Kloves.

3e NUIT DE L'ASTRONOMIE

JUIN 2021

AKENIUM

Acknowledgments

French version :
Je voudrais tout d'abord exprimer ma gratitude envers mes trois encadrants de thèse, Emmanuel Marcq, Jean-Philippe Beaulieu et Benjamin Charnay de m'avoir soutenu durant ces trois années de thèse. Je les remercie de m'avoir laissé, chacun à leur manière, toute la liberté de travailler sur les sujets qui m'intéressaient tout en facilitant les collaborations internationales. La diversité de leurs expériences et leur expertise dans des domaines variés a enrichi nettement mon travail et a certainement permis d'élargir ma vision des sciences planétaires et exo-planétaires.

Je tiens également à remercier Alain Lecavelier pour sa confiance lors de mon stage de Master 2 en 2019. Cette première expérience d'analyse de données Hubble a façonné de bien des aspects mon travail de thèse et aiguisé ma curiosité pour ce domaine. Je le remercie également de son soutien pendant la thèse, la recherche de post-doctorat et la rédaction d'un article dont je suis fière.

Je remercie l'ensemble des membres de mon jury de thèse d'avoir accepté de participer à ma soutenance. Je remercie en particulier Néstor Espinoza et Michaël Gillon, les rapporteurs, d'avoir fourni des rapports complets et encourageants. Leurs remarques ont enrichi mon manuscrit et m'ont aidé à prendre de la hauteur sur le travail effectué.

Je remercie chaleureusement Quentin Changeat et Billy Edwards pour leur incroyable soutien lors de la rédaction de mes articles d'analyse des données Hubble sur les petites planètes. Leur disponibilité et leur confiance m'ont aidé à prendre confiance en moi et en mon travail. Je suis contente de pouvoir continuer à travailler avec eux, en particulier Quentin que je vais retrouver à Baltimore. Nous partageons une vision commune de ce que le domaine peut et doit devenir un monde plus collaboratif et plus ouvert.

Je tiens à remercier également les doctorants et post-doctorants de l'IAP avec lesquels j'ai passé de bons moments, mais aussi tous les élèves de l'école d'été ARIEL. Merci à Emilie et Natalia d'avoir rejoint le groupe exoplanète à l'IAP durant ces dernières années. Ces rencontres ont marqué ma thèse. En particulier, je tiens à remercier Michelle Bieger et Jack Skinner pour leur indéfectible soutien (et leur relecture de mes candidatures, proposal et articles en anglais !). Je suis fière de pouvoir les compter parmi mes amis proches.

Je pense aussi à mes vieux copains de classe préparatoire à Saliège. Eux seuls savent à quel point ce n'était pas gagné que j'écrive une thèse en Astrophysique après mes premiers devoirs surveillés de Maths et de Physique. Je remercie mes amis de l'ENAC, en particulier mes copines de la Team Rugby : Marion, Alex, Alexia, Sandra, Eléanor et Camille pour leur soutien et encouragements ! Leur présence le jour de ma soutenance me touche beaucoup.

Il me reste à remercier mes parents et ma famille, mes sœurs Lise et Manon, mon cousin Clément, mon beau-frère Adrien et mes nièces Judith et Nina avec qui j'ai partagé de nombreux moments durant ces mois de confinement. J'ai eu la chance de grandir dans un environnement culturel, intellectuel et financier qui m'a permis de rêver très tôt de faire de ma passion pour l'univers, des études et un métier. Je me rends compte de cette chance et j'en profite ici pour rappeler que, malgré la gratuité des études en France, la recherche académique, et en particulier l'astrophysique reste réservée à une élite sociale et culturelle. Il est temps d'ouvrir les yeux sur les inégalités non seulement de genre, mais aussi d'origine sociales. La diversité ne peut qu'amener le progrès.

Je tiens à remercier Anatol, 3 ans de thèse à deux, nous y sommes parvenus. Merci de me tirer vers le haut et d'être mon parachute au quotidien.

Arrivée au terme de ces trois années de thèse, j'ai une pensée pour ma sœur Manon qui n'est plus là. Rien ne remplacera la présence d'une grande sœur le jour d'une soutenance de thèse qui marque, malgré tout, une étape importante de ma vie.

English version :
First, I would like to express my gratitude to my three thesis supervisors, Emmanuel Marcq, Jean-Philippe Beaulieu and Benjamin Charnay, for supporting me during these three years of my thesis. I want to thank them for having given me, each in their way, the freedom to work on the subjects that interested me while facilitating international collaborations. Their diverse experience and expertise in various fields have enriched my work and broadened my vision of planetary and exo-planetary sciences.

I would also like to thank Alain Lecavelier for his trust during my Master 2 internship in 2019. This first experience with Hubble data analysis has shaped my thesis work in many aspects and sharpened my curiosity about this field. I also thank him for his support during the thesis, the post-doctoral search and the writing of a paper I am proud of.

I thank all the members of my thesis jury for having accepted to participate in my defence. In particular, I thank Néstor Espinoza and Michaël Gillon, the rapporteurs, for providing a complete and encouraging report. Their remarks enriched my manuscript and helped me to gain perspective on my work.

I warmly thank Quentin Changeat and Billy Edwards for their incredible support in writing my papers analysing the Hubble small planet data. Their availability and trust helped me to gain confidence in myself and my work. I am happy to be able to continue working with them, especially Quentin, whom I will meet again in Baltimore. We share a vision of how the field can and should become a more collaborative and open world.

I would also like to thank the IAP PhD students and post-docs with whom I had a great time and all the ARIEL summer school, students. Thanks to Emilie and Natalia for joining the exoplanet group at IAP during these last years. These meetings have marked my thesis. In particular, I would like to thank Michelle Bieger and Jack Skinner for their unfailing support (and their proofreading of my applications, proposals and papers in English!) I am proud to count them among my close friends.

I also think of my old friends from the preparatory class at Saliège. Only they know how difficult it was for me to write a thesis in Astrophysics after my first supervised Maths and Physics assignments. I want to thank my friends at ENAC, particularly my friends from the Rugby Team: Marion, Alex,

Alexia, Sandra, Eléanor and Camille, for their support and encouragement! Their presence on the day of my defence means a lot to me!

It remains for me to thank my parents and my family, my sisters Lise and Manon, my cousin Clément, my brother-in-law Adrien and my nieces Judith and Nina, with whom I shared many moments during these months of confinement. I was lucky to grow up in a cultural, intellectual and financial environment that allowed me to dream of turning my passion for the universe into a study and a profession. I realise how lucky I was, and I take this opportunity to remind you that, even though studies are free in France, academic research, particularly astrophysics, is still reserved for a social and cultural elite. It is time to open our eyes to the inequalities not only of gender but also of social origin. Diversity can only bring progress.

I want to thank Anatol for three years of the thesis together, and we made it. Thank you for pulling me up and being my daily parachute.

At the end of these three years of the thesis, I have a thought for my sister Manon who is no longer here. Nothing can replace the presence of an older sister on the day of a thesis defence, which marks, despite everything, an important stage in my life.

Contents

List of Figures

List of Tables

Introduction

On July 12, 2022, NASA released the first spectrum of an exoplanet's atmosphere taken by the James Webb Space Telescope (JWST). The spectrum of the hot-Jupiter WASP-96b in the near-infrared and the apparent transit light curve of this same planet was the first steps of a new and fascinating era in exoplanet science. A few weeks later, The JWST Transiting Exoplanet Community Early Release Science Team revealed the carbon dioxide detection in the atmosphere of the gas giant WASP-39 b, proving the outstanding capabilities of the JWST in characterising exoplanet atmospheres. An exoplanet's spectrum might not be the most impressive picture from JWST's first image release at first glance. However, it highlights the incredible rise of exoplanet atmosphere characterisation. Without resolving the planet spatially, we can tell what molecule and atomic species compose the atmosphere if clouds are present and determine its thermal structure. This is achievable with only a few data points from observing the star light years away. These measurements can help us constrain the planet's formation and evolution, learn about its climate, and even determine if it is habitable.

The thousands of exoplanets discovered over the past decades and the progress towards in-depth spectroscopic characterisation of their atmospheres have made the field evolve rapidly. Space and ground-based facility observations added to detailed theoretical modelling provide insights into the variety of exoplanet's physical and chemical processes. As we explore this new range of possibilities with JWST, let us take a step back and acknowledge what the Hubble Space Telescope (HST) has taught us about the atmospheres of exoplanets. This thesis focuses on HST observations using the transmission spectroscopy technique.

The present manuscript is structured around the published and submitted articles from the work that constitutes the thesis. It is divided into four parts and nine chapters, the majority presenting the results of one or more of the publications I have contributed to. The chapters are structured in two axes: from giant gas-rich planets to smaller planets and from current HST to future JWST and ARIEL capabilities.

The first part discusses the general aspect of the characterisation of exoplanet atmospheres and details the observational fundamental techniques and results. We specially focus on Super-Earth, and Sub-Neptune demography and space-based observational results as these objects constitute an essential part of the thesis. The second part details the data analysis techniques of HST near ultraviolet (NUV) observations and gives an interpretation of the atmosphere at high altitudes of several hot-Jupiters. In the second chapter, we transpose the method applied to hot-Jupiters to a Super-Earth.

The third part deals with characterising the deeper region of the atmospheres of smaller planets using HST near-infrared data, particularly the one obtained using the Wide Field Camera 3 (WFC3). The first chapter presents the data analysis methods and the atmospheric Bayesian retrieval code used to characterise the atmosphere of the planets studied in this part. We present the atmospheric characterisation of two Sub-Neptunes and then move on to a temperate terrestrial planet. The third chapter

of this part reviews the main findings of a large sample study. Twenty-six transmission HST spectra are consistently analysed to explore the transition from Super-Earth to Sub-Neptune. This chapter reviews what has been possible to achieve and discover with Hubble about these small planets.

The fourth part deals with the modelling and simulated observations of warm Sub-Neptune atmospheres. First, we present the model grid created with a self-consistent radiative-convective model. Then we used this grid to study two points: the impact of cloud sedimentation on the transmission spectrum and the nature of the carbon-bearing species. We discuss the importance of optical observations in differentiating a clear from a cloudy atmosphere using CHEOPS unprecedented observations. In the last chapter, we investigate JWST and ARIEL observational strategies to unveil the ambiguities highlighted by HST for Super-Earth and Sub-Neptune. In particular, we explore distinguishing a primary cloudy from a heavier atmosphere. In both cases, spectral features are muted. Last, we compare HST and JWST abilities in detecting methane in Sub-Neptune atmospheres using transmission spectroscopy, which has not been done yet, differentiating methane from water absorption.

Part I

Twenty years of extra-solar planet atmospheric characterisation

Chapter 1

Characterisation of exoplanet atmospheres

Contents

1.1 Observing methods

The characterisation of exoplanet atmospheres is based upon simple principles, and different methods have been developed: transmission spectroscopy, emission and reflection spectroscopy, and full-orbit phase curve. All these techniques can be applied to transiting exoplanets: planets that pass periodically in front of and behind the host star blocking a small fraction of the light. We observe the portion of the stellar light filtered through the planet's atmosphere during the transit before it gets to us. During the planetary eclipse, thermal emissions and reflections are blocked. Both transit and eclipse geometry are illustrated in Figure 1.1. It is challenging on a technical level, as the star outshines the planet by a factor of at least a thousand to one. However, by comparing these effects to the stellar constant baseline flux, we can measure relative changes and infer atmospheric properties (Kreidberg, 2018).

1.1.1 Transmission spectroscopy

During a planetary transit, the planet passes in front of its host star and blocks a small portion of the stellar light. The total measured flux which encompasses the planet and the star is called the transit

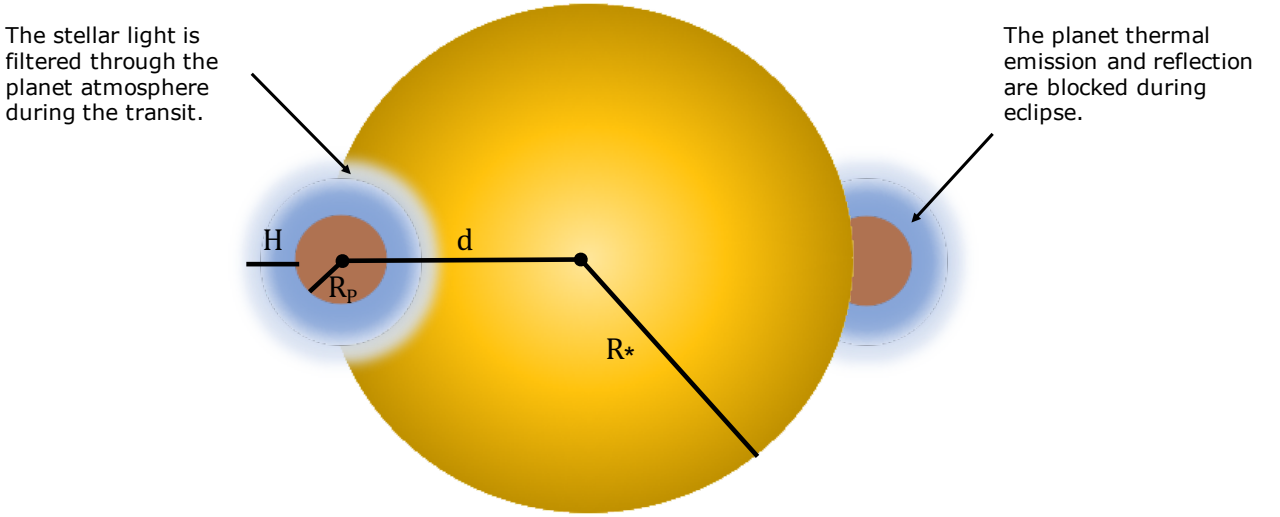

Figure 1.1: Illustration of the transit and eclipse geometry for a planet and its atmosphere. The planet orbits periodically around the star. When it passes in front of the star, there is a transit event; when it passes behind, the secondary eclipse occurs. We presented the stellar $R_\star$ and planetary R_P radii, along with the scale height H and d, the separation of centres in the plane of the sky. This figure is adapted from Kreidberg (2018).

white light curve. The fraction of the flux blocked by the planet, leading to a slight drop in total brightness, corresponds to the planet's sky-projected area relative to the star's area and is called the transit depth (δ). When it is entirely in front of the star, the absorption depth can be approximated by the area ratio of the stellar and planetary disks, with F_{int} and F_{out} the stellar fluxes in and outside the transit, R_P and $R_\star$ the radii of the planet and the star:

$$\delta \approx 1 - \frac{F_{int}}{F_{out}} = \left(\frac{R_P}{R_\star}\right)^2 \tag{1.1}$$

In front of a star the size of the Sun, the transit depth is 1% for a planet the size of Jupiter and 0.01% for a planet the size of the Earth.

This quantity is wavelength dependant and allows atmospheric properties to be inferred. Suppose atoms, molecules, clouds, or hazes absorb light. In that case, the atmosphere will appear more opaque at the wavelength where an atomic or molecular transition occurs and for which the corresponding element is abundant (Seager & Sasselov, 2000). If the planet has an atmosphere, it will block more stellar light, and the planetary radius will appear larger at that specific wavelength. The measurement results in the planet's apparent radius variation with the wavelength. To measure the transit depth as a function of wavelength and obtain the transmission spectrum, we typically bin the total white light curve in wavelength into spectro-photometric channels. Each spectral light curve is then fitted separately with a transit model. To model the transmission spectrum correctly, we need radiative transfer computation of the light on the path through the atmosphere of the planet (Seager & Sasselov, 2000). However to define the detectability of a planet's atmosphere, we can use a good approximation, the expression of the effective radius defined in Lecavelier des Etangs et al. (2008a) with F, the flux, measured during the transit, $S_{planet}(\lambda)$ the effective surface (apparent radius) of the planet and its atmosphere at λ, T_{atm}, μ_{atm} the temperature and the mean molecular weight of the atmosphere, ρ_{planet} the density of the planet, σ the absorption cross-section of the dominant species at λ, independent of the pressure, and $R_\star$ the stellar radius:

$$\frac{d\Delta F/F}{d\lambda} \propto \frac{dS_{planet}(\lambda)}{d\lambda} \propto \frac{T_{atm}}{R_\star^2 \mu_{atm} \rho_{planet}} \frac{d\ln\sigma}{d\lambda} \tag{1.2}$$

Similarly, we can predict the size of the atmospheric features using the scale height. The scale height is the change in altitude over which the pressure drops by a factor of e. It is defined assuming the hydrostatic equilibrium and ideal gas law, where K_b is the Boltzmann constant, T_{eq} is the planet's equilibrium temperature, μ_{atm} is the mean molecular mass of the atmosphere, and g is the surface gravity:

$$H = \frac{K_b T_{eq}}{\mu_{atm} g} \tag{1.3}$$

The size of the atmospheric features can be defined as in Kreidberg (2018), where n is the number of scale heights crossed at wavelengths with high opacity (n is equal to two for clear atmospheres at low-resolution (Stevenson, 2016)):

$$\Delta\delta_\lambda = \left(\frac{R_P + nH}{R_\star}\right)^2 - \left(\frac{R_P}{R_\star}\right)^2 \propto \frac{2nR_PH}{R_\star^2} \tag{1.4}$$

The detection of an atmosphere is favoured for a nearby (within 15 parsecs because of the brightness leading to a better signal-to-noise ratio) small host star (M-dwarf), high equilibrium temperature, a low mean molecular weight, i.e. a hydrogen-dominated atmospheric composition, and low surface gravity. Atmospheric measurements are also most feasible for short-period planets, which are statistically more likely to transit and easier to schedule. In the ideal case, the size of the atmospheric features can reach 0.1% for a hot-Jupiter around a K-dwarf, which could fall to 0.001% for an Earth-like planet. We computed the size of the atmospheric features for planets around a Sun-like star and found the following:

- for a hot-Jupiter with a temperature of 1300 K, a surface gravity of 25 m/s^2 and a mean molecular mass of 2.3 g/mol: $\delta \approx 0.01$ and $\Delta\delta \approx 4.10^{-4}$
- for an Earth-like planet with a temperature of 280 K, a surface gravity of 10 m/s^2 and a mean molecular mass of 28 g/mol: $\delta \approx 10^{-4}$ and $\Delta\delta \approx 2.10^{-6}$

For similar planets around Trappist-1 star:

- for a hot-Jupiter with a temperature of 1300 K, a surface gravity of 25 m/s^2 and a mean molecular mass of 2.3 g/mol: $\delta \approx 0.7$ and $\Delta\delta \approx 2.10^{-2}$
- for an Earth-like planet with a temperature of 280 K, a surface gravity of 10 m/s^2 and a mean molecular mass of 28 g/mol: $\delta \approx 6.10^{-3}$ and $\Delta\delta \approx 10^{-4}$

This method is the most popular in atmospheric characterisation because it allows the constraint if molecular abundances and cloud properties. Most of this thesis's observations and modelling used transmission spectroscopy.

1.1.2 Occultation spectroscopy

Occultation spectroscopy aims to measure the transiting planet's thermal emission and reflection. When the planet passes behind the star, it is occulted, and we can measure the stellar baseline flux. When the planet comes out of the eclipse and back into view, the increase in the total brightness can be attributed to the planet's reflected light and thermal emission.

The thermal emission source for detected exoplanets is the incident stellar flux. Thus the emission signal can be approximated as defined in Kreidberg (2018), where $F_P/F_\star$ is the planet-to-star flux ratio, $B(\lambda, T)$ is the blackbody spectral radiance, $R_P/R_\star$ is the planet-to-star radius ratio and T_{eq} the equilibrium temperature:

$$\frac{F_P}{F_\star} \approx \frac{B_\lambda(T_{eff})}{B_\lambda(T_\star)} \left(\frac{R_P}{R_\star}\right)^2 \tag{1.5}$$

The flux ratio increases with the wavelength because the planet has a temperature lower than the star. As for transmission spectroscopy, we can construct the emission spectrum of an exoplanet atmosphere and study the opacity of the planet with the wavelength. The emitted flux comes from the photosphere of the planet; the more opaque the atmosphere is, the higher in altitude the photosphere will be located. However, the wavelength is not always equivalent to the pressure. A thermal emission spectrum is an excellent tool for establishing the thermal structure of the atmosphere. The size and shape of spectral features depend on the atmosphere's temperature. If there is a thermal inversion, i.e. a temperature increase with altitude, the features will be seen in emission rather than absorption.

The reflected light can be measured at short wavelengths and is usually approximated using the perfect Lambertian surface: a flat, perfectly diffusing disk with the same cross-sectional area as the planet. The total reflected light is defined as in Kreidberg (2018) where A_g is the geometric albedo, a is the orbital separation and $\Phi(\alpha)$ is the phase function:

$$F_{\text{reflected}} = A_g(R_P/a)^2\Phi(\alpha)F_\star \tag{1.6}$$

Finally, we can also observe a continuous time series of photometry or spectroscopy of a planet over its entire orbital period. A full-orbit phase curve uses the secondary eclipse and the stellar baseline flux to measure the emission and reflection at each phase. Phase curves are mainly observed for short-period tidally locked planets whose orbital period is equal to the rotation one. In one orbit, we can probe all longitudes. Phase curves have a clear advantage compared to a single transit or eclipse as it probes a broader space and time parameter space.

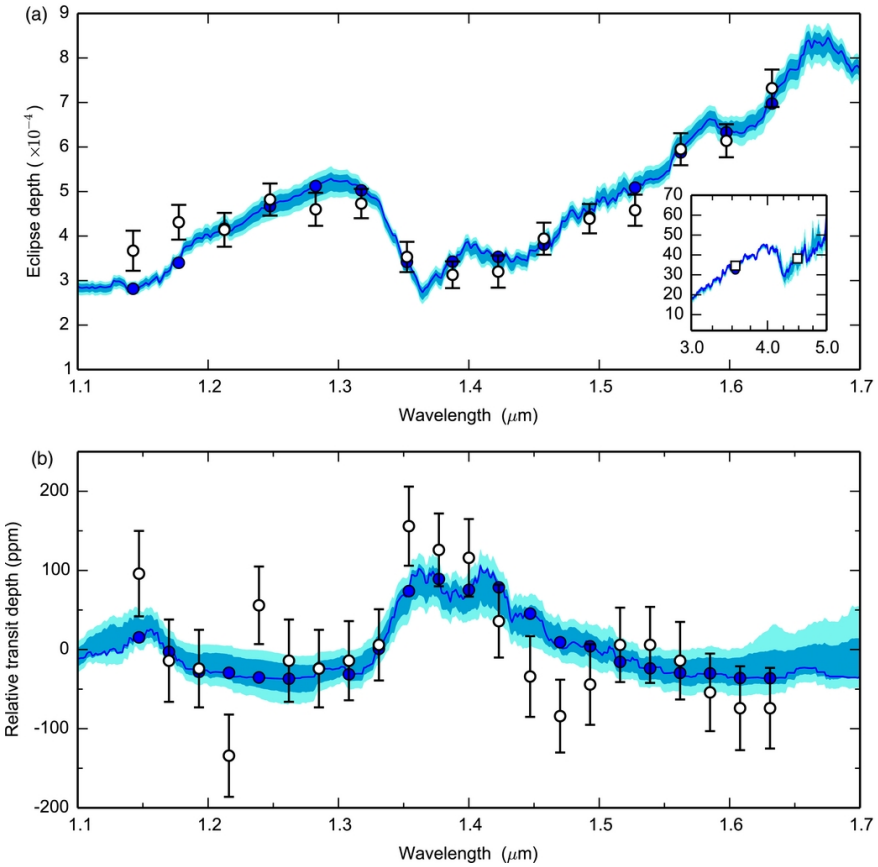

Figure 1.2: Thermal emission spectrum (top) and transmission spectrum (bottom) for the hot-Jupiter WASP-43 b from Kreidberg et al. (2014b). The data points, in white, are from the Hubble Space Telescope Wide Field Camera 3 (1.1 to 1.7 µm) and Spitzer IRAC (3.6 and 4.5 µm). The best fit model from an atmospheric retrieval analysis with 1- and 2-σ uncertainty ranges are in blue.

Transmission and occultation observations can be made at different resolutions. Low spectral resolution observations can reveal broad molecular absorption bands while observing at very high-resolution (R ∼100,000) can better resolve individual absorption lines (Snellen et al., 2010). However, high-resolution spectra are most impacted by the stellar light and techniques of stellar-light suppression must be employed (Lovis et al., 2017; Wordsworth & Kreidberg, 2021). Figure 1.2 presents the thermal emission spectrum and the transmission spectrum of the hot-Jupiter WASP-43 b. This figure is taken from Kreidberg et al. (2014b) to illustrate the contributions of the two techniques, occultation and transmission, as proposed in Kreidberg (2018). The data points in white are from the Hubble Space Telescope (HST) Wide Field Camera 3 (WFC3) instrument IR channel (1.1 to 1.7 µm) and Spitzer IRAC (3.6 and 4.5 µm). Water is detected in the atmosphere of this planet with high confidence (5-σ). The broadband water absorption feature is seen in both spectra at low resolution. It is an average of numerous rotational and vibrational line transitions (Kreidberg, 2018). The planet's flux decreases in the water band centred at 1.4 µm for the thermal emission spectrum while it increases in the transmission spectrum.

1.2 Observing facilities and strategies

Detecting an atmosphere around an exoplanet is challenging because the signal is small (one part per thousand of the total stellar flux), and the observation is mostly indirect. Even for favourable systems, these observations require many photons, thus a large telescope and a very stable environment (Kreidberg, 2018). Consequently, the observation must be carefully prepared. This section is based on the review of Kreidberg (2018).

1.2.1 Which processes observed in which wavelength range?

In transmission spectroscopy, the absorption is higher as the wavelength decreases, except when a high-altitude cloud deck is blocking the signal. Therefore, the spectral range allows probing different atmospheric regions, hence different processes (Madhusudhan, 2019). First, we will present the main atmospheric processes for gaseous planets and how the electromagnetic spectrum can probe them. The study of atmospheric processes is usually explained as a function of pressure. The atmosphere is considered at equilibrium for gaseous planets deep in the atmosphere (P> 1 to 10 bar). We assume that chemical reactions happen faster than disequilibrium processes (such as atmospheric mixing and UV photolysis) so that thermo-chemical and radiative-convective equilibrium are reached. The region higher up, between 10^{-3} and 1 bar, can be probed using the near-infrared (NIR) and infrared (IR) wavelength range. This part of the atmosphere is sensitive to stellar radiation but is also the location of various processes such as thermal inversions, clouds and hazes sedimentation, and atmospheric dynamics. These processes depend on the temperature profile and the atmospheric chemical composition. As a result, the atmosphere can be out-of-equilibrium. IR and NIR observations give access to the molecular composition of the atmosphere because of rovibrational transitions; molecules like H_2O, CO, CO_2, NH_3, CH_4 absorb in this part of the electromagnetic spectrum. IR observations give access to a higher part of the atmosphere than the optical and are less sensitive to the presence of clouds. Above this layer, the atmospheric composition is dominated by photo-dissociation processes between 10^{-6} and 10^{-3} bar. This upper part of the atmosphere can be reached using optical to near ultra-violet (NUV) observations. Heavy metal species like TiO and VO, but also atomic metals like Fe, Mg, and Si have strong absorption in the optical or in the NUV depending on their excitation and ionisation states. The upper part of the atmosphere is accessible using mid-to-far Ultra-Violet (UV) observations and is where atmospheric escape by atomic species occurs. Photochemistry reactions can also change the composition at deeper layers given enough mixing or UV mean free path. The spectral range is

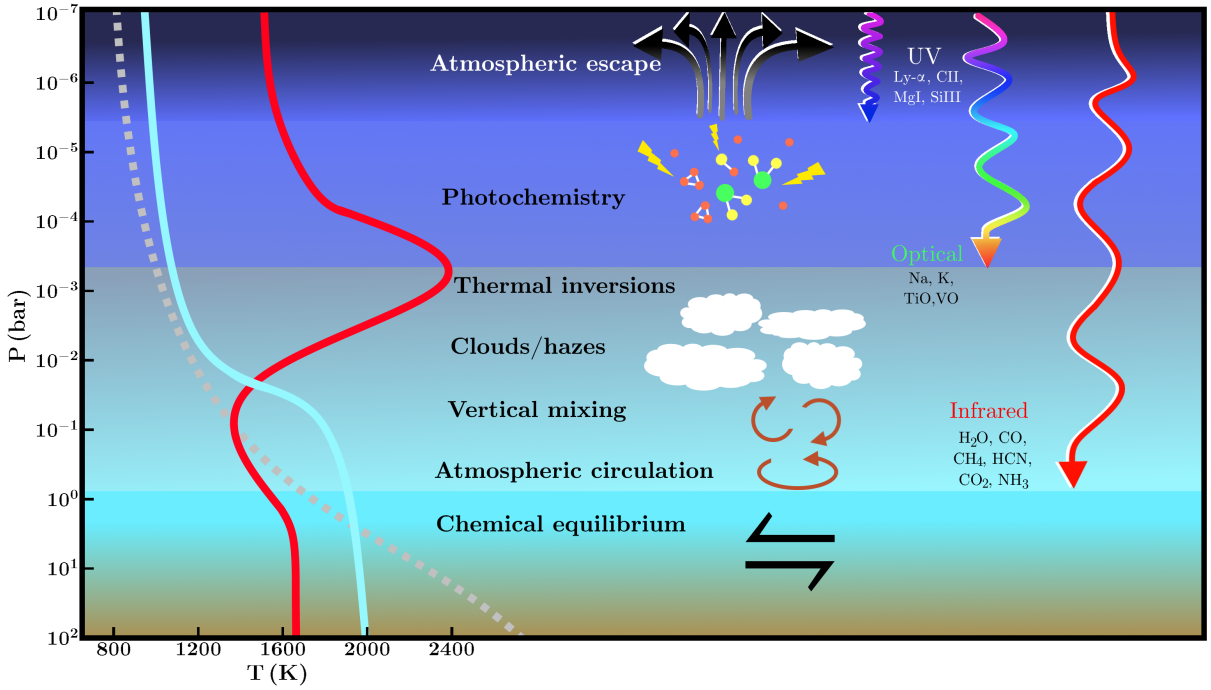

Figure 1.3: Summary of the atmospheric processes in a gaseous exoplanet atmosphere and how the electromagnetic spectrum probes them. This figure is taken from the review of (Madhusudhan, 2019).

a crucial parameter in observing exoplanets as it gives access to a different part of the atmosphere and, thus, to various physical and chemical processes. This is illustrated and summarised in Figure 1.3 taken from the review of Madhusudhan (2019).

While most of the general principles above hold for rocky planets, the presence of a surface modifies the observational strategies as the surface, and the atmosphere interact. Taking the example of Solar-system rocky planets, we can draw a basic thermal structure for rocky exoplanet atmospheres. At high pressure (> 1 bar), there is a turbulent region called the planetary boundary layer, which connects the low troposphere to the surface. The troposphere is located up to 0.1 bar, where convection processes dominate. The temperature decreases with altitude following a near adiabatic law. Above the troposphere, the temperature decreases more slowly or even increases due to UV absorption. This region is called the mesosphere or the stratosphere when thermal inversion occurs, and the radiative balance is reached. The upper part of the atmosphere is the thermosphere, which is sensitive to atmospheric escape. The temperature can increase rapidly due to heating by absorption of extreme ultraviolet or X-ray (XUV) stellar photons (Wordsworth & Kreidberg, 2021).

1.2.2 Facilities for exoplanets atmospheric observations

Exoplanet atmospheric exploration is carried out from space but also from the ground. The Hubble and the Spitzer Space Telescopes have been the most employed facilities from space until now. Contrary to the ground facilities, they offer the advantage of being free of the Earth's atmosphere, which is time-varying and adds noise to the observations. Earth's atmosphere allows observations in specific windows where it is transparent, but turbulence, variable water vapour content, clouds, and hazes complicate the observations of tiny signals from other planets. An additional benefit of space-based observations is that we can observe in a wavelength range where the Earth's atmosphere absorbs, particularly the water absorption band in the near-infrared and ultra-violet ranges. They can also perform infrared observations with low background noise (Deming & Seager, 2017). The Space Telescope Imag-

ing Spectrograph (STIS) and the Wide Field Camera 3 (WFC3) are the main Hubble instruments used to perform exoplanet atmospheric spectroscopy from the ultra-violet (UV) to the near-infrared (NIR) ($\sim$ 0.1 µm to 1.1 µm). The Spitzer IRAC instrument allows broadband photometric measurements at 3.6 and 4.5 µm. The James Webb Space Telescope, launched in December 2021, has four instruments and, by combining them, provides a wavelength coverage of 0.6 µm to 12 µm (up to 28 µm in specific configurations). The Atmospheric Remote-sensing Infrared Exoplanet Large-survey (ARIEL) will provide a continuous wavelength coverage of 0.5 to 7.8 µm with the same instrument. We summarise in Figure 1.4 the current and planned space facilities for exoplanets' atmospheric characterisation. We also indicate the Characterising Exoplanets Satellite (CHEOPS) photometric channel in dotted lines, as it will be later on used in this thesis.

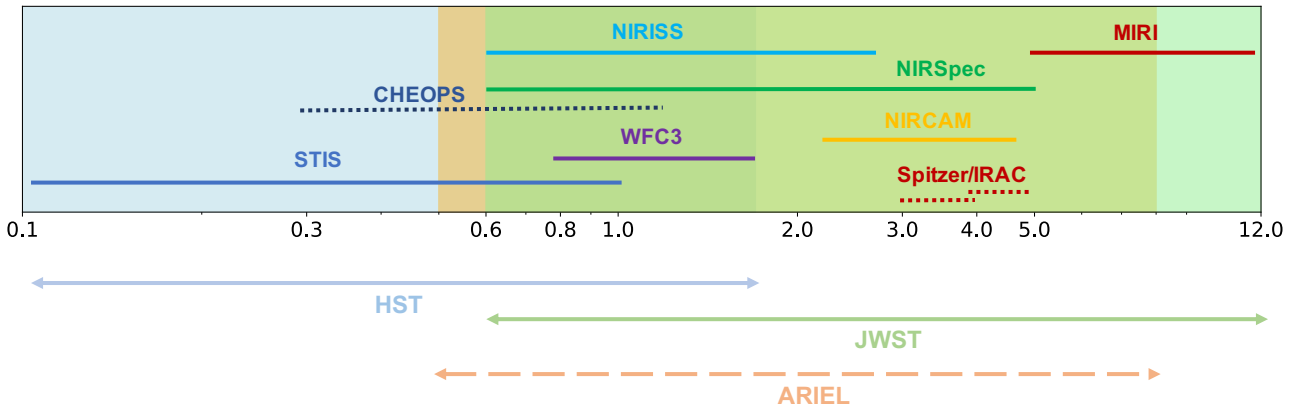

Figure 1.4: Summary of the current and planned space abilities for atmospheric characterisation. We indicate the HST/STIS and WFC3 instruments coverages (0.1 to 1.7 µm). The four instruments of the JWST, NIRISS, NIRCAM, NIRSpec and MIRI cover the 0.6 to more than 12 µm. ARIEL will provide spectroscopy from 0.5 to 8 µm. The resolution of these instruments is between 20 to 1000. We also indicate the photometric channels of Spitzer/IRAC and CHEOPS in dotted lines.

Ground-based observations are difficult because of the variation of the Earth's atmosphere properties. The cloud coverage, the mean molecular weight, and the amount of water vapour vary, which creates additional noise in the measured light curve. One way of correcting the signal from the systematic trends is to monitor these variations by pointing at nearby stars. On the other hand, observing from the ground allows for high-resolution spectroscopy based on the Doppler effect. The planetary spectrum is shifted due to the orbital motion, which can be distinguished from the stellar lines and the Earth's atmosphere. This technique uses the cross-correlation method to identify the atmospheric components (Snellen et al., 2010; Kreidberg, 2018).

1.2.3 Source of uncertainties in time series observations

As previously stated, observing an exoplanet's atmosphere is challenging, and we aim to detect a signal in the order of 0.1% in the best-case scenarios. It is thus essential to monitor and study the source of errors and learn how to deal with them to disentangle the signal from the noise. Getting a precise atmospheric signal also requires a good knowledge of the host star, especially when it is active. Several sources of noise have been noted and can be classified as follows (Kreidberg, 2018):

1. Photon noise
2. Instrument systematics
3. Astrophysical systematics

Photon noise

The photon noise is equal to $\sqrt{(N)}$, where N is the number of photons emitted by the star per unit of time if the star emits N$\pm$ $\sqrt{(N)}$ photons. Each atom in the star emits a photon with a probability per unit of time, and the count rate follows a Poisson distribution. This noise limits the precision of the light curve measurement. Thus, to improve the precision, we have to stack together as many observations as possible. The brighter the star is, the larger the photon noise is; the SNR however, is higher for the brighter stars. For atmospheric characterisation, the best targets have a magnitude in H-band below 10. This limit changes with facility and mode.

Instrument systematics

The noise introduced by the instruments can impact the light curves and mask the planet's signal by several orders of magnitude. It is a significant noise source in time series observations (TSO) for exoplanet characterisation. The first common instrument-based noise source is the *charge trapping effect* (Smith et al., 2008). This effect is mainly seen in infrared detectors, such as the WFC3, where impurities trap photo-electrons. The trap is filled up exponentially with a time constant dependent on the detector properties and illumination (Zhou et al., 2017). When the traps are released, an afterglow effect appears. It can be corrected analytically by modelling (Deming et al., 2013; Line et al., 2016).

Secondly, there is an *intra-pixel effect* because the detector does not have a uniform spatial sensitivity. The flux is then correlated to the position of the centroid in the image. This effect also arises for infrared detectors, particularly Spitzer/IRAC, and it can be corrected by modelling the intra-pixel variations (Stevenson et al., 2012; Deming et al., 2015; Morello et al., 2015).

The position of the spectrum on the detector can shift during the observation, causing a *variable illumination effect*. This effect can be due to a defocus of the telescope or a change in telescope pointing. The light falls on a pixel with different sensitivity and thus creates a considerable flux variation (Kreidberg, 2018). Sing et al. (2011) proposes to correct this effect with a polynomial model for HST STIS observations. Last, *the thermal breathing* of the telescope, observed in particular for HST, periodically modifies the point-spread function (PSF). This variation in the detector's temperature at the start of the observation creates large ramps in the observations of the light curve that can be corrected using a polynomial model (see Chapter 3).

Astrophysical systematics

The astrophysical noise sources are mainly due to a lack of information or incomplete modelling of the host-star. This is the case for the *background stars* noise, or dillution. If the host-star has a companion, the flux from the planet can be mixed with the companion. This is common as more than one star over two has a companion (Raghavan et al., 2010). To correct this effect, the transit or eclipse depth is multiplied by a correction factor $1 + \beta(\lambda)$ where β is the background to host star flux ratio.

The *stellar activity* is also an important source of uncertainty in atmospheric characterisation. In transmission spectroscopy, it can mimic atmospheric features and mislead atomic and molecular detection. The stellar activity corresponds to the variation of star spot coverage that impacts the transit depth. The temperature difference between the stellar photosphere and the spot (cooler regions) creates a slope in the transmission spectrum. For example, water can form in this cold region, which will be wrongly associated with the planet's atmosphere because we can not differentiate the spot absorption from the planet's. Correctly accounting for the stellar activity would require precise long-term, photometric monitoring of the host-star to estimate the changes in the spot covering fraction.

The astrophysical noise can also find its origin in the planet itself. During the transit, the thermal emission from the planet's night side can have a non-negligible contribution to the observed flux. This effect is predicted for the hottest planets and depends on the temperature, the cloud coverage and the

heat redistribution, which is only accessible with phase curve observations. This effect can be corrected by multiplying the transit depth with a factor $1/(1+F_P/F_s)$ where F_P is the planet's night side flux and F_s is the stellar flux (Kipping & Tinetti, 2010).

1.3 Major results from 20 years of atmospheric observations

Combining precise spectroscopic observations with in-depth theoretical modelling led to the characterisation of more than a hundred exoplanets' atmospheres and major discoveries. In this section, we highlight some of the main results from the past twenty years with a focus on space-based observations.

1.3.1 Diversity of the chemical composition

The atmospheric composition can be predicted by studying the composition of the proto-planetary disk during the planet's formation. The gas and the dust surrounding the star are the first building blocks that form planets, and their composition is similar to that of the host star. The proto-planetary disk is thus made of a majority of hydrogen (H) and helium (He). It contains metals in smaller amounts, and the most abundant are oxygen (O), carbon (C) and nitrogen (N). However, by studying the solar system giant and telluric planets, we know that the atmospheric composition can be more complex and depends on the planet's evolution and history. The main constituents recombine in planetary atmospheres to form molecules like dihydrogen (H_2), water (H_2O), carbon monoxide (CO) and dioxide (CO_2), ammonia (NH_3), methane (CH_4), dioxygen (O_2) and nitrogen (N_2). This recombination depends on the temperature pressure profile and the atmosphere's composition. The atmospheric dynamics and the elemental atmospheric composition can be altered by photochemical reactions induced by the stellar X-UV flux.

Atomic and ionic detections

Observations of exoplanet atmospheres have enabled the detection of molecular and atomic species. Many species mentioned above have been detected in the infrared because they have strong absorption features due to the rovibrational transitions. Heavier molecules like titanium oxide (TiO) and vanadium oxide (VO) absorb in the optical. Atomic and ionic species have electronic transitions and are detected in UV and optical. We represent in Figure 1.5 the opacity contributions to the transmission spectrum for a hot-Jupiter around a sun-like star, with an equilibrium temperature of 1500 K, a solar composition at equilibrium chemistry for a cloud-free atmosphere. We performed this simulation using the radiative-convective modelling code `Exo-REM` (Exoplanet Radiative-convective Equilibrium Model) (Baudino et al., 2015; Charnay et al., 2018; Blain et al., 2021). We note the absorption features of H_2O and CO in the infrared and the strong lines of the alkali metals, potassium (K) and sodium (Na), in the optical. The first detection of an absorbing species and, thus, the first proof of an atmosphere around an extra-solar planet, was the sodium doublet at 0.589 µm in the hot-Jupiter HD 209458 b by Charbonneau et al. (2002). Since then, Na and K have been discovered in other hot-Jupiters using HST STIS observations in the optical (Nikolov et al., 2013, 2014; Sing et al., 2014, 2016; Nikolov et al., 2018; Carter et al., 2020). Additionally, atomic and ionic species have been discovered using UV transit observations. In particular, hydrogen was detected with Lyman-α measurements obtained with HST STIS (Vidal-Madjar et al., 2003; Bourrier & Lecavelier des Etangs, 2013; Ehrenreich et al., 2015), but also heavy metals in the upper atmosphere with NUV observations (Vidal-Madjar et al., 2004; Fossati et al., 2010; Vidal-Madjar et al., 2013; Sing et al., 2019). These measurements revealed large exosphere and escaping atmospheres for hot-Jupiter and Neptune-like planets (Ehrenreich et al., 2015). Dihydrogen was interpreted as a possible source of the Rayleigh scattering identified in the transmission spectrum of HD 209458 b by Lecavelier des Etangs et al. (2008b). Besides, the slope of

the optical HD 189733 b transmission spectrum suggested the presence of a haze of submicrometre particles in the upper atmosphere (Pont et al., 2008).

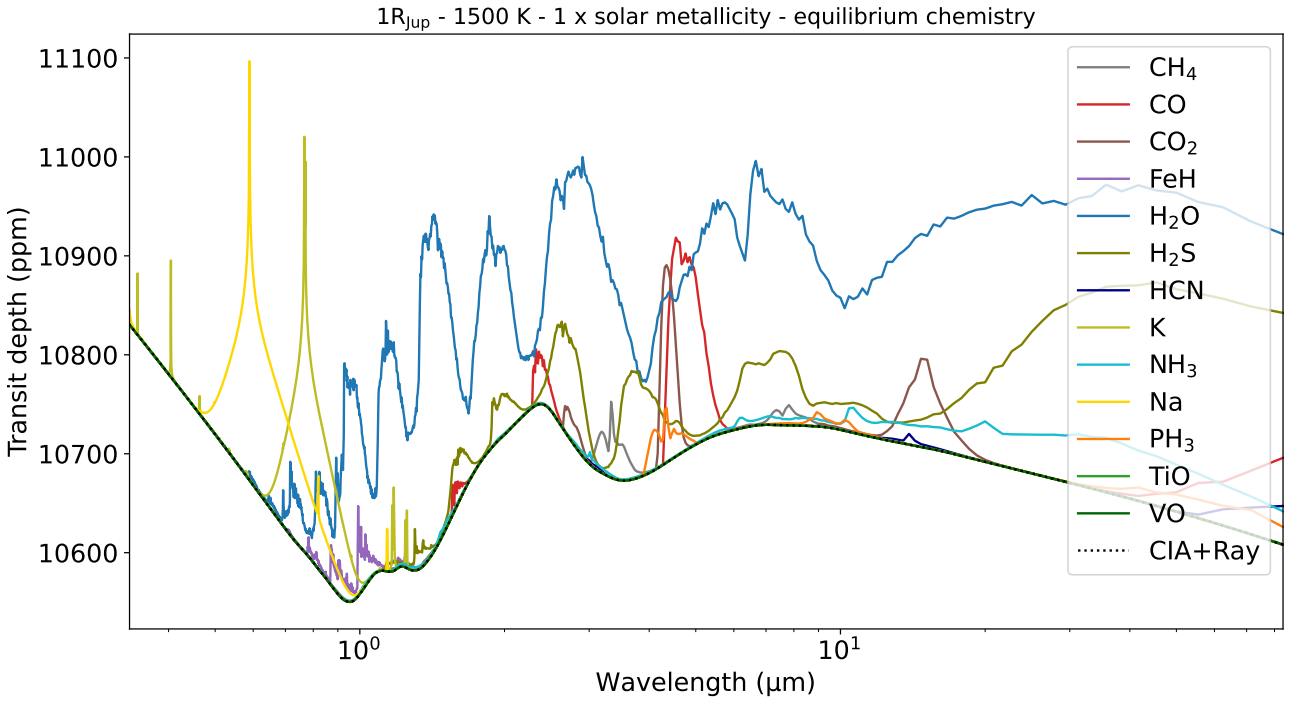

Figure 1.5: Opacity contributions to the transmission spectrum for a hot-Jupiter around a sun-like star, with an equilibrium temperature of 1500 K, a solar-composition at equilibrium chemistry for a cloud-free atmosphere. Sodium and potassium are the dominant absorbing species in the optical, while water and carbon dioxide dominates in the near-infrared. At lower temperatures, CH_4 and NH_3 become more abundant and contribute to the transmission spectrum in the infrared. This figure is made using a radiative-convective model `Exo-REM`(Baudino et al., 2015; Charnay et al., 2018; Blain et al., 2021).

Molecular detections

Volatile molecules have also been looked for and found in exoplanets' atmospheres. Most of the molecular detection has been made using the HST WFC3 instrument IR mode using the G141 grism (1.1 to 1.7 μm) in transmission, but also emission has shown in Figure 1.2. This instrument is excellent for detecting water which presents a strong and large absorbing feature around 1.4 μm and is expected to be one of the main oxygen-bearing species. Thus it makes it the most observed and detected molecule in hot-Jupiters (Tinetti et al., 2007; Deming et al., 2013; Huitson et al., 2013; Mandell et al., 2013; Wakeford et al., 2013; McCullough et al., 2014; Kreidberg et al., 2014b, 2015; Line et al., 2016; Evans et al., 2016; Damiano et al., 2017; Wakeford et al., 2017; Tsiaras et al., 2018) but also Sub-Neptune and Super-Earth (Fraine et al., 2014; Wakeford et al., 2017; Tsiaras et al., 2019; Benneke et al., 2019; Benneke et al., 2019; Guilluy et al., 2020; Edwards et al., 2021). Water was also detected using Spitzer IRAC measurements and Ground-based observations (Beaulieu et al., 2008, 2010; Swain et al., 2010). These detections are made in transmission spectroscopy but also using thermal emission, and then water is detected on the day-side of the planet. They are more or less robust, but we can say that H_2O has been strongly confirmed in more than ten exoplanets. Besides H_2O, other molecules have been suggested in exoplanets' atmospheres but have proven to be more challenging to detect. In particular, carbon-bearing species absorb strongly in the infrared, but until now, this wavelength range was not accessible with HST, and only hints of detection are available (Guilluy et al., 2020). Last August, the JWST Transiting Exoplanet Community Early Release Science Team revealed the carbon dioxide

detection in the atmosphere of the gas giant WASP-39 b using NIRSpec time series observations from 3.0 to 5.5 µm. They reported an absorption feature at 4.3 µm corresponding to a 26-σ significance (The JWST Transiting Exoplanet Community Early Release Science Team et al., 2022). Spitzer observations previously suggested the absorption of carbon-bearing species, but it remained difficult to identify precisely due to the lack of unambiguous spectroscopic identification (Désert et al., 2009; Stevenson et al., 2010; Madhusudhan et al., 2010; Morley et al., 2017; Beaulieu et al., 2011; Knutson et al., 2011). HCN, NH_3 and TiO and VO have been suggested, but there is no definitive proof of their detection (Haynes et al., 2015; Tsiaras et al., 2016a; Evans et al., 2017; Kilpatrick et al., 2018; Guilluy et al., 2020). The first JWST result shows that we have entered a new era of unambiguous detections, and we will be able to have a final word on these previously tentative detections.

We note that CH_4 and NH_3 are not commonly and easily detected. Swain et al. (2008) detected methane in HD 1897333 b, but it was then contested in (Gibson et al., 2012). These species are sensitive to photo-dissociation and are expected to dominate at lower temperatures than what is usually probed in hot-Jupiters. Besides, CH_4 has similar absorbing features to H_2O around 1.4 µm, which makes it ambiguous to detect with WFC3. Methane depletion has been noticed and discussed for close-in Sub-Neptunes (Benneke et al., 2019; Bézard et al., 2022) and we will go into more detail and compare HST and JWST abilities in detecting methane in Chapter 9.

Constraining the abundances, the metallicity and the C/O ratio

Once the molecule is detected, its *abundance* is estimated as the molecule's volume mixing ratio (VMR) or the enrichment over the solar value. The abundance of one molecule is a crucial parameter to understanding, as a first step, the planet's formation and evolution through the estimation of accretion rates (Fortney et al., 2013). However, constraining the abundance of one molecule is highly challenging and requires transmission and/or emission spectra with broad spectral coverage and precise observations. Using only one technique generally leads to highly degenerated solutions. In transmission spectroscopy, the degeneracies are between the abundances and the atmospheric pressure but also with clouds or hazes. In emission, degeneracies are between the chemical ratios and the temperature profile. Probing multiple absorbing features in a transmission spectrum can help better constrain the molecular abundance (Benneke & Seager, 2012). In transmission spectroscopy, the temperature also influences the spectrum's shape, but there is a degeneracy between the abundance and the temperature. In emission, this degeneracy is reduced because the temperature is better constrained and thus the abundance.

However, most of the best molecular abundance constraints come from HST observations in transmission spectroscopy for H_2O. Combining HST STIS observations in the optical, sensitive to clouds and hazes, with HST WFC3 measurements where H_2O absorbs resolves some degeneracies. Wakeford et al. (2017) used this method to constrain H_2O's abundance in the atmosphere of HAT-P-26 b to 0.8-26 x solar. Thermal emission observations with the WFC3 constrained H_2O's abundance on the day-side of the planet (Kreidberg et al., 2014b; Line et al., 2016). Most hot-Jupiter population studies using transmission spectroscopy reported sub-solar H_2O abundances (Barstow et al., 2016; Pinhas et al., 2018; Tsiaras et al., 2018). Using phase curve observations of WASP-43 b with Spitzer, Stevenson et al. (2017) reported a 0.3-1.7 x solar metallicity for the global abundance of CO and CO_2.

The metallicity of Solar-System giant planets follows a power law with the planet's mass. The metallicity increases with decreasing mass. Jupiter has a 3 × solar metallicity atmosphere, while Uranus and Neptune have a strongly enriched atmosphere by 80 × solar. Some efforts have been carried out to look for a similar pattern in exoplanet metallicity using H_2O abundance. This pattern is a natural outcome of planet formation because the massive planets are less impacted by planetesimal infalls (Mordasini et al., 2012; Fortney et al., 2013). However, recent works suggest a more complex process given the observed bulk planet metallicity relationship with the mass (Thorngren et al., 2016;

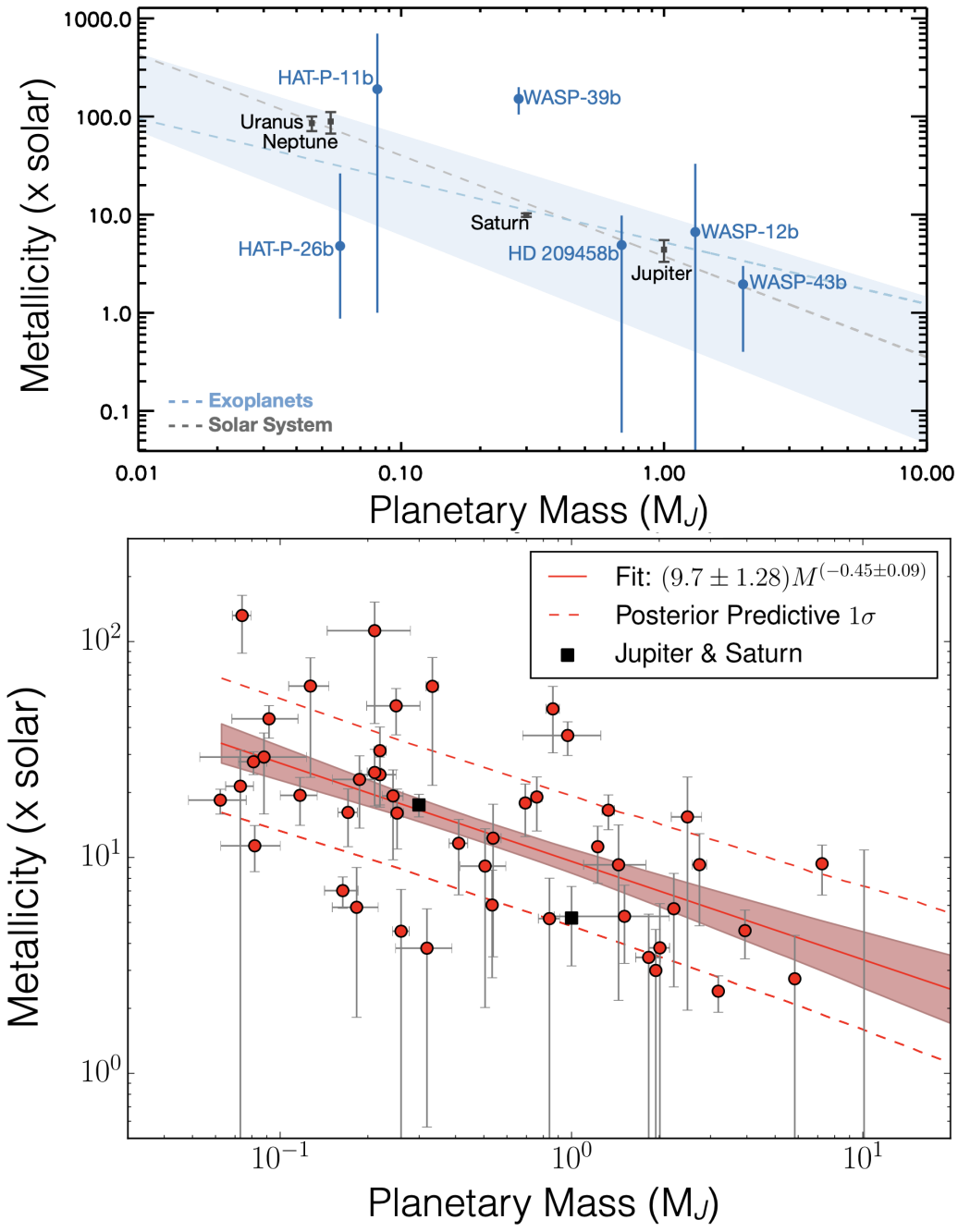

Figure 1.6: Mass-metallicity relations for Solar System giant planets and exoplanets from Sing (2018) (top) using transmission spectroscopy observations and from Thorngren et al. (2016) (bottom) using interior modelling. The Solar System planets show a trend of decreasing metallicity with increasing mass. Exoplanets seem to follow a similar pattern, but the distribution is scattered, and the uncertainties are large.

Mordasini et al., 2016). Giant planets are expected to retain their primordial atmosphere of hydrogen and helium. Kreidberg et al. (2014b) first showed that the observed metallicity of WASP-43 b agrees with the Solar-System trend. On the contrary, the Sub-Neptune HAT-P-26 b displays a lower metallicity than expected, showing the diversity of atmospheric compositions in exoplanets (Wakeford et al., 2017). This result suggests that Neptunes and Sub-Neptunes might have a different formation and evolution process than gas giants. We illustrate the mass-metallicity power law using Figure 1.6 from adapted from Thorngren et al. (2016) and Sing (2018) and taken from the ARIEL red book. Sing (2018) estimated the metallicity using individual transit spectroscopy measurements while Thorngren et al. (2016) used interior modelling. Bulk metallicity estimates can not be directly compared with atmospheric metallicity estimates. The former puts limits on the latter (Thorngren & Fortney, 2019; Thorngren et al., 2021). Welbanks et al. (2019) studied 19 exoplanets transmission spectra from warm Sub-Neptune to hot-Jupiters and, using a Bayesian retrieval code, retrieved the abundance of H_2O, Na and K. They found a mass-metallicity trend of increasing H_2O abundances with decreasing mass, with substellar values for gas giants and superstellar for Neptunes like planets. This trend is lower than the pattern found for Solar-System planets using the abundance of CH_4. In the Solar System giant planet atmospheres, CH_4 is more easily constrained because it is well mixed in the atmosphere at these temperatures. In contrast, the amount of H_2O is not well constrained because it condenses in the deep layers of the atmosphere (Showman & Ingersoll, 1998; Mousis et al., 2014). However, in hot exoplanets, H_2O is well mixed in the gas phase, and it seems the natural choice to constrain the metallicity. Yet it must be noted that in most cases, the metallicity is constrained using one H_2O feature at 1.4 µm and remains degenerate. The JWST and the ARIEL mission will provide precise measurements of the atmospheric metallicity for hundreds to thousands of exoplanets, enabling an actual statistical constraint on the metal enrichment and going beyond the four giant Solar system planets.

The abundance ratio between carbon-bearing molecules and oxygen-bearing molecules (C/O) is also an essential quantity in constraining planets formation and evolution (Madhusudhan et al., 2014). The C/O ratio holds the physical properties of the proto-planetary disk and the planet's position within the disk (Sing, 2018). The temperature decreases with the radial distance to the centre of the disk, allowing the identification of the frozen lines of molecules like H_2O, CO and CO_2. The evolution of the amount of gas versus dust and solid can be traced in a planetary atmosphere. In the case of migrating hot-Jupiter, a high C/O ratio (> 1) could indicate that the planet was formed beyond the snow line and accreted carbon-rich gas. In contrast, a low C/O ratio (< 1) could indicate the accretion of oxygen-rich solid materials (Öberg et al., 2011; Espinoza et al., 2017). Once again, constraining the C/O ratio is difficult, but it is an important tracer of disequilibrium chemistry as the equilibrium abundances change when the carbon is more abundant than the oxygen. First attempts to evaluate the C/O ratio in hot-Jupiters revealed an oxygen-rich atmosphere (Line et al., 2014; Kreidberg et al., 2015; Barstow et al., 2016).

1.3.2 Clouds and photochemical hazes

Condensates are ubiquitous in the atmosphere of Solar System gas giants and telluric planets, and we expect them to form in exoplanet atmospheres. Cloud formation depends on complex couplings between atmospheric dynamics, chemistry, and microphysics (Marley et al., 2013). Taking the example of the hot-Jupiter around a sun-like star described above, we show in Figure 1.7 that the typical temperature pressure profile is close to the condensation curves of several components. Like H, C, O, and N recombine to form molecules, they can combine to form condensates via chemistry (driven by the temperature) or photochemistry. Photochemical hazes are present in reducing atmospheres, carbon-rich atmospheres. The photolysis of CH_4 produces radicals such as CH_3, which can combine to

form a longer chain and hydrocarbon soots and finally, haze particles (Kempton et al., 2011; Morley et al., 2013).

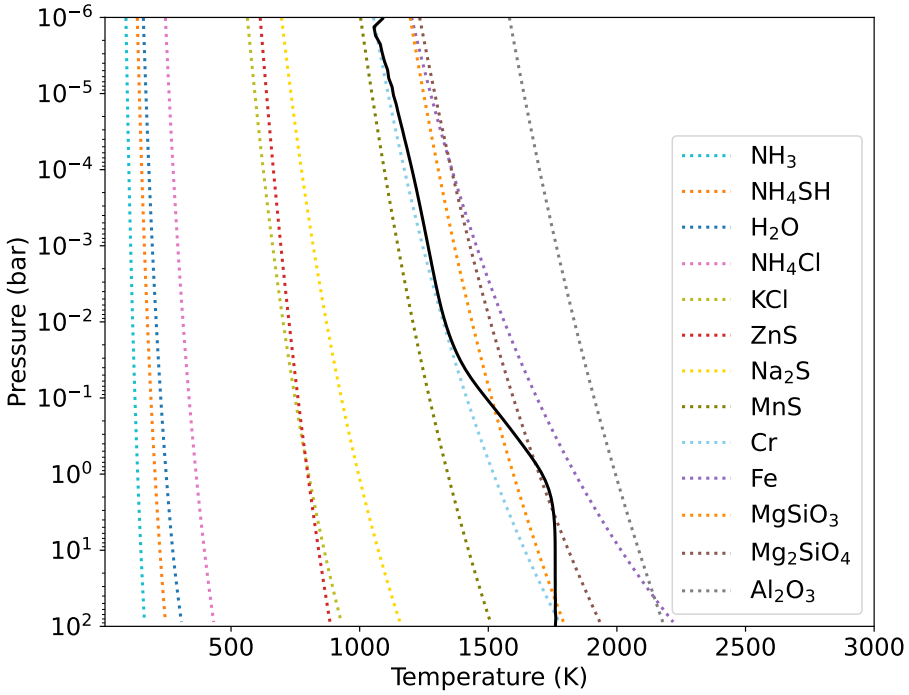

Figure 1.7: Temperature pressure profile of a hot-Jupiter around a sun-like star, with an equilibrium temperature of 1500 K, a solar-composition at equilibrium chemistry. This figure is made using a radiative-convective model `Exo-REM` (Baudino et al., 2015; Charnay et al., 2018; Blain et al., 2021).

Clouds and haze formation have a strong impact on the transmission spectrum. First, they can block the transmission of the stellar flux and mask atmospheric spectral features below the opaque cloud layer. The first detection of Na in the atmosphere of HD 209458 b is also the first indication of clouds as the spectral feature does not reach the expected one in a clear atmosphere (Charbonneau et al., 2002). Truncated spectral features to completely flat spectra have been observed for hot-Jupiters and Neptune-like planets for which we expect an extended atmosphere (Deming et al., 2013; Crossfield et al., 2013; Kreidberg et al., 2014a; Knutson et al., 2014a). Depending on the height of the cloud deck, spectral features can be masked partially to entirely. The water features are partially blocked in the atmosphere of HD 209458 b (Deming et al., 2013) while it is completely masked for the Sub-Neptune GJ 1214 b (Kreidberg et al., 2014a). The transmission spectrum is featureless and has a precision of around 30 ppm, corresponding to an optically thick absorber at a pressure level of 0.1 millibars. This result is explained by a very high cloud layer or efficient haze formation (Morley et al., 2015).

Condensates can also create a slope at short wavelengths, and the scattering of particles introduces a steep increase in transit depth in the optical part of the spectrum. A large slope in the optical has been observed in several transmission spectra and interpreted as particle scattering (Pont et al., 2008; Lecavelier des Etangs et al., 2008a; Sing et al., 2011, 2013; Dragomir et al., 2015; Sing et al., 2016). The large slope observed in NUV HST observations of WASP-78 b's was interpreted by SiO absorption (Lothringer et al., 2022). Condensates are more likely to be formed in temperate to warm atmospheres (Stevenson, 2016; Charnay et al., 2018); however, the microphysics of clouds is complex and depends on the temperature pressure profile and the atmospheric circulation. That is why phase curve observations are best suited to study the impact of clouds in tidally-locked planets and infer condensate properties (Demory et al., 2013; Parmentier et al., 2016).

1.3.3 Exoplanets climate: atmospheric dynamics

Transiting planets orbit in synchronous rotation around their host star, making them tidally locked and highly irradiated. This geometry affects the dynamics of the atmosphere, particularly the day-night temperature structure and the chemistry through photochemical processes.

Thermal emission measurements give access to the planet's climate, and until now, observations have been mainly carried out for hot-Jupiters. Secondary eclipse observations have been used to constrain the day-side temperature and the temperature-pressure profile. One of the most important results is the thermal inversion in hot-Jupiter atmospheres. Thermal inversion occurs when strong optical absorbers, like TiO and VO, absorb the stellar radiation at a higher altitude than they thermally radiate, which heats the atmosphere's upper layers and increases the temperature with altitude (Fortney et al., 2008). TiO and VO are expected in the hottest atmosphere, where we can observe a stratosphere. Hot-Jupiter and, most notably, ultra-hot-Jupiters (UHJ) are new objects with unique physical processes. The presence of a stratosphere transforms the atmospheric circulation and dynamics of the planet. For a hot-Jupiter without strong absorbers, the stellar radiation is absorbed deep in the atmosphere at a pressure of around 1 bar. This results in a temperature-pressure profile decreasing with the altitude while it increases with altitude when the stellar radiation heats optical absorbers. Additionally, winds high in the atmosphere are not efficient enough to redistribute the energy, creating a strong day-night temperature gradient. With a thermal inversion, the hottest part of the atmosphere is located at the sub-stellar point, and the temperature decreases towards the limb (Sing, 2018).

First Spitzer observations of HD 209458 b by Knutson et al. (2008) proposed a thermal inversion but it was later disputed (Diamond-Lowe et al., 2014; Schwarz et al., 2015; Line et al., 2016). A search for thermal inversions with Spitzer was conducted but did not provide definitive detections. A strong thermal inversion was more recently discovered by Evans et al. (2017) in the atmosphere of WASP-121 b. The H_2O feature is thermally inverted and is seen in emission using HST secondary eclipses observations. A stratospheric thermal inversion and evidence of TiO were observed in the atmosphere of WASP-33 b (Haynes et al., 2015; Nugroho et al., 2017). TiO was not detected in WASP-18 b's atmosphere, but H^- opacity could be the cause of the observed inversion (Sheppard et al., 2017; Arcangeli et al., 2018). These planets have a day side temperature above 2500 K, which could be the limit for thermal inversion; however, this is not a sufficient condition as it is not systematically observed for ultra-hot-Jupiters (Beatty et al., 2017b). Most of the planets observed to date do not show thermal inversion, implying a lack of UV and optical absorbers for irradiated atmospheres.

Thermal phase curves give access to detailed constraints on atmospheric circulation. Phase curve observations can be carried out in individual photometric channels or full-phase spectroscopy. Phase curves are precious for atmospheric characterisation. They give information on the temperature profile as a function of the orbital phase and the brightness temperature as a function of the atmospheric pressure, but also provide the location of the day-side hot spot (Madhusudhan, 2019). Exoplanet phase curves are observed with current facilities such as HST, Kepler, and Spitzer, from which we can now add JWST. The first phase curve observations and analysis were led by Knutson et al. (2007) for the hot-Jupiter HD 189733 b using Spitzer. They showed an offset of the peak brightness eastwards to the substellar point, which is predicted by Global Circulation Models (GCMs). Eastward equatorial jets are caused by the Rossby wave's interaction with the planet's rotation (Showman et al., 2009). Besides, Knutson et al. (2007) showed a small difference between the day and night sides temperatures, suggesting an efficient heat redistribution. The first phase curve spectroscopic observations was made for WASP-43 b using HST WFC3 instrument (Stevenson et al., 2014). They could infer the planet's thermal structure in longitude and altitude and constrain the bond albedo to 0.2. They also highlighted a strong day-night gradient likely caused by cloud formation on the night side. Most phase curve observations were initially conducted for hot-Jupiters but are now more commonly done for smaller

planets. Demory et al. (2016) realised a thermal phase curve of the Super-Earth, 55 Cnc e using Spitzer. This observation highlighted the large temperature difference between the day side, which reaches 2700 K and the night side at 1300 K, and the host spot offset 40 degrees eastward of the sub-stellar point. 55 Cnc e observations are consistent with either a magma ocean, molten rocks on the day-side or a thick atmosphere with no heat redistribution. Phase curve measurements of irradiated rocky planets can help determine if they retained an atmosphere and even constrain the nature of their surface. Kreidberg et al. (2019) revealed a symmetric amplitude of the thermal phase curve using Spitzer observations at 4.5 µm of LHS 3844 b. This result suggests a large day-night temperature contrast and rules out the presence of a thick atmosphere around LHS 3844 b. We present in Figure 1.8 Spitzer phase curves observations of 55 Cnc e and LHS 3844 b. The asymmetric phase curve for 55 Cnc e might suggest atmospheric circulation, while the symmetry in LHS 3844 b observations suggest the absence of a thick atmosphere.

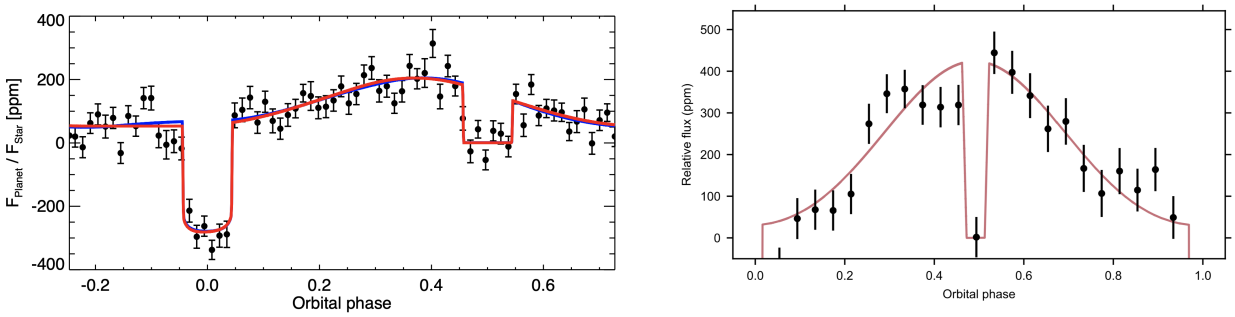

Figure 1.8: Thermal phase curves for the Rocky planets 55 Cnc e (Demory et al., 2016) (left) and LHS 3844 b (Kreidberg et al., 2019) (right). The asymmetric phase curve for 55 Cnc e might suggest atmospheric circulation, while the symmetry in LHS 3844 b observations suggest the absence of a thick atmosphere.

Phase curve measurements first confirmed for hot-Jupiters that the heat redistribution efficiency decreases with the stellar irradiation and that the hot spot is located eastwards to the sub-stellar point as predicted by GCM. At the same time, observations of rocky planets showed that phase curves could be used to infer the presence of an atmosphere.

1.3.4 Atmospheric escape

We showed in Section 1.3.1 that NUV and optical observations led to the detection of atomic species in the upper part of the atmosphere. Atomic H and heavy metals have been reported in several giant planets and Sub-Neptune at the level where they are no longer gravitationally bound to the planet and escape the atmosphere (Vidal-Madjar et al., 2003; Bourrier & Lecavelier des Etangs, 2013; Ehrenreich et al., 2015; Sing et al., 2019). To confirm that an atmosphere is escaping, it has to extend beyond the Roche lobe radius. The most common observation is the transit depth measurement in the Lyman-α line, where the density of neutral hydrogen is very low. Vidal-Madjar et al. (2003) measured a transit depth of 15% whereas Charbonneau et al. (2002) measured an optical transit depth of 1.5% which showed that hydrogen is extended to very large radii (Owen, 2019). The absorption depth reaches 56% in Lyman-α for GJ 436 b compared to the optical value, 0.69% (Ehrenreich et al., 2015; Kulow et al., 2014). This incredible absorption difference is proof that the Sub-Neptune is undergoing atmospheric escape. Other measurements can be a good probe for atmospheric escape. HST NUV measurements were used to detect escaping metal in the magnesium and iron lines in the atmosphere of WASP-121 b (Sing et al., 2019). Spake et al. (2018) used the He triplet line in HST WFC3 to detect an extended atmosphere around WASP-107 b. Observational discoveries are detailed in the introduction of Chapter 3, which presents the analysis of HST NUV observations.

Theoretical models suggest that stellar X-Ray and extreme ultraviolet (EUV) radiation leads to the instability of the upper layers of a hydrogen-rich atmosphere and the extension to a hydrodynamic state. This vertical flow of hydrogen accelerates to several kilometres per second at the exobase, where it becomes possible to escape the planetary gravity (Koskinen et al., 2013). The dynamics of the escaped gas depend on acceleration mechanisms such as radiation pressure or interactions with the stellar wind. These two mechanisms can accelerate the gas away from the planet at high velocities and give it the shape of a cometary tail, as observed for GJ 436 b (Ehrenreich et al., 2015). The depth of the profile is related to the atmospheric escape rate. At the same time, its spectral range depends on the gas acceleration mechanisms and allows the study of the stellar wind's properties. Observing and constraining the hydrodynamic escape processes give access to the composition of the exosphere and the planetary mass loss. The Lyman-α line is a probe of the extended exosphere. In contrast, lines of other heavy elements probe the extended atmosphere of hot planets in more detail and constrain the location and temperature of the thermosphere (Bourrier et al., 2014b,a). The mechanism of hydrodynamic escape suggests that evaporation can affect all planets with a massive hydrogen envelope that is irradiated. This is the case for gas giants at short orbital distances. Nevertheless, giant planets are so massive that they can only lose a small fraction of their mass during their lifetime (Owen, 2019). Atmospheric escape is stronger the lower the density of the planet. However, its impact is more significant for a low-mass planet and probably the most important escape mechanism for a hydrogen-rich atmosphere on low-mass planets. The study of atmospheric escape for Sub-Neptune is a hot topic as this could explain the formation of the radius valley (Fulton et al., 2017; Eylen et al., 2018).

One of the most striking discoveries of the past decades is the bi-modal distribution of low-mass exoplanets, also called the Fulton Gap or radius valley (Fulton et al., 2017; Fulton & Petigura, 2018; Eylen et al., 2018). Exoplanets in the 1.5 to 2$R_\oplus$ radius range are less common than planets with a lower or higher radius. This result was predicted by hydrodynamical escape modelling (Lopez & Fortney, 2014; Owen & Wu, 2013). It could explain the abundance of small planets at short orbital distances as they could be the remnant of the rocky cores of Sub-Neptune, whose atmosphere has been completely stripped. The existence of the Fulton gap is discussed in Chapter 7. A large part of this thesis deals with intermediate-sized planets' observation and nature. Most of the observations and results discussed in this first chapter focus on hot-Jupiters; the next chapter details the major results for rocky to sub-Neptune planets.

Chapter 2

Small exoplanets characterisation

Contents

2.1 Small exoplanets demography

Since the first exoplanet was discovered around a main sequence star by Mayor & Queloz (1995), recognised with the Nobel prize in 2019, more than 5000 exoplanets have been discovered around different stars, even around pulsars (Wolszczan & Frail, 1992)–actually before 51 Pegasi b in 1995–, binaries (Doyle et al., 2011; Welsh et al., 2012) and ultra-cool dwarfs (Gillon et al., 2017). It has been shown that, on average, every star in the galaxy host at least one planet (Cassan et al., 2012; Howard et al., 2010) and the planets discovered are far from being an unbias sample. However, ongoing space missions (e.g the ESA Gaia Perryman et al. (2014), the NASA Kepler and K2 Batalha (2014); Mayo et al. (2018); Borucki (2016); Petigura et al. (2018), the NASA Transiting Exoplanet Survey Satellite TESS Ricker et al. (2016); Barclay et al. (2018)), and ground-based surveys (e.g. SPECULOOS Gillon (2018), HARPS Pepe et al. (2018), Micro-lensing Batista (2018), Gemini Nielsen et al. (2019), SPHERE Boccaletti et al. (2020)) and future missions (the ESA PLATO) will enable the discovery of thousands of new exoplanets, from hot-Jupiters to Earth-sized around bright stars.

2.1.1 Key questions and classification

This thesis deals with the observation and modelling of exoplanet atmospheres. In particular, we hold a special focus on studying small planets, with a size between the Earth and Neptune (1-4$R_\oplus$ and 1-20

$M_\oplus$). The discovery of such planets on short-period orbits, by far the most common, identified by the NASA Kepler mission (Howard et al., 2012; Fressin et al., 2013), has brought new perspectives to our understanding of exoplanet formation. These intermediate-sized planets, also called transitional planets, have no equivalent in the Solar System and have raised new key questions. What is this type of exoplanet made of? What is the atmospheric composition, and is it linked to physical, stellar, and orbital parameters? How were these planets formed? Figure 2.1 is a schematic illustration of the different pathways of planet formation and evolution. We will not discuss the details of the formation process. However, categorising planets is the first step to understanding their variety and demography (Chen & Kipping, 2016).

- **Gas-Giants** have a radius superior to the one of Neptune and are composed, in a significantly large fraction, of primordial hydrogen and helium.
- **Terrestrial planets**, with a high density, are rocky objects with a radius roughly below $1.5R_\oplus$. These planets have probably lost their primordial envelope. They can have a secondary atmosphere created by impacts or outgassing. Depending on their irradiation, they consist of bare rock, an icy core, a magma-ocean planet or feature similarities to the four inner planets and the satellites of gas giants in the Solar System.
- **Transitional planets** probably have a bulk composition dominated by heavy elements, but they could have retained a primary atmosphere of hydrogen and helium. These planets are between the two categories above and are crucial in understanding planetary system formation.

This classification gives us a first view of the planets discovered as a function of the radius. However, the separation in radius is not set in stone. For example, the definition of Super-Earth and Sub-Neptune is unclear: can we find a rocky core with an extended atmosphere and a radius of $1.5R_\oplus$?

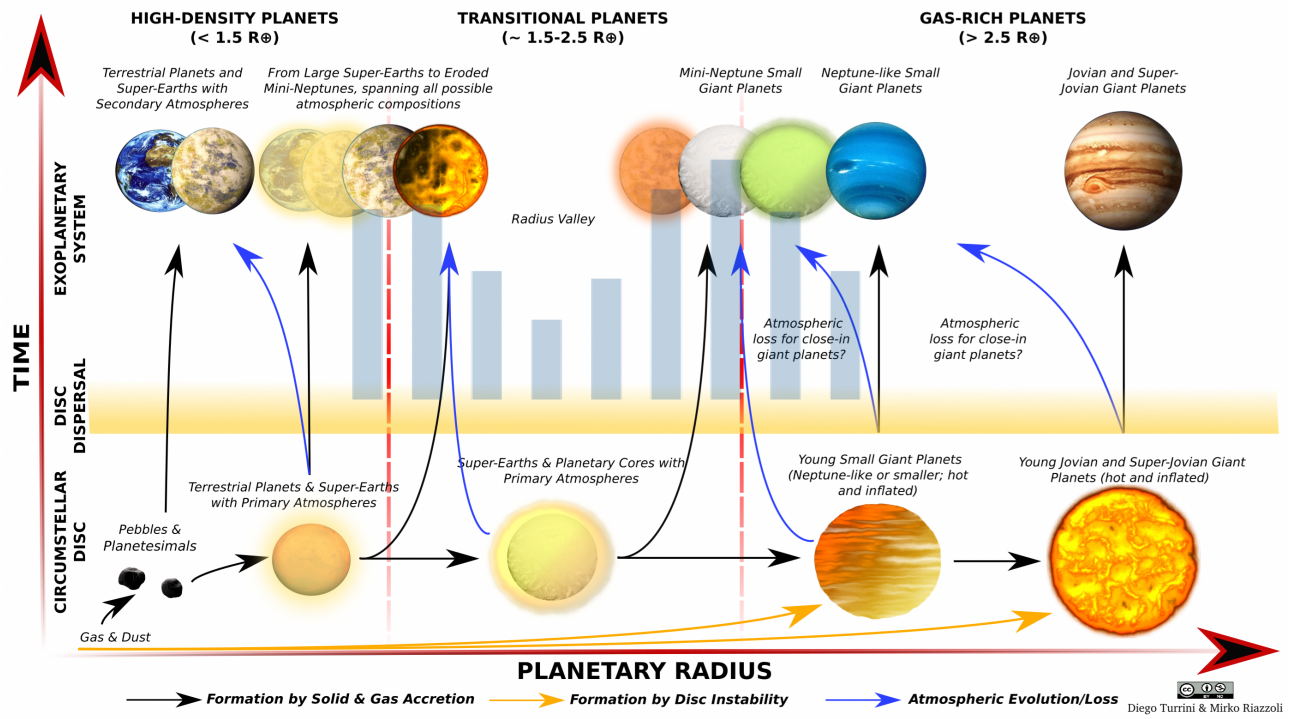

Figure 2.1: Illustration of the different pathways on how planet form (orange arrows) and evolve (blue arrows). They are divided into three groups: high-density planets, gas-rich planets and intermediate-sized planets. This figure is taken from the ARIEL Definition Study Report (study report, 2020) and adapted from (Turrini et al., 2018). The light blue histogram on the backs is the occurrence rate of planets as a function of the radius from (Fulton et al., 2017; Fulton & Petigura, 2018)

2.1.2 The Radius Valley

As previously stated, one of the most surprising findings of the past years in exoplanets survey is the high occurrence of rocky planets and the bi-modal distribution of intermediate-sized planets. Exoplanets with a radius between 1.5 and $2R_\oplus$ are less numerous than those with lower and higher radii, with a gap centred at $1.7R_\oplus$ (Fulton et al., 2017; Eylen et al., 2018). This result has shaped the population of intermediate-sized planets, dividing them into two groups and consequently has shaped the classification presented above. Planets with a radius below $1.5_\oplus$ are thought to be rocky, have probably lost their primordial atmosphere and thus might have a heavy secondary atmosphere. Planets with a size above $2_\oplus$ are likely gaseous planets, with a large portion of their atmosphere dominated by hydrogen and helium (see Figures 2.2). The transition between rocky and gaseous is poorly understood, we know it should occur between roughly 1 and $3R_\oplus$, but we do not know if it is an abrupt or continuous process. The Kepler mission revealed this deficit in the occurrence rate of Sub-Neptunes, but it

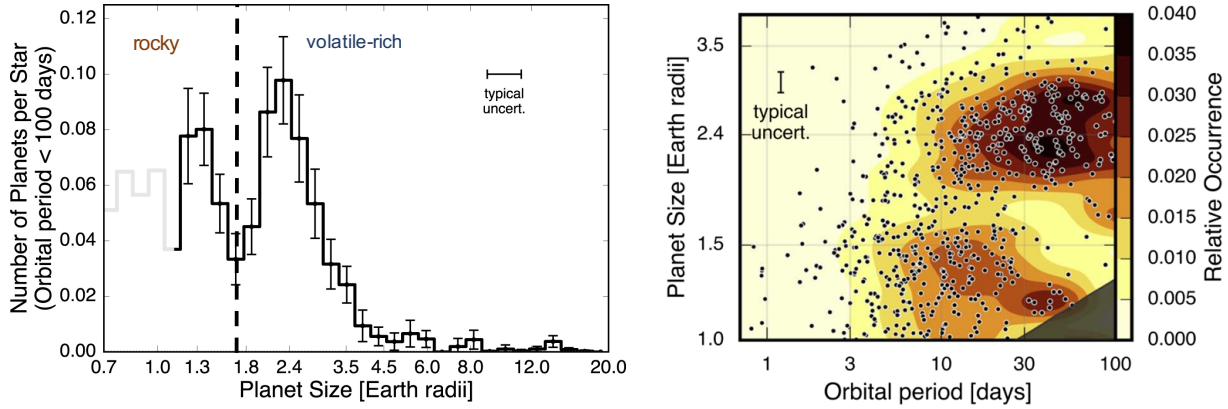

Figure 2.2: Occurence rate of planets with a period below 100 days (left) and distribution of planets as a function of size and orbital period (right). The figures are taken and adapted from Fulton & Petigura (2018).

was predicted by hydrodynamical escape modelling (Lopez & Fortney, 2014; Owen & Wu, 2013) and called the "photo-evaporation valley". It could explain the abundance of small planets at short orbital distances as they could be the remnant of the rocky cores of Sub-Neptune, whose atmosphere has been completely stripped. However, other pathways could be considered (Ginzburg et al., 2018). The location of the gap varies depending on the host star (Fulton & Petigura, 2018; Cloutier & Menou, 2020), and its appearance is blurred while plotting a radius-temperature diagram. Two planets of similar size could have very different bulk compositions, making the Radius Valley interpretation even more complex. This reinforces the need for atmospheric constraints.

2.1.3 The hot-Neptune desert

The hot-Neptune desert, also called the sub-jovian desert, can be understood as an extension of the Radius Valley in a different parameter space at high stellar irradiation and radius. While we can find ultra-hot-Jupiters ($R>10R_\oplus$) or rocky planets ($R<2R_\oplus$) with an orbital period of less than a day around Sun-like stars, there is a lack of planets between these two categories. This dearth of planets can be explained by the intense stellar radiation that removes the primary envelope from low-mass planets, leaving a bare rocky core, or by the enrichment of the atmosphere through outgassing (Davis & Wheatley, 2009; Szabó & Kiss, 2011; Mazeh et al., 2016; Winn et al., 2018). The effective temperature of these planets can reach 2000 K (Jenkins et al., 2020), making them unique objects to analyse. How they manage to keep their hydrogen atmosphere remains unclear. If the planets formed as a hot-Jupiter, atmospheric mass loss removal through photo-evaporation can not be the only mechanism

to explain present-day mass and radius. Studying the hydrodynamical escape mechanism and the potential evaporation and Roche Lobe overflow is crucial to understand the demography.

2.2 Nature of intermediate-sized planets

2.2.1 Mass-radius diagram

Intermediate-sized planet composition remains an open question. These planets could have a rocky core with an extended gaseous hydrogen and helium envelope, or even heavier elements. We could find steamy atmospheres, dominated by water, around a water ice core (Valencia et al., 2013; Zeng et al., 2019). Although the density is essential to constrain the bulk composition of exoplanets, the knowledge of only the mass and the radius is not enough to constrain the nature of these planets. Many different combinations of materials can yield the same planetary density. We represent in Figure 2.3 (left) the degeneracy of the internal composition of GJ 1214 b. This figure is taken from Valencia et al. (2013) and adapted by study report (2020). The ternary diagram proposes internal composition depending on the Earth-like nucleus fraction, water and ice fraction and the hydrogen and helium fraction to the total mass. The thick black dashed lines represent the constraints on GJ 1214 b mass and radius. Two very different compositions are consistent with the observations: either a pure water composition or a 90% rocky core with a 10% envelope of hydrogen helium and trace of water. We also plot the

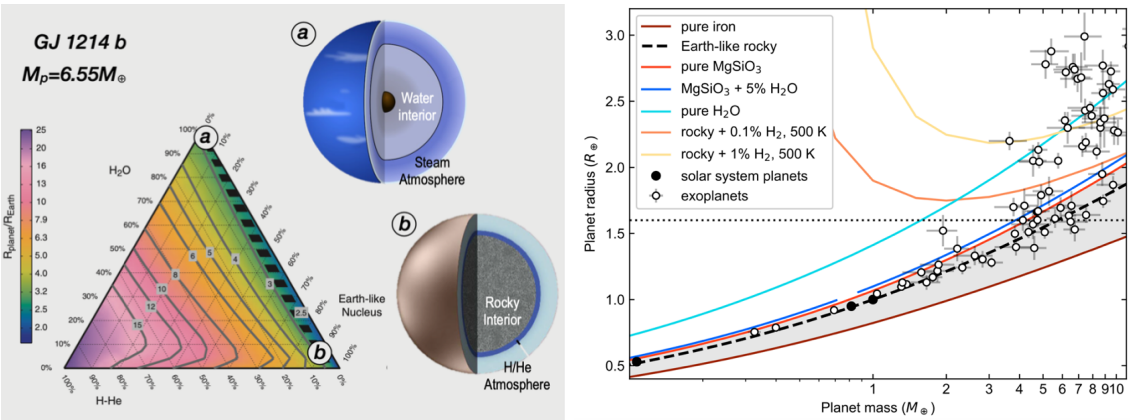

Figure 2.3: Internal composition of GJ 1214 b with the density (left). The ternary diagram proposes internal composition depending on the Earth-like nucleus fraction, water and ice fraction and the hydrogen and helium fraction to the total mass. Grey lines are for constant radius. The plot is from (Valencia et al., 2013). Mass-radius diagram for exoplanets and solar system planets compared to model compositions (right). Only planets with a 5-σ measurement are plotted. The grey-shaded area corresponds to rocky planets. The dotted lines represent the limit set in (Rogers, 2015) above which planets have retained hydrogen and helium. The plot is from Wordsworth & Kreidberg (2021), the measurement from NASA Exoplanet Archive (`https://exoplanetarchive.ipac.caltech.edu/`) and the model composition from Zeng et al. (2019).

mass-radius diagram from Wordsworth & Kreidberg (2021)'s review. It represents the mass and radius measurements for exoplanets and solar system terrestrial planets. They represent exoplanets with a radius below $3R_\oplus$ and a mass below $10M_\oplus$. The grey-shaded area corresponds to rocky planets. The dotted line corresponds to the limit set in (Rogers, 2015) above which planets have retained hydrogen and helium. The measurements are from NASA Exoplanet Archive [1] and the model composition are from Zeng et al. (2019). This representation supports the classification presented in section 2.1.1. Planets with a radius below $1.5R_\oplus$ are consistent with a rocky composition (Weiss & Marcy, 2014; Rogers, 2015; Wolfgang & Lopez, 2014) while planets with a larger radius require volatiles species and

[1] `https://exoplanetarchive.ipac.caltech.edu/`

are scattered in terms of density. The Radius Valley is identified with fewer planets in the 1.5 to $2R_\oplus$ range. The planetary radius increases rapidly with the amount of hydrogen in the model. We note that mass-radius measurements of Sub-Neptunes are consistent with several internal compositions, including a pure-water model. The density must be confronted with atmospheric measurements and modelling to constrain intermediate-sized planets' nature fully.

2.2.2 The existence of Water-worlds

Recently, Luque & Pallé (2022) revisited the mass-radius diagram of transitional planets. They analysed the mass and the radius of all transiting planets with a size below $4R_\oplus$ around M-dwarfs. They identify three populations of planets: rocky, water-rich and gas-rich. Their observations are inconsistent with the bimodal radius distribution explained by atmospheric loss. They look at the planetary distribution in terms of density and find a gap between rocky and water-rich exoplanets. Rocky planets could form within the slow line, whereas water-world form beyond the water frost line and then migrate inward. Orbital migrations can thus explain the gap in density that separates planets. We represent in Figure 2.4 two plots from their study. The first one is the mass-radius diagram of exoplanets around M-dwarfs. They use two internal models from Zeng et al. (2019): an Earth-like model (green) and a 50% water dominate ices added to 50% silicates (blue). We can see the alignment of two populations of planets on these two lines regardless of the temperature. We represent the frequency of planets as a function of the density normalised to the Earth. Once again, three populations of planets appear rocky, water-world and puffy Sub-Neptunes. This study questions the appearance and understanding of the Fulton Gap and the existence of water-world planets. The classification made in section 2.1.1 would see a new class of planet appear: water-rich planets.

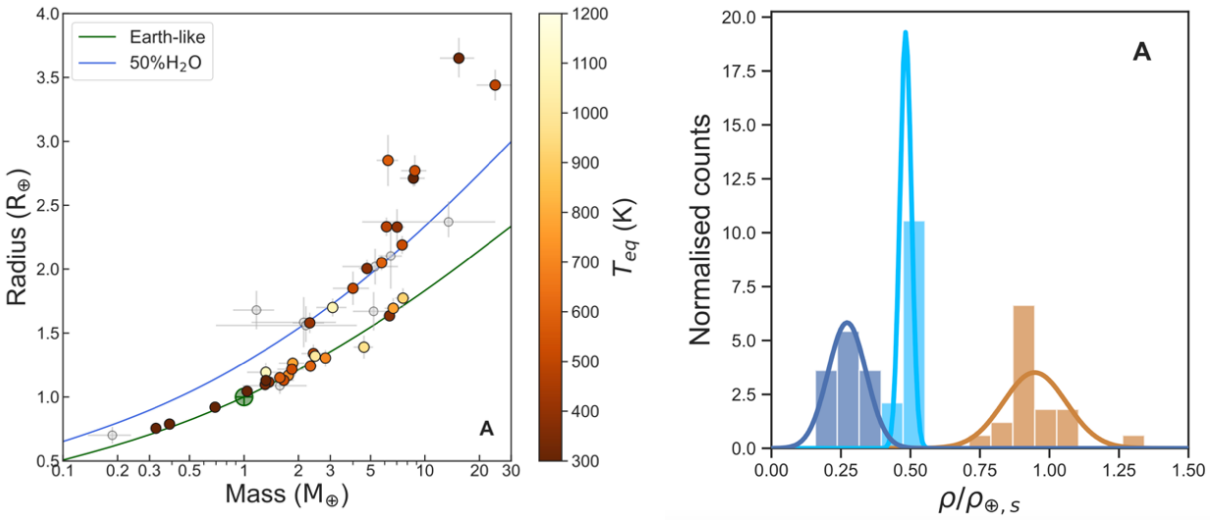

Figure 2.4: Mass-radius diagram for small planets around M-dwarfs (left). They include nine new planets' mass-radius measurements and represent two model compositions from Zeng et al. (2019). The green line is the Earth-like composition, and the blue line is a 50% water dominant ices added to 50% silicates. Frequency of small planets as a function of density (right). Solid lines are Gaussian models fitted to the distributions. Brown histograms are for rocky planets, light blue for water-worlds and dark blue for puffy Sub-Neptunes.

Mousis et al. (2020) studied the mass-radius diagram of irradiated terrestrial water-worlds. They showed that close-in ocean planets affected by the greenhouse effect display hydrospheres in a super-critical state. This phenomenon generates inflated atmospheres without invoking the presence of large hydrogen-dominated envelopes. Their models suggest that super-Earths and water-rich Sub-Neptunes could belong to the same family of planets, hydrogen and helium-free planets, with differences between their interiors simply resulting from the variation in the water content. Besides, Turbet et al. (2019a,

2020a) showed that irradiated water-rich planets might have a hot interior made of steam because of a strong runaway greenhouse effect.

2.3 Observations of transitional to rocky planets

2.3.1 Probing the atmosphere to break degeneracies

Atmospheric characterisation is the most reliable method to constrain the nature of Sub-Neptune and Super-Earth. First, we must define the type of atmosphere we observe. A low mean molecular weight (2.3g/mol, 1 × solar) corresponds to what we call a **primary atmosphere**. The atmosphere can contain gas traces in a low amount (VMR$\sim 10^{-3}$). Sub-Neptunes are expected to have atmospheres enriched with heavy elements leading to a mean molecular weight above 4g/mol (100 to 300 × solar). This type of atmosphere is still dominated by hydrogen and helium, but their composition is unclear. We expect to find volatile species in larger amounts. A **secondary atmosphere** is an Earth-Like atmosphere, no longer dominated by hydrogen and helium and formed by cometary impacts or outgassing. We could also find water-rich atmosphere from the Luque & Pallé (2022) analysis.

Identifying the dominant molecular species and constraining the mean molecular weight or the atmospheric metallicity will help discriminate planets that retained their primordial hydrogen and helium from those that did not. Thus, a classification through the mean molecular weight can be used to separate atmospheric models.

2.3.2 Major results from Space Observations

Most of the small planets' atmospheric characterisation results were obtained with the Hubble Space Telescope and Spitzer. We already discussed discoveries in the Sub-Neptune regime in Chapter 1, and we recall some major results :

- Water identification using HST STIS and WFC3: HAT-P-11 b(Fraine et al., 2014), HAT-P-26 b(Wakeford et al., 2017; MacDonald & Madhusudhan, 2019), HD 106315 c (Guilluy et al., 2020; Kreidberg et al., 2020), HD 3167 c (Guilluy et al., 2020; Mikal-Evans et al., 2020), K2-18 b(Tsiaras et al., 2019; Benneke et al., 2019), GJ 3470 b (Benneke et al., 2019)
- Flat transmission spectra interpreted as clouds or hazes condensation: GJ 1214 b(Kreidberg et al., 2014a), GJ 436 b(Knutson et al., 2014a)
- Atmospheric mass loss using Lyman-α and NUV observations: GJ 436 b (Ehrenreich et al., 2015), GJ 3470 b(Bourrier et al., 2018), HAT-P-11 b(Allart et al., 2018; Ben-Jaffel et al., 2022; dos Santos et al., 2022)

Pushing to terrestrial planets observations is challenging and reaches the limit of current facilities. Most of the observations have been performed for transiting planets around M-dwarfs, motivated by the discovery of the seven-rocky planets TRAPPIST-1 system (Gillon et al., 2016, 2017). M-dwarfs have several advantages in transmission spectroscopy. They are more numerous than Sun-like stars leading to more favourable targets. They have a smaller radius, which increases the signal-to-noise of the planet's atmospheric features (see Chapter 1.1.1), and they have a cooler temperature, leading to temperate Earth-like planet located closer to the star where they are more likely to transit (Dressing & Charbonneau, 2013; Dressing & Charbonneau, 2015). Transmission spectroscopy was obtained for about ten rocky planets around M-dwarfs.

In particular, transit spectroscopy with the Hubble WFC3 G141 has been performed on all seven planets of the ultra-cool TRAPPIST-1 star (de Wit et al., 2016, 2018; Wakeford et al., 2019; Gressier et al., 2021; Garcia et al., 2022). Atmospheric features can reach ten ppm; however, all the transmission

spectra are featureless, and a primary atmosphere is ruled out with at least 2-σ. Flat transmission spectrum results in a constant transit depth over the observed wavelength range. An in-depth analysis of TRAPPIST-1 h data is detailed in Chapter 7 along with an atmospheric comparison of other TRAPPIST-1 planets. Southworth et al. (2017) and Swain et al. (2021) found evidence of atmospheric features and claimed an atmosphere around the warm rocky planet GJ 1132 b (Berta-Thompson et al., 2015). However, this detection is inconsistent with Diamond-Lowe et al. (2018); Mugnai et al. (2021); Libby-Roberts et al. (2022); Waalkes et al. (2019); studies that rejected H_2 dominated atmosphere and did not find evidence for atmospheric features. While the signal-to-noise of these transmission spectra allows rejecting hydrogen-rich atmospheres, we can not yet rule out heavier atmospheric scenarios with smaller features. An atmosphere dominated by N_2, H_2O or CO_2 with a high mean molecular weight has spectral features of the order of the observations uncertainties. A flat transmission spectrum could also result from no atmosphere or a high-altitude cloud or haze layer that blocks the stellar flux through the atmosphere.

A water feature is tentatively identified in the 1.7$R_\oplus$ planet, LHS 1140 b, HST observation (Edwards et al., 2021). This water detection is not statistically significant (2-σ) and is also consistent with stellar activity. TRAPPIST-1 b-g also shows hints of water features consistent with water contamination from the stellar photosphere.

Thermal emission measurement was carried out for LHS 3844 b, a 1.3$R_\oplus$ planet with an 11 hours orbital period (Vanderspek et al., 2019). We presented the phase curve of this rocky planet in Chapter 1, Figure 1.8. Kreidberg et al. (2019) revealed a symmetric amplitude of the thermal phase curve using Spitzer observations at 4.5 µm. This result suggests a large day-night temperature contrast and rules out the presence of a thick atmosphere.

Last, 55 Cnc e, a 1.9$R_\oplus$ Super-Earth (Demory et al., 2016) is the only planet around a Sun-like star for which transmission and thermal emission measurements are available. It is a prime target for transmission spectroscopy with a bright host star visible to the naked eye. This planet orbits in less than a day resulting in an elevated temperature of 1960 K. It is still unclear whether the planet has a rocky surface or a thick volatile envelope from its parameters. However, a light atmosphere dominated by hydrogen and helium is not the favoured scenario, as extreme UV radiation would remove such an atmosphere. Lyman-α measurements (Ehrenreich et al., 2012) and high-resolution spectroscopy (Deibert et al., 2021) are consistent with this hypothesis but disagree with Tsiaras et al. (2016a) analysis of Hubble NIR spectrum consistent with HCN features in a light atmosphere. Demory et al. (2016) realised a thermal phase curve of the Super-Earth, 55 Cnc e using Spitzer (see Figure 1.8). This observation highlighted the large temperature difference between the day side, which reaches 2700 K and the night side at 1300 K, and the host spot offset 40 degrees eastward of the sub-stellar point. 55 Cnc e observations are consistent with either a magma ocean, molten rocks on the day-side or a thick atmosphere with no heat redistribution. 55 Cnc e is an outlier. This planet is poorly understood, with variability in transmission and emission spectroscopy. NUV observations of this planet are presented in Chapter 4.

2.3.3 Population studies

The statistical study of exoplanets' atmosphere remains challenging due to the small amount and the low quality of the available data. It is thus mostly reserved for hot-Jupiters (Sing et al., 2016; Tsiaras et al., 2018; Gao et al., 2020). However, population studies of exoplanets are key to unlocking their statistical properties.

Sing et al. (2016) carried out a comparative study of ten hot Jupiters covering the wavelength range 0.3 to 5 µm. Combining HST STIS, WFC3 and Spitzer measurements allows them to resolve optical scattering and infrared molecular absorption. They reveal a diverse group of hot-Jupiters that exhibit a continuum from clear to cloudy atmospheres. They define a metric by computing a difference

between the optical and infrared planetary radii to distinguish atmospheric scenarios. The difference correlates with the spectral strength of water so that strong water absorption lines are seen in clear-atmosphere planets, and the weakest features are associated with clouds and hazes. The water feature metric is used in several studies to compare hot-Jupiter atmospheres (Stevenson, 2016; Fu et al., 2017; Gao et al., 2020). In particular, (Gao et al., 2020) uses the amplitude of the water feature correlation to the temperature to constrain the condensation of silicate hazes in gaseous atmospheres. They find that silicates dominate aerosol opacity above equilibrium temperatures of 950 K, while hydrocarbon aerosols dominate below 950 K due to increased methane abundance.

Changeat et al. (2022) analysed spectroscopic and photometric data of 25 hot Jupiters obtained with the Hubble and Spitzer Space Telescopes via the eclipse technique. They perform a consistent retrieval analysis of the entire set of 25 planets and extract robust trends in the thermal structure and chemical properties of hot Jupiters. Tsiaras et al. (2018), consistently reduced 30 gaseous planets HST WFC3 G141 data and analysed them with a Bayesian retrieval tool. They develop methods to quantify atmospheric detectability and infer atmospheric properties. Even more recently, Edwards et al. (2022) extended this study to 65 HST transmission spectra. However, all of these studies deal with gas giants, and small planets' atmospheres have not yet been looked at in a consistent large-scale survey until this thesis.

Crossfield & Kreidberg (2017) proposed the first study of six Sub-Neptunes HST transmission spectra. They use the water feature amplitude around 1.4 µm and investigate the correlation with other parameters. They show a correlation between the amplitude of atmospheric features in the near-infrared with the temperature and its bulk H/He mass fraction. These correlations could indicate either more optically thick or photochemically produced hazes at a lower temperature. They linked the correlation to the formation of clouds and hazes in Sub-Neptunes atmospheres. They showed that the temperature limit between clear and cloudy/hazy atmospheres could be found around 850 K.

One of the goals of this thesis is to improve our knowledge of the atmospheric composition of intermediate-size planets. This is linked to the formation and evolution of these planets. Getting closer to the atmospheric composition will inform us about its formation. This question will be addressed in Part III and IV using Hubble NIR observations and modelling, while Part II deals with gas giant atmospheric escape through NUV observations. However, the last chapter of this part discloses unprecedented NUV observations of a Super-Earth linking this part to the study of the transitional planets. We perform a Hubble transmission survey of rocky to intermediate-sized planets in Chapter 7. This is the first large-scale transmission survey of small planets, building upon the initial work of Crossfield & Kreidberg (2017).

Part II

Observations: Hubble Near-UV data analysis

Chapter 3

Probing the high atmosphere of hot-Jupiters with Hubble STIS NUV observations

Contents

3.1 Introduction

This chapter is based on the publication **The Hubble PanCET Program: The near-UV transmission spectrum of WASP-79 b (Gressier et al. submitted**, which addresses WASP-79 b Hubble STIS data analysis and interpretation. This paper was submitted to A&A in July 2022 (seeList of Publications).

Exoplanet atmospheric characterisation has been mainly carried out using observations of close-in transiting planets. Transit spectroscopy in the visible or in the infrared enabled the detection of atomic

and molecular species (Tinetti et al., 2007; Swain et al., 2008, 2010; Deming et al., 2013; Kreidberg et al., 2014b; Sing et al., 2016; Tsiaras et al., 2018; Madhusudhan, 2019), as well as clouds and hazes (Pont et al., 2008; Lecavelier des Etangs et al., 2008a; Bean et al., 2010; Kreidberg et al., 2014a) in the lower parts of the atmosphere. Absorption spectroscopy in the ultraviolet (UV) gives access to the upper part of the atmosphere up to the exosphere (10^{-6}-10^{-7} bar) and enables the detection of atomic and ionic species (Redfield et al., 2008; Fossati et al., 2010; Wyttenbach et al., 2015; Arcangeli et al., 2018; Spake et al., 2018). Exoplanets orbiting close to their star receive stellar X-ray and extreme UV radiations leading to heating at the base of the thermosphere and to the hydrodynamical expansion of the upper layers (Watson et al., 1981; Lecavelier des Etangs et al., 2004; Murray-Clay et al., 2009; Erkaev et al., 2016; Salz et al., 2016). Highly irradiated hot-Jupiter and Neptune-mass planets are sensitive to hydrodynamic outflows and atmospheric mass escape (Bourrier et al., 2013; Bourrier et al., 2018; Ehrenreich et al., 2015; Owen, 2019). Lyman-α measurements in the far-UV (FUV) revealed extended hydrogen atmosphere around HD 209458 b (Vidal-Madjar et al., 2003), HD 189733 b (Lecavelier des Etangs et al., 2010, 2012; Bourrier & Lecavelier des Etangs, 2013), GJ 436 b (Kulow et al., 2014; Ehrenreich et al., 2015; Lavie et al., 2017; dos Santos et al., 2019), GJ 3470 b (Bourrier et al., 2018) and HAT-P-11 b (Allart et al., 2018; Ben-Jaffel et al., 2022; dos Santos et al., 2022) producing a much larger transit depth (10% to 50%) than the transit of the planet at optical and IR wavelengths (0.1-1%). The atmospheric outflow carries heavier elements from the 0.1–1 bar atmospheric level up to the thermosphere (García Muñoz, 2007). The velocities of metal species range between a few hundred m/s to several km/s at the base of the exosphere and escape the planet's gravitational pull. Those heavy species are detectable in the near UV (NUV) absorption spectroscopy. During the transit, they cover 2% to 10% of the stellar disk. Atomic oxygen, magnesium and iron, and also ionized carbon, magnesium and iron have been detected on HD 209458 b (Vidal-Madjar et al., 2004; Linsky et al., 2010), HD 189733 b (Redfield et al., 2008; Ben-Jaffel & Ballester, 2013; Wyttenbach et al., 2015) and WASP-121 b (Sing et al., 2019). Helium was detected in the atmosphere of WASP-107 b using HST G102 measurement in the near-infrared (Spake et al., 2018). Nikolov et al. (2022) recently observed the complete pressure-broadened profile of the sodium absorption feature in the cloud-free atmosphere of the hot-Saturn, WASP-96 b, with the Very-Large Telescope. They could measure a precise, absolute sodium abundance for this planet.

STIS NUV observations presented here aim to understand the connection between the formation of heavy elements through haze dissociation (Parmentier et al., 2015, 2016) and the upper expanding atmosphere (Bourrier & Lecavelier des Etangs, 2013; Bourrier et al., 2014b,a) and hot-Jupiters. Deep clouds cannot be observed directly but can be detected through Rayleigh scattering (Lecavelier des Etangs et al., 2008a,b; de Mooij et al., 2013; Dragomir et al., 2015). Moreover, observing heavy elements at high altitudes can bring information on physical processes lower in the atmosphere. First, we detail the method developed to correct systematic effects in HST/STIS E230M data and adjust the raw light curves in Section 3.2. Then, we present WASP-121 b and WASP-79 b data analysis results in Section 3.3. WASP-121 b's analysis is a confirmation of Sing et al. (2019)'s findings, while WASP-79 b's data analysis is a new result. Consequently, Section 3.4 discusses WASP-79 b's observations and focuses on interpreting the NUV transmission spectrum of this planet.

3.2 Methodology

3.2.1 Observations

Observations of WASP-79 b and WASP-121 b used in the present analysis are part of the Panchromatic Exoplanet Treasury (PanCET) program (HST GO Proposal #14767, PI D.K. Sing and M. Lopez-Morales). We analysed two transit observations for each planet with the Hubble Space Telescope Imaging Spectrograph (HST/STIS) instrument. The observations were conducted with the NUV-Multi-Anode Microchannel Array (NUV-MAMA) detector using the E230M echelle grating with a 0.2"x0.2" aperture. E230M has a resolving power of about 30 000 and covers the wavelength range of 2280 to 3070 Å. The spectra have an average dispersion of 0.049 Å per pixel, about two pixels per resolution element. Each Observation consists of five consecutive orbits covering the full transit before and after. The two observations of WASP-79 b were taken on January 12, 2018 and March 11, 2018 and February 23, 2017 and April 10 2017 for WASP-121 b.

The data were acquired in time-tag mode. We extracted a sequence of 350-second long sub-exposures from these using `calstis` version 3.4. From the shorter Observation of the first orbit of each visit, we obtained 6 sub-exposures, and from the extended Observation of the second to the fifth orbit, we obtained 8 sub-exposures per orbit. This yields a total of 38 sub-exposures per visit.

Table 3.1: System and transit parameters used in the analysis.

Parameters	WASP-79 b	WASP-121 b
Spectral Type	F5	F6
$R_\star$ [$R_\odot$]	$1.51^{+0.04}_{-0.03}$	1.458 ± 0.030
$M_\star$ [$M_\odot$]	1.39 ± 0.06	$1.353^{+0.080}_{-0.079}$
[Fe/H]$_\star$	0.03 ± 0.10	0.13±0.09
Teff$_\star$ [K]	6600 ± 100	6459 ± 140
$\log_{10}\ g_\star$ [cgs]	4.20 ± 0.15	$4.242^{+0.011}_{-0.012}$
R_P [R_{Jup}]	1.53 ± 0.04	1.865 ± 0.044
M_P [M_{Jup}]	0.85 ± 0.08	$1.183^{+0.064}_{-0.062}$
T_{eq}[K]	$1716.2^{+25.8}_{-24.4}$	2358±52
P [days]	3.662392 ± 0.000004	$1.27492550^{+0.00000020}_{-0.00000025}$
i [deg]	86.1 ± 0.2	89.1±0.5
e [deg]	0.0	0.0
ω [deg]	90.0	90.0
$a/R_\star$	7.407 ± 0.109	3.86±0.02
$R_P/R_\star$	0.10440 ± 0.00048	$0.12454^{+0.00047}_{-0.00048}$
Reference	Brown et al. (2017)	Delrez et al. (2016); Evans et al. (2018)

3.2.2 Systematics correction

Spectrophotometric light curves taken with STIS aboard the Hubble Space Telescope (HST) are highly affected by instrument-related systematics. For instance, the thermal "breathing" effect periodically modifies the point-spread function (PSF). Systematic effects are correlated to instrumental parameters or external factors that vary with time during the observations (Sing et al., 2019). Usually, only the thermal "breathing" effect characterised by the correlation with the HST orbital phase is considered in HST STIS E230M data analysis. However, corrections limited to only these systematic effects are not enough for data with a high level of correlated noise, especially for the first HST orbit with different systematic effects. Most of the time, this led to the removal of all the data of this first orbit from the analysed data set.

We implemented a method to analyse and correct systematic effects in HST/STIS E230M data using all the information available. Similar to Sing et al. (2019), we decided to include in the systematic effects correction model the measured parameters (see Table 3.2) that describe HST's Pointing Control System performance during the observation run. Those parameters are created by the Engineering Data Processing System (EDPS). For computational efficiency, we normalised each measurement by subtracting the mean and dividing it by the standard deviation. We decided to keep the first HST orbit, but we discarded the first exposure of each orbit that systematically presents a lower flux level. We discarded the latitude and longitude because of the possible correlation to the HST's phase. These parameters were later re-included in the list to analyse 55-Cnc e data. However, this does not impact the rest of the analysis as they were not selected as a dominant effect for WASP-79 b and WASP-121 b visits.

Table 3.2: Details of the jitter engineering parameters used in the detrending method of HST STIS E230M data. The parameters from `v2_dom` to `si_v3_p2p` are tabulated in arcsec. The parameters from `ra` to `los_zenith` are tabulated in degrees. The magnetic field strengths tabulated in the three last rows are tabulated in Gauss.

Parameters	Meaning
`v2_dom`	Dominant guide star V2 coordinate
`v3_dom`	Dominant guide star V3 coordinate
`v2_roll`	Roll FGS V2 coordinate
`v3_roll`	Roll FGS V3 coordinate
`si_v2_avg`	Mean of jitter in V2 over 3 seconds
`si_v2_rms`	Mean of jitter in V2 over 3 seconds
`si_v2_p2p`	Peak-to-peak jitter in V2 over 3 seconds
`si_v3_avg`	Mean of jitter in V3 over 3 seconds
`si_v3_rms`	Mean of jitter in V3 over 3 seconds
`si_v3_p2p`	Peak-to-peak jitter in V3 over 3 seconds
`ra`	Right Ascension of aperture reference
`dec`	Declination of aperture reference
`roll`	Position angle between north and +V3 axis
`lat`	Latitude of the Telescope
`long`	Longitude of the Telescope
`limbang`	Angle between V1 axis and Earth limb
`los_zenith`	Angle between HST zenith and target
`mag_v1`	Magnetic field along V1
`mag_v2`	Magnetic field along V2
`mag_v3`	Magnetic field along V3

Detrending parameters selection

The EDPS file contains 20 parameters (Table 3.2) to which we add the 96 minutes of HST's orbital phase (ϕ_{HST}). Each parameter describes the spacecraft's configuration, which varies with time and potentially impacts the photometric measurements. To determine whether it is necessary to take a parameter into account in the detrending model, we perform a first fit of the white light curve by testing each parameter independently. For that, we model the correlation of the residuals as a function of the parameter value using a first-degree polynomial. The quality of the fit to the light curve is then quantified using the corrected Akaike statistical criterion, $AICc$, which is calculated as a function of k

(the number of free variables), n (the total number of exposures), and χ^2 the Chi-squared:

$$\mathrm{AICc} = \mathrm{AIC} + \frac{2\mathrm{k}^2 + 2\mathrm{k}}{\mathrm{n} - \mathrm{k} - 1} \tag{3.1}$$

$$\mathrm{AIC} = \chi^2 + 2 \times \mathrm{k} \tag{3.2}$$

The effect of a parameter whose correction produces AICc improvement (compared to an initial uncorrected adjustment) is integrated into the model. Note that we decided to use the corrected AIC rather than the classical AIC or BIC criteria because of the small size of the statistical sample, which here are only 33 points (38 sub-exposures minus 5 first sub-exposures of each HST orbit).

Polynomial degree selection

Once we identified the parameters to be considered to improve the fit to the light curve, we modelled the correction factor as a function of the parameter value using a polynomial function. (Equations. 3.3 and 3.4), whose degree is chosen to obtain the best fit, that is, the fit to the light curve that produces the lowest AICc value. We obtain a systematic effect correction model composed of the product of polynomials. The parameter values for a given visit are x_i for i ranging from 1 to 21. The number of parameters used in the model depends on the visit. For each jitter parameter, we increase the polynomial degree n until the AICc value no longer decreases from its previous value. We also systematically test the $n+1$ degree polynomial if $n-1$ has improved AICc, but n does not. At this step, the correction of the tested parameter is incorporated into the light curve fit, and the other parameters are tested again (see section 3.2.2) by including the correction of the identified effects in the fit. The procedure for the parameters and polynomial degree selection is carried out iteratively until the systematics correction no longer improves the AICc criterion.

$$\mathrm{S(X)} = \prod_{\mathrm{i}=1}^{\mathrm{N}} \mathrm{S_i(x_i)} \tag{3.3}$$

$$\mathrm{S_i(x_i)} = 1 + \mathrm{a_1} \times \mathrm{x_i} + \mathrm{a_2} \times \mathrm{x_i^2} + ... + \mathrm{a_n} \times \mathrm{x_i^n} \tag{3.4}$$

3.2.3 White light curve fitting

We integrated the flux over the entire wavelength range to obtain a white light curve, with 33 measurements for each of the two transits for each planet. We normalised each light curve with respect to the average flux over a visit, and we modelled the transit using the `batman` python package (Basic Transit Model Calculation in Python; Kreidberg (2015)). We held fixed the inclination, semi-major axis to star radius ratio and limb-darkening coefficients to the values in Table 3.3. We modelled the flux measurement over time $f(t)$ as a combination of the theoretical transit model $T(t, \theta)$, where θ is the set of the transit parameters, the total baseline flux from the host star $\mathrm{F_0}$ and the systematic error correction model S(X), derived as described in Section 3.2.2:

$$f(t) = T(t, \theta) \times \mathrm{F_0} \times \mathrm{S(X)} \tag{3.5}$$

We include a linear baseline time trend in S(X) to correct flux variations over time. The number of free parameters depends on the corrections and S(X) terms. In the search for the best fit, the planet-to-star radius ratio, the polynomial coefficients, and the baseline flux are left free. We used `batman`'s convention and normalised the time with respect to the transit centre. We do not fit for the mid-transit time in our analysis as that did not improve the fitting results. However, our code is flexible, and this parameter can be easily added as a free parameter if necessary. The best-fit parameters are

determined using Levenberg-Marquardt's least squares method (L-M) (Markwardt, 2009). The limb-darkening effect is modelled using a non-linear law given by the equation (Claret, 2000):

$$I(\mu) = I_0 \times [1 - c_1(1 - \mu^{\frac{1}{2}}) - c_2(1 - \mu) - c_3(1 - \mu^{\frac{3}{2}}) - c_4(1 - \mu^2)] \tag{3.6}$$

where $\mu = \sqrt{1 - x^2}$, x is the normalised radial coordinate and I_0 is the normalised star flux.

Transit parameters are initialised for the rest of the analysis with values found in Brown et al. (2017) for WASP-79 b. There are set to those of Delrez et al. (2016) and Evans et al. (2018) for WASP-121 b, following Sing et al. (2019) initialisation and allowing further comparison (see Table 3.1). The coefficients (c_1,c_2,c_3,c_4), detailed in Table 3.3, are computed using Sing (2010) with the effective temperature, metallicity [Fe/H] and surface gravity given in Table 3.1. The UV spectral region contains strong stellar atomic lines that can behave anomalously at the limb, especially in temperature inhomogeneities. However, the present HST NUV light curves do not allow us to precisely sample the ingress and egress portions of the transit, so it is not straightforward to constrain the limb darkening coefficients to high accuracy. Besides, we tested other limb-darkening laws and found similar results to those presented below. Sing (2010) non-linear four parameters law is a good approximation for fitting HST NUV light curves.

Table 3.3: Limb-darkening coefficients for STIS E230M data analysis of WASP-79 b and WASP-121 b.

Bands		Limb darkening coefficient			
λ_C(Å)	$\Delta\lambda$(Å)	c1	c2	c3	c4
2673	799	0.44589384	-0.22547123	1.14667951	-0.42635197
2387	236	0.41620878	-0.5781367	1.29633765	-0.1709417
2600	200	0.53356331	-0.67401008	1.80463859	-0.70370411
2800	200	0.46217923	-0.23965174	1.08129327	-0.3632111
2986	172	0.39608196	0.15363096	0.79375784	-0.42174585

3.2.4 Spectral light curve fitting

We created a correction model for the white light curve using jitter correlation parameters and then applied this correction to all light curves obtained in various spectral wavelength ranges. The correction model is constructed by dividing the best-fit analytic white light curve model by the jitter parameters polynomial. We first divided the spectrum into several broadband spectral ranges (∼200 Å) adopting the same selection as Sing et al. (2019). We also calculated higher-resolution transmission spectra in 4 Å bins. The transit (∼ 1%) can still be resolved at this resolution except in spectral regions with strong stellar absorption and at the edge of spectral orders. We removed points where the transit was not detected. The planet-to-star radius ratio is a free parameter in the model, and its value is adjusted to get the best-fit spectrum. To validate the value found by the L-M method and estimate the 1-σ error, we used the χ^2 variation method by varying the planet-to-star radius ratio and estimating the value of the χ^2 as a function of the radius ratio. The minimum is found for the best-fit planet-to-star radius ratio, and the 2-σ error bars are taken at $\Delta\chi^2 = 4$, i.e.:

$$\sigma = \left|\frac{R_P/R_\star(\chi^2_{min} + 4) - R_P/R_\star(\chi^2_{min})}{2}\right| \tag{3.7}$$

3.3 Results

3.3.1 WASP-121 b data analysis: method validation

To validate our fitting method described above, we applied it to WASP-121 b's STIS data. WASP-121 b is a Hot-Jupiter orbiting an F6V star with a similar temperature as WASP-79, 6459 K (Delrez et al., 2016). The planet has an inflated radius, i.e, 1.865 R_J and an equilibrium temperature reaching 2358 K (Delrez et al., 2016) (see Table 3.1). These observations are also part of the PanCET program and were studied and published in Sing et al. (2019). Our analysis includes all HST NUV-observations of WASP-121 b, except for the first exposure of each orbit. We represent in Figure 3.1 the white light curve fitting results on both observations of WASP-121 b. The planetary transit is visible in the raw data. The latter is not highly affected by systematics. The correction model only includes a linear polynomial of the planetary phase for Observation 2, while the first Observation requires a more complex correction with a total of 7 free parameters:

$$S(X) = (1 + a_1\phi_t) \times (1 + a_2\phi_{HST} + a_3\phi_{HST}^2) \times (1 + a_4 \text{mag\_v3}) \times (1 + a_5 \text{ si\_v2\_avg}) \quad (3.8)$$

The correlations of the normalised raw flux with jitter parameters are plotted in Figure 3.2 for the first Observation on WASP-121 b. We find a $R_P/R_\star$ of 0.135 ± 0.002 for both visits, which is consistent within 1-σ with the values found by Sing et al. (2019), i.e 0.1364 ± 0.0110 and 0.1374 ± 0.0026 for the first and second visit, respectively.

Table 3.4: WASP-121 b radius measured in different broad bands.

			Observations 1		Observations 2		Observations 2 Sing et al. (2019)	
	λ_C(Å)	$\Delta\lambda$(Å)	$R_P/R_\star$	error	$R_P/R_\star$	error	$R_P/R_\star$	error
White	2673	799	0.1353	0.0022	0.1347	0.0022	0.1374	0.0026
Bin 1	2387	236	0.1482	0.0066	0.1457	0.0081	0.1530	0.0085
Bin 2	2600	200	0.1441	0.0037	0.1363	0.0040	0.1396	0.0045
Bin 3	2800	200	0.1363	0.0031	0.1396	0.0029	0.1376	0.0037
Bin 4	2986	172	0.1262	0.0036	0.1268	0.0036	0.1273	0.0039

We fitted ∼200 Å bins with the same systematic model to fit the white light curve for the different visits optimally. We observed an increase in the wavelength-dependent $R_P(\lambda)/R_\star$ at short wavelength with $R_P(2387 \pm 118 \text{ Å})/R_\star = 0.1457 \pm 0.0081$ for the first transit which is within 1-σ of the Sing et al. (2019) result: 0.1530 ± 0.0084. We present in Table 3.4 and in Figure 3.3 the broadband transmission spectrum for both observations and for the second visit of Sing et al. (2019). We also obtained 4 Å bins NUV transmission spectrum of WASP-121 b using the second transit, that confirms the FeI, FeII and MgII detection (see Figure 3.3. For instance, we find $R_P/R_\star(2348\text{Å}) = 0.292 \pm 0.053$, that is in the FeII absorption domain, and $R_P/R_\star(2796\text{Å}) = 0.297 \pm 0.040$ in the MgII h-line of the doublet around 2800 Å. Therefore, we confirm that FeII and MgII are no longer gravitationally bound to the planet.

In conclusion, our WASP-121 b analysis yields the same results as the ones found by Sing et al. (2019); this validates our procedure for the systematics correction and the planet radius estimates, as described above.

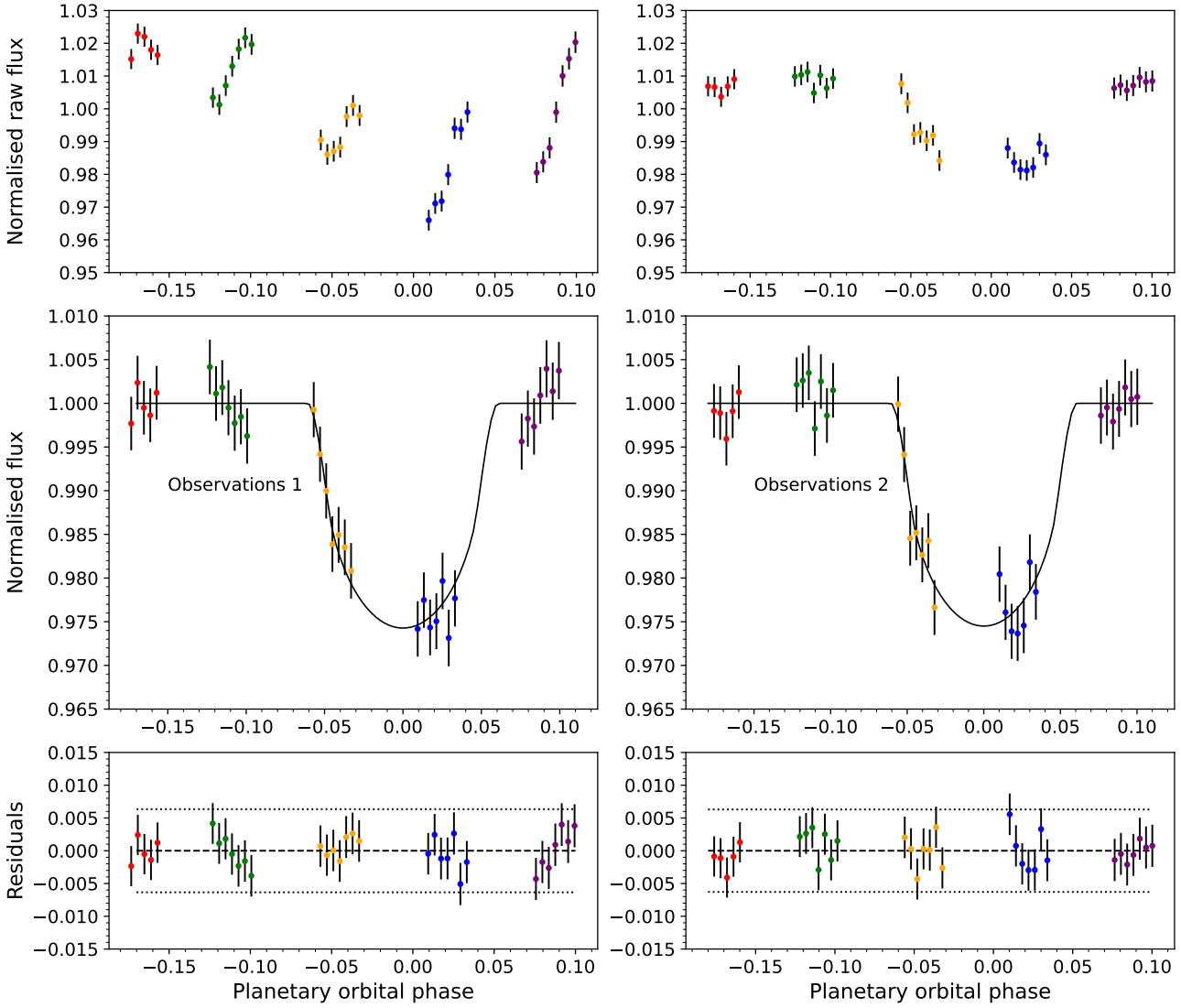

Figure 3.1: WASP-121 b white light curves for Observations 1 (left) and Observations 2 (right). Top: normalised raw light curves. Middle: flux corrected from systematic errors and fitted with a transit model. Bottom: residuals between the flux corrected spectra and the best-fit models and 2-σ error bars (dotted line).

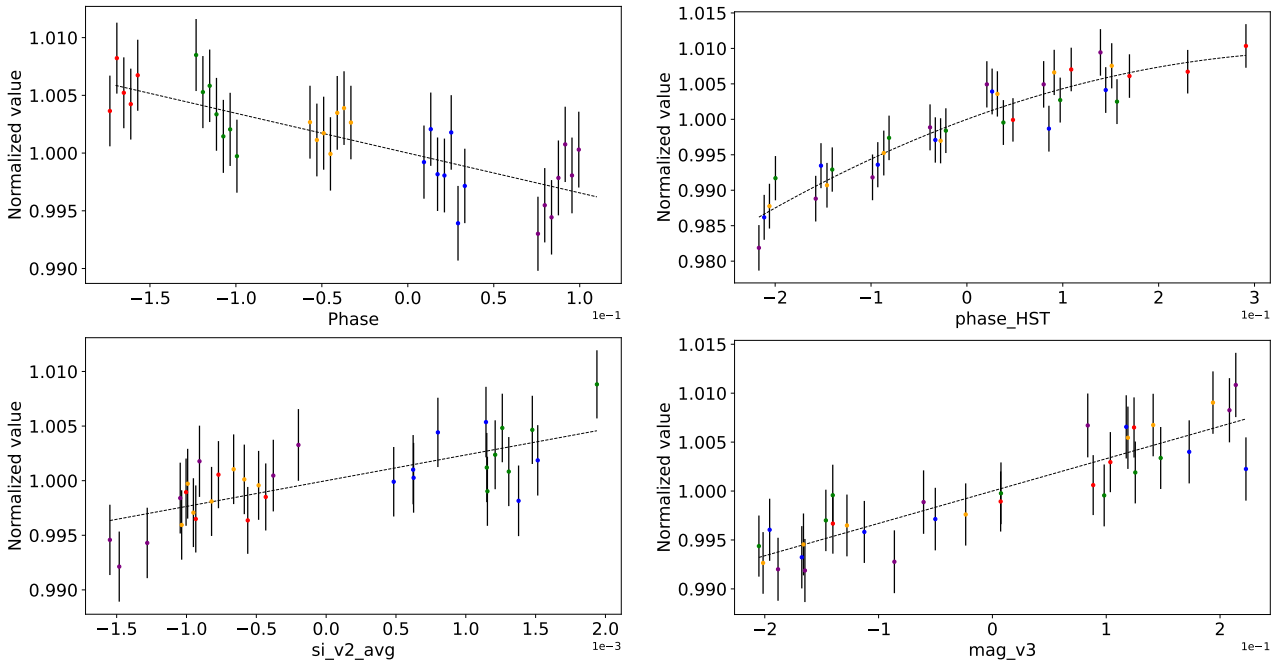

Figure 3.2: Polynomial fit (dotted line) included in the correction model for the white light curve of Observations 1 on WASP-121 b. All polynomials are of degree one except for the polynomial with regards to the HST orbital phase, whose degree is 2.

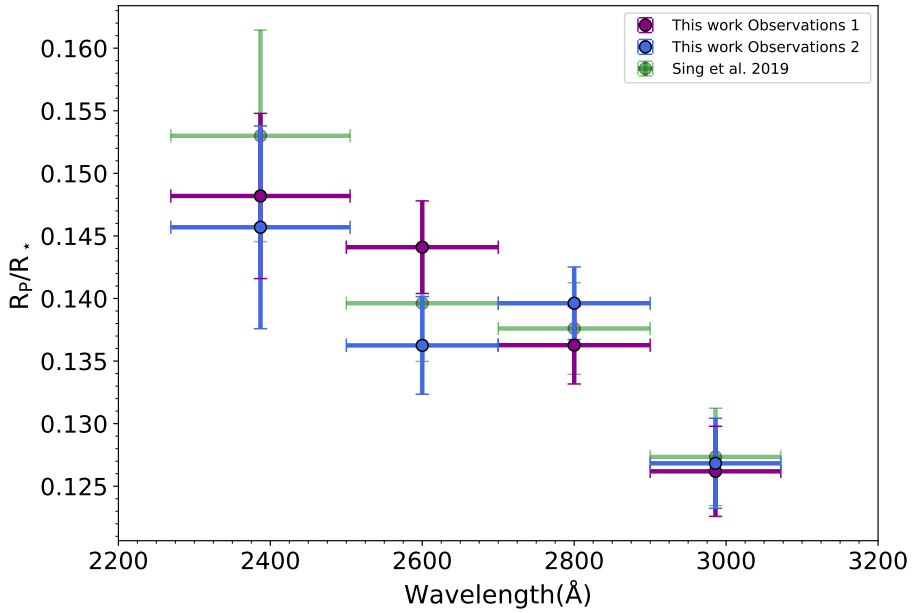

Figure 3.3: WASP-121 b planet-to-star radius ratio measured in the broadband transmission spectra of the first visit (purple) and second visit (blue from this work, green from Sing et al. (2019)).

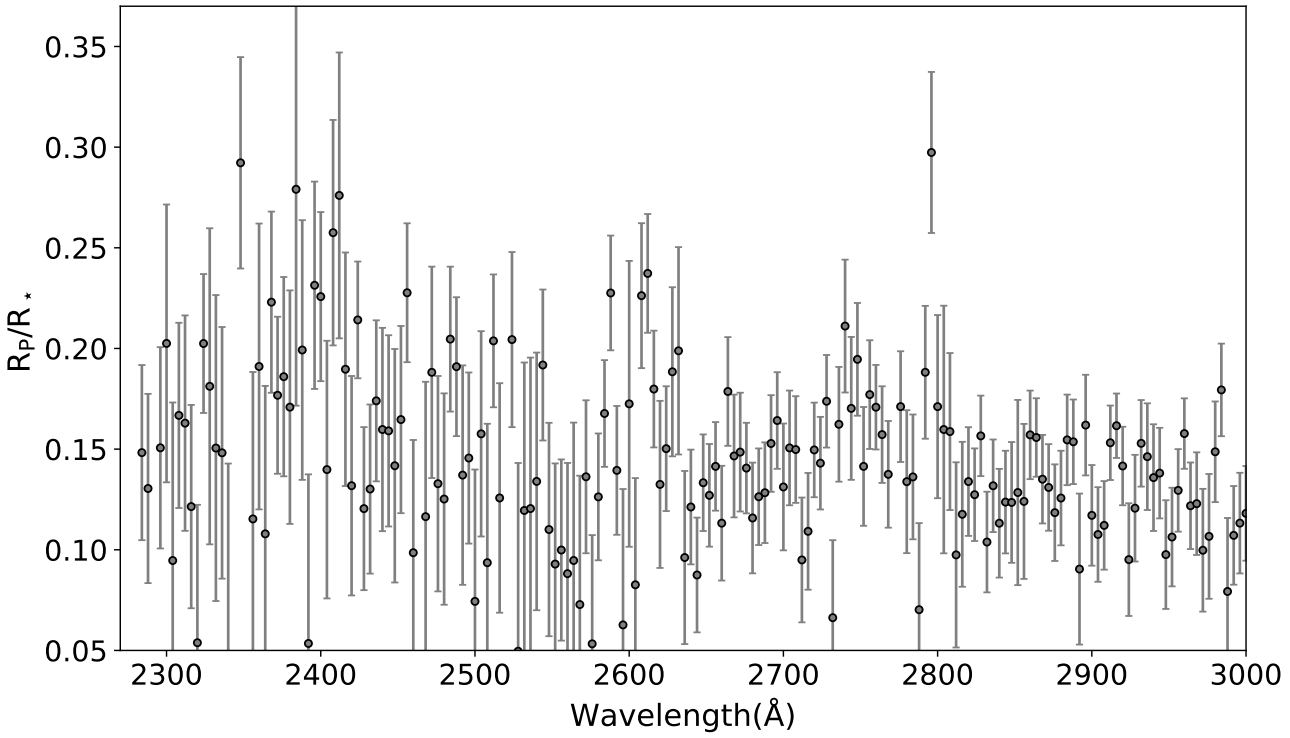

Figure 3.4: WASP-121 b NUV transmission spectra in 4 Å bins for Observations 2.

3.3.2 WASP-79 b data analysis

WASP-79b was discovered by Smalley et al. (2012) with the WASP-South and TRAPPIST telescopes. Using a main-sequence mass-radius constraint on the Monte-Carlo Markov Chain process, they found a mass of 0.90±0.08M_J and a radius of 1.70±0.11R_J. The radius was found to be larger, 2.09±0.14R_J while using a non-main-sequence constraint. Brown et al. (2017) refined the parameters and found a planetary radius of 1.53±0.04R_J and a mass of 0.85±0.08M_J (Table 3.1). The large radius and the mass close to one Jupiter mass yield a low density of $\rho \sim 0.31\,\mathrm{g\,cm^{-3}}$, suggesting an inflated atmosphere. The planet orbits its F-type star in 3.7 days and has a high equilibrium temperature ∼1700 K. Addison et al. (2013) showed that the Rossiter-McLaughlin signal of the planet suggests a nearly polar orbit. Sotzen et al. (2020) analyzed HST/WFC3 and Magellan/LDSS-3C data along with Spitzer data and reported the 0.6 to 4.5 µm transmission spectrum of WASP-79 b. They found evidence of vapour water and presented a retrieval analysis favours the presence of FeH and H^- in the atmosphere. Another independent study on HST/WFC3 G141 data confirmed the water detection and the possible presence of iron hydride (Skaf et al., 2020). More recently, a full 0.3 to 5.0 µm spectrum was published by Rathcke et al. (2021) with an analysis of HST PanCET data between 0.3 and 1.0 µm. In this work, the transmission spectrum blueward of 1.0 µm decreases toward shorter wavelengths with no evidence of hazes or Rayleigh scattering in the planet's atmosphere. On the other hand, they confirmed the water detection with more than 4-σ confidence and displayed a moderate detection of H^- with 3.3σ significance. Finally, they detected the effect of unocculted stellar faculæ on the observed spectrum of the planet's atmosphere.

White light curves fitting

We apply our method to the STIS data obtained during the transit of WASP-79 b. For each set of transit observations, we used all 5 HST orbits but excluded the first exposure of each orbit. The two visits show highly different trends: the first visit presents more than 10% variations in the normalised

raw flux. This visit is highly affected by systematic effects, whereas the second visit is of better quality with lower systematics (Figure 3.5). Following the procedure described in Section 3.2.2, we use a correction model to obtain the global fit. The data of Observation 1 requires a complex model with 15 free parameters in total:

$$S(X) = (1 + a_1\phi_t) \times (1 + a_2\phi_{HST} + a_3\phi_{HST}^2 + ... + a_9\phi_{HST}^8) \times (1 + a_{10}\ \text{mag\_v1}) \times (1 + a_{11}\ \text{si\_v2\_rms}) \times (1 + a_{12}\ \text{los\_zenith}) \times (1 + a_{13}\ \text{roll}) \quad (3.9)$$

Correlations of the normalised raw flux with jitter parameters are plotted in Figure 3.6.

Values of the polynomial coefficients corresponding to the parameter involved in the correction model are detailed in Table 3.5. The analysis of the white light curve of the first Observation yields $R_P/R_\star = 0.1285 \pm 0.0021$. Even in the corrected light curve, some exposure points are outliers beyond 2-σ, and the light curve obtained within the orbits 3 and 4 still presents systematic trends (see Figure 3.5). We performed a broadband analysis using the formalism of Sing et al. (2019) and obtained the following values: $R_P/R_\star(2400\,\text{Å}) = 0.1362 \pm 0.0063$, $R_P/R_\star(2600\,\text{Å}) = 0.1254 \pm 0.0045$, $R_P/R_\star(2800\,\text{Å}) = 0.1305 \pm 0.0035$ and $R_P/R_\star(3000\,\text{Å}) = 0.1255 \pm 0.0035$. This visit yields a deeper transit that is not compatible with previous studies.

Therefore we consider that the results of the first transit are most likely affected by strong instrumental systematics or suffer from stellar activity. Considering the large amplitude of the systematics in the raw measurements obtained during the Observation 1 (see top left panel of Figure 3.5), we decided to focus our analysis on the transmission spectra obtained with the Observations 2 and to use the results from the observations of the first visit only for confirmation or consistency checks. Nonetheless, we note an increase in the transit depth at low wavelength with a relative difference between the radius at 2400 Å and at 3000 Å of $\Delta R_P/R_\star = 0.0107 \pm 0.0072$. This result is consistent and gives confidence with what is found with the data of the second visit, as described in the following sections.

The raw light curve of Observation 2 shows less systematics and can be fitted with only 4 free parameters :

$$S(X) = (1 + a_1\phi_t) \times (1 + a_2\ \text{si\_v3\_avg}) \quad (3.10)$$

The correlations of the normalised raw flux with jitter parameters are plotted in Figure 3.7. The value of the polynomial coefficients, including the jitter parameter `si_v3_avg` (the mean jitter in V3 over 3 seconds) are in Table 3.5. Compared to Observations 1, the second visit presents a better transit phase coverage and all residuals are below 2-σ (see Figure 3.5). The white light curve of the second visit yields $R_P/R_\star = 0.1059 \pm 0.0025$. Table 3.6 shows the different planet to star radius ratio measurements from previous published studies (Rathcke et al., 2021; Sotzen et al., 2020). Our new measurement is consistent with all previous published values for WASP-79 b, in particular with the Brown et al. (2017) value of 0.10440 ± 0.00048.

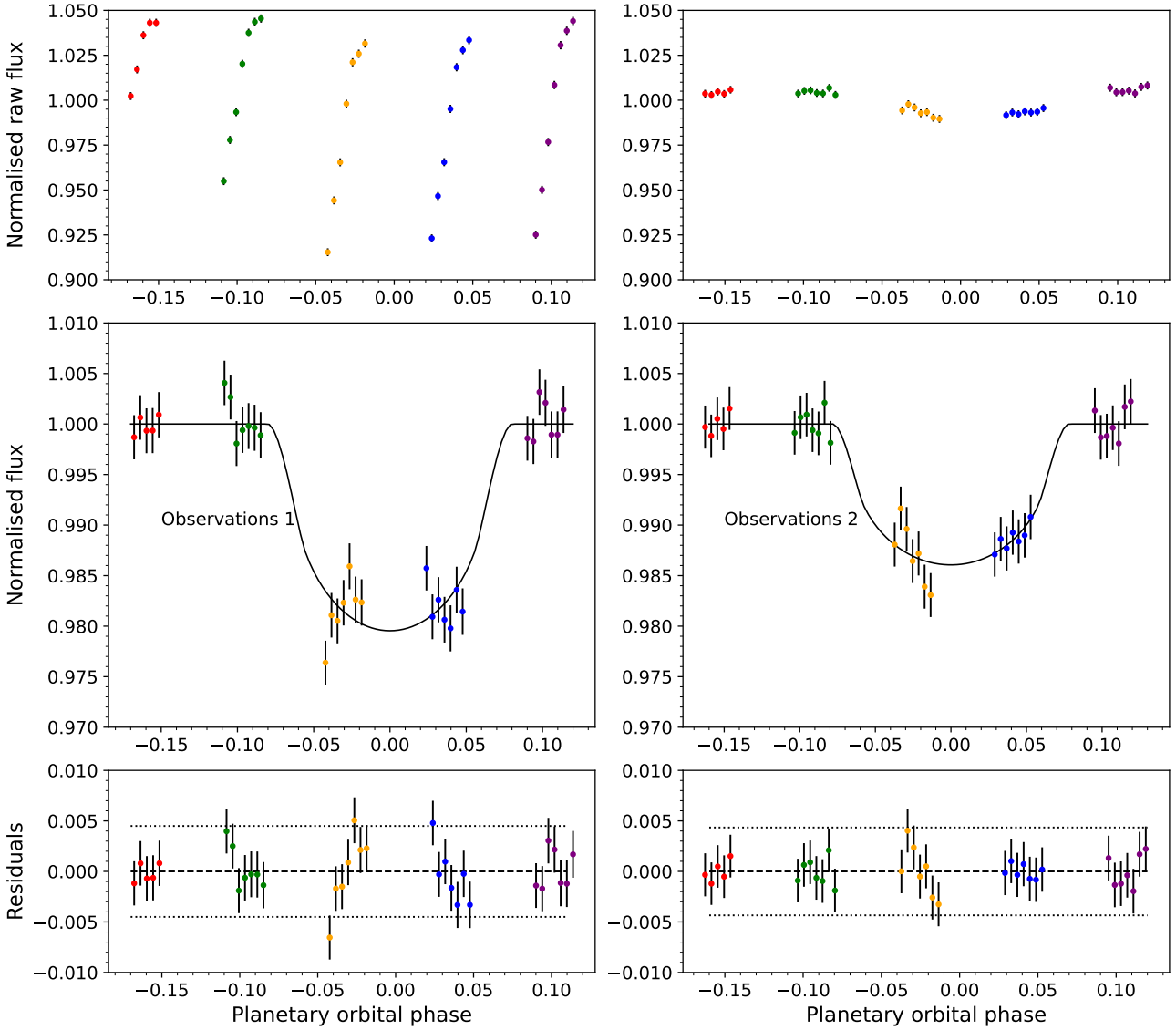

Figure 3.5: WASP-79 b white light curves for Observations 1 (left) and Observations 2 (right). Top: normalised raw light curves. Middle: flux corrected from systematic errors and fitted with a transit model. Bottom: residuals between the flux corrected spectra and the best-fit models and 2-σ error bars (dotted line). Observations 1's raw data display a larger ramp effect than Observation 2. This ramp is mainly correlated to the HST orbital phase.

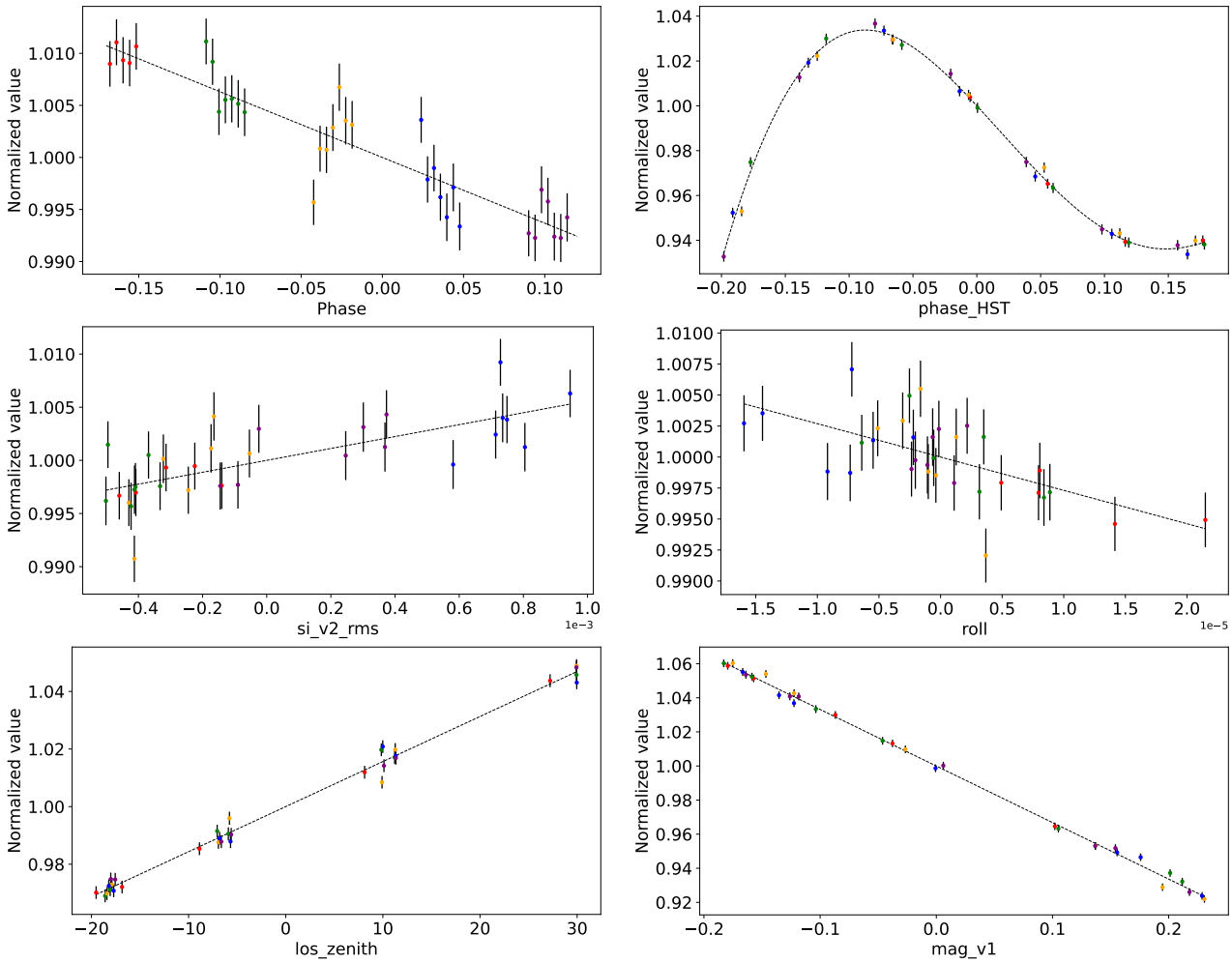

Figure 3.6: Polynomial fit (dotted line) included in the correction model for the white light curve of Observations 1 on WASP-79 b. All polynomials are of degree one except for the polynomial with regards to the HST orbital phase, whose degree is eight.

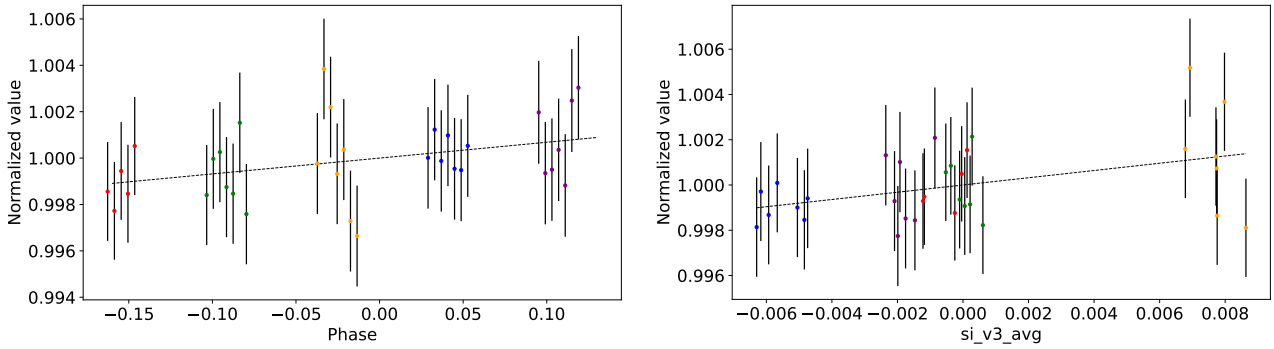

Figure 3.7: Polynomial fit of degree 1 (dotted line) included in the correction model for the white light curve of the second visit on WASP-79 b.

Table 3.5: List of the jitter engineering parameters and values of polynomial coefficients included in the white-light curves correction model for the two visits on WASP-79 b. All polynomials are of degree 1 in this case. The correction model of Observation 1 of the PanCET program also includes a polynomial of degree 8 of the HST orbital phase correlated to the large ramp effect (see Figure 3.5). The coefficients are the following in increasing degree order: -0.5844569, -1.05257, 17.27887, -20.33507, -37.87583, 251.4479, 7.275825, -1671.329. We also corrected the linear effect correlated to the planetary phase. The coefficients are 0.12850 and 0.006832 for Observations 1 and 2, respectively.

Parameters	Observations 1	Observations 2
v2_dom	-	-
v3_dom	-	-
v2_roll	-	-
v3_roll	-	-
si_v2_avg	-	-
si_v2_rms	5.429995	-
si_v2_p2p	-	-
si_v3_avg	-	0.163022
si_v3_rms	-	-
si_v3_p2p	-	-
ra	-	-
dec	-	-
roll	-267.9753	-
limbang	-	-
los_zenith	0.0015797	-
mag_v1	-0.3187546	-
mag_v2	-	-
mag_v3	-	-

Table 3.6: Extracted planet to star radius ratio comparison with values found in the literature.

Instrument	Bandpass	$R_P/R_\star$
STIS E230M this work	0.22-0.32 µm	0.10590±0.0025
STIS G430L Rathcke et al. (2021)	0.29-0.57 µm	0.10519±0.00025
STIS G750L Rathcke et al. (2021)	0.53-0.57 µm	0.10482±0.00040
STIS G750L Rathcke et al. (2021)	0.59-1.02 µm	0.10662±0.00024
TESS Sotzen et al. (2020)	0.59-1.02 µm	0.10675±0.00014
LDSS-3C Sotzen et al. (2020)	0.60-1.0 µm	0.10782±0.00070
WFC3 G141 Sotzen et al. (2020)	1.10-1.70 µm	0.10621±0.00015
Spitzer Sotzen et al. (2020)	3.18-3.94 µm	0.10594±0.00038
Spitzer Sotzen et al. (2020)	3.94-5.06 µm	0.10675±0.00048

Broadband analysis

We used the same broadband bin width of ∼200 Å as used by Sing et al. (2019) in their broadband analysis of WASP-121 b's STIS data. We fitted the broadband data of WASP-79 b using the same systematic detrending model to correct the white light curve optimally. Broadband results are presented in Table 3.7 and Figure 3.8. We indicate values for Observation 1 for information even though the rest of the analysis is done with results from Observation 2. We observe an increase in the planet-to-star radius ratio toward shorter wavelengths. In the white light curve and in the broad bands around 2600 Å, 2800 Å and 2900 Å, the planet-to-star radius ratio is found compatible within 1-σ with Rathcke et al. (2021) findings at 0.3 µm. However, at shorter wavelength around 2400 Å, the ratio $R_P/R_\star$(2400 Å)=0.1207±0.0067 is found to be significantly higher. For this reason, we computed the planet-to-star radius ratio for the band 2500-3000Å, where no variation in wavelength is detected. We found $R_P/R_\star$=0.1031±0.0027.

The relative difference between the planet-to-star radius ratio at 2400 Å and 3000 Å is $\Delta R_P/R_\star = 0.0191 \pm 0.0079$. This result is consistent within 1-σ with the value of 0.0107 ± 0.0072 found using Observations 1 data in Section 3.3.2. This increase in the absorption depths at short wavelengths can be explained by the absorption of heavy ionic or atomic species (Lothringer et al., 2020) or by the presence of hazes in the upper part of the atmosphere. In short, we observe a significant increase in the apparent radius of the planet at a shorter wavelength could be due to the presence of clouds or hazes.

Figure 3.9 shows the overall HST transmission spectrum of WASP-79 b, including our NUV measurements obtained with the data of the second visit, Sotzen et al. (2020) measurements in the NIR (HST/WFC3) and Rathcke et al. (2021) measurements in the NUV and visible wavelength range (HST/STIS G430L and HST/G750L). We represent the value around 2400 Å in a 200 Å band and the large band value after 2500 Å to show the steep increase in the planet-to-star radius ratio at short wavelength. Combining different transmission spectroscopy datasets is even more difficult when there is no spectral overlap. The orbital parameters and limb-darkening coefficients can be different from one study to another, the treatment of systematic effects and stellar activity can vary as well, leading to variations in planet to star radius ratio and transit depth measurements (Tsiaras et al., 2018; Yip et al., 2020; Changeat et al., 2020a; Pluriel et al., 2020a; Edwards et al., 2021). Even while using the same system parameters, prescriptions for limb darkening and a lack of stellar activity, Nikolov et al. (2013) already highlighted differences in absolute radius level for HAT-P-1 b, when combining STIS with WFC3. We decided to keep the values only from the HST instruments even though Sotzen et al. (2020) and Rathcke et al. (2021) showed the compatibility of LDSS-3C transmission values on WASP-79 b in the optical and NIR. Our measurement in the NUV obtained using the white light curve of the second visit is compatible within 1-σ with all other transmission spectra. Nonetheless, it shows a trend of increasing absorption towards shorter wavelengths.

Table 3.7: WASP-79 b radius measured in different broad bands.

			Observations 1		Observations 2	
	λ_C(Å)	$\Delta\lambda$(Å)	$R_P/R_\star$	error	$R_P/R_\star$	error
White	2673	799	0.1285	0.0021	0.1059	0.0025
Bin 1	2786	572	0.1266	0.0028	0.1031	0.0027
Bin 2	2387	236	0.1362	0.0063	0.1207	0.0067
Bin 3	2600	200	0.1254	0.0045	0.1072	0.0051
Bin 4	2800	200	0.1305	0.0035	0.1028	0.0043
Bin 5	2986	172	0.1256	0.0035	0.1016	0.0042

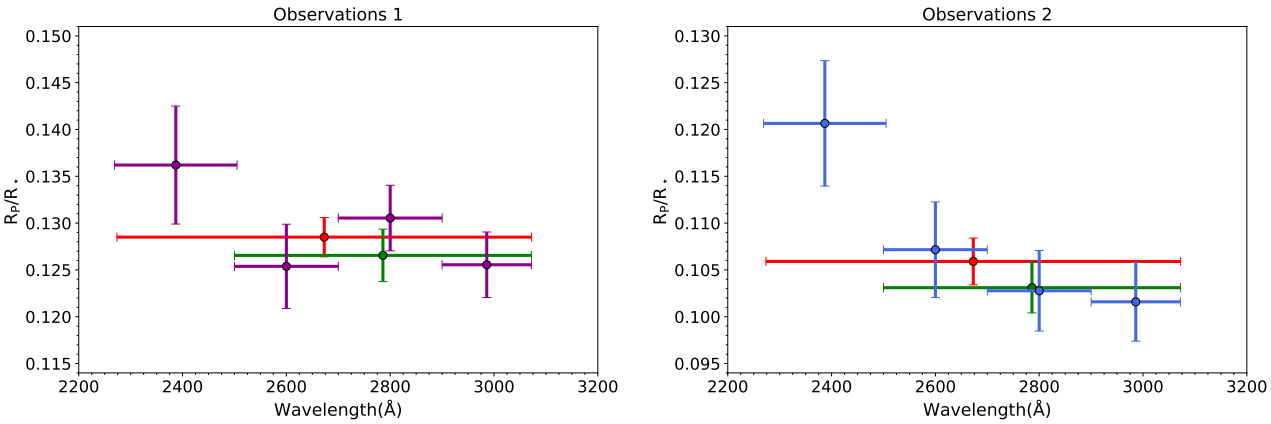

Figure 3.8: WASP-79 b planet-to-star radius ratio measured in the broadband transmission spectra of the first visit (left) and second visit (right). The value from the white light curve is plotted in red, and the value from Bin 1 (2500 to 3100 Å) is green.

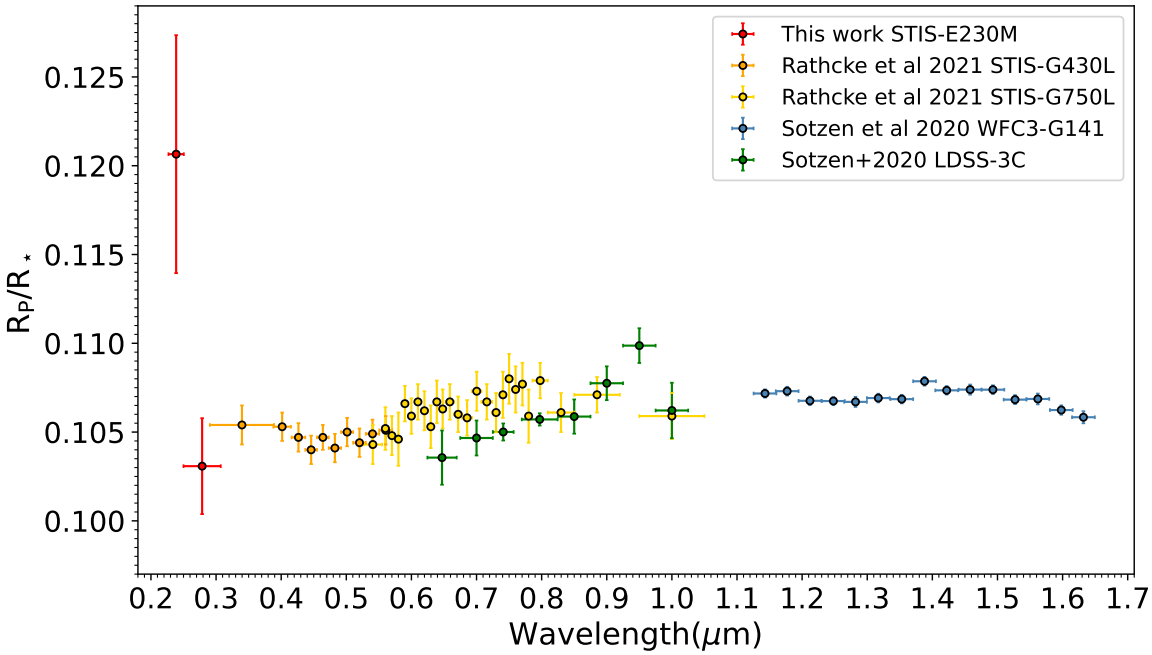

Figure 3.9: WASP-79 b HST transmission spectrum. NUV values are from the broadband analysis of Observations 2 obtained here using the STIS E230M observations (in red). We represent two values around 2400 Å and 2700 Å for clarity (Bin 1 and 2 in Table 3.7). In the optical, the values are from Rathcke et al. (2021) analysis of STIS G430L and G750L data (orange and yellow). HST/WFC3 observations in the NIR are from Sotzen et al. (2020) (blue).

Narrow band analysis

To investigate the possibility of the presence of heavy species in the upper atmosphere producing a dense forest of narrow absorption lines, we calculated the transmission spectrum in narrow bands of 4Å width (Figure 3.10). We search for an increase in the apparent radius of the planet at specific wavelengths that could be due to the presence of heavy metal species at very high altitudes or escaping the atmosphere. The wavelengths of the highest absorption in the transmission spectrum can be seen in Figure 3.10, some exceeding 0.18 in planet-to-star radius ratio. None of them corresponds to known metallic species absorbing in this part of the spectrum. We note that the value at 2384 Å could correspond to a Fe II line, usually found at 2382 Å. However, there is no detection of excess absorption of Fe II in other lines with similar oscillator strength. We note that the data reduction process described in Section 3.2.4 does not converge in the vicinity of two strong FeI lines (2484 and 2719 Å). This is likely due to the very low flux level in the middle of the line because of the stellar atmosphere absorption.

All things considered, the spectrum does not provide clear evidence of Fe I or Fe II absorption that could have explained the observed increase in the apparent radius at short wavelengths. Nonetheless, the absorption spectrum in narrow bands confirms the global increase in the apparent radius of the planet at short wavelengths. The planet-to-star radius ratio weighted average is 0.1233 ± 0.0052 below 2500 Å and 0.1022 ± 0.0021 beyond. This simple computation compares nicely to the broadband analysis and the value found around 2400 Å, $R_P/R_\star$(2400 Å) = 0.1207±0.0067, and after 2500 Å, $R_P/R_\star$(>2500 Å) = 0.1031±0.0027. We also computed each bin's transmission spectrum shifted by 2 ÅThis analysis confirmed the shape of the spectrum.

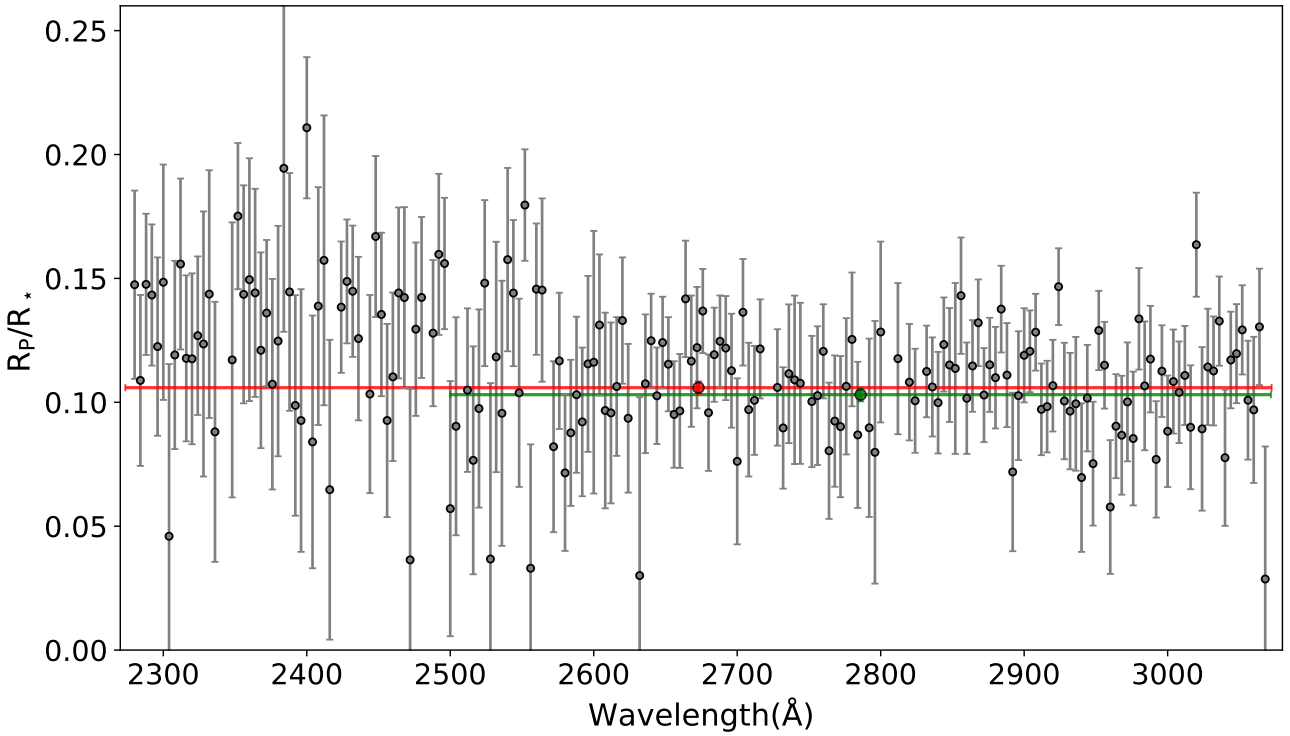

Figure 3.10: WASP-79 b NUV transmission spectra in 4 Å bins for Observations 2. We indicate the overall NUV transmission spectrum (white light curve) $R_P/R_\star$(NUV) = 0.1059 in red, along with the planet-to-star radius ratio after 2500(Å) in green $R_P/R_\star$(>2500 Å) = 0.1031.

3.4 Discussion

3.4.1 Scale height of the atmospheric absorption

At shortest wavelengths (∼2400 Å), the radius of the planet measured in the broadband and the narrow band is significantly higher than at longer wavelengths (≥ 2600 Å). Although this increase in planetary radius is consistently observed in the two visits, we consider only the quantitative estimates obtained with the second visit (Observations 2), which provided better quality data with fewer systematic errors. In the broadband at 2400 Å we obtain $R_P/R_\star$=0.1207±0.0067, that is about 16% bigger than the planet size as seen in the optical. From 3000 Å to 2400 Å, the increase in planet size is measured to be $\Delta R_P/R_\star = 0.0191 \pm 0.0079$. In the broadband at 2400 Å we obtain $R_P/R_\star$=0.1207±0.0067, which is about 16% bigger than the planet size as seen in the optical. From 3000 Å to 2400 Å, the increase in planet size is measured to be $\Delta R_P/R_\star = 0.0191 \pm 0.0042$.

We performed a joint fit of the two light curves to accurately compute the difference between the planetary radius and the uncertainty. We concatenate the two light curves into one matrix and adjust each light curve with the same correction model as for the broadband analysis. However, instead of fitting for the two planet-to-star radius ratios in the two separate bins, we fit for the planet-to-star radius ratio of the first bin and the $\Delta R_P/R_\star$. The other parameters are held fixed. We then computed the uncertainty by using the variation of the χ^2 described above. This method is justified to find the increase in planetary size and absorption as we are looking for a relative measurement, not two independent, absolute planetary radii. Our finding corresponds to an increase in radius short ward of 2400 Åto a 4.5-σ effect which rules out a statistical fluctuation. The increase in the apparent planet size at specific wavelengths is commonly interpreted as due to extra absorption in the atmosphere. Here the increase of 16% in the planet's size is so large that the variation of the planet's gravity reaches 30% between the bottom atmosphere and the altitude at which the atmosphere is optically thick at 2400Å, so the usual derivation of the atmospheric scale height has to be adapted.

With a constant gravity, the hydrostatic equilibrium equation is $dP/P = -(\mu g/kT)dr$, where P are the pressure, μ the mean molar mass of the atmosphere, g the gravity, T the temperature and r is the distance to the planet centre. This allows defining the atmospheric scale height $H = kT/\mu g$. The pressure P as a function of the altitude z is then $P(z) = P_0 \exp(-z/H)$, where P_0 is the pressure at zero altitude. However, with an atmospheric thickness that is not negligible compared to the planet's radius, we need to consider the planet's gravity's decrease with altitude. The new hydrostatic equilibrium equation is $dP/P = -(\mu G M_p/kTr^2)dr$, where M_p is the mass of the planet and G the gravitational constant. The pressure vertical profile becomes $P(z) = P_0 \exp(-zR_p/H(R_p + z))$ or $P(z) = P_0 \exp(-z/H')$, where the modified altitude dependent scale height is $H'(z) = H \cdot (R_p + z)/R_p$. Interestingly, the pressure limit in this model when z tends to infinity becomes non-zero. This result could be discussed with regard to hydrodynamical escape formalism.

For WASP-79 b, we have a temperature $T = 1716 \pm 25$ K and a planet gravity $g = GM_p/R_p^2 = 10.6 \pm 1.6\,\mathrm{ms}^{-2}$ (Brown et al., 2017). Assuming an hydrogen-helium atmosphere with $\mu = 2.3$, this yields a scale height of $H = 580 \pm 100$ km, and a ratio $H/R_\star = 5.5 \times 10^{-4} \pm 1.0 \times 10^{-4}$. Finally with an atmospheric absorption thickness of $\Delta R_P/R_\star = 0.0191 \pm 0.0079$, we find a ratio $\Delta R_P/H \approx 34$. Considering the gravity variation with altitude, this ratio is decreased to $\Delta R_P/H' \approx 29$. This value remains very large, and the absorption at high altitude, as observed at 2400 Å takes place at a pressure that is $e^{-29} = 2 \times 10^{-13}$ lower than at the altitude where the atmosphere is optically thick at ∼ 3000 Å.

We identified two other processes that could increase the scale height and thereby require less strong absorption than computed above. First, the scale height value uses a calculated equilibrium temperature, not a measured temperature. Spitzer secondary eclipses of this planet give a day side temperature of about 1950±85 K Garhart et al. (2020). The planet is irradiated sufficiently strongly

that it may not redistribute heat efficiently, and the limb temperatures may not be much less than the Spitzer day side temperatures. However, we re-computed the scale height using the day-side temperature, and we find $H = 660 \pm 130$ km, which translates to a ratio of $\Delta R_P/H \approx 30$. We find a ratio of ≈ 25 while considering the gravity variation with altitude, which remains very large. The impact of the temperature is marginal. Besides, the mean molecular weight could be lower than 2.3 amu due to hydrogen dissociation. Even if we consider that the hydrogen molecules may be partially dissociated, leading to a smaller mean molar mass ($\mu \sim 1$), we find $\Delta R_P/H' \approx 13$, and ≈ 11 with a temperature of 1950 K and the conclusion remains the same. Although identifying the main absorber at $\sim$2400 Å remains puzzling, it must have an extremely large cross-section to be optically thick at such a low density. Clouds and hazes appear to be the most plausible carrier of the detected absorption at the shortest wavelengths, even though the pressure is really low.

3.4.2 Comparison with the Roche Lobe equivalent radius

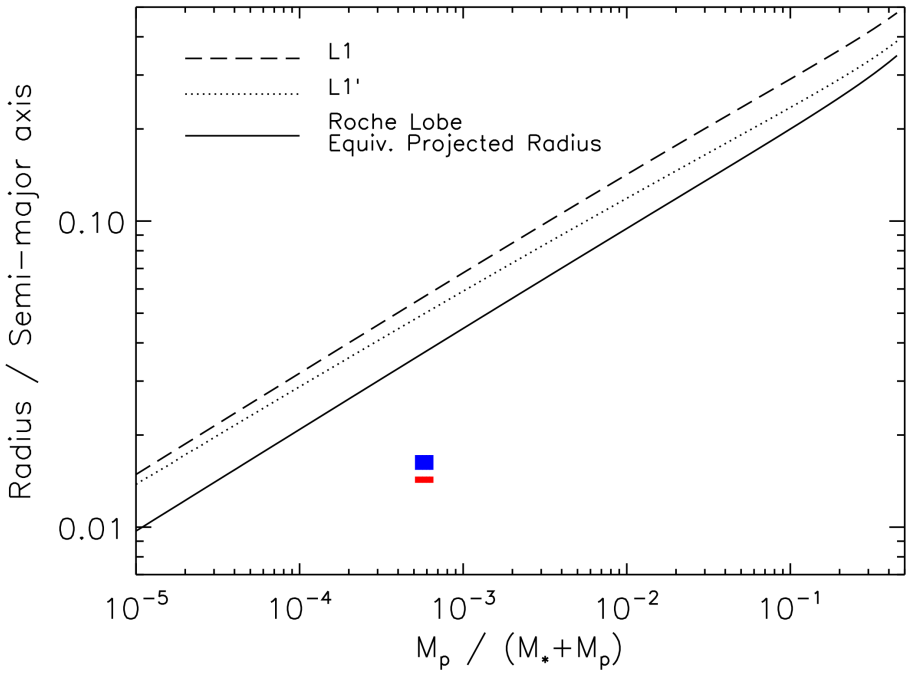

Figure 3.11: ratio of the Roche lobe size to the orbital semi-major axis as a function of the planet-to-star mass ratio. The size of the Roche lobe can be calculated using the distance of the planet centre to the L1 point (dashed line), to the L1′ point (dotted line) or by calculating the projected size of the Roche lobe occulting the stellar disk during a transit observation. This last size is about 2/3 of the size calculated by considering the L1 or L1′ points. The measurements for WASP-79 b in the NUV white light curve and at 2400Å are plotted in red and blue, respectively.

The high thickness of the atmosphere detected at 2400 Å raises the question of possible geometrical escape as defined by Lecavelier des Etangs et al. (2004), which occurs when the Roche lobe is filled up with the upper atmospheric gas. Thus, the high altitude of absorbers detected at the shortest wavelengths needs to be compared to the size of the Roche lobe. For that purpose, we calculated the distance of the L1 and L1′ Lagrange points of the equipotential surface to the planet centre as a function of the planet-to-star mass ratio (Figure 3.11). We also calculated the equivalent radius of the occulted area during a Roche lobe transit. Because of the elongated shape of the Roche lobe, this equivalent radius is about 2/3 of the distance between L1 and the planet center (Vidal-Madjar et al., 2008; Sing et al., 2019).

For WASP-79 b, we found that with a planet-to-star mass ratio of 5.8×10^{-4} and a semi-major

axis to star radius ratio of $a/R_\star = 7.407$, the transit of the Roche lobe corresponds to an occultation by a disk with a radius of 0.276 times the radius of the star. The measured radius at 2400 Å is only 44% this size. Even the highest values in the narrow band spectrum correspond to about 76% the size of the Roche lobe. Therefore, none of the absorption depths measured in the spectrum of WASP-79 b reaches the absorption that an optically thick Roche Lobe would cause. We are left to consider that the detected absorptions are due to components at high altitudes of the upper atmosphere.

None of the absorption features exceeds the theoretical Roche Lobe radius. There is no evidence of atmospheric hydro-dynamical escape in our NUV transmission spectrum.

3.4.3 Impact of Faculæ on the transmission spectrum

In their analysis of the transit spectrum of WASP-79 b, Rathcke et al. (2021) have shown that the spectrum from 0.3 to 1.0 µm is significantly affected by the presence of faculæ on the stellar surface. They found that about 15% of the stellar photosphere is covered by faculæ that is ~ 500 K hotter than the mean temperature of the star. Because of their different black body temperatures, faculæ and spots modify the planet-to-star radius ratio measured through transit observations, even if the planet does not pass in front of these features (Pont et al., 2013; McCullough et al., 2014).

In the presence of unocculted stellar spots or faculæ the measured radius ratio $(R_P/R_\star)_{mes}$ is given by

$$\left(\frac{R_P}{R_\star}\right)_{mes} = \left(\frac{R_P}{R_\star}\right)_{real} \Bigg/ \sqrt{1 - f \cdot \left(1 - \frac{F_{spot}(\lambda)}{F_\star(\lambda)}\right)}$$

where $(R_P/R_\star)_{real}$ is the real physical radius ratio, f is the fraction of the stellar area covered by the spots or faculæ, and $F_{spot}(\lambda)$ and $F_\star(\lambda)$ are the specific intensities of the spots (or faculæ) and the star, respectively. Assuming a black body at 6600 K, we have $F_\star(2300\,\text{Å}) = 1.4 \cdot 10^7\,\mathrm{W\,m^{-2}\,str^{-1}\,\mu m^{-1}}$, and $F_\star\,(3000\,\text{Å}) = 3.4 \cdot 10^7\,\mathrm{W\,m^{-2}\,str^{-1}\,\mu m^{-1}}$. With a 500 K higher temperature of 7100 K for the faculæ we have $F_{spot}(2300\,\text{Å}) = 2.76 \cdot 10^7\,\mathrm{W\,m^{-2}\,str^{-1}\,\mu m^{-1}}$, and $F_{spot}(3000\,\text{Å}) = 5.72 \cdot 10^7\,\mathrm{W\,m^{-2}\,str^{-1}\,\mu m^{-1}}$.

Finally, with $f = 0.15$, we obtain that the measured radius ratio is larger than the actual ratio by a factor of 1.07 at 2300Å and 1.05 at 3000Å. Therefore, the increase in the planet-to-star ratio toward shorter wavelengths between 3000 Å and 2300 Å due to the faculæ is only about 2%. Even if we consider the extreme case of the error bars given by Rathcke et al. (2021), that is 25% of the stellar surface covered by faculæ with ΔT=900 K, we found an increase of only 6%. To reproduce the observed ∼20% increase in planet ratio, the faculæ should have a brightness temperature of at least 9 000 K over 15% of the stellar disk. So, even if a blackbody is a poor approximation of the faculæ in the UV, unrealistic brightness for those would be required to explain the observations. Although the unocculted faculæ have some effect on the measured radius ratio, this effect is negligible. It does not explain the observed amplitude of the increase in the radius ratio toward shorter wavelengths.

3.4.4 1D and 2D atmospheric simulations

The NUV transmission does not show evidence of photo-evaporation. Yet, it presents high atmospheric features proving the presence of clouds, hazes or atomic species at very high altitudes in the atmosphere of WASP-79 b while optical observations (Sotzen et al., 2020; Skaf et al., 2020) using HST/WFC3 G141 suggest the presence of H_2O and FeH in deeper layers. We decided to compare the observations to the predicted atmospheric composition and temperature profile by modelling the interior of the planet using `Exo-REM` (Exoplanet Radiative-convective Equilibrium Model) (Baudino et al., 2015; Charnay et al., 2018; Blain et al., 2021). `Exo-REM` is a self-consistent software for brown dwarfs and giant exoplanet atmospheric simulations. The model will be presented in more detail in Chapter 5.

The stellar and planetary parameters are set to those of Table 3.1. The light source spectrum

is modelled using PHOENIX (Allard et al., 2012) with an effective temperature of 6600 K, a surface gravity of $\log g = 4$ and solar metallicity. We calculate the structure of the atmosphere of WASP-79 b using 71 layers between 10^{-8} and 10^{3} bar. We included 13 absorbing species (CH_4, CO, CO_2, FeH, H_2O, H_2S, HCN, K, Na, NH_3, PH_3, TiO, VO) using k-coefficient tables computed with a resolving power of 500 and 3 collision induced absorption sources (H_2-H_2, H_2-He, H_2O-H_2O). The chemistry is allowed to be out of equilibrium for the different species. We used a 10 × solar metallicity and a constant eddy diffusion coefficient of 10^8 cm^2/s. We initialised the temperature/pressure profile to an isothermal one using the equilibrium temperature of WASP-79 b. Then we used the results of the first 25 iterations of the modelling to set the a priori temperature profile. We obtained a solution using a retrieval tolerance for the flux convergence of 0.01.

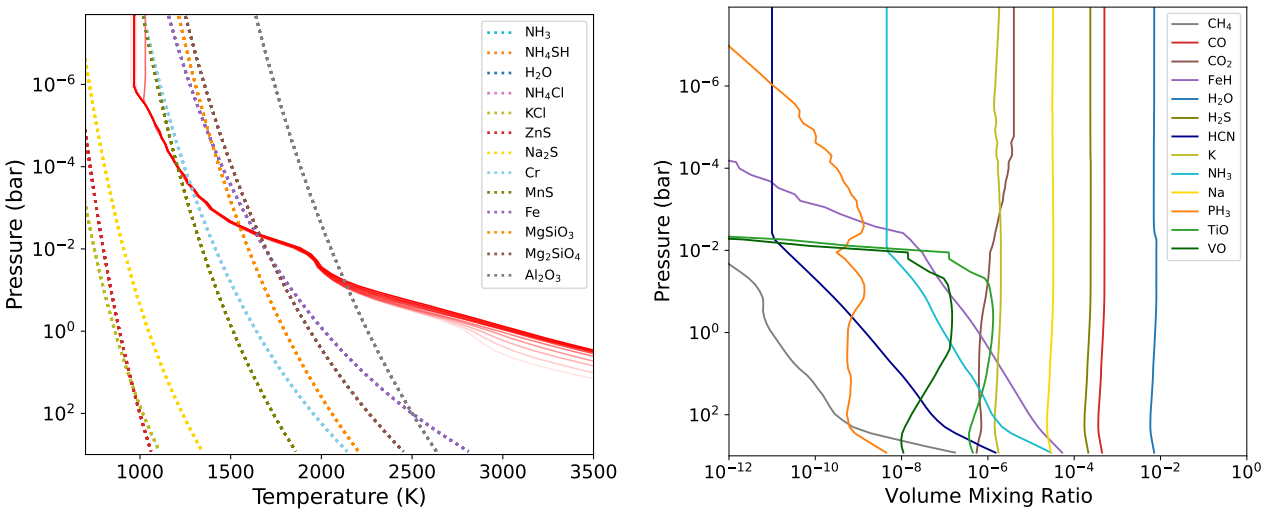

Figure 3.12: Temperature-pressure profiles (solid line) of WASP-79 b atmosphere (top) assuming radiative transfer equilibrium and condensation curves (dotted lines). The atmospheric structure is computed for different interior temperatures from 350 K (light red) to 800 K (red). Gas species abundances in WASP-79 b atmosphere (bottom) obtained with `Exo-REM`, assuming a 10 × solar metallicity, non-equilibrium chemistry, an Eddy diffusion coefficient of 10^8 cm^2/s and an interior temperature of 600 K.

Figure 3.12 shows the calculated abundances in volume mixing ratios of gas species and the temperature pressure profiles of WASP-79 b atmosphere using `Exo-REM` between 10^{-8} and 10^{3} bar for various interior temperatures ranging from 350 to 800 K. The gas abundances are represented for the T-P profile obtained with an interior temperature of 600 K and all the simulations are made using a clear atmosphere and metallicity of 10 × the solar value. At high altitudes, the main gas species are H_2O, CO, H_2S in the atmosphere of WASP-79 b. FeH abundance remains below 10^{-6} even at pressure probed by HST/WFC3 ($\sim 10^{-1}$ and 10^{-3} bar). The temperature profile crosses the condensing lines of Cr, MnS, $MgSiO_3$, Mg_2SiO_4 between 10^{-5} and 10^{-2} bar. Deeper in the atmosphere, below 10^{-2} bar, different species like TiO and VO are becoming more abundant with volume mixing ratios reaching 10^{-6} and 10^{-7}, respectively. We note that a very hot thermosphere could also explain large transit depths at short wavelengths (Yelle, 2004), and we will consider it as future modelling improvements.

According to the Gao et al. (2020) study on hot-Jupiter cloudiness as a function of temperature, the WASP-79 b spectrum should be dominated by clouds, in particular by Mg_2SiO_4 around 1700 K. After simulating a clear atmosphere with no clouds, we include different clouds in separate simulations with a fixed sedimentation parameter set to 2. The metallicity is set to 10 × the solar value, and the interior temperature is fixed to 600 K. Figure 3.13 (top) compares the HST transmission observations with forward models that include different condensing species. We indicate the Chi-squared (χ^2) results for each model. We use our NUV measurements from the broadband analysis on Observations 2 and include the large band value after 2500 Å, similar to Figure 3.9. The value around 2400 Å does not

appear in Figure 3.13 for clarity, but is taken into account for Chi-squared computations. χ^2 results indicate that forward models tested here fit the HST transmission spectrum of WASP-79 b poorly. However, it seems to be best explained by a clear atmosphere. None of the clouds presented here can explain the high planet-to-star radius ratio above 0.12 found in both the broad and narrow bands analysis. Figure 3.13 (bottom) shows the simulated spectra using 1, 10, and 100 $\times$ solar metallicity as a comparison. The resolution of the spectra in the NUV does not allow us to distinguish between the three different metallicities. The observations in the NIR are best explained by the 10 $\times$ solar metallicity scenario, especially for the absorption feature of water at 1.4 µm. However, we note that the slope observed after 1.5 µm is not well fitted, and the atmosphere of WASP-79 b might have a slightly higher metallicity. WASP-79 b spectrum is consistent with a clear atmosphere, yet the planet could also present a cold cloudy limb and a clear limb on the other side that would differently shape the spectrum. We explore this 2D effect using the temperature grid presented in Moses et al. (2021) based on the `2D-ATMO` circulation model described in Tremblin et al. (2017). Figure 3.14 shows the temperature-pressure profiles for four different longitudes, where the 0° longitude corresponds to the sub-stellar point, using an effective temperature of 1700 K and a metallicity 10 $\times$ the solar value. The condensation curves are from `Exo-REM` simulations of WASP-79 b's atmosphere using the temperature-pressure profiles from the grid of Moses et al. (2021). KCl, ZnS and Na_2S could condense on the night 270° limb (purple line). As seen before, WASP-79 b spectrum suggests a clear atmosphere. We would then have a clear limb on the day side at 90° and a cloudy limb on the other side.

We used the two temperature-pressure profiles at longitudes of 90° and 270° as inputs for WASP-79 b simulations. We include clouds, i.e., KCl, Na_2S, and ZnS, for the cloudy limb simulation, and we remove them for the clear limb one. Figure 3.15 shows the modelled spectra for the clear and cloudy cases and the combined spectrum (blue) corresponding to a weighted mean of the two limbs' spectra. The combined spectrum does not improve the fit of WASP-79 b, and in particular, it does not fit water features around 1.4 µm. However, we must recall that the 2D grid was built for sub-Neptune planets and not for hot-Jupiters. Besides, H^- was not included in `Exo-REM` and therefore it is not present as an opacity source in those simulations, although H^- was detected in Sotzen et al. (2020) and Rathcke et al. (2021) analysis of the HST data. These species could also be affected by 3D effects, created on one limb and eliminated on the other, causing the spectrum to be shaped differently.

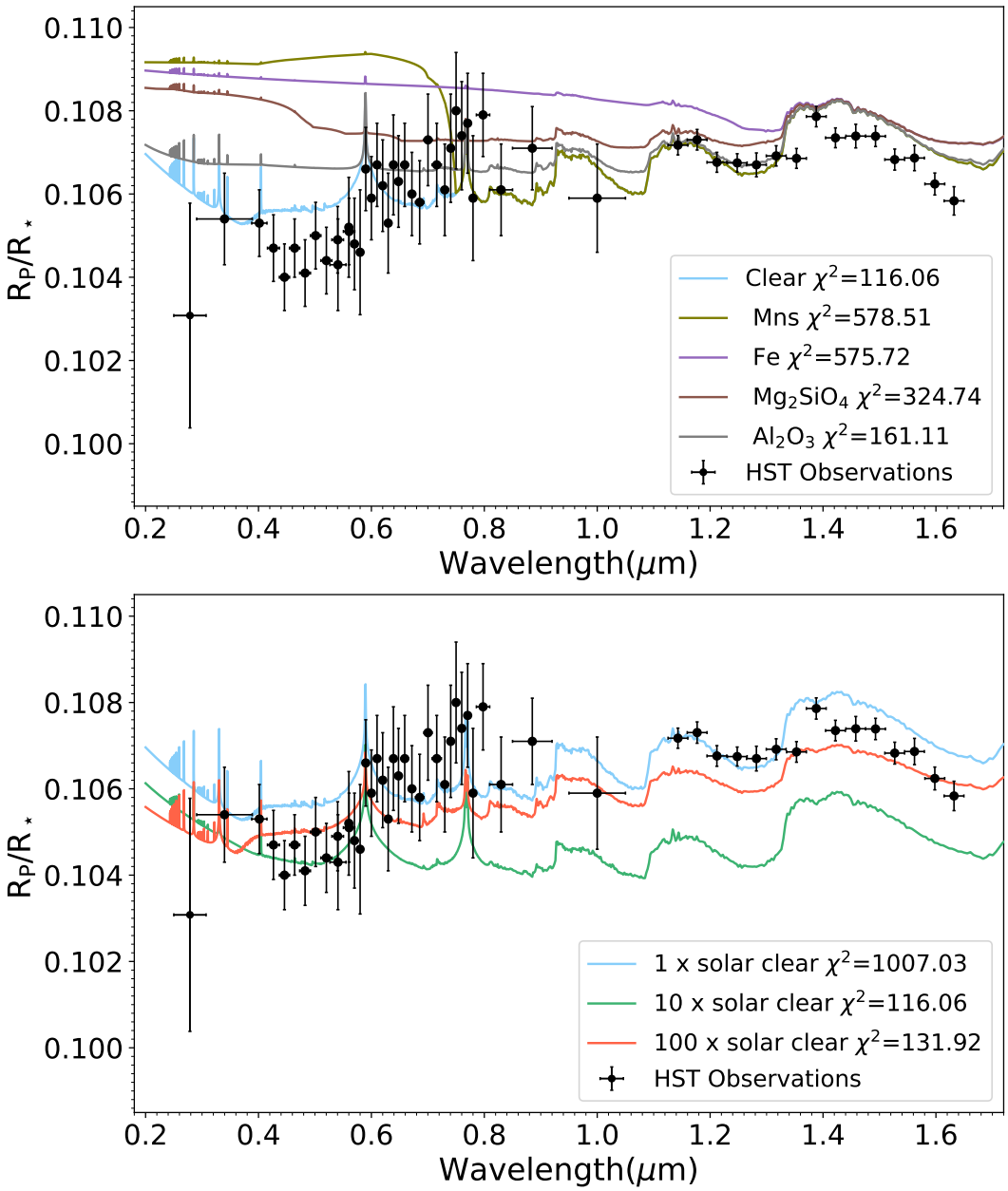

Figure 3.13: WASP-79 b HST transmission spectrum observations (black) and simulated spectra using `Exo-REM` (colors). WASP-79 b atmosphere is simulated using a 10 × solar metallicity, an interior temperature of 600 K, and we include different clouds (top). We also test a clear atmosphere while changing the metallicity of the atmosphere (bottom).

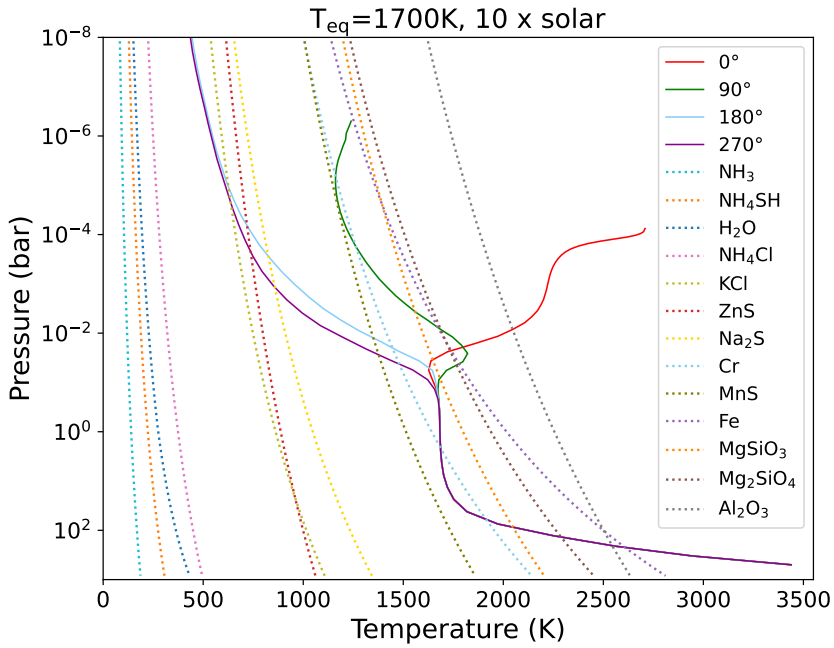

Figure 3.14: Temperature pressure profiles (solid lines) for four different longitudes. The 0° longitude corresponds to the sub-stellar point. The profile is obtained from the grid presented in Moses et al. (2021) based on the `2D-ATMO` circulation model described in Tremblin et al. (2017) for an effective temperature of 1700 K and a 10 × solar metallicity. Condensation curves (dotted lines) are from `Exo-REM` simulation using the same temperature and metallicity.

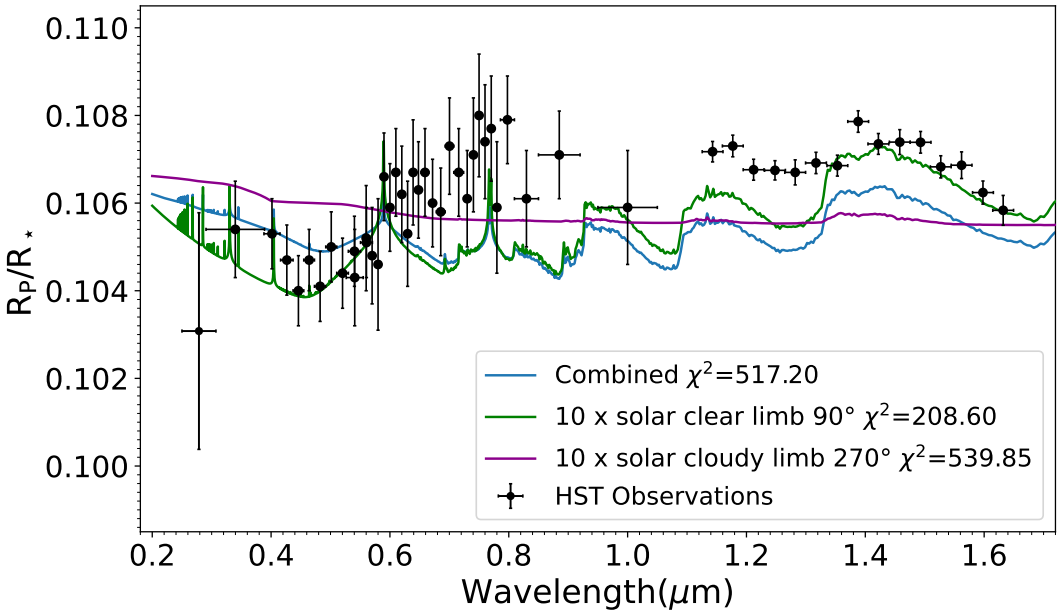

Figure 3.15: WASP-79 b HST transmission spectrum observations (black) and simulated spectra using `Exo-REM` (colors). WASP-79 b atmosphere is simulated using a 10 × solar metallicity and interior temperature of 600 K. We include KCl, ZnS and Na_2S on the night side (purple) simulation and remove clouds on the day side (green). The combined spectrum is in blue.

3.4.5 hot-Jupiter near-UV absorption

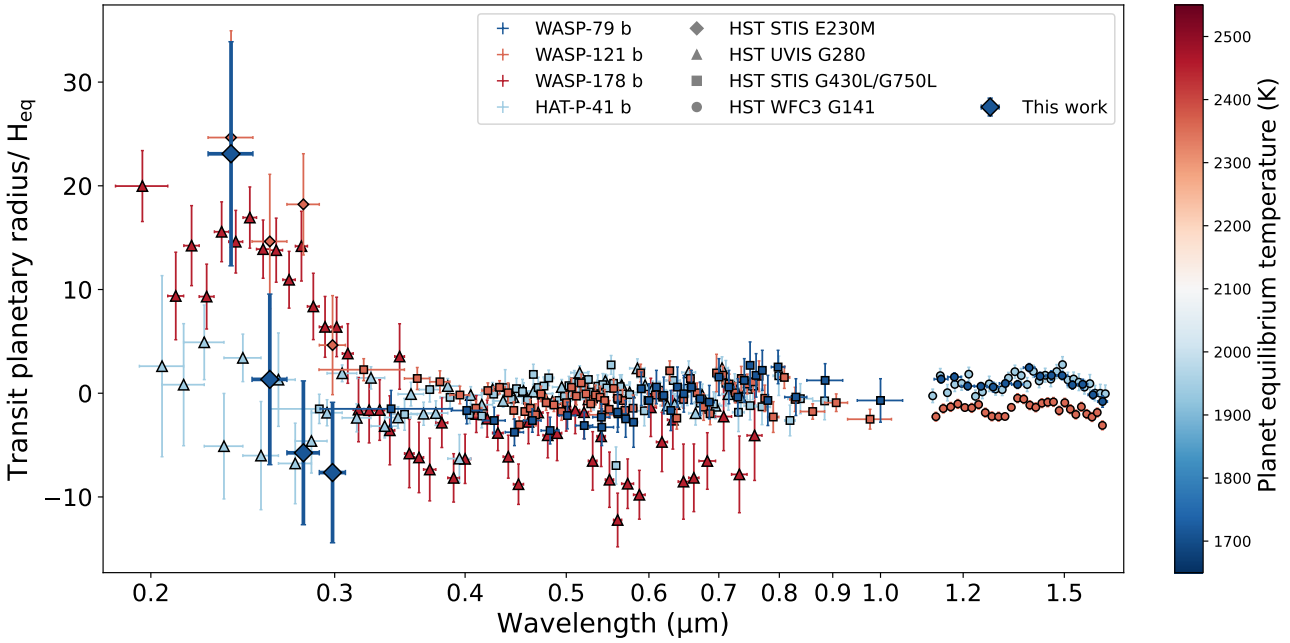

Figure 3.16: NUV to NIR transmission spectra normalised by the scale height for WASP-79 b (T_{eq}=1716 K) and additional three hot-Jupiters: WASP-121 b (T_{eq}=2358K) (Evans et al., 2017, 2018), HAT-P-41 b (T_{eq}=1941 K) (Wakeford et al., 2020; Sheppard et al., 2021) and WASP-178 b (T_{eq}=2450 K) (Lothringer et al., 2022). WASP-121 b and WASP-79 b's HST STIS E230M measurements are from this work. The formalism is similar to Figure 2 in Lothringer et al. (2022).

In Figure 3.16, we present the planetary transit radius normalised by the scale height with respect to the wavelength for four hot-Jupiters. We followed Lothringer et al. (2022) formalism and added our measurements of WASP-121 b and WASP-79 b planetary radius using HST STIS E230M (see Figure 2 of Lothringer et al. (2022)). We used HAT-P-41 b HST WFC3 UVIS observations from Wakeford et al. (2020) and HST STIS G430L/G750L and HST WFC3 G141 from Sheppard et al. (2021). WASP-121 b's HST STIS G430L/G750L and WFC3 G141 observations are from Evans et al. (2017, 2018), while WASP-178 b WFC3 UVIS G280 measurements are from Lothringer et al. (2022). Surprisingly, WASP-79 b's transit spectrum appears to show an absorption in the NUV similar to WASP-121 b and WASP-178 b, while their equilibrium temperatures are higher (∼2350 K and ∼2450 K for WASP-121 b and WASP-178 b, respectively). Among those, WASP-121 b's has the largest increase in the NUV absorption depth, with a depth increase larger than 30 times the atmospheric scale height. Conversely, the transit spectrum of HAT-P-41 b shows no increase in the absorption depth in the NUV despite its intermediate temperature (∼1950 K).

Lothringer et al. (2022) has interpreted the increase in the planet-to-star radius ratio at short wavelengths by the absorption of SiO, a precursor of condensate clouds, using simulations based on equilibrium chemistry. By comparing WASP-121 b, HAT-P-41 b and WASP-178 b transmission spectra, they put a first temperature constraint on silicate cloud formation. The condensation could begin on exoplanets with effective temperatures between 1950 and 2450 K. At short wavelengths, WASP-79 b displays a similar feature to WASP-121 b and WASP-78 b. Our large absorption measurement in the atmosphere of WASP-79 b, with an equilibrium temperature of 1716 K, challenges this direct interpretation. We showed that none of the strong absorption lines in the narrow band analysis was attributed to iron. Thus, the large absorption feature below 2400 Å could be interpreted as SiO absorption. Extended Figure 3 in Lothringer et al. (2022) shows the partial pressures of iron and silicon-bearing species as a function of temperature. Silicates and iron condense between 1500 and

2000 K, between 1 mbar and 10 bar for atmosphere with metallicities between 1 and 10 × solar. The lack of absorption in the atmosphere of HAT-P-41 b was explained in Lothringer et al. (2022) by the rainout of refractory species from the gas phase. We observed an absorption for WASP-79 b as high as for WASP-121 b and WASP-178 b (see Figure 3.16), making it a strong spectral feature observed in an exoplanet in terms of atmospheric scale heights at this temperature. How WASP-79 b avoided rainout whereas HAT-P-41 b did not remain puzzling.

3.5 Conclusion

We developed a method to analyse hot-Jupiters Hubble STIS/NUV E230M observations consistently and presented results for two hot-Jupiters. WASP-121 b 's data has already been analysed in Sing et al. (2019), but the application of our method on the same dataset confirmed the detection of Mg II and Fe II in the upper layers of WASP-121 b. We obtained a Near-UV transmission spectrum of WASP-79 b's atmosphere using new HST/STIS E230M data. We found an increase in the transit depth at short wavelengths (below 2600 Å). The difference between the radius ratios at 2400 Å and 3000 Å reaches 0.0191 ± 0.0042 ($\sim 4.5-\sigma$). A narrow band transmission spectrum at a resolution of 4 Å did not reveal particular absorption lines but confirmed the global increase in the planet's apparent radius at short wavelengths. Contrary to the exoplanet WASP-121 b, the highest values of the planet radius in the narrow band transmission spectrum do not exceed the Roche Lobe's equivalent radius but reach about 75% of its value. The absorption observed below 2500 Å corresponds to about 44% of the Roche lobe equivalent radius.

A rapid and straightforward evaluation of the possible impact of spot and faculæ on the transmission spectrum is performed in the discussion section using a black-body spectrum. A more realistic evaluation of the fraction of the stellar area covered by the spots or faculæ could be assessed using an atmospheric model. However, non-solar type stars spectra and faculæ are poorly known. Our first approximation shows that the effect of stellar activity on the planet's radius is negligible and does not explain the amplitude of the observed features. Given the order of magnitude, a more advanced model would not affect the overall result, and the conclusion would remain similar.

A 1D simulation of the deeper layers of the atmosphere was performed using `Exo-REM` with non-equilibrium chemistry and a ten times solar metallicity. The temperature pressure profile crosses condensation curves of radiative clouds like MnS, Fe, Mg_2SiO_4, or Al_2O_3. Nevertheless, none of those absorbing species (i.e. Fe, Mg) can explain the observed increase in the planet's radius at short wavelengths. The overall HST transmission spectrum suggests a clear atmosphere for WASP-79 b, but the planet might be tidally locked, and 3D effects could play an important role. We explored the 3D/2D effects using the temperature-pressure profiles grid from Moses et al. (2021) based on `2D-ATMO` of Tremblin et al. (2017). Clouds made of KCl, Na_2S, and ZnS could be created on one side and evaporated on the other.

The comparison of WASP-79 b's transmission spectrum with three other hot-Jupiters at short wavelength shows a surprisingly similar absorption around 2400 Å. While the HAT-P-41 b spectrum is flat, WASP-79 b, WASP-121 b and WASP-178 b display a large absorption features between 0.2 and 0.3 µm. This has been interpreted as SiO absorption by Lothringer et al. (2022) in the atmosphere of WASP-178 b. WASP-79 b's NUV excess absorption corresponds to more than 20 scale height, making it one of the largest spectral features observed in an exoplanet at this temperature (1716 K). If this feature is attributed to absorption by SiO, silicate cloud formation must be investigated to understand the disparity in this sample of hot-Jupiters. Further observations of WASP-79 b in UV could better

characterise this absorption. A combination of the present STIS E230M measurement with WFC3 UVIS observation could be of great interest, as suggested in Lothringer et al. (2022). Ground-based high-resolution observations of WASP-79 b 's atmosphere could also detect species like Fe or atomic Si and help us understand whether species are raining out. An increase in the number of exoplanets observed in the UV will help investigate the cloud formation in hot-Jupiters.

Chapter 4

Generalising the method: application to the Super-Earth 55-Cnc e

Contents

4.1 Introduction

This chapter takes the method described in Section 3.2 for processing hot-Jupiters HST STIS E230M observations and applies it to a Super-Earth: 55-Cnc e. The main difference is the signal level. The planet-to-star radius ratio of WASP-79 b is around 0.105 in the optical, which yields a transit depth of 1.10%. The planet-to-star radius ratio appears 16% bigger in the NUV with $R_P/R_\star$=0.1207, corresponding to a transit depth of 1.46%. 55-Cnc e has a planet-to-star radius ratio of 0.0182±0.0002 (Bourrier et al., 2018), corresponding to a transit depth in percentage of 0.033%. The result presented in this chapter are preliminary and not published.

4.2 Planet description

55-Cnc e is a Super-Earth, first discovered with a period of 2.808 days in 2004 by McArthur et al. (2004) using radial velocity observations with the Hobby-Eberly Telescope. The period was refined to 0.73 days in Dawson & Fabrycky (2010) and it was later detected in transit by Winn et al. (2011); Demory et al. (2012).

55-Cnc e has been massively studied as it is a prime target for transit spectroscopy. It has a very short period of 0.015 (AU), an elevated temperature of 1960 K (Demory et al., 2016) and orbits a nearby (12 pc) and very bright (V = 6.0) G8 type star. This is one of the brightest stars known to host planets. The planet's proximity to the star makes it a fascinating and complex planet to analyse, as intense planet-to-star interactions must occur. A large phase modulation has been detected by Winn

et al. (2011) and later shown to vary with time. The eclipse variability has been contested and might be due to instrumental systematic noise. 55-Cnc e has been shown to orbit within the Alfven surface of the stellar wind (Folsom et al., 2020). Demory et al. (2016) showed that the 300 % difference in occultation depth taken by Spitzer/IRAC between 2012 and 2013 could translate into a change in day-side brightness temperature of around 1200 K. Different scenarios could cause such a large occultation depth: volcanic activity on the surface, volatile loss through surface evaporation, or the presence of an inhomogeneous circumstellar torus of dust (Demory et al., 2016; Tamburo et al., 2018; Sulis et al., 2019). 55 Cancri e was already observed in several wavelength ranges: in IR (Demory et al., 2011, 2015; Demory et al., 2016), NIR (Tsiaras et al., 2016a) optical (Winn et al., 2011; Sulis et al., 2019), far-UV (Bourrier et al., 2018) and X-ray (Ehrenreich et al., 2014).

4.3 Methodology

4.3.1 Observations

The four available transit observations are from two HST programs, ID 14094 and 14917, of PI Vincent Bourrier and have not been published yet. The observations have been taken using the aperture of 0.2 x 0.2 centred at 2707 Å .The first observation consists of four HST orbits, while the other three have five HST orbits. The first orbit of each visit consists of 7 exposure points of 220 seconds. The other orbits are made of 8 exposure points of 234 seconds. The second orbit of Observation 3 has been deleted during the extraction. We have a total of 31 for Observations 1 and 3 and 39 for Observations 2 and 4.

Table 4.1: 55-Cnc e transit observations details from programs ID 14094 and 14917 of PI Vincent Bourrier.

Observations	**1**	**2**	**3**	**4**
Observing date	2016/04/17	2016/04/24	2017/05/12	2017/06/07
Number of orbits	4	5	4	5
Number of exposure per orbit	7/8	7/8	7/8	7/8
Exposure time (s)	220/234	220/234	220/234	220/234
Total exposures	31	39	31	39
Deleted exposures	exp.1 orb.1, 2, 4	exp.1 orb.1, 2, 3, 5 and exp.8 orb.3	exp.1 orb.5 and exp.2 orb.3,4	exp.1 orb.1, 2, 3, 5 and exp.6 orb.4
Total exposures for fitting	28	34	28	34

4.3.2 Data analysis

We applied the method previously described to HST observations of 55-Cnc e in the NUV using STIS E230M measurements to correct the systematics and adjust the light curves. In the previous analysis, the planet-to-star radius ratio is a free parameter and could take any value. For the analysis of 55-Cnc e, we applied an asymmetric lower constraint to the fitting process. The value is fitted between [-50%, + inf] of the latest fitted planet-to-star radius ratio. During the correction process, if the fitted planet-to-star radius ratio is out of the prior, the correction is not applied, and the value is set to the latest found planet-to-star radius ratio. This prior was added to the fitting method for 55-Cnc e's observations because we obtained unrealistic negative values during the fitting process.

Each transit observation is fitted separately, and we deleted specific data points by eye, to adjust the white light curve. In Figure 4.1, we plot the raw light curve for each visit normalised to the mean raw flux, and the deleted exposures are crossed out. The transit is represented in dotted lines and is

Table 4.2: Stellar and planetary parameters used in the white light curve fitting of 55-Cnc e observations. The mid-transit time is held fixed to the value of Endl et al. (2012) while the other parameters are taken from Bourrier et al. (2018). Limb-darkening coefficients are computed with a non-linear law using Claret et al. (2013) formalism.

Parameter	Values
Spectral Type	G8
$R_\star$ [$R_\odot$]	0.943 ± 0.010
$[Fe/H]_*$	0.35 ± 0.10
Teff$\star$ [K]	5172 ± 18
$\log_{10}\ g_\star$ [cgs]	4.43 ± 0.02
$R_p/R_\star$	0.0182±0.0002
$a/R_\star$	3.52 ± 0.01
i (deg)	$83.59^{+0.47}_{-0.44}$
e	0
P_{orb} (days)	$0.7365474^{+0.0000013}_{-0.0000014}$
T_{mid} (BJD_{TDB})	2 455 568.005±0.026
Limb-darkening coefficients	0.421889067, 0.175900403, 0.03832787, -0.067419199

barely visible as the planet-to-star radius ratio is set to 0.0182±0002 (Bourrier et al., 2018), hence a diminution of the total flux of around 0.03%, while the amplitude of the observed systematics reaches 6% of the total raw flux. For Observations 1, 2 and 4, we deleted the first exposure of out-of-transit orbits. Observation 3 is less affected by systematics; we decided to suppress three individual data located abnormally off the transit model (see Figure 4.1 bottom left). The last exposure of orbit 3 in Observation 2 and orbit 4 in Observation 4 is deleted. Once again, we can see that these specific data points are off the transit model by more than 100%. Keeping these exposures in the model can lead to over-fitting data during the engineering parameter and the corresponding polynomial degree selection. When possible, we kept all the exposures of the transiting orbit to capture the egress or ingress. We end up with 28 data points for Observations 1 and 3 and 34 or Observations 2 and 4. 55-Cnc e transit observations information and details on which exposure is deleted are summarised in Table 4.1. The planetary parameters used to adjust the light curve are in Table 4.2. We also indicate the limb-darkening coefficients, computed with the Claret et al. (2013) formalism using a non-linear law. The values where obtained with the `PyLightcurve`[1] (Tsiaras et al., 2016a) python package that uses `ExoTETHyS` (Morello et al., 2020)[2].

We fit only for the planet-to-star radius ratio, the normalised stellar baseline flux and coefficients of polynomials for the correction model. We include a linear correction of the planetary phase to correct for HST's thermal breathing for every observation except for Observation 3. The last orbit data points are located between phase 0 and phase 0.05 at the ingress of the transit. As the transit might not be totally captured, a phase correction could compromise the planet-to-star radius ratio fitting. The mid-transit time is used to extract the data and compute the planetary phase; it is then set to zero and not adjusted. We note that all available visits on 55-Cnc e are strongly affected by systematics (more than 100% of the transit value); hence the value found after correction must be carefully considered. Table 4.3 lists jitter engineering parameters and the corresponding degree of polynomial included in the white-light curves correction model for the four visits on 55-Cnc e. Polynomials included in the correction model for the four visits are presented in Appendix A.1, A.2, A.3 and A.4.

[1] https://github.com/ucl-exoplanets/pylightcurve
[2] https://github.com/ucl-exoplanets/ExoTETHyS

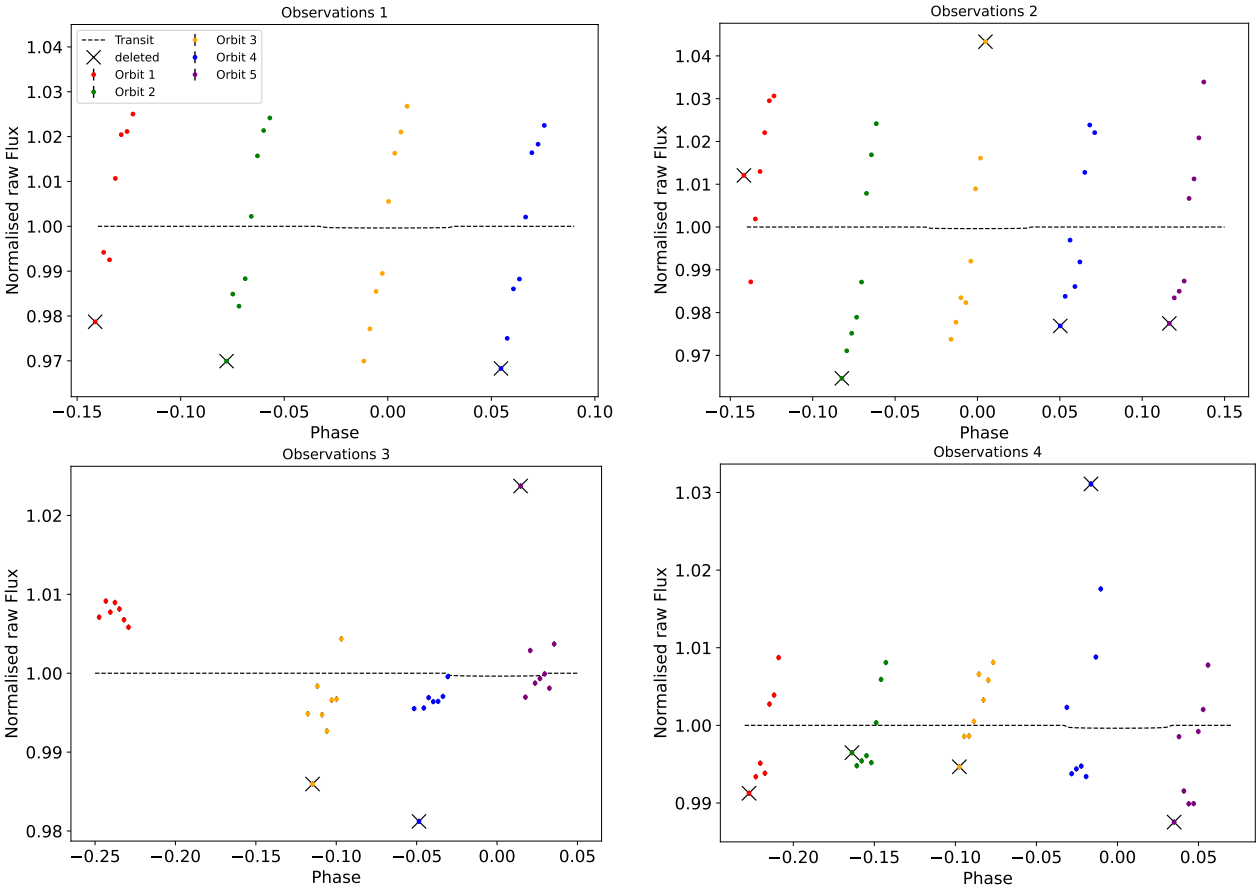

Figure 4.1: Normalised raw flux of 55-Cnc e four transit observations: Observations 1 (top left), Observations 2 (top right), Observations 3 (bottom left), Observations 4 (bottom right). The transit model is in a dotted line, computed for a planet-to-star radius ratio of 0.0182±0002 and centred at phase zero. Deleted exposure from the analysis are crossed out. Exposure data points are in red, green, yellow, blue and purple for Orbits 1, 2, 3, 4 and 5.

Table 4.3: List of the jitter engineering parameters and degree of polynomial included in the white-light curves correction model for the four visits on 55-Cnc e.

Parameters	**Observations 1**	**Observations 2**	**Observations 3**	**Observations 4**
phase	1	1	-	1
phase HST	-	1	-	2
v2_dom	-	1	3	-
v3_dom	2	1	-	-
v2_roll	-	3	1	1
v3_roll	-	4	4	-
si_v2_avg	-	-	1	1
si_v2_rms	2	1	-	-
si_v2_p2p	1	-	-	4
si_v3_avg	-	-	2	-
si_v3_rms	1	-	1	-
si_v3_p2p	3	1	-	-
ra	-	-	-	-
dec	-	-	-	-
roll	1	2	2	1
lat	1	3	-	-
long	-	-	1	-
limbang	2	2	-	-
los_zenith	-	-	-	1
mag_v1	-	7	-	-
mag_v2	-	-	-	8
mag_v3	7	-	4	3

4.4 Results

However, we present in Table 4.4 planet-to-star radius ratio and the corresponding uncertainty found from the best-fit of every visit. Even though the values are not consistent within 1σ, there are all significantly higher (four to five times) than the planet-to-star radius ratio found in the optical: between 0.08397±0.00150 and 0.10103±0.00119 for Observations 4 and 3 respectively, compared to 0.0182±0.0002. This result corresponds to a maximum transit depth of 1.021±0.024% in the NUV compared to 0.033±0.0007% in the optical. In Figure 4.2 we present the four corrected visits and the corresponding residuals. Observation 3 corresponds to the best fit in terms of χ^2. We have the start of the ingress and a clear-fitted egress. However, there is no post-transit baseline flux which could have dragged down the planet-to-star radius ratio. We computed the average planet-to-star radius ratio using all four visits and obtained 0.09353±0.00056. We used this value in Figure 4.3 to generate the transit model, and we over-plot the raw and corrected white light curves from the four observations. All visits are fitted independently, yet there is an overall good agreement when considering the high systematic level in the raw flux. The transit seems reconstructed while adding all the observations.

Using the same formalism as in the publication, the increase in planet size between the optical and the NUV is $\Delta R_P/R_\star$=0.075, which results in $\Delta R_P/H \approx 150$ with a scale height equal to 314km for a 2.31g/mol mean molecular weight and a constant gravity. If we consider that the gravity decreases with the altitude, we obtain a $\Delta R_P/H^{'} \approx 30$. However, the atmosphere of 55-Cnc e is unlikely to be hydrogen-dominated. Thus the weight of the atmosphere might be more elevated, resulting in a lower scale height and a more important absorption.

Table 4.4: 55-Cnc e white light curve planet-to-star radius ratio results

	Observations 1	**Observations 2**	**Observations 3**	**Observations 4**
$R_P/R_\star$	0.08582±0.00156	0.09626±0.00113	0.10103±0.00119	0.08397±0.00150
χ^2	164.86	114.38	61.70	162.19
Data points	28	34	28	34
Variables	23	28	21	24

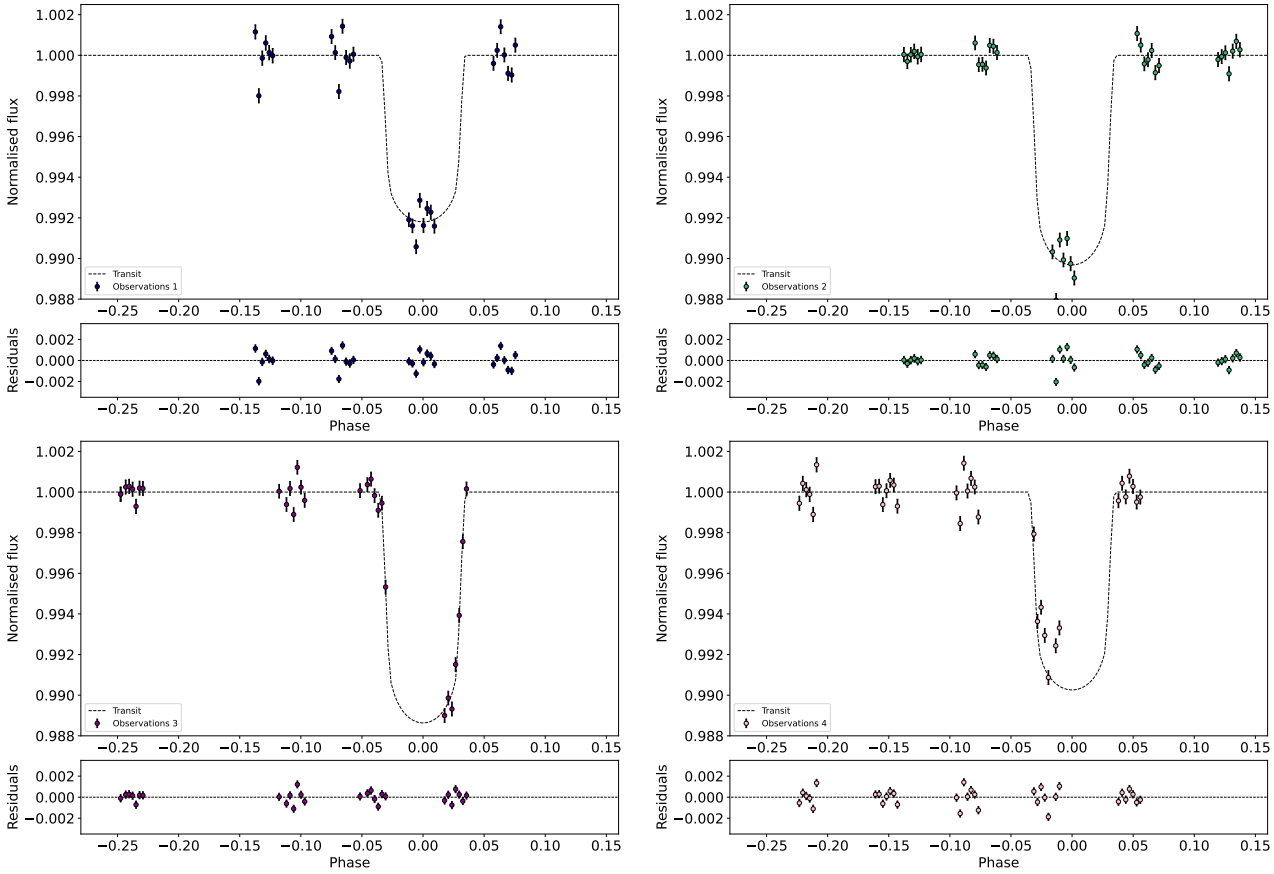

Figure 4.2: Normalised corrected flux of 55-Cnc e four transit observations. The transit model is in a dotted line and computed independently with the best fit planet-to-radius ratio found for each visit. Residuals are computed between the best-fit model and the corrected flux.

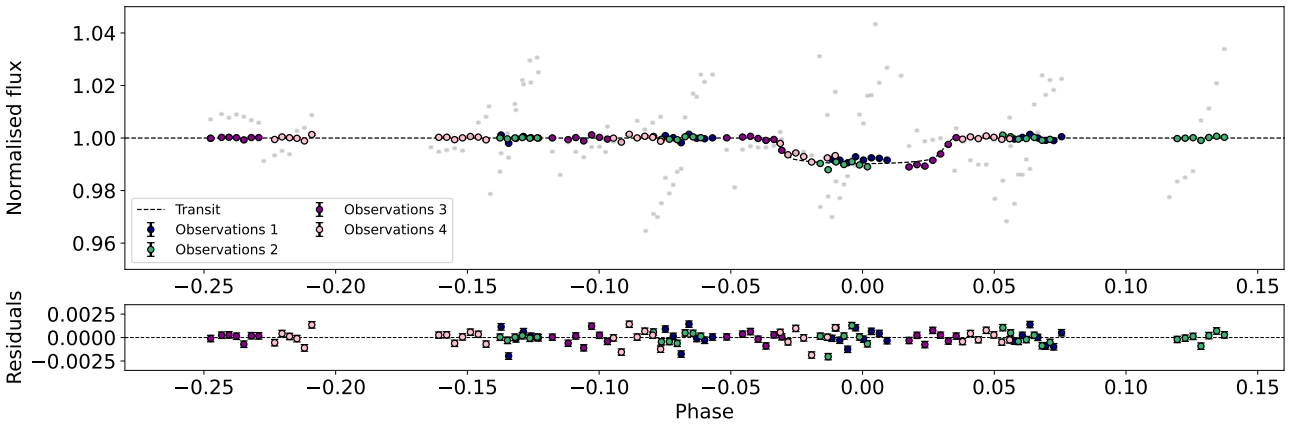

Figure 4.3: Normalised raw (grey) and corrected (colours) flux of 55-Cnc e four transit observations. The transit model is in a dotted line, computed for a planet-to-star radius ratio of 0.09353±0.00056 and centred at phase zero.

4.5 Conclusion

These results being preliminary, we decided not to go into more profound interpretations and implications of the observed absorptions. With low changes to the correction and fitting method described in Chapter 3 for hot-Jupiters, we adjusted the four observations of a very different planet: 55-Cnc e. The method is designed to automatically adjust HST/STIS/E230M planetary transit observations.

55-Cnc e data analysis is an excellent transition to the rest of the thesis, which addresses the observations and the modelling of smaller planets. We go deeper into the atmosphere and focus on Hubble NIR observations with the WFC3 to probe molecular absorption and understand the composition of Super-Earth and Sub-Neptune.

Part III

Observations: Hubble Near-IR data analysis

Chapter 5

Characterising two Neptune-like planets atmospheres with Hubble NIR observations

Contents

5.1 Introduction

This chapter is based on the publication **ARES IV: Probing the atmospheres of two warm small planets HD 106315 c and HD 3167 c with the HST/WFC3 Camera (Guilluy, Gressier et al. 2021)**. The paper was published in the Astrophysical Journal in January 2021 (see List of Publications). This work results from a collaboration with Gloria Guilluy started during the ARIEL 2019

summer school. I extracted, corrected and fitted the light curves of HD 106315 c and led the atmospheric retrieval analysis on both planets.

In this chapter, we analyse the transmission spectrum of the Neptune-type HD 106315 c and of the sub-Neptune HD 3167 c, using publicly available observations from the Hubble Space Telescope (HST) Wide Field Camera 3 (WFC3) operating in its spatial scanning mode. First, we briefly describe the planetary systems studied in this chapter. In Section 5.3, we detail the extraction and reduction process to obtain a 1D transmission spectrum from the WFC3 G141 raw images and present the data analysis through atmospheric modelling. We present the results of the light curve fitting and the atmospheric retrieval analysis in Section 5.4 before discussing our findings in Section 5.5. Two independent analyses of the same dataset for HD 106315 c and HD 3167 c, were led by Kreidberg et al. (2020) and Mikal-Evans et al. (2020). We refine parameters and figures and add a part comparing these two publications to our work compared to the initial publication **ARES IV: Probing the atmospheres of two warm small planets HD 106315 c and HD 3167 c with the HST/WFC3 Camera (Guilluy, Gressier et al. 2021)** (see List of Publications). We analyse the difference in the extraction of the 1D transmission spectrum and the consequence of the retrieval analysis results. We also attempt to compare the Bayesian modelling tools employed for atmospheric characterisation.

5.2 Planets description

5.2.1 HD 106315 c

HD 106315 c is a Neptune-like planet with a mass of 14.6±4.7 $M_\oplus$, a radius of 4.98±0.23 $R_\oplus$, and a density of 0.65±0.23 g cm^{-3}. It orbits an F5V star with a period of 21.05731±0.00046 days (this work, Table 5.1). Its equilibrium temperature, computed by assuming an albedo of 0.2 (Crossfield & Kreidberg, 2017), is 835±20 K. The planet has an inner-smaller companion HD 106315 b (R_P=2.18±0.33 $R_\oplus$, this work). The discovery of this multi-planetary system was simultaneously announced by Crossfield et al. (2017) and Rodriguez et al. (2017) using data from the K2 mission.

Due to the paucity of radial velocities measurements, both teams could not derive a precise measurement of the planetary mass, and only the High Accuracy Radial velocity Planet Searcher (HARPS) radial velocity observations by Barros et al. (2017) allowed a mass estimation. More recently, Zhou et al. (2018) reported also an obliquity measurement ($\lambda = -10.9^{\circ}{}^{+3.6}_{-3.8}$) for HD 106315 c from Doppler tomographic observations gathered with the Magellan Inamori Kyocera Echelle (MIKE), HARPS, and Tillinghast Reflector Echelle Spectrograph (TRES). We computed the atmospheric scale height assuming a primary mean molecular weight of 2.3 g/mol and found H∼518 ± 174 km. We also estimated the contribution to the transit depth of 1 scale height (40 ± 14 ppm) calculated by using the relationship that the change in transit depth due to a molecular feature scales as $2\,H\,R_p/R_\star^2$, Brown et al. (2001)). Given the host-star's brightness (V=8.951±0.018 mag, Crossfield et al. (2017)) and the precedent computations, HD 106315 c is an excellent target for transmission spectroscopy.

Planetary parameters refinement

From the comparison of the papers mentioned above (Crossfield et al., 2017; Rodriguez et al., 2017; Barros et al., 2017; Zhou et al., 2018), a difference emerges in the light-curve parameters of HD 106315 c, and in particular in the value of the planetary radius (R_P). On the one hand, the photometric studies by Crossfield et al. (2017); Rodriguez et al. (2017), and Barros et al. (2017) seem to converge toward a lower planetary radius (∼4 $R_\oplus$), but with big error bars (this is probably a consequence of having a light curve with a high impact parameter). More precisely, Crossfield et al. (2017) measured a planetary radius of $3.95^{+0.42}_{-0.39}$ $R_\oplus$, Rodriguez et al. (2017) of $4.40^{+0.25}_{-0.27}$ $R_\oplus$, and Barros et al. (2017) of

Table 5.1: Stellar and planetary parameters used in the observations analysis of HD 106315 c and HD 3167 c.

Parameter	HD 106315 c	HD 3167 c
Spectral type	F5V	K0V
$R_\star$ ($R_\odot$)	1.31 ± 0.04	0.835 ± 0.026
$M_\star$ ($M_\odot$)	1.079 ± 0.037	0.877 ± 0.024
$T_\star$ (K)	6256 ± 51	5286 ± 40
log(g)	4.235 ± 0.030	4.53 ± 0.03
Fe/H	-0.276 ± 0.083	0.03 ± 0.03
R_p ($R_\oplus$)	4.98 ± 0.23	$2.740^{+0.11}_{-0.10}$
M_p ($M_\oplus$)	14.6 ± 4.7	$8.33^{+1.79}_{-1.85}$
a (AU)	0.1531 ± 0.0017	0.1806 ± 0.0080
T_{eq} (K)	835 ± 20	518 ± 12
$a/R_\star$	25.10 ± 0.79	46.5 ± 1.5
$R_p/R_\star$	0.03481 ± 0.00099	$0.03006^{+0.00065}_{-0.00055}$
i (deg)	88.17 ± 0.11	89.6 ± 0.2
e	0.052 ± 0.052	$0.05^{+0.07}_{-0.04}$
b	0.798 ± 0.032	$0.30^{+0.11}_{-0.18}$
P_{orb} (days)	21.05731 ± 0.00046	$29.84622^{+0.00098}_{-0.00091}$
T_{mid} (BJD_{TDB})	2457569.0211 ± 0.0053	$2457394.97831 \pm 0.00085$
references	This work	Gandolfi et al. (2017)

4.35 ± 0.23 $R_\oplus$. On the other hand, the independent analysis by Zhou et al. (2018) resulted in a higher R_P value with smaller uncertainties (i.e. $R_P = 4.786 \pm 0.090$ $R_\oplus$). We decided to perform a combined analysis using spectroscopic and photometric observations to overcome these inconsistencies. More precisely, we included in our analysis ESO/HARPS radial velocities (Barros et al., 2017), space-based K2 data and three ground-based transits, namely one observation gathered with the Las Cumbres Observatory (LCO) telescopes (Barros et al., 2017) and two with the EULER telescope (Lendl et al., 2017). We modelled these data by employing the Markov Chain Monte Carlo (MCMC) Bayesian Planet Analysis and Small Transit Investigation Software (PASTIS) code (Dí az et al., 2014) as done in Barros et al. (2017). The improved system's parameters are listed in Table 5.1. In particular, if we compare our results to the previous papers, trying to break the inconsistency mentioned above on the R_P value, we note that our planetary radius is in agreement with that found by the spectroscopic analysis of Zhou et al. (2018).

5.2.2 HD 3167 c

HD 3167 c was discovered, together with an inner planet HD 3167 b ($R_P = 1.574 \pm 0.054$ $R_\oplus$), by Vanderburg et al. (2016b). Gandolfi et al. (2017) and Christiansen et al. (2017) then revised the system parameters and determined radii and masses for the two exoplanets. HD 3167 c has a mass of $M_P = 8.33^{+1.79}_{-1.85}$ $M_\oplus$, a radius of $R_P = 2.740^{+0.106}_{-0.100}$ $R_\oplus$ (Gandolfi et al., 2017), and a temperature of $T_{eq} = 518 \pm 12$ K (assuming an albedo of 0.2). It orbits its K0V host star with a period of $29.84622^{+0.00098}_{-0.00091}$ days. Given a mean density of $\rho = 2.21^{+0.56}_{-0.53}$ g cm^{-3}, HD 3167 c should have had a solid core surrounded by a thick atmosphere (Gandolfi et al., 2017). The brightness of the host star (V=8.94± 0.02mag, Vanderburg et al. (2016b)) combined with the atmospheric scale height (171 ± 40 km, calculated by assuming a primary mean molecular weight of 2.3 g/mol) and the contribution to the transit depth of one scale height (18±4 ppm, this work) make the planet a suitable target for atmospheric characterisation.

Table 5.2: Proposal information for the data used in the HST analysis of HD 106315 c and HD 3167 c

Planet	Proposal ID	Proposal PI	Transits used	HST orbit used
HD 106315 c	15333	Crossfield I.	4	20
HD 3167 c	15333	Crossfield I.	5	28

5.3 Methodology

5.3.1 Observations: Hubble WFC3 data reduction and extraction

We used the raw spatially scanned observations on HD 106315 c and HD 3167 c, part of the HST proposal GO 15333 (PI: Ian Crossfield) and downloaded from the public Mikulski Archive for Space Telescopes (MAST) archive. We use four and five transit observations of HD 106315 c and HD 3167 c, respectively, acquired with the G141 infrared Grism (1.125 - 1.650 μm) of the Hubble Wide Field Camera 3 (see Table 5.2). Each transit was observed over six and seven HST orbits for HD 106315 c and HD 3167 c, respectively. The observations were obtained with both forward (increasing row number) and reversed (decreasing row number) scanning.

To reduce and analyse the data, we used `iraclis`[1] (Tsiaras et al., 2016b,a, 2018), a publicly available pipeline, dedicated to the analysis of the scanned spectroscopic observations obtained with the near-infrared grism (G102, G141) of Hubble's Wide Field Camera 3. This tool includes data reduction and calibration, Light-curves extraction, Limb-darkening coefficients calculation, White light-curves fitting and Spectral light-curve fitting.

Data reduction and calibration

The reduction of the raw observations follows these steps: zero-read subtraction, reference pixels correction, non-linearity correction, dark current subtraction, gain conversion, sky background subtraction, flat-field correction, and corrections for bad pixels and cosmic rays.

Light-curve extraction

After the reduction and calibration of the raw images, we extracted the wavelength-dependent light-curves. In performing this operation, the geometric distortions caused by the tilted detector of the WFC3/IR channel are taken into account, as explained in Tsiaras et al. (2016b). Two kinds of light-curve were extracted: the white and spectral light curves. The white light curve is calculated from a broad wavelength band (1.09-1.68μm) covering the whole wavelength range of WFC3/G141. The spectral light curves consist of a set of light curves extracted using a narrow band with a specific resolving power. The 'high', 'low' and 'very low' resolutions correspond to a resolving power of 70, 50 and 10 at 1.4μm. We chose the spectral 'high' resolution to analyse HD 106315 c and HD 3167 c light curves. The bins were selected such that the signal-to-noise is approximately uniform across the planetary spectrum. We ended up with 25 bands, with bin widths in the range of 188.0-283.0nm.

Limb darkening coefficients

The stellar limb darkening effect is modelled using the non-linear formula with four terms from Claret et al. (2012, 2013); Claret (2018). The coefficients are calculated by fitting the stellar profile from an ATLAS model (Kurucz, 1970) and using the stellar parameters presented in Table 5.1. Table 5.3 shows the limb-darkening coefficients calculated for the white light-curve (between 1.125 - 1.650 μm).

[1] https://github.com/ucl-exoplanets/Iraclis

White light-curves fitting

The products of the previous steps are the white and spectral light curves. However, to obtain a transmission spectrum and go further with the atmospheric characterisation, we have to correct the data from the systematics and fit the light curves with a transit model. We correct for the time-dependent systematics introduced by HST: one long-term 'ramp' (which affects all the observations) with a linear (and, in some cases, a quadratic) trend and one short-term 'ramp' (which affects every HST orbit) with an exponential trend. To remove the systematics, we fit the white light curves with a transit model from the python package `PyLightcurve`[2] (Tsiaras et al., 2016a), multiplied by a model for the systematics. We account for the systematics in the white light curve fitting using the following formula, where t is time, T_0 is the mid-transit time, t_0 is the starting time of each HST orbit, r_{a1} and r_{a2} are the linear and quadratic systematic trend's slope, r_{b_1} and r_{b_2} are the exponential systematic trend's coefficients, and $n_W^{\rm scan}$ is a normalisation factor that changes for forward scanning ($n_W^{\rm for}$), and for reverse scanning ($n_W^{\rm rev}$):

$$\mathrm{R_w(t) = n_w^{scan}(t)(1 - r_a(t - T_0))(1 - r_{b_1} e^{r_{b_2}(t - t_0)})}. \tag{5.1}$$

Second-order (quadratic) observation-long ramps were also fitted for HD 3167 c observations because they were more affected by systematics. The parameter space was sampled using the package emcee (Foreman-Mackey et al., 2013). We used 300000 steps, 200 walkers, and 100000 burned iterations. We employed this setup for all the observations of both planets. The only exception is represented by the fourth observation of HD 106315 c, where we had to use 200000 iterations to obtain a good fit to our data.

Spectral light-curves fitting

We then fit for the planet-to-star radius ratio in every wavelength band. We used the white light curve divide method (Kreidberg et al., 2014a), each spectral light-curve is fitted with a model that includes the white light curve and its best-fit model, along with a spectral-dependent visit-long slope (Tsiaras et al., 2018) model to account for the systematic effects. Each spectral light curve is fitted with the following formula, with χ_λ being the slope for the wavelength-dependent systematic effects along each orbit, $\mathrm{LC_w}$ the white light curve signal, and $\mathrm{M_w}$ the white light curve best-fit model:

$$\mathrm{R_\lambda(t) = n_\lambda^{scan}(t)(1 - \chi_\lambda(t - T_0))\frac{LC_w}{M_w}}. \tag{5.2}$$

The only free parameter is $\mathrm{R_P/R_\star}$, while the other parameters are similar to the white light-curve fitting. Using the divide-white method presents the advantage that the residuals from fitting spectral light-curves do not show similar trends to the white light-curve. After the initial white light curve fit, the errors on each exposure were scaled to match the root mean square of the residuals. The white fitting was then performed a second time with these scaled errors. A similar scaling was also applied to the spectral light curves. This method ensures that the recovered uncertainties on the transit depth are not underestimated (Tsiaras et al., 2016b). As for the white light-curves fitting, the parameters space was sampled using the emcee method. In this case, we used 50000 emcee iterations, 100 walkers and 20000 burned iterations.

[2] https://github.com/ucl-exoplanets/pylightcurve

5.3.2 Data analysis: Atmospheric modelling

Description of the retrieval setups

We used `Tau-REx 3` [3] (Waldmann et al., 2015b,a; Al-Refaie et al., 2021) and the nested sampling algorithm Multinest (Feroz et al., 2009) with an evidence tolerance of 0.5 and 1500 live points to perform the atmospheric retrieval analysis. We used the software `PyMultinest` (Buchner et al., 2014) that connects Multinest to python. `Tau-REx 3` is a fully Bayesian code that maps the atmospheric parameters space to find the best-fit model for the transmission spectrum. It includes the molecular line lists from the ExoMol project (Tennyson et al., 2016; Chubb et al., 2021), HITEMP (Tennyson & Yurchenko, 2018), and HITRAN (Rothman et al., 1987; Rothman et al., 2013).

The atmosphere of the two planets was simulated by assuming an isothermal temperature-pressure (T/P) profile with molecular abundances constant as a function of altitude. These assumptions are acceptable since, due to the short wavelength covered by HST/WFC3, we are probing a restricted range of the planetary T/P profile (Tsiaras et al., 2018). We note that this may not be the case with next-generation space telescopes (Rocchetto et al., 2016; Changeat et al., 2019). We calculated the equilibrium temperatures of the two planets with the following formula where $R_\star$ is the stellar radius, a is the semi-major axis, and A is the geometric albedo.

$$\mathrm{T_{eq}} = \mathrm{T_\star} \left(\frac{\mathrm{R_\star}}{2\,\mathrm{a}} \right)^{1/2} (1 - \mathrm{A})^{1/4} \tag{5.3}$$

Assuming an albedo of 0.2 (Crossfield & Kreidberg, 2017), we obtained a temperature of 835 ± 20 K and 518 ± 12 K for HD 106315 c and HD 3167 c, respectively. We then used a wide range of temperature priors $\pm 60\%$ $T_{\rm eq}$ (334–1336 K for HD 106315 c, and 207–829 K for HD 3167 c) to allow different temperatures around the expected $T_{\rm eq}$. The planetary radius is also fitted in the model ranging from $\pm 50\%$ of the values reported in Table 5.1 (0.22-0.68 $\mathrm{R_J}$ for HD 106315 c, and 0.12-0.38 $\mathrm{R_J}$ for HD 3167 c).

We simulated atmospheres with pressures between 10^{-2} and 10^{6} Pa, uniformly distributed in log space across 100 layers. We considered the following trace-gases: H_2O (Polyansky et al., 2018), CH_4 (Yurchenko & Tennyson, 2014), CO (Li et al., 2015), CO_2 (Rothman et al., 2010), NH_3 (Yurchenko et al., 2011) and assumed the atmosphere to be H_2/He dominated. Each trace-gas abundance was allowed to vary between 10^{-12} and 10^{-1} in volume mixing ratios (log-uniform prior). We used absorption cross-sections at a resolution of 15000 and include Rayleigh scattering and collision-induced absorption of H_2–H_2 and H_2–He (Abel et al., 2011; Fletcher et al., 2018; Abel et al., 2012). Clouds are modelled assuming a grey opacity model, and cloud top pressure bounds are set between 10^{-2} and 10^{6} Pa. All priors are listed in Table 5.6. Recently, Kreidberg et al. (2020) presented a transmission spectrum of HD 106315 c based on HST/WFC3, K2, and Spitzer observations. They chose to add N_2 in the retrieval analysis of HD 106315 c to compensate for invisible molecular opacities that could impact the mean molecular weight. The high equilibrium temperature of HD 106315 c ($\sim$800 K) suggests the favoured presence of N_2. However, no further constraints have been found regarding N_2 opacity in the posterior distributions presented in Kreidberg et al. (2020). Considering this result and for consistency with HD 3167 c whose equilibrium temperature is lower ($\sim$500 K), we decided to consider NH_3 instead of N_2 in the retrieval analysis for both planets. This choice is mainly motivated by the low density of HD 106315 c ($\sim$600 kg/m^3), indicating, most likely, a primary light atmosphere. We did not add N_2 to the analysis to maintain a primary mean molecular weight ($\mu \sim$2.3 amu).

[3] https://github.com/ucl-exoplanets/TauREx3_public

Bayes factor and significance

We used a Bayes factor, $\Delta\log(\mathrm{E})$, to assign significance to our detection. The ADI (Atmospheric Detectability Index) described in (Tsiaras et al., 2018) is used to perform a similar analysis. It is positively defined as a function of the Bayes factor. The definition used here is a Bayes Factor between the nominal atmospheric and flat-line models. A flat-line model, only including a cloud deck, was performed to assess the significance of the different scenarios compared to a baseline. A baseline represents the lack of an atmosphere (e.g. an atmosphere with no spectral features) or a flat spectrum that a high-altitude cloud deck can only fit. The significance was computed using a Bayes factor, the logarithm difference between the best-fit model and the baseline model. The Bayesian evidence was computed using Bayes' theorem for a set of θ parameters in a model H for the data D (Feroz et al., 2009)

$$\mathrm{P}(\theta|\mathrm{D},\mathrm{H}) = \frac{\mathrm{P}(\mathrm{D}|\theta,\mathrm{H})\mathrm{P}(\theta|\mathrm{H})}{\mathrm{P}(\mathrm{D}|\mathrm{H})}, \tag{5.4}$$

where $\mathrm{P}(\theta|\mathrm{D},\ \mathrm{H}) \equiv \mathrm{P}(\theta)$ is the posterior probability distribution, $\mathrm{P}(\mathrm{D}|\theta,\ \mathrm{H}) \equiv \mathrm{L}(\theta)$ is the likelihood, $\mathrm{P}(\theta|\mathrm{H}) \equiv \pi(\theta)$ is the prior, and $\mathrm{P}(\mathrm{D}|\mathrm{H}) \equiv \mathrm{E}$ is the Bayesian evidence. The nested sampling method estimates the Bayesian evidence of a given likelihood volume, and the evidence can be expressed as follows:

$$\mathrm{E} = \int \mathrm{L}(\theta)\pi(\theta)\,\mathrm{d}\theta. \tag{5.5}$$

To compare the two H_0 and H_1 models, in our case, the flat-line model and the primary or secondary scenario, we can compute the respective posterior probabilities, given the observed data set D,

$$\frac{\mathrm{P}(\mathrm{H}_1|\mathrm{D})}{\mathrm{P}(\mathrm{H}_0|\mathrm{D})} = \frac{\mathrm{P}(\mathrm{D}|\mathrm{H}_1)\mathrm{P}(\mathrm{H}_1)}{\mathrm{P}(\mathrm{D}|\mathrm{H}_0)\mathrm{P}(\mathrm{H}_0)} = \frac{\mathrm{E}_1\mathrm{P}(\mathrm{H}_1)}{\mathrm{E}_0\mathrm{P}(\mathrm{H}_0)}, \tag{5.6}$$

where $\mathrm{P}(\mathrm{H}_1)/\mathrm{P}(\mathrm{H}_0)$ is the a priori probability ratio for the two models, which can often be set to unity (Feroz et al., 2009). We used the logarithm version of the model selection to compute the Bayes factor, $\Delta\log(\mathrm{E})$, between the flat-line and the tested model. The significance (σ) represents the strength of a detection, and it was estimated using a Kass & Raferty (1995), Trotta (2008), and Benneke & Seager (2013) formalism. We used Table 2 in Trotta (2008) and Table 2 in Benneke & Seager (2013) to find the equivalence between the Bayes factor and the significance σ and evaluate the strength of a detection. A Bayes factor of one corresponds to a significance of 2.1σ and is considered weak, a Bayes factor greater than three (3σ) is considered significant, and one superior to eleven (5σ) is considered as a strong detection. We define $\Delta\log(\mathrm{E})$ as:

$$\Delta\log(\mathrm{E}) = \log(\mathrm{E}_{\text{Atmospheric Model}}) - \log(\mathrm{E}_{\text{Flat line}}) \tag{5.7}$$

The atmospheric model can be considered a better fit than the flat-line if the $\Delta\log(\mathrm{E})$ is superior to the three. We also computed two other Bayes factors. $\Delta\log(\mathrm{E}_1)$ is used to compute the significance of molecule detection using a Bayes factor between the nominal atmospheric model and the same model without the considered molecule.

$$\Delta\log(\mathrm{E}_1) = \log(\mathrm{E}_{\text{Atmospheric Model with X}}) - \log(\mathrm{E}_{\text{Atmospheric Model without X}}) \tag{5.8}$$

The second one, $\Delta\log(\mathrm{E}_2)$, compares a given model to a model containing only water, Rayleigh scattering and collision-induced absorption as the reference Bayesian's evidence.

$$\Delta\log(\mathrm{E}_2) = \log(\mathrm{E}_{\text{Atmospheric Model}}) - \log(\mathrm{E}_{\text{Water only}}) \tag{5.9}$$

It is used to assess the necessity of a complex model to explain the atmosphere of the observed planet.

5.4 Results

5.4.1 Light curves fitting

Figures 5.1 and 5.2 show the light curves for all the transit observations of bot planets divided by the best-fit systematic model. In the fit we took T_0 and $R_P/R_\star$ as free parameters, and we used fixed values for P, ω, i, $a/R_\star$, and e parameters, as reported in Table 5.1. We decided to eliminate data gathered during the first HST orbit and the first two points of each orbit for both planets because of the observed stronger systematics. An incorrect fitting of the instrument's behaviour at this stage would have introduced additional uncertainties in the final values of the transit parameters. The original output images from `iraclis`, and used in the publication **ARES IV: Probing the atmospheres of two warm small planets HD 106315 c and HD 3167 c with the HST/WFC3 Camera (Guilluy, Gressier et al. 2021)** (see List of Publications) are in appendix B.1 and B.2. They present the distinction between forward and reverse scans and the auto-correlation of the residuals.

Processing Observations 3 and 4 for HD 3167 c required additional steps. HD 3167 b is also transiting the stellar disk during these observations causing a poor fitting of the white light curve. Strong auto-correlation in the fit residuals for Observations 3 and 4 led to an investigation of the orbits for both the transiting planets in the HD 3167 system: b and c. Theoretical transit light curves were plotted for all four HD 3167 observation windows, again using `PyLightcurve` and taking parameters for both planets from Gandolfi et al. (2017). The theoretical light curves showed no overlap between transits for the first two observations but contamination of the third and fourth observations by concurrent transits of HD 3167 b. This effect was limited to a single HST orbit in each affected observation in both cases. These two orbits were then disregarded, leaving six orbits for each of Observations 1, 2, and 5 and five orbits apiece for Observations 3 and 4. These affected orbits can be seen in Figure 5.3. The final fitting results and their uncertainties can be found in Table 5.3.

The spectral light curve fits for the first observation on each planet are plotted in Figures 5.4 and 5.5. All the spectral light curves fits for both planets and all observations are in Appendix B.3 and B.4. The final spectrum is extracted and combined from the spectral light-curves by computing the average of the transit spectra weighted by their respective uncertainties. First, we subtracted each spectrum by the corresponding white light-curve depth, and then we computed the weighted average of all the transit observations. Finally, we added the weighted average of all white light-curves values to the averaged spectrum. The white light transit depths were consistent between transits, except for Observations 3 on HD 3167 c (0.0291±0.0005 compared to the weighted mean 0.03058±0.00015). This is probably due to remaining systematics or stellar activity. The combined extracted spectrum and the increased S/N ratio are presented in Tables 5.4 and 5.5. The transmission spectra and the recovered final transit depth are over-plotted in Figure 5.6, which we then used for atmospheric retrieval.

Table 5.3: White light-curve fitting results for HD 106315 c and HD 3167 c.

Planet	Visit	T_0 HJD_UTC	Transit depth ppm	Limb darkening coefficients a_1	a_2	a_3	a_4
HD 106315 c	1	$2458453.3973^{+0.0003}_{-0.0002}$	1122±22	0.795044	-0.783874	0.928023	-0.395789
	2	$2458474.4537^{+0.0003}_{-0.0003}$	1040±22				
	3	$2458516.5668^{+0.0003}_{-0.0003}$	1084±29				
	4	$2458811.3661^{+0.0007}_{-0.0022}$	1048±26				
HD 3167 c	1	$2458260.52574^{+0.00016}_{-0.00014}$	920±20	0.853939	-0.762504	0.927610	-0.402020
	2	$2458320.2132^{+0.0018}_{-0.0016}$	944±21				
	3	$2458648.52966^{+0.00017}_{-0.00019}$	848±26				
	4	$2458708.220^{+0.005}_{-0.003}$	950±31				
	5	$2459036.5327^{+0.0019}_{-0.0022}$	956±14				

Table 5.4: Combined transit depth, associated uncertainties and limb-darkening coefficients. The final transmission spectrum was computed in ppm using the four HST/WFC3 G141 transit observations on HD 106315 c.

Wavelength	Bandwidth	Transit depth	Error	Limb-darkening coefficients			
μm	μm	ppm	ppm	a1	a2	a3	a4
1.1263	0.0219	1064	27	0.8644	-1.1412	1.4546	-0.6042
1.1478	0.0211	1098	19	0.8453	-1.0800	1.3799	-0.5748
1.1686	0.0206	1060	18	0.8388	-1.0537	1.3377	-0.5586
1.1888	0.0198	1065	19	0.8294	-1.0246	1.3038	-0.5473
1.2084	0.0193	1068	17	0.8162	-0.9786	1.2477	-0.5263
1.2275	0.0190	1063	19	0.8078	-0.9208	1.1763	-0.4992
1.2465	0.0189	1082	19	0.7953	-0.8977	1.1484	-0.4899
1.2655	0.0192	1029	18	0.7924	-0.8791	1.1243	-0.4848
1.2848	0.0193	1078	19	0.8103	-0.8370	0.9890	-0.4301
1.3038	0.0188	1046	17	0.7745	-0.8015	1.0185	-0.4424
1.3226	0.0188	1068	18	0.7696	-0.7734	0.9719	-0.4211
1.3415	0.0189	1080	19	0.7627	-0.7360	0.9229	-0.4034
1.3605	0.0192	1130	18	0.7604	-0.7152	0.8868	-0.3882
1.3801	0.0199	1096	18	0.7531	-0.6685	0.8136	-0.3568
1.4000	0.0200	1099	17	0.7511	-0.6382	0.7618	-0.3343
1.4202	0.0203	1086	17	0.7620	-0.6529	0.7644	-0.3345
1.4406	0.0206	1130	17	0.7597	-0.6218	0.7107	-0.3117
1.4615	0.0212	1126	19	0.7661	-0.6195	0.6967	-0.3072
1.4831	0.0220	1111	19	0.7728	-0.6291	0.6935	-0.3045
1.5053	0.0224	1116	17	0.7737	-0.6125	0.6555	-0.2864
1.5280	0.0230	1074	19	0.7781	-0.5887	0.6044	-0.2629
1.5516	0.0241	1106	20	0.7875	-0.5997	0.5936	-0.2535
1.5762	0.0253	1044	19	0.8026	-0.6526	0.6329	-0.2622
1.6021	0.0264	1062	19	0.8079	-0.6274	0.5694	-0.2309
1.6295	0.0283	1018	20	0.8038	-0.5891	0.5084	-0.2059
1.3750	0.5500	1074	12	0.7950	-0.7834	0.9280	-0.3958

Table 5.5: Combined transit depth, associated uncertainties and limb-darkening coefficients. The final transmission spectrum was computed in ppm using the five HST/WFC3 G141 transit observations on HD 3167 c.

Wavelength	Bandwidth	Transit depth	Error	Limb-darkening coefficients			
μm	μm	ppm	ppm	a1	a2	a3	a4
1.1263	0.0219	950	12	0.9786	-1.3596	1.7291	-0.7069
1.1478	0.0211	945	12	0.9515	-1.2748	1.6297	-0.6697
1.1686	0.0206	926	11	0.9293	-1.1977	1.5356	-0.6359
1.1888	0.0198	924	12	0.9176	-1.1635	1.4888	-0.6169
1.2084	0.0193	930	11	0.9041	-1.1196	1.4426	-0.6035
1.2275	0.0190	935	11	0.8800	-1.0354	1.3494	-0.5697
1.2465	0.0189	909	11	0.8710	-1.0034	1.3127	-0.5577
1.2655	0.0192	915	11	0.8573	-0.9471	1.2404	-0.5304
1.2848	0.0193	903	12	0.8583	-0.9165	1.1966	-0.5249
1.3038	0.0188	913	11	0.8358	-0.8621	1.1395	-0.4964
1.3226	0.0188	912	11	0.8262	-0.8153	1.0715	-0.4677
1.3415	0.0189	920	11	0.8131	-0.7556	1.0001	-0.4433
1.3605	0.0192	928	11	0.8059	-0.7123	0.9380	-0.4185
1.3801	0.0199	949	11	0.7936	-0.6385	0.8371	-0.3794
1.4000	0.0200	955	11	0.7922	-0.6039	0.7848	-0.3593
1.4202	0.0203	961	11	0.8066	-0.6400	0.8313	-0.3825
1.4406	0.0206	970	11	0.7881	-0.5412	0.6946	-0.3273
1.4615	0.0212	937	11	0.7894	-0.5070	0.6403	-0.3073
1.4831	0.0220	958	12	0.7894	-0.4730	0.5674	-0.2727
1.5053	0.0224	925	12	0.7932	-0.4536	0.5140	-0.2462
1.5280	0.0230	944	12	0.7958	-0.3606	0.3543	-0.1766
1.5516	0.0241	938	12	0.8126	-0.3496	0.2923	-0.1430
1.5762	0.0253	957	12	0.8467	-0.4497	0.3714	-0.1643
1.6021	0.0264	937	12	0.8740	-0.4581	0.3290	-0.1388
1.6295	0.0283	932	12	0.8950	-0.4586	0.3235	-0.1291
1.3750	0.5500	934	9	0.8539	-0.7625	0.9276	-0.4020

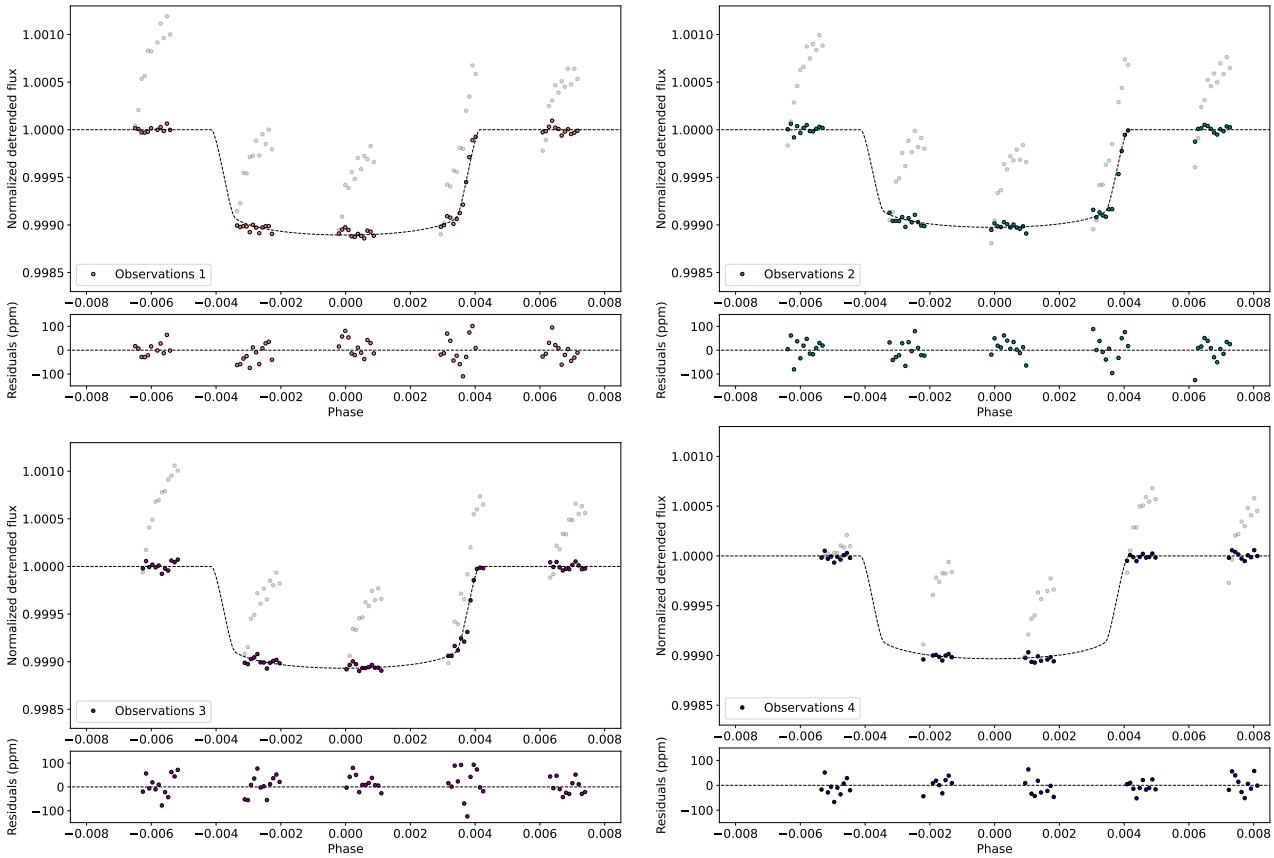

Figure 5.1: White light curve fits for the four observations on HD 106315 c. For every observation, we show the raw (grey) and de-trended flux (colour points), and the best-fit model (dotted lines) along with the residuals from the best-fit model.

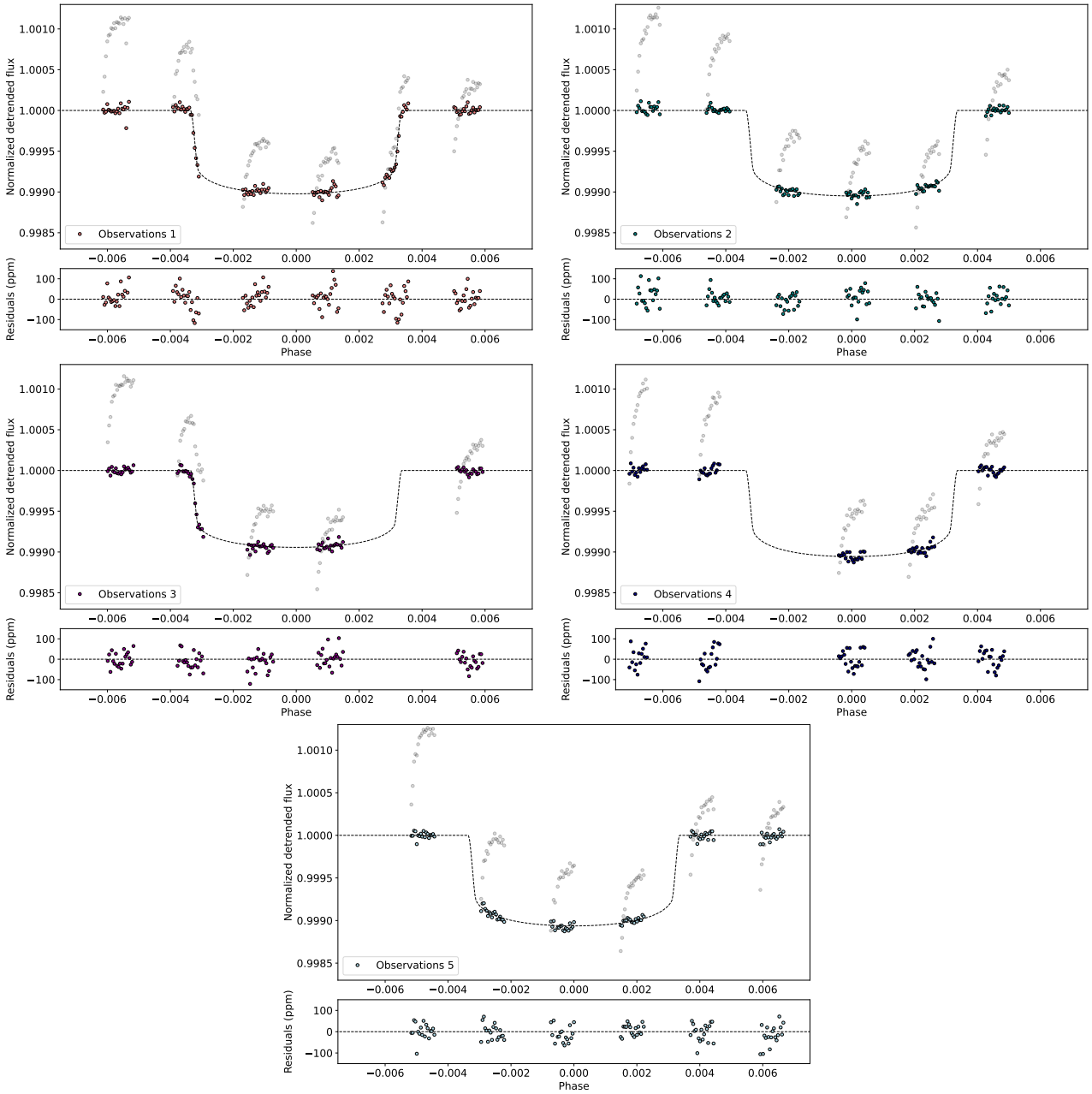

Figure 5.2: Same as Figure 5.1 for the five observations on HD 3167 c

.

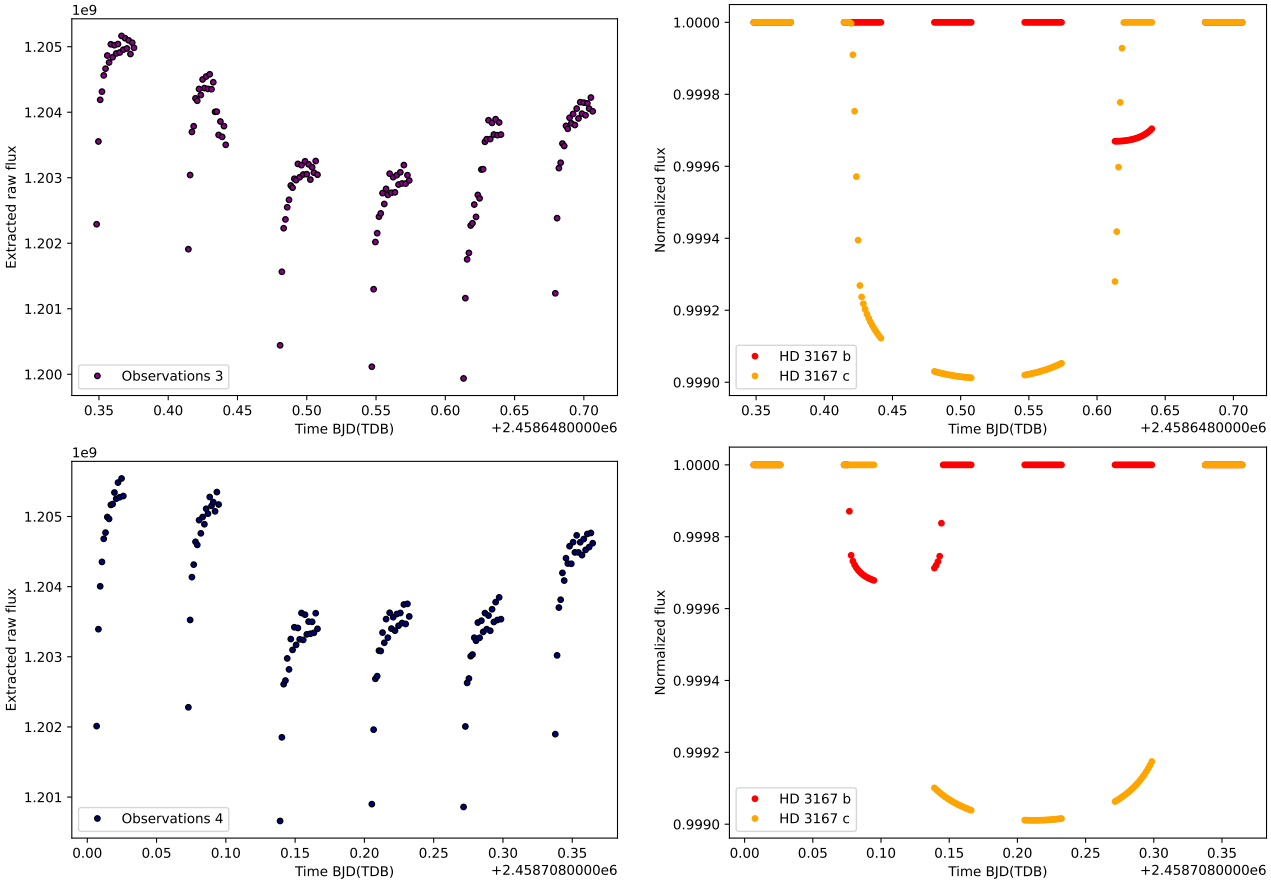

Figure 5.3: Left: Raw extracted light curves for HD 3167 c observations (top: Observations 3, bottom Observations 4). Right: Predicted planetary transits using `PyLightcurve` transits model and Gandolfi et al. (2017) system parameters at the time of the observations. HD 3167 b is transiting on orbit 6 of Observations 3 and orbit 3 of Observations 4.

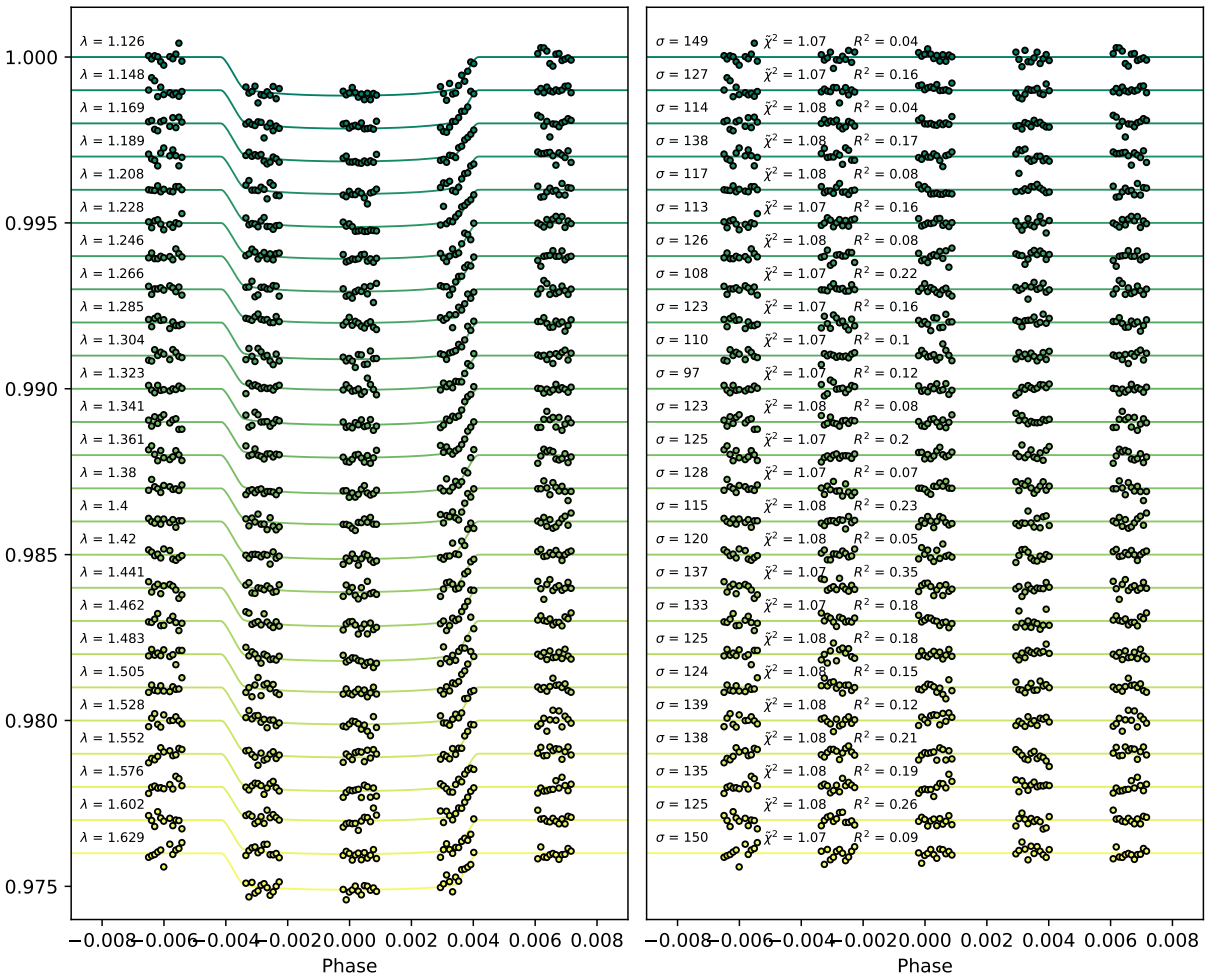

Figure 5.4: Spectral light curve fits for the first observation on HD 106315 c. An artificial offset in the y-axis was applied for clarity. For each light curve, the left panel shows the de-trended spectral light curves with the best-fit model in dotted lines, and the right panel shows the residuals and values for the standard deviation (σ) in ppm, the reduced Chi-squared ($\tilde{\chi}^2$), and the auto-correlation (R^2).

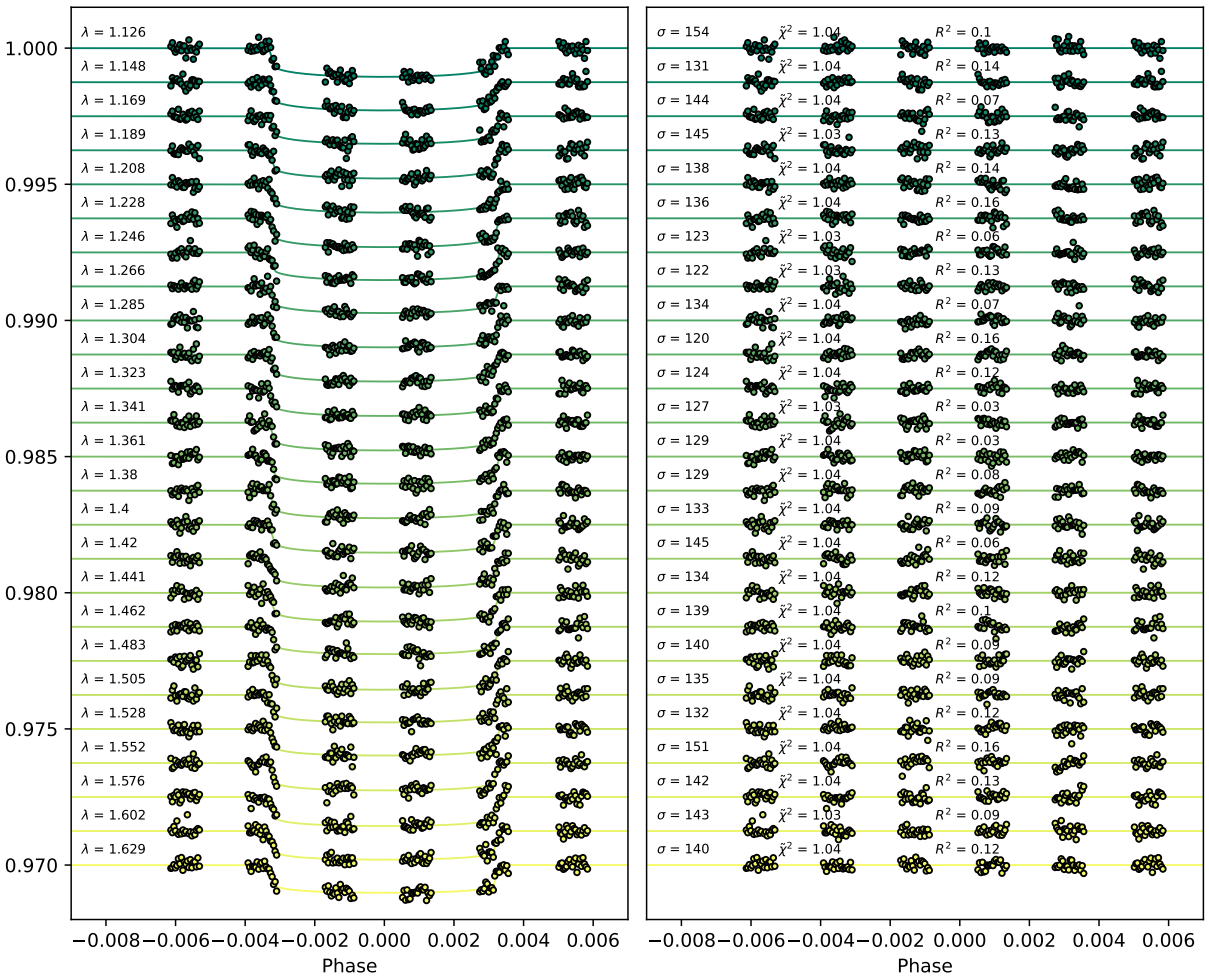

Figure 5.5: Spectral light curve fits for the first observation on HD 3167 c. An artificial offset in the y-axis was applied for clarity. For each light curve, the left panel shows the de-trended spectral light curves with the best-fit model in dotted lines, and the right panel shows the residuals and values for the standard deviation (σ) in ppm, the reduced Chi-squared ($\tilde{\chi}^2$), and the auto-correlation (R^2).

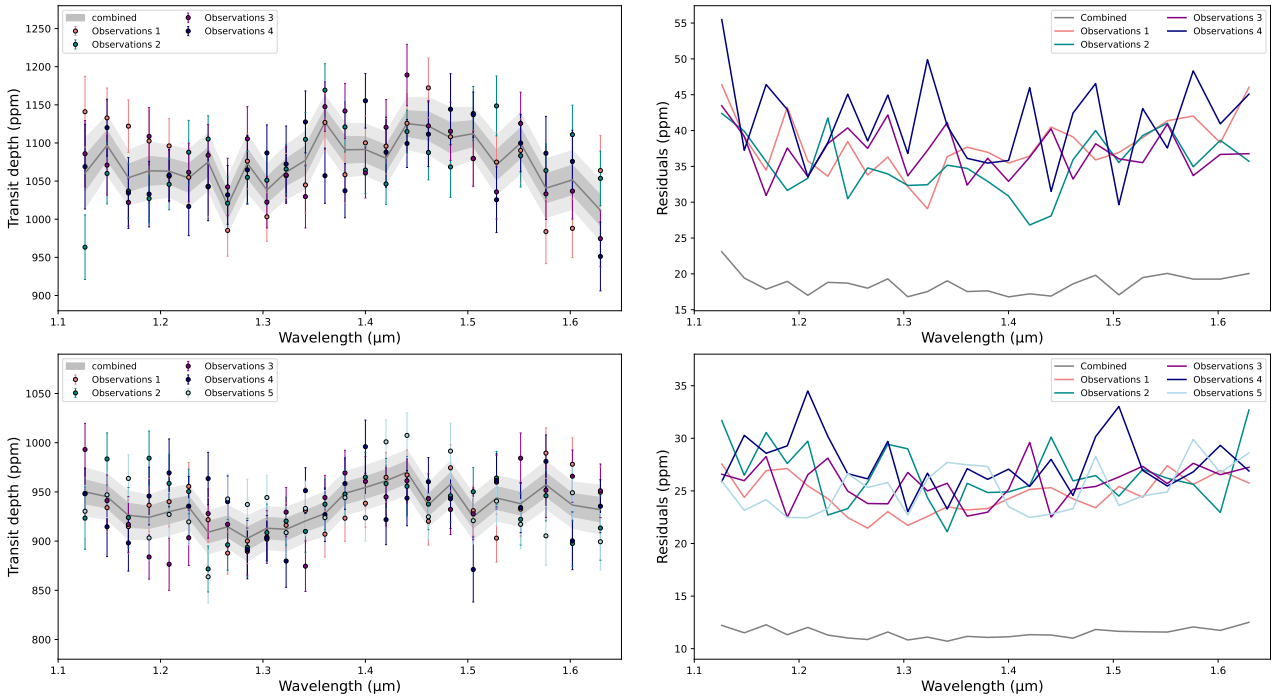

Figure 5.6: Recovered transit depths for all observations HD 106315 c (top) and HD 3167 c (bottom), and combined transmission spectrum with 1 and 2σ uncertainty ranges (left). First, we suppressed the white light curve values from each visit raw flux, computed the weighted mean, and added the mean white light curve value to obtain the transit depths. Residuals are from the spectral light curves analysis and the combined spectrum (right).

5.4.2 Atmospheric modelling

Table 5.6 lists `Tau-REx 3` retrieval results for the two planets, while retrieved best-fit spectra and corresponding best-fit molecular opacity contributions are shown in Figure 5.7. Posterior distributions are plotted in Figure 5.8 and Figure 5.9. For each opacity source, the contribution function is the transit depth we would obtain if the molecule were alone in the atmosphere. Therefore, the opacity sources, like H_2O in HD 3167 c (Figure 5.7 bottom right) are never fully dominant since there are always some residuals CIA, Rayleigh or other molecules that contribute to the model. Opacity contributions are represented for the best-fit model: the best solution is the one with the highest log evidence. The offset opacities correspond to molecules that do not contribute to the fit and are found to be unconstrained. The grey line in Figure 5.7 (bottom) represents the top cloud pressure retrieved by `Tau-REx 3` for the best fit solution. This layer theoretically blocks the signal, and nothing can be observed at higher pressures. Opacities found below this line are unconstrained. Using the Bayesian log evidences, we computed the $\Delta\log(E)$, $\Delta\log(E_1)$ and $\Delta\log(E_2)$ as explained in Section 5.4.2.

For both planets, retrieval results are consistent with water absorption features detectable in the spectral band covered by the G141 grism. We note a moderate detection of carbon-bearing species in the atmosphere of HD 3167 c consistent with CO_2 absorption features. This result is unexpected considering the planetary equilibrium temperature. CH_4 features are more likely to be present than CO_2 (Venot et al., 2020). Other species like NH_3, CO and CH_4 have either unconstrained or low abundances. They could be present in both atmospheres, but spectra do not present significant absorption features. We note, however, that NH_3 abundance is better constrained in the atmosphere of HD 106315 c (see Figure 5.8). Cloud top pressure is retrieved at different levels, $10^{3.7}$ Pa for HD 106315 c and $10^{5.3}$ Pa for HD 3167 c, corresponding to an upper bound (see the posterior distribution in Figure 5.8, and 5.9). The presence of molecular features in our spectra suggests a clear atmosphere for both planets. However, HD 106315 c atmospheric model might require a thick absorber at a higher level than HD 3167 c to fit the water feature correctly. However, the layer is probably located deep in the atmosphere, and if opaque clouds are present, they are located below the region probed by WFC3/G141 observations.

Table 5.6: Fit evaluation criteria and maximum a-posteriors retrieval results for HD 106315 c and HD 3167 c HST/WFC3 G141 data.

		HD 106315 c		**HD 3167 c**	
Parameter	Unit	Prior	Value	Prior	Value
T_P	K	$\mathcal{U}(334, 1336)$	630^{+326}_{-115}	$\mathcal{U}(207, 829)$	440^{+119}_{-79}
R_P	R_J	$\mathcal{U}(0.22, 0.68)$	$0.40^{+0.01}_{-0.02}$	$\mathcal{U}(0.12, 0.38)$	$0.25^{+0.01}_{-0.01}$
$\log_{10}(H_2O)$	dex	$\mathcal{U}(-12, -1)$	$-2.1^{+0.7}_{-1.3}$	$\mathcal{U}(-12, -1)$	$-4.1^{+0.9}_{-0.9}$
$\log_{10}(NH_3)$	dex	$\mathcal{U}(-12, -1)$	$-4.3^{+0.7}_{-2.0}$	$\mathcal{U}(-12, -1)$	< -5
$\log_{10}(CO_2)$	dex	$\mathcal{U}(-12, -1)$	unconstrained	$\mathcal{U}(-12, -1)$	$-2.4^{+0.7}_{-1.0}$
$\log_{10}(CO)$	dex	$\mathcal{U}(-12, -1)$	unconstrained	$\mathcal{U}(-12, -1)$	unconstrained
$\log_{10}(CH_4)$	dex	$\mathcal{U}(-12, -1)$	< -5	$\mathcal{U}(-12, -1)$	< -5
$\log_{10}(P_{clouds})$	Pa dex	$\mathcal{U}(-2, 6)$	$3.7^{+1.4}_{-1.3}$	$\mathcal{U}(-2, 6)$	$5.3^{+0.5}_{-0.5}$
μ (derived)	g/mol	-	$2.38^{+0.52}_{-0.07}$	-	$2.44^{+0.66}_{-0.13}$
$\Delta\log(E)$	-	-	15.97	-	9.58
$\Delta\log(E_2)$	-	-	6.07	-	6.65
χ^2	-	-	22.4	-	24.6
σ-level[4]	-	-	6σ	-	5σ

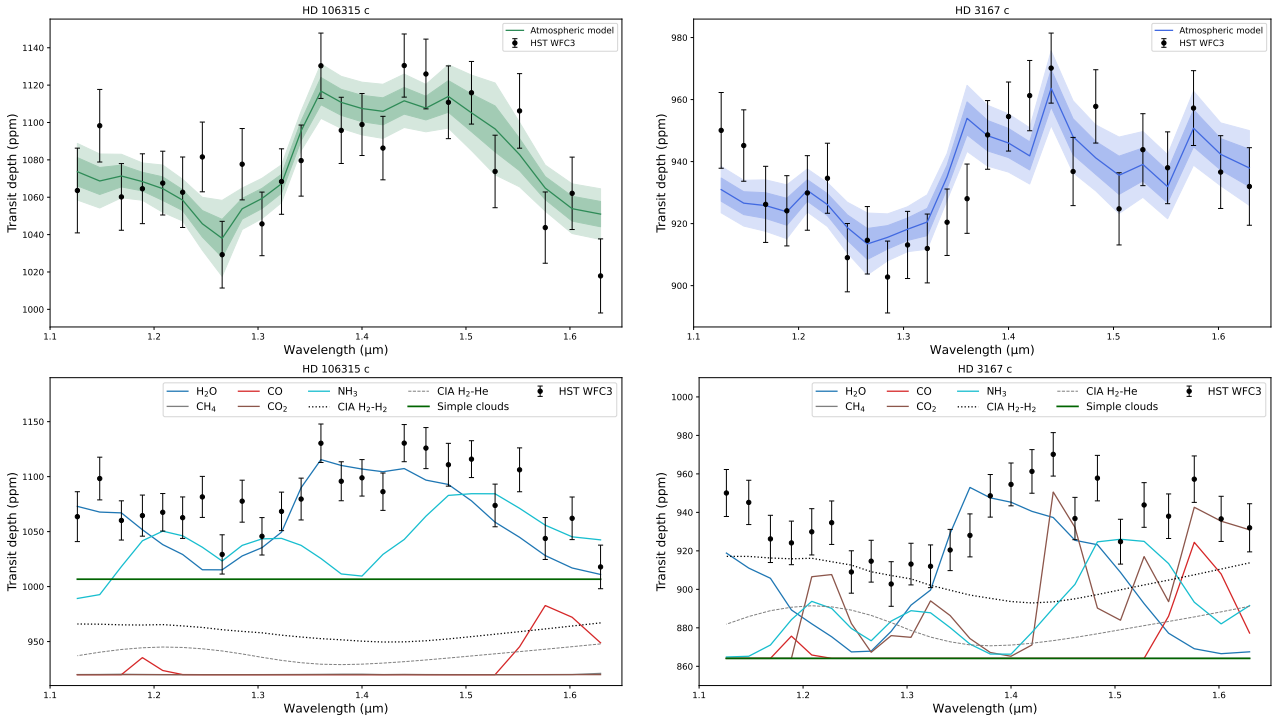

Figure 5.7: Best-fit models to HD 106315 c (left) and HD 3167 c (right) HST/WFC3 G141 data. Top panels: best fit spectra, 1σ and 2σ uncertainty ranges. Bottom panels: contributions of active trace gases, Rayleigh scattering, collision-induced absorption (CIA), and clouds. Some opacity contributions are offset from the data, corresponding to molecules that do not contribute to the fit.

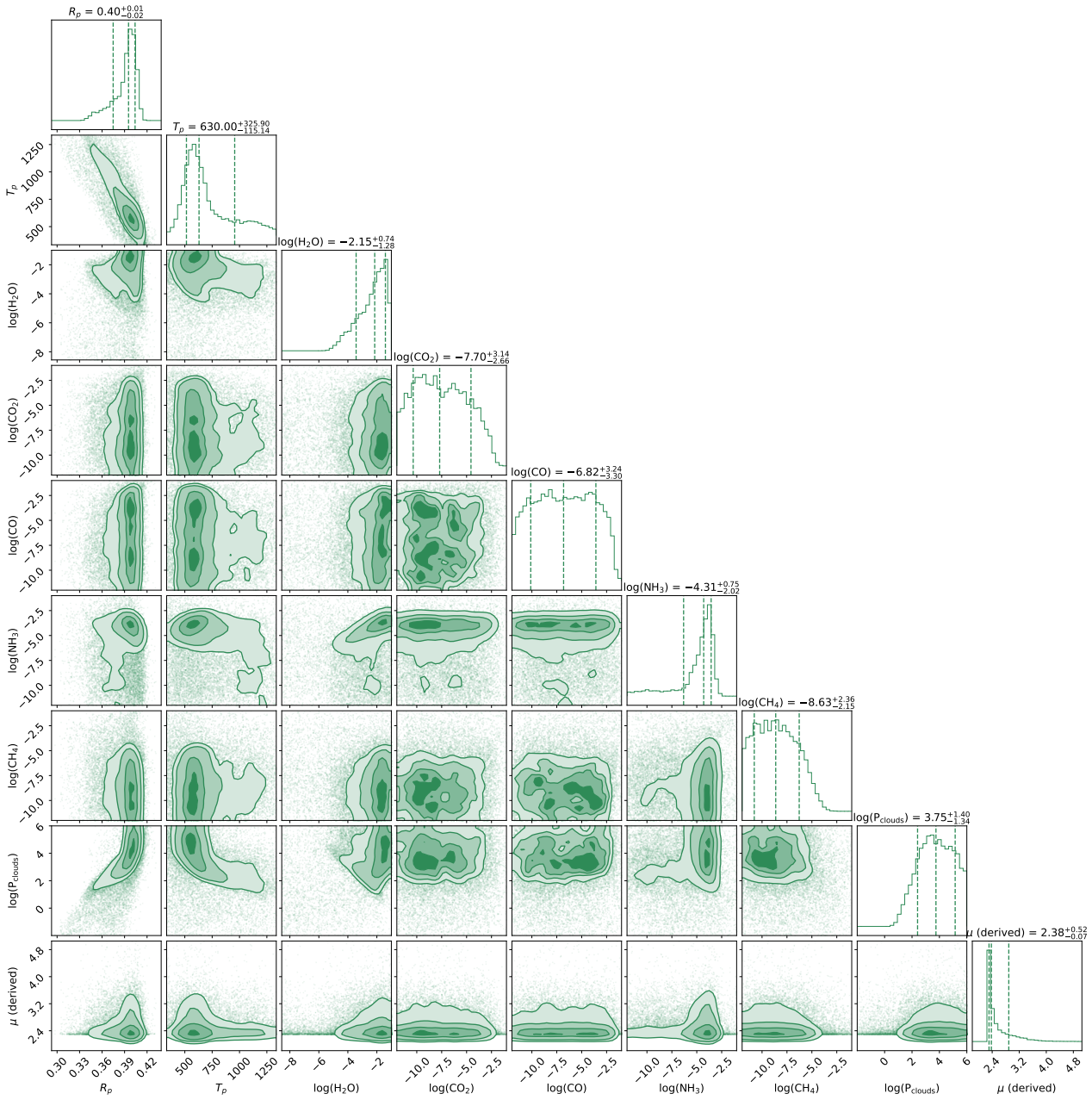

Figure 5.8: Posterior distributions for the atmospheric retrieval on the extracted HD 106315 c spectrum.

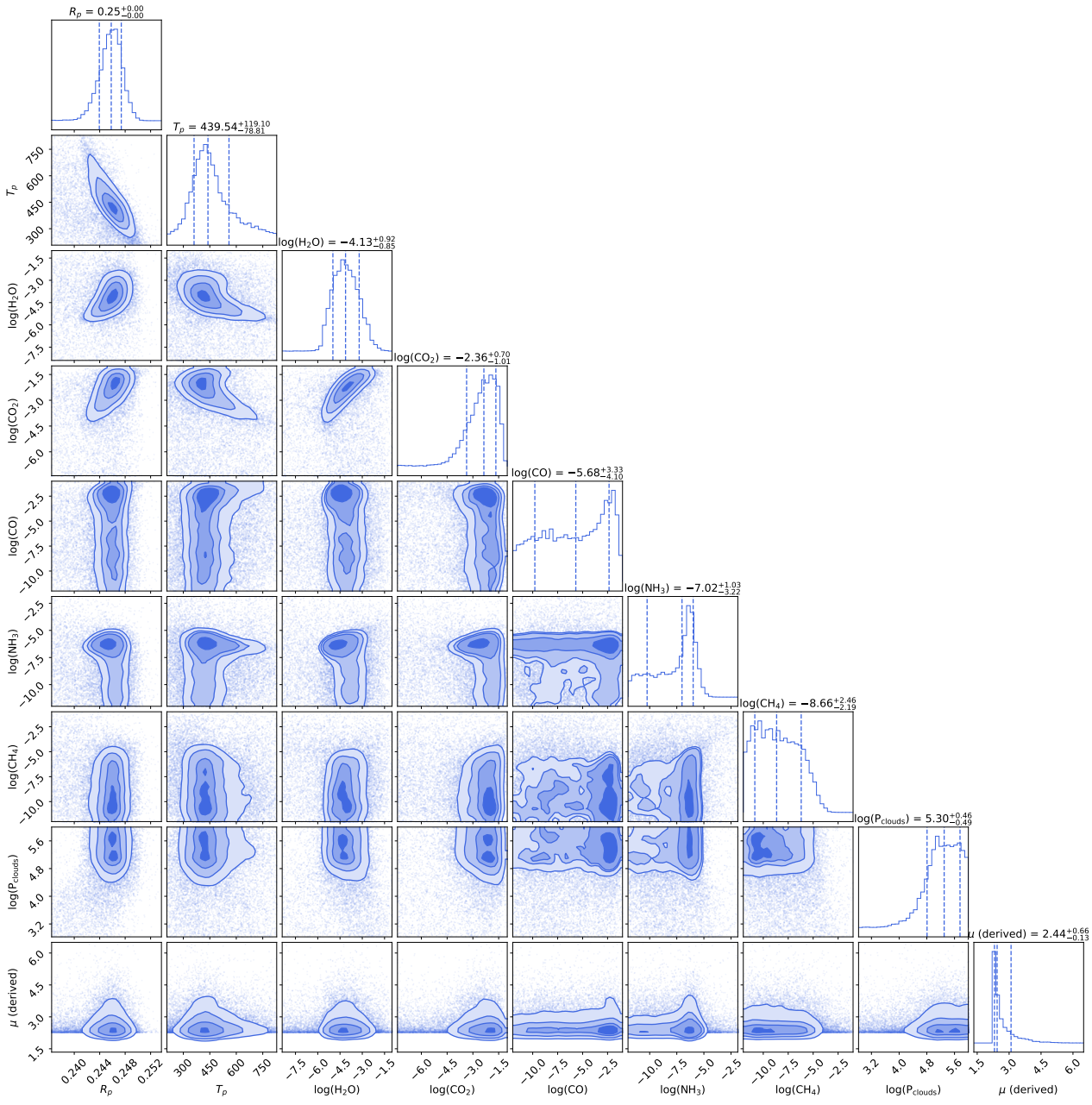

Figure 5.9: Posterior distributions for the atmospheric retrieval on the extracted HD 3167 c spectrum.

HD 106315 c

According to the $\Delta\log(E)$, we retrieved a significant (6-σ) atmosphere around the warm Neptune HD 106315 c with a notable water detection. H_2O is the only species that explains the absorption features between 1.3 and 1.5 μm (Figure 5.7). We obtained a temperature of 630^{+326}_{-115} K, which is lower than the equilibrium temperature, but consistent within 1σ. This result could be explained by the fact that we are probing the atmosphere in the terminator area, and we modelled the atmosphere in 1D using an isothermal profile (Caldas et al., 2019; MacDonald et al., 2020; Pluriel et al., 2020b). Skaf et al. (2020) analysed three hot-Jupiters (WASP-127 b, WASP-79 b and WASP-62 b) together with the exoplanets from Tsiaras et al. (2018) and highlighted the existence of a global trend between the equilibrium and the retrieved temperatures, with the retrieved temperatures showing almost always lower values. In Figure 5.10 we updated Figure 6 from Skaf et al. (2020) by adding the retrieved/equilibrium temperatures of the two Neptunes-like planets analysed in this work. We can see that HD 106315 c follows the global Trend. A discussion on retrieved and irradiation temperatures is lead for Super-Earth and Sub-Neptune in Chapter 7. The best-fit solution contains a notable amount of water,

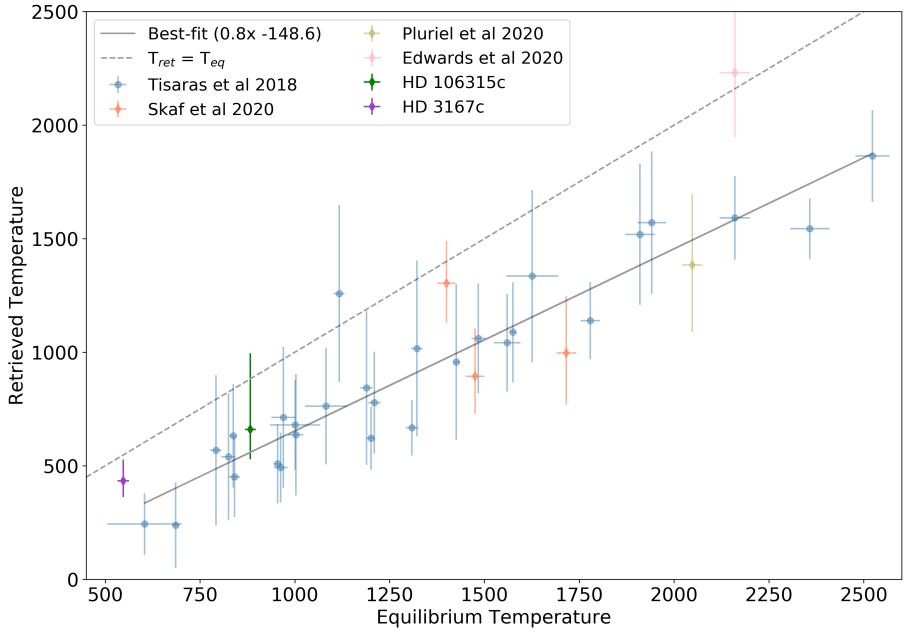

Figure 5.10: Trend between the retrieved and the equilibrium temperatures (or irradiation temperature) for the planets studied in Tsiaras et al. (2018), Skaf et al. (2020), and the two planets analysed in this work. A zero albedo has been assumed to calculate the equilibrium temperature for consistency with the two works mentioned above. For completeness, the planets studied in ARES I (Edwards et al., 2020) and ARES III (Pluriel et al., 2020a) are shown too.

$\log_{10}(H_2O) = -2.1^{+0.7}_{-1.3}$. Figure 5.8 shows that the right wing of the water's abundance Gaussian Distribution is incomplete. The abundance of H_2O could take even higher values ($\log_{10}(H_2O) \sim -1$), but this is an unrealistic solution for a primary atmosphere expected here for this Neptune-type planet. This result is likely due to the limited coverage of HST/WFC3 G141. We note that the Bayes factor between a pure water model and the full chemical model $\Delta\log(E_2)$ is equal to 6.1 (see Table 5.7), meaning that the complexity of the full chemical model is justified with a strong significance (4σ).

The temperature retrieved by `Tau-REx 3` (~600 K) is compatible with absorption from NH_3, which strengthens our choice to consider NH_3 as active gas instead of N_2. However, NH_3 contribution is debatable – the detection is driven by a few points at 1.28, 1.55 μm and 1.60 μm, hence the weak abundance of $\log_{10}(NH_3) = -4.3^{+0.7}_{-2.0}$. We note that a high-temperature solution gives no constraint on NH_3 abundance, whereas a lower temperature requires the molecule to be present (Figure 5.8). NH_3

abundance is also correlated to the amount of H_2O.

Moreover, we can only put constraints on the higher abundance of CH_4: it could be found below 10^{-5}. CO and CO_2 abundances are unconstrained. The model finds a cloud top pressure of $10^{3.7}$ Pa correlated to the amount of H_2O: the deeper the clouds are, the more water we have. The best-fit solution suggests a transparent atmosphere with a significant amount of water. In order to give an estimation of the planetary C/O ratio, we employed the following formula re-adapted from MacDonald & Madhusudhan (2019): $C/O = (XCH_4+XCO+XCO_2)/(XH_2O+XCO+2CO_2)$, where the numerator indicates all species containing C atoms, and the denominator indicates all other O-bearing species. As we obtained a constrained value only for the water abundance, we decided to explore the range of valid C/O by using the mean abundances and the upper/lower possible values allowed by the posteriors (see Table 5.6). In this way, we obtained a C/O ratio that could vary in the range (7.5 $\times 10^{-9}$-0.60).

HD 3167 c

The $\Delta\log(E)$ value found for HD 3167 c retrieval is lower than the one computed for HD 106315 c (Table 5.6), yet it corresponds to a 5σ significance detection of an atmosphere around this sub-Neptune. The temperature retrieved by `Tau-REx 3` (440^{+119}_{-79} K) is lower than the equilibrium temperature, assuming an albedo equal to 0.2, but it is consistent within 1σ.

The main difference with HD 106315 c's atmosphere is the detection of CO_2 and, more generally, the presence of carbon-bearing species. Opacity source contributions in Figure 5.7 show both water and carbon dioxide features; these two species seem required to fit the data obtained by HST/WFC3, and their abundances are highly correlated (see Figure 5.9). $\Delta\log(E_2)$ is equal to 6.6 (Table 5.7) meaning that the full chemical model is statistically significant (4σ) compared to a pure water model. This is probably driven by the carbon dioxide detection that explains the absorption features at 1.20 µm, 1.46 µm, and 1.60 µm. The best-fit solution contains a significant amount of carbon dioxide $\log_{10}(CO_2) = -2.4^{+0.7}_{-1.0}$ and a lower amount of water $\log_{10}(H_2O) = -4.1^{+0.9}_{-0.9}$. We would have expected CH_4 to be the main carbon-bearing species instead of CO_2, which will be discussed in Chapter 8.

Looking at the posterior distributions in Figure 5.9, we can constrain the higher limits of ammonia and methane abundances, which are below 10^{-5}. The monoxide abundance posterior distribution is highly degenerate, hence the weak detection. Carbon dioxide and monoxide features are difficult to distinguish in WFC3/G141 observations because they have similar features between 1.5μm and 1.6μm, potentially leading to degeneracies between the two abundances. The amounts of H_2O and CO_2, as well as the planetary temperature and radius, are correlated. For less water and carbon dioxide, the model requires a higher temperature and lower radius at 10 bar atmospheric pressure (see Figure 5.9). The best-fit solution suggests a clear atmosphere with a top cloud pressure retrieved at 1 bar. As for HD 106315 c, we derived a range of possible values in which the C/O ratio could vary, i.e. (0.49-0.85).

Table 5.7: Statistical results of the atmospheric retrieval analysis on HD 106315 c and HD 3167 c HST/WFC3 G141 data.

HD 106315 c											
N°	Setup	Log E	$\Delta\log(E)$	$\Delta\log(E_1)$	$\Delta\log(E_2)$	T(K)	R_P (R_J)	$\log_{10}(P_{clouds})$	$\log_{10}(H_2O)$	$\log_{10}(NH_3)$	$\log_{10}(CH_4)$
A0	No active gas	210.94	N/A	N/A	N/A	798^{+356}_{-315}	$0.39^{+0.03}_{-0.04}$	$2.5^{+2.5}_{-3.2}$	N/A	N/A	N/A
A1	Full chemical	226.91	15.97	N/A	6.07	630^{+326}_{-115}	$0.40^{+0.01}_{-0.02}$	$3.7^{+1.4}_{-1.3}$	$-2.1^{+0.7}_{-1.3}$	$-4.3^{+0.7}_{-2.0}$	< -5
A2	H_2O only	220.84	9.52	N/A	N/A	859^{+66}_{-99}	$0.40^{+0.01}_{-0.01}$	N/A	$-5.1^{+0.3}_{-0.2}$	N/A	N/A
A3	No H_2O	212.70	1.76	14.21	N/A	417^{+156}_{-56}	$0.40^{+0.01}_{-0.01}$	$4.1^{+1.3}_{-1.8}$	N/A	$-3.4^{+1.0}_{-1.5}$	$-3.0^{+1.0}_{-2.9}$
A4	No clouds	226.98	16.04	N/A	6.14	546^{+93}_{-87}	$0.40^{+0.01}_{-0.01}$	N/A	$-2.1^{+0.7}_{-1.5}$	$-4.3^{+0.7}_{-1.0}$	< -5
A5	No NH_3	226.00	15.06	0.91	5.16	1004^{+223}_{-278}	$0.37^{+0.02}_{-0.02}$	$2.5^{+1.1}_{-0.9}$	$-2.6^{+1.1}_{-1.3}$	N/A	< -5

HD 3167 c											
N°	Setup	Log E	$\Delta\log(E)$	$\Delta\log(E_1)$	$\Delta\log(E_2)$	T(K)	R_P (R_J)	$\log_{10}(P_{clouds})$	$\log_{10}(H_2O)$	$\log_{10}(CO_2)$	$\log_{10}(CO)$
B0	No active gas	225.84	N/A	N/A	N/A	473^{+225}_{-180}	$0.24^{+0.01}_{-0.02}$	$2.2^{+2.6}_{-2.6}$	N/A	N/A	N/A
B1	Full chemical	235.41	9.58	N/A	6.65	440^{+119}_{-79}	$0.25^{+0.01}_{-0.01}$	$5.3^{+0.5}_{-0.5}$	$-4.1^{+0.9}_{-0.9}$	$-2.4^{+0.7}_{-1.0}$	unconstrained
B2	H_2O only	228.76	2.92	N/A	N/A	785^{+33}_{-73}	$0.24^{+0.01}_{-0.01}$	N/A	$-5.62^{+0.19}_{-0.18}$	N/A	N/A
B3	No H_2O	231.80	5.97	3.61	N/A	449^{+100}_{-88}	$0.25^{+0.01}_{-0.01}$	$5.1^{+0.6}_{-0.6}$	N/A	$-1.9^{+0.5}_{-0.8}$	unconstrained
B4	No clouds	236.45	10.62	N/A	7.69	426^{+127}_{-75}	$0.25^{+0.01}_{-0.01}$	N/A	$-4.2^{+0.9}_{-0.8}$	$-2.4^{+0.7}_{-1.0}$	unconstrained
B5	No CO_2	231.48	5.64	3.93	2.72	605^{+151}_{-237}	$0.25^{+0.01}_{-0.01}$	$5.2^{+0.5}_{-0.7}$	$-4.8^{+1.4}_{-0.6}$	N/A	$-1.9^{+0.5}_{-1.6}$
B6	No CO	234.84	9.00	0.60	6.08	440^{+110}_{-82}	$0.25^{+0.01}_{-0.01}$	$5.3^{+0.5}_{-0.6}$	$-3.9^{+1.1}_{-1.0}$	$-2.1^{+0.7}_{-0.9}$	N/A
B7	No CO_2, CO	229.86	4.03	5.55	1.10	732^{+60}_{-105}	$0.24^{+0.01}_{-0.01}$	$5.4^{+0.4}_{-0.4}$	$-5.5^{+0.3}_{-0.2}$	N/A	N/A

5.5 Discussion

Considering the limited wavelength coverage and the low data resolution, the results obtained must be considered carefully and put into perspective. The model we tested has eight free parameters and 25 observation data points. Molecular abundances and temperatures retrieved by `Tau-REx 3` are sensitive to the users' inputs and bounds. `Tau-REx 3` gives us the first insight into these exoplanets' atmospheres and, particularly for HST/WFC3, helps us infer the presence of water. To better constrain the molecular detections found in Section 5.4.1 we analysed different simulations (**A0-A5** and **B0-B7** in Table 5.7, for HD 106315 c and HD 3167 c, respectively) that include the expected molecules considering the wavelength coverage and the equilibrium temperature **A0** and **B0** are flat-line models that help us compute the ADI and **A2** and **B2**, pure water models are used to compute $\Delta\log(E_2)$.

5.5.1 Strength of water detection

To assess the significance of H_2O detection for both planets, we removed this active gas from the full chemical model and analysed the Bayes factor $\Delta\log(E_1)$. It decreases from 226.91 (**A1**) to 212.70 (**A3**) (see Table 5.7) and from 235.41 (**B1**) to 231.80 (**B3**) for HD 106315 c and HD 3167 c, respectively. H_2O detection is statistically confirmed for both planets with a strong (Kass & Raferty, 1995; Benneke & Seager, 2013) significance (5σ) for HD 106315 c, and a moderate one (3σ) for HD 3167 c. To date, water has been detected on several Neptune and sub-Neptune planets, which allows comparisons. HD 106315 c could be compared to HAT-P-11 b (with a water detection's significance, hereafter σ_{H_2O}, of 5σ, Fraine et al. 2014), and to GJ 3470 b (σ_{H_2O}= 5σ, Benneke et al. 2019). While HD 3167 c has a lower water detection, appearing more similar to K2-18 b (σ_{H_2O}=4σ, Tsiaras et al. 2019, and σ_{H_2O}=4σ, Benneke et al. 2019).

Crossfield & Kreidberg (2017) studied the water features amplitude of six warm Neptune planets and highlighted correlations with the equilibrium temperature and the mass fraction of hydrogen and helium. To verify the correlation of H_2O amplitude, in units of atmospheric scale height, with the equilibrium temperature, we computed HD 106315 c, HD 3167 c and K2-18 b water amplitude using HST/WFC3 spectra obtained here and in Tsiaras et al. (2019). We used the same method described in Crossfield & Kreidberg (2017). We fitted a carbon-free template of GJ 1214 b normalised in units of scale height (Crossfield et al., 2011) to the observations using the Levenberg and Marquardt's least squares method (L-M) (Markwardt, 2009). Then, we measured the amplitude taking the normalised average value from 1.34μm to 1.49μm and subtracting it from the average value outside this wavelength range. The scale height $H=K_BT_{eq}/\mu g$ is computed assuming a hydrogen-rich atmosphere (μ=2.3 g/mol) and the equilibrium temperature is calculated for an albedo of 0.2.

We find a water feature amplitude of 1.02±0.18 for HD 106315 c, of 1.04±0.24 for HD 3167 c, and of 1.28±0.49 for K2-18 b. We note that Kreidberg et al. (2020) recent paper found a lower absorption feature, i.e 0.80±0.4 for HD 106315 c. We plot our values in Figure 5.11 along with the amplitudes computed in Crossfield & Kreidberg (2017) and the ones found in Libby-Roberts et al. (2020) for Kepler 51 b and Kepler 51 d. Finally, we fitted a linear relation and compared the Pearson correlation coefficient and the probability. We find a correlation coefficient of 0.43 and a p-value of 0.18. The strong correlation highlighted in Crossfield & Kreidberg (2017) is not found here, mostly because of K2-18 b high water feature amplitude at low temperature. While removing K2-18 b and Kepler 51 d amplitudes – to focus on planets with temperature between 500 and 1000 K as in Crossfield & Kreidberg (2017)- we find a correlation coefficient of 0.70 and p-value of 0.04 while they found a coefficient of 0.83 for a p-value equal to 0.04.

A more in-depth analysis of the HST/WFC3 water feature amplitude for intermediate-size planets is detailed in Chapter 8. The present analysis is a comparison with Crossfield & Kreidberg (2017) study, while Chapter 8 proposes a new metric of the amplitude of the spectrum in the water absorption band

and a comparison with self-consistent modelling. We build a grid of Sub-Neptune atmospheres to study the impact of radiative clouds on the size of the water feature and compare it to 26 HST/WFC3 transmission spectra.

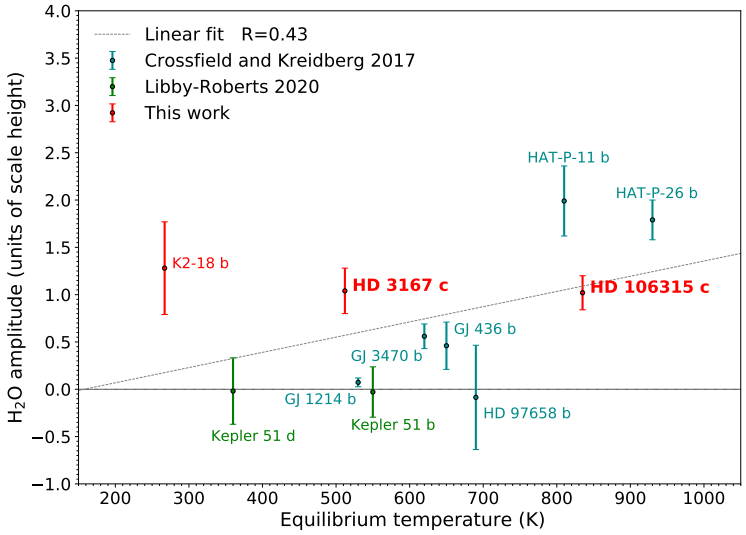

Figure 5.11: Normalized H_2O amplitude in units of scale height as a function of equilibrium temperatures. Blue points are from Crossfield & Kreidberg (2017) and green points are from Libby-Roberts et al. (2020). Red points are computed using the method described in Crossfield & Kreidberg (2017) and spectra obtained in this work and from Tsiaras et al. (2018) for K2-18 b. The dotted line corresponds to a linear fit. The correlation coefficient was found to be lower than in Crossfield & Kreidberg (2017), 0.43 compared to 0.83.

5.5.2 Clear or cloudy atmospheres

In Section 5.4.2, we retrieved a clear atmosphere for both planets, but we expect species to condense and clouds to form on warm Neptune and sub-Neptune planets. The flat spectra of GJ 436 b (Knutson et al., 2014a), GJ 1214 b (Kreidberg et al., 2014a) and HD 97658 b (Knutson et al., 2014b) were interpreted as high cloud or haze at low pressure. We confirm the clear atmosphere by removing the cloud top pressure parameter from the full chemical model. $\Delta\log(E)$ of cloud-free models (**A4** and **B4** in Table 5.7) are higher than $\Delta\log(E)$ of full chemical models with clouds (**A1** and **B1** in Table 5.7). Clouds do not impact retrieval results, even for HD 106315 c with a lower top cloud pressure, and this means that the planet has a clear atmosphere or the clouds are located below the visible pressure where the atmosphere is opaque. HD 106315 c's cloud top pressure correlations with H_2O abundance (see Figure 5.8), a second mode appears, meaning that clouds could be present in the region we are probing.

`Tau-REx 3` retrieval analysis does not bring any information on cloud composition, and we must recall that the wavelength coverage is not wide enough to constrain cloud chemistry. All things considered, models have predicted that for hot atmospheres (900 to 1300 K) we could find condensates like KCl, ZnS and Na_2S, and for colder atmospheres (400 to 600 K) KCl and $NH_4H_2PO_4$ (Lodders, 2010; Morley et al., 2012; Charnay et al., 2018). GJ 1214 b (6.26 ± 0.86 $M_\oplus$, 2.85 ± 0.20 $R_\oplus$, Harpsøe et al. 2012), K2-18 b (7.96 ± 1.91 $M_\oplus$, 2.38 ± 0.22 $R_\oplus$, Cloutier et al. 2017) and HD 3167 c (this work) have a similar mass and radius, and yet present very different atmospheric properties. The equilibrium temperature is lower for K2-18 b (283±16 K, Cloutier et al., 2017), but presents water detection. GJ 1214 b has a similar equilibrium temperature (571±44 K, Harpsøe et al., 2012), but exhibits a flat spectrum suggesting the presence of clouds.

5.5.3 Ammonia in HD 106315 c's atmosphere

HD 106315 c's best fit solution includes a small amount of NH3, i.e $\log_{10}(NH_3) = -4.3^{+0.7}_{-2.0}$. Looking at the posteriors distribution (Figure 5.8), NH_3 abundance converges toward a solution. To confirm this detection, we removed this gas from the full chemical model and computed Δ_{E1} (see **A5** in Table 5.7). The difference is 0.91 meaning that NH_3's detection has to be considered not-significant (2σ) (Kass & Raferty, 1995; Benneke & Seager, 2013). However, we observe some differences: the temperature rises to 1004 K with fewer constraints, and consequently, the radius decreases to 0.374 R_J. Clouds are found at a higher level: $10^{2.5}$ Pa. The cloud deck compensates for NH_3 features by cutting H_2O ones and shrinking the spectrum. From this analysis, we conclude that HD 106315 c can be surrounded by either a clear primary atmosphere with H_2O and traces of NH_3 or by a primary atmosphere with H_2O and deep clouds.

As mentioned in Section 5.3.2, the high equilibrium temperature of HD 106315 c should have favoured the presence of N_2 instead of NH_3. NH_3 is expected to disappear above 500-550 K. However, we retrieve at the terminator, so we should expect a lower temperature (closer to this 500 K limit) and more NH_3. Moreover, N_2 is an inert gas with no spectral feature, which means that the 'free' retrieval we perform – a retrieval in 'free' mode is used to retrieve the abundance for active molecules that have features in the spectrum- will not pick up this molecule except if it influences the mean molecular weight. To test this, we added N_2 in the analysis to see the possible consequences this molecule could have had on the mean molecular weight. We assumed an initial N_2 abundance of 10^{-4}, and we allowed it to vary between 10^{-12} and 10^{-1} in volume mixing ratios (log-uniform prior) -as for the other molecules. The inclusion of N_2 does not affect the mean molecular weight. NH_3 detection remains around 10^{-4} (see Figure 5.12).

5.5.4 Carbon dioxide in HD 3167 c's atmosphere

HD 3167 c best fit solution includes an important amount of CO_2 (i.e $\log_{10}(CO_2) = -2.4^{+0.7}_{-1.0}$). This detection is supported by the data points from ~1.5 to 1.6 μm, but water explains better the absorption features around 1.4 μm (see Figure 5.7). We removed CO_2 from the full chemical and compared log evidences; it decreases from 235.41 (**B1**, Table 5.7) to 231.48 (**B5**) corresponding to a 3σ moderate detection. The ADI decreases as well to 5.64. We note that CO is now compensating for CO_2 features and its log abundance increases to $\log_{10}(CO) = -1.9^{+0.5}_{-1.6}$. This exact value is too high for the realistic primary hydrogen-rich atmosphere that we expect for this planet but errorbars are large. We successively removed CO from the full chemical model, but it does not impact the retrieval results (**B6** in Table 5.7) and Δ_{E1} is below 1 (not significant). Finally, we removed both CO and CO_2 to asses the detection of those carbon-bearing species (**B7**). The difference in log evidence is now equal to Δ_{E1}=5.55 and corresponds to more than 3σ carbon detection. This test does not impact the abundance of water nor the top cloud pressure but constrains the abundance of ammonia to $10^{-6.4}$. We note that CH_4 does not compensate for the lack of the other carbon-bearing species. Its abundance remains constrained below 10^{-5}. The temperature increases to keep a primary atmosphere hypothesis and an extended clear atmosphere.

This unexpected carbon-bearing species moderate detection could be explained by noise or systematic effects that were not removed during the white light curve fitting step (see Section 5.3.1). It could also be the result of phenomena that our 1D equilibrium chemistry modelling cannot reproduce, e.g. 3D transport cross-terminator. Another interpretation could be the actual presence of CO_2 in the atmosphere of HD 3167 c due to very high metallicity and C/O ratio. The abundance of CO_2 scales quadratically with metallicity (see, e.g. Moses, 2014). Examples of CO_2' abundance interpreted by a high metallicity can be found in the literature (see, e.g. Madhusudhan & Seager, 2011). However, suppose we use the water abundance as a proxy of metallicity (see, e.g., Kreidberg et al., 2014b). In

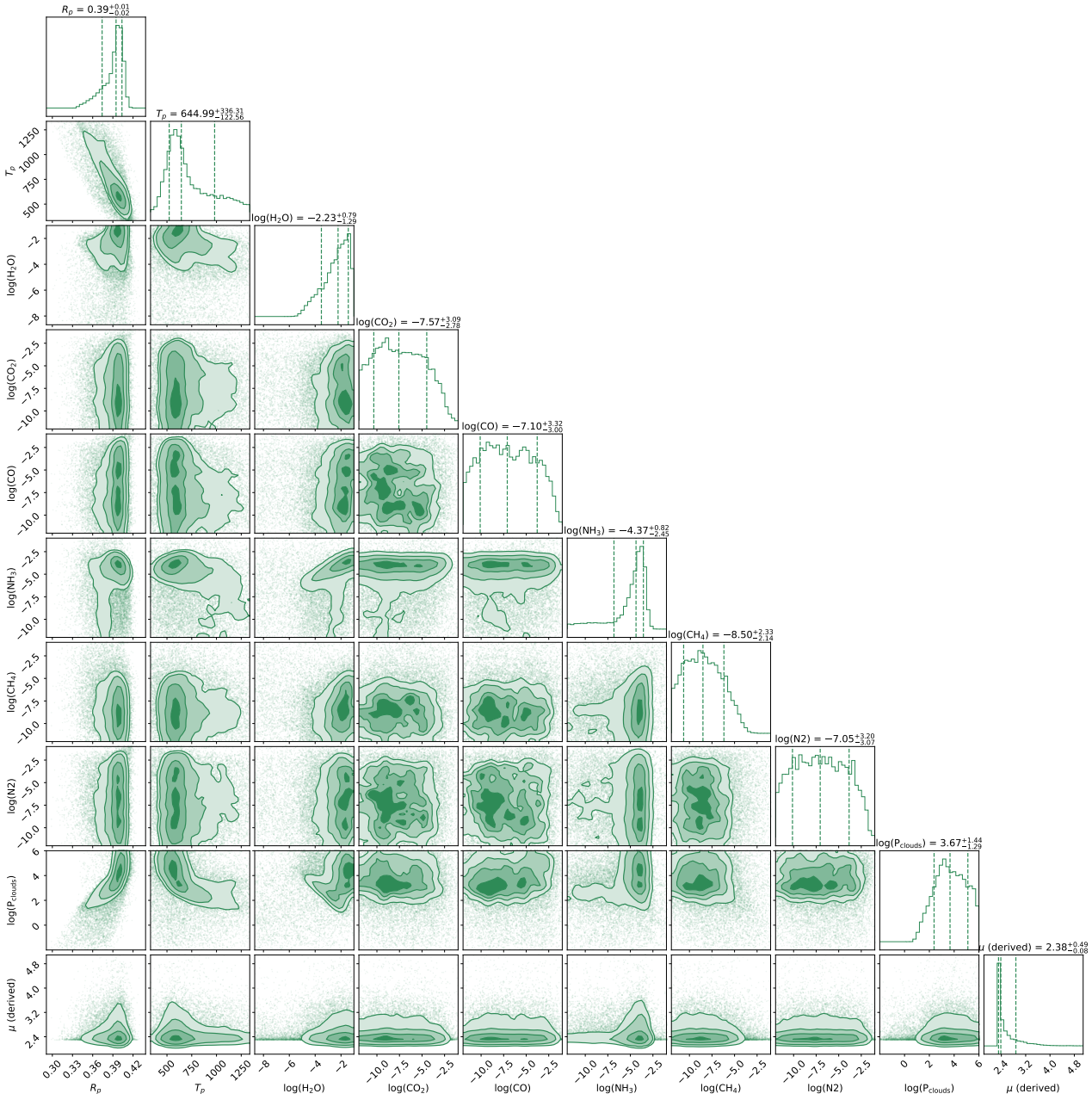

Figure 5.12: Posterior distributions including N_2 for the atmospheric retrieval on the extracted HD 106315 c spectrum.

that case, we infer a solar or sub-solar metallicity for HD 3167 c, which would be in tension with the possibility that CO_2 is present due to high metallicity or disequilibrium chemistry processes. More observations are thus necessary to better constrain a possible presence of CO_2 in the atmosphere of HD 3167 c.

Modelling of HD 3167 c's atmosphere using a radiative-convective self-consistent code is proposed in Chapter 8. We investigate the presence and the nature of carbon-bearing species in Sub-Neptune atmospheres. In particular, we aim to constrain methane's presence regarding atmospheric metallicity.

5.5.5 Inferences from the Mass and Radius

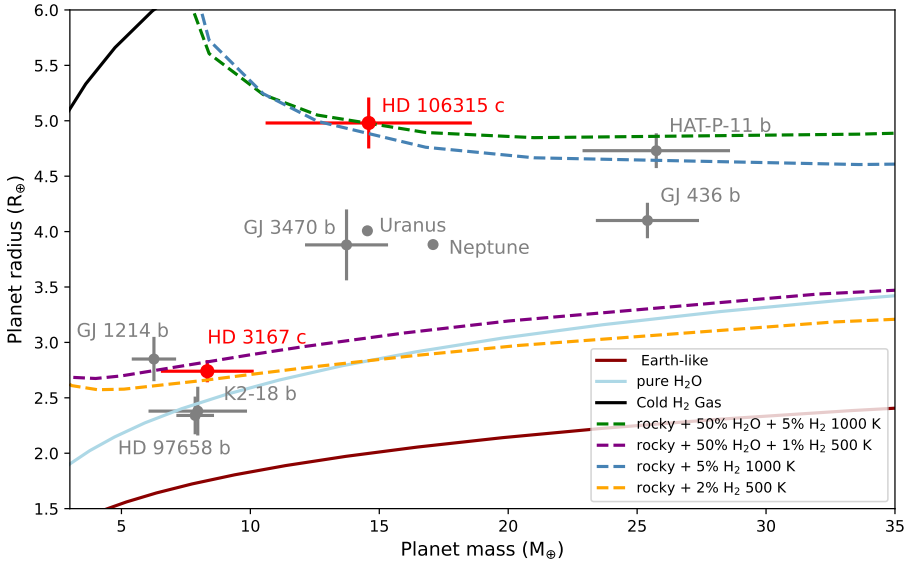

Figure 5.13: Distribution of the planetary mass and radius for eight Neptune-like planets with size between 1.5-4 $R_\oplus$ and published atmospheric characterisation studies. Planetary parameters of HD 106315 c and HD 3167 c are from Table 5.1, GJ 3470 b (Biddle et al., 2014), GJ 436 b (Lanotte et al., 2014), GJ 1214 b (Harpsøe et al., 2012), HD 97658 b (Dragomir et al., 2013), HAT-P-11 b (Bakos et al., 2010), K2-18 b (Cloutier et al., 2017)- and Uranus and Neptune (`https://nssdc.gsfc.nasa.gov/planetary/factsheet/`). The mass and radius models are from Zeng et al. (2019).

There is a strong degeneracy in exoplanet interiors as many compositional models are compatible with the observed mass and radius. However, by combining our study's mass, radius, and spectroscopic results, we can infer the interior composition of HD 106315 c and HD 3167 c. Our discovery of icy constituents, such as H_2O in both planetary atmospheres (and maybe NH_3 in the envelope of HD 106315 c) could indicate an ice-rich embryo. However, atmospheric metal content might not represent bulk and core content (Thorngren & Fortney, 2019). Curiously, the mass and radius of HD 106315 c and HD 3167 c are also consistent with an ice-rich core which we explain below.

For the following results, we adopted the planetary models from Zeng & Sasselov (2013), Zeng et al. (2016), and Zeng et al. (2019). Based on the mass and radius of HD 106315 c and HD 3167 c, they are both consistent with icy cores with hydrogen envelopes ~ 5 wt.% and $0.3 - 1$ wt.% of their total planetary masses, respectively. We show these results in Figure 5.13. Nevertheless, there is still enough uncertainty in the results that a silicate embryo engulfed by a hydrogen atmosphere is still plausible for both planets. Certainly, with improved mass and radius measurements and more accurate spectroscopic observations, the interior structure of exoplanets such as HD 106315 c and HD 3167 c will get further constrained. An updated version of this plot for 26 planets and different composition models is presented in Chapter 7. Besides, Mousis et al. (2020) showed that close-in planets could have water-rich hydrospheres in a super-critical state. Their model suggests that intermediate-size

planets could be hydrogen/helium-free, and their interiors would vary from one another depending on the water content.

5.5.6 Comparison with independent studies

Two independent analyses of the same datasets have been performed simultaneously with ours. Kreidberg et al. (2020) analysed HD 106315 c WFC3 observations while Mikal-Evans et al. (2020) studied HD 3167 c observations. They use different extraction algorithms and atmospheric inference models. Kreidberg et al. (2020), reported a tentative detection (with a Bayes factor of 1.7 or 2.6, depending on prior assumptions) of water vapour with a small amplitude of 30 ppm. Mikal-Evans et al. (2020) find evidence for absorption by at least one of H_2O, HCN, CO_2, and CH_4 (Bayes factor 7.4; 2.5σ significance).

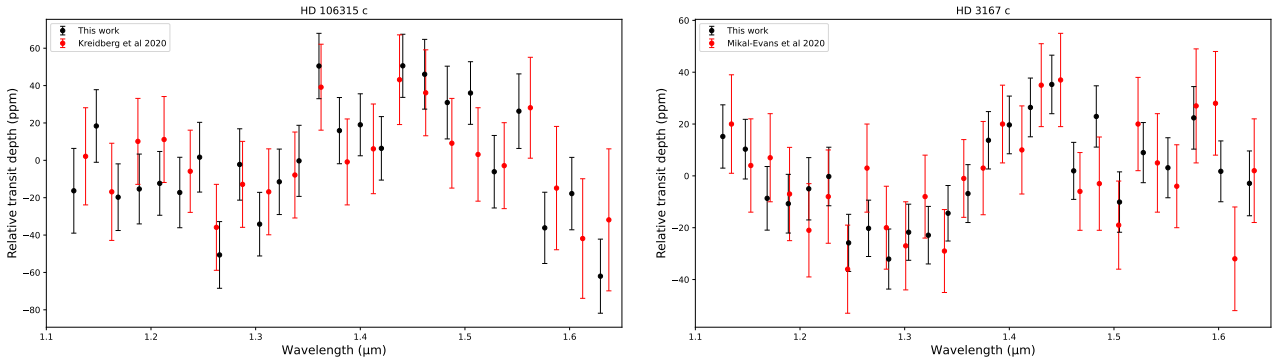

Figure 5.14: Relative transit depth for HD 106315 c (left) and HD 3167 c (right) spectra. The spectra are from this work (in black) and from Kreidberg et al. (2020) and Mikal-Evans et al. (2020) (in red).

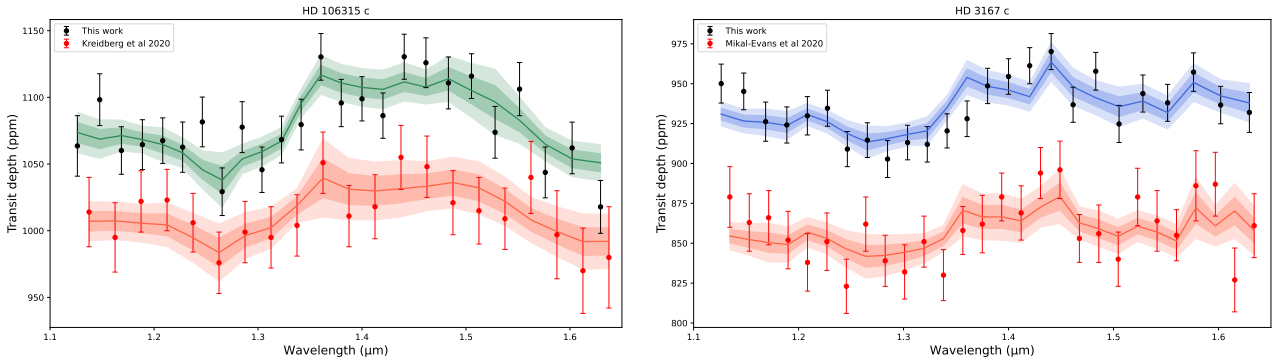

Figure 5.15: Comparison of the best-fit models to HD 106315 c (left) and HD 3167 c (right) HST/WFC3 G141 data extracted with different method. HD 106315 c and HD 3167 c spectra and best-fits from Kreidberg et al. (2020) and Mikal-Evans et al. (2020) are in red while models from this work are in green and blue. The model represented corresponds to the result of the retrieval analysis **A1** 'Full chemical' in Table 5.7.

Atmospheric inference comparison

First, we compare the atmospheric result using the same Bayesian atmospheric retrieval code on the different extracted spectra. We plot in Figure 5.14 the relative transit depth (transit depth with the mean subtracted) for all spectra. The relative transit depth agrees well despite the different methods used to extract and correct the raw flux. The error bars are bigger in the Kreidberg et al. (2020) and Mikal-Evans et al. (2020) than in our analysis. The mean error of our extracted spectrum is 18 ppm compared to 25 ppm for HD 106315 c and 11 ppm to 17 ppm for HD 3167 c. This difference of around

6 ppm, might be due to the model used to correct the instrument systematics. They use an analytic ramp model rather than the dividing white light curve systematics to adjust the spectral light curves. This method increases the size of the error bars. However, one can argue that the analytics models are more reliable as the systematics might also depend on the detector flux level (Zhou et al., 2017).

Table 5.8: Comparison of the best-fit results of the atmospheric retrieval analysis on HD 106315 c and HD 3167 c HST/WFC3 G141 data with two independent analyses.

	HD 106315 c Full chemical		**HD 3167 c Full chemical**	
Parameter	Kreidberg et al. (2020)	This work	Mikal-Evans et al. (2020)	This work
$\Delta\log(E)$	0.95	15.97	1.43	9.58
$\Delta\log(E_1)$ w/o H_2O	1.1	14.21	0.88	3.61
$\Delta\log(E_1)$ w/o CO_2	N/A	N/A	0.59	3.93
$\Delta\log(E_2)$	1.55	6.07	2.64	6.65
T(K)	669^{+377}_{-220}	630^{+326}_{-115}	418^{+191}_{-127}	440^{+119}_{-79}
$R_P(R_J)$	$0.38^{+0.02}_{-0.03}$	$0.40^{+0.01}_{-0.02}$	$0.23^{+0.01}_{-0.01}$	$0.25^{+0.01}_{-0.01}$
$\log_{10}(P_{clouds})$	$2.9^{+1.5}_{-1.7}$	$3.8^{+1.4}_{-1.3}$	$4.3^{+1.1}_{-2.2}$	$5.3^{+0.5}_{-0.5}$
$\log_{10}(H_2O)$	$-3.7^{+1.6}_{-2.3}$	$-2.1^{+0.7}_{-1.3}$	$-4.9^{+1.7}_{-3.3}$	$-4.1^{+0.9}_{-0.9}$
$\log_{10}(NH_3)$	unconstrained	$-4.1^{+0.8}_{-2.0}$	unconstrained	unconstrained
$\log_{10}(CO_2)$	unconstrained	unconstrained	$-3.3^{+1.3}_{-5.1}$	$-2.4^{+0.7}_{-1.0}$

We performed the retrieval analysis on the extracted spectrum of HD 106315 c by Kreidberg et al. (2020) and of HD 3167 c by Mikal-Evans et al. (2020) using `Tau-REx 3` for a consistent analysis. We tested the models corresponding to the **A0**, **A1**, **A2** and **A3** retrieval setups. We represent in Figure 5.15 the best-fit model results corresponding to the **A1** 'Full chemical' retrieval setups (see Table 5.6), for HD 106315 c and HD 3167 c spectra from this work and Kreidberg et al. (2020) and Mikal-Evans et al. (2020). The retrieval setups, including parameters, units and priors, are similar to those in Table 5.6. There is a positive offset between our extracted spectrum and the ones from both analyses. This difference is probably caused by the initial choice of the stellar and planetary parameters in the extraction and light curves fitting and the correction model used in the light curves fitting. As shown in Figure 5.14, the offset should have little impact on the atmospheric conclusion as the shape of the transmission spectrum, and the features are similar. In Table 5.8 we summarise the best-fit retrieval results and statistical criteria obtained with `Tau-REx 3`. The fitted parameters from the two independent studies are compatible within one or two σ with our result. The radius is found to be lower in both cases. The top cloud layer is higher using Kreidberg et al. (2020) spectrum for HD 106315 c and Mikal-Evans et al. (2020) spectrum for HD 3167 c but consistent with our values. The retrieved abundance of water is similar for HD 3167 c and HD 106315 c, within 1-σ. Carbon dioxide is also retrieved with a non-negligible abundance for HD 3167 c but ammonia is not constrained for HD 106315 c using Kreidberg et al. (2020) spectrum. Reassuringly, we reproduced the result using the same atmospheric inference model on a different data spectrum, particularly water detection. The difference resides in the statistical criteria and, thus, the significance of the detection. Using Kreidberg et al. (2020) spectrum, the water is only tentatively detected (Bayes factor equal to 1.1, 2.1σ detection). $\Delta\log(E)$ is below one, which means that we cannot confidently confirm the presence of the atmosphere. In contrast, we find a Bayes factor above 15, corresponding to a 5σ confidence atmospheric detection using our reduction process. The atmospheric signal significance is 2.1σ using Mikal-Evans et al. (2020) spectrum, formally a non-detection, while we confirmed the presence of the atmosphere with more than 3σ significance. Neither H_2O nor CO_2 is detected strongly with Mikal-Evans et al. (2020) spectrum (Bayes factor below one). The main driving factor in the difference is the ∼6ppm larger error bars on both spectra. Surprisingly, such a small difference greatly impacts the Bayes factor and the strength of the atmospheric conclusions.

Finally, Mikal-Evans et al. (2020) included HCN in the atmospheric inference and found evidence of this molecule with around 2σ confidence. We ran one last retrieval analysis based on the Full Chemical model with added HCN as a molecular opacity source for both our spectrum and Mikal-Evans et al. (2020) 's. While we find a small contribution of HCN using our extracted spectrum, the abundance is poorly constrained $\log(\mathrm{HCN})=-4.9^{+1.7}_{-3.72}$. H_2O and CO_2 are still found as the main spectral contributors, and their abundance is similar. $\Delta\log(E)$ is equal to 10.08, which is not significantly higher than the Bayes factor without HCN (9.58). We find similar result using Mikal-Evans et al. (2020) spectrum with `Tau-REx 3`. HCN is not constrained with an abundance of $\log(\mathrm{HCN})=-5.3^{+2.5}_{-4.2}$ while H_2O and CO_2 are unchanged. $\Delta\log(E)$ equals 1.70, which is close to the Bayes factor found without HCN (1.43). This difference with Mikal-Evans et al. (2020) atmospheric retrieval might be due to the model employed and the selected line lists.

Comparison of the atmospheric Bayesian models

We used the spectra, setups and results described in Kreidberg et al. (2020) and Mikal-Evans et al. (2020) to compare the Bayesian retrieval analysis codes. In both their analysis, they use `SCARLET` (Benneke & Seager, 2012, 2013; Kreidberg et al., 2014a; Knutson et al., 2014a; Benneke et al., 2019; Benneke et al., 2019; Wong et al., 2020) and `petitRATRANS` Mollière et al. (2019) retrieval frameworks in free mode to analyse the atmospheric composition. The idea is to use `Tau-REx 3` in free retrieval mode with a similar setup and spectrum than found in their paper. We tried to reproduce a similar retrieval analysis, to have a consistent comparison. However, line lists differ; we do not have information on the stellar and planetary parameters used. As they do not retrieve the planetary radius, we fixed it to the best-fit value, 0.38 R_J for HD 106315 c and 0.23 R_J for HD 3167 c.

We present in Table 5.9 the retrieval setups and results on HD 106315 c's spectrum obtained in Kreidberg et al. (2020). We note that the prior on the temperature and the molecular opacities are not the same from `SCARLET` to `petitRATRANS` analysis. The `petitRATRANS` analysis also includes the fit of P_0, which is a reference pressure at a given radius. The molecular abundances are fitted with a uniform prior between 10^{-10} and one and the top cloud pressure between 10^{-3} and 10^7 Pa. This setup differs from our retrieval analysis setup described in Section 5.3.2. The molecular abundances are fitted between 10^{-12} and 10^{-1} and the pressure range is 10^{-2} and 10^6 Pa. the temperature is fitted between 400 and 1000 K. The main difference between `Tau-REx 3` and the two other Bayesian frameworks is found in the fitted abundance of the main absorber water. All three retrieval analyses identify water as the main spectral opacity contributor but with different abundances. While fixing the upper prior to 1 for molecular mass fraction, the abundance constrained by `Tau-REx 3` for water reaches $\log(H_2O)$=-0.7. It favours a heavy atmosphere, with a large amount of water in a cloud-less atmosphere, while the two other codes find a low amount of water, below 10^{-3}, with a high cloud deck around 100 Pa. However, in their paper, Kreidberg et al. (2020) indicates that they use these priors but require that the sum of all mass fractions is below unity, possibly forcing the abundances to take lower values.

We present in Table 5.10 the retrieval setups and results on HD 3167 c's spectrum obtained in Mikal-Evans et al. (2020). The molecular abundances are fitted using uniform priors, between 10^{-10} and 1. The temperature is between 400 and 800 K and is poorly constrained for all three retrievals. The abundance of the main spectral contributor, HCN, is found high using `Tau-REx 3` and `SCARLET` around 10^{-1} while `petitRATRANS` finds a lower value around 10^{-3} and find evidence of CO_2 with an abundance of around 10^{-2}. All three frameworks agree on a cloud-free atmosphere for HD 3167 c.

We also performed a similar retrieval setup using our extracted spectra for HD 106315 c and HD 3167 c. HD 106315 c retrieval results are similar to those obtained with Kreidberg et al. (2020) spectrum (see the third column of `Tau-REx 3` in Table 5.9). The increase of the prior in `Tau-REx 3` seems to be the main differentiating factor with our analysis in Section 5.4.2. The second column of

Tau-REx 3 in Table 5.10 presents the retrieval result using this setup on our HD 3167 c's spectrum. Using the opacity contribution results and the posterior distributions, we find evidence of H_2O, CO_2 and HCN in a cloud-free atmosphere, but the abundance is poorly constrained. Even with a prior up to 1, Tau-REx 3 does not find high values of molecular abundances.

To conclude, Bayesian atmospheric retrieval codes are sensitive to user inputs and priors. Increasing the molecular abundance priors in Tau-REx 3 tends to favour a heavy atmospheric composition solution instead of including clouds to adjust a small spectral feature. Similar behaviour was found for SCARLET. However, we note that Kreidberg et al. (2020) and Mikal-Evans et al. (2020) did not perform a flat-line retrieval and thus did not evaluate the strength of the atmospheric detection. The absence of a baseline reference retrieval provides us to compare the goodness of the different atmospheric fits and models. From our result with Tau-REx 3 in the section above, we did not strongly prove the presence of an atmosphere using their spectrum, which questions the comparison of the codes. Using a simulated spectrum would be better for comparing Bayesian retrieval codes. This work briefly compares the Bayesian frameworks with a similar setup and spectrum but cannot be considered a fully comprehensive comparison as too much information is missing and this highlights the need for atmospheric studies to report precisely priors and assumptions.

Table 5.9: Comparison of the retrieval analysis on HD 106315 c HST/WFC3 G141 data using three different Bayesian frameworks. The spectrum is taken from Kreidberg et al. (2020). The third column Tau-REx 3 presents the result obtained with this setup on our extracted spectrum of HD 106315 c.

		SCARLET		petitRADTRANS		Tau-REx 3		
Parameter	Unit	Prior	Value	Prior	Value	Prior	Value	
T(K)	K	$\mathcal{U}(620, 1150)$	866^{+188}_{-166}	$\mathcal{U}(400, 1000)$	594^{+188}_{-129}	$\mathcal{U}(400, 1000)$	746^{+175}_{-218}	916^{+57}_{-102}
$\log_{10}(P_{clouds})$	Pa dex	$\mathcal{U}(-3, 7)$	$1.6^{+2.4}_{-2.0}$	$\mathcal{U}(-3, 7)$	$2.8^{+1.9}_{-1.5}$	$\mathcal{U}(-3, 7)$	$4.0^{+1.8}_{-1.6}$	$3.1^{+2.5}_{-1.0}$
$\log_{10}(P_0)$	Pa dex	-	-	$\mathcal{U}(-3, 7)$	$2.7^{+1.6}_{-1.4}$	-	-	-
$\log_{10}(H_2O)$	dex	$\mathcal{U}(-10, -0.5)$	$-3.0^{+1.9}_{-3.1}$	$\mathcal{U}(-10, 0)$	$-3.4^{+2.1}_{-3.8}$	$\mathcal{U}(-10, 0)$	$-0.70^{+0.2}_{-3.8}$	$-0.75^{+0.1}_{-0.1}$
$\log_{10}(CO_2)$	dex	$\mathcal{U}(-10, -0.5)$	$-5.2^{+3.4}_{-3.2}$	$\mathcal{U}(-10, 0)$	$-5.5^{+3.3}_{-3.6}$	$\mathcal{U}(-10, 0)$	$-5.8^{+2.7}_{-2.7}$	$-6.5^{+2.6}_{-2.2}$
$\log_{10}(CO)$	dex	$\mathcal{U}(-10, -0.5)$	$-4.9^{+3.4}_{-3.4}$	$\mathcal{U}(-10, 0)$	$-5.4^{+3.0}_{-3.3}$	$\mathcal{U}(-10, 0)$	$-6.1^{+2.9}_{-2.5}$	$-6.7^{+2.7}_{-2.1}$
$\log_{10}(N_2)$	dex	$\mathcal{U}(-10, -0.5)$	$-5.3^{+3.2}_{-3.2}$	$\mathcal{U}(-10, 0)$	$-5.9^{+3.3}_{-3.0}$	$\mathcal{U}(-10, 0)$	$-5.7^{+2.7}_{-2.9}$	$-6.7^{+2.8}_{-2.2}$
$\log_{10}(CH_4)$	dex	$\mathcal{U}(-10, -0.5)$	$-6.6^{+2.8}_{-2.3}$	$\mathcal{U}(-10, 0)$	$-6.8^{+2.4}_{-2.3}$	$\mathcal{U}(-10, 0)$	$-6.8^{+2.6}_{-1.9}$	$-6.6^{+2.1}_{-2.1}$

Table 5.10: Comparison of the retrieval analysis on HD 3167 c HST/WFC3 G141 data using three different Bayesian frameworks. The spectrum is taken from Mikal-Evans et al. (2020). The second column Tau-REx 3 presents the result obtained with this setup on our extracted spectrum of HD 3167 c

Parameter	Unit	Prior	SCARLET	petitRADTRANS	Tau-REx 3	
T(K)	K	$\mathcal{U}(400, 800)$	558^{+109}_{-108}	488^{+119}_{-66}	610^{+116}_{-120}	737^{+53}_{-123}
$\log_{10}(P_{clouds})$	Pa dex	$\mathcal{U}(-3, 7)$	$4.1^{+1.9}_{-2.0}$	$4.6^{+1.5}_{-1.9}$	$5.0^{+1.3}_{-1.5}$	$4.6^{+1.5}_{-1.1}$
$\log_{10}(H_2O)$	dex	$\mathcal{U}(-10, 0)$	$-3.6^{+2.3}_{-3.4}$	$-3.8^{+1.7}_{-1.1}$	$-3.6^{+2.6}_{-3.6}$	$-5.0^{+1.7}_{-0.4}$
$\log_{10}(HCN)$	dex	$\mathcal{U}(-10, 0)$	$-1.6^{+1.0}_{-4.3}$	$-3.7^{+1.9}_{-3.4}$	$-0.9^{+0.3}_{-4.1}$	$-5.4^{+2.0}_{-1.3}$
$\log_{10}(CO_2)$	dex	$\mathcal{U}(-10, 0)$	$-4.1^{+2.5}_{-3.9}$	$-2.1^{+1.0}_{-4.6}$	$-5.3^{+3.0}_{-2.9}$	$-3.6^{+1.3}_{-0.6}$
$\log_{10}(CO)$	dex	$\mathcal{U}(-10, 0)$	$-5.0^{+3.3}_{-3.3}$	$-5.3^{+3.1}_{-3.0}$	$-5.8^{+3.5}_{-2.6}$	$-6.3^{+2.7}_{-2.4}$
$\log_{10}(N_2)$	dex	$\mathcal{U}(-10, 0)$	$-5.0^{+3.3}_{-3.3}$	$-5.5^{+3.1}_{-2.9}$	$-5.5^{+3.3}_{-2.8}$	$-6.5^{+2.5}_{-2.3}$
$\log_{10}(CH_4)$	dex	$\mathcal{U}(-10, 0)$	$-5.9^{+2.7}_{-2.7}$	$-6.5^{+2.2}_{-2.2}$	$-6.0^{+2.9}_{-2.4}$	$-7.5^{+1.6}_{-1.6}$
$\log_{10}(NH_3)$	dex	$\mathcal{U}(-10, 0)$	$-7.0^{+2.2}_{-1.9}$	$-7.3^{+1.8}_{-1.7}$	$-7.1^{+1.9}_{-1.7}$	$-7.3^{+1.1}_{-1.7}$

5.6 Conclusion

This chapter presents an atmospheric characterisation study of two medium-sized planets bracketing the radius of Neptune: HD 106315 c (R_P=4.98 ± 0.23 $R_\oplus$) and HD 3167 c (R_P=$2.740^{+0.106}_{-0.100}$ $R_\oplus$). We analysed spatially scanned spectroscopic observations obtained with the G141 grism (1.125 - 1.650 μm) of the Wide Field Camera 3 (WFC3) onboard the Hubble Space Telescope. We use the publicly available `iraclis` pipeline and `Tau-REx 3` atmospheric retrieval code and we detected water vapour in the atmosphere of both planets with an abundance of $\log_{10}(H_2O) = -2.1^{+0.7}_{-1.3}$ ($\sim 6\sigma$) and $\log_{10}(H_2O) = -4.1^{+0.9}_{-0.9}$ ($\sim 3\sigma$) for HD 106315 c and HD 3167 c, respectively. The analysis of the transmission spectrum of HD 106315 c offered a tentative detection of ammonia absorption ($\log_{10}(NH_3) = -4.3^{+0.7}_{-2.0}$, $\sim 2\sigma$). A deep cloud deck is required to fit the spectrum when removing ammonia. We can only put an upper bound on methane abundance (10^{-5}), while carbon dioxide and monoxide abundances are unconstrained. HD 3167 c analysis resulted in both a water vapour ($\log_{10}(H_2O) = -4.1^{+0.9}_{-0.9}$, Δ_{E1}=3.61) and a carbon dioxide ($\log_{10}(CO_2) = -2.4^{+0.7}_{-1.0}$, Δ_{E1}=3.93) moderate detection. As CO_2 is not explained by 1D equilibrium chemistry models at low metallicity for planets with equilibrium temperature below 600 K, its presence could be due to noise and highlights the limitations of our data quality. More precise constraints on the chemical abundances could be given if 3D models were employed instead of 1D ones. The shortcomings of retrieval analyses performed with 1D forward models have already been highlighted in previous papers (see, e.g. Caldas et al., 2019). On the contrary, if we assume a high metallicity, CO_2 could be present in the atmosphere of HD 3167 c (an increase in metallicity by a factor of x tends to increase the abundance of CO_2 by a factor of x^2, see Moses see e.g. 2014). Thus, further observations are needed to establish whether the CO_2 might be present in the atmosphere of this exoplanet.

Upcoming facilities could help resolve degeneracies in the atmosphere of low-mass planets. Cowan et al. (2015), Greene et al. (2016), Tinetti et al. (2018), and Edwards et al. (2019) have shown the potential of the JWST, Twinkle, and Ariel space missions to characterise exo-atmospheres. Additionally, ground-based instruments such as the European Extremely Large Telescope (E-ELT), -and in particular, the Mid-Infrared E-ELT Imager and Spectrograph (METIS) instrument (Brandl et al., 2018)-, the Thirty Meter Telescope (TMT, Skidmore et al. 2018), and the Giant Magellan Telescope (GMT, Fanson et al. 2018), will become available. The availability of the new data will lead to the systematic study of thousands of exoplanets' day sides and terminators at high-(HRS, from the ground) and low-(LRS, from space) spectral resolution. By combining HRS with LRS and thus probing different regions of the exoplanetary atmospheres (higher atmospheric altitudes with HRS, lower atmospheric altitudes with LRS), we will better understand the atmospheric compositions and thus be able to apply more constraints on their formation and evolution. The Transit Spectroscopy Metric (TSM) proposed in Kempton et al. (2018) indicates the potential of spectroscopy measurements for exoplanets. The TSM value respectively 98 and 86 for HD 106315 c and HD 3167 c. However, in light of the results obtained with HST and given the brightness of their respective host stars and the large-scale heights, we can conclude that these two planets are suitable targets for these upcoming instruments.

To support this point, we updated Figure 6 in Tsiaras et al. (2018), which represents the planetary radius as a function of the Atmospheric Detectability Index (ADI) or $\Delta\log(E)$ here. The analysis presented in this chapter results from work carried out during the ARES Summer School, where we used algorithms and data available to the public, thus allowing our results to be tested and reproduced. It is based on the publication **ARES IV: Probing the atmospheres of two warm small planets HD 106315 c and HD 3167 c with the HST/WFC3 Camera (Guilluy, Gressier et al. 2021)** (see List of Publications). The latter is the fourth paper output of this summer school. In the first work, ARES I(Edwards et al., 2020) and the third one, ARES III (Pluriel et al., 2020a), we analysed

the transmission and the emission spectra of WASP-76 b and KELT-7 b respectively. In contrast, in the second one ARES II (Skaf et al., 2020), the atmospheric study of WASP-42 b, WASP-79 b, and WASP-127 b was performed. For consistency, we used the ADI metric as a significance index. Figure 5.16 shows the gaseous exoplanets studied by Tsiaras et al. (2018) (in black), K2-18b examined in Tsiaras et al. (2019) (in blue), the hot-Jupiters analysed in ARES I, ARES II, ARES III (in red) and the Neptune-like planets, HD 106315 c (in green) and HD 3167 c (in violet). This figure shows that the ADI is not smaller even if the two exoplanets have smaller radii than most other targets. Together with Tsiaras et al. (2019), our study shows that even smaller planets' atmospheres can be highly significant. This result opens the way for the atmospheric study of planets with smaller radii than the hot-Jupiter targets, which have mainly been analysed so far. A revised version of this figure is proposed in Chapter 7 for the HST survey on 26 Sub-Neptune and Super-Earth planets.

Tools presented in this chapter are designed to automatically analyse Hubble Observations in the NIR, from the raw images to the atmospheric composition. We used already developed open access codes `iraclis` and `Tau-REx 3` to perform the analyses. We applied it to two Neptune-like planets with a warm gaseous atmosphere. Even though we could find evidence of molecular absorption, particularly water, in these atmospheres, this study also highlights the limitation of using Hubble data to characterise exoplanet atmospheres. The retrieved abundances have large uncertainties because of the low spectral resolution and the short wavelength coverage. Different atmospheric modelling will find other solutions. In the next chapter, we will adapt the analysis and the methodology to infer atmospheric properties on a temperate terrestrial planet and look for evidence of an atmosphere. We will thus highlight even more limitations in studying smaller and smaller planets with Hubble data quality.

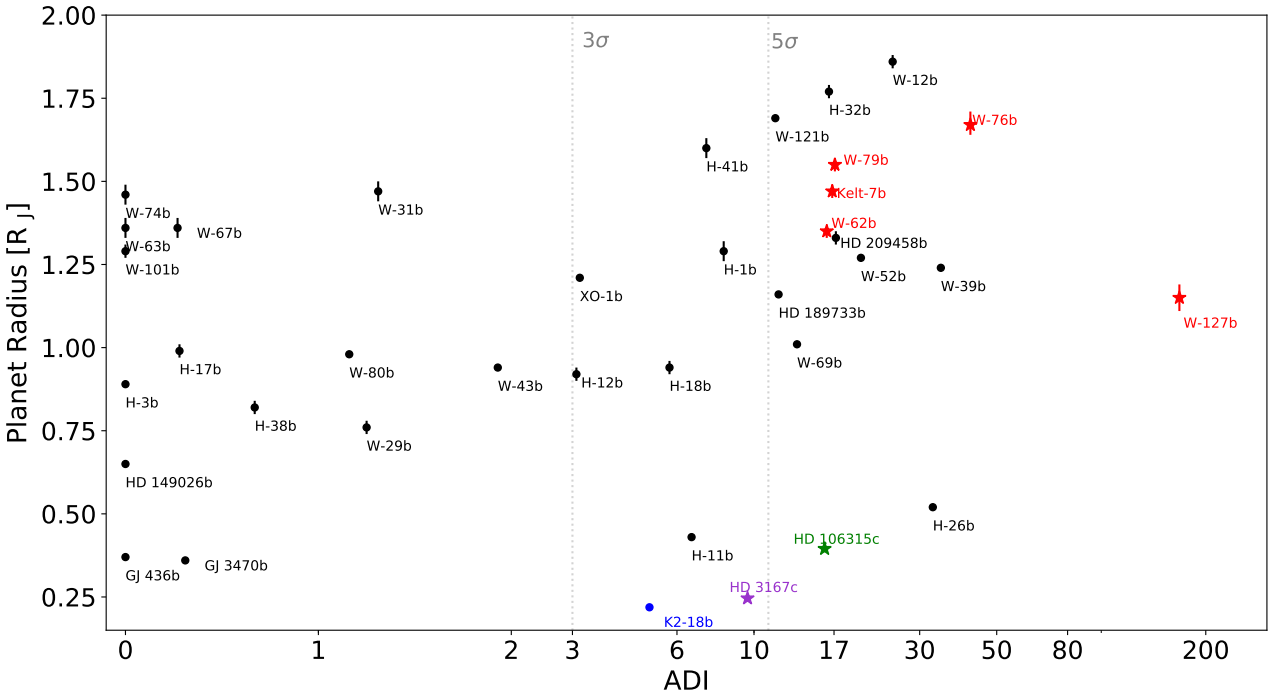

Figure 5.16: Exoplanetary radii as a function of the Bayes factor, Atmospheric Detectability Index (in logarithmic scale) for the targets analysed in this work (in green and in violet), in ARES I-II-III (in red), in Tsiaras et al. (2018) (in black), and in Tsiaras et al. (2019) (in blue).

Chapter 6

Constraining the atmosphere of a rocky temperate planet with Hubble NIR observations

Contents

6.1 Introduction

This chapter is based on the publication **Near infrared spectrum of TRAPPIST-1h using Hubble WFC3 G141 observations (Gressier et al. 2022)**. The paper was published in A&A in February 2022, and the link to the article is in List of Publications .

We present the first attempt to characterise the atmosphere of the seventh planet of the TRAPPIST-1 planetary system, TRAPPIST-1 h. We present in Section 6.1 the specific configuration of the planetary system. In Sections 6.3.1 and 6.3.2 we analyse the HST/WFC3 G141 raw data using the python

package `iraclis` (Tsiaras et al., 2016b,a, 2018) and detail the stellar contamination models used to correct our spectrum. Section 6.3.3 presents the atmospheric characterisation of TRAPPIST-1 h. First, different atmospheric scenarios are discussed based on the recent review by Turbet et al. (2020a). Then, we detail the atmospheric retrieval set-ups we performed using the Bayesian radiative transfer code Tau-REx 3 (Al-Refaie et al., 2021)[1]. We present the results in Section 6.5 and discuss our findings in Section 6.5.

6.2 Planet description

The TRAPPIST-1 planetary system was discovered by Gillon et al. (2016) and Gillon et al. (2017), using the Transiting Planets and PlanetIsimals Small Telescope (Gillon et al., 2011, 2013). TRAPPIST-1 h is the most outer planet detected in this system. Its detection was first suggested in Gillon et al. (2017) but later confirmed in Luger et al. (2017b). Further observations using Spitzer and K2 photometry followed the discovery to constrain planetary parameters better (Delrez et al., 2018; Ducrot et al., 2018; Burdanov et al., 2019; Ducrot et al., 2020). Since then, important scientific efforts have been carried out to observe, characterise, and model the seven planets orbiting this M8-type star. This is motivated by the TRAPPIST-1 system, which offers the most favourable conditions to study rocky planets in the habitable zone, that is, planets that could harbour liquid water on their surface as defined in Kasting et al. (1993).

Table 6.1: Stellar and planetary parameters used in the observations analysis of TRAPPIST-1 h

Parameter	Value
Spectral type	M8-V
$R_\star$ ($R_\odot$)	0.1170 ± 0.0036
$M_\star$ ($M_\odot$)	0.0802 ± 0.0073
$T_\star$ (K)	2559 ± 50
log(g)	5.21
Fe/H	0.040 ± 0.080
R_p ($R_\oplus$)	0.752 ± 0.032
M_p ($M_\oplus$)	$0.331\ ^{+0.056}_{-0.049}$
a (AU)	0.059 ± 0.004
T_{eff} (K)	173 ± 4
S ($S_\oplus$)	0.165 ± 0.025
$a/R_\star$	109 ± 4
$R_p/R_\star$	0.0588 ± 0.0016
i (deg)	$89.76^{+0.05}_{-0.03}$
e	0
b	0.45
P_{orb} (days)	$18.767\ ^{+0.004}_{-0.003}$
T_{mid} (BJD_{TDB})	$2\,458\,751.06983 \pm 0.00021$[2]
references	Gillon et al. (2017) Luger et al. (2017a)

TRAPPIST-1 is close (39.14 light years), cool (2559 K), and small (0.117 $R_\odot$), making it favourable for observations (Gillon et al., 2017). On the other hand, the star is also the limiting factor in studying the atmosphere of TRAPPIST-1 planets. M-type stars stay for millions of years in the pre-main sequence (PMS) phase, during which planets are exposed to strong non-thermal extreme UV (EUV)

[1] https://github.com/ucl-exoplanets/Tau-REx3_public
[2] Obtained in this work

and far-UV irradiation, which is expected to lead to atmospheric hydrodynamical escape (Vidal-Madjar et al., 2003; Bourrier et al., 2017b) and a runaway greenhouse effect (Ramirez & Kaltenegger, 2014). TRAPPIST-1 is a very cold M-dwarf, but it is supposedly very active with strong flaring events (Vida et al., 2017) and EUV flux (Wheatley et al., 2017). Atmospheric erosion might have stripped all planets in the TRAPPIST-1 system of their atmospheres (Lammer et al., 2003; Bolmont et al., 2017). Whether or not an atmosphere was sustained depends on the initial amount of accreted volatiles during the planetary formation phase and the intensity of the atmospheric escape due to the star activity.

The TRAPPIST-1 planetary system is very compact, all the planets are within 0.06 AU, and they are co-planar (Luger et al., 2017a,b; Delrez et al., 2018). In addition, they all have a circularised orbit with eccentricities below 0.01 (Gillon et al., 2017; Luger et al., 2017b) and present gravitational interactions forming a resonant chain, thus suggesting that the system had a relatively peaceful history. TRAPPIST-1 h is this planetary system's furthest and smallest known planet. It has a radius of 0.752 ± 0.032 R$\oplus$ and a mass of $0.331^{+0.056}_{-0049}$ M$\oplus$ (Luger et al., 2017b; Gillon et al., 2017), which suggests a density similar to that of Mars ($\sim$ 4000 kg/m^3). The planetary parameters are detailed in Table 6.1 along with stellar and orbital parameters of the system.

Two possible formation scenarios have been proposed for the TRAPPIST-1 system, particularly for TRAPPIST-1 h. The first suggests that all the planets formed beyond the water frost line migrated inwards, causing the resonance. This possibility was proposed in the discovery papers Gillon et al. (2017) and Luger et al. (2017b), but also detailed in Ormel et al. (2017), Tamayo et al. (2017), and Coleman et al. (2019). If TRAPPIST-1 h formed far from the host star, it could be volatiles-rich because the atmospheric escape would only remove between 1 and 10% of the total planet mass (Tian & Ida, 2015; Bolmont et al., 2017; Bourrier et al., 2017b; Turbet et al., 2020a). TRAPPIST-1 h could also have formed in situ, and a short migration or an eccentricity damping could have caused the resonant chain (MacDonald & Dawson, 2018). In this case, the planet is probably dry (Turbet et al., 2020a) because of the strong atmospheric erosion.

On the other hand, TRAPPIST-1 h, being the furthest planet of the system, might have had a more important quantity of initial gas than the inner planets. It could have formed with TRAPPIST-1 f and g in a different part of the proto-planetary disk leading to a different bulk composition (Papaloizou et al., 2018; Turbet et al., 2020a). Volatiles could also have been brought after by cometary impacts or degassing (Kral et al., 2018; Dencs & Regály, 2019; Turbet et al., 2020a; Kimura & Ikoma, 2020), and this is favoured for outer planets because volatiles' impacts dominate over the impact erosion mechanism (Kral et al., 2018).

For close-in planetary systems, the effects of gravitational tides by the star on the planets are important and shape the orbital dynamics. They slow the rotation rate, reduce the obliquity, and circularise the orbit. As shown in Turbet et al. (2018), the evolution timescales for TRAPPIST-1 h are 7 million years for the rotation and 80 million years for the obliquity. Given the age of the TRAPPIST-1 system, 8 billion years old (Burgasser & Mamajek, 2017), it is likely that TRAPPIST-1 h is in a synchronous rotation state. However, tidal heating is unlikely to be the dominant interior heating process for outer planets (Turbet et al., 2018; Makarov et al., 2018; Dobos et al., 2019) compared to direct atmospheric warming. The received stellar flux is two orders of magnitude higher than the tidal heating for TRAPPIST-1 h (Turbet et al., 2020a). It is then unlikely that TRAPPIST-1 h tidal heating caused the melting of the mantle leading to the out-gassing of volcanic gases (Turbet et al., 2020a).

At the time of publishing, TRAPPIST-1 h was the only planet in the system for which the near-infrared (NIR) spectrum (1.1-1.7 µm) from the Hubble Space Telescope (HST) Wide Field Camera 3 Grism 141 (WFC3/G141) had not been published. The other planets' spectra have already been studied with different pipelines and stellar contamination models in de Wit et al. (2016) and de Wit et al. (2018), Zhang et al. (2018), and Wakeford et al. (2019). From these analyses, we learned that the TRAPPIST-1 planets probably do not have a H_2, He extended atmosphere. However, it was impossible

to rule out this hypothesis using only HST/WFC3 (de Wit et al., 2018; Moran et al., 2018). All spectra are consistent with flat spectra and could be fitted with different models, including a high-altitude cloud cover and/or a high metallicity hydrogen-rich atmosphere. A featureless spectrum could also result from the absence of an atmosphere around these planets. However, Bourrier et al. (2017b) and Bourrier et al. (2017a) analysed Lyman-α HST/STIS transits of TRAPPIST-1 b and c and detected a decrease in the flux, which might hint at the presence of an extended hydrogen exosphere.

6.3 Methodology

6.3.1 Observations: Hubble WFC3 data reduction and extraction

We used the raw spatially scanned spectroscopic images obtained from Proposal 15 304 (PI: Julien de Wit) in the Mikulski Archive for Space Telescope (MAST) [3]. Three transit observations of TRAPPIST-1 h were acquired using the Grism 256 aperture and 256 x 256 sub-array with an exposure time of 112.08 s. We refer to the data taken in July 2017, September 2019, and July 2020 as Observations 1, 2, and 3, respectively. Each visit comprises four HST orbits, with 60 exposures in Observation 2 and 50 for Observations 1 and 3, each being made in the forward spatial scan mode.

To reduce and analyse the data, we used `iraclis`, presented in the previous Chapter 5 Section 5.3. We will then summarise the steps and precise the adjustments made for these observations. The reduction of the raw observations follows these steps: zero-read subtraction, reference pixels correction, non-linearity correction, dark current subtraction, gain conversion, sky background subtraction, flat-field correction, and corrections for bad pixels and cosmic rays. We used the reduced spatially scanned spectroscopic images for all three observations to extract the white and spectral light curves. We used the default 'low' resolution from Iraclis for the spectral light curves bins, which correspond to a resolving power of around 50 at 1.4 µm.

Using the extracted light curves and the time of the observations, we first looked for contamination from other TRAPPIST-1 planets transits using the python package PyLightcurve (Tsiaras et al., 2016a) [4]. The planets and transit parameters were set to those of Gillon et al. (2017). TRAPPIST-1 c was also transiting during the second orbit of the first observation (July 2017), and we then suppressed this orbit from the rest of the analysis. We plot in Figure 6.1 the extracted raw flux, and the corresponding predicted transits of the TRAPPIST-1 planets for the three visits. The first orbit always presents a stronger wavelength-dependent ramp than the other orbits and is usually suppressed from the analysis. However, we decided to keep the first HST orbit in every transit observation to conserve an out-of-transit baseline and correctly fit the transit parameters. Indeed, every attempt was made to keep as many exposures as possible. For Observations 1 and 2, we removed the first two exposures of these first orbits but kept all exposures of every subsequent orbit. However, for Observation 3, a good fit could only be obtained by removing the first exposure of every orbit, a practice which is expected as these exposures present significantly lower counts than the following exposures (e.g. Deming et al., 2013; Tsiaras et al., 2016b; Edwards et al., 2021).

We fitted the white light curves and the spectral light curves using the transit model from `PyLightcurve` (Tsiaras et al., 2016a) and the Markov chain Monte Carlo (MCMC) method implemented in emcee (Foreman-Mackey et al., 2013). For the white light curve fitting of all the observations, the only free planetary parameters are the mid-transit time and the planet-to-star radius ratio. The other planetary parameters were fixed to the values from Luger et al. (2017a) ($a/R_\star$=109±4 and i=89.76°) and stellar parameters are from Gillon et al. (2017) ($T_\star$=2559±50 K, log(g)=5.21, Fe/H=0.04). We also fitted for the coefficients ra, rb_1, and rb_2. We adopted the parameterisation of Claret et al. (2012) and Claret

[3] https://archive.stsci.edu
[4] https://github.com/ucl-exoplanets/pylightcurve

et al. (2013) with four parameters to describe the limb-darkening coefficient. We used the PHOENIX model (Claret, 2018) and `ExoTETHyS` package (Morello et al., 2020) to obtain the limb-darkening coefficients for the white light curve analysis but also in every wavelength bin for the spectral curves fitting (see Table 6.2). We accounted for the ramp time-dependent systematic effect and fitted for the planet-to-star radius ratio in every wavelength band using the same method and formulas presented in Chapter 5 Section 5.3 (see equations 5.1 and 5.2).

The white light curve fits for the three different observations are shown in Figure 6.2. The planet-to-star radius ratio are found to be compatible with 0.0575±0.0006 for Observation 1, 0.0565±0.0009 for Observation 2, and 0.0575±0.0012 for Observation 3. We found the following mid-transit times in BJD_{TDB}: 2 458 319.4282 ± 0.0020 for Observation 1, 2 458 751.06983 ± 0.00021 for Observation 2, and 2 459 051.3428 ± 0.0053 for Observation 3. The spectral light curve fit for the three observations is presented in Figure 6.4. We computed the final transmission spectrum by combining the three spectral fits using a weighted mean of the transmission spectra. After the initial white light curve fit, the errors on each exposure were scaled to match the root mean square of the residuals. The white fitting was then performed a second time with these scaled errors. A similar scaling was also applied to the spectral light curves. This method ensures that the recovered uncertainties on the transit depth are not underestimated (Tsiaras et al., 2016b). The transmission spectra and the recovered final transit depth are over-plotted in Figure 6.5, along with the corresponding residuals. We note a rise in the transit depth around 1.3 µm. All three observations exhibit similar features over these regions, suggesting this is of astrophysical origin and part of the transit spectrum and not contamination, or poor fitting, of a single visit. We also present in Figure 6.3 the three white light curves in the same plot using a planet-to-star radius ratio weighted by the mean of the three white light curve best-fits for the transit model. The combined extracted spectrum and the uncertainties are presented in Table 6.2.

Table 6.2: Combined transit depth, associated uncertainties and limb-darkening coefficients. The final transmission spectrum was computed in ppm using the three HST/WFC3 G141 transit observations from July 2017, September 2019, and July 2020 on TRAPPIST-1 h.

Wavelength	Bandwidth	Transit depth	Error	Limb-darkening coefficients			
µm	µm	ppm	ppm	a1	a2	a3	a4
1.1262	0.0308	3128.22	129.30	2.0139	-1.6261	0.8709	-2.0398
1.1563	0.0293	2981.61	132.61	2.1956	-2.0725	1.2403	-0.3147
1.1849	0.0279	3224.87	121.09	2.1292	-1.9036	1.0964	-0.2708
1.2123	0.0269	3275.06	112.69	1.9514	-1.5303	0.8020	-0.1849
1.2390	0.0265	3476.20	95.97	1.9236	-1.5957	0.8838	-0.2137
1.2657	0.0269	3264.82	95.65	2.0255	-1.8405	1.0765	-0.2698
1.2925	0.0267	3589.24	115.10	2.1105	-2.1495	1.3561	-0.3578
1.3190	0.0263	3686.39	110.98	2.1650	-2.2486	1.4262	-0.3772
1.3454	0.0265	3368.20	126.87	1.2204	-0.1088	-0.1857	0.0789
1.3723	0.0274	2900.07	108.34	1.0023	0.4493	-0.6644	0.2195
1.4000	0.0280	3271.69	109.38	0.9553	0.4582	-0.6187	0.1988
1.4283	0.0285	3321.59	103.01	0.7774	0.7086	-0.7252	0.2128
1.4572	0.0294	3111.09	113.41	0.9247	0.4694	-0.6071	0.1921
1.4873	0.0308	3070.67	113.98	1.0279	0.2998	-0.530181	0.18063
1.5186	0.0318	3037.95	112.45	1.2541	-0.1103	-0.2727	0.1188
1.5514	0.0337	3125.30	102.78	1.5025	-0.6408	0.1247	0.0082
1.5862	0.0360	3472.00	114.20	1.7942	-1.3368	0.6809	-0.1553
1.6237	0.0390	3045.52	95.82	1.9296	-1.7566	1.0358	-0.2629
1.3750	0.5500	3268.70	51.38	2.009	-1.7704	1.0225	-0.2546

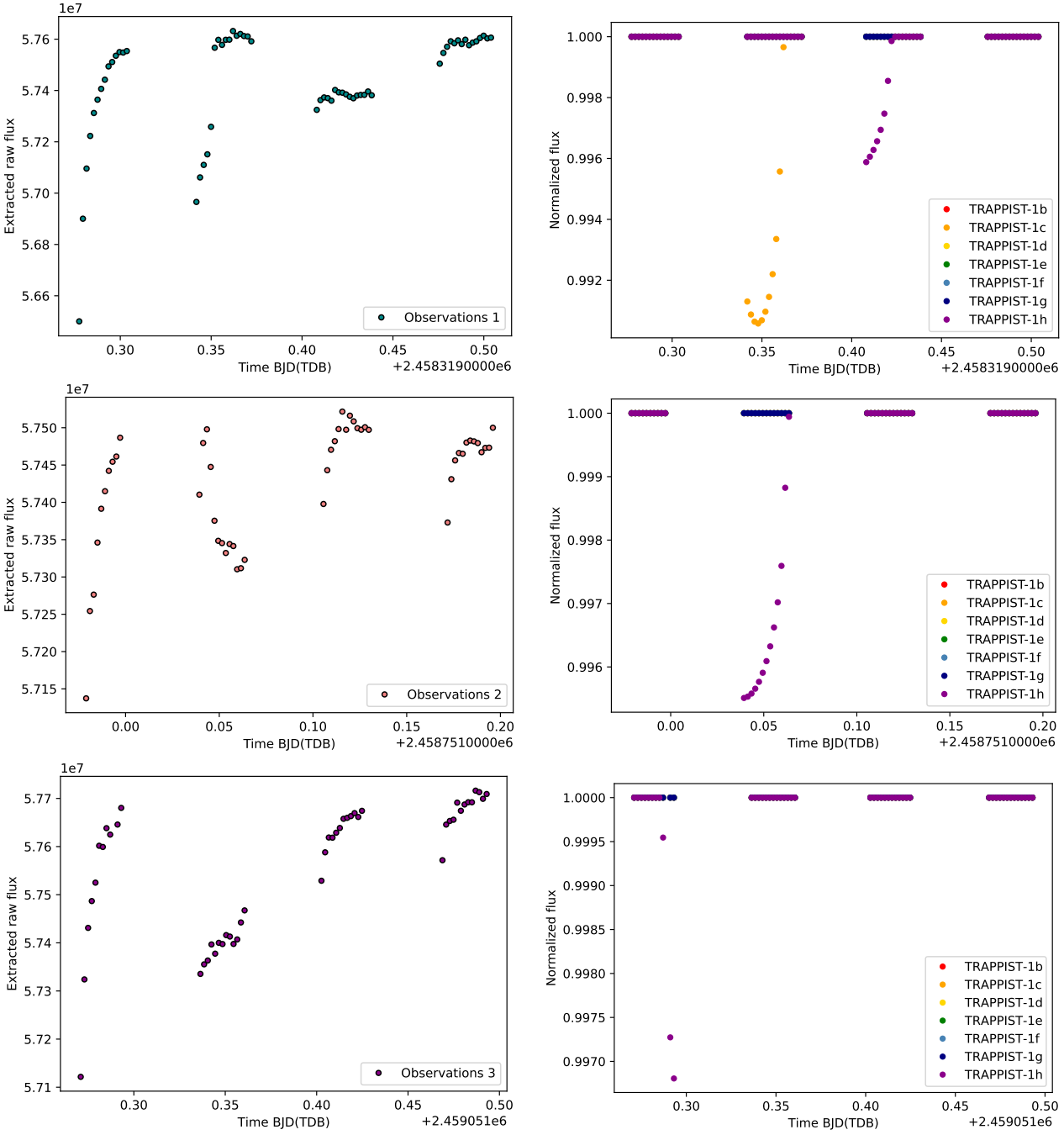

Figure 6.1: Left: Raw extracted light curves for the TRAPPIST-1 h observations (top: Observations 1 July 2017, middle: Observations 2 September 2019, and bottom Observations 3: July 2020). Right: Predicted planetary transits using `PyLightcurve` transits model and Gillon et al. (2017) system parameters at the time of the observations.

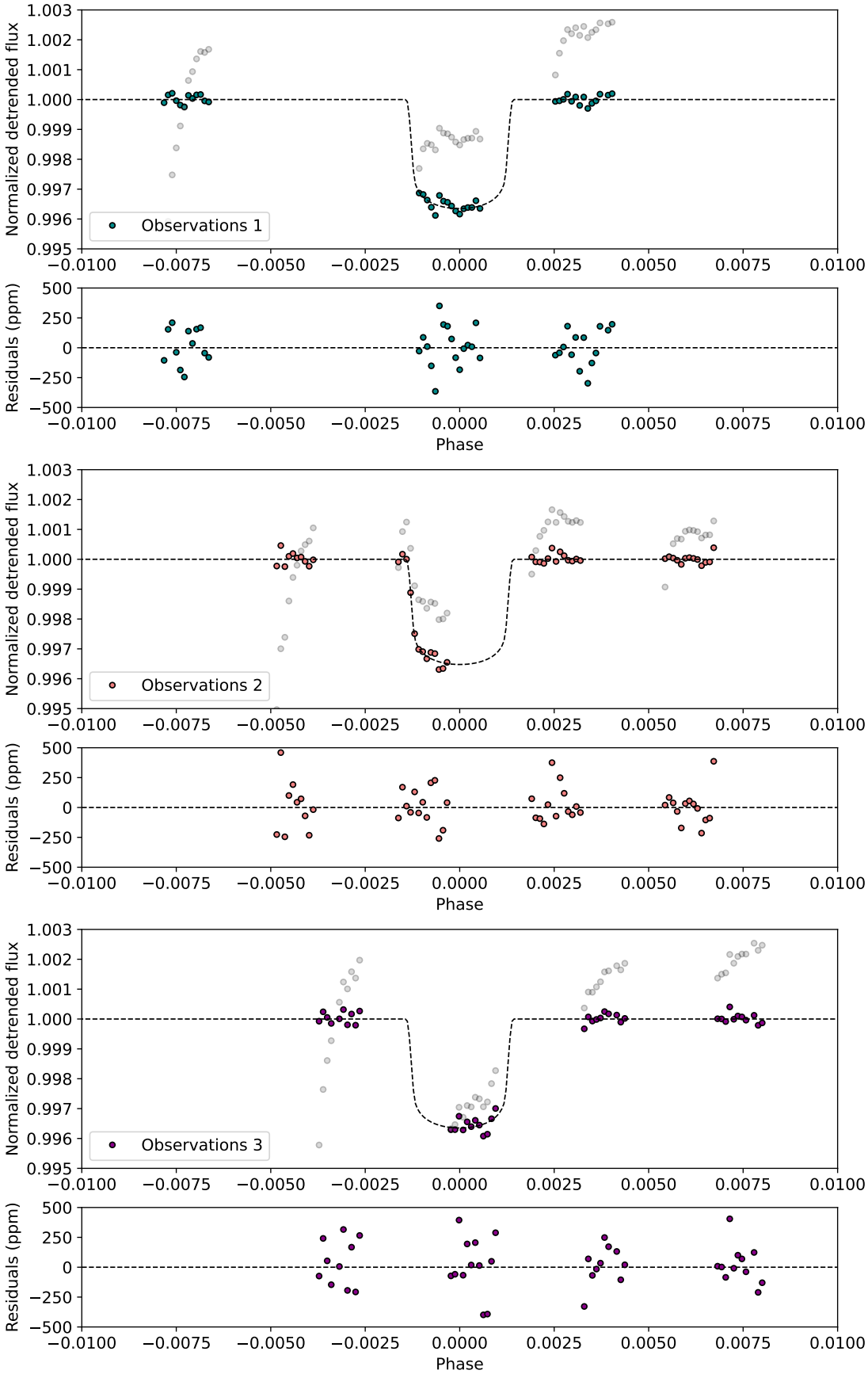

Figure 6.2: White light curve fits for the three observations on TRAPPIST-1 h (top: July 2017, middle: September 2019, and bottom: July 2020). For every observation, we show the raw (grey), the de-trended flux (colour points) and the best-fit model (dotted lines) along with the residuals from the best-fit model.

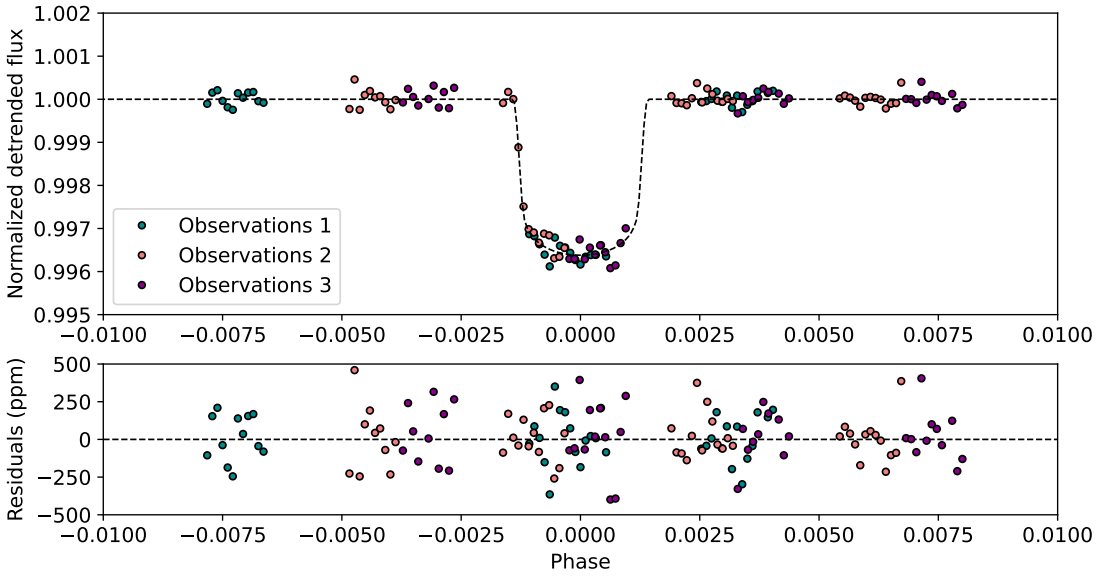

Figure 6.3: Combined white light curve fits for the three visits on TRAPPIST-1 h (top). The transit model (dotted line) was simulated using a weighted mean of the three observations' planet-to-star radius ratios, i.e. 0.0572.

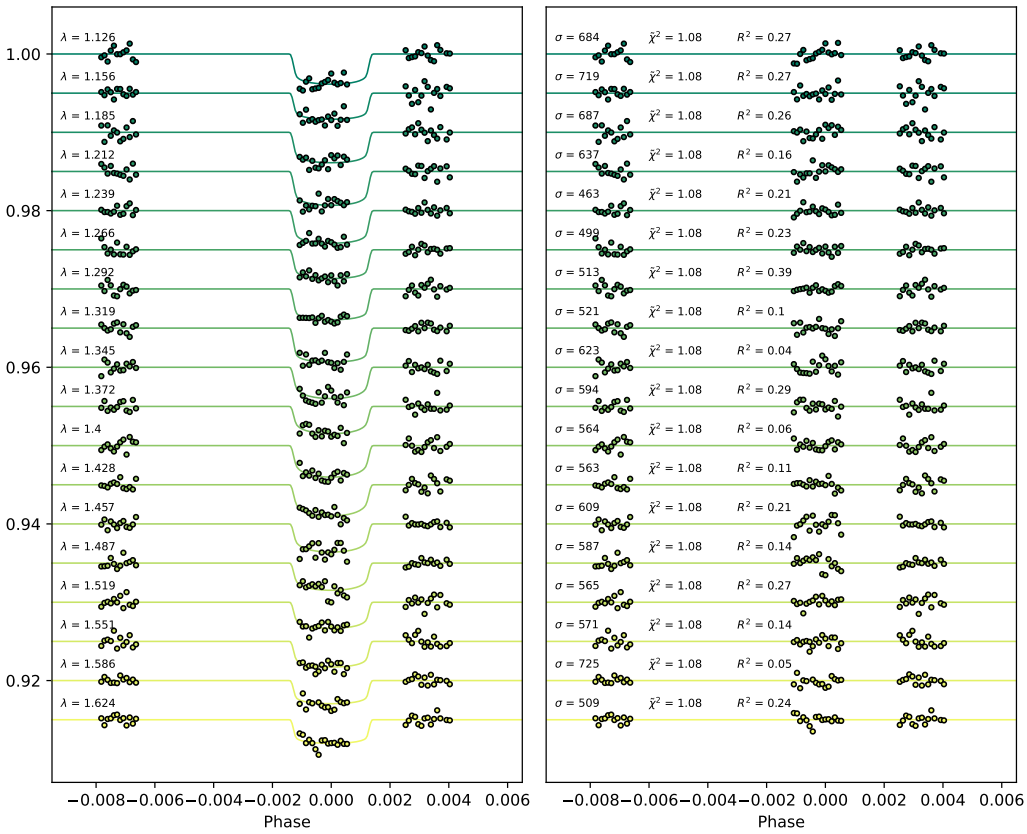

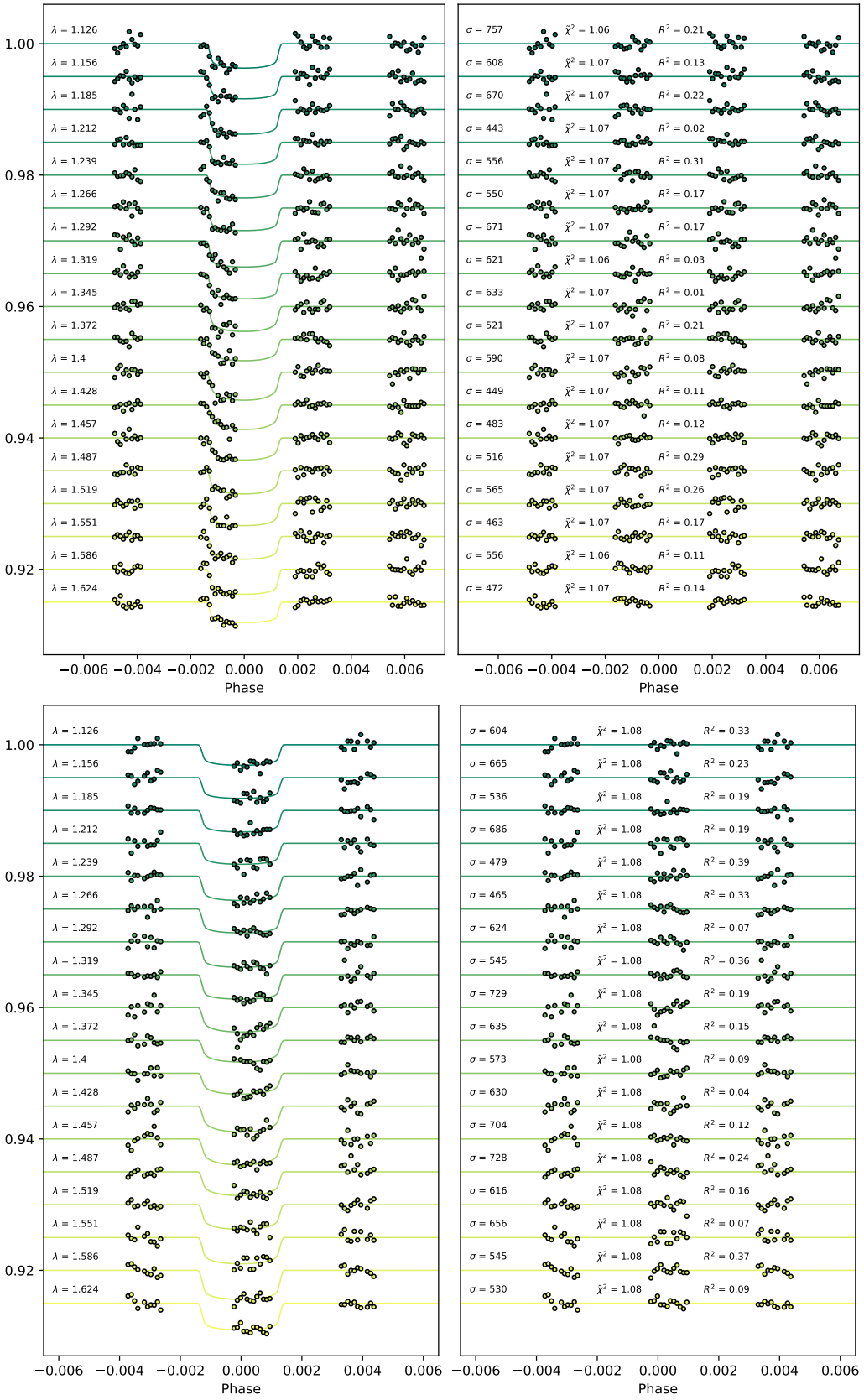

Figure 6.4: Spectral light curve fits for the three observations on TRAPPIST-1 h (top: July 2017, middle: September 2019, and bottom: July 2020). An artificial offset in the y-axis was applied for clarity. For each light curve, the left panel shows the de-trended spectral light curves with the best-fit model in dotted lines with the central wavelength, and the right panel shows the residuals and values for the standard deviation (σ) in ppm, the reduced Chi-squared ($\tilde{\chi}^2$), and the auto-correlation (R^2).

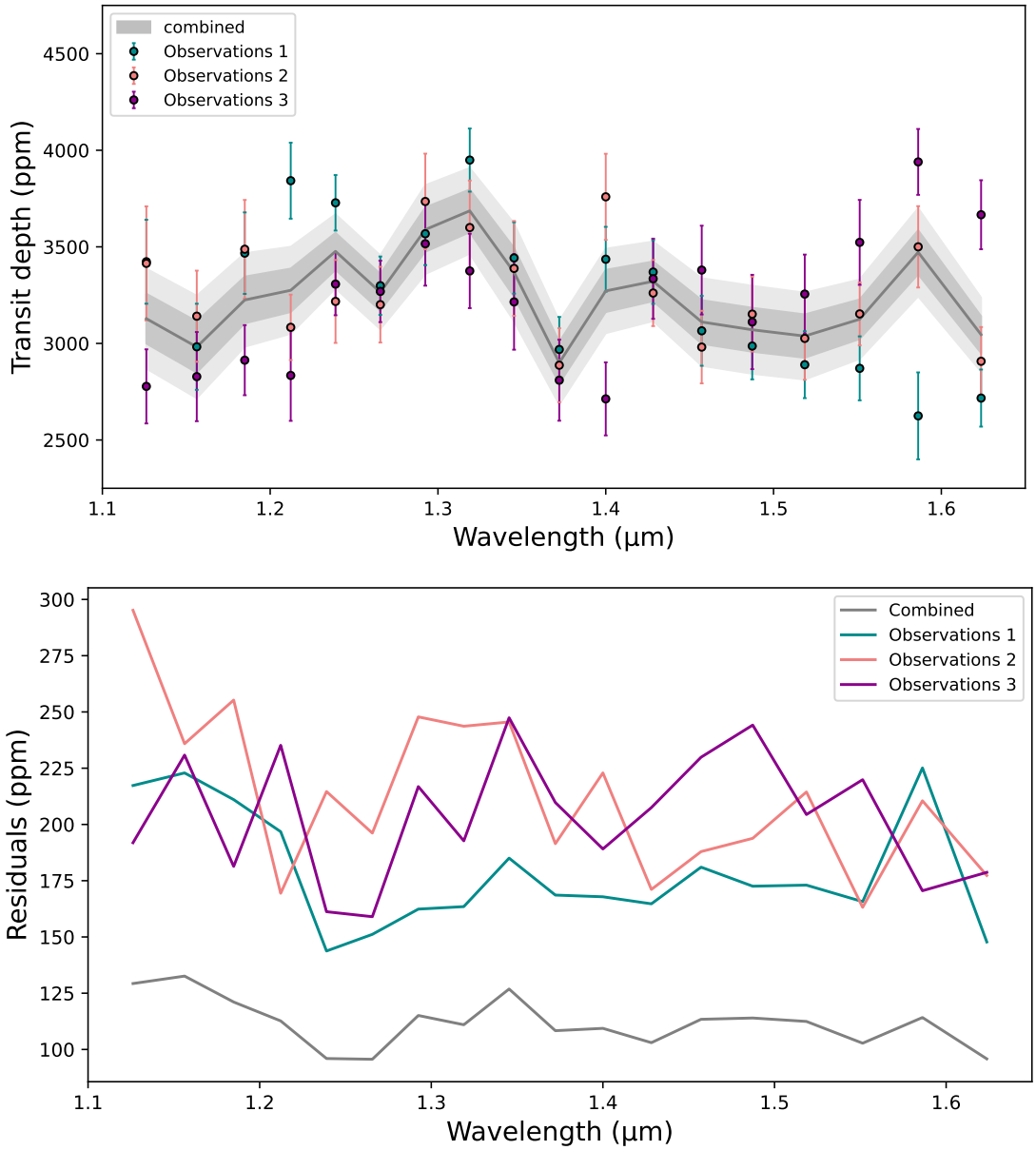

Figure 6.5: Recovered transit depths for the three observations and combined transmission spectrum with 1 and 2-σ uncertainty ranges (left). First, we suppressed the white light curve values from each visit raw flux, then computed the weighted mean, and finally added the mean white light curve value to obtain the transit depth. Residuals are from the spectral light curves analysis and the combined spectrum (right).

6.3.2 Data analysis: Modelling the stellar contamination

TRAPPIST-1 is known for presenting a heterogeneous photosphere that can lead to a misinterpretation of the transmission spectra. This Section aims to use different existing models to correct our spectrum for a stellar contribution. The star presents a $\sim$ 1% photometric variability in the I+z bandpass interpreted as active regions rotating in and out of view (Gillon et al., 2016). Rackham et al. (2018) show that it would cause a non-negligible effect (transit light source effect, TLSE) on the transmission spectrum if the variability is consistent with rotational modulations. Several previous studies have examined the stellar surface models using various methods, but their results are inconsistent. In the present study, three stellar models from three studies, Zhang et al. (2018), Morris et al. (2018), and Wakeford et al. (2019), were introduced and examined.

Table 6.3 shows the temperature and the covering fraction of each component for each model. We note that T_i is the temperature, f_i is the covering fraction at the photosphere, and f'_i is the covering fraction at the transit chord. The M18 model is the best-fit model from Morris et al. (2018). Z18 is the best-fit contamination model from Table 16 in Zhang et al. (2018). W19 is the $3T_{c+m}$ model from Wakeford et al. (2019). We note that what we call the W19 model here is not the best-fit model in their analysis, as they conclude that TLSE is not significant in their data, but they did not exclude $3T_{c+m}$.

We define the wavelength-dependent contamination factor ε_λ as

$$\delta_\lambda = \varepsilon_\lambda \times \delta_{real,\lambda}, \tag{6.1}$$

where δ_λ is the measured transit depth and $\delta_{real,\lambda}$ is the actual transit depth. For each stellar surface model, ε_λ was calculated as

$$\varepsilon_\lambda = \frac{f'_1 S_{1,\lambda} + f'_2 S_{2,\lambda} + f'_3 S_{3,\lambda}}{f_1 S_{1,\lambda} + f_2 S_{2,\lambda} + f_3 S_{3,\lambda}} \tag{6.2}$$

$$f_3 = 1 - f_1 - f_2 \tag{6.3}$$

$$f'_3 = 1 - f'_1 - f'_2, \tag{6.4}$$

where $S_{i,\lambda}$ is the stellar flux of each temperature component. We used the BT-Settl model for each temperature, with the metallicity [Fe/H]= 0 dex and the stellar surface gravity log g at 5.2, from the SVO theoretical spectra web server ([5]).

Table 6.3: Summary of the adopted TRAPPIST-1 stellar models.

Model	Z18	M18	W19
T_1(K)	2000	2500	2400
T_2(K)	2400	5300	3000
T_3(K)	3000	–	5800
f_1	0.38	0.999952	0.64
f_2	0.14	4.8×10^{-5}	0.35
f'_1	0.10	1.0	0.646
f'_2	0.45	0.0	0.354

[5] http://svo2.cab.inta-csic.es/theory/newov2/

6.3.3 Data analysis: Atmospheric modelling

Possible atmospheric scenarios

Turbet et al. (2020a) reviewed the different atmospheric scenarios for TRAPPIST-1 planets. We discuss the possibilities mentioned for TRAPPIST-1 h, such as a H_2/He rich atmosphere, a H_2O envelope, and an O_2, a CO_2, a CH_4/NH_3, or an N_2 dominated atmosphere. First, numerical modelling using mass and radius measurements has shown that a H_2/He envelope is unlikely for all TRAPPIST-1 planets. Turbet et al. (2020a) constructed a mass-radius relation using the Grimm et al. (2018) atmospheric climate calculation and estimated that for a 'cold' scenario assuming 100 x solar metallicity and based on TRAPPIST-1 h irradiation, the maximum hydrogen to core mass fraction is 4×10^{-4} for a clear atmosphere. Using the estimation of Wheatley et al. (2017) for the EUV flux received by the planet (10^2 erg.s^{-1}.cm^{-2}) and the results from Bolmont et al. (2017), Bourrier et al. (2017b) and Bourrier et al. (2017a), they computed the equivalent mass loss over the age of the system (8 billion years) and found 10^{22} kg (i.e. 5×10^{-3} mass fraction). A hydrogen-rich envelope could be ripped out in ∼100 million years for TRAPPIST-1 h (Turbet et al., 2020a), meaning that this type of atmosphere is not completely impossible but unstable and unlikely to be sustained around this low-mass planet. The recent publication by Hori & Ogihara (2020) has also shown that the total mass loss over the planet's lifetime is supposedly higher than the initial amount of accreted gas.

Regarding a water-rich atmosphere scenario, Turbet et al. (2019a), Turbet et al. (2020b) and Turbet et al. (2020a) estimated the water content in TRAPPIST-1 planets by taking the runaway greenhouse limit into account, while Bourrier et al. (2017b) investigated the hydrodynamic water loss. Combining those two pieces of information leads to the conclusion that TRAPPIST-1 h could have lost less than three of Earth's oceans and retained water in its atmosphere or surface. Lincowski et al. (2019) show that O_2 atmospheres would be the best candidate for TRAPPIST-1 planets as a remnant of H_2O erosion and Wordsworth et al. (2018) determine that O_2 build-up is limited to one bar for TRAPPIST-1 h.

NH_3 and CH_4 are highly sensitive to photo-dissociation (Turbet et al., 2018), and for TRAPPIST-1 h to sustain a CH_4 or an NH_3 rich atmosphere would require an important source of those species. Assuming an Earth-like methane production rate, the planet could have a concentration up to 0.3% (Rugheimer et al., 2015). However, methane or ammonia photolysis rates could decrease via the formation of high-altitude clouds or hazes (Sagan & Chyba, 1997; Wolf & Toon, 2010; Arney et al., 2016).

An Earth-like atmosphere, that is one bar and a N_2 rich atmosphere, might be stable against stellar wind for TRAPPIST-1 h if CO_2 is abundant (Dong et al., 2018, 2019); CO_2 could accumulate in TRAPPIST-1 planets (Lincowski et al., 2019) because it is less sensitive to atmospheric escape (Dong et al., 2017, 2018, 2019). However, Turbet et al. (2018) and Turbet et al. (2020a) show that TRAPPIST-1 h would probably experience a CO_2 collapse. The planet is far from the star and probably tidally locked, favouring CO_2 surface condensation. Furthermore, CO and O_2 could also be found in the case of a CO_2 rich atmosphere due to the photo-dissociation of CO_2 and the low recombination of CO and O_2 (Gao et al., 2015; Hu et al., 2020).

Finally, a water ocean at the surface of TRAPPIST-1 h, implying potential habitability, is unlikely. As the planet is beyond the CO_2 collapse region, the atmosphere does not warm the surface (Turbet et al., 2020a). To counterbalance the CO_2 condensation, the planet would require a very thick CO_2 atmosphere with volcanic gases such as H_2 and CH_4, but, as explained above, neither H_2 nor CH_4 are expected to be stable in the TRAPPIST-1 h atmosphere (Pierrehumbert & Gaidos, 2011; Wordsworth et al., 2017; Ramirez & Kaltenegger, 2017; Lincowski et al., 2018; Turbet et al., 2018, 2019b, 2020b). Few observational constraints have been brought on TRAPPIST-1 planets, leaving a wide range of atmospheric possibilities. The following Section aims to analyse the TRAPPIST-1 h IR spectrum with regard to the predictions mentioned above to bring new constraints and prepare further observations.

Retrieval analysis set-up

We used `Tau-REx 3`, the nested sampling algorithm Multinest, the software `PyMultinest` and similar line lists from the ExoMol project presented in Chapter 5 Section 5.3.2. We simulated the atmosphere assuming a constant temperature-pressure profile, and every layer of the simulated atmosphere is uniformly distributed in log space, with a total of 100 ranging from 10^{-2} to 10^{5} Pa. We included the collision-induced absorption (CIA) of H2-H2 (Abel et al., 2011; Fletcher et al., 2018), H_2-He (Abel et al., 2012), and Rayleigh scattering. We used a wide range of temperatures (50-1000 K) to adjust the planet's temperature, using the effective temperature (∼173 K) as the initial value. The planetary radius was also fitted as a free parameter in the model, and its value ranges from ±50% of the published value reported in Table 6.1. The planetary radius fitted corresponds to the bottom of the atmosphere, assumed at one bar here. Clouds were included using a simple grey opacity model, and the top clouds pressure varies from 10^{-2} to 10^{5} Pa. We considered the following opacity sources: H_2O (Polyansky et al., 2018), CO_2 (Rothman et al., 2010), NH_3 (Yurchenko et al., 2011), and CO (Yurchenko & Tennyson, 2014).

We performed two different atmospheric retrievals by forcing a primary and a secondary atmosphere. We modelled the TRAPPIST-1 h atmosphere using H_2, He, and N_2 as fill gas and H_2O, CO, CO_2, NH_3, and CH_4 as trace gases. We note that H_2, He, and N_2 do not display features in the spectrum; they contribute to the continuum and shape the mean molecular weight. The ratio between H_2 and He abundances was fixed to the solar value of 0.17, while the ratio between the abundance of N_2 over the abundance of H_2 varied between 10^{-12} and 10^{-2} for the primary model and between 10^{-12} and 10^{4} for the secondary scenario. The mean molecular weight can then evolve towards higher values, and we tested a hydrogen-rich and nitrogen-rich atmosphere. The abundance of the other molecular absorption sources was included in the fit as a volume mixing ratio, allowing us to vary between 10^{-12} and 10^{-2}. A flat-line model, only including a cloud deck, was performed to assess the significance of the different scenarios compared to a baseline. A baseline represents the lack of an atmosphere (e.g. an atmosphere with no spectral features) or a flat spectrum that a high-altitude cloud deck can only fit. We used a similar formalism than in Chapter 5, Section 5.3.2 to compute the Bayes factor and evaluate the significance of a detection (see equations 5.4,5.5 and 5.6). The significance (σ) represents the strength of a detection, and was estimated using a Kass & Raferty (1995), Trotta (2008), and Benneke & Seager (2013) formalism. We used Table 2 in Trotta (2008) and Table 2 in Benneke & Seager (2013) to find the equivalence between the Bayes factor and the significance σ. A Bayes factor of one corresponds to a 2.1σ detection and is considered weak. A Bayes factor greater than three (3σ) is considered significant, and one superior to eleven (5σ) is considered a strong detection. We define $\Delta\log(E)=\log(E_{\text{Atmospheric Model}})-\log(E_{\text{Flat line}})$. The atmospheric model can be considered a better fit than the flat-line if the $\Delta\log(E)$ is superior to the three.

6.4 Results

6.4.1 Atmospheric retrieval results

The two retrieval results show no evidence of molecular absorption in the recovered spectrum of TRAPPIST-1 h. Both primary and secondary retrieval analyses have logarithm evidence (109.92 and 110.18, respectively) comparable to the flat-line model, 110.55. This result favours a bare rock planet, a high cloud layer in a primary atmosphere, or a secondary envelope. It is consistent with previous work on other TRAPPIST-1 planets (de Wit et al., 2018; Wakeford et al., 2019; Zhang et al., 2018).

Figure 6.6 (left) shows the extracted spectrum with the best-fit atmospheric results: flat-line (red), primary (blue), and secondary model (purple). The flat-line and the secondary best-fit models are similarly flat with a transit depth of around 3220 ppm, while the primary models are found to be

around 3274 ppm. This difference is due to the different radius and temperature estimations depending on the scale height and the weight of the atmosphere. We present the correlations among parameters for the primary and the secondary model in Figure 6.7. We over-plotted the two posterior distributions for a direct comparison, but the values are displayed for the secondary best-fit model. The primary model posterior distribution alone is presented in Appendix C.1.

The secondary atmospheric retrieval analysis estimates the radius to be $0.69^{+0.03}_{-0.07}R_{\oplus}$ and the temperature reaches 345^{+326}_{-196} K. The mean molecular weight distribution is bi-modal, and the code can retrieve two solutions: a light atmosphere with a 2.3 g/mol mean molecular weight and a heavier solution with a mean molecular weight reaching $25.35^{+2.46}_{-23.02}$ g/mol corresponding to a 16 km scale height. This is correlated to the abundance of N_2 retrieved as the ratio of inert gases, that is, $\log(N_2/H_2)$. When we allowed this ratio to increase beyond one, the best-fit value was constrained to $1.01^{+1.18}_{-6.13}$. However, we note that a second solution, around seven, corresponds to the primary analysis retrieved value and creates the bi-modal distribution in the mean molecular weight. Nitrogen is the only parameter that impacts the value of the mean molecular weight as no constraints can be put on H_2O, CH_4, CO, CO_2, and NH_3.

We found the anti-correlation between the radius, temperature, and layer for top clouds from both posteriors distributions. The radius decreases with increasing temperature and decreasing layers for top clouds. The latter is found high in the atmosphere, $\log(P_{clouds})=1.02^{+1.90}_{-1.72}$, which corresponds to a cloud layer at approximately 10^{-4} bar. Considering the pressure of this layer, it is likely that these clouds may not be condensation clouds but rather photochemical mists or hazes with particles big enough not to have a spectral slope. From those two retrievals analyses, we show that the atmosphere must be either secondary (probably dominated by nitrogen) or primary with a very high photochemical haze layer. The two retrieval analyses have similar statistical results, so we cannot favour one solution. We cannot rule out the hypothesis of a lack of an atmosphere either, as the log(E) of the flat-line model remains the highest. We can reject a clear primary atmosphere as expected for this planet as the primary model requires a layer of clouds to correctly fit the spectrum (see Section 6.5.1).

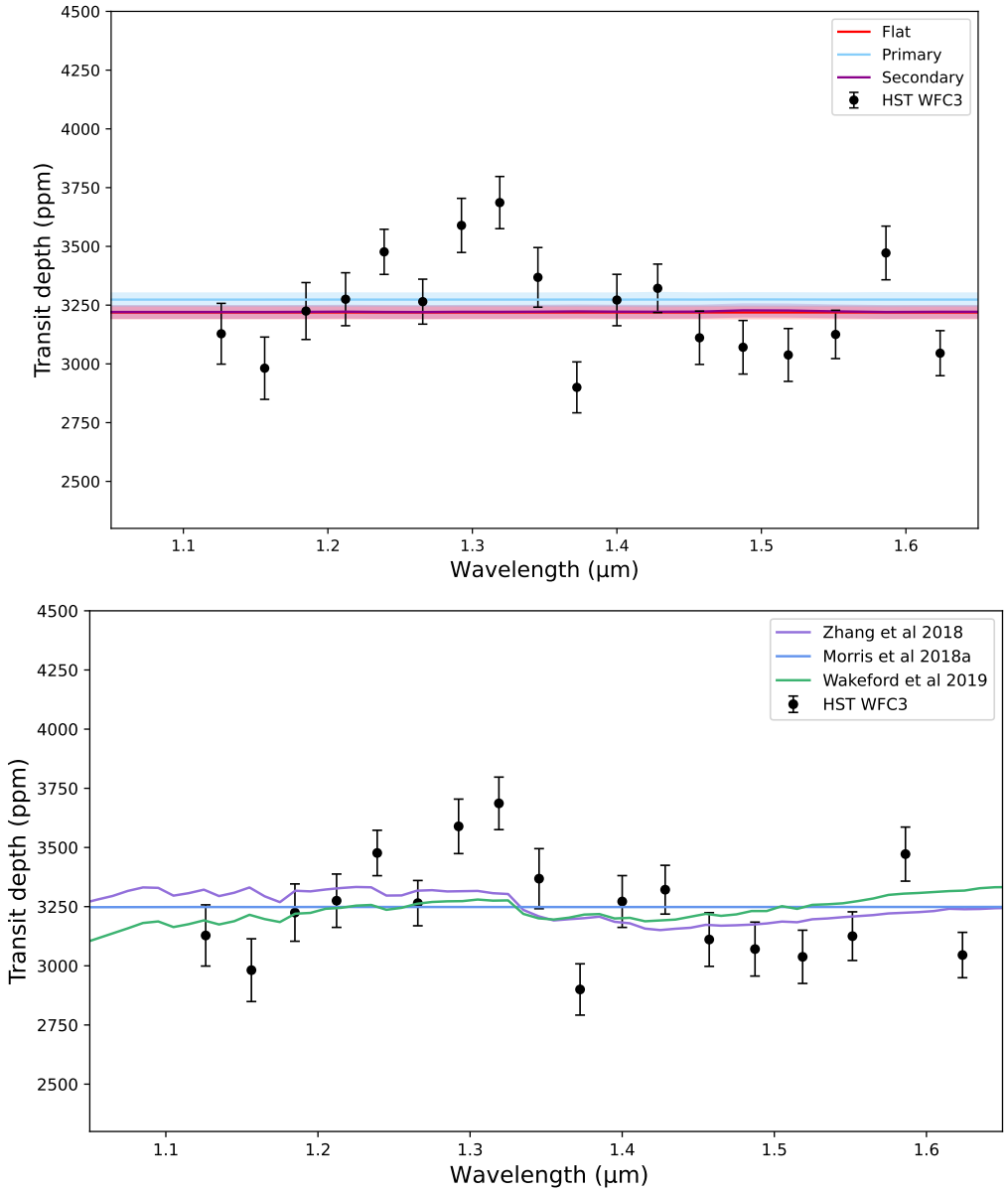

Figure 6.6: best-fit models to TRAPPIST-1 h HST/WFC3 G141 data from atmosphere retrievals (left) and stellar contamination models based on Zhang et al. (2018), Wakeford et al. (2019), and Morris et al. (2018) (right).

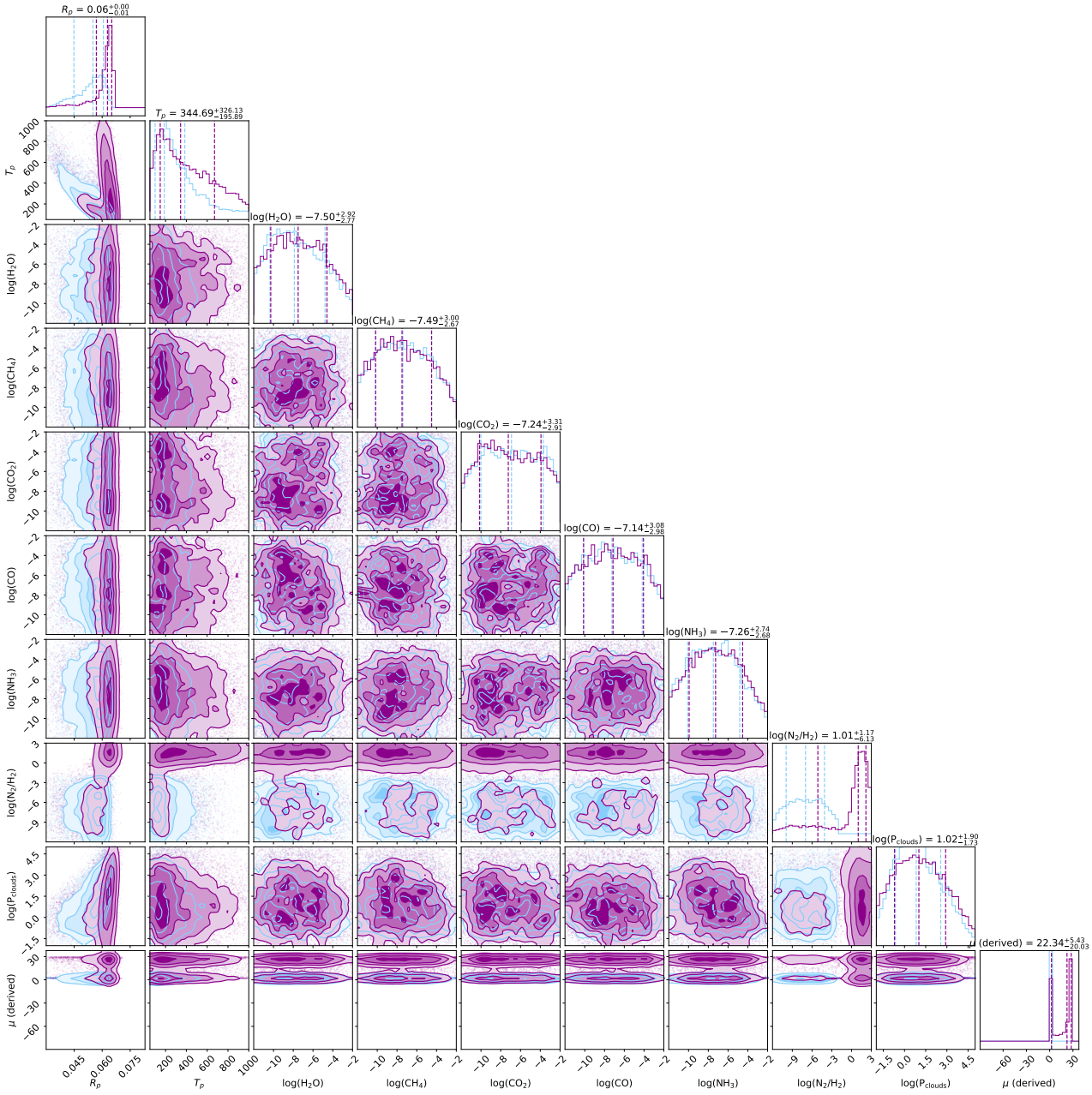

Figure 6.7: Posterior distributions for the primary (blue) and the secondary retrieval (purple) on the extracted TRAPPIST-1 h spectrum. Only the values from the secondary best-fit analysis are displayed.

Table 6.4: Statistical results of the atmospheric retrieval analysis and the stellar contamination modelling on TRAPPIST-1 h HST/WFC3 G141 data. Chi-squared (χ^2) and reduced chi-squared ($\tilde{\chi}^2 2$) were computed using the result of the retrieval best-fit model and the stellar contamination models. Bayesian logarithm evidence (log(E)) and the Bayes factor (Δlog(E)) were computed when applicable, i.e. only for the atmospheric retrieval analysis.

Model	χ^2	$\tilde{\chi}^2$	log(E)	Δlog(E)
Flat-line	64.95	3.61	110.55	N/A
Atmosphere primary	65.20	3.62	109.92	-0.63
Atmosphere secondary	65.25	3.62	110.18	-0.37
Stellar Zhang et al. (2018)	54.02	3.00	N/A	N/A
Stellar Wakeford et al. (2019)	60.70	3.37	N/A	N/A
Stellar Morris et al. (2018)	63.91	3.55	N/A	N/A
Corrected by Zhang et al. (2018)				
Flat-line	54.94	3.05	115.48	N/A
Atmosphere primary	50.54	2.81	115.02	-0.46
Atmosphere secondary	54.77	3.04	115.20	-0.28
Corrected by Wakeford et al. (2019)				
Flat-line	61.41	3.41	112.13	N/A
Atmosphere primary	61.91	3.44	111.51	-0.62
Atmosphere secondary	61.80	3.43	112.01	-0.12
Corrected by Morris et al. (2018)				
Flat-line	65.11	3.62	110.39	N/A
Atmosphere primary	65.28	3.63	109.79	-0.60
Atmosphere secondary	65.23	3.62	110.12	-0.27

6.4.2 Including the stellar contamination

We present in Figure 6.6 (left) the stellar contamination models and in Table 6.4 the statistical results on both the atmosphere and stellar models. We computed the chi-squared ($\chi 2$) and the reduced chi-squared ($\tilde{\chi}^2 2$) for all models and indicated the logarithm evidence (log(E)) from the retrieval analysis. According to the chi-squared computation, the stellar contamination model of Zhang et al. (2018) is favoured. However, none of the models we tested here is significant and can explain variations in the TRAPPIST-1 h spectrum. In particular, the rise in the transit depth around 1.3 µm is not reproduced. To account for stellar contamination, we corrected our HST/WFC3 extracted spectrum by subtracting the stellar contributions using the Zhang et al. (2018), Wakeford et al. (2019), and Morris et al. (2018) formalism.

We present in Table 6.5 the transit depth after subtraction of the stellar contamination for the three models and conduct the same retrieval analysis as in Section 6.4.1 on those corrected spectra. We over-plotted all the different spectra as a comparison in appendix C.2. Statistical results on the retrieved corrected spectra are detailed in Table 6.4. The flat-line is the favoured model for all the corrected spectra, but the correction by Zhang et al. (2018) leads to the highest log(E). We present in Figure 6.8 best-fit atmospheric retrieval results on the three spectra, while posterior distributions are in appendix C.4. We note transit depth variations at 1.2 µm, 1.45 µm, and 1.6 µm on the primary best-fit model on the spectrum corrected by Zhang et al. (2018). This is due to the contribution of CO_2 to the best-fit solution, but the amount of CO_2 is not constrained (see posterior distributions in appendix C.4), and the model is not statistically significant. We also observe variations in the transit depth around 1.5 µm on the primary best-fit model on the spectrum corrected by Morris et al. (2018). This is due to the absorption of ammonia. Once again, this absorption is not constrained in terms of abundance and the log(E) remains below the one of the flat-line. As an indication, we put the best-fit opacity contributions from those two models in appendix C.3. The correction made here to the spectra does improve the statistical retrieval results in the case of the Zhang et al. (2018) correction. However, it does not lead to molecular detection and does not allow us to provide further constraints on the atmosphere of TRAPPIST-1 h.

To better constrain the stellar contamination, we also tried to add the optical value found in Luger et al. (2017a) using K2 photometry. As seen in the plot of Appendix C.5 and in the χ^2 computation results in appendix C.1, the existing stellar models discussed here fit the spectrum poorly. First, we cannot ensure inter-instrument calibration at this accuracy and combining a different transit depth could lead to misinterpretations of the spectrum (Yip et al., 2020). In addition, the stellar spot distribution may have changed in the intervening time between the observations, but this is unlikely as they are not that far apart. K2 light curves were taken between 15 December 2016 and 4 March 2017, while the HST data were taken in July 2017, September 2019, and July 2020. A more likely explanation is that for both K2 and HST data, multiple transits were stacked, regardless of the phase of the star's rotation. If the stellar rotational phase and activity were different from time to time, the effect in the transmission spectrum would be suppressed when they are stacked. Adding this point does not further constrain the stellar contamination models in the case of TRAPPIST-1 h.

Table 6.5: Corrected transit depth in ppm using stellar contamination models. (1) Zhang et al. (2018); (2) Wakeford et al. (2019); (3) Morris et al. (2018)

Wavelength (µm)	Transit depth (ppm)		
1.1262	3072.99	3193.93	3129.83
1.1563	2934.85	3032.81	2983.10
1.1849	3171.13	3259.82	3226.35
1.2123	3202.19	3283.50	3276.38
1.2390	3406.64	3477.46	3478.10
1.2657	3207.19	3257.41	3266.07
1.2925	3520.20	3564.16	3590.50
1.3190	3643.19	3673.80	3687.80
1.3454	3388.59	3396.28	3369.86
1.3723	2948.59	2939.83	2901.69
1.4000	3341.90	3318.92	3273.55
1.4283	3414.44	3373.99	3323.56
1.4572	3193.82	3149.00	3112.83
1.4873	3141.10	3090.15	3072.24
1.5186	3093.99	3037.20	3039.34
1.5514	3165.61	3101.84	3126.55
1.5862	3499.04	3418.90	3473.19
1.6237	3057.41	2980.84	3046.45
References	1	2	3

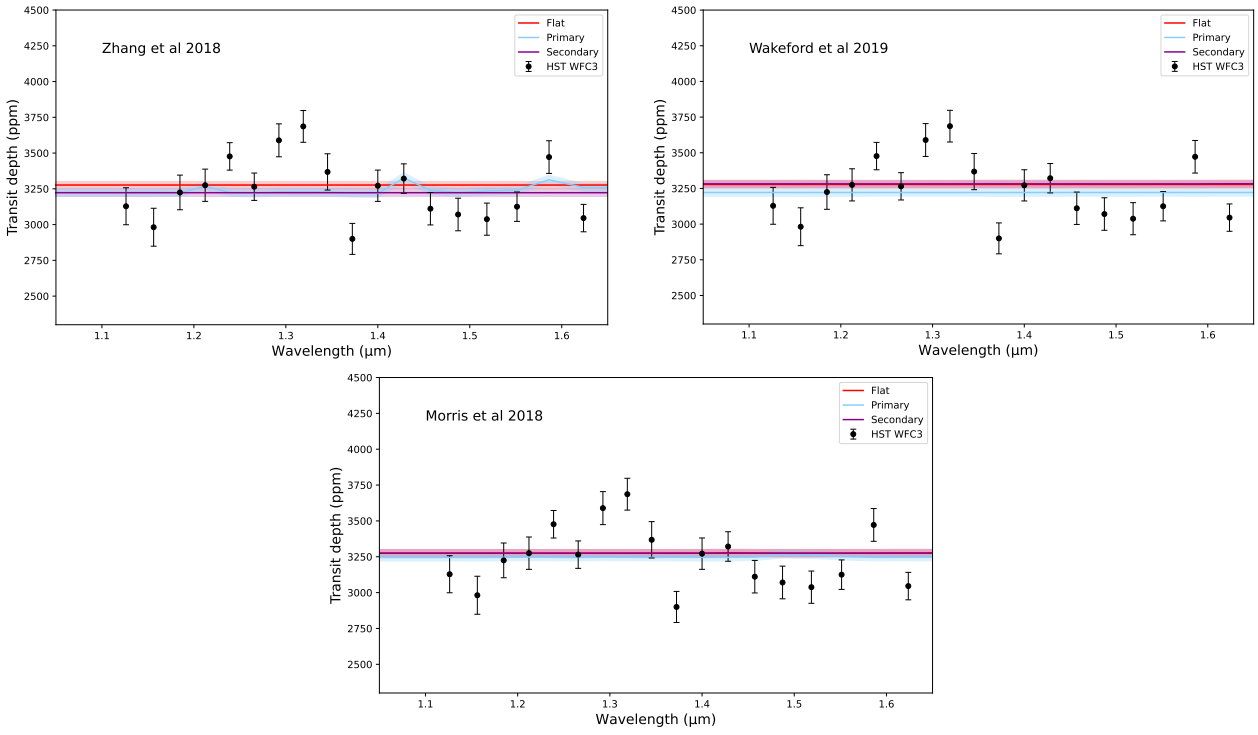

Figure 6.8: Best-fit models to TRAPPIST-1 h HST/WFC3 G141 data after subtraction of stellar contamination contributions according to the Zhang et al. (2018) (top), Wakeford et al. (2019) (middle), and Morris et al. (2018) (bottom) formalism.

6.5 Discussion

6.5.1 Primary clear atmosphere

We show in Section 6.4.1 that the HST/WFC3 extracted spectrum was compatible with either a secondary or a primary cloudy and hazy atmosphere if we retain the hypothesis of a presence of an atmosphere. In this Section, we explore the case of a primary clear atmosphere by fixing the molecular absorption of the different species to 10^{-3}, which forces spectral features. The temperature was allowed to vary between ±20% of the equilibrium one (173 K), and the radius was fitted between ±50% of the published value. We tested six different opacity sources, H_2O, CO_2, CO, CH_4, NH_3, and N_2, separately by running a retrieval for each source. We included collision-induced absorption and Rayleigh scattering and fixed the He/H_2 ratio to 0.17. The atmosphere was simulated as in Section 6.4.1, with 100 layers ranging between 10^{-2} and 10^5 Pa.

We measured the size of a clear atmosphere in the case of TRAPPIST-1 h in those six configurations and showed that a primary clear atmosphere is rejected in each case. We present in Table 6.6 best-fit results from the six tested scenarios. We indicate the radius, the temperature, and the mean molecular weight, and we estimate the corresponding scale height. For comparison, we also indicate the results from the flat-line model of Section 6.4.1. Statistical results, that is, the logarithm evidence from primary clear models, are below the one of the flat-line with an absolute difference of 3 or more while including H_2O, CH_4, NH_3, or N_2. This result indicates that a primary clear atmosphere is rejected with high confidence (i.e. 3σ). Primary clear atmospheric scenarios with traces of CO or CO_2 have higher Δlog(E), remaining below the one of the flat-line models, but they cannot be rejected as firmly as the others (see also Figure 6.11 in Section 6.5.2).

A primary clear atmosphere scenario was previously rejected for TRAPPIST-1 planets using HST/WFC3 G141 spectra (de Wit et al., 2018; Zhang et al., 2018; Wakeford et al., 2019). Performing the same exercise with a fixed 10^{-3} water abundance for the other six TRAPPIST spectra from Zhang et al. (2018), we also confirm that a primary clear atmospheric model does not fit their spectra. We note that we simulated planet atmospheres with the same 100 layers between 10^{-2} and 10^{-5} even though they have different sizes, radii, and masses. We present in Figure 6.9 the best-fit atmospheric retrieval results in the case of a Hydrogen-dominated atmosphere with water as a trace gas (the volume mixing ratio was fixed to 10^{-3}) for the seven planets of the TRAPPIST-1 system. The results are presented in a number of scale heights, and we can see that TRAPPIST-1 planets are unlikely to possess a clear atmosphere dominated by hydrogen with water in a low quantity. The comparison of logarithm evidence between a flat-line model and a clear primary atmosphere for all seven planets is detailed in appendix C.2. This is in agreement with theoretical modelling as detailed in Section 6.3.3 and in Turbet et al. (2020b) and Hori & Ogihara (2020).

Table 6.6: Best-fit atmospheric results and derived parameters for a primary clear retrieval analysis on TRAPPIST-1 h spectrum. The primary clear atmospheric scenario was simulated, including the molecular absorption with a volume mixing ratio fixed to 10^{-3} in an H-dominated atmosphere.

Model	$R_P(R_\oplus)$	T(K)	μ(g/mol)	H(km)	χ^2	$\tilde{\chi}^2$	log(E)	Δlog(E)
Flat-line	0.61±0.110	296±225	2.30	71.28	64.95	3.61	110.55	N/A
H_2O	0.70±0.003	140±2	2.32	75.27	128.68	7.15	74.78	-35.77
CO_2	0.71±0.003	157±26	2.35	86.84	68.37	3.80	108.99	-1.56
CO	0.72±0.003	158±25	2.33	88.84	70.53	3.92	107.93	-2.62
CH_4	0.69±0.003	139±2	2.32	72.20	146.35	8.13	65.48	-45.07
NH_3	0.68±0.003	140±3	2.32	70.56	107.58	5.98	85.38	-25.17
N_2	0.72±0.003	156±26	2.33	87.85	69.71	3.87	106.82	-3.73

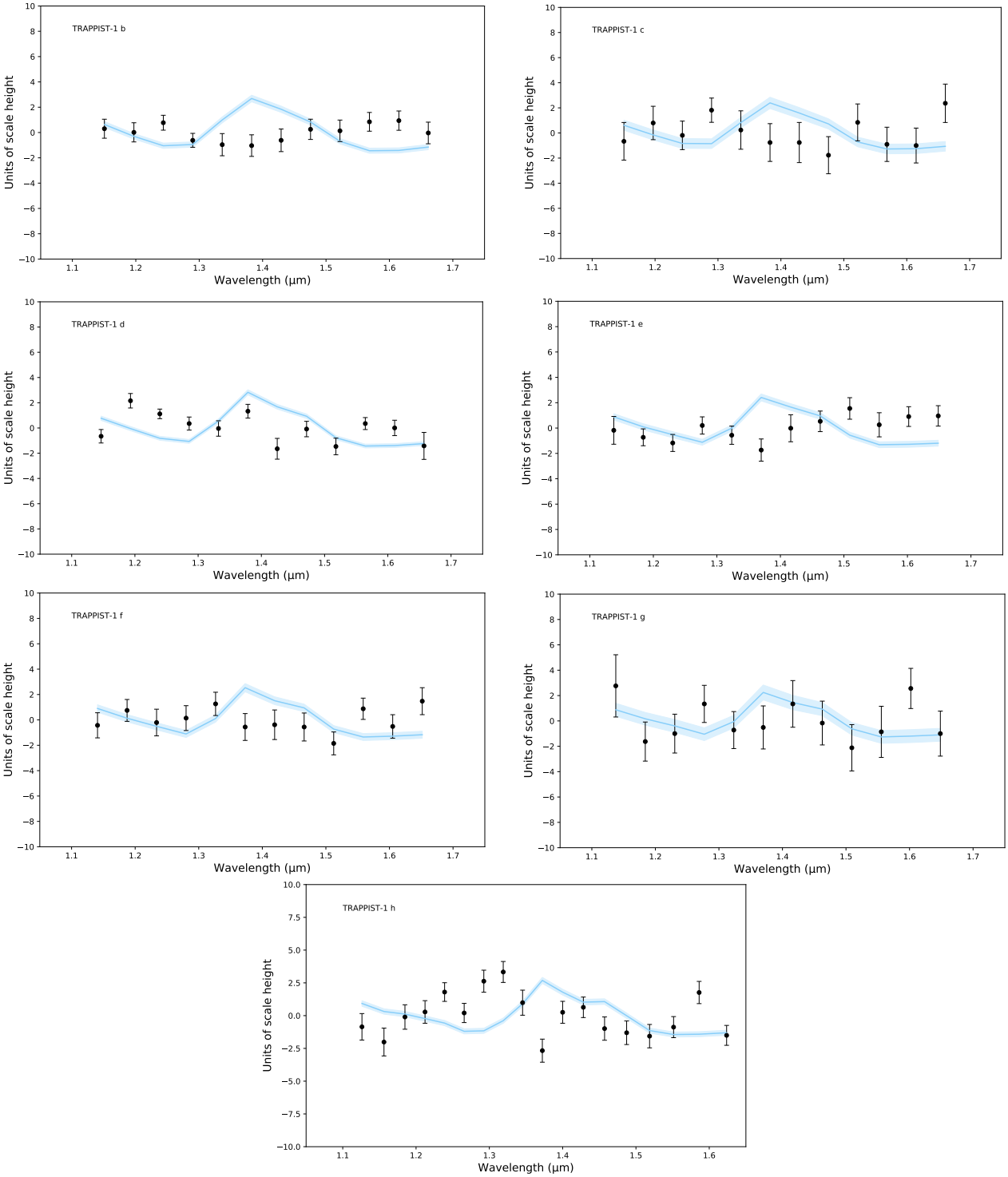

Figure 6.9: comparison of the best-fit atmospheric results for TRAPPIST-1 planetary spectra in the case of a forced primary clear atmosphere with a volume mixing ratio of water fixed to 10^{-3} in an H-dominated atmosphere. We used spectra from Zhang et al. (2018) for the TRAPPIST-1 b to g retrievals and presented the results in units of scale height.

6.5.2 Steam atmosphere

From the review of the possible atmospheric scenario (Turbet et al., 2020b), TRAPPIST-1 h could have water-, methane-, ammonia-, nitrogen-, or even a carbon-dioxide-rich atmosphere depending on the evolution of the planet, on the species collapses, and on the photo-chemistry. A steam atmosphere is unlikely for TRAPPIST-1 h as it would require the planet to retain its atmosphere and be stable against the stellar wind (see Section 6.3.3). However, we tested those different hypotheses using a similar approach as in Section 6.5.1 but allowed for heavier atmospheres by increasing the volume mixing ratio of the tested molecular absorber from 0.01 to 0.8 progressively. Best-fit atmospheric results, derived parameters and statistical criteria are detailed in appendix C.3. We note that some forced secondary steam atmospheric models have log(E) equal to or slightly above the one of the flat-line model. The difference in log(E) is above one for one case, with the CO-rich atmosphere having a volume mixing ratio fixed to 0.2. This model has a Δlog(E) of 1.01 corresponding to 2.1σ confidence, hence a 'weak detection' in Benneke & Seager (2013) classification. The best-fit spectrum of the models presenting an elevated log(E) is plotted in Figure 6.10. They correspond to the model of 20% CO_2 and CO and 80% of N_2 and NH_3. Carbon dioxide and carbon monoxide have similar absorption features in the HST/WFC3 wavelength range, which leads to similar best-fit results. Moreover, as the features are tiny, we obtained the same volume mixing ratios for those species. We note that N_2 acts as a fill gas in the atmosphere as it does not have features; the best-fit spectrum is then similar to that of the flat-line. We can add a CO-rich atmosphere to the possible atmospheric scenario for TRAPPIST-1 h.

We note that Δlog(E) remains below one for most tested models, meaning they are not statistically significant. We present in Figure 6.11 the comparison of the log evidence for a flat-line to that of single molecule retrievals from the primary clear analysis of Section 6.5.1 and the secondary models of Section 6.5.2 following the formalism of Figure 6 in Mugnai et al. (2021). We decided to represent the Δlog(E) as a function of the mean molecular weight of the modelled atmospheres to compare the different scenarios, as similar molecular abundances could lead to different weights and metallicities. Primary atmospheric models with metallicity below 50 $\times$ solar (i.e. mmw=2.70 g/mol) are rejected with more than 5σ confidence (i.e. the Bayes factor is inferior to -11), except for CO and CO_2. In addition, if the atmosphere were primary, it would be unlikely that it does not contain any water. The equivalence between abundances, the mean molecular weight, and solar metallicity is presented in appendix C.3. A figure of all Δlog(E) as a function of the abundances is presented in appendix C.6. The area between dashes represents the set of Bayes factor values for which it is impossible to conclude compared to a flat-line, with absolute Δlog(E) below 3. Models with a Δlog(E) between -3 and -11 can be significantly rejected compared to a flat-line, while the ones below -11 are strongly disfavoured.

6.5.3 Impact of changing the spectral resolution

Neither stellar contamination nor atmospheric absorption can explain the rise in the transit depth around 1.3 µm. This is probably due to scattering noise remaining after the extraction and the spectral light curve fitting. By changing the resolution of the data extraction, we investigated if the scattering at 1.3 µm remains significant and if a single narrow band of the spectrum caused this 'feature'. We performed the same data analysis as in Section 6.4.1 using two other binning resolutions with a resolving power of 25 and 70 around 1.4 µm, respectively. We also performed the same retrieval analysis using the two spectra' primary, secondary, and flat-line setups. We obtained similar results; the flat-line model is the best fit according to the Bayes factor.

We present in Figure 6.12 the best-fit atmospheric results on the two spectra of TRAPPIST-1 h. The log(E) of the flat-line is 47.52 and 163.62 for the very low and the high-resolution spectra, whereas the log(E) of the primary model reaches 47.04 and 163.15, respectively. Log(E) of the secondary model is also below the one of the flat-line models, 47.42 and 163.42. Changing the resolution of the spectrum

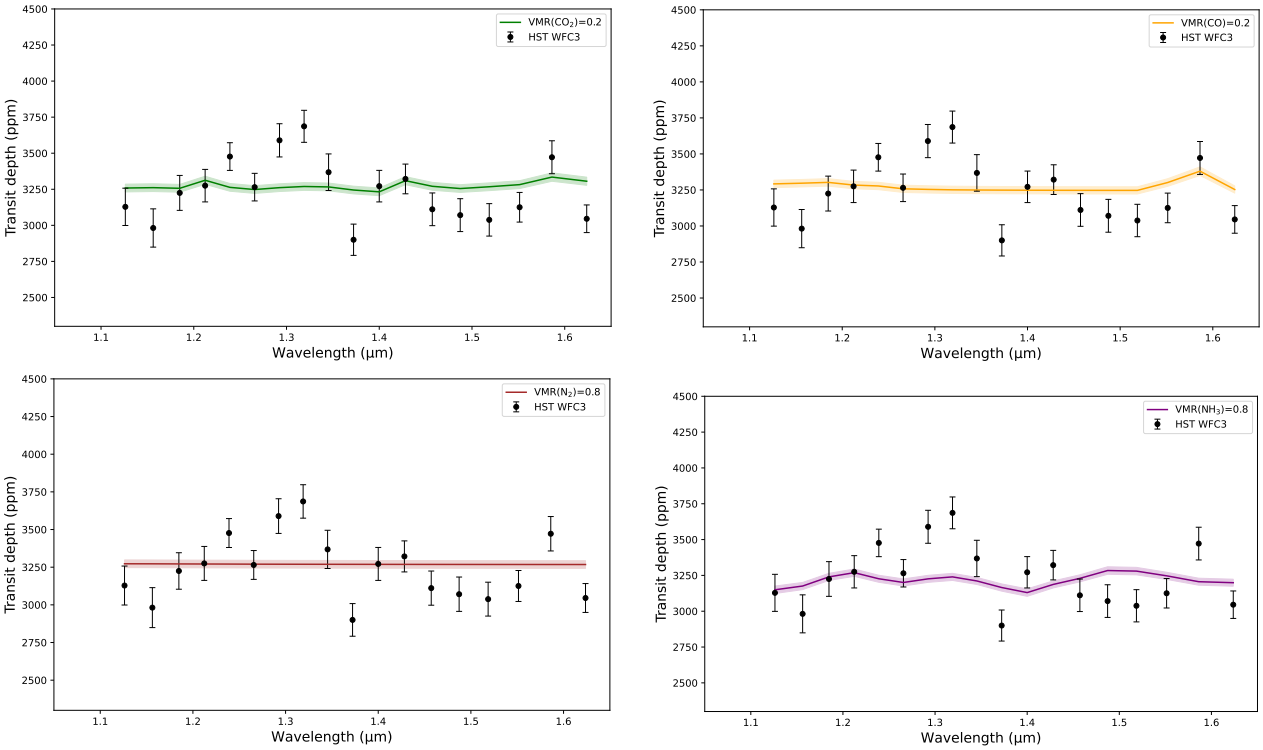

Figure 6.10: comparison of the best-fit atmospheric results for the TRAPPIST-1 h spectrum in the case of four forced secondary clear atmospheres with a volume mixing ratio of CO_2 fixed to 0.2 (upper left), CO to 0.2 (upper right), N_2 to 0.8 (bottom left), and ammonia to 0.8 (bottom right).

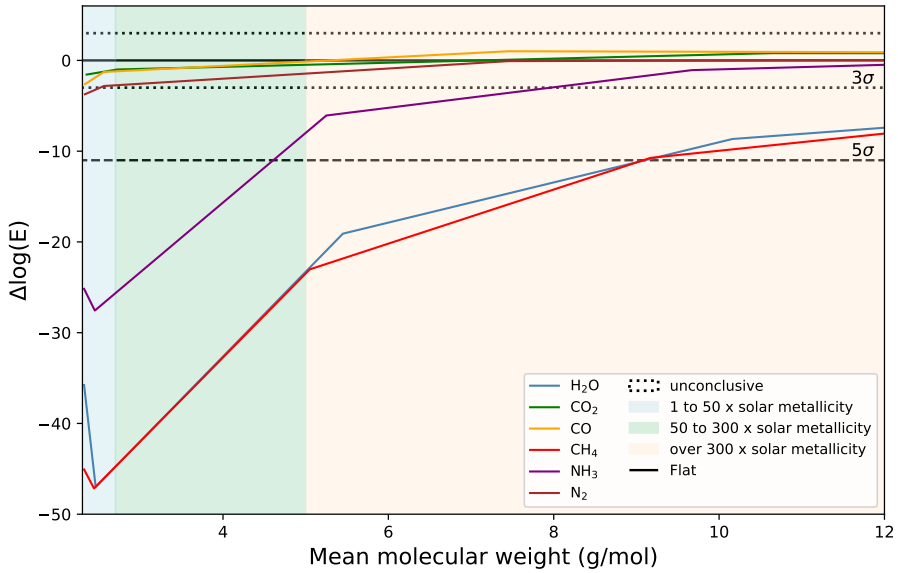

Figure 6.11: Comparison of the log evidence for a flat-line to that of single molecule retrievals where the abundance of the molecule is fixed, and no clouds were included. We represent the Delta log(E) as a function of the mean molecular weight of the tested atmospheres. The region between dashes represents the set of Bayes factor values for which it is impossible to conclude compared to a flat-line, with absolute Δlog(E) below 3. Models below the large dashed lines are strongly disfavoured compared to the flat-line.

does not flatten or increase the rise of the transit depth at 1.3 µm, and it was recovered in each case. Results from Section 6.4.2 are confirmed while using different resolutions. A flat-line model best fits the TRAPPIST-1 h spectrum.

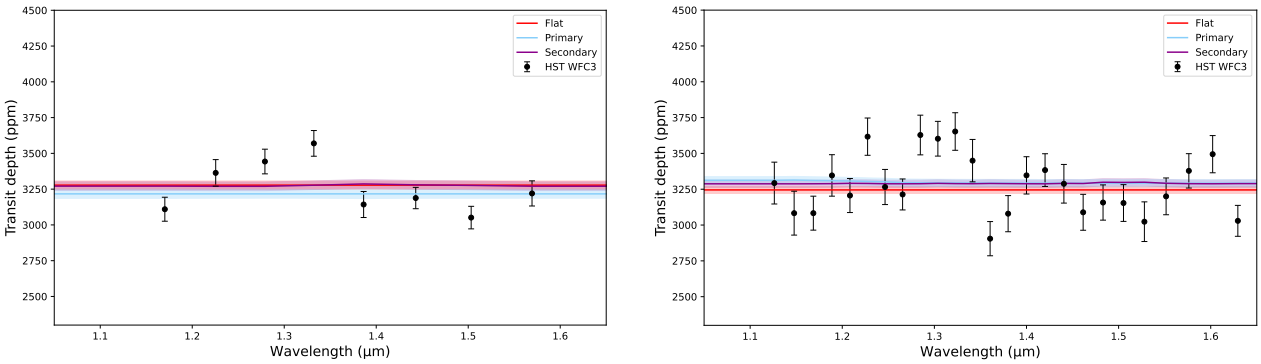

Figure 6.12: Best-fit models to TRAPPIST-1 h HST/WFC3 G141 data using a very low (left) and a high (right) resolution with a resolving power of 25 and 70 around 1.4 µm.

6.5.4 Comparison with an independent study

An independent analysis on the same dataset has been performed in Garcia et al. (2022). To extract, reduce and correct the raw data, they use both `iraclis`, the `prose` framework and Kreidberg et al. (2014a) method. They use Ducrot et al. (2020)'s result to set the orbital period and the impact parameter while we use Luger et al. (2017a). Contrary to our analysis, they exclude the first HST orbit of each observation to adjust the white and spectral light curves. The suppression of the first orbit and, thus, a fitting without a pre-baseline transit for Observations 2 and 3 could explain the difference in the fitted transit parameters, particularly in the mid-transit time. However, the extracted transmission spectra are similar. We plot in Figure 6.13 the transmission spectrum found by Garcia et al. (2022) (in red) and our transmission spectrum using two different resolutions (in black and grey). The overall transit depth is similar, as there is no observed offset between the two studies. The shape of the transmission spectra are similar, and they also find an increase in the transit depth at around 1.3 µm.

The treatment of the stellar activity is based on Wakeford et al. (2019) formalism. They conclude that TRAPPIST-1 surface might be covered by ∼15% of cold spots (2000±100 K) and by a tiny fraction (185.2±8.8 ppm) of hot spots (hotter than 5000 K). However, they reach a similar conclusion, none of the photosphere models provides a good fit for the data. A need for better constraints on the photospheric structure of TRAPPIST-1 and, in general, on ultra-cool M-dwarf; is required to break degeneracies and will be crucial to go further in the atmospheric analysis.

They use a forward atmospheric model, `CHIMERA` (Line et al., 2013) to constrain the atmosphere of TRAPPIST-1h. `CHIMERA` is a one-dimensional radiative transfer code based on the correlated-k method for radiative transfer and the five-parameter, double, grey, one-dimensional temperature-pressure profile of Guillot (2010). It has been adapted for TRAPPIST-1 planetary system analyses by Batalha et al. (2018) and Moran et al. (2018). Regarding the atmosphere of TRAPPIST-1h, they reach once again similar conclusions. They find that the planet is unlikely to possess an aerosol-free hydrogen-dominated atmosphere. In agreement with our findings, the likeliest scenario is that the planet has a very high mean molecular weight (>1000 × solar metallicity) atmosphere, is enshrouded by an opaque aerosol layer, or is devoid of atmosphere.

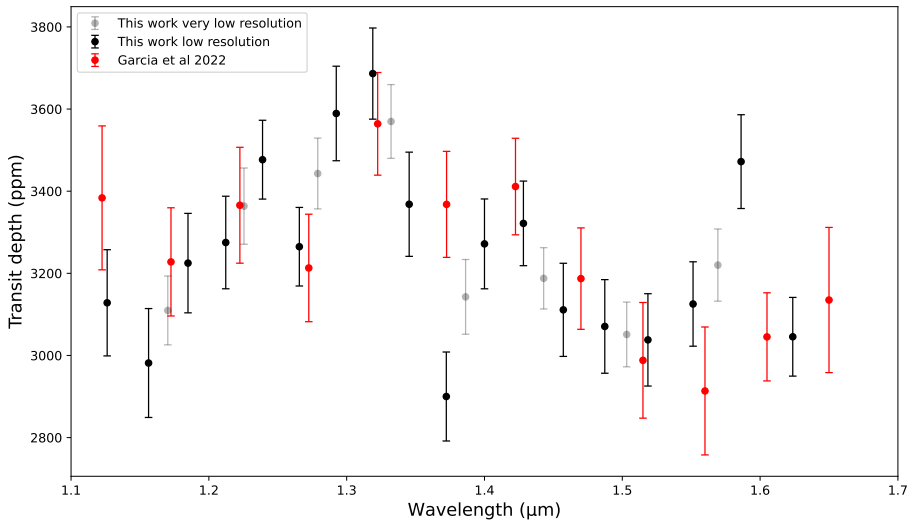

Figure 6.13: TRAPPIST-1h transit depths from this work at low resolution (black) and very low resolution (grey) and from Garcia et al. (2022) (in red).

6.6 Conclusion

Terrestrial planets with a secondary envelope are challenging to characterise, especially given HST's low resolution and limited wavelength coverage. Here, we have presented a transmission spectrum of a 0.7 R⊕ planet, TRAPPIST-1 h, the seventh planet of the highly studied TRAPPIST-1 system. This planet is the furthest and the smallest planet in the system, yet we obtained a spectrum by combining three different HST observations. We cannot make a strong claim from the spectrum analysis as it is a better fit using a flat-line. However, as for the other TRAPPIST planets, we could rule out a primary clear atmosphere with more than 3σ confidence. Given these observations, we cannot distinguish between a featureless cloudy H-dominated atmosphere and a clear or cloudy secondary envelope with smaller spectral features. The two models have similar statistical significance and cannot be distinguished using retrieval analysis.

We cannot completely rule out the possibility that TRAPPIST-1 h has lost its atmosphere over its lifetime, as the evidence for a flat-line model is favoured. We tested secondary clear atmospheric scenarios and found that a CO-rich atmosphere with a volume mixing ratio of 0.2 in a hydrogen atmosphere obtained the best statistical result with a Bayes factor of 1.01 (i.e. a 2.1σ detection). However, this result is not significant enough and is mainly driven by the last points of the spectrum. This could be due to stellar activity, even though all the stellar contamination models tested here could not reproduce those points and the rise of the transit depth around 1.3 μm. Other absorbing species, such as H_2S or H_2CO, could also create features around 1.3 μm, but they are unlikely to be produced in the TRAPPIST-1 h atmosphere with such a high level of absorption. The feature is likely caused by either stellar contamination or by the planet. However, as previously stated in this paper, we cannot find an explanation. While these scatter data points will cause the atmospheric model to be poorly fit, the same is true of the flat and cloudy models. Therefore, as each will feature these points equally poorly, the evidence between the two will be independent of this and so not overly affected. Future observations with the JWST will hopefully remove the ambiguity; however, as shown in Figure 6.11, we can rule out clear H/He atmospheres with high confidence. It is then necessary to obtain more data on this planet and on the other six planets of the system to prove the presence of an atmosphere and better constrain the nature of this intriguing planetary system.

The observations presented in the first two chapters of this part are individual analyses of a transmission spectrum. The next step in exo-planetary science is to carry out comparative exo-planetology and consistently analyse a population of objects. The tools presented in this chapter can be applied to more than one planet, allowing atmospheric properties inference automatisation. In the next chapter, we apply the same method to a large-scale survey to study exoplanet's atmosphere, particularly, Super-Earth and Sub-Neptune and perform a first population study for small planets.

Chapter 7

Exploring the transition from Super-Earth to Sub-Neptune with a Hubble transmission survey

Contents

7.1 Introduction

This chapter is based on the observational part of the publication **Exploring the transition from Super-Earth to Sub-Neptune with a Hubble transmission survey (Gressier et al. submitted)**, which is a consistent re-analysis of 26 transmission spectra. The simulations presented in this publication will be detailed in Chapters 8 and 9. This paper was submitted to A&A in September 2022 (see List of Publications).

Sub-Neptunes, exoplanets with a size between Earth and Neptune (1-4$R_\oplus$), are the most common type of planets in our Galaxy. Despite their ubiquitous nature, they have no equivalent in our solar system and remain challenging to characterise today. Planet formation models (Howard et al., 2012; Lopez & Fortney, 2014; Owen & Wu, 2013) predict that planets with masses between Earth and

Neptune are a natural outcome of planetary formation. Those planets are abundant, even though our Solar-System does not host an equivalent. Those planets span a wide range of radii, from the Earth to Neptune. Consequently, while distinguishing between rocky planets and ice giants is straightforward in our Solar-System, this has remained a challenge in the field of exoplanets. The occurrence rate of these planets showed that rocky planets are abundant and highlighted a different formation pathway for rocky planets: the radius valley also called the Fulton gap (Fulton et al., 2017). Super-Earth (below 1.7 $R_\oplus$) and Sub-Neptune (2 to 4 $R_\oplus$) are divided between the planetary radius and orbital period space by a valley where planets are less common. Super-Earth might be formed by the shrinking of a H_2 rich atmosphere(Eylen et al., 2018).

What is the nature of transitional planets? Is a Sub-Neptune a small gaseous planet with heavy elements, or can it be rocky with an extended atmosphere? Can a Super-Earth have a hydrogen-dominated atmosphere or only an Earth-like, secondary atmosphere? Comparative exoplanetary science is just beginning. We can expect breakthrough results with the James Webb Space Telescope (JWST) observations and the dedicated survey of 1000 planets by the ESA Ariel space mission.

So far, exoplanets population studies have been carried out using up to 65 Hubble Space Telescope (HST) observations in the optical and near-infrared. In particular, mainly hot-Jupiters, transiting gaseous planets, have been studied systematically to derive trends, molecular features, clouds and hazes properties (Sing et al., 2016; Tsiaras et al., 2018; Fu et al., 2017; Welbanks et al., 2019; Gao et al., 2020; Changeat et al., 2022; Edwards et al., 2022). Studying low-mass planets as a group is more difficult due to their observations' lack and lower signal-to-noise. Crossfield & Kreidberg (2017) performed the first population study of six Sub-Neptunes planets using the Hubble Space Telescope Wide Field Camera 3 Grism 141 (HST WFC3 G141). They pointed out atmospheric trends with temperature and linked them to the formation of clouds and hazes.

The present study is the first large-scale study of small planets. Twenty-six HST/WFC3 G141spectra for planets with a radius less than 6 Earth radii were collated from the literature. By expanding the study from Crossfield & Kreidberg (2017)'s to a broader sample and consistently re-analysing 26 transmission spectra in the near-infrared, we aim to extract population-level trends and distinguish primary and secondary atmospheres.

As constraints on atmospheric composition are usually difficult to obtain for small planets, mass and radius measurements are usually used to try to separate rocky and gaseous worlds. A large amount of hydrogen will indeed increase the measured radius of the planet (Valencia et al., 2010). Figure 7.1 (top) shows the mass-radius relationship for the 26 planets in the sample together with theoretical interior models of Zeng et al. (2019). The scattered point is coloured according to the temperature calculated for zero albedo and complete heat redistribution (see Table 7.2). We give the gap position in the radii double-peaked distribution at $1.7R_\oplus$(Fulton et al., 2017). Planets with a radius below $1.7R_\oplus$ are consistent with a rocky composition (Weiss & Marcy, 2014; Rogers, 2015; Wolfgang & Lopez, 2014; Wordsworth & Kreidberg, 2021) and the observations in our sample follow the Earth-like rocky composition. Planets with a larger radius are more scattered in the mass-radius relation and require a larger amount of volatiles (Wordsworth & Kreidberg, 2021). In this diagram, we see the radius gap and two populations of planets: 8 planets have a radius below $1.5R_\oplus$ and a mass below $2M_\oplus$ and 18 planets have a radius above $1.7R_\oplus$ and a mass above $4M_\oplus$. The distribution of the planets in terms of orbital period and radius is shown in Figure 7.1 (bottom). We also present values for transiting planets with an orbital period below 300 days and a radius below $8R_\oplus$.

First, we present the HST observations used for the data analysis in Section 7.2.1. Section 7.2.2 explains the Bayesian retrieval setups used to analyse the 26 spectra homogeneously. The results are presented in Section 7.3. First, we quantify the detection of an atmosphere for Super-Earths and Sub-Neptunes. Then, we assess the strength of molecular detections and discuss the observed degeneracies.

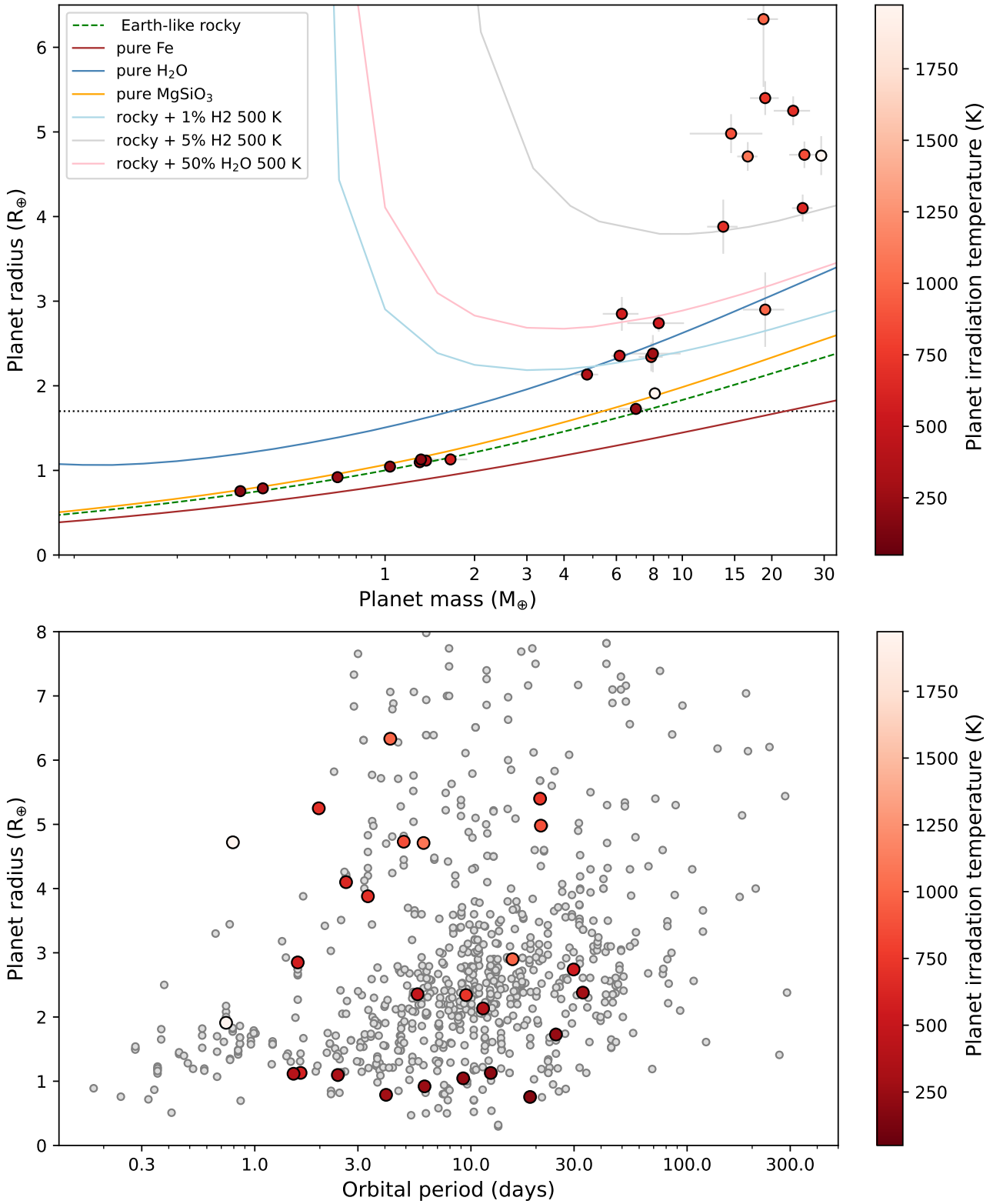

Figure 7.1: Mass radius measurements as a function of the irradiation temperature for planets studied here (top). Models compositions are from Zeng et al. (2019), and the horizontal dotted lines are set to the radius gap from Fulton et al. (2017). Distribution of the orbital period and the radius for planets in the sample (bottom). Known transiting planets with a published mass are shown in grey.

7.2 Methodology

7.2.1 Observations

This study will analyse planets with radii spanning from $\sim$ 1-6$R_\oplus$. Fulton et al. (2017) showed that the gap in the planet radius distribution appears at 1.7 $R_\oplus$ and that the number of planets per star decreases for planets with a radius larger than 6 $R_\oplus$. Crossfield & Kreidberg (2017) studied trends in the atmospheres of 6 warm Sub-Neptunes, excluding planets with a temperature larger than 600 K. We expanded the sample to include planets with higher temperatures, such as 55-Cnc e and LTT 9779 b, but also temperate planets, K2-18 b, LHS 1140 b and TRAPPIST-1 b to h, although the presence of an atmosphere was not confirmed for all of them. Our sample comprises 26 planets with a radius of less than 6 $R_\oplus$ observed with the Hubble Space Telescope Wide Field Camera 3 Grism 141 (HST/WFC3 G141). The sample covers a wide range of temperatures, planet masses and planet radii. All stellar and planetary parameters and references can be found in the tables 7.1 and 7.2.

Table 7.1: Stellar parameters

Name	$R_\star$ ($R_\odot$)	$T_\star$ (K)	References
55-Cnc	0.943	5196	Von Braun et al. (2011)
GJ 436	0.455	3416	Lanotte et al. (2014)
GJ 1132	0.207	3270	Berta-Thompson et al. (2015)
GJ 1214	0.216	3026	Harpsøe et al. (2012)
GJ 3470	0.48	3652	Biddle et al. (2014)
HAT-P-11	0.75	4780	Bakos et al. (2010)
HAT-P-26	0.788	5079	Hartman et al. (2011)
HD 3167	0.835	5286	Gandolfi et al. (2017)
HD 97658	0.703	5119	Dragomir et al. (2013)
HD 106315	1.312	6256	Guilluy et al. (2020)
HD 219666	1.03	5527	Esposito et al. (2019)
HIP 41378	1.40	6199	Vanderburg et al. (2016a)
K2-18	0.411	3457	Benneke et al. (2017)
K2-24	1.16	5625	Petigura et al. (2018)
LHS 1140	0.2139	3216	Ment et al. (2019)
LTT 9779	0.949	5443	Jenkins et al. (2020)
TOI-270	0.378	3506	Van Eylen et al. (2021)
TOI-674	0.420	3514	Murgas et al. (2021)
TRAPPIST-1	0.1192	2566	Agol et al. (2021)

For consistency, we collected spectra mostly extracted with the `iraclis` (Tsiaras et al., 2016b) pipeline. Thus, most spectra come from the population studies of Tsiaras et al. (2018) and Edwards et al. (2022). We add the spectra analysed as part of the Ariel Retrieval of Exoplanets School (ARES IV Guilluy et al. (2020) and ARES V (Mugnai et al., 2021)). The LHS 1140 b spectrum is from Edwards et al. (2021) and TRAPPIST-1 h from Gressier et al. (2021). The TRAPPIST-1 b to g spectra are from Zhang et al. (2018) and were extracted with a different pipeline with similar performance to `iraclis`. We list in Table 7.3 the different planets with information about the observing proposals and the reference of the published spectra. Most of the spectra were extracted at the defined 'high' resolution of `iraclis`, i.e. with a resolving power of 70 around 1.4μm. K2-18 b, LHS 1140 b, and TRAPPIST-1 h have 'low' resolution ($\lambda/\Delta\lambda$=50) and TRAPPIST-1 b to g have 'very low' resolution ($\lambda/\Delta\lambda$=30).

Table 7.2: Planetary parameters

Name	R_P ($R_\oplus$)	M_P ($M_\oplus$)	a (AU)	T_{irr} (K)	References Parameters
55-Cnc e	1.91	8.08	0.01544	1960	Demory et al. (2016)
GJ 436 b	4.10	25.4	0.0308	633	Lanotte et al. (2014)
GJ 1132 b	1.13	1.66	0.0153	585	Bonfils et al. (2018)
GJ 1214 b	2.85	6.26	0.01411	571	Harpsøe et al. (2012)
GJ 3470 b	3.88	13.73	0.031	692	Biddle et al. (2014)
HAT-P-11 b	4.73	25.743	0.053	867	Bakos et al. (2010)
HAT-P-26 b	6.333	18.751	0.0479	993	Hartman et al. (2011)
HD 3167 c	2.74	8.33	0.1806	548	Gandolfi et al. (2017)
HD 97658 b	2.341	7.86	0.0796	733	Dragomir et al. (2013)
HD 106315 c	4.98	14.59	0.1531	883	Guilluy et al. (2020)
HD 219666 b	4.71	16.6	0.06356	1073	Esposito et al. (2019)
HIP 41378 b	2.90	-	0.12692	992	Vanderburg et al. (2016a)
K2-18 b	2.38	7.96	0.143	283	Cloutier et al. (2017)
K2-24 b	5.4	19.0	0.154	744	Petigura et al. (2018)
LHS 1140 b	1.727	6.98	0.0936	234	Ment et al. (2019)
LTT 9779 b	4.72	29.32	0.01679	1973	Jenkins et al. (2020)
TOI-270 c	2.355	6.15	0.04526	488	Van Eylen et al. (2021)
TOI-270 d	2.133	4.78	0.07210	387	Van Eylen et al. (2021)
TOI-674 b	5.25	23.6	0.0250	694	Murgas et al. (2021)
TRAPPIST-1 b	1.116	1.374	0.01154	398	Agol et al. (2021)
TRAPPIST-1 c	1.097	1.308	0.01580	340	Agol et al. (2021)
TRAPPIST-1 d	0.788	0.388	0.02227	286	Agol et al. (2021)
TRAPPIST-1 e	0.920	0.692	0.02925	250	Agol et al. (2021)
TRAPPIST-1 f	1.045	1.039	0.03849	218	Agol et al. (2021)
TRAPPIST-1 g	1.129	1.321	0.04683	197	Agol et al. (2021)
TRAPPIST-1 h	0.755	0.326	0.06189	172	Agol et al. (2021)

Table 7.3: Proposal ID, PI and spectrum's reference for the data used in the HST transmission survey.

Name	Proposal ID and PI	References Spectrum
55-Cnc e	13665 Benneke	Tsiaras et al. (2016a)
GJ 436 b	11622 Knutson	Tsiaras et al. (2018)
GJ 1132 b	14758 Berta-Thompson	Mugnai et al. (2021)
GJ 1214 b	13021 Bean	
GJ 3470 b	13665 Benneke	Tsiaras et al. (2018)
HAT-P-11 b	12449 Deming	Tsiaras et al. (2018)
HAT-P-26 b	14260 Deming	Tsiaras et al. (2018)
HD 3167 c	15333 Crossfield	Guilluy et al. (2020)
HD 97658 b	13501 Knutson	Edwards et al. (2022)
HD 106315 c	15333 Crossfield	Guilluy et al. (2020)
HD 219666 b	15698 Beatty	Edwards et al. (2022)
HIP 41378 b	15333 Crossfield 13665 Benneke	Edwards et al. (2022)
K2-18 b	14682 Benneke	Tsiaras et al. (2019)
K2-24 b	14455 Petigura	Edwards et al. (2022)
LHS 1140 b	14888 Dittmann	Edwards et al. (2021)
LTT 9779 b	16457 Edwards	Edwards et al. (2022)
TOI-270 c	15814 Mikal-Evans	Edwards et al. (2022)
TOI-270 d	15814 Mikal-Evans	Edwards et al. (2022)
TOI-674 b	15333 Crossfield	Edwards et al. (2022)
TRAPPIST-1 b	14500 de Wit	Zhang et al. (2018)
TRAPPIST-1 c	14500 de Wit	Zhang et al. (2018)
TRAPPIST-1 d	14873 de Wit	Zhang et al. (2018)
TRAPPIST-1 e	14873 de Wit	Zhang et al. (2018)
TRAPPIST-1 f	14873 de Wit	Zhang et al. (2018)
TRAPPIST-1 g	14873 de Wit	Zhang et al. (2018)
TRAPPIST-1 h	15304 de Wit	Gressier et al. (2021)

7.2.2 Data analysis: Atmospheric modelling

We performed the retrieval of the atmospheric properties of the 26 planets from their observed spectra using TauREx 3 (Al-Refaie et al., 2021)[1]. We use the nested sampling algorithm Multinest (Feroz et al., 2009; Buchner et al., 2014) to explore the parameter space. Each atmosphere is simulated using 100 layers, uniformly distributed in log-space, ranging from 10^{-3} and 10^{6} Pa. We adopted an evidence tolerance of 0.5 and 500 live points. We note that some rocky planets in the sample might not be correctly represented by a 10-bar atmosphere, but we fixed this value for consistency. The stellar and planetary parameters used in the retrieval are set to the values given in Tables 7.1 and 7.2. We include molecular line lists and continuum from the ExoMol project (Tennyson et al., 2016; Chubb et al., 2021), HITEMP (Tennyson & Yurchenko, 2018), and HITRAN (Rothman et al., 1987; Rothman et al., 2013). In all our retrievals, the ratio of helium over hydrogen is set to the solar value of 0.17. We tested different atmospheric scenarios using six retrievals analysis to investigate the atmospheric properties of the selected planets. These are all described below.

The first three retrieval setups represent "complete" retrieval scenarios, whereas the last three are "forced" scenarios. In the "forced" scenarios, we fit only for the radius and the temperature, which allows us to test for a specific composition. The first three retrievals are not model oriented and are designed to span the whole parameter space. We should find similar cloud coverage and molecular abundance results if the atmospheric properties are well-constrained.

1-Primary: We include the following active molecular opacities: H_2O (Polyansky et al., 2018), CO (Li et al., 2015), CO_2(Rothman et al., 2010), CH_4(Yurchenko & Tennyson, 2014), NH_3(Yurchenko et al., 2011) and HCN (Barber et al., 2014) in a H/He dominated atmosphere. The choice of the molecules is motivated by the previous spectra analysis. In particular, HCN was found in the analysis of 55-Cnc e by Tsiaras et al. (2016a). All active molecules are considered as gas traces, and thus, the volume mixing ratio (VMR) is fitted between 10^{-12} and 10^{-2}. We also include collision-induced absorption (CIA) for all molecules for H_2-H_2 and He-H_2 and Rayleigh scattering. We model clouds as grey clouds, using a uniform opaque layer, and we fit for the top pressure of the cloud deck between 10^{-3} and 10^{6} Pa. If the clouds are retrieved below 10^{5}, the atmosphere is consistent with a primary clear scenario.

2-Active clear: This setup is similar to the **1-Primary** scenario, but we allow for a heavier atmosphere and remove clouds. We increase the higher bound of the molecular abundances to 1 (pure molecule atmosphere). We include the same molecular opacities, CIA and Rayleigh. This setup lets us know if the active molecular opacities alone can fit the spectral features. If the retrieved molecular abundance is low, the scale height is large, and the atmosphere is primary. In this case, we should retrieve similar atmospheric properties as for **1-Primary** with no clouds. On the contrary, if the molecular abundance is high, the atmosphere is heavier and more compact.

3-Hidden absorber: This setup is based on the same setup as the previous two, but we also include N_2 as an inert gas. The ratio of N_2/H_2 is fitted between 10^{-12} and 10^{4}. The molecular opacities list is similar to the first **1-Primary** setup, and we fit their abundance between 10^{-12} and 10^{-2}. We test if, in a clear atmosphere, a hidden absorber is required to increase the weight of the atmosphere and adjust the spectrum. If the N_2/H_2 is found low, the case of a primary clear atmosphere is retrieved again, and we should find similar results as in **1-Primary** with no clouds and **2-Active clear** with low molecular abundances. If the ratio is high, we should find similar molecular abundances than for **1-Primary** with clouds. We note that, for heavier atmospheres, the molecular line lists are no longer adapted because there are computed for a hydrogen-dominated atmosphere. However, this

[1] https://github.com/ucl-exoplanets/TauREx3_public

approximation might not be too impacting while using HST-restricted wavelength range and resolution.

4-Primary clear with a trace of H_2O: In this setup, we only include H_2O as the active molecular opacity, and we fix its abundance to 10^{-3} in VMR. We arbitrarily set this value to keep a light atmosphere and a low molecular weight of around 2.3 g/mol We still include CIA and Rayleigh scattering, but we remove grey clouds.

5-Water world 100% H_2O: Similarly to the previous setup, we only included H_2O as the only molecular source, and we fixed its abundance to 1 to simulate a pure water atmosphere.

6-Flat line: This retrieval only includes a cloud deck, and the top pressure is fitted between 10^{-3} and 10^6 Pa. No molecular opacities are included, and we fit for the planet's radius and temperature. This setup is used to assess the strength of the atmospheric detection in the previously described models by computing the Bayes factor, $\Delta\log(E)$ or, positively defined, the Atmospheric Detectability Index (ADI) in Tsiaras et al. (2018). The latter is the difference in logarithm evidence between the tested model and the flat line (Kass & Raferty, 1995). The equivalence between the Bayes factor and the significance is estimated using Table 2 in Trotta (2008) and Table 2 in Benneke & Seager (2013). A Bayes factor greater than 3 (3σ) is considered significant, and one superior to 11 (5σ) is considered a strong detection. The detection is considered weak if the Bayes factor is between 1 and 3 (2σ). We defined $\Delta\log(E)$ as in Gressier et al. (2021): $\Delta\log(E)=\log(E_{\rm Model})-\log(E_{\rm Flat\ line})$.

In every retrieval, the radius is fitted between ±50% of the literature value given in Table 7.2. The planet mass is fixed to the value from Table 7.2. In the case of HIP 41378 b, where no information on the mass has yet been provided, we run the first retrieval with the model based on **1-Primary** setup and also fitted for the mass between 1 and 30 Earth masses. We retrieved a mass of 19 ±3 $M_\oplus$. We then fixed HIP 41378 b's mass to this value and reran each retrieval. We note that fixing the planet mass did not modify the result of the fit for the rest of the parameters as predicted in Changeat et al. (2020b).

We assumed an isothermal temperature/pressure (T/P) profile in each planet's atmosphere. The temperature is then fitted between ±50% of the irradiation temperature and reported in Table 7.2. It is computed with the stellar and planetary parameters from Table 7.1 and 7.2, assuming zero albedo and full heat redistribution. As the albedo is unknown, we can not properly speak of an equilibrium temperature. We will then call this quantity the irradiation temperature ($T_{\rm irr}$), which gives an upper bound on the temperature.

$$T_{\rm irr} = T_\star \left(\frac{R_\star}{2\,a}\right)^{1/2} \tag{7.1}$$

The albedo of the planets in the sample is unknown. We decided to use the irradiation temperature with wide prior ranges to account for higher albedos and, thus, lower temperatures. While these atmospheres are unlikely to have an iso-thermal T/P profile, this approximation is not entirely wrong regarding the short-wavelength coverage and, the low resolution and the transit observation technique. The HST data quality restricts us to this simplification, and a more complex model would not be constrained. In a broader view, Caldas et al. (2019) and Pluriel et al. (2022) showed that 3D effects shape the transmission spectrum and, by not taking them into account, this could lead to biases in the retrieved molecular abundances or the retrieved temperature (Skaf et al., 2020; MacDonald et al., 2020). In the case of a temperate to warm Sub-Neptune, these effects might not be as important as they are for Ultra hot-Jupiter.

7.3 Results

We performed the six retrieval setups for the 26 spectra and determined the best fit model using the logarithm Bayesian evidence (log(E)). A summary of the best fit atmospheric results for each planetary spectrum is presented in Table 7.4. We indicate the best fit model along with the Bayes factor and the strength of the detection, the main absorber, and the derived mean molecular weight. Figure 7.2 presents the spectra and the best-fit models from the retrieval results: **1-Primary** (blue), **2-Active clear** (green), **3-Hidden absorber** (red), **4-Primary clear** (light blue) and **5-Water world** (purple). The model is in the solid line when it is significant compared to the flat line (i.e., the Bayes factor is superior to three) and in dotted lines otherwise. H_2O is the molecule targeted in this part of the spectrum as it presents an important absorption feature around 1.4μm. It is the retrieved main absorber in almost all cases. HCN is retrieved for 55-Cnc e. HD 97658 b's best fit spectrum is a combination of HCN, NH_3, CO_2 and H_2O. NH_3 and CO_2 are also constrained for some planets but do not spectrally contribute as strongly as H_2O. CH_4 is never retrieved, which is surprising. As explained in Bézard et al. (2022), methane should be the main spectral contributor in Sub-Neptune's atmospheres with low metallicity and an equilibrium temperature below 600 K. We find ten planets are consistent (Bayes factor is superior to three) with a **1-Primary** model. Those planets are 55-Cnc e, HAT-P-11 b, HAT-P-26 b, HD 3167 c, HD 987658 b, HD 106315 c, HD 219666 b, LTT 9779 b, TOI-270 d and TOI-674 b. The same sample is consistent with a **2-Active clear** and a **3-Hidden absorber** model. The **2-Active clear** model is often found to be the best-fit model. We note that K2-18 b is consistent with **2-Active clear** and a **3-Hidden absorber** model but not with the **1-Primary** model. GJ 1214 b is found to be statistically consistent with only the **3-Hidden absorber** model, and this is the first time that an atmospheric model has been found significant for this planet. The data for this planet has been re-analysed in Edwards et al. (2022) using `iraclis` pipeline and led to this new detection.

Among these ten planets, seven are consistent with a **4-Primary atmosphere with a trace of water**. The Bayes factor is lower than the best-fit model except for HAT-P-26 b and LHS 1140 b. Nine planets are consistent with a **5-Water world**. Once again, the Bayes factor is lower than one of the best-fit models except for TOI-674 b. GJ 3470 b's best fit is the **5-Water world** model, but Δlog(E) does not exceed three and is considered a weak detection. Except for HAT-P-26 b, LHS 1140 b and TOI-674 b's spectra, we need a more complex model to fit the other spectra correctly. A pure water world is unlikely for a Neptune planet like TOI-674 b (see Figure 7.1). This result shows the limitation of HST's short-wavelength coverage and low resolution to determine the abundance of a detected molecule, mainly water. Once detected, the fit will be significant, regardless of the water's amount we set in the retrieval. The detailed best fit results of all retrieval setups are in Appendix Tables D.1 to D.5 and log(E) results for each model and every spectra, are presented in Appendix Table D.6.

[2]The best fit includes also H_2O and NH_3

[3]The 2-Active clear model also includes NH_3

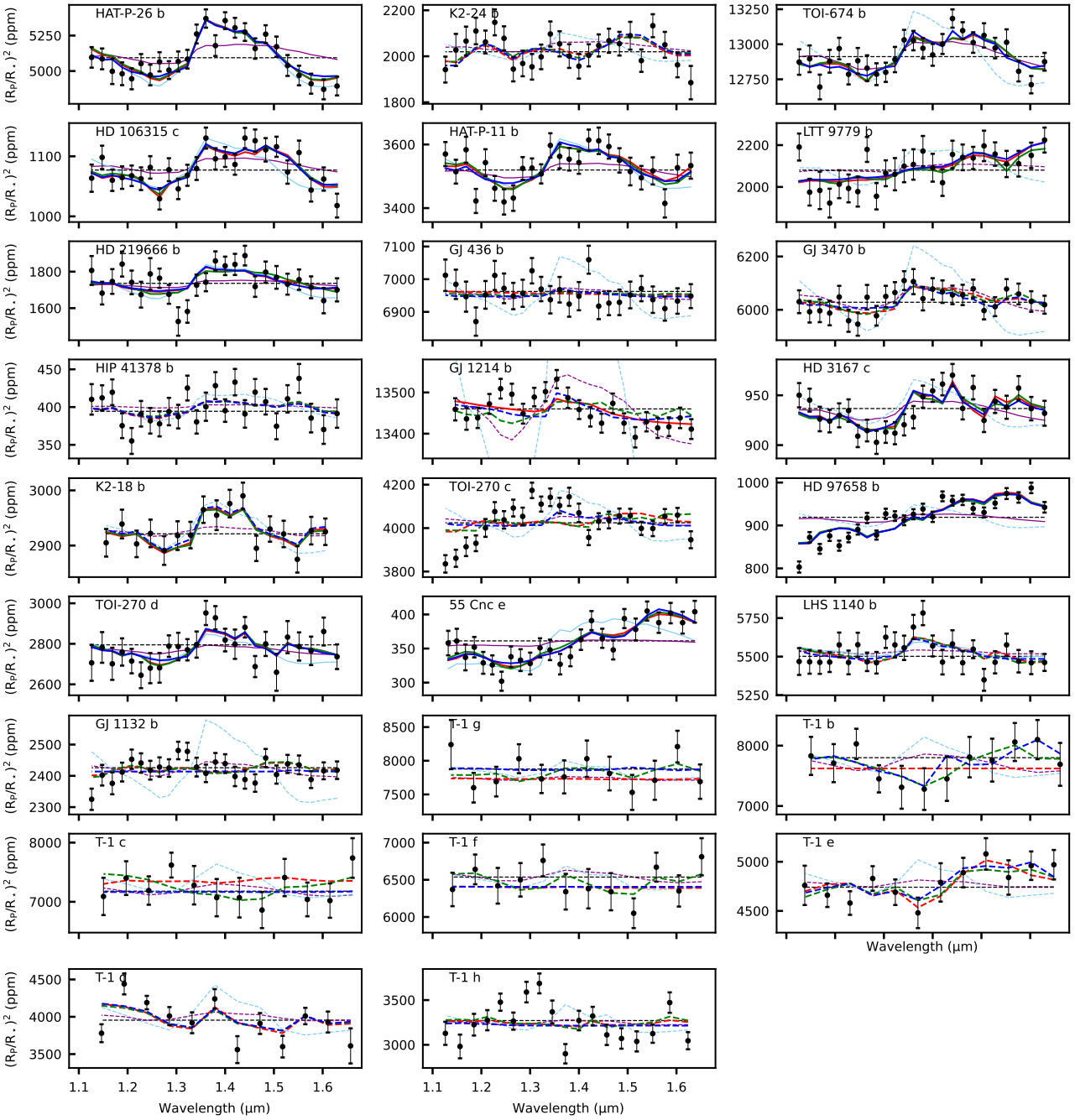

Figure 7.2: HST/WFC3 G141(1.1-1.65 μm) spectrum for the 26 planets along with five retrieval models: the **1-Primary** (blue), the **2-Active clear** (green), the **3-Hidden absorber** (red), the **4-Primary clear** (light blue) and the **5-Water world** (purple). We also represent the flat line model with the black dotted line. The model is in solid lines when it is significant compared to the flat line (i.e. the Bayes factor is superior to 3) and in dotted lines otherwise. The spectra are ordered in increasing radii.

Table 7.4: Best-fit retrieval results for the 26 Sub-Neptune and Super-Earth transmission spectra covering the HST/WFC3 G141wavelength range.

Planet	Best-fit model	Δlog(E)	Detection	Absorbers (X)	μ (g/mol)
55-Cnc e	**2-Active clear**	29.94	strong	HCN	2.34
GJ 436 b	1-Primary	0.04	none	H_2O	2.31
GJ 1132 b	6-Flat-line	-	none	-	2.30
GJ 1214 b	**3-Hidden absorber**	3.53	strong	H_2O, N_2	27.90
GJ 3470 b	5- Water world	2.15	weak	H_2O	18.02
HAT-P-11 b	**2-Active clear**	9.99	strong	H_2O	4.43
HAT-P-26 b	**4-Primary clear**	43.12	strong	H_2O	2.32
HD 3167 c	**2-Active clear**	11.13	strong	H_2O, CO_2	2.84
HD 97658 b	**2-Active clear**	103.34	strong	HCN, CO_2[2]	2.85
HD 106315 c	**2-Active clear**	16.63	strong	H_2O, NH_3	5.94
HD 219666 b	**2-Active clear**	5.02	strong	H_2O	2.60
HIP 41378 b	4-Primary clear	2.44	weak	H_2O	2.32
K2-18 b	**2-Active clear**	3.47	strong	H_2O	2.43
K2-24 b	2-Active clear	0.39	none	NH_3	4.71
LHS 1140 b	**4-Primary clear**	3.70	strong	H_2O	2.32
LTT 9779 b	**2-Active clear**	5.71	strong	CO_2	2.31
TOI-270 c	2-Active clear	1.36	weak	CO_2	27.51
TOI-270 d	**2-Active clear**	5.19	strong	H_2O, CO_2	2.44
TOI-674 b	**5-Water world**	17.86	strong	H_2O[3]	8.87
TRAPPIST-1 b	2-Active clear	1.05	weak	CO, NH_3	2.39
TRAPPIST-1 c	6-Flat-line	-	none	-	2.30
TRAPPIST-1 d	3-Hidden absorber	0.59	none	H_2O	2.32
TRAPPIST-1 e	1-Primary	0.49	none	NH_3	2.32
TRAPPIST-1 f	1-Primary	0.10	none	-	2.31
TRAPPIST-1 g	6-Flat-line	-	none	-	2.30
TRAPPIST-1 h	6-Flat-line	-	none	-	2.30

7.4 Discussion

7.4.1 Strength of the atmospheric detection

Using the best fit results for each planet (see Table 7.4), we quantify the atmospheric detectability, and we confirm the detection of an atmosphere around a planet by computing $\Delta\log(E)$ between the best fit atmospheric model and the flat line. We present the Bayes factor as a function of the planetary radius and the Transmission Spectroscopy Metric (TSM) (Kempton et al., 2018) for each planet in Figure 7.3. HIP 41378 b appears in grey as no TSM has yet been computed. If the Bayes factor, $\Delta\log(E)$, is superior to 3 or 11, the planet's atmosphere is detected with more than 3σ and 5σ confidence, respectively. We

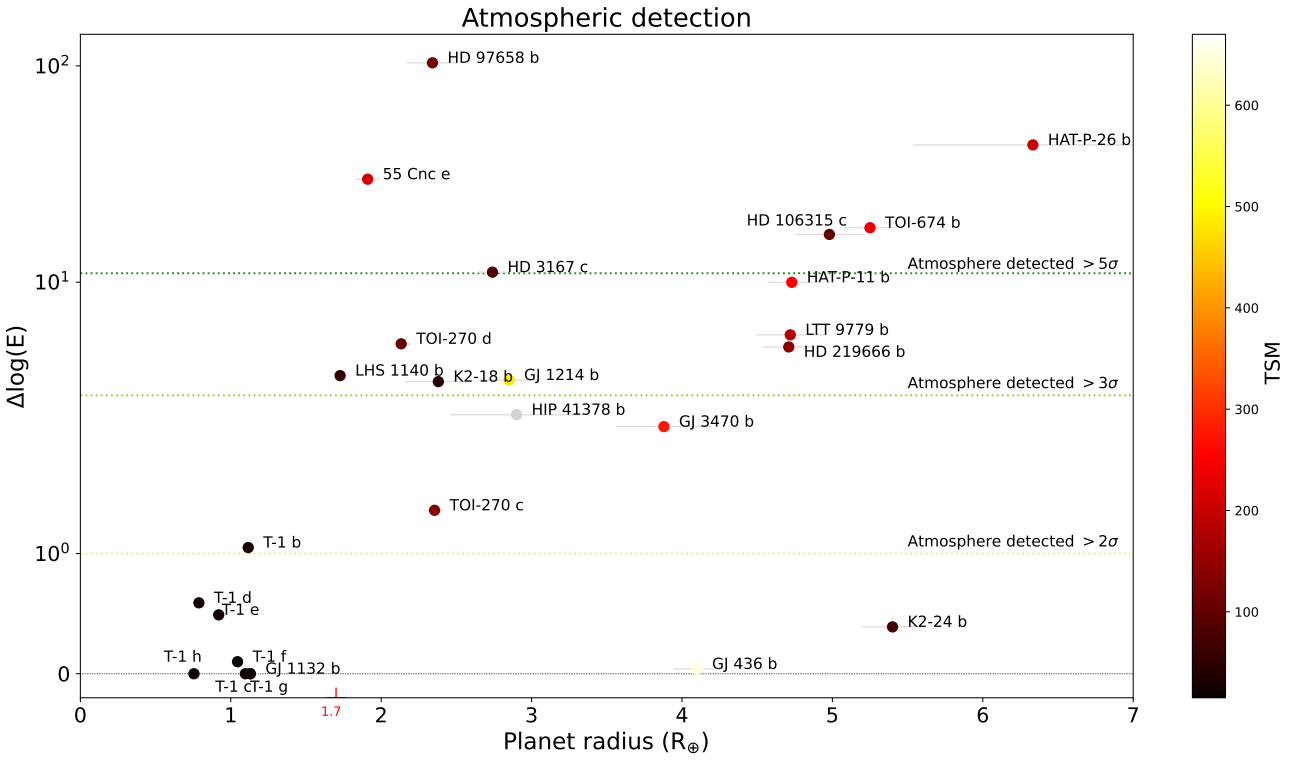

Figure 7.3: Atmospheric detection for Sub-Neptune and Super-Earth in the sample using HST WFC3 spectra covering 1.1 to 1.65 μm. Bayes factor, computed with the Bayesian evidence from the best fit model, as a function of the planet radius and the TSM (Kempton et al., 2018). We indicate the position of the radius gap at 1.7 $R_\oplus$. If the Bayes factor, $\Delta\log(E)$, is superior to 3, the planet's atmosphere is detected with more than 3σ confidence.

confirm the detection of an atmosphere for 13 planets. For the other half of the sample, we cannot strongly confirm the presence of an atmosphere. The Bayes factor is between plus or minus three; thus, we can not conclude that the model with an atmosphere is strongly favoured compared to the flat line model. As the best fit, we note that a flat line could also suggest the presence of a high cloud deck or a layer of photochemical hazes in the planet's upper atmosphere. GJ 3470 b, HIP 41378 b, TOI-270 c, and TRAPPIST-1 b present a Bayes factor above one, corresponding to a 2σ detection. These planets might possess an atmosphere, but the Bayesian log evidence result is classified as a 'weak detection' in Benneke & Seager (2013)'s formalism.

All the planets with a radius below 1.7 $R_\oplus$, (i.e. the position of the radius valley and the supposed limit for the planet to be rocky), TRAPPIST-1 b to h and GJ 1132 b, have a Bayes factor around or below 1. On the other hand, 55-Cnc e and LHS 1140 b, which have a density superior to 6 g/cm^{-3} and, thus, are probably rocky planets, present a more elevated Bayes factor and might have sustained an atmosphere. The high Bayes factor found for HD 97658 b is probably due to the slope shape of

the transmission spectrum. We note that the TSM and the Bayes factor are sometimes in disagreement, particularly for warm Sub-Neptunes like GJ 436 b, whose spectra are flat in the Near Infrared but present an elevated TSM. We also observe a disagreement the other way around; for example, HD 3167 c's atmosphere has been detected with more than 5σ but displays a TSM below 100.

7.4.2 Strength of molecular detections

To assess the strength of the molecular detection claimed in Section 7.3, we suppressed the molecule from the best-fit model and performed the retrieval analysis. We compare the logarithm evidence of both retrievals, with and without the molecule, by computing a Bayes factor as follows: $\Delta\log(E) = \log(E_{withX})\text{-}\log(E_{withoutX})$. If this quantity exceeds three, the molecule is detected with high confidence. If it is between one and three, it is a tentative detection. The molecule is not detected if $\Delta\log(E)$ is below one. In short, we remove species from the model and examine whether the loss of fit quality is significant, and we call this method *Ablation study*. We performed this test for 17 planets in the sample. These planets have a weak to strong atmospheric detection associated with an identified absorber (see Table 7.4). We present the results of the ablation study in Table 7.5. This table summarises the

Table 7.5: Summary of molecular detection for Sub-Neptune and Super-Earth atmospheres using the HST/WFC3 G141 wavelength range. Green is for detected with more than 3σ, orange is for tentative detection, and grey is for non-detection after the ablation study. Cells are left empty when there is no evidence of the given molecule in the spectrum.

Planet	H_2O	CH_4	CO	CO_2	NH_3	HCN	references [4]
55-Cnc e							T16a
GJ 436 b							
GJ 1132 b							
GJ 1214 b							
GJ 3470 b							B19a, E22
HAT-P-11 b							F14,E22
HAT-P-26 b							W17, MD19, E22
HD 3167 c							G20, ME20, E22
HD 97658 b							E22
HD 106315 c							G20, K20, E22
HD 219666 b							
HIP 41378 b							
K2-18 b							T19, B19b, E22
K2-24 b							
LHS 1140 b							E22
LTT 9779 b							
TOI-270 c							
TOI-270 d							E22
TOI-674 b							B22, E22
TRAPPIST-1 b							
TRAPPIST-1 c							
TRAPPIST-1 d							
TRAPPIST-1 e							
TRAPPIST-1 f							
TRAPPIST-1 g							
TRAPPIST-1 h							

molecules detected in Sub-Neptune atmospheres using the HST/WFC3 G141 wavelength range. Green cells are for strong detections (ΔlogE >3), orange ones are for tentative detections (1< ΔlogE <3) and grey ones are for non-detections. Cells are left empty when there is no indication of the molecule in the spectrum. We also indicate references for each planet that confirmed a detection using the same dataset. We confirm the detection of H_2O with strong confidence for nine planets: HAT-P-11 b, HAT-P-26 b, HD 3167 c, HD 97658 b, HD 106315 c, HD 219666 b, LHS 1140 b, TOI-270 d and TOI-674 b. HCN is detected in the atmosphere of 55-Cnc e. Water is not confirmed in the atmosphere of GJ 1214 b. However, a hidden absorber, like N_2, is required to increase the weight of the atmosphere and match the observed features. Added to H_2O, NH_3 and HCN are also required to fit HD 97658 b's transmission spectrum correctly. We note that H_2O is only a tentative detection in K2-18 b's atmosphere. Others detection from Table 7.4 are either tentative or non-detection.

7.4.3 Retrieval analysis degeneracies

From Section 7.4.1 and the analysis of the best-fit model, we showed that 13 planets over 26 have an atmosphere detected with more than 3σ. We presented the best-fit model results, i.e. the model with the highest log evidence. However, one must note that others models fit the data correctly and presented elevated evidence for these planets. The log evidence results of all six retrieval analyses for the 26 transmission spectra are presented in Table D.6. As detailed in Section 7.2.2, we designed the first three retrieval analyses to find similar results for the same spectrum and test at the same time a specific aspect. By constraining the molecular abundances, the **1-Primary** retrieval checks if the atmosphere is primary. The model also includes grey clouds. The **2-Active clear** setup allows abundances to take higher values if necessary. The **3-Hidden absorber** model uses N_2, the hidden absorber, as a fill gas to fit the molecular features with a heavier atmospheric scenario. If this is not required, the model should find similar results as the **1-Primary** model.

We show in Table 7.6, the main results of the three first retrieval analysis (**1-Primary**, **2-Active clear** and **3-Hidden absorber**) for these 13 planets. We also computed the scale height from the results. We can conclude on a primary clear atmospheric scenario for four planets, 55-Cnc e, HAT-P-26 b, LHS 1140 b and LTT 9779 b. All three retrieval analyses converge towards a light atmosphere with a mean molecular weight of around 2.3 g/mol, and we find the grey clouds' top cloud pressure below 10^4 Pa. The main absorber's volume mixing ratio is low, below 10^{-3}.

GJ 1214 b retrieval solutions are degenerate. A combination of a high cloud deck, in a primary atmosphere, with a low amount of H_2O (10^{-5}) or a large amount of N_2/H_2 (10^2) with a low amount of H_2O (10^{-7}) can fit the observed spectral features. For two planets, HD 3167 c and HD 97658 b, the amount of the main detected species is poorly constrained, but we do not detect clouds. We can conclude in a clear atmosphere but cannot distinguish a primary from a higher metallicity atmosphere. For the remaining transmission spectra, the solutions are more or less degenerate. The issue resides mainly in differentiating the **1-Primary** and the **2-Active clear** models for planets, which present similar Bayesian statistical results (see Table D.6) but imply a different type of atmosphere. The spectra are either fitted with a light amount of the main absorber, here water and grey clouds (**1-Primary**), or by a larger amount of water with no clouds (**2-Active clear**). The first scenario corresponds to an atmosphere dominated by hydrogen, with a mean molecular weight of around 2.3 g/mol (1 metallicity). The second one allows heavier atmospheric scenarios from 2.4 to 9.1 g/mol (15 to 500 x solar). This difference may be important for estimating the C/O and H/O ratio and, consequently, the planet's formation process.

[4]B19a:Benneke et al. (2019); B19b: Benneke et al. (2019); B22: Brande et al. (2022); E22: Edwards et al. (2022); F14: Fraine et al. (2014); G20: Guilluy et al. (2020); K20: Kreidberg et al. (2020); MD19: MacDonald & Madhusudhan (2019); ME20: Mikal-Evans et al. (2020); T16a: Tsiaras et al. (2016a); T19:Tsiaras et al. (2019); W17: Wakeford et al. (2017)

We present in Figures 7.5 the posterior retrieval distributions from the three models of the radius, the temperature, the mean molecular weight and the molecular abundances for 55-Cnc e, HD 3167 c and HAT-P-11 b. In the case of 55-Cnc e, for which we concluded in a clear atmosphere, the parameter's Gaussian distributions overlap, particularly the abundance of HCN. We found similar results for the three retrievals. For the two other planets, the distributions of the molecular VMR of the **2-Active clear**'s solution, in green, peak at a higher solution than the **1-Primary** and **3-Hidden absorber** models. We illustrate the degeneracies with the abundance of water in HAT-P-11 b's retrieval posteriors (bottom). The water abundance distributions overlap for the first and the third model in blue and red while the Gaussian distribution of the **2-Active clear**'s model, in green, peaks at 10^{-1} and is separated by more than 2σ.

To follow up on the water-clouds specific degeneracy, we present in Figure 7.4 the HAT-P-11 b's spectrum and the best fit opacity contributions from water and grey clouds for the two models. In the primary scenario, grey clouds are required to cut the large water feature and to fit the data points, whereas a larger amount of water in a heavier atmosphere fits the spectrum. This ambiguity in the fitting of these spectra is probably due to the short wavelength coverage and the low resolution of the HST data, which leads to biases in the interpretation of the retrieval analysis while increasing the priors bounds of the molecular species. We find this degeneracy on giant planets, like HAT-P-11 b, for which there is little doubt about its gaseous nature. We find a similar result for smaller planets like TOI-270 d, for which there is room for doubt on their nature: a rocky core with a large H/He envelope or an icy core with heavier elements.

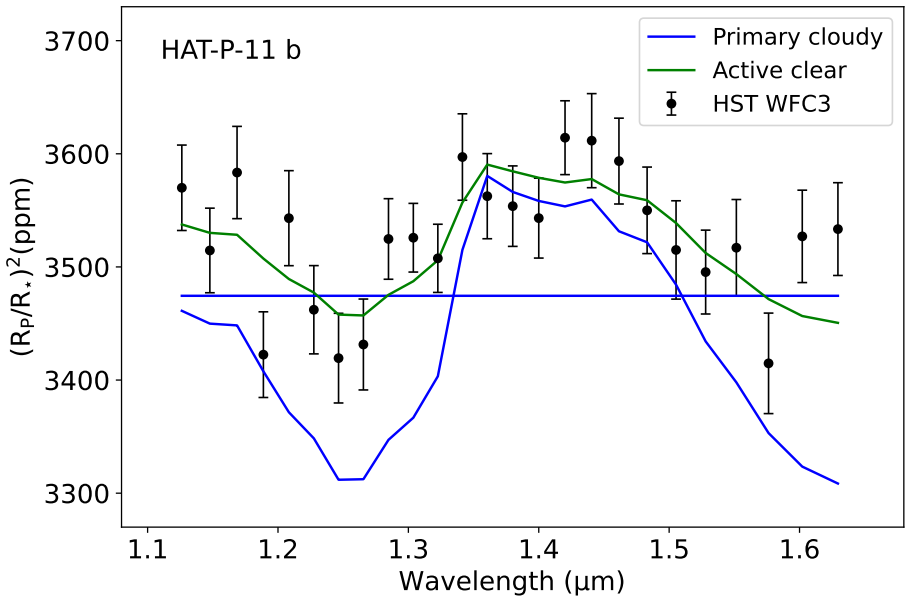

Figure 7.4: Best fit opacity contribution of water, and grey clouds (straight line) for the **1-Primary** (blue) and **2-Active clear** (green) models in the case of HAT-P-11b.

Table 7.6: Comparison of the best-fit models for 13 planets for which we detected a significant atmosphere (i.e. $\Delta\log(E)>3$).

Planet	$\log_{10}(X)$			$\log_{10}(P_{clouds})$	$\log_{10}(N_2/H_2)$	μ(g/mol)			Scale Height(km)			Conclusion
Model	**1**	**2**	**3**	**1**	**3**	**1**	**2**	**3**	**1**	**2**	**3**	
55-Cnc e	-2.92	-3.21	-3.49	>4	<-3	2.34	2.34	2.33	269	255	254	Primary clear
GJ 1214 b	-4.95	-1.51	-6.68	2.01	2.43	2.31	39.26	27.90	197	8	26	Degenerated
HAT-P-11 b	-3.01	-0.93	-3.84	3.20	3.80	2.33	4.43	2.34	233	95	203	Degenerated
HAT-P-26 b	-2.99	-3.51	-3.73	3.46	<-3	2.32	2.31	2.31	546	437	437	Primary clear
HD 3167 c	-2.66	-2.85	-2.72	>5	<-3	2.32	2.84	2.41	136	127	135	Clear degenerated
HD 97658 b	-2.21	-1.95	-2.20	>4	<-3	2.60	2.85	2.61	242	221	241	Clear degenerated
HD 106315 c	-2.92	-0.64	-2.99	3.07	-5.79	2.33	5.94	2.36	496	213	350	Degenerated
HD 219666 b	-3.19	-2.45	-4.48	3.19	<-2	2.32	2.60	2.31	465	362	382	Degenerated
K2-18 b	-4.01	-3.84	-4.22	4.14	<-2	2.33	2.43	2.35	73	58	66	Degenerated
LHS 1140 b	-3.22	-3.26	-3.61	4.30	<-3	2.33	2.34	2.33	39	32	34	Primary clear
LTT 9779 b	<-3	-6.37	<-3	5.19	<-3	2.31	2.31	2.31	647	664	674	Primary clear
TOI-270 d	-3.56	-3.53[5]	-3.89	4.06	<-3	2.33	2.44	2.35	135	109	116	Degenerated
TOI-674 b	-2.92	-0.44	-3.17	2.63	-0.37	2.34	8.87	9.14	286	84	87	Degenerated

[5] CO_2 is also constrained and found at -3.93 which leads to a higher mean molecular weight

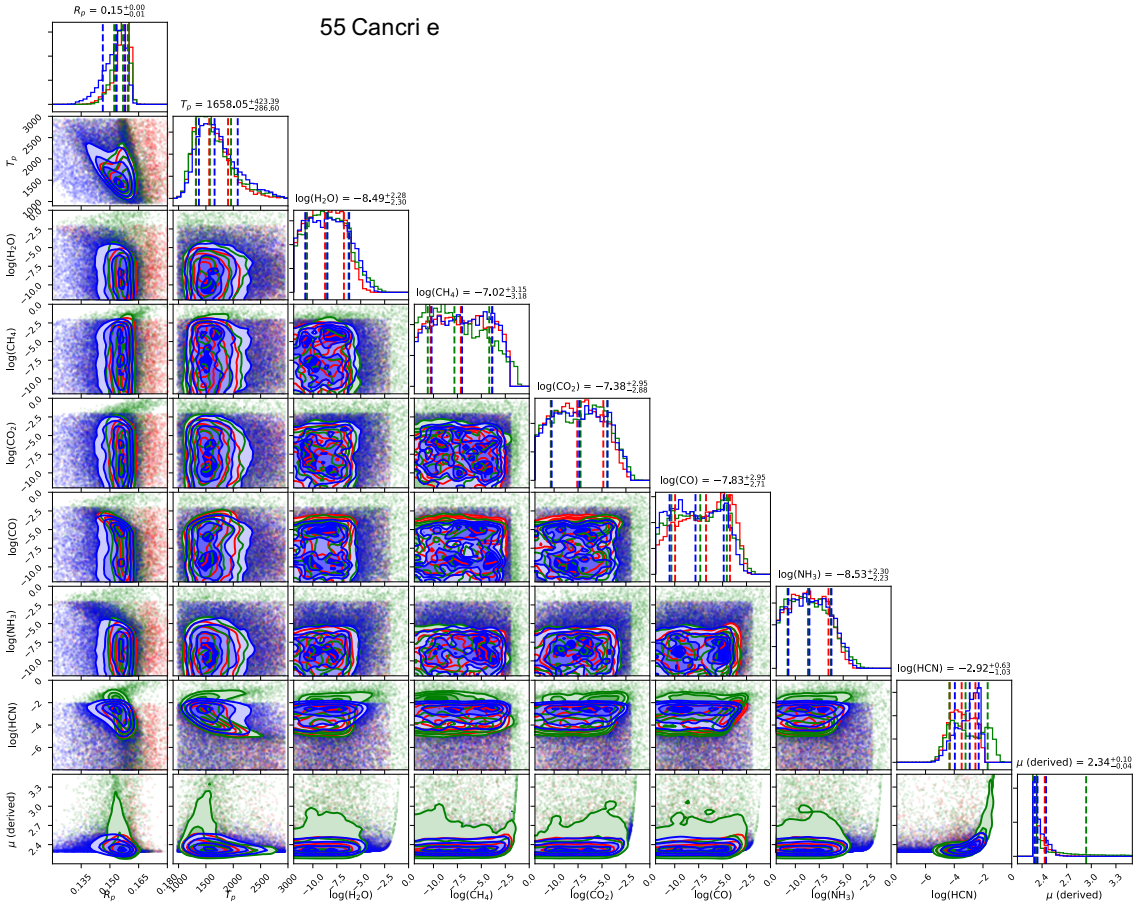
55 Cancri e
$R_p = 0.15^{+0.00}_{-0.01}$
$T_p = 1658.05^{+423.39}_{-286.60}$
$\log(H_2O) = -8.49^{+2.28}_{-2.30}$
$\log(CH_4) = -7.02^{+3.16}_{-3.18}$
$\log(CO_2) = -7.38^{+2.95}_{-2.88}$
$\log(CO) = -7.83^{+2.95}_{-2.71}$
$\log(NH_3) = -8.53^{+2.39}_{-2.23}$
$\log(HCN) = -2.92^{+0.63}_{-1.03}$
μ (derived) $= 2.34^{+0.10}_{-0.04}$
R_p
T_p
$\log(H_2O)$
$\log(CH_4)$
$\log(CO_2)$
$\log(CO)$
$\log(NH_3)$
$\log(HCN)$
μ (derived)

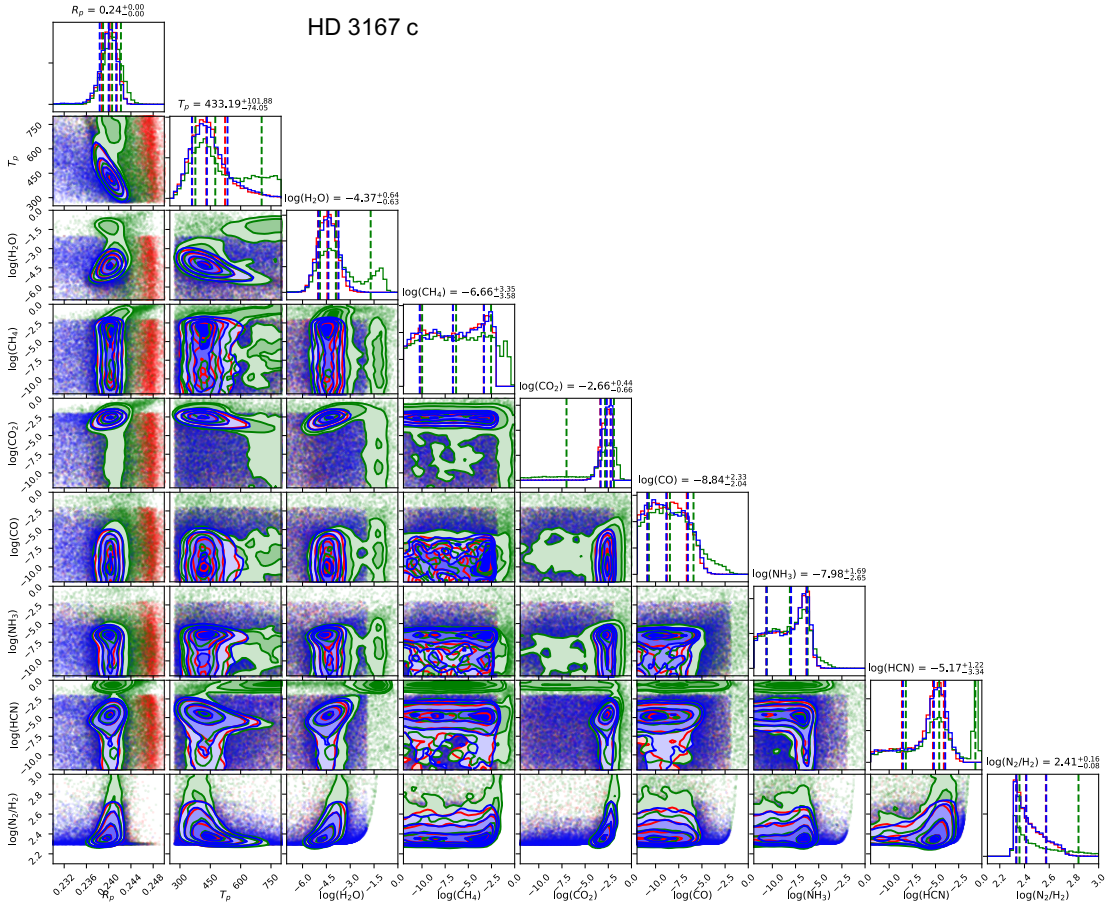
HD 3167 c
$R_p = 0.24^{+0.00}_{-0.00}$
$T_p = 433.19^{+101.88}_{-74.05}$
$\log(H_2O) = -4.37^{+0.64}_{-0.63}$
$\log(CH_4) = -6.66^{+3.35}_{-3.38}$
$\log(CO_2) = -2.66^{+0.44}_{-0.66}$
$\log(CO) = -8.84^{+2.33}_{-2.04}$
$\log(NH_3) = -7.98^{+1.69}_{-2.65}$
$\log(HCN) = -5.17^{+1.22}_{-3.34}$
$\log(N_2/H_2) = 2.41^{+0.16}_{-0.08}$
R_p
T_p
$\log(H_2O)$
$\log(CH_4)$
$\log(CO_2)$
$\log(CO)$
$\log(NH_3)$
$\log(HCN)$
$\log(N_2/H_2)$

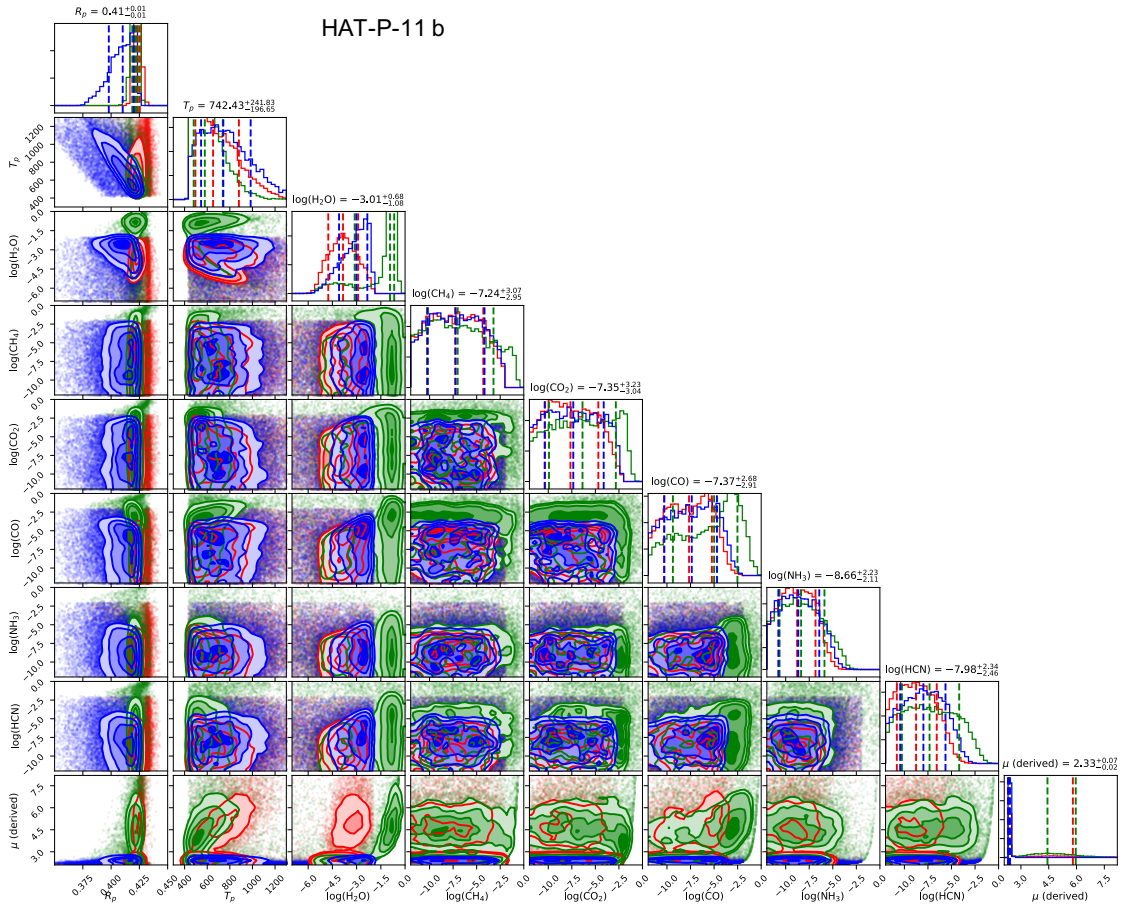

Figure 7.5: Posteriors retrieval distributions for the **1-Primary** (blue), **2-Active clear** (green) and **3-Hidden absorber** (red) for 55-Cnc e, HD 3167 c and HAT-P-11 b HST/WFC3 G141transmission spectra.

7.4.4 Estimation of the temperature in the retrieval analysis

The temperature is a complex parameter to infer from transmission spectra retrieval analysis. We use an isothermal temperature profile because we are probing a small portion of the atmosphere at the terminator region. To constrain the temperature profile, we need emission spectroscopy observations. We plot in Figure 7.6 the best-fit retrieved temperature as a function of the effective temperature for 14 planets. These planets have a strong spectral signature from which we add GJ 3470 b. When the best-fit model is the **4-Primary clear** or **5-Water World**, we indicate the retrieved temperature from the **2-Active clear** model. We also represent the range of possible temperatures probed in transit and depending on the albedo with the following formula (top panel in Figure 7.6) :

$$T(Ab) = T_{irr} \times (1 - Ab)^{1/4} \tag{7.2}$$

However, this formula might overestimate the probed temperature. If the heat redistribution is effective, then the temperature probed in transit is closer to the skin temperature. We represent the range of albedos computed with the skin temperature (bottom panel in Figure 7.6):

$$T(Ab) = 0.5^{1/4} \times T_{irr} \times (1 - Ab)^{1/4} \tag{7.3}$$

This computation is a rough evaluation of the retrieved temperature compared to the range of possible albedos. The probed temperature formula depends on the region of the atmosphere. Around 0.1 bar, close to the radiative boundary layer, 7.2 can be used. However, at lower pressure, 1 mbar to 100 mbar, the skin temperature is more accurate (7.3), closer to the probed temperature in transit. Both of these equations assume a transparent atmosphere with no thermal inversion. Warm Sub-Neptunes probably do not present thermal inversion caused by TiO or VO because the atmosphere is not hot enough. Nevertheless, they might have photochemical hazes. In the first case (Figure 7.6 top), the mean albedo is roughly 0.5, while it is around 0 with T_{skin} factor (Figure 7.6 bottom). This result is closer to what has been observed in reflected light for warm gaseous planets.

The retrieved temperature is roughly within 1-σ of the possible albedo range for each planet except HD 97658 b. This planet has an irradiation temperature of 733 K, and the best-fit retrieved temperature is above 1000 K. The absorption of HCN probably drives this result as the main spectral contributor. However, the transmission spectrum displays a large slope over the entire wavelength range, which remains challenging to interpret. Further observations of this planet with the JWST might help understand the HST's results. On the contrary, HAT-P-26 b's retrieved temperature is 500 K while its irradiation temperature is 993 K. The corresponding albedo is thus 0.9. The terminator region is colder than the rest of the atmosphere, which might explain this result. The uncertainties on the retrieved temperature are large, and we cannot constrain an albedo from this measurement. It highlights the limitations of HST observations and puts our interpretation of the retrieval analysis into perspective.

7.4.5 Metallicity and C/O ratio

The metallicity and the C/O ratio are complex parameters to infer using HST short-wavelength coverage. As we show in this section, there are highly degenerated parameters, and so retrievals remain challenging. First, we create a database of corresponding mean molecular weight and metallicity using solar elemental abundances from Lodders (2010). Then, we used the derived mean molecular weight from the retrieval results and the database to convert it into a solar metallicity. The C/O ratio is also estimated using the best-fit retrieval results as follows with n_X the abundance of specie X:

$$C/O = \frac{n_{CH_4} + n_{CO} + n_{CO_2} + n_{HCN}}{n_{H_2O} + n_{CO} + 2n_{CO_2}} \tag{7.4}$$

For both the metallicity and the C/O ratio, we give an upper and lower estimation of the value using the error bars on the given parameters from the retrieval posteriors (see Table D.1, D.2 and D.3).

In Figure 7.7 (left), we compare the estimated values for the metallicity from the best-fit retrieval results of three main models to the mass and metallicity power law using values from the solar system giants as introduced in Kreidberg et al. (2014a). This comparison is purely qualitative. The estimated metallicities do not follow the power law between the mass and the metallicity. The results from the **1-Primary** model are below what is found in the Solar System giants planet. The **3-Hidden absorber** presents similar results to the first model, especially for planets with a mass around 10 $M_{\oplus}$, while low-mass planets, mainly TRAPPIST-1 planets, have a much higher metallicity. The **2-Active clear** model presents a mass-metallicity closer to the one of the solar system for planets with a mass around 10 $M_{\oplus}$, but the uncertainties are significant, and no conclusion can be drawn. None of the best-fit results follows the trend proposed in Kreidberg et al. (2014a). This can be explained by the variety of exoplanets investigated here and how the retrieval is designed. We still note that a primary atmosphere model deviates from what is expected from Solar System giants.

We present in Figure 7.7 (right) the estimation of the C/O regarding the reduced semi-major axis. We restricted the range of the C/O ratio below 3 for clarity. The C/O ratio is poorly constrained because of the short HST wavelength coverage. The abundances of the molecules used to compute the ratio are not all constrained in this part of the spectrum. When the main absorber is found, and the value is retrieved, it will directly impact the C/O ratio and drag it towards either very high or very low values. This is the case for 55-Cnc e and all the models tested. The elevated and constrained abundance of HCN (around 0.01 in VMR) in the atmosphere of 55 Cnc e, compared to O-bearing species, results in an estimation of the C/O ratio above 10^3.

The metallicity and the C/O ratio are not constrained well enough using HST/WFC3 to analyse trends in the atmosphere of Super-Earth and Sub-Neptune.

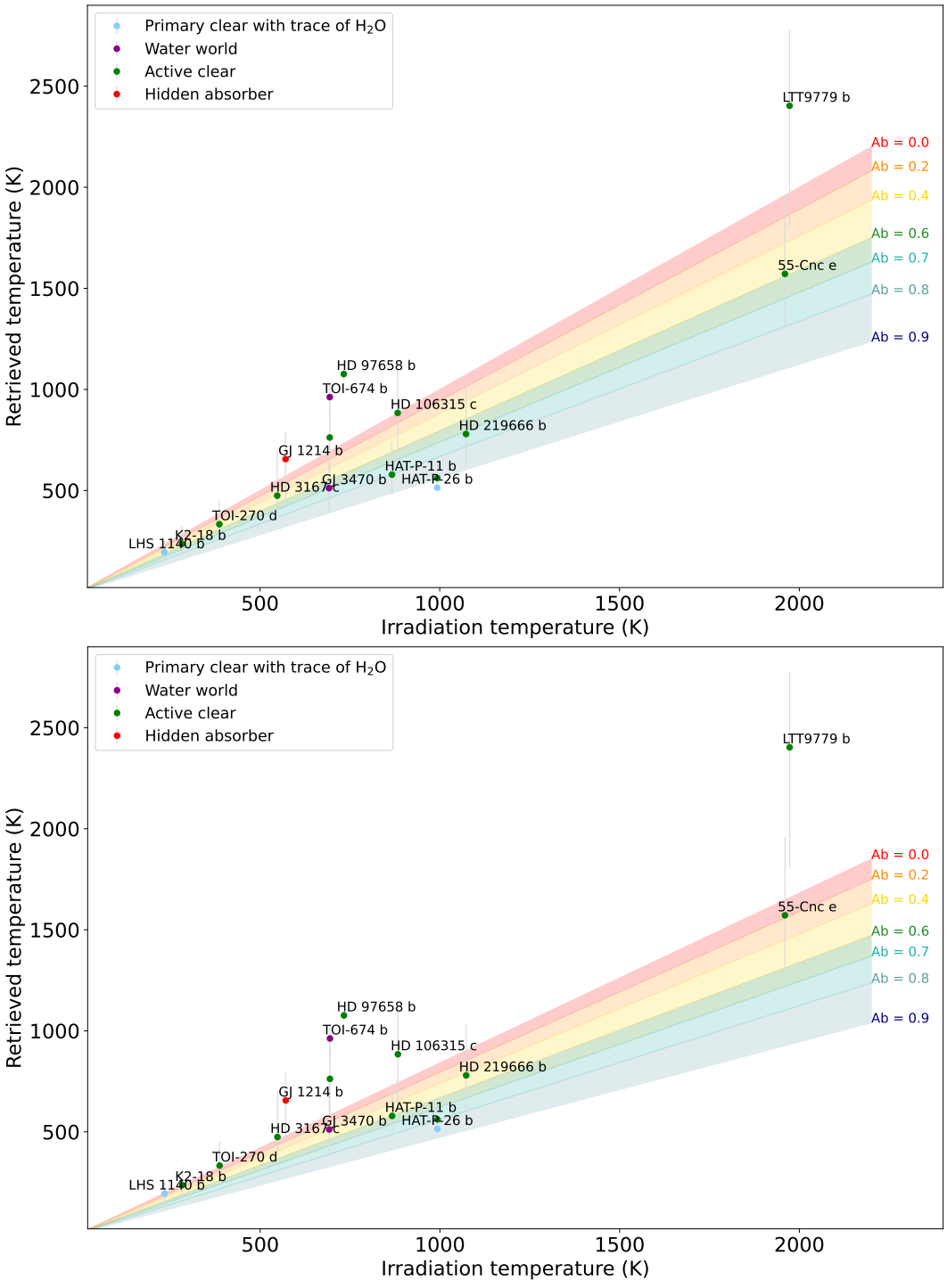

Figure 7.6: Best-fit retrieved temperature as a function of the effective temperature and range of possible temperatures with respect to the albedo. The probed temperature is computed using two formulas $T_{\rm irr} \times (1 - {\rm Ab})^{1/4}$ as a first estimation (top) and then the skin temperature $T_{\rm skin} = 0.5^{1/4} \times T_{\rm irr} \times (1 - {\rm Ab})^{1/4}$ (bottom).

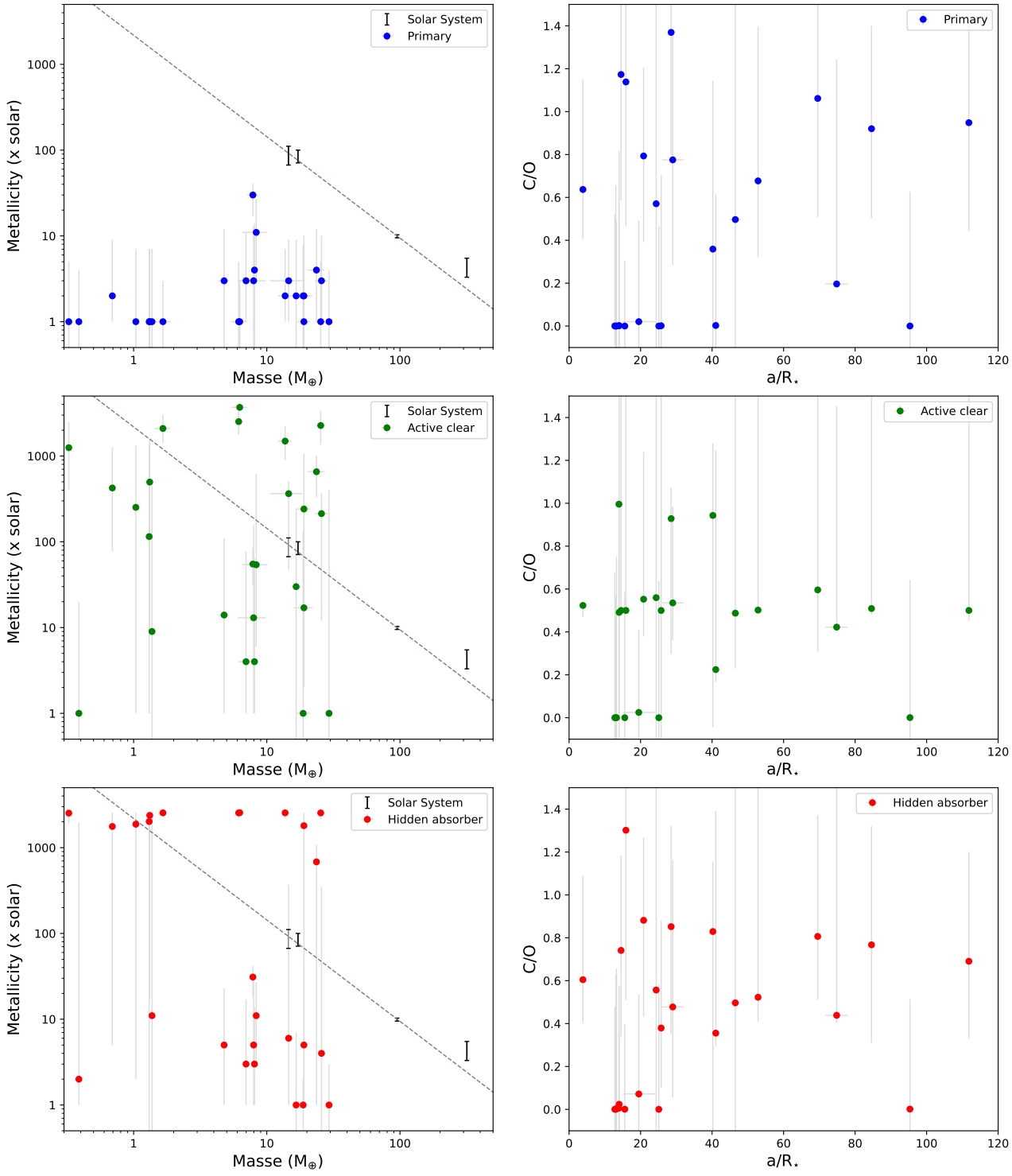

Figure 7.7: Mass and metallicity power law using Solar System giants values from Kreidberg et al. (2014a) and estimation of the metallicity from the best-fit results of the three main retrieval analyses (left). Inferred C/O ratio regarding the reduced semi-major axis (right). We restricted the range of the C/O ratio below 3 for clarity.

7.5 Conclusion

Sub-Neptunes, exoplanets with a size between Earth and Neptune (1-4$R_\oplus$), are the most common type of planets in our Galaxy. Despite their ubiquitous nature, they have no equivalent in our solar system and remain challenging to characterise today. Their distribution (or occurrence rate) forms a bimodal distribution, with a noticeable gap in the number of planets around 1.7$R_\oplus$, suggesting that dominant planetary formation or evolution processes shape the nature of this population. Planets with a radius below 1.7$R_\oplus$ are believed to be primarily rocky and are often referred to as Super-Earths, while planets above this radius threshold are most likely gaseous and commonly named Sub-Neptunes. In this work, we have used the available near-infrared data from the Hubble Space Telescope and collected 26 transmission spectra of planets smaller than 6$R_\oplus$. We investigated this transition region between rocky and gaseous planets by analysing this data with the Bayesian Retrieval Framework, TauREx-3.0. We have tested six atmospheric retrieval scenarios, assuming various primary to secondary atmospheres, and compared the results of those retrievals via the Bayesian Evidence. With this analysis, we confirmed, with high confidence (3σ), the detection of an atmosphere for 13 planets with a radius larger than 1.7$R_\oplus$, the limit set to distinguish between rocky and gaseous planets. The retrieval analysis converges toward a clear primary atmosphere for four planets: 55-Cnc e, HAT-P-26 b, LHS 1140 b and LTT 9779 b. We provided the first summary of molecular detections for Super-Earth and Sub-Neptunes using HST/WFC3 G141. We performed an ablation study on molecular opacities and confirmed the detection of at least one molecule in 11 planets. We detected water vapour with high confidence for nine planets. HCN is strongly detected in the atmosphere of 55-Cnc e and HD 97658 b, for which we can add NH_3. A re-analysis of GJ 1214 b's transmission spectrum highlighted the need for a hidden absorber to explain the observed features. However, once a molecule is detected, the abundance is poorly constrained, leading to degeneracies in molecular abundances and grey clouds' top pressure. Among 13 transmission spectra showing strong features, we concluded that eight of them have a degenerate solution. The fit requires either grey clouds to cut the molecular features or heavy elements to adjust the size of the observed atmospheric features.

This chapter ends the observational part on Sub-Neptune and Super-Earth atmospheres. Observing small planet atmospheres with HST is challenging. Although these observations give us valuable initial information about their atmosphere, the limits of interpretation are quickly reached. Our study has revealed numerous degeneracies in the Bayesian analysis of the transmission spectra. The last part of this thesis is an attempt to break them, first by comparing the observations to self-consistent simulations and then by proposing observational strategies with the JWST and ARIEL. We will focus on two aspects directly linked to the observational survey results: the impact of cloud coverage on the transmission spectrum and the nature of carbon and oxygen-bearing species in Sub-Neptune atmospheres.

Part IV

Modelling and observability predictions for Sub-Neptune atmospheres

Chapter 8

Modelling Sub-Neptune atmospheres with a radiative-convective model

Contents

8.1 Introduction

This chapter presents 1D/2D simulations of warm Sub-Neptune atmospheres and deals with two aspects directly linked to the conclusion of the observations led in the previous chapters. First, we have found the absence of methane detection but carbon dioxide in the analysis of our observations. Thus we examine the presence and nature of carbon-bearing species in Sub-Neptune atmospheres. We study the competition of H_2O-CO-CH_4 in Sub-Neptune atmospheres and determine the main spectral contributor in the NIR wavelength range. Secondly, we investigate the impact of radiatively active clouds on the transmission spectrum of warm Sub-Neptune. The first section of this chapter presents the grid of models we used to investigate Sub-Neptune atmospheres. Then we discuss the chemical compositions of these planets and the nature of carbon-bearing species. The fourth section of this chapter is based on the simulation part of the publication **Exploring the transition from Super-Earth to Sub-Neptune with a Hubble transmission survey (Gressier et al. submitted)**. We constrain the nature of clouds and sedimentation parameters and study the 2D effects of cloud formation. The last

section is based on the accepted CHEOPS proposal, for which I am the PI **The cloudiness of three warm sub-Neptunes**. We highlight the contribution of optical observations in differentiating clear from cloudy atmospheres. We presented the observations and the retrieval analysis of 26 transmission spectra in Chapter 7, and we compare, in this chapter, the observations with a grid of models developed using `Exo-REM`.

8.2 `Exo-REM` models grid

We used `Exo-REM` (Exoplanet Radiative-convective Equilibrium Model) (Baudino et al., 2015; Charnay et al., 2018; Blain et al., 2021) to create a grid of transmission spectra for Sub-Neptune atmospheres. `Exo-REM` is a 1D self-consistent radiative-convective code for exoplanet and brown dwarf atmospheres. The grid is based on HD 3167 c planetary and stellar parameters and has two main dimensions: temperature and metallicity. The atmosphere is modelled using 80 layers between 10^{-2} and 10^{7} Pa. We vary the stellar irradiation to scan an equilibrium temperature range from 200 to 1200 K, and we scan metallicity values from 1 × solar to 1000 × solar. Metallicity is the factor by which all the elemental abundances except H are multiplied compared to their solar abundances. The solar abundances are from Lodders (2010). The elemental abundances are calculated using the metallicity value. We fixed the Eddy diffusion coefficient to 10^{8} cm^2/s^{-1}. We include 13 absorbing species in a hydrogen-rich atmosphere, allowing for out-of-equilibrium chemistry. `Exo-REM` includes disequilibrium chemistry processes for CH_4–CO, CO–CO_2 , N_2–NH_3–HCN reactions systems based on Zahnle & Marley (2014) formalism. The quenching level is determined by comparing the reaction timescale to the mixing time H^2/K_{zz}, where H is the atmospheric scale height and K_{zz} the Eddy diffusion coefficient. The abundance of the species is governed by the thermochemical equilibrium below the quenching level, where the temperature and pressure are high enough so that the kinetics dominates. In contrast, above this level, the mixing ratios of the quenched species are held constant (Blain et al., 2021). We fixed the internal temperature to 70 K, and this parameter controls the position of the convective layer. Below the convective layer, the atmosphere is opaque, and the stellar irradiance does not reach these layers making internal heating the dominant process to heat the atmosphere. The position of the convective layers affects the species abundances in the upper layers if the quenching effect level is at a pressure below the region where stellar irradiance dominates.

We created transmission spectra from 1.1 to 1.7µm in the case of a clear and cloudy atmosphere. We account for the radiative effects of clouds using self-consistent condensation computations of KCl and Na_2S, with a full cloud cover and a sedimentation efficiency (fsed) of 0.5 and 2, as expected for this type of planet and as observed in the Solar System (Charnay et al., 2018; Morley et al., 2015). The sedimentation parameter represents the relative velocity scale between the cloud particle sedimentation and the atmospheric convection. It is a ratio of sedimentation and convection rates. This parameter controls the vertical extent of the clouds and determines how efficiently the particles can settle out of the cloud. A low efficiency, fsed below 1, represents extended clouds made of small particles. On the contrary, a higher efficiency, fsed above 1, corresponds to vertically compressed clouds with large particles (Ackerman & Marley, 2001; Gao et al., 2018). We included KCl and Na_2S radiative clouds separately and simulated two sedimentation efficiency (fsed=0.5 and 2). We computed the 1.4 µm feature amplitude for each simulated transmission spectrum and constructed a metallicity, temperature and amplitude database.

8.3 Carbon-bearing species in Sub-Neptune atmospheres

We use the grid described above to study the competition of H_2O-CO-CH_4 in the atmosphere of Sub-Neptunes and determine the main spectral contributor in the NIR spectral wavelength band. We study the impact of temperature and metallicity on the atmospheric composition and the transmission spectrum in the case of a clear atmosphere. We represent a fraction of this model grid in Figures 8.1 and 8.2. We show the abundance profiles of the chemical components and the corresponding opacity contributions in the 1.1 to 1.7 µm wavelength range for 1 and 300× solar composition and an equilibrium (irradiation) temperature of 300, 500, 800, and 1000 K. The simulations for the metallicity 10, 100 and 1000 × solar are in Appendix E.1 E.2 and E.3. We focus on H_2O, CH_4, CO, and CO_2 species represented respectively in blue, grey, red and brown for the abundances profiles and the spectral contributions. The total transmission spectrum is the thin black line, and the y-axis scale is set for a given metallicity for clarity. H_2O and CO compete for the oxygen component, while CH_4 and CO compete to be the main carbon-bearing species and determine the oxidation level of the atmosphere. CO and H_2O react to form CO_2. Out-of-equilibrium reactions are allowed, driven by the vertical transport, and computed with the quenching level. We will jointly explore the two dimensions of the grid: the impact of the metallicity and the temperature on the composition and the transmission spectrum.

8.3.1 Joint impact of the metallicity and the temperature

Global trends

The amplitude of the spectrum decreases with the metallicity. Two processes compete when the metallicity increases. First, trace gases abundance increases which increase the spectrum's amplitude. The molecular features are increased because the impact of pressure broadening and CIA in spectral windows is reduced. However, heavy elements abundance increases as well, which increases the mean molecular mass of the atmosphere and decreases the spectrum's amplitude. The first effect is dominant for atmospheric composition between 1 and 10 × solar because heavy species constitute only 1% of the total composition. In contrast, the second effect dominates for heavier atmospheric composition, above 10 × solar. This effect was previously observed in Moses et al. (2013, 2021); Blain et al. (2021). We illustrate in Figure 8.3 (left) the competition of these two effects using the grid of models for a 500 K equilibrium temperature and five atmospheric compositions. The spectrum's amplitude of the 10 × solar simulation is more significant than the 1 × solar composition. The amplitude of the water feature will be further discussed and quantified below.

The main carbon-bearing species changes with increasing metallicity and temperature. CH_4 is more abundant than CO at low temperatures and low metallicities, while CO becomes prominent in warm and heavy atmospheres. The temperature at which the switchover occurs decreases as the metallicity increases. CH_4 is more abundant than CO until 800 K for a 1 × solar atmospheric composition, then decreases to 300 K for a 1000 × solar atmospheric composition. CO_2 is never the main carbon-bearing species, but its abundance increases with increasing metallicity and temperature.

Bézard et al. (2022) showed that methane should be the main contributor to the absorption features in the NIR spectrum for Sub-Neptunes with temperatures below 600 K, even though water might be more abundant. We find similar results and refine the transition temperature by metallicity. H_2O and CH_4 are the main spectral contributors in the NIR wavelength range. The temperature for which we see the opacity change decreases with increasing metallicity. For a 1 × solar atmospheric composition, CH_4 dominates the spectrum until 800 K, while it dominates only until 400 K at 1000 × solar. Even though H_2O is the most abundant species, CH_4 remains the main contributor even for a warm (500 K) Sub-Neptune with a 300 × solar atmospheric composition. CO and CO_2 do not have strong spectral features in this part of the wavelength range and thus do not contribute strongly

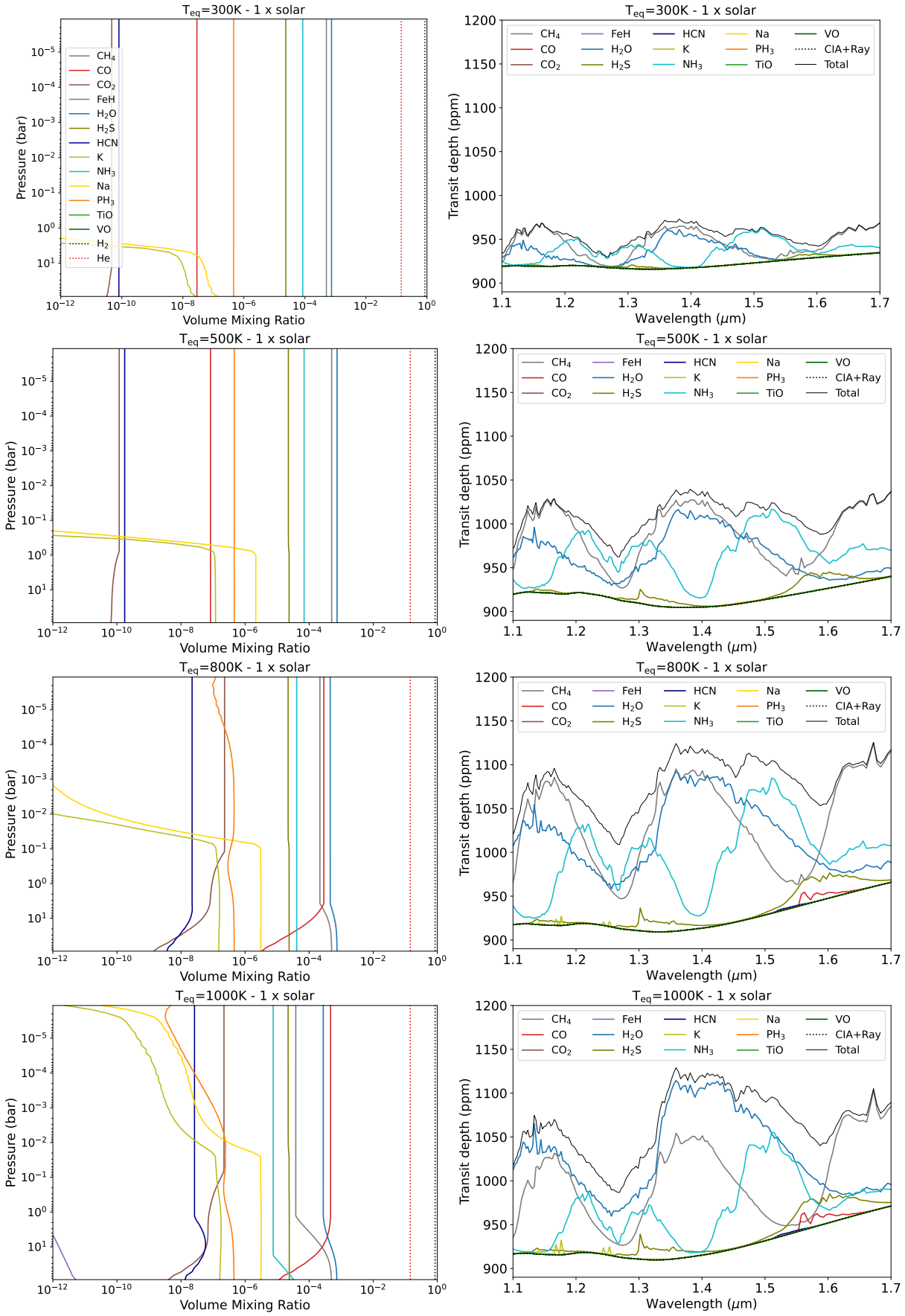

Figure 8.1: Volume mixing ratios and NIR spectral opacity contributions for a 1 × solar atmospheric composition at 300, 500, 800 and 1000 K.

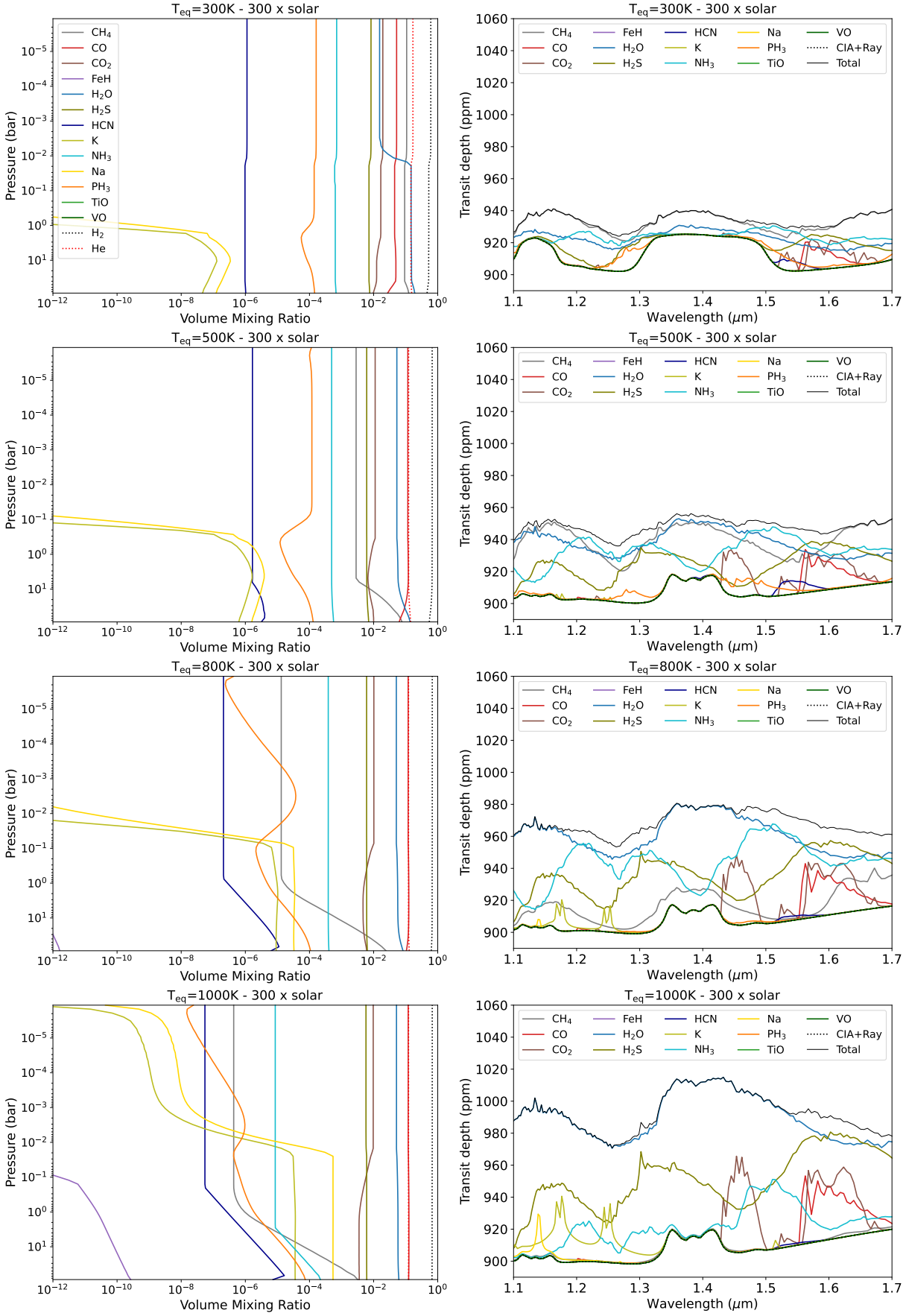

Figure 8.2: Volume mixing ratios and NIR spectral opacity contributions for a 300 × solar atmospheric composition at 300, 500, 800 and 1000 K.

to the total transmission spectrum. However, CO and CO_2 have stronger absorption lines around 2.5 µm and 4.5 µm. These species are/ will be easily detected using the NIRSpec instrument of the JWST. We present in Figure 8.3 (right) the spectral opacity contributions for a 300 × solar atmospheric composition at 800 K from 0.6 to 5 µm spanning roughly the wavelength range of NIRISS and NIRSpec combined. H_2O dominates the transmission spectrum spectrally, especially at low wavelengths, but CO and CO_2 display strong and recognisable atmospheric spectral features at 2, 2.5, 2.8 and 4.5 µm.

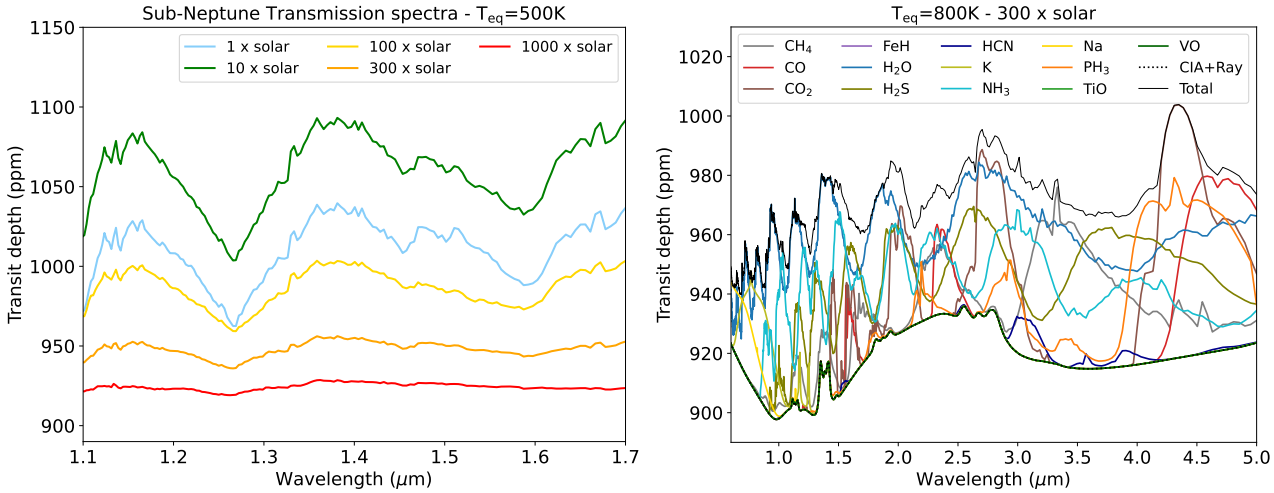

Figure 8.3: Impact of the metallicity on the spectrum's amplitude in the HST WFC3 spectral range (1.1 to 1.7 µm) (left) and spectral opacity contributions in the JWST NIRISS and NIRSpec combined wavelength range (0.6 to 5 µm) for a Sub-Neptune at 800 K with a 300 × solar atmospheric composition (right).

The metallicity also has an impact on the saturation pressure level of H_2O. For metallicities above 100 × solar at 300 K, (top left panel in Figures 8.2, E.2, E.3) the abundance of H_2O decreases above 10^{-2} bar as the temperature-pressure profile crosses the condensation curve of H_2O. Clouds form in the atmosphere with increasing metallicities because the partial pressure of H_2O increases, and the condensation profile is shifting towards higher temperatures (Blain et al., 2021).

We detail below our findings, categorised by atmospheric metallicity.

1 × solar atmospheric composition

We first study the case of solar atmospheric composition and focus on Figure 8.1. A 1 × solar atmospheric composition corresponds to an atmosphere with a mean molecular weight of 2.3 g/mol and is dominated by hydrogen and helium. Until 800 K, the most abundant species are H_2O, CH_4 with a VMR of roughly 10^{-3} while CO and CO_2 are below 10^{-7}. The abundance profiles are constant with altitude. Even though H_2O is the most abundant species, CH_4 is the main spectral contributor and shapes the total NIR transmission spectrum. At 800 K, CO is more abundant than CH_4 above 10 bar, while H_2O remains the most abundant species. H_2O and CH_4 contributions shape the total transmission spectrum, and the 1.4 µm spectral features of these two species overlap. At 1000 K, CO is now the most abundant trace gas, and H_2O is the main spectral contributor between 1.1 and 1.7 µm. However, CH_4 still spectrally contributes to the transmission spectrum where H_2O does not absorb. It has a strong spectral feature at 1.65 µm. CO_2 abundance remains below 10−6. We note that above 800 K, the trace gases' abundance profiles are no longer constant with altitudes.

10 × solar atmospheric composition

The 10 × solar atmospheric simulations are in Appendix Figure E.1. The results are similar to the 1 × solar scenario, but the mean molecular weight is now equal to 2.5 g/mol and the abundance of the main

trace gases, H_2O and CH_4, reach 10^{-2}. CO is globally more abundant than at 1 × solar, even at low temperatures (around 10^{-5} at 300 K), while CO_2 remains below 10^{-6}. The profiles are constant at low temperatures, but CO becomes more abundant than CH_4 at 800 K (10^{-2} and 10^{-4} respectively). CO VMR profile decreases with decreasing altitude below 10 bar while CH_4's increases. CH_4 is the main spectral contributor in the NIR below 700K, while H_2O dominates for higher temperatures. At 800 K, the CH_4 spectral feature at 1.65 µm is not as strong as in the 1 × solar atmospheric composition. NH_3 contributes around 1.55 µm. At 1000 K, the transmission spectrum is fully dominated by H_2O.

100 × solar atmospheric composition

The 100 × solar atmospheric simulations are consistent with a mean molecular weight atmosphere of around 3.3 g/mol. The results are in Appendix Figure E.2. H_2O and CH_4 are again the most abundant species at 300 and 500 K. The VMR increases compared to the previous composition, reaching 10−1.5. CO abundance decreases from the simulation at 300 to 500 K before increasing again at 800 K, where it becomes the prominent species. At 300 K, H_2O saturation is reached at 10^{-2} bar, and the abundance profile decreases slightly above this limit. CO_2 abundance reaches 10^{-3} above 800 K. CH_4 is the main spectral contributor in the NIR below 600 K, while H_2O dominates for higher temperatures. At 800 K, the total transmission spectrum is also shaped by the absorption of NH_3 at 1.55 µm, while at 1000 K, it follows the H_2O spectral features.

300 × solar atmospheric composition

An atmosphere of 300 × solar is often used to represent a Sub-Neptune atmosphere. It is still dominated by hydrogen, but volatile abundance reaches 10% of the total atmospheric composition, and the mean molecular weight is around 5.3 g/mol. H_2O saturation is clearly seen at 300 K, where H_2O profile abundance decreases from 10^{-1} to 10^{-2} at 10^{-2} bar. CH_4 is thus the most abundant species, followed by CO with an abundance of around 10^{-1} and $10^{-1.3}$. CO_2 abundance reaches $10^{-1.8}$ and is roughly constant at this metallicity. CO becomes the prominent species at 500K, and CH_4 VMR decreases to $10^{-2.5}$. CH_4 abundance globally decreases with increasing temperature. However, CH_4 abundance decreases with increasing altitudes below 1 bar, where the quenching level is reached, and the abundance is fixed above. CH_4 is the dominant spectral opacity only at 300K. At 500K, the 1.4 µm feature of H_2O and CH_4 overlap. H_2O dominates the spectrum above 500K with an input of NH_3 at 1.5 µm, especially at 800K. CO and CO_2 spectral features at 1.45 and 1.65 µm start to be more significant, but H_2O contributes the most. H_2S is also present spectrally around 1.6 µm.

1000 × solar atmospheric composition

Last, we simulated a 1000 × solar atmospheric composition. At this metallicity, the atmosphere's mean molecular weight is around 12.3 g/mol, and the most abundant species, CO, at all temperatures, reaches a VMR of 0.3. H_2 remains the dominant species with an abundance of 0.4. CH_4 is now the least abundant species among CO, CO_2 and H_2O. At 300K, we still note H_2O saturation that decreases the abundance of the molecule above 10^{-2} bar. CO abundance profiles are constant for all temperatures. H_2O is roughly constant for temperatures above 500K with an abundance of 10^{-1}. We see a similar process for CH_4 than for the 300 × solar composition. It is destroyed in the deep regions of the atmosphere until 1 bar, where the abundance is then fixed. Even though CO is the most abundant species, CH_4 still contributes the most to the transmission spectrum at 300K and is then replaced by H_2O above 400K. CO_2 spectral features at 1.45 and 1.65 µm and CO at 1.6 µm appear firmly above 500K, but H_2S wide feature from 1.5 µm to 1.7 µm overlap. The transmission spectrum's shape is driven by H_2O absorption.

8.3.2 Comparison with HST observations survey

We use the grid of simulations to compare with the atmospheric retrieval analysis of Chapter 7. This grid is based on HD 3167 system parameters. Even though it is not representative of all the Neptune-like planets studied in the survey in Chapter 7, it is a first step to confronting the results. In particular, we aim to understand if a self-consistent model explains the molecular absorption we retrieved. We focus on the planets that fit our grid parameter space, with a temperature between 200 and 1200 K, a retrieved mean molecular weight below 12 g/mol and a detected atmosphere (e.g. ten planets). We compare in Table 8.1 the best fit atmospheric results from Chapter 7 with the model grid described above. We indicate the retrieved temperature, the inferred mean molecular weight, the observed spectral contributor and the chosen simulation (metallicity, temperature) with the expected spectral contributor in the NIR. The uncertainty on the retrieved parameter is considerable, making the result consistent with several simulations of the model grid. Thus, we chose to show a comparison with one simulation but discuss below the uncertainty. However, as the temperature is poorly constrained, we perform a similar comparison using the fixed irradiation temperature from Table 7.2 in Chapter 7. The results from this comparison are in Appendix Table E.1.

Table 8.1: Best-fit retrieval results comparison with self-consistent computations grid. The best-fit results are from the survey atmospheric retrieval analysis with `Tau-REx 3` (see Chapter 7).

	Retrieval analysis			Model grid		
Planet	Spectral contributors	μ (g/mol)	T_P (K)	metallicity (x solar)	T (K)	Expected
HAT-P-11 b	H_2O	$4.4^{+1.5}_{-2.0}$	579^{+160}_{-99}	300	600	H_2O
HAT-P-26 b	H_2O	$2.3^{+0.1}_{-0.1}$	705^{+212}_{-136}	1	700	CH_4
HD 3167 c	H_2O, CO_2	$2.8^{+5.6}_{-0.3}$	475^{+230}_{-98}	10	500	CH_4
HD 97658 b	H_2O, CO_2, HCN, NH_3	$2.9^{+0.3}_{-0.2}$	1076^{+17}_{-32}	10	1100	H_2O
HD 106315 c	H_2O, NH_3	$5.9^{+1.5}_{-3.1}$	884^{+215}_{-288}	300	900	H_2O
HD 219666 b	H_2O	$2.6^{+2.1}_{-0.3}$	752^{+288}_{-247}	10	800	H_2O, NH_3
K2-18 b	H_2O	$2.4^{+1.4}_{-0.1}$	236^{+90}_{-62}	10	200	CH_4, NH_3
LHS 1140 b	H_2O	$2.3^{+0.1}_{-0.1}$	194^{+55}_{-48}	1	200	CH_4, NH_3
TOI-270 d	H_2O, CO_2	$2.4^{+1.0}_{-0.1}$	333^{+120}_{-78}	10	300	CH_4, NH_3
TOI-674 b	H_2O, NH_3	$8.8^{+3.5}_{-3.3}$	762^{+165}_{-180}	1000	800	H_2O

The lack of apparent methane detection

The first striking result is the absence of methane detection in Sub-Neptune atmospheres. This molecule is predicted to be the main spectral contributor using the observational results and the model grid for five planets over ten but is never retrieved as so. H_2O is constantly retrieved as the main opacity with inputs of CO_2 for HD 3167 c and TOI-270 d. From HAT-P-26 b's retrieval results, we found a solar atmospheric composition with a strong H_2O feature in a clear atmosphere. The grid predicts CH_4 absorption at 700K. However, the retrieved temperature is also consistent with higher values, and the irradiation one reaches 993K. For a solar composition, 1000K H_2O is the main spectral contributor with inputs of CH_4 at 1.65 µm, which is consistent with the retrieval analysis.

HD 3167 c retrieval results suggest a 10 × solar atmospheric composition with a temperature around 500K and opacity contributions from H_2O and CO_2. For these parameters, CH_4 is predicted in the NIR transmission spectrum, with an abundance of 10^{-2}, while CO_2 VMR is below 10^{-5} with no spectral features expected. The observations are thus not consistent with the models that include out-of-equilibrium chemistry. Considering the upper bound on the error bars of both the temperature and the mean molecular weight, we obtain 705K and 8.4 g/mol. Using a simulation from the grid at 700K with a 300 × solar atmosphere, H_2O is the main opacity contributor at 1.4 µm, and NH_3 contributes at 1.5 µm. CO_2 features appear at 1.45 and 1.6 µm, but not as strongly as H_2O and NH_3. However, its

expected abundance reaches 10^{-2} in VMR, compatible with our retrieval analysis ($10^{-2.85}$). We can easily explain the discovery of H_2O in the atmosphere of HD 3167 c while increasing the temperature and weight slightly, but the carbon dioxide's detection is more challenging to interpret. However, it is not entirely unrealistic for a 300 × to a 500 × atmospheric composition with a temperature around 700K. For the temperature and the mean molecular weight retrieved in the NIR transmission

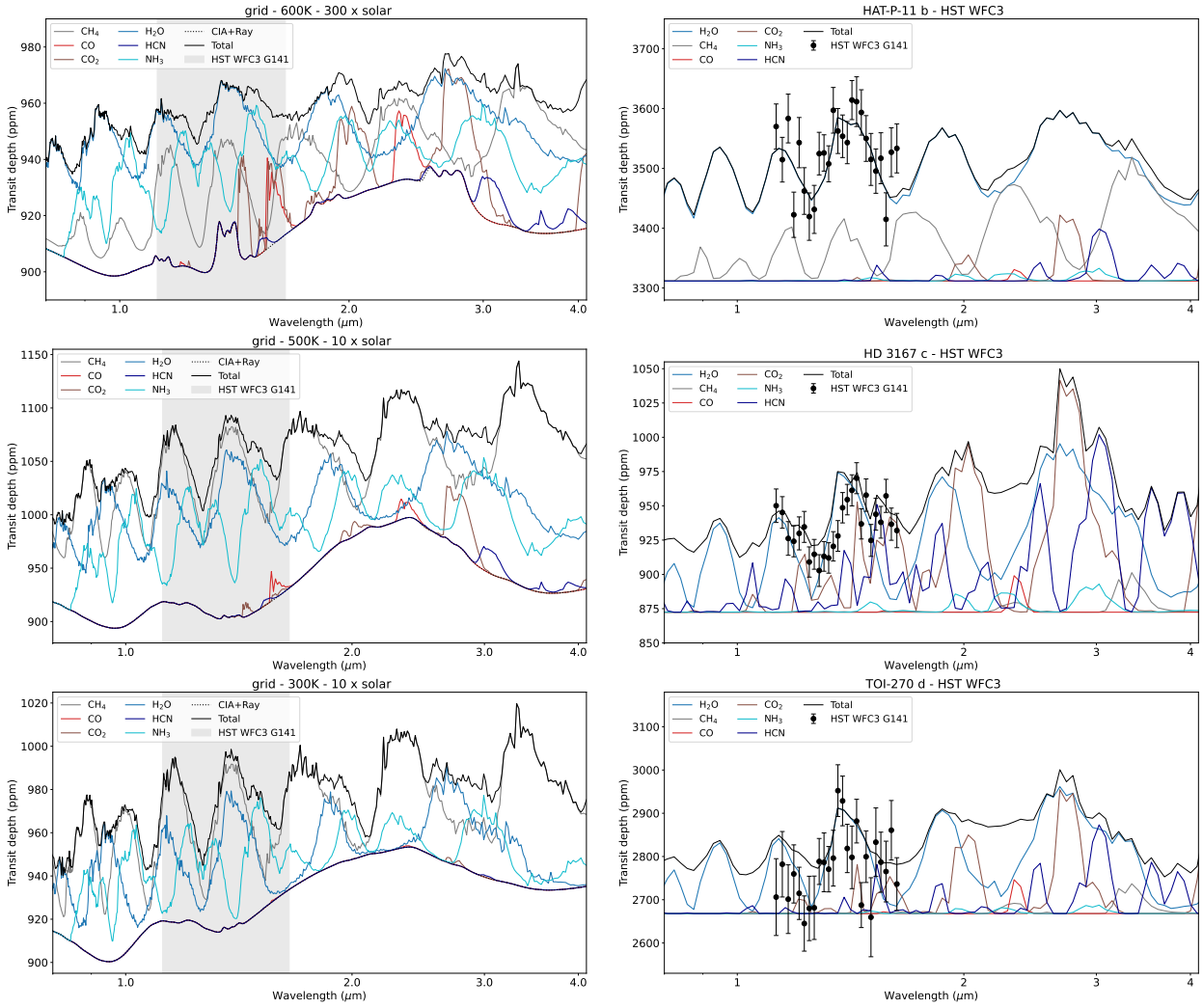

Figure 8.4: HAT-P-11 b (top), HD 3167 c (middle) and TOI-270 d (bottom) best-fit retrieval results (right) comparison with self-consistent computations grid (left). We represent in shaded area the HST WFC3 G141 wavelength range in the simulations and in thin black line the total transmission spectrum.

spectrum of HD 97658 b, we should expect H_2O to completely dominate the transmission spectrum with a strong feature around 1.4 µm. We do not observe this feature in the HST NIR transmission spectrum. It presents a slope over the entire wavelength range and suggests the presence of HCN, CO_2, NH_3 and H_2O. If we use a simulation with a temperature of 700K, close to the irradiation one (733K), we find contributions of H_2O, NH_3 and CH_4. We never find hints of HCN or CO_2 even while increasing the atmospheric composition to 100 × solar. The carbon-bearing species at this metallicity and temperature should be CH_4. We can explain the presence of H_2O and NH_3, but something is missing either in the retrieval analysis (stellar activity) or in the model grid to explain the HCN and CO_2 absorption.

The lack of methane is surprising for planets with temperatures between 200 and 400K, K2-18 b, LHS-1140 b and TOI-270 d. The retrieval analysis for these three planets suggests that H_2O is responsible for the transit depth's increase at 1.4 µm. We could constrain the mean molecular weight between

1 and 100 × solar composition for the three analyses, suggesting a light atmosphere and even cloudless for LHS-1140 b. We scan the grid from 1 to 100 × solar and from 200 to 400K. Even though H_2O is present and even more abundant than CH_4 in most cases, it is never the main spectral contributor. CH_4 absorbs at 1.15, 1.4 and 1.65 µm more strongly and shape the transmission with three "bumps". NH_3 contributes at 1.5 µm. However, LHS-1140 b has a radius and a mass of $1.73R_\oplus$ and $1.98M_\oplus$ compatible with 7.5 g/cm^{-3} density. It is located on the Earth-like rocky line in the diagram mass-radius of Figure 7.1 in Chapter 7. Even though its transmission spectrum suggests a hydrogen-dominated clear atmosphere, the surface is not considered in the model grid. Besides, its density is much higher than the one of K2-18 b and TOI-270 d (i.e 3.3 and 2.7 g/cm^{-3} respectively) located near the pure H_2O line (see Figure 7.1 in Chapter 7). The formation of the planet and the amount of initial carbon might explain the deviation from the modelling grid.

Figure 8.4 compares for HAT-P-11 b, HD 3167 c and TOI-270 d the retrieval best-fit opacity contributions and the predictions from the grid. We represent in a grey-shaded area the HST WFC3 G141 wavelength range. We extend the best-fit retrieval models from 0.8 to 4 µm to highlight where the retrieval models and simulations deviate the most. For HAT-P-11 b, the retrieved water features at 1.4 µm are consistent with the simulation at 600 K and 300 × solar. The difference occurs at longer wavelengths with the apparition of CO and CO_2 features in the simulation, obviously not predicted in the retrieval analysis. TOI-270 d and HD 3167 c retrieval analyses and predictions are inconsistent. Methane is supposed to dominate both atmospheres spectrally. However, the retrieval analysis found hints of CO_2 and HCN, whose spectral features become prominent around 3 µm. This illustration shows the ambiguity due to the HST's short wavelength coverage. In Chapter 9, we explore the advantages of increasing the wavelength range using JWST and ARIEL simulations in discriminating atmospheric scenarios.

Observations and model consistency

Four HST transmission spectra are consistent with the prediction of the modelling grid. This is the case for Neptune-like planets with a warm atmosphere (above 700 K). HAT-P-11 b's transmission spectrum displays a strong H_2O feature well explained and predicted by the model grid at 300 × solar and 600 K (see top panel in Figure 8.4). However, the retrieved quantities, temperature, and mean molecular weight are not well constrained, and the uncertainties span different simulations. The results are consistent with a metallicity from a 10 to a 300 × solar composition and a temperature of 500 to 700 K. Increasing the metallicity and the temperature reinforces the result and confirms that H_2O is predicted as the main detectable species. However, for a 10 × and a 100 × solar atmospheric compositions at 500 K, CH_4 dominates the NIR spectrum. If we use simulations at 900 K, close to the irradiation temperature (867K), H_2O is always the main spectral contributor. H_2O has been detected in this planet by several studies (Fraine et al., 2014; Tsiaras et al., 2018) and considering the strong detection, and we might use the model grid to constrain the atmosphere. For H_2O to dominate the NIR transmission spectrum, the temperature must be over 600 K, whatever the metallicity; or the metallicity must be above 300 × solar for a temperature of at least 500 K.

HD 106315 c transmission spectrum analysis suggest H_2O and NH_3 absorption in a 5.9 g/mol cloudy atmosphere. The amount of H_2O retrieved is 0.22 (VMR) and NH_3 is 10^{-6}. The retrieved temperature is close to the irradiation one, 884 and 883, respectively. However, the uncertainties are large, and the retrieval results span the simulations 100 × to 300 × and 600 to 1100 K. H_2O is always predicted as the main spectral contributor. NH_3 contributes for a 100 × solar composition until 900 K and 800 K for a 300 × solar composition. The observations are consistent with the modelling grid.

HD 219666 b transmission spectrum is consistent with a 10 × solar atmospheric composition with trace of H_2O (10^{-3} VMR) and clouds. The temperature retrieved is lower than the irradiation one, 752 and 1073 K, respectively. The uncertainties on the retrieved parameters make the result compatible

with a 1 to 100 × solar composition and 500 to 1000 K. Thus, H_2O dominates the transmission spectrum for the simulations above 800, 700 and 600 K for a metallicity of 1, 10 and 100 × solar. If we fix the temperature to 1100K, H_2O is always the main spectral contributor. There are no hints of NH_3 in the retrieval analysis, but it is predicted to absorb at 1.5 µm for the atmospheric compositions considered below 900 K. This might indicate that the planet's temperature is probably higher than the one retrieved. We note that the presence of a grey cloud deck might hide NH_3 spectral features.

Last, we compare the modelling grid to TOI-674 b transmission spectrum. We found that H_2O is the main spectral contributor with an abundance of 0.36, and NH_3 as a gas trace (10^{-3}). The temperature and the mean molecular weight are 762^{+165}_{-180} K and $8.8^{+3.5}_{-3.3}$ g/mol, consistent with metallicities 300 to 1000 × solar and temperatures 600 to 900 K. H_2O is always predicted as the main spectral contributor, and NH_3 contributes until 900K for a 300 × solar and 600K for a 1000 × solar composition.

Comparison with the ablation study

Blain et al. (2021) argued that the over-fitting of the observations or the omission of CH_4 in the retrieval analysis might be the reason for its non-detection. This would result in a retrieval analysis bias, not an actual atmospheric result. H_2O has been detected with other retrieval analysis code than `Tau-REX 3` in Sub-Neptune atmospheres (Fraine et al., 2014; Mikal-Evans et al., 2020; Benneke et al., 2019; Benneke et al., 2019). However, we use the analysis of the 26 transmission spectra from Chapter 7 to test if detecting H_2O is a bias of the retrieval analysis. In Chapter 7, we performed an ablation study for all the molecules detected in the Bayesian retrieval analysis. We suppressed the molecule from the fit and compared the Bayesian evidence of the two models to confirm the necessity of having the molecule as an absorber to fit the spectrum correctly. Thus, we suppressed H_2O from all the detections above. We can then compare the retrieval result obtained with and without H_2O and confront it to the model grid. We present in Table 8.2 a statistical comparison of the retrieval analysis. We indicate the Bayesian logarithm evidence and the main contributors of the different models for the planets mentioned above.

Table 8.2: Best-fit retrieval results comparison with and without H_2O. The results are from the survey atmospheric retrieval analysis with `Tau-REx 3` (see Chapter 7).

	Best-fit model		Model without H_2O			
Planet	Spectral contributors	log(E)	Spectral contributors	μ (g/mol)	T_P (K)	log(E)
HAT-P-11 b	H_2O	208.2	CH_4, NH_3	$5.8^{+1.9}_{-1.4}$	633^{+224}_{-127}	203.8
HAT-P-26 b	H_2O	195.9	CH_4, NH_3	$2.3^{+0.1}_{-0.1}$	512^{+28}_{-12}	161.1
HD 3167 c	H_2O, CO_2	237.0	CH_4, NH_3, CO_2, HCN	$9.3^{+3.4}_{-4.5}$	673^{+100}_{-206}	233.9
HD 97658 b	H_2O, CO_2, HCN, NH_3	185.9	CO_2, HCN, NH_3	$3.9^{+0.5}_{-0.4}$	1073^{+20}_{-37}	180.0
HD 106315 c	H_2O, NH_3	227.5	CH_4, NH_3	$4.1^{+10.1}_{-1.7}$	517^{+143}_{-54}	211.9
HD 219666 b	H_2O	197.8	CH_4, NH_3	$2.9^{+0.7}_{-0.6}$	676^{+224}_{-103}	193.3
K2-18 b	H_2O	149.8	CH_4, NH_3, CO2	$4.8^{+4.3}_{-2.4}$	234^{+103}_{-65}	148.5
LHS 1140 b	H_2O	195.3	CH_4, HCN	$2.6^{+25.2}_{-0.2}$	191^{+87}_{-48}	191.7
TOI-270 d	H_2O, CO_2	198.5	CH_4, HCN, CO_2	$4.3^{+4.7}_{-01.8}$	308^{+124}_{-72}	195.4
TOI-674 b	H_2O, NH_3	188.9	CH_4, NH_3	$5.5^{+6.5}_{-1.5}$	416^{+104}_{-45}	174.3

CH_4 and NH_3 or HCN compensate for H_2O absorption in almost every case. CH_4 is not detected in HD 97658 b atmosphere even after suppressing H_2O from the opacity line lists. However, the Bayes factor of the CH_4 rich model is always significantly lower (< 3)) than the H_2O-rich one. We illustrated this result in Table 7.5 in Chapter 7. This table summarises the molecule detections in Sub-Neptune atmospheres using the ablation methodology. There is one exception: K2-18 b's transmission spectrum. The Bayesian logarithm evidence of the CH_4-rich model is 148.5, while the evidence of the best-fit model, including H_2O, reaches 149.8. The difference is 1.3, which is not statistically significant enough to rule out CH_4 absorption instead of H_2O completely. The model grid agrees with this retrieval result apart from the CO_2 input that is not predicted and is probably an artefact. The grid never predicts

HCN and CO_2 in the configurations obtained for a CH_4-rich model. As we artificially suppressed H_2O from the model, the grid does not agree with the new result for planets with an equilibrium temperature above 600 K. However, the model grid is consistent with CH_4 and NH_3 as the main contributors for planets with a retrieved temperature around 500K and below. The non-detection of CH_4 might be due to a chemical disequilibrium stronger than expected or a low C/O ratio.

While this model grid reproduces the best-fit retrieval analysis transmission results for five planets out of ten, we note some inconsistencies between what is expected to be found in a Sub-Neptune atmosphere with what we observed. However, we used a clear atmosphere to compare the chemical composition, but clouds are present in the atmosphere of Sub-Neptune and were found in the retrieval analysis. Clouds impact the transmission spectrum, mask spectral features and could explain the degeneracies between H_2O and CH_4 detections. In the next section, we investigate the impact of clouds on Sub-Neptune NIR transmission spectra.

8.4 Impact of radiative clouds on Sub-Neptune NIR transmission spectra

Substantial efforts have been made to analyse and interpret exoplanetary atmospheres this past decade. However, while the development of forward and retrieval codes leads to atomic and molecular absorption discoveries in emission and transmission spectroscopy, clouds remain challenging to characterise and detect. Cloud formation inhabits the complexity of atmospheric dynamics, chemistry, and microphysics, which makes it difficult to account for in transit modelling. Optically thick clouds in the upper layers of the atmosphere can significantly block the spectroscopic features of gas species, while thinner clouds allow atmospheric features to be partially detected. The first detection of clouds in a Sub-Neptune atmosphere, GJ 1214 b by Kreidberg et al. (2014a) pointed out the importance of clouds in the atmosphere of this population of planets and its impact not only in the optical but also in the NIR. Our survey analysis also showed the importance of including clouds in the retrieval analysis and highlighted the need for more in-depth modelling.

We propose to investigate the impact of radiative clouds on the 1.4 µm feature using HST/WFC3 G141 observations and a radiative-convective model. To tackle this complex issue, we focus on the correlation of the feature size with the temperature and consider only KCl and Na_2S condensation to begin with. Then, we decided to extend the wavelength range. By combining HST and CHEOPS photometric observations in the optical, we propose a method to differentiate a clear from a cloudy atmosphere.

The simple parametrisation of grey clouds in the retrieval analysis is insufficient to model the complexity of clouds' condensation in the atmosphere of Super-Earth and Sub-Neptunes. However, the first step we can perform with HST data is assessing the necessity of another optically thick absorber in the model. Our observational retrieval survey, presented in Chapter 7, showed that 13 spectra in our sample are flat, and 13 spectra display features. Most of them require grey clouds to fit the molecular features accurately. We decided to investigate the cloudiness of Sub-Neptunes and Super-Earth with the temperature by measuring the 1.4 µm amplitude feature. The water band absorption amplitude around 1.4μm in HST WFC3 G141 data has already been computed to establish statistics on hot-Jupiter spectra Sing et al. (2016); Stevenson (2016); Fu et al. (2017). Gao et al. (2020) derived clouds and aerosols properties using the water band amplitude correlation with the equilibrium temperature. This study remains challenging for low-mass planets due to the lack of data and difficulty obtaining a proper spectrum. Crossfield & Kreidberg (2017) studied the water features amplitude of six warm Neptune planets and highlighted correlations with the equilibrium temperature and the mass fraction of hydrogen and helium. We showed in Chapter 6 that this correlation was not obvious anymore while adding HD 106315 c, HD 3167 c and K2-18 b data points.

8.4.1 1.4 microns feature metric

The amplitude of the spectrum in the water band absorption, A_{H_2O} is measured by taking the weighted average transit depth from 1.35μm to 1.45μm (Sing et al., 2016) and subtracting it from the weighted mean of the transit depth where the water does not absorb, between 1.22 and 1.29μm. Following Stevenson (2016); Fu et al. (2017), we divided it by $2R_P H_P/R_\star^2$ which corresponds to a factor of one scale height change in transit depth. We define the metric as follows:

$$A_{H_2O} = \frac{\bar{x}_{[1.35-1.45\mu m]} - \bar{x}_{[1.22-1.29\mu m]}}{2R_P H/R_\star^2} \tag{8.1}$$

We computed the 1.4 µm amplitude feature for all the transmission spectra. The scale height is computed assuming a 2.31 g/mol mean molecular weight for all planets. The temperature corresponds to the irradiation temperature, and the gravity is calculated with parameters from Chapter 7 Table 7.2. We present in Table 8.3 the value of the 1.4 µm features amplitudes for 26 transmission spectra using HST/WFC3 G141.

We note that this quantity estimates the size of a feature. We can not summarise the complexity of the atmosphere with only one measurement. However, it contains information on the possible absorption of vapour water and the impact of cloud sedimentation. More importantly, it allows the comparison of different planetary systems and compositions.

Table 8.3: 1.4 µm features amplitudes for 26 transmission spectra using HST/WFC3 G141.

Planet	A_{H_2O}
55 Cnc e	1.84±0.53
GJ 436 b	-0.12± 0.35
GJ 1132 b	-0.11± 0.17
GJ 1214 b	-0.03±0.04
GJ 3470 b	0.71±0.22
HAT-P-11 b	1.86±0.41
HAT-P-26 b	1.33±0.21
HD 3167 c	1.98±0.40
HD 97658 b	2.34±0.33
HD 106315 c	1.11±0.29
HD 219666 b	1.79±0.63
HIP 41378 b	3.67± 1.83[1]
K2-18 b	2.38±0.80
K2-24 b	-0.45±0.80
LHS 1140 b	3.59±1.35
LTT 9779 b	0.93±0.58
TOI-270 c	-0.15±0.38
TOI-270 d	3.19±0.78
TOI-674 b	0.93± 0.22
TRAPPIST-1 b	-1.27±1.11
TRAPPIST-1 c	-1.56±1.20
TRAPPIST-1 d	-0.48±0.52
TRAPPIST-1 e	-0.52±0.78
TRAPPIST-1 f	-0.64±1.48
TRAPPIST-1 g	0.12±1.63
TRAPPIST-1 h	-1.30±0.59

[1]There is no published mass for HIP-41378 b, the scale height used in the normalisation is computed with a mass set

8.4.2 Correlation of the 1.4 microns feature's size with temperature

In Figure 8.5, we plot the observed amplitudes for 15 planets with an equilibrium temperature between 200 and 1200K and a published mass and the simulated amplitudes. We represent in dotted lines the amplitude for a clear atmosphere and, in a shaded area, the amplitudes between two different sedimentation parameters, 0.5 and 2, for each metallicity. A sedimentation efficiency of 0.5 is the most impacting, i.e. the lowest amplitudes. We evaluate radiative clouds' impact on the water features' size around 1.4 µm.

For clear atmospheres, two processes impact the water feature amplitudes—the amplitude increases between 1 and 10 × solar metallicity except for temperatures between 600 and 1000K. For metallicities above 10 × solar, amplitudes decrease with increasing metallicities, whatever the temperature. We find the highest amplitudes passed 1000 K. KCl clouds impact most of the transmission spectrum for planets with temperatures between 600 and 900 K. Between 300 and 600 K, KCl clouds are present but do not impact the amplitude strongly. We can see a drop in amplitudes after 600 K, especially for metallicities 10 and 100 × solar. Above 1000 K, there is no KCl condensation, and we find the amplitudes at the same level as a clear atmosphere. Na_2S condensate at higher temperatures than KCl. For 1 and 10 × solar metallicity, Na_2S mask features for temperatures between 700 and 1000 K. For higher metallicities, the amplitude of the water feature is lower than the clear atmosphere level even for temperatures above 1000 K.

The uncertainties on the observed amplitudes are high, and we cannot make strong claims regarding the tested models. However, the modelling results are consistent with the retrieval analysis, and we find similar degeneracies as described in Chapter 7, Table 7.6. The amplitude of HAT-P-11 b, HD 106315 c, HD 219666 b, K2-18 b, TOI-270 c and TOI-674 b spectra are consistent with a cloudless high metallicities (above 10) atmosphere and a cloudy low metallicities (between 1 and 10) models (see Figure 8.5). We can refine the nature of clouds present in the atmosphere of Sub-Neptune regarding the temperature. According to this modelling, it seems that KCl clouds can be present in the atmosphere of HAT-P-11 b and HD 97658 b, while Na_2S is found for HD 219666 b. We note that the lowest observed amplitudes, between 500 and 800 K (i.e. TOI-270 c, GJ 436 b, GJ 1132 b, and K2-24 b), are only compatible with high metallicity (300 to 1000 × solar) cloudy atmospheres. GJ 1214 b is inconsistent with any clear and cloudy models. Something is missing in the `Exo-REM` models to fit flat spectra between 500 and 800 K. Clouds and photochemical hazes have proven hard to explain, model, and predict in the atmospheres of Sub-Neptunes. Optically thick clouds forming in the atmosphere's upper layers can significantly block the spectroscopic features of gas species, while thinner clouds allow atmospheric signatures to be partially detected. Specifically, methane photo-dissociation could also lead to the creation of photochemical hazes in the high atmosphere of Sub-Neptune and could explain low amplitudes at lower metallicities.

`Exo-REM` simulations are consistent with the retrieval analysis. KCl and Na_2S clouds can be present in the atmosphere of Sub-Neptune and Super-Earth. These simulations support the primary cloudy scenario found in the retrieval analysis for HAT-P-11 b, HD 106315 c, HD 219666 b, K2-18 b, TOI-270 d and TOI-674 b.

to $19M_\oplus$.

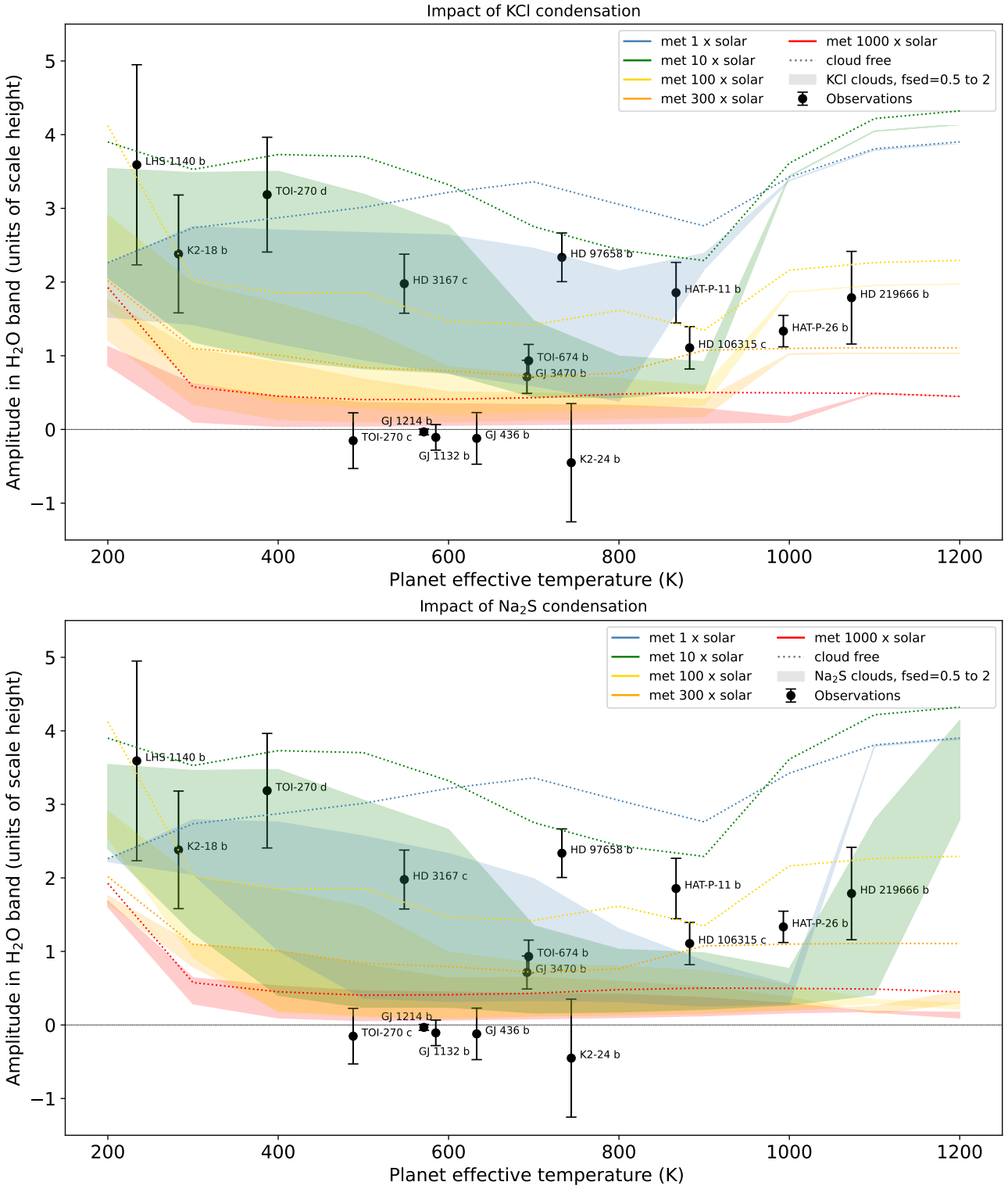

Figure 8.5: Size of the 1.4 µm features in observational (black data points) and simulated (colours) transmission spectra in the NIR wavelength range. We created transmission spectra with `Exo-REM` for clear (dotted lines) and cloudy (straight) scenarios with varying temperatures, metallicities and sedimentation efficiencies to evaluate the impact of radiative clouds on water features.

8.4.3 2D effect on clouds formation

We could not reproduce the spectral feature's amplitude for Sub-Neptune with an irradiation temperature around 600 K. This is the case particularly for GJ 1214 b, and GJ 436 b, whose transmission spectrum in the NIR is flat. We decided to investigate if 2D effects could be a critical parameter in shaping the transmission. We established that photochemical hazes, not included in `Exo-REM` could be the culprit, but the temperature variation from one limb to another could also impact the chemistry and the condensation of various species. Planet studied here are close-in Sub-Neptune around M-dwarf and probably tidally-locked. Clouds could form on the night side and evaporate on the day side.

We present an investigation of 2D effects on cloud formation for Sub-Neptune. This work is ongoing and was not published in the survey. We used Moses et al. (2021) grid based on `2D-ATMO` circulation model described in Tremblin et al. (2017). The grid is in temperatures and metallicity and computed for GJ 436 b-like planet with a radius of $0.4 R_{Jup}$ ($4.5 R_{\oplus}$) and gravity of 1000 cm/s^2. The planet orbits around a K5 V star with a radius of $0.7 R_{\odot}$, a temperature of 4500K and a log(g) of 4.5 cgs. We combined the temperature-pressure profiles at different longitudes with the self-consistent computation of clouds from `Exo-REM` to study the 2D effect impact on the transmission spectrum. We used Moses et al. (2021) 's simulations at 500 and 700 K for 1, 10, 100 and 1000 times the solar metallicity. The four temperature-pressure profiles at longitudes 0°) (substellar point), 90°), 180°) and 270°) are used as a proxy for `Exo-REM` simulations. We fixed the Eddy diffusion coefficient to 10^{10} cm^2/s.

We present in Figure 8.6 the temperature-pressure profiles at different longitudes for an equilibrium temperature of 500 and 700 K and four atmospheric metallicities. The substellar point's temperature profile is in red (0°), the day-side limb is in green (90°) and the night-side limb in purple (270°). We over-plot the condensation curves of several components computed with `Exo-REM`. The main result is that below a pressure level of 10^{-2} bar, the temperature profiles are similar for all longitudes and thus cross the condensation curves of KCl and Na_2S similarly. The condensation of these species should happen symmetrically in both limbs. The temperature-pressure profiles differ in the upper layer of the atmosphere and start to diverge above 10^{-3} or 10^{-2} bar, depending on the metallicity. The temperature decreases with higher metallicities in the upper layers of the atmosphere. For a 500 K equilibrium temperature and metallicities above 100 × solar, the night-side's temperature pressure profile crosses the condensation curve of H_2O, NH_4Cl, NH_4SH and NH_3. At an equilibrium temperature of 700 K, the night-side's temperature profile only crosses the NH_4Cl condensation line at a 1000 × solar metallicity. This species is not radiatively active and do not impact the transmission spectrum.

Water can condense on the planet's night-side and evaporate on the day-side. Water's condensation occurs deep in the atmosphere when stellar radiation decreases and metallicity increases. The temperature decreases with less irradiation, and the partial pressure of H_2O increases with metallicity. The bond albedo should increase with condensation and high metallicity. This phenomenon could occur for a planet with an equilibrium temperature around 500K and a metallicity above 100 × solar, which corresponds roughly to a 4.2 g/mol mean molecular mass. We represent in Figure 8.7 the transmission spectrum in the NIR from the previous simulation of a Neptune-like planet with a 1000 × solar composition at 500K. The cloudy limb simulation, in purple, includes H_2O condensation with full coverage and the flat transmission spectrum. The clear limb is in green, and we can see an absorption feature around 1.4 µm attributed to H_2O. We averaged these two transmission spectra and obtained the full transmission spectrum in black. We note that the condensation of H_2O on the night side could impact the transmission spectrum. The amplitude of the water absorption band is 5.6 in units of scale height for the clear limb,-0.01 for the cloudy limb and 2.8 for the averaged spectrum. This is computed with the formalism of Section 8.4.1. We note that we kept a clear day-side, but a condensation of KCl and Na_2S could also occur. 2D effects have to be taken into account to interpret transmission spectra, however, we found that the impact of H_2O condensation is most important for high metallicity atmosphere and low temperature.

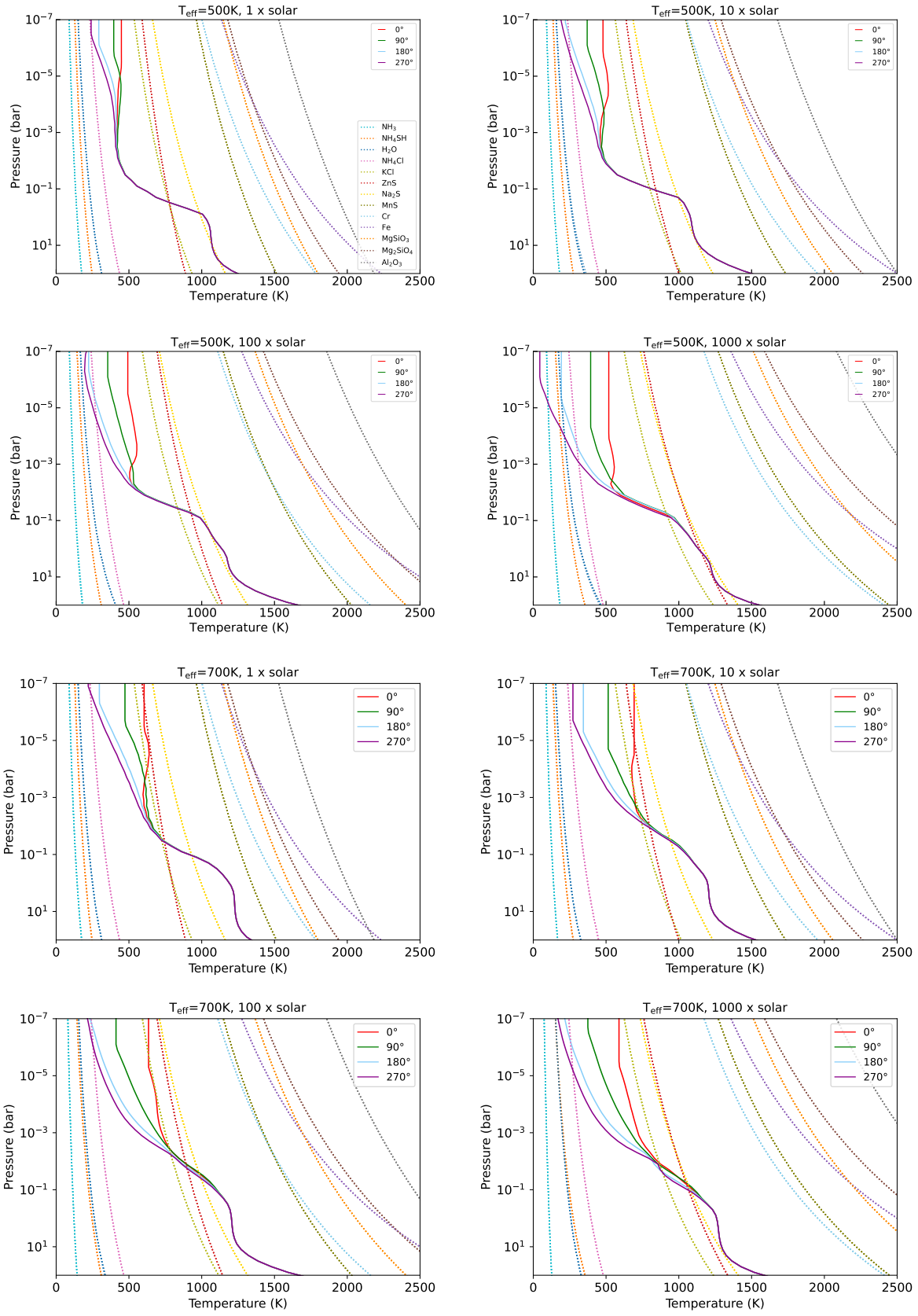

Figure 8.6: Temperature pressure profiles as a function of longitude for an equilibrium temperature of 500 and 700 k and a 1, 10, 100 and 1000 × solar compositions. The substellar point corresponds to the longitude 0° (red line), the day limb is at 90° (in green), and the night limb is at 270° (purple line). We plot the corresponding condensation curves of several components from `Exo-REM` self-consistent computations.

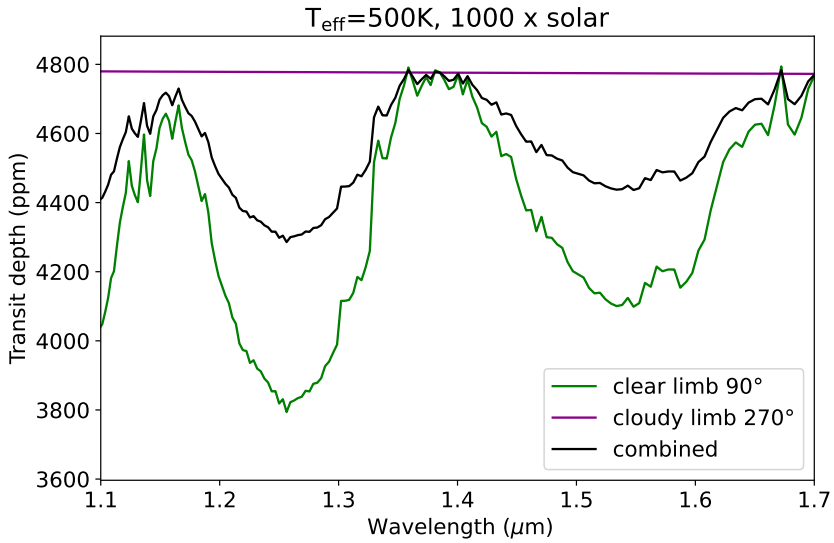

Figure 8.7: Transmission spectra in the HST WFC3 G141 band for different longitudes for a Neptune-like planet. The atmosphere is simulated using a 1000 × solar metallicity. We include H_2O clouds on the night side (purple) and remove clouds on the day side (green). The combined spectrum is in black.

8.5 The need for optical observations: synergy with CHEOPS

We initially identified three planets of interest observable with CHEOPS in the timeline of the AO-3 observations campaign: GJ 3470 b (3.88 $R_\oplus$, 13.73 $M_\oplus$, 692 K) (Biddle et al., 2014), HAT-P-26 b (6.33 $R_\oplus$, 18.75 $M_\oplus$, 957 K) (Hartman et al., 2011) and HD 219666 b (4.71 $R_\oplus$, 16.6 $M_\oplus$, 1040 K) (Esposito et al., 2019). All of them are part of our HST transmission survey (see Chapter 7 and thus are within 2-6 $R_\oplus$, and are complemented by an observation in the NIR. While there is no doubt that these planets have a light, hydrogen-dominated atmosphere, the presence of clouds or hazes in the upper atmosphere is more difficult to assess, especially in NIR (1.1-1.65 µm), and this has to be investigated with an accurate optical measurement for which CHEOPS is in an excellent position to provide. The proposal's idea was to refine the planetary transit depth in the optical. Secondly, by comparing the value found by CHEOPS in transmission to atmospheric clear and cloudy forward models, confirm or refute the presence of clouds in the atmosphere of Sub-Neptunes. We also wanted to link these observations with the previous section 8.2 and, by adding a photometric point in the optical, we could homogeneously investigate the effect of the temperature in the cloud cover of Sub-Neptunes. While we concluded in a clear atmosphere for HAT-P-26 b, KCl and Na_2S could condensate in GJ 3470 b and HD 219666 b atmospheres which makes it a perfect sample. However, only HD 219666 b was awarded time with CHEOPS by the Time Allocation Committee (TAC), as the two other planets have been previously observed in the optical with HST. The CHEOPS observation of HD 219666 b provides the first optical measurement for this planet, and with good accuracy, i.e. we estimated the noise to be ±60 ppm with three transit observations. We will then present the simulations for GJ 3470 b used in our initial proposal to make our case and unprecedented early analysis of HD 219666 b CHEOPS observations confronted to simulations.

8.5.1 GJ 3470 b predictions and modelling

Once again, we used `Exo-REM` to simulate the atmosphere of GJ 3470 b. The atmosphere is described using 80 layers between 10^{-3} and 10^7 Pa. We included 13 absorbing species in a hydrogen-rich atmosphere, allowing for out-of-equilibrium chemistry. We fixed the atmospheric metallicity to 1 × solar and the Eddy Diffusion coefficient to 10^8 cm^2/s. We will explore higher metallicity atmospheres for

HD 219666 b in section 8.5.2.

We present in Figure 8.8 the temperature-pressure profile of the planet along with the condensation curves to predict the condensates that could be found in this type of atmosphere. We can find KCl, ZnS and Na_2S for GJ 3470 b and expect similar results in the atmospheres of other Sub-Neptune planets that fall in the 500-1500 K temperature range. We illustrate in Figure 8.9 the impact of the radiative clouds in the transmission spectrum using GJ 3470 b's simulation and two different atmospheric models: a clear atmosphere and a cloudy one. Clouds radiative effects were accounted for using self-consistent condensation computations of KCl with a full cloud cover and a sedimentation efficiency (fsed) of 0.5,1 and 2, as expected for this type of planet observed in the Solar System (Morley et al., 2015; Charnay et al., 2018). The sedimentation parameter represents the relative velocity scale between the cloud particle sedimentation and the atmospheric convection. It is described in the section above 8.2. We also represent in grey the region probed by HST in the NIR.

Our simulations show a shift towards higher transit depths between the clear and cloudy scenarios at short wavelengths. We expect this effect to be even more critical while considering hazes or Na_2S condensations. To ensure that we could measure this effect, we computed the average transit depth in the CHEOPS bandpass (0.33 to 1.1 µm) for the different scenarios. We obtain an average transit depth of 6650 ppm for the clear atmosphere, 6772, 7037 and 7263 ppm for the cloudy atmosphere, with respectively 2,1 and 0.5 sedimentation efficiency. The differences in transit depth are over 120 ppm, which means that we can distinguish between the models with CHEOPS accuracy, ±60ppm, even for the most constraining models, i.e. fsed=2 with 2 σ, and with more than 5 σ for the other models.

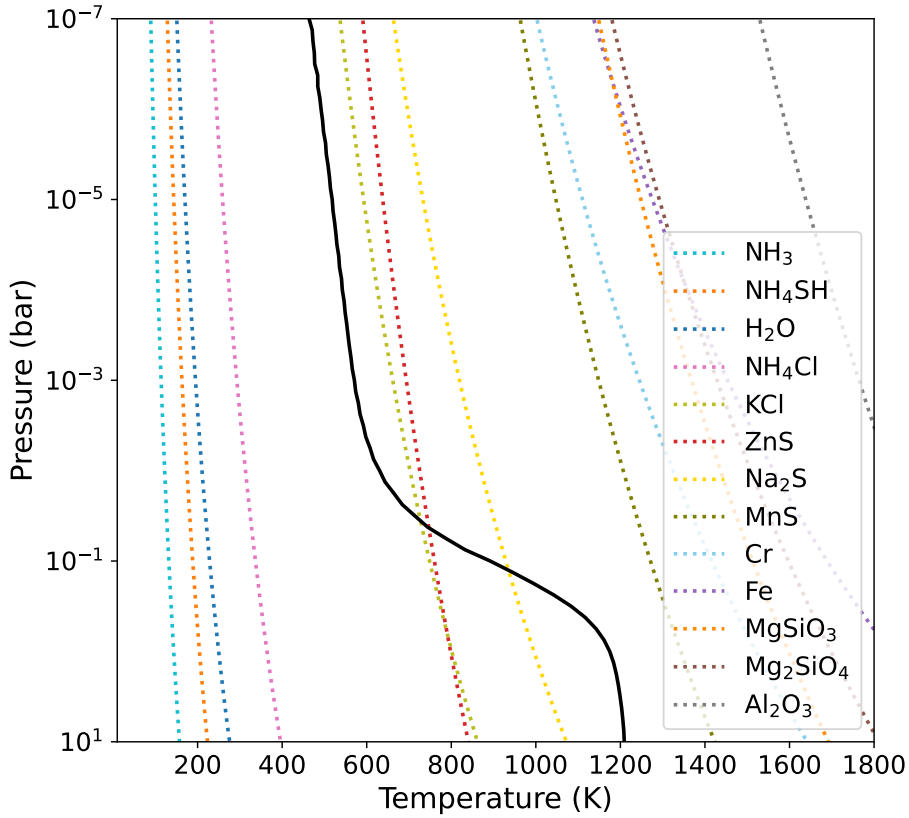

Figure 8.8: Simulated temperature-pressure profiles for GJ 3470 b (solid black lines) and condensation profiles (dotted lines) using `Exo-REM`. GJ 3470 b's atmosphere is computed for a 1 × solar metallicity composition.

By comparing this measure to the HST observations in the NIR, we could also assess the cloudiness of the atmosphere in a second way. It is more challenging to distinguish models using only HST observations in the NIR (see the grey area in Figure 8.9), and this is why we need a CHEOPS measurement

in the optical. However, we can see clearly that atmospheric features are muted and that the overall spectrum is flatter while including clouds. The difference in transit depth between CHEOPS bandpass and the value at 1.4 µm, where H_2O is expected to absorb, is large in the case of a clear atmosphere (over 600 ppm) and becomes ten times smaller when including KCl clouds high in the atmosphere. The difference will be easily measured and compared using CHEOPS measurement. We have simulated the case for GJ 3470 b as it is the smallest and coldest planet in our initial sample of three planets. We expect the difference to be more pronounced with other planets with the increasing scale height of the atmosphere. However, we must remember that combining different instruments is subject to errors as it is complicated to ensure consistency among measurements. Consequently, JWST and ARIEL might be more suited to investigate this issue. Besides, the simulations have been made for a 1 × solar metallicity, but it is more than likely that the Sub-Neptune atmospheres have a more elevated atmospheric metallicity. Thus, the atmospheric features' amplitude is smaller, making it more difficult to distinguish among models.

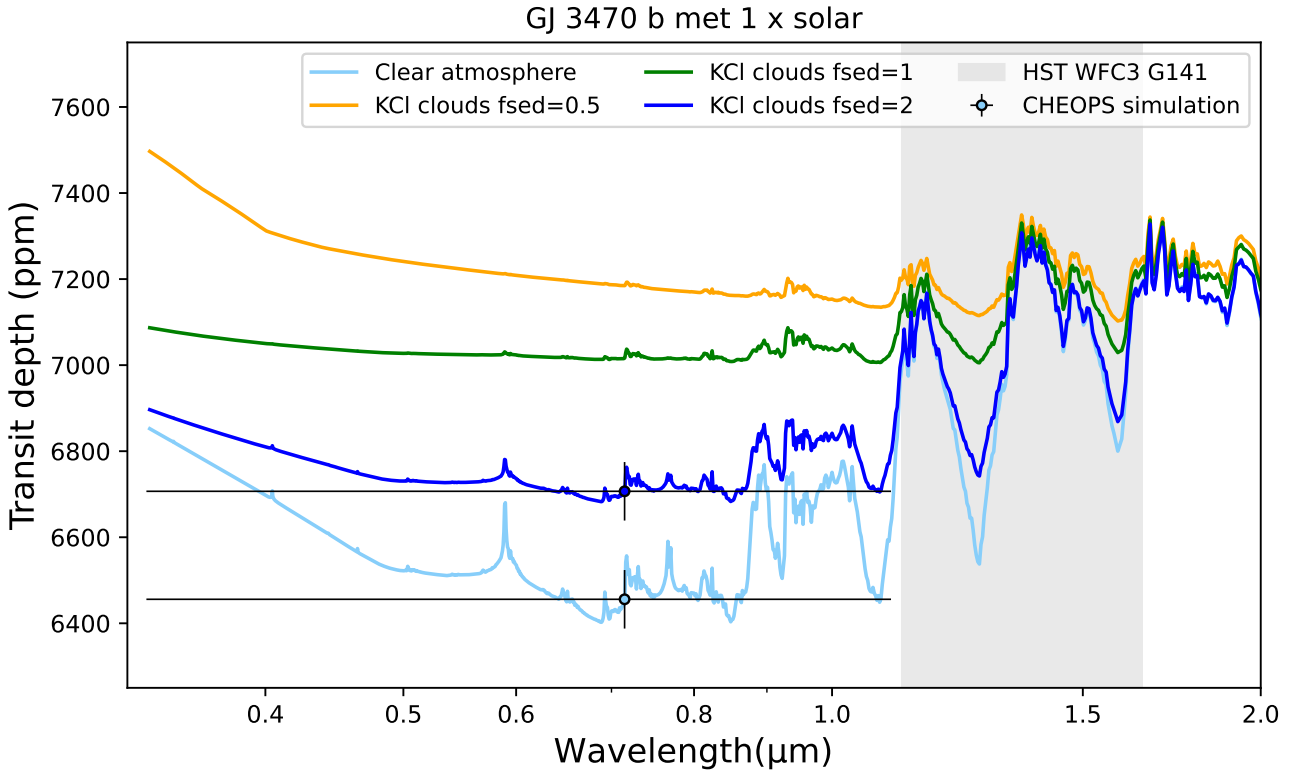

Figure 8.9: Impact of radiative clouds in the transmission spectrum of GJ 3470 b for a 1 × solar metallicity atmosphere. We include KCl clouds with three different sedimentation parameters and highlight the region probed by HST WFC3 G141 in grey. Simulations are from `Exo-REM`.

8.5.2 HD 219666 b observations and modelling

CHEOPS light curve analysis

CHEOPS observed HD 219666 b during the writing of the manuscript, and we present an early analysis of the three observations on this planet. The data are automatically analysed with the CHEOPS data reduction pipeline (DRP), and the raw data processing follows the below steps. The pipeline calibrates the raw images, considering bias and gain corrections, linearisation, dark currents, event flagging and flat field corrections. Then the raw images are corrected from environmental effects such as depointing, smearing trails and background light and finally, the DRP performs aperture photometry to extract

the target flux. The time variable contamination in the photometric aperture due to the CHEOPS Point Spread Function (PSF) shape and nearby background stars is accounted for by the DRP using GAIA DR2 Catalog to simulate CHEOPS images of the field of view. We check for systematics by looking at correlations with instrumental and environmental parameters: background, PSF centroid position on the CCD, dark current, and cosmic rays. HD 219666 b is not part of multiple planetary systems and contamination from outer planetary transits should be avoided. The data files are directly accessed using the CHEOPS archive. We use `pycheops` (Maxted et al., 2021) a dedicated, open-access python package developed to analyse CHEOPS light curves efficiently. This software reduces and corrects the planetary light curves accounting for systematics such as ramp and smearing effects. We perform an individual light curve fitting of each visit following the process described in (Maxted et al., 2021). A Monte-Carlo Markov Chain (MCMC) method is employed and implemented in the emcee package(Foreman-Mackey et al., 2013). We chose the `OPTIMAL` aperture from the DRP report for each light curve. We set the model with the latest published stellar, planetary parameters and ephemerides and the limb-darkening coefficients are described with a quadratic law as implemented in `pycheops`.

The information on the three CHEOPS observations is in Table 8.4. We indicate the start of each observation, the duration of the observation, the exposure time, the number of frames (data points), and the optimal radius aperture. We fit the light curves using `pycheops` software based on the `qpower2` algorithm (Maxted & Gill, 2019). They use a power 2 law for the modelling of the limb-darkening coefficients $I_\lambda(\mu)$=1-c(1-μ^α), where μ is the cosine of the angle between the surface normal and the line of sight. The parameters of the transit model used in `pycheops` are described below with a the orbital semi-major axis and i the orbital inclination:

- T_0: mid-transit time (fitted parameter)
- P: orbital period (fixed to the value of Patel & Espinoza (2022) 6.0357970± 0.0003070)
- b=acos(i)/$R_\star$: impact parameter for a circular orbit (fitted parameter)
- D=$(R_P/R_\star)^2$= k^2: transit depth (fitted parameter)
- W=$(R_\star/a)\sqrt{((1+k^2)-b^2)}/\pi$: transit width in phase units for a circular orbit (fitted parameter)
- f_c=$\sqrt{e}\cos\omega$: with e and ω the eccentricity and the periastron (fixed to 0: circular orbit)
- f_s=$\sqrt{e}\sin\omega$: (fixed to 0: circular orbit)
- h_1=$I_\lambda(1/2)$=1-c(1-$2^{-\alpha}$) (fitted parameter)
- h_2=$I_\lambda(1/2)$ - $I_\lambda(0)$=c$2^{-\alpha}$ (derived parameter)

We used (Patel & Espinoza, 2022) parameters to initialise the transit model parameters and set the orbital period to 6.0357970± 0.0003070. This update on HD 219666 b was not available at the start of our HST transmission survey in Chapter 7, which uses Esposito et al. (2019) parameters. We summarise the result of the individual light curve fitting in Table 8.4 and over-plot the three transit light curves in Figure 8.10. The raw and corrected light curves are plotted individually in Appendix F.1 and F.2. The posterior distributions from the Gaussian process analysis of `pycheops` are in Appendix F.3, F.4 and F.5. Observation 3 is more affected by systematics than the two other visits. We obtained a larger transit depth of 1902.42±124.47 ppm, which is consistent within 1-σ with the first observations' result 1788.47±79.52 ppm but not with the second observation 1708.11±78.64 ppm. The transit width is larger for Observation 2 and not consistent with values found for Observations 1 and 3. Observation 2 covers part of the transit ingress and none of the egress, whereas Observations 1 and 3 cover both the ingress and egress. However, we combined the observations to obtain an averaged transit depth of **1773.80±51.01 ppm** and use this value for the rest of the analysis. We reached an uncertainty better than we expected ($\sim$ 60ppm), which can be compared to the HST transmission spectrum. Using all three observations, we can revise the planet's orbital period to **6.0345422±0.00011** and the inclination

Table 8.4: HD 219666 b CHEOPS observations information

Observations	G Mag	Start date (UTC)	Duration (s)	T_{exp} (s)	N_{frames}	Radius aperture (pixel)
1	9.65	2022-08-03 21:35	10.55	1× 60	380	30.5
2		2022-09-03 00:46	10.94	1× 60	411	31
3		2022-09-27 04:04	11.41	1× 60	402	35.5

Table 8.5: Summary of the individual light curve fitting. The decorrelation parameters of the initial fit are time, t; spacecraft roll angle (ϕ), PSF centroid position (x,y); smear position, smear; and image background level, bg.

Observations	1	2	3
Input parameters			
$T_{\rm eff}$ (K)	5539±18		
log g (cgs)	4.32±0.04		
[Fe/H]	0.06±0.01		
P (days)	6.0357970± 0.0003070		
e	0		
Model parameters			
T_0 ($\rm BJD_{TDB}$) -245900	795.57881722±0.00046702	825.75673853±0.00088703	849.88965584±0.00053802
D (ppm)	1788.47±79.52	1708.11±78.64	1902.42±124.47
W(phase unit)	0.015126±0.00027	0.01770 ±0.00048	0.015065±0.00029
b	0.86±0.02	0.80±0.03	0.87±0.02
h_1	0.7196±0.0096	0.7184±0.0101	0.7188±0.0104
h_2	0.446	0.446	0.446
Decorrelation parameter	y, bg, smear	y, bg, $\cos\phi$	t, x, bg, $\cos\phi$, $\cos^2\phi$, $\sin\phi$, $\sin^2\phi$, $\sin^3\phi$
Derived parameter			
$R_{\rm P}$ ($\rm R_\oplus$)	5.87±0.43	5.93 ± 0.46	6.09±0.48
$R_{\rm P}/R_\star$	0.04223± 0.00098	0.04133± 0.00102	0.04362±0.00131
$log(\rho_\star/\rho_\odot)$	-0.154±0.079	-0.201±0.098	-0.163±0.091
$g_{\rm P}$ ($\rm m/s^2$)	19.1±3.3	18.8±3.3	17.8±3.2
$\rho_{\rm P}$ ($\rm g/cm^3$)	1.82±0.44	1.77±0.44	1.64±0.41
$a/R_\star$	12.39±0.76	11.96±0.88	12.31±0.86
i (deg)	86.02±0.09	86.16±0.18	85.96±0.10

to **86.01±0.06**°. A more in-depth analysis of the derived parameter linked to a joint-simultaneous fit of the three light curves is planned. It will allow us to refine the stellar and planetary system parameters. We first wanted to show that CHEOPS observations can also be used to characterise the atmosphere of exoplanets and, in synergy with HST and JWST observations, constrain the cloudiness of Sub-Neptune. This point is explored in the next subsection.

Comparison with self-consistent modelling

Similarly to the Section 8.5.1, we simulate the atmosphere of HD 219666 b using `Exo-REM`, with 80 layers between 10^{-3} and 10^7 Pa. We used Table 8.5 stellar and planetary parameters from Table 8.5. We included 13 absorbing species in a hydrogen-rich atmosphere, allowing for out-of-equilibrium chemistry. HD 219666 b is warmer than GJ 3470 b, thus KCl condensation do not occur (see Figure 8.11). The cloudy atmospheric configuration includes Na_2S condensations with sedimentation parameters 0.5, 1 and 2. We vary the atmospheric metallicity to 1, 10, 100, and 300 × solar. We aim to distinguish a clear from a cloudy atmosphere by adding the optical observation from CHEOPS to the HST transmission spectrum in the NIR and constraining the atmospheric metallicity. We note that combining

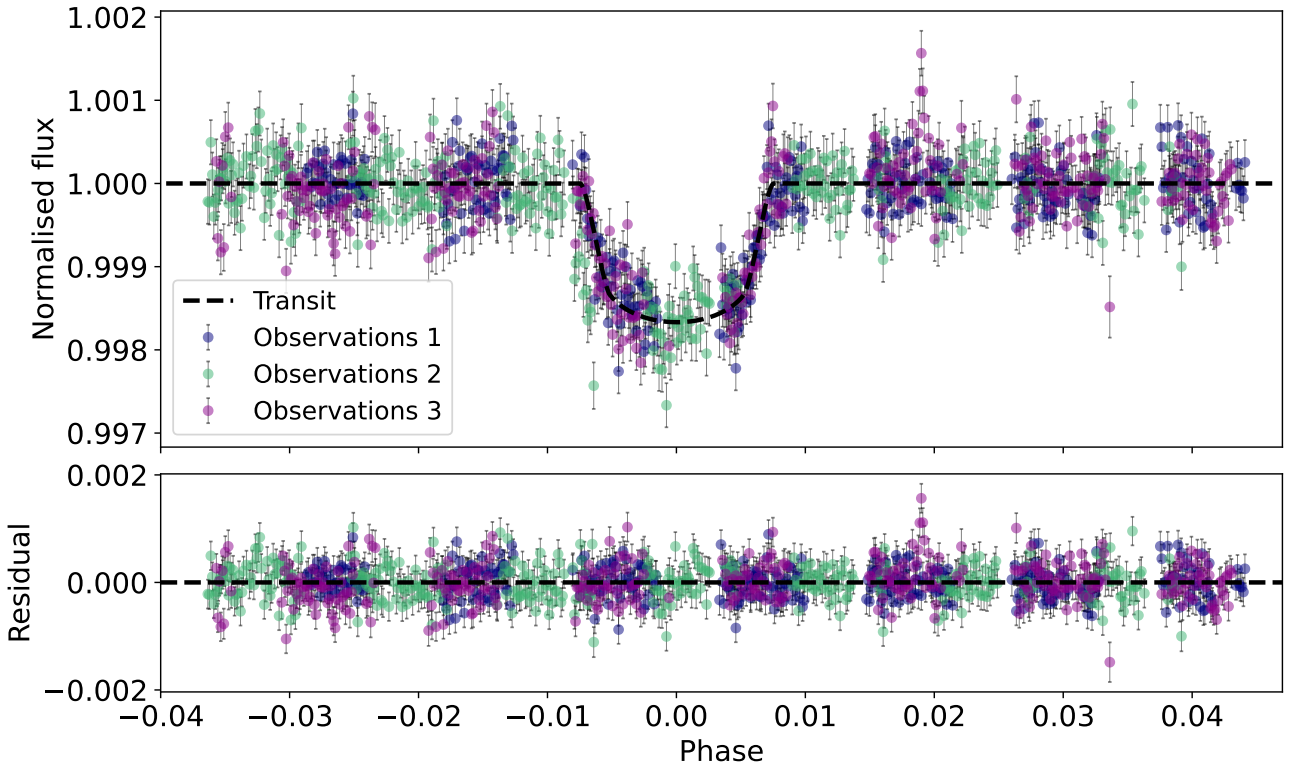

Figure 8.10: CHEOPS phase-folded transit light curves of HD 219666 b. The corrected light curves are in the upper panel: blue for Observation 1, green for Observation 2 and purple for Observation 3. We over-plot the transit model (black dotted line) from `pycheops`. We plot the residual from the best-fit models in the lower panel.

photometric and spectroscopic measurements can lead to an inaccurate interpretation of transit depth variations. However, the value found with CHEOPS is compatible with HST measurements, and no offset is required (see Figure 8.12).

First, we compare clear atmospheric scenarios for different metallicity with the 0.3-1.7 µm transmission spectrum in Figure 8.12. Using only HST observations with a 60 to 70 ppm precision seems difficult to distinguish among clear atmospheric scenarios for different metallicities. If we focus only on the CHEOPS data point, we restrict the possible atmospheric between 1 and 100 × solar. We include Na_2S condensation clouds with fixed sedimentation efficiency: 0.5, 1 and 2. The impact of Na_2S condensation on the simulated transmission spectra for 1, 10 and 100 × solar is presented in Figure 8.13 along with CHEOPS and HST transit depths. A similar figure, including ZnS condensation, is in Appendix F.6. We can rule out a cloudy atmosphere with more than 4-σ and 2-σ for a 1 and a 10 × solar configuration. For the 100 × solar composition, we can rule out with 1-σ the most impacting cloudy scenarios but not Na_2S condensation with a sedimentation parameter of 2. This ambiguity could also translate to partial cloud coverage. We compute the Chi-squared (χ^2) between the combined transmission spectrum with the simulated transmission spectra, and the best fit is the 100× solar with χ^2 = 31.2 (see Appendix F.1 for a full table of χ^2 computation). We note that ZnS condensation impacts most of the transmission spectrum at short wavelengths, and these variations can not be accounted for with CHEOPS's large band photometric point (see Appendix F.6). Combining the information brought by CHEOPS in the optical with the shape of the transmission spectrum in the NIR helps us break a part of the degeneracies highlighted in Chapter 7. We can use CHEOPS's single photometric measurement to refine planetary parameters and characterise the atmosphere. HD 219666 b has probably a cloud-free light atmosphere (below 100 × solar). This method will have to be tested on a larger scale and be confronted with other optical measurements.

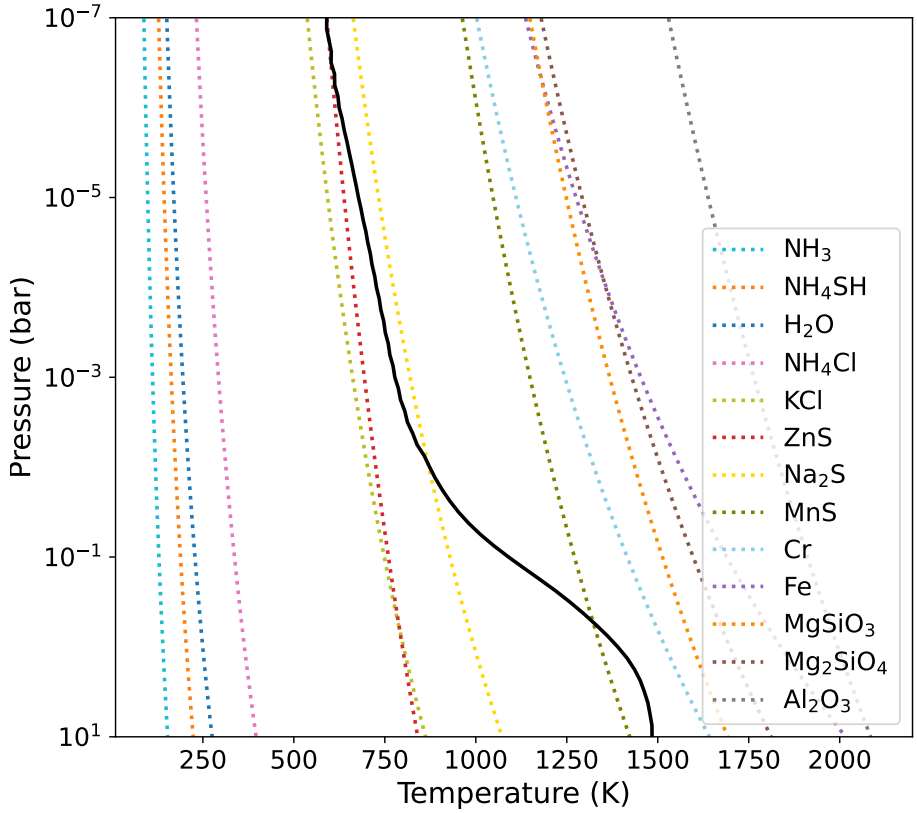

Figure 8.11: Simulated temperature-pressure profiles for HD 219666 b (solid black lines) and condensation profiles (dotted lines) using `Exo-REM`. HD 219666 b's atmosphere is computed for a 1 × solar metallicity composition.

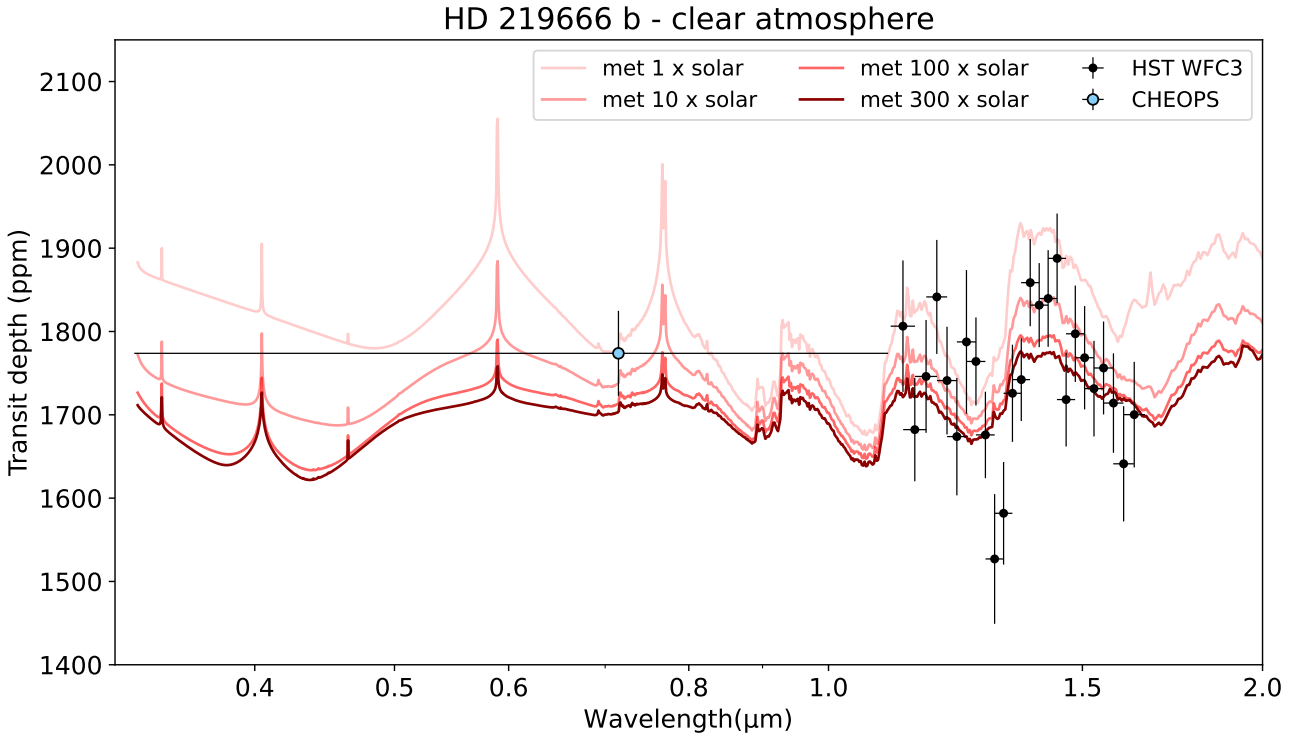

Figure 8.12: CHEOPS (blue) and HST (black data points) transit observations of HD 219666 b and simulated transmission spectra for a clear atmosphere. The simulations are from `Exo-REM` self-consistent computations for 1, 10, 100, and 300 × solar atmospheric composition.

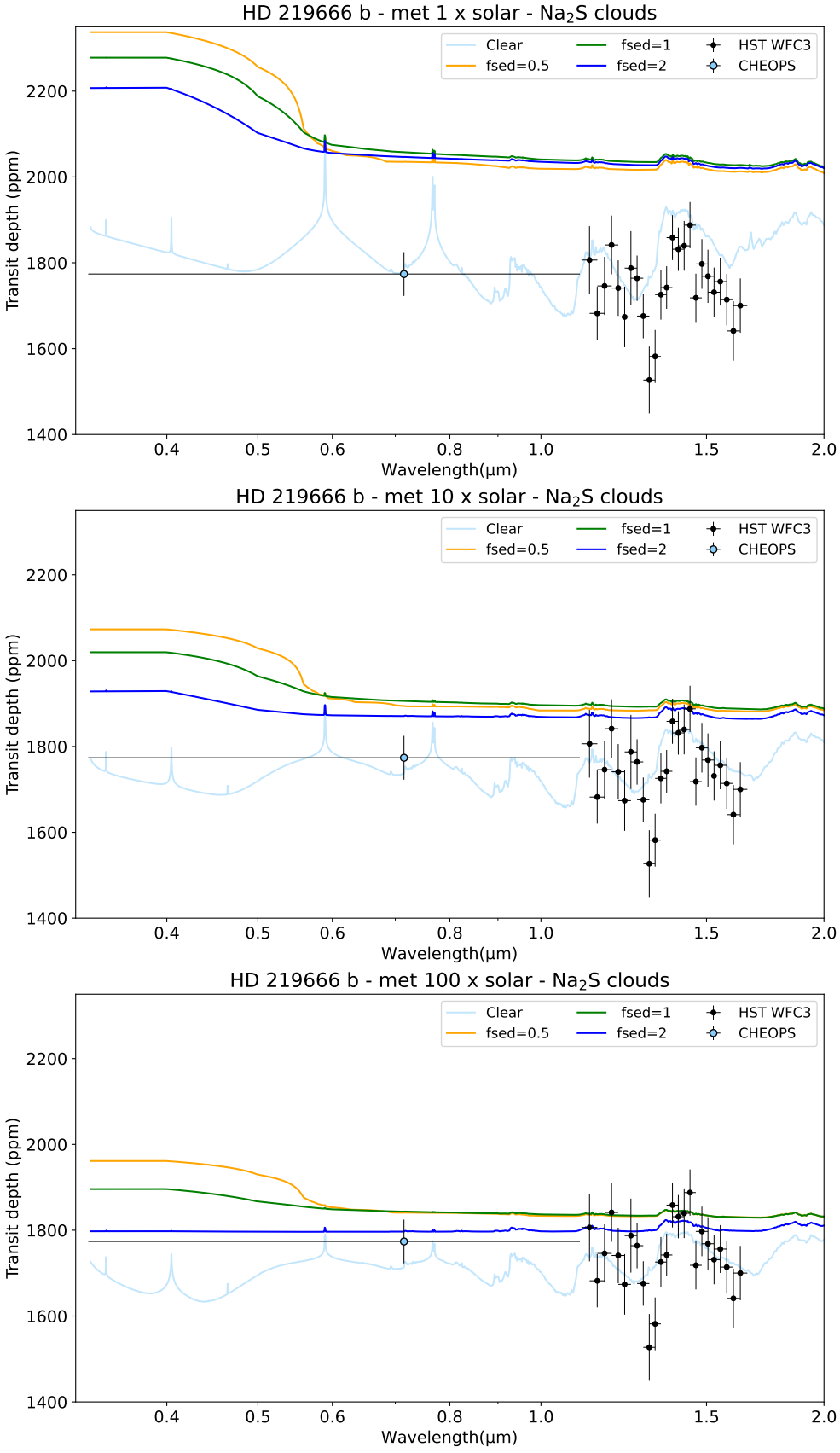

Figure 8.13: CHEOPS (blue) and HST (black data points) transit observations of HD 219666 b and simulated transmission spectra for a cloudy atmosphere. The simulations are from `Exo-REM` self-consistent computations for 1 (top), 10 (middle), and 100 (bottom) × solar atmospheric composition. We include Na_2S clouds with three different sedimentation parameters

8.6 Conclusion

We built a grid of models and NIR transmission spectra by varying the metallicity, the temperature and the atmospheric clear or cloudy scenario. The grid is based on the Sub-Neptune, HD 3167 c from which we vary the irradiation and the atmosphere's composition. First, we span the model grid to investigate the abundance of H_2O, CH_4, CO and CO_2 and identify the carbon-bearing species depending on the temperature and metallicity. We highlight the transition of the carbon-bearing species, CH_4 to CO and the oxygen-bearing species, H_2O to CO and CO_2. CH_4 is more abundant than CO at low temperatures and low metallicities, while CO becomes prominent in warm and heavy atmospheres. CO_2 abundance increases with temperature and metallicity but remains lower than CO and H_2O. Besides, we determine the expected main spectral contributors in the NIR (1.1-1.7 µm) and compare the result to the observations of the HST transmission survey (see Chapter 7). Even though H_2O is the most abundant species, CH_4 remains the main contributor for temperate to warm Sub-Neptune with low atmospheric metallicity atmosphere.

The retrieval analysis of the warm Sub-Neptune transmission spectra suggests the presence of H_2O at 1.4 µm in different atmospheric configurations in terms of metallicity and temperature. We detail the results of ten planets and compare the best-fit retrieval results with the closest simulation from the grid. The most important result is the lack of apparent methane detection in these atmospheres. Among ten planets, we expect, for at least four of them, that CH_4 is the carbon-bearing species and, most importantly, that this molecule's spectral features dominate the transmission spectrum. H_2O is retrieved as the main spectral contributor, and CO_2 is found for two planets as the carbon-bearing species. The lack of methane was already noticed and discussed in Blain et al. (2021) and Bézard et al. (2022) for K2-18 b. They show that CH_4 should be the main carbon-bearing species for Sub-Neptune below 600 K. They tentatively explained it by over-fitting the transmission spectrum or omitting CH_4 in the retrieval analysis. This result is surprising for K2-18 b, TOI-270 d and LHS-1140 b whose retrieved and equilibrium temperatures are below 400 K and the retrieval analysis suggests a 1 to 10 × solar atmospheric composition.

HD 3167 c transmission spectrum analysis includes H_2O and CO_2 absorption at 500 K for a 10 × solar atmosphere. Both of these detections are unexpected in this configuration. Taking into account the uncertainties on the retrieved parameters, H_2O is easily formed at slightly higher temperatures and metallicity while CO_2 spectral features appear at the upper bound of the uncertainties range and are still masked by H_2O and NH_3 features. CO_2 detection remains challenging to interpret in this Sub-Neptune atmosphere. We note that the `Exo-REM` model grid reproduces the retrieval analysis results for five warm (above 600 K) Sub-Neptune to Neptune-like planets. In particular H_2O detection in HAT-P-11 b and HAT-P-26 b but also NH_3 in the atmosphere of HD 106315 c and TOI-674 b.

We tested the presence and the impact of radiative clouds in the atmosphere of Sub-Neptunes using self-consistent computations of KCl and Na_2S condensations with `Exo-REM`. We used the size of the water feature, around 1.4 µm, as a metric to compare observations and simulations. By using a more accurate parameterisation of clouds, we refined the nature of clouds in Sub-Neptune atmospheres. In particular, we proved that KCl clouds could be present in the atmosphere of HAT-P-11 b and HD 97658 b while Na_2S could condensate in HD 219666 b atmosphere. We confirmed that HAT-P-26 b is clear. The same degeneracies are found between the atmosphere's weight and cloudiness.

Flat spectra for planets with an equilibrium temperature between 500 and 800 K can not be explained only by the cloud's condensation. Crossfield & Kreidberg (2017), showed a correlation of the amplitude of atmospheric features in the near-infrared with the temperature and linked that to the formation of clouds and hazes in Sub-Neptunes atmospheres. They showed that the temperature limit

between clear and cloudy/hazy atmospheres could be found around 850 K. We showed in our simulations that cloud condensation could explain the size of observed atmospheric features even for planets within this range. However, some observations are found to be inconsistent with most of the cloudy models. Photochemical hazes, not included in `Exo-REM`, are probably present in the atmosphere of GJ 1214 b, K2-24 b, TOI-270 c, GJ 436 b and GJ 1132 b and thus would explain the very low observed amplitudes. The creation of clouds and hazes in Sub-Neptune atmospheres remains complicated; temperature is a parameter that drives it but is not the only one.

While the modelling grid in clear and cloudy configurations reproduces the retrieval analysis and explains, by condensation, the observed atmospheric features, we note inconsistencies between the model and observations. However, these discrepancies might be explained by the variety of planets chosen in the sample. As stated above, some planets have a large density suggesting a rocky surface which is not accounted for in the modelling. The lack of methane detection is surprising, but this molecule, along with NH_3, is highly sensitive to photochemistry and is probably destroyed in the upper layers of irradiated atmospheres. They are easily photodissociated to form haze precursors, but this chain of reactions is not yet implemented in `Exo-REM`. The presence of clouds and hazes in Sub-Neptune is a contested subject, and photochemistry shapes the transmission spectra in a way we did not reproduce here. Still, it could explain some unexpected results, particularly warm Sub-Neptune flat transmission spectra. 2D and 3D effects are also important parameters in the formation of clouds. We showed that the condensation of H_2O on the night side and the evaporation on the day side could happen for a warm Sub-Neptune (500 K). Lastly, we build a grid using HD 3167 c stellar and planetary parameters; thus, the gravity is fixed to 10 m/s^2. However, this parameter impacts the scale height and the amplitude of the spectral features. The following points will have to be looked into to improve the grid:

- add the gravity dimension to the construction of the grid
- explore the C/O ratio dimension and its impact on H_2O, CO, CO_2 and CH_4 abundances
- include photochemistry reactions
- determine the impacts of NH_3, H_2O, ZnS, Si-bearing clouds in 1D
- determine the impact of changing the cloud's sedimentation parameters to lower values (fsed=0.1)
- adapt and include 2D/3D effects to the grid and investigate the effects at higher temperatures
- deal with higher density planets: Super-Earth surface interactions with the atmosphere

Finally, the accuracy of CHEOPS in 0.33 to 1.1 µm bandpass allows the differentiation of a cloudy from a clear atmosphere where Rayleigh scattering dominates. First, we proved this point using GJ 3470 b simulations. Then, we disclose unprecedented CHEOPS observations of HD 219666 b and propose a method to use the photometric measurement to characterise the atmosphere. We combined CHEOPS and HST transit observations and compared them to self-consistent computations. These simulations were explicitly made for this planet. We did not use the modelling grid to compare transit depths. We concluded on a light, cloud-free atmosphere, proving that CHEOPS can refine planetary parameters and be used to constrain atmospheric models. We note that the planetary radius is a degenerate parameter in the forward modelling, and thus the conclusions presented here are only assumptions. We will use these observations to refine HD 219666 b stellar and planetary parameters.

Our findings could be linked to previous analyses of the same planets and compared to our grid of models with `Exo-REM`, testing Crossfield & Kreidberg (2017) 's hypothesis. The observation of HD 219666 b could be included in a broader study, using previous measurements of CHEOPS on other

Sub-Neptunes that populate the Radius Valley (Fulton et al., 2017) and span a wider temperature range. In particular, GJ 436 b (633 K) and HD 97658 b (733 K) analyses from the Early Release Science program studied in Maxted et al. (2021), but also data on HD 3167 c (548K), HD 106315 c (883 K) or LTT 9779 b (1973 K), could offer the unique opportunity to study the cloudiness of an intriguing population of planets consistently.

Chapter 9

From Hubble to James Webb Space Telescope and ARIEL: unveiling small planets atmospheres

Contents

9.1 Introduction

This chapter presents simulated transmission observations of the Hubble (HST), James Webb (JWST), and the Atmospheric Remote-sensing Infrared Exoplanet Large-survey (ARIEL) space telescopes. We aim to compare the abilities of each facility in answering two main questions: how to differentiate a heavy clear atmosphere from a primary cloudy atmosphere? Is the apparent lack of methane in Sub-Neptune a bias of detection, and can we detect methane with JWST? The first section uses a test case, HAT-P-11 b, to tackle the differentiation of a secondary clear from a primary cloudy atmosphere by comparing JWST and ARIEL functionalities. The second section deals with the apparent methane depletion in Sub-Neptune atmospheres and is based on the rejected HST proposal **Atmospheric characterisation of the warm Sub-Neptune LTT 3780 c**.

9.2 Primary cloudy or secondary atmosphere: HAT-P-11 b a test case

Using the short-wavelength coverage and low resolution of HST makes it impossible to differentiate a primary cloudy atmosphere from heavier atmospheric scenarios. To accurately retrieve the abundance of water, we need the molecular absorption lines' shape; it is not achievable using the resolution of HST. In this section, we test if it is possible to remove this degeneracy for HAT-P-11 b using JWST and the European Space Agency mission, ARIEL (Tinetti et al., 2018) simulations. We saw in Chapter 7 Figure 7.4 that HAT-P-11 b's spectrum could be fitted by either a high cloud deck and a low amount of water in a primary atmosphere or by a higher amount of water in a clear, heavier atmosphere. For this reason, we chose HAT-P-11 b to perform the simulation and develop the method to distinguish among atmospheric scenarios. The transmission spectrum seems to offer the best example of this degeneracy among the 26 transmission spectra we analysed in Chapter 7. This planet is a Neptune-like planet with a very low density of 1.34g/cm^3, and its atmosphere is likely dominated by hydrogen and helium with a trace of volatiles. However, the retrieval analysis on the HST transmission spectrum suggests the presence of a thick absorber or a larger amount of either N_2 or H_2O that increases the mean molecular weight. This result is driven by the fact that the water feature at 1.4 µm is smaller than what would be expected in a cloudless hydrogen-dominated atmosphere for a Neptune-like planet.

9.2.1 Forward models

We used `Tau-REx 3` in forward mode to create synthetic spectra with three different models using HAT-P-11 b best-fit results from Chapter 7 Section 7.3 for the radius and the cloud top layer. The stellar parameters are fixed to those of Chapter 7 Table 7.1. The atmosphere is simulated between 10^{-3} and 10^6, with 100 layers. We define three simple models based on the results from Section 7.3 on HAT-P-11 b:

Model 1: We include H_2O with a VMR of 10^{-3} in a hydrogen-rich atmosphere. The radius is fixed according to the **1-Primary** best fit result, i.e. to 4.5 $R_\oplus$. We include a grey cloud top layer at 1585 Pa.

Model 2: We include H_2O with a VMR of 10^{-1} in a hydrogen-rich atmosphere. The radius is set according to the **2-Active clear** best fit result, i.e 4.61 $R_\oplus$.

Model 3: We include H_2O with a VMR of 10^{-4} in a hydrogen-rich atmosphere. The radius is set according to the **2-Active clear** best fit result, i.e 4.61 $R_\oplus$. We fixed the ratio of N_2/H_2 to 1.5×10^{-4}.

We used an isothermal temperature profile and fixed the temperature to the irradiation temperature, 867K, for all the models.

9.2.2 Instruments setups

We assumed the JWST observations are performed with NIRISS SOSS and NIRSpec G395H. The combination of these two instruments ensures a wavelength coverage from 0.8 to 5 µm and can be compared to the ARIEL wavelength coverage (0.5 to 8 µm). We used `Pandexo` (Batalha et al., 2017) to simulate JWST observations, and we used only one transit of each mode. The instrumental setups for NIRISS and NIRSpec are detailed in Table 9.2. To simulate the performances of ARIEL, we used the noise simulator, `ARIELRad` (Mugnai et al., 2020), for HAT-P-11 b in TIER 3 resolution. We created three spectra using one, five and ten transits observations. We did not scatter the spectra for JWST and ARIEL simulations. Transit spectra were generated at high resolution and then binned down.

Table 9.1: Description of the models and retrieval priors for the simulations on HAT-P-11 b

Parameter	**Model 1**	**Model 2**	**Model 3**	Retrieval
R_P ($R_\oplus$)	4.5	4.61	4.61	50% R_P
T (K)	867	867	867	50% T_{irr}
He/H_2	0.17	0.17	0.17	fixed
N_2/H_2	-	-	$1.6x10^{-4}$	$[10^{-12}$-$10^{4}]$
CIA	H_2-H_2, H_2-He	H_2-H_2, H_2-He	H_2-H_2, H_2-He	-
Rayleigh	all species	all species	all species	-
P_{clouds} (Pa)	1585	None	None	$[10^{-3}$-$10^{6}]$
VMR(H_2O)	10^{-3}	10^{-1}	10^{-4}	$[10^{-12}$-$10^{-1}]$
VMR(CO)	None	None	None	$[10^{-12}$-$10^{-1}]$
VMR(CO_2)	None	None	None	$[10^{-12}$-$10^{-1}]$
VMR(CH_4)	None	None	None	$[10^{-12}$-$10^{-1}]$
VMR(NH_3)	None	None	None	$[10^{-12}$-$10^{-1}]$
VMR(HCN)	None	None	None	$[10^{-12}$-$10^{-1}]$

Table 9.2: JWST instrumental setups from Pandexo (Batalha et al., 2017) simulations.

Parameter	NIRISS	NIRSpec
Aperture	SOSS	s1600a1
Mode	SOSS	BOTS
Disperser	GR700xd	G395H
Subarray	substrip96	sub2048
Filter	clear	f290lp
Spectral coverage (μm)	0.83-2.81	2.87-5.18
Exposure time (s)	7228.8	8574.8
Saturation level (e^-)	57600	52000
Number groups	2	2
In transit integration	1085	3145
Out of Transit integration	1085	3145
Observations duration (hrs)	6.65	4.72

JWST spectra have a resolving power of around R∼100 while ARIEL spectra have a resolving power of ∼ 20/100/30. Likely, binning real JWST spectra obtained at high resolution will not be the best strategy as we might lose information on species-absorbing lines. However, this is justified here as we only include water in our model and want to compare it with ARIEL simulations.

9.2.3 Retrieval models

These simulated spectra were then used as inputs to `Tau-REX 3` in retrieval mode to assess whether we could distinguish a primary cloudy from heavier atmospheric scenarios. Thus, we performed a mock retrieval on these spectra using a similar retrieval setup as described in Chapter 7 Section 7.2.2. We include the molecular opacity from H_2O, CO, CO_2, NH_3, CH_4 and HCN, with a large prior range (10^{-12} and 10^{-1}) as well as the N_2/H_2 ratio fitted between 10^{-12} and 10^4. We also retrieve the top cloud layer pressure between 10^{-3} and 10^6 Pa. The two forward models and the retrieval priors are detailed in Table 9.1. We present in Figure 9.1 the simulated spectra along with the best fit atmospheric model

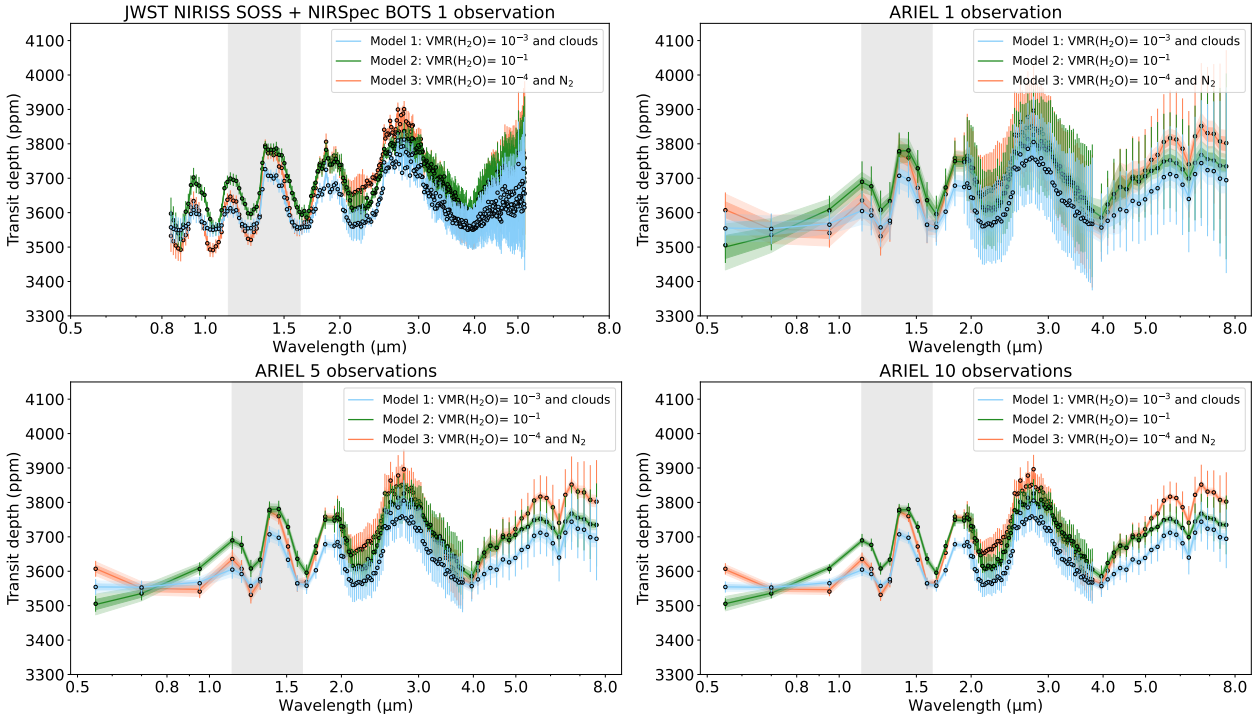

Figure 9.1: Simulated observed spectra and best-fit retrieval models for three models of HAT-P-11 b obtained with two transits, one of NIRISS and one of NIRSpec (top left) and one transit of ARIEL (top right), five transits of ARIEL (bottom left), ten transits of ARIEL (bottom right). The grey area represents the region probed by HST WFC3 G141.

from the retrieval analysis for one, five, and ten transits observations with ARIEL and one transit of NIRISS and NIRSpec. We represent in grey the region probed by HST WFC3 G141. Retrieval posterior distributions for the three models are over-plotted in Figure 9.2 for the JWST simulated spectrum and in and Figure 9.3 for the spectrum created with five transits of ARIEL. The posteriors distributions for the simulations obtained with one and ten simulated transits of ARIEL are in Appendix G.1 and G.2. We recall that **Model 1**, in blue, is representative of a primary cloudy atmosphere, **Model 2** in green is a water-rich atmosphere and **Model 3** in orange is a nitrogen-rich atmosphere.

We present the best fit results for the main parameters in Table 9.3 for one transit of JWST instruments and five transits of ARIEL. The retrieval results comparison of one, five and ten transits of ARIEL is in Appendix G.1. Using five observations of ARIEL, one can start to differentiate between the models with more than 2σ (see Figure 9.1 and posterior distributions 9.3). The abundance of H_2O

Table 9.3: Comparison of the retrieval results on HAT-P-11 b simulated spectra with the JWST and ARIEL.

Number of transits	1 NIRISS+ 1 NIRSpec			5 ARIEL		
Model	1	2	3	1	2	3
R_P ($R_\oplus$)	$4.50^{+0.11}_{-0.11}$	$4.61^{+0.01}_{-0.01}$	$4.61^{+0.01}_{-0.01}$	$4.50^{+0.01}_{-0.01}$	$4.61^{+0.01}_{-0.01}$	$4.61^{+0.01}_{-0.01}$
T (K)	868^{+39}_{-38}	870^{+32}_{-31}	868^{+15}_{-12}	866^{+117}_{-120}	878^{+62}_{-57}	871^{+45}_{-46}
$\log_{10}(N_2/H_2)$	$-7.61^{+3.16}_{-2.97}$	$-7.53^{+3.27}_{-2.94}$	$-7.67^{+3.27}_{-2.94}$	$-7.58^{+3.32}_{-2.93}$	$-7.27^{+3.55}_{-3.12}$	$-7.59^{+3.38}_{-3.03}$
$\log_{10}(P_{clouds})$	$3.15^{+0.20}_{-0.23}$	$4.77^{+0.83}_{-0.88}$	$5.48^{+0.36}_{-0.38}$	$3.04^{+0.42}_{-0.57}$	$4.64^{+0.89}_{-0.92}$	$5.30^{+0.47}_{-0.47}$
$\log_{10}(H_2O)$	$-2.91^{+0.27}_{-0.24}$	$-0.93^{+0.04}_{-0.04}$	$-3.86^{+0.06}_{-0.06}$	$-2.65^{+0.51}_{-0.53}$	$-0.93^{+0.09}_{-0.10}$	$-3.85^{+0.20}_{-0.18}$
μ (g/mol)	$2.33^{+0.02}_{-0.01}$	$4.15^{+0.17}_{-0.15}$	$2.31^{+0.01}_{-0.01}$	$2.34^{+0.08}_{-0.03}$	$4.15^{+0.39}_{-0.37}$	$2.31^{+0.01}_{-0.01}$

and the cloud top layer pressure are retrieved correctly for all models (see Table 9.3). We can distinguish between a cloudy light atmosphere and a clear heavier atmosphere with five observations of ARIEL. One transit observation is not enough to separate the solutions. Even though the distribution peak at the right value, they overlap for the water abundance and the pressure of the top cloud. The solutions found are not accurate enough to ensure the differentiation between models. One transit of NIRISS and NIRSpec is enough to distinguish models, but only receive similar uncertainties when using ten transits of ARIEL. We retrieved the ground truth using five ARIEL transits and one JWST transit.

Five ARIEL observations of HAT-P-11 b and one transit of NIRISS and NIRSpec could fulfil the main objective of this study: remove the ambiguity pointed out with HST in Chapter 7 Section 7.4.3 for small planets. This result illustrates one planet and will have to be investigated in more depth to be adapted to the whole sample of Sub-Neptune studies in the HST survey (Chapter 7). ARIEL has been conceived to observe warm exoplanets around bright stars (Edwards et al., 2019), and this result might not be directly transposed to colder and smaller exoplanets such as K2-18 b. In particular, Changeat et al. (2021) investigated different atmospheric scenarios for K2-18 b, observed with ARIEL and JWST. They show that 20 observations with ARIEL should be enough to distinguish between a cloudy light and a secondary atmosphere, while only two transits are required with JWST if combining NIRISS and NIRSpec data.

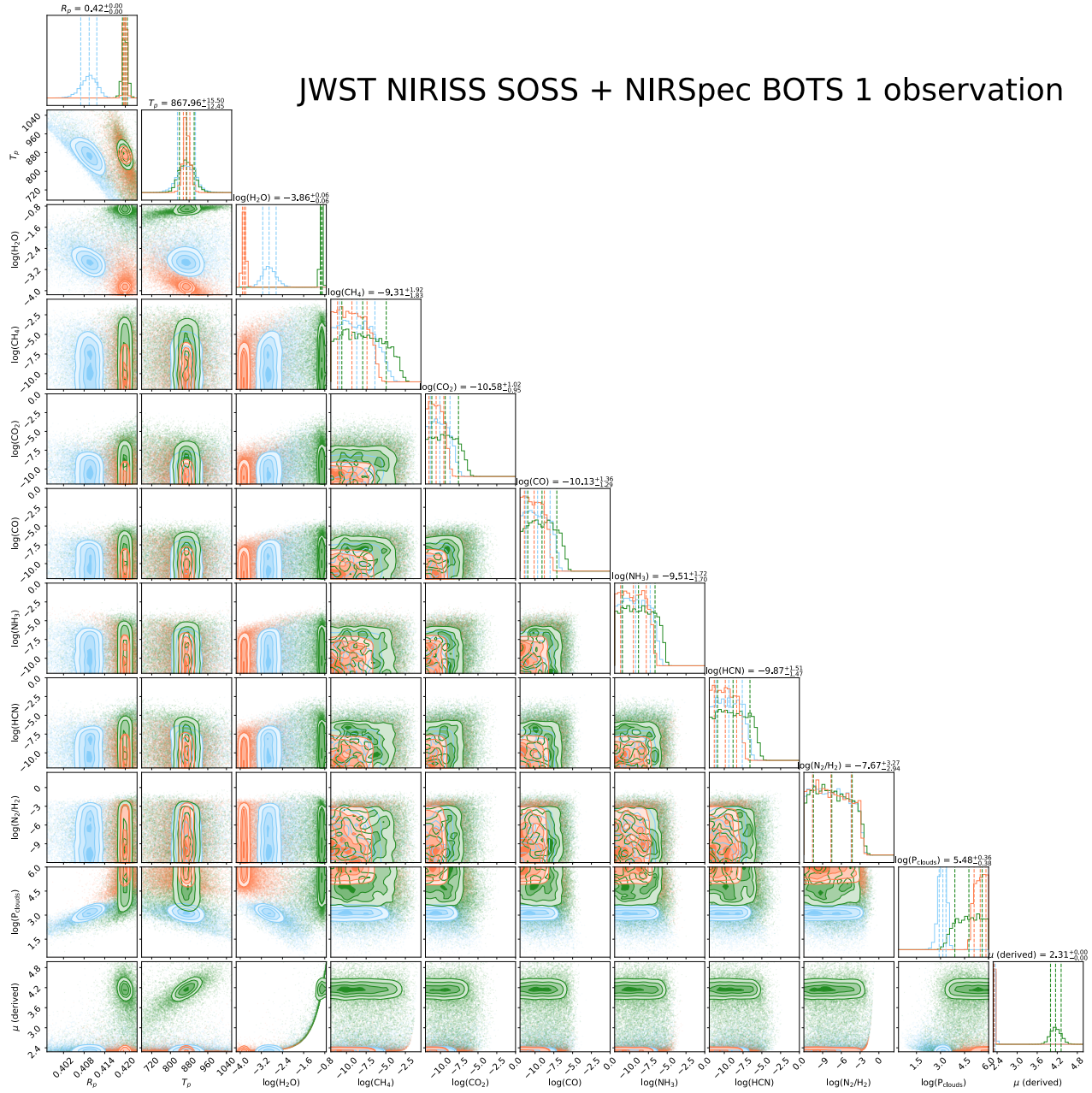

Figure 9.2: Posteriors distributions for the three models of HAT-P-11 b obtained with two transits, one of NIRISS and one of NIRSpec. Model 1, in blue, is representative of a primary cloudy atmosphere, Model 2, in green, is a water-rich atmosphere and Model 3, in orange is a nitrogen-rich atmosphere.

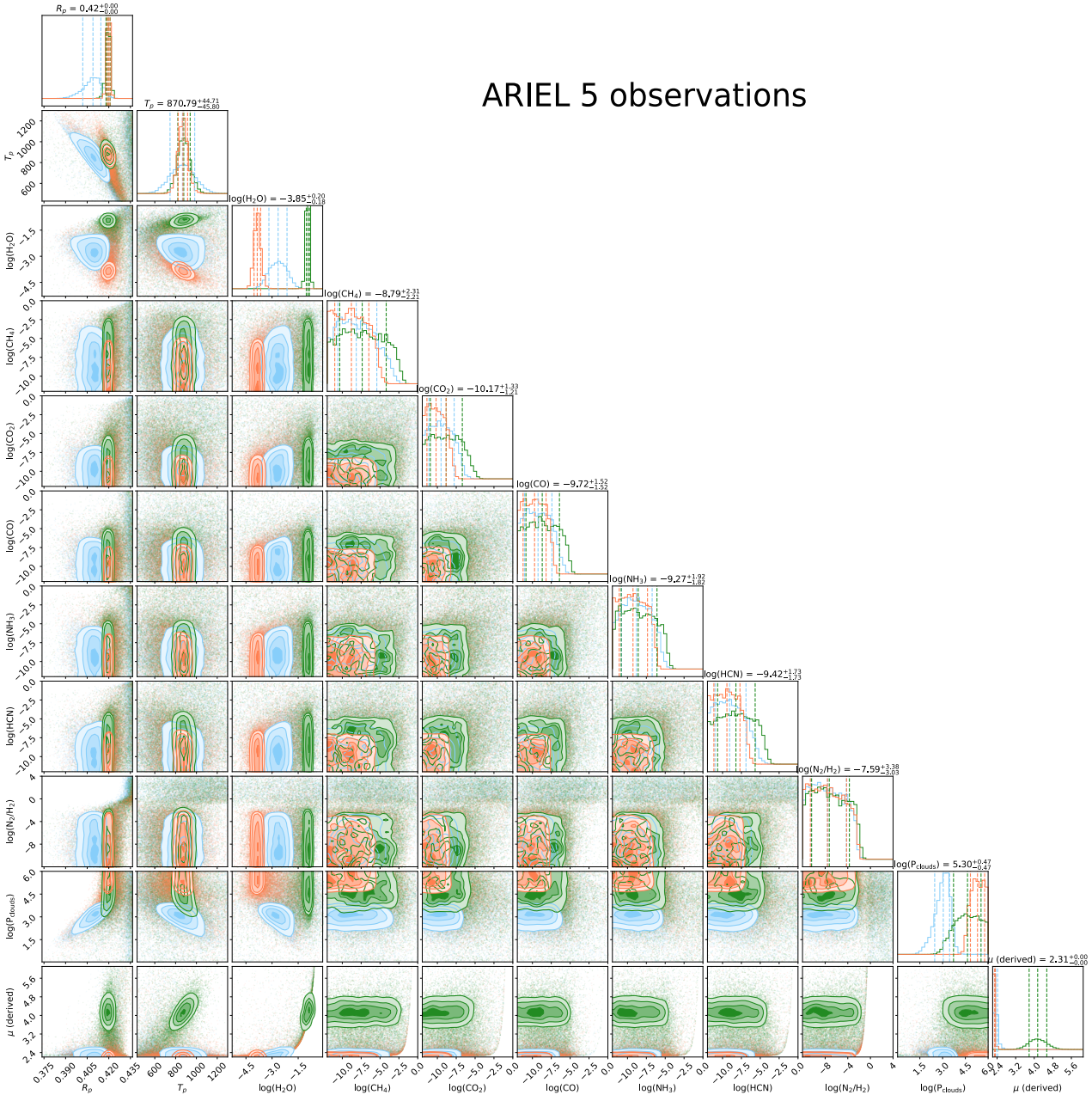

Figure 9.3: Posteriors distributions for the three models of HAT-P-11 b obtained with five transits of ARIEL. Model 1, in blue, is representative of a primary cloudy atmosphere, Model 2, in green, is a water-rich atmosphere and Model 3, in orange, is a nitrogen-rich atmosphere.

9.3 Detecting methane in Sub-Neptune atmospheres from HST to JWST

Methane is thermochemically expected to exist in cool planets, but previous observations in the NIR have shown an apparent lack of this molecule. We showed in Chapter 7 that among 26 Sub-Neptune transmission spectra (HST WFC3) spanning 300 to 1900K, none showed evidence of CH_4 absorption. Close-in planets could have a near solar metallicity atmosphere created by primordial gas accretion (Lee & Chiang, 2015; Ginzburg et al., 2016), while others could have formed beyond the frost-line and migrated forward, allowing a higher metallicity atmosphere, and even water worlds (Rogers & Seager, 2010). The unexpected apparent lack of methane, in particular in GJ 3470 b (Benneke et al., 2019), and in K2-18 b (Benneke et al., 2019; Tsiaras et al., 2019) atmospheres, were tentatively explained by internal heating, where carbon monoxide becomes prominent (Kreidberg et al., 2018; Morley et al., 2017) or by photochemical destruction of methane in deep layers, but, these results are more than 3σ away from predicted equilibrium chemistry (Benneke et al., 2019). As shown in Bézard et al. (2022), methane should be the main contributor to the absorption features in this part of the spectrum for Sub-Neptunes with temperatures below 600K, even though water might be more abundant. We reach similar conclusions in Chapter 8, where we built a grid of Sub-Neptune atmospheres spanning 200 to 1200K and 1 to 1000 $\times$ solar metallicity. CH_4 is expected to be the main spectral contributor below 500K for metallicity below 300 $\times$ solar. This result is in disagreement with the retrieval analysis on HST WFC3 G141 observations, especially for K2-18 b (T$\sim$300K) (Tsiaras et al., 2019) (Benneke et al., 2019): they claim evidence of water absorption around 1.4 µm. Blain et al. (2021) compared 1D self-consistent models and HST observations on K2-18 b and showed that this result could either be due to the omission of methane or the over-fitting of the data during the retrieval analysis. We showed in Chapter 8 that the retrieval analysis favours H_2O absorption over CH_4. However, the Bayes factor between the model with and without H_2O (with CH_4) is not significant. We can not completely rule out CH_4 as the main spectral contributor but the detection is not clear.

9.3.1 LTT 3780 c: a perfect target for methane detection

In this context, LTT 3780 c, with a radius of 2.42±0.10$R_\oplus$, a mass of 6.29±0.63$M_\oplus$ (i.e ρ=2.42 g/cm^3) and an equilibrium temperature of 363±11 K (Nowak et al., 2020) is an excellent target for the atmospheric characterisation of a cool world around a small cool star ($R_\star$=0.382±0.012$R_\odot$ and $T_{\rm eff}$=3360±51K). We proposed in the Cycle 30 HST proposal **Atmospheric characterisation of the warm Sub-Neptune LTT-3780 c** to observe five transits of LTT 3780 c using the HST WFC3 G141 (1.1-1.65 µm) to characterise its atmosphere and detect for the first time methane in a Sub-Neptune's atmosphere. The ideas behind this proposal were to investigate the cloud cover in the atmosphere of LTT 3780 c and better adjust the feasibility and usefulness of the JWST Cycle 2 observations. Then, providing the atmosphere is cloudless, we could probe the upper layers of the atmosphere to detect methane or water with high significance (5-σ) and test the possible methane depletion of close-in Sub-Neptunes. While there is little doubt that the atmosphere of this planet is consistent with a hydrogen-dominated composition, it is unclear whether H_2O or CH_4 should dominate the spectrum around 1.4 µm.

LTT 3780 c can be considered as a "warm K2-18 b". K2-18 b (2.61±0.087$R_\oplus$, 8.63±1.35$M_\oplus$), and, LTT 3780 c present similar planetary and stellar parameters ($R_\star$0.445±0.015$R_\odot$, $T_{\rm eff}$=3457 ± 39K). Contrary to the temperate K2-18 b ($T_{\rm eq}$=254±4K (Benneke et al., 2019)), LTT 3780 c is warm ($T_{\rm eq}$=363 ± 11K) and the TSM (Kempton et al., 2018) reaches 112.5. This is more than 2.5 times that of K2-18 b, which makes it one of the best warm Sub-Neptunes for transmission spectroscopy. This planet is also warm enough to prevent H_2O condensation, which could complicate the interpretation of

the transmission spectrum. Thus, comparing K2-18 b observations with LTT 3780 c makes sense and would be useful to constrain formation and evolution models. If the planet formed beyond the frost line, it could have retained volatile species – specifically, H_2O – which we can detect. For this reason, we requested five transit observations to reach a similar uncertainty on the spectrum data point than for K2-18 b, i.e ∼25ppm around 1.4 µm (Tsiaras et al., 2019; Benneke et al., 2019).

9.3.2 HST cloud free simulations

We used `Exo-REM` to simulate the atmosphere of LTT 3780 c. We used a similar parametrisation to Blain et al. (2021) on the Sub-Neptune K2-18 b. The atmosphere is modelled using 80 layers between 10^{-2} and 10^7 Pa, with an equilibrium temperature of 363 K. We include 13 absorbing species in a hydrogen-rich atmosphere, allowing for out-of-equilibrium chemistry. We vary the atmospheric metallicity from 1 to 500 × solar, but we fixed the Eddy diffusion coefficient to 10^8 cm^2/s. Then, we used `Pandexo` Batalha et al. (2017) to simulate a NIR spectrum using five transit observations, 18 spectral channels (allowing the power of resolution of $\lambda/\Delta\lambda$=48 at 1.4 µm), and the spectrum parameterisation given by `Exo-REM` in the case of 100 × solar metallicity. Using fewer observations with the same resolution will lead to higher estimated noise, between 30 and 50 ppm, and, thus, more uncertainties in our ability to distinguish between atmospheric scenarios.

Figure 9.4 (top) shows five transits are able to distinguish between a light atmosphere (1 × solar) and a heavier atmosphere (superior to 100 × solar) with more than 3σ confidence. Figure 9.4 (bottom) confirms that the spectrum is dominated by CH_4 absorption features in the case of a 100 × solar metallicity for the calculated temperature/pressure profile. We present in Figure 9.5, the volume mixing ratios and the spectral opacity contributions in the 1.1 to 1.7 µm for 1, 10, 100 and 300 × solar atmospheric compositions. Until 300× solar composition, the transmission spectrum is dominated by CH_4 absorption even though H_2O is more abundant.

We compare in Figure 9.4 (top), the simulated spectrum (100 × solar) with different atmospheric models from `Exo-REM` including 13 absorbing species, H_2O only and CH_4 only in a H_2/He rich atmosphere. The mean amplitude of the spectrum in three bands: [1.12-1.20 µm], [1.35-1.45 µm] and [1.55-1.65 µm] is computed by subtracting the mean transit depth value to the one in a reference band where CH_4 nor H_2O absorbs [1.25-1.30 µm]. The presence of CH_4 increases the amplitude of the features in all three bands, but the main differences with the model, including only H_2O, are seen in the first and the third bands. We find the amplitude of 172 ppm and 83 ppm for the CH_4 and H_2O only models, respectively, in the first band and 103 ppm versus -13 ppm in the third band. The amplitudes for the simulated HST observations that include CH_4 are 114±22 ppm and 75±22 ppm in the first and third bands, respectively. With five transits observations of HST WFC3, the uncertainties on the spectrum will allow the differentiation of the main contributor with more than 1-σ for the first band and more than 3-σ for the third one. This would only be at the detection limit for a similar resolution spectrum with three transits and not achievable with only one or two transits observations.

Note that methane and water have an overlapping band around 1.4 µm that could lead to confusion in a retrieval analysis. On the other hand, methane also has absorbing features between 1.1 and 1.2 µm and after 1.55 µm. The latter strongly shapes the transmission spectrum and should constrain the interpretation. Without these lines, the overall transmission spectrum would not display an elevated transit depth at a low wavelength and would decrease after 1.5 µm following water features. Moreover, chi-squared (χ^2) and reduced chi-squared ($\tilde{\chi}^2$2) computations presented in Table 9.4, show that we can quantitatively distinguish CH_4 and H_2O molecular absorptions. The chi-squared (χ^2) and the reduced chi-squared ($\tilde{\chi}^2$2) are computed using models plotted in Figure 9.4 and 9.6, and, the HST simulated spectrum obtained with `Pandexo` (Batalha et al., 2017) based on the 100 × solar (all species) simulations. Models including CH_4 fit significantly better the spectrum with a χ^2 around 50, while models including water present a χ^2 over 200. This quantifies the ability to detect methane and

differentiates it with water features for a 100 × solar metallicity atmosphere. For a 500 × solar metallicity atmosphere, the spectrum between 1.1 and 1.7 µm is no longer dominated by methane. In particular, in the 1.35-1.45 µm band, water is the main contributor. Methane features shape the third band around 1.6 µm, where water does not absorb, and the amplitude in this band is 74 ppm. As seen in Figure 9.4, the features amplitudes are smaller and other carbon-bearing species (CO and CO_2) might contribute, especially around 1.6 µm.

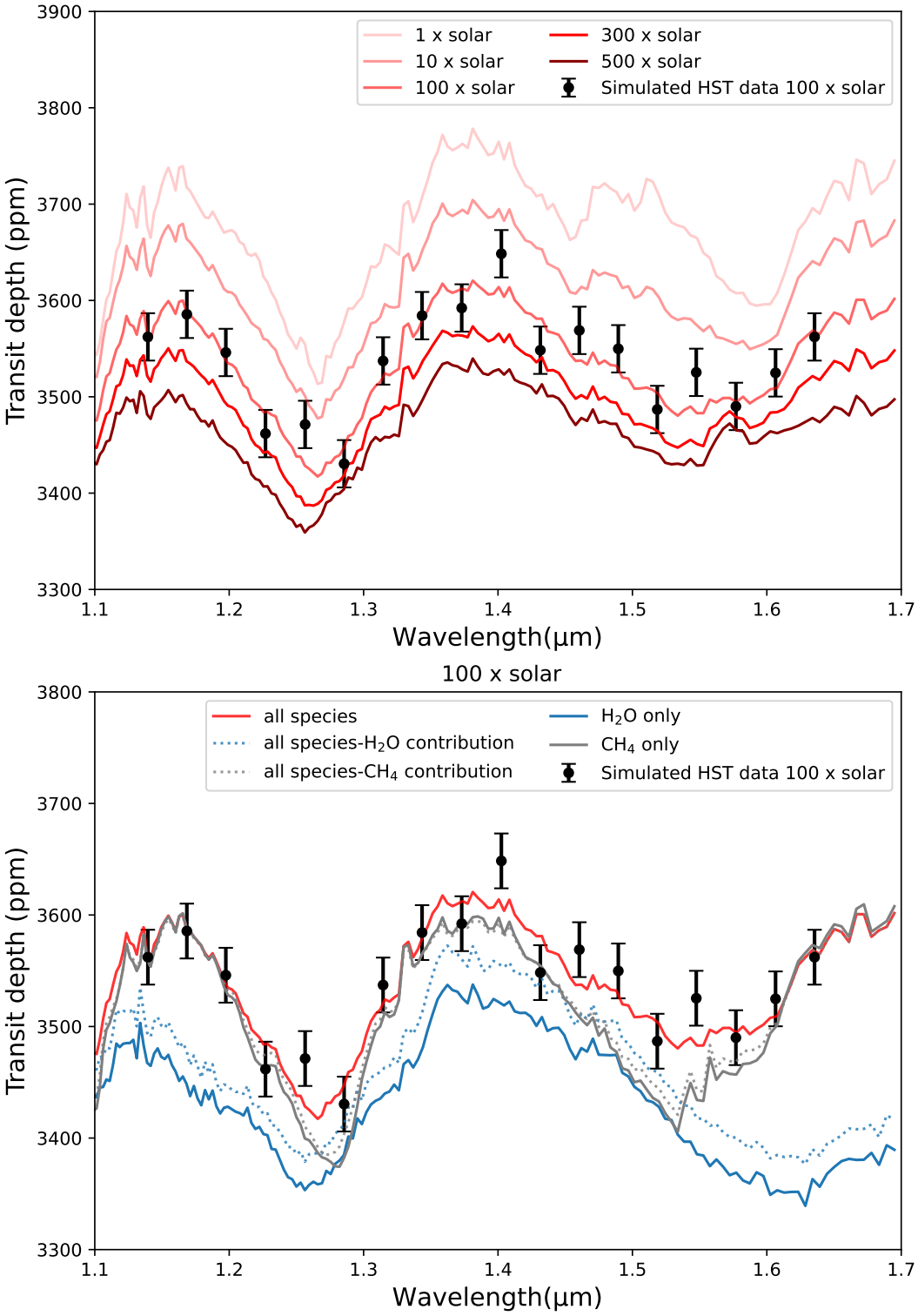

Figure 9.4: Effect of metallicity on the transmission spectrum (top). Comparison of different models and opacity contributions in the HST/WFC3 G141 wavelength range from`Exo-REM` computations (bottom).

Model	χ^2	$\tilde{\chi}^2$	Model	χ^2	$\tilde{\chi}^2$	Model	χ^2	$\tilde{\chi}^2$
1 × solar	561.7	31.2	all species	16.33	0.9	clear 100 × solar	16.33	0.9
10 × solar	163.6	9.1	all species H_2O contribution	222.2	12.3	KCl fsed=2	15.6	0.9
100 × solar	16.3	0.9	all species CH_4 contribution	44.4	2.5	KCl fsed=1	19.1	1.1
300 × solar	75.5	4.2	H_2O only	375.4	20.9	KCl fsed=0.5	93.6	5.2
500 × solar	188	10.4	CH_4 only	57.7	3.2			

Table 9.4: Chi-squared (χ^2) and reduced chi-squared ($\tilde{\chi}^2 2$) computed using `Exo-REM` simulations.

9.3.3 HST cloudy simulations

Clouds and photochemical hazes have proven hard to explain, model, and predict in the atmospheres of Sub-Neptunes. Optically thick clouds forming in the atmosphere's upper layers can greatly block the spectroscopic features of gas species, while thinner clouds allow atmospheric signatures to be partially detected. Specifically, methane photo-dissociation could also produce photochemical hazes in the high atmosphere of LTT 3780 c. The non-detection of atmospheric features, as expected in previous simulations, will prove the presence of optically thick absorbers, which is also one of the goals of this observation. Figure 9.6 (top) shows the temperature/pressure (T/P) profile of LTT 3780 c for a 100 × solar metallicity atmosphere. Note that the T/P profile crosses the condensation curves of NH_4Cl and KCl. Decreasing the metallicity could lead to higher temperatures below 10^1 bar and the formations of ZnS and Na_2S. However, increasing the metallicity will decrease the temperature, though not enough to create water clouds. NH_4Cl condensation clouds are too thin to influence the transmission spectrum optically. KCl condensates at pressures probed by HST WFC3 G141 could flatten molecular absorption features by blocking the signal from below. The radiative effects of clouds were accounted for using self-consistent condensation computations of KCl, with a full cloud cover and a sedimentation efficiency (fsed) of 0.5,1 and 2, as expected for this type of planet and as observed in the Solar System (Morley et al., 2015; Charnay et al., 2018). Figure 9.6 (bottom) shows the impact of radiative KCl clouds in the transmission spectrum for three different sedimentation efficiencies. To account for a possible opaque layer blocking the signal, we also indicate the relevant altitude of grey clouds. Below 130 km, the layer is found too deep to impact the transmission spectrum, while above 570 km, no molecular features can be detected. Here, 450 km and 350 km are the maximum altitudes at which the spectral signatures could still be detected with ∼1- and 3-σ confidence. This is computed using the maximum of the [1.35-1.45 µm] band (∼ 3600 ppm) and the estimated uncertainty (∼ 25 ppm). KCl clouds are located at 450 km in the opacity contribution plot when the sedimentation parameter is set to 0.5.

9.3.4 Mock retrievals

To understand the sensitivity of the data to the absorption of methane and water, we performed a mock retrieval on the simulated spectrum for a clear and cloudy atmosphere with all the species included and for a model including only H_2O using 1 to 5 transit observations. For the cloudy model, we used the most constraining simulation, i.e. the one that considers KCl clouds with a sedimentation parameter of 0.5. The position of the clouds in this simulation also corresponds to the opaque layer's maximum authorised altitude for which we can still detect an atmosphere. We include H_2O, CO, CO_2, NH_3 and CH_4 as molecular opacity sources, Rayleigh scattering, Collision-Induced Absorption (CIA), a cloud deck, and we fit an isothermal T/P profile. We also performed a flat-line retrieval, including only a cloud deck without any molecular opacity source. This setup is used to assess the strength of the atmospheric detection in the previously described models by computing the Bayes factor. The latter is the difference in logarithm evidence between the tested model and the flat line Kass & Raferty (1995). The equivalence between the Bayes factor and the significance is estimated using Table 2 in Trotta

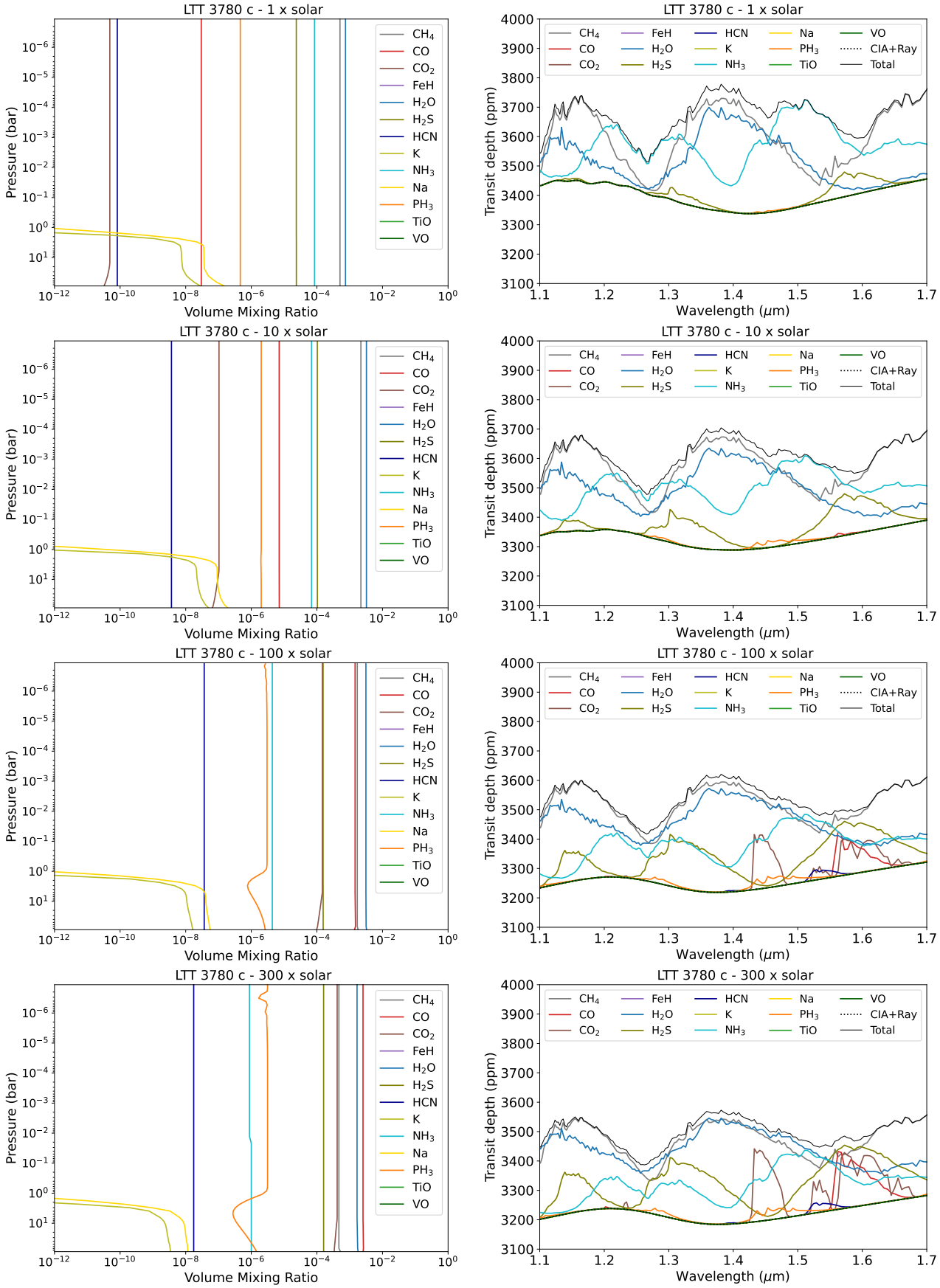

Figure 9.5: LTT 3780 c's volume mixing ratios and NIR spectral opacity contributions for 1, 10, 100 and 300 × solar atmospheric compositions. The calculation are from `Exo-REM` computations.

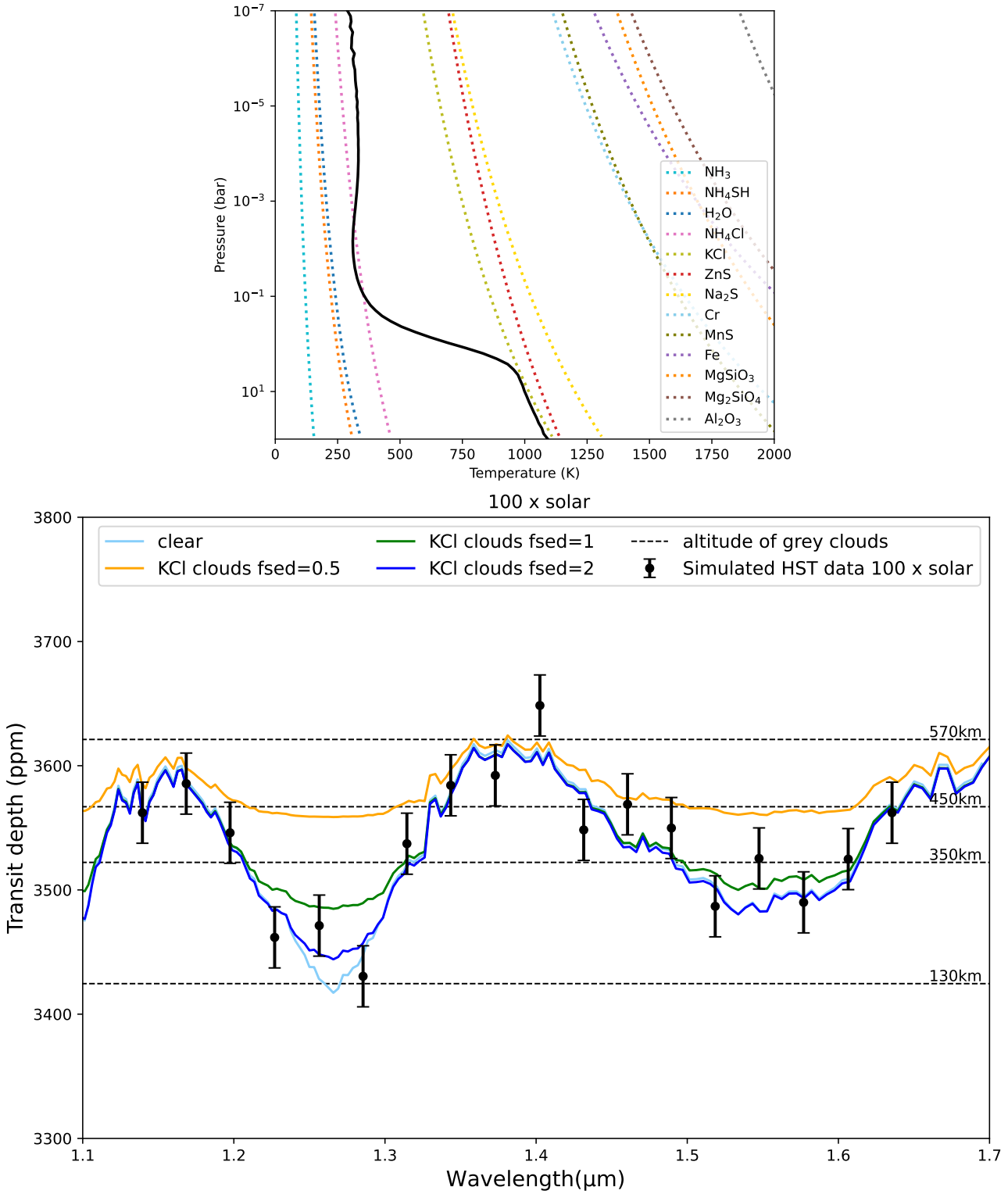

Figure 9.6: Simulated temperature-pressure profiles for LTT 3780 c (solid black lines) and condensation profiles (dotted lines) for a 100 × solar metallicity atmosphere (top). Impact of radiative clouds in the transmission spectrum and altitudes of possible optically thick grey clouds (bottom).

(2008) and Table 2 in Benneke & Seager (2013). Here a Bayes factor greater than 3 (3-σ) is considered significant.

Our retrievals found that the main contributor is CH_4 in the case of a clear atmosphere with 3-σ confidence using three observations and with more than 5-σ using five observations (see the contributions plot (top) in Figure 9.7 and Table 9.5). CH_4's volume mixing ratio is better constrained than that of H_2O (see bottom left in Figure 9.7 and Table 9.5). The value found (i.e -2.68 in log space) is close to the one predicted (i.e -2.77). At least three transit observations are required to detect methane, and five transits are required to obtain a constrained and precise value (see Table 9.5). We determined the main contributor between water and methane, with one transit for the H_2O only simulation, and three transits for a complete model. If the planet's atmosphere is clear and contains water and no methane, we can detect water with more than 5-σ confidence. Including KCl clouds with a sedimentation efficiency of 0.5 in our simulation significantly influences the retrieval analysis because neither methane nor water is constrained with less than five transit observations. This proves the presence of another thick absorber. Methane (see Figure 9.7 (bottom middle)), contributes to the spectrum opacity (see Figure 9.7 (middle)), but the significance of the retrieval is around 1-σ. The top grey cloud layer is found at a pressure of $10^{2.39}$ Pa (or 340 km in our previous formalism), which is close to the ground truth (350km). Five transits are required to retrieve the contribution of methane and the correct altitude of the layer of clouds in a cloudy atmosphere (see Table 9.5). The posterior distribution in Figure 9.7 (bottom right) shows we can distinguish a clear from a cloudy atmosphere using three transits and with a good accuracy using five. Note that the mock retrieval on the cloudy atmospheric spectrum shown here is a worst-case scenario. That is, the altitude of the clouds corresponds to the maximum level for which atmospheric detection is possible. Hence, if a layer of clouds or hazes is located deeper in the atmosphere (as is likely), we would be able to detect methane or water with higher confidence. Conversely, if an opaque layer is higher in the atmosphere, it would more easily be detected and differentiated from a clear atmosphere.

	1 transit	2 transits	3 transits	4 transits	5 transits
all species × 100 solar metallicity clear atmosphere					
$\log(CH_4)$	unconstrained	unconstrained	$-2.80^{+1.17}_{-2.39}$	$-2.59^{+0.88}_{-0.73}$	$-2.68^{+0.89}_{-0.64}$
$\log(H_2O)$	unconstrained	unconstrained	$-5.98^{+3.04}_{-3.73}$	$-5.19^{+2.65}_{-4.02}$	$-6.07^{+3.24}_{-3.73}$
$\log(P_{clouds})$ (Pa)	unconstrained	$4.97^{+1.21}_{-1.35}$	$4.95^{+1.12}_{-1.18}$	$5.11^{+1.22}_{-1.21}$	$5.27^{+1.07}_{-1.16}$
Bayes Factor	0.26	1.74	4.12	10.82	20.45
H_2O only × 100 solar metallicity clear atmosphere					
$\log(CH_4)$	< -4	< -5	< -5	< -5	< -5
$\log(H_2O)$	$-2.64^{+0.98}_{-1.56}$	$-2.30^{+0.74}_{-1.02}$	$-2.01^{+0.57}_{-0.93}$	$-1.37^{+0.26}_{-0.73}$	$-1.29^{+0.21}_{-0.58}$
$\log(P_{clouds})$ (Pa)	$4.63^{+0.87}_{-1.51}$	$4.80^{+0.74}_{-1.10}$	$5.04^{+0.60}_{-0.66}$	$5.05^{+1.21}_{-0.95}$	$5.23^{+1.14}_{-0.90}$
Bayes Factor	2.61	7.69	13.73	17.70	23.71
all species × 100 solar metallicity cloudy atmosphere					
$\log(CH_4)$	unconstrained	unconstrained	unconstrained	unconstrained	$-4.34^{+1.66}_{-4.33}$
$\log(H_2O)$	unconstrained	unconstrained	unconstrained	unconstrained	unconstrained
$\log(P_{clouds})$ (Pa)	unconstrained	unconstrained	$2.10^{+1.41}_{-2.00}$	$1.94^{+1.43}_{-1.99}$	$2.39^{+1.31}_{-1.89}$
Bayes factor	-0.40	-0.37	-0.07	0.27	0.30

Table 9.5: Retrieved CH_4, H_2O VMR and top pressure of a grey cloud layer for a spectrum made with 1 to 5 transits.

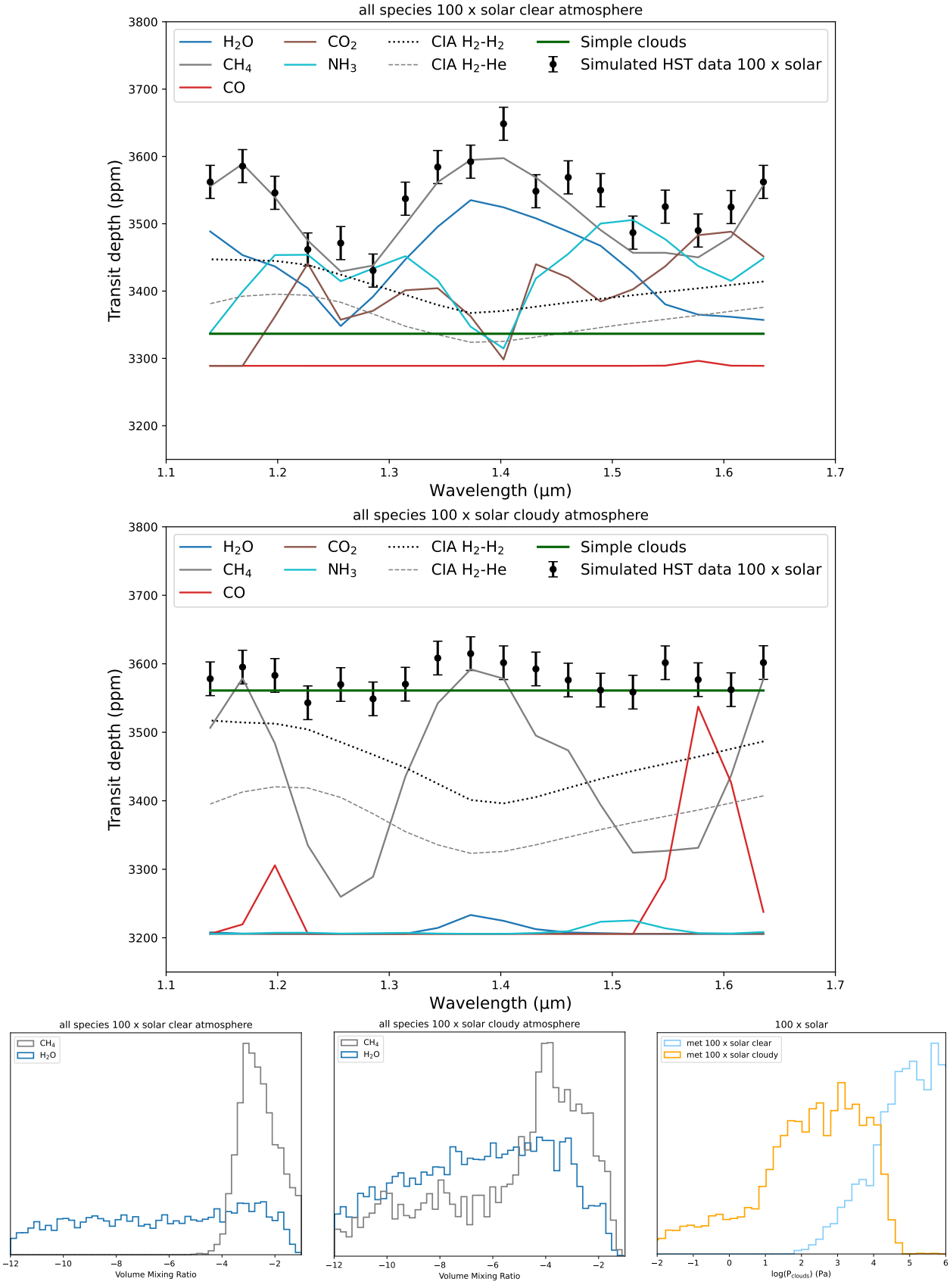

Figure 9.7: Results of the retrieval analysis on HST simulated data with CH_4 included as the main contributor and five transits observations.

9.3.5 JWST's contribution to the detection of methane

We created three JWST transmission spectra of LTT 3780 c based on the 100 × solar atmospheric composition simulations from `Exo-REM`: a clear atmosphere with 13 absorbing species (CH_4 being the main spectral contributor), a cloudy atmosphere, and a H_2O only atmosphere. As in Section 9.2.2, we used `Pandexo` and combined two instruments of the JWST. The observations are performed assuming one transit of NIRISS SOSS and one transit of NIRSpec G395H. We did not add scattering noise to the spectra and binned down the spectrum to an R∼100 resolution as in Section 9.2.2. Table 9.6 summarises the JWST instrumental setups for the NRISS and NIRSpec observations. Figure 9.8 presents the opacity contributions to the transmission spectrum of LTT 3780 c in the combined NIRISS and NIRSpec wavelength range (0.8 to 5 µm) for a clear atmosphere with a metallicity of 100 × solar. The total transmission spectrum is in a thin black dotted line. The grey line is the CH_4 absorptions, dominating the entire transmission spectrum above 1 µm. We note several broad absorptions features at 0.9, 1.0, 1.2, 1.4, 1.7, 2.3 and 3.4 µm. Probing a wider wavelength range will help identify the main spectral contributor.

Table 9.6: JWST instrumental setups from Pandexo (Batalha et al., 2017) simulations.

Parameter	NIRISS	NIRSpec
Aperture	SOSS	s1600a1
Mode	SOSS	BOTS
Disperser	GR700xd	G395H
Subarray	substrip96	sub2048
Filter	clear	f290lp
Spectral coverage (µm)	0.83-2.81	2.87-5.18
Exposure time (s)	7217.1	8574.8
Saturation level (e^-)	57600	52000
Number groups	7	3
In transit integration	407	1787.0
Out of Transit integration	407	1787.0
Observations duration (hrs)	4.01	3.58

We then perform a mock retrieval analysis on the three simulated spectra using the same parametrisation as in Section 9.3.4. We aim to show that CH_4 is the main spectral contributor in the clear and cloudy configuration and show it is easily distinguishable from H_2O absorption. Figure 9.9 presents the best-fit retrieval results for the three simulated spectra. We represent the best-fit opacity contributions to the spectra for the three configurations. First, CH_4 is the main spectral contributor for the clear and cloudy scenarios, including all the species (see the top and middle panels). The Bayesian code identifies the cloudy scenario and the best-fit model includes a cloud deck (green line) to adjust the CH_4 spectral signatures. The best-fit model also includes CO and CO_2 broad absorptions features at 4 and 4.5 µm that the model predicts (see Figure 9.8). We could retrieve the correct opacity contributions and differentiate CH_4 from H_2O. In particular, we find the broad absorption features of CH_4 identified in Figure 9.8 and the 1.4 µm is attributed to CH_4. In the case of a H_2O only clear atmosphere, all the spectral features are easily identified and attributed to H_2O absorptions. We note that the best-fit model includes weak absorption features of CH_4, CO, CO_2, likely due to the simulated spectrum's uncertainties. We compute the Bayes factor of the atmospheric model with a flat line. It is over 27 for the clear atmospheric models and reaches 6 for the cloudy model. Using only one transit of NIRISS combined with one transit of NIRSpec allows identifying with high confidence the opacity source, even in a cloudy configuration.

The opacity contributions are accurately derived, but what about the retrieved values of the molecular abundances? We over-plot in Figure 9.10 the retrieved VMR profiles and the initial simulated

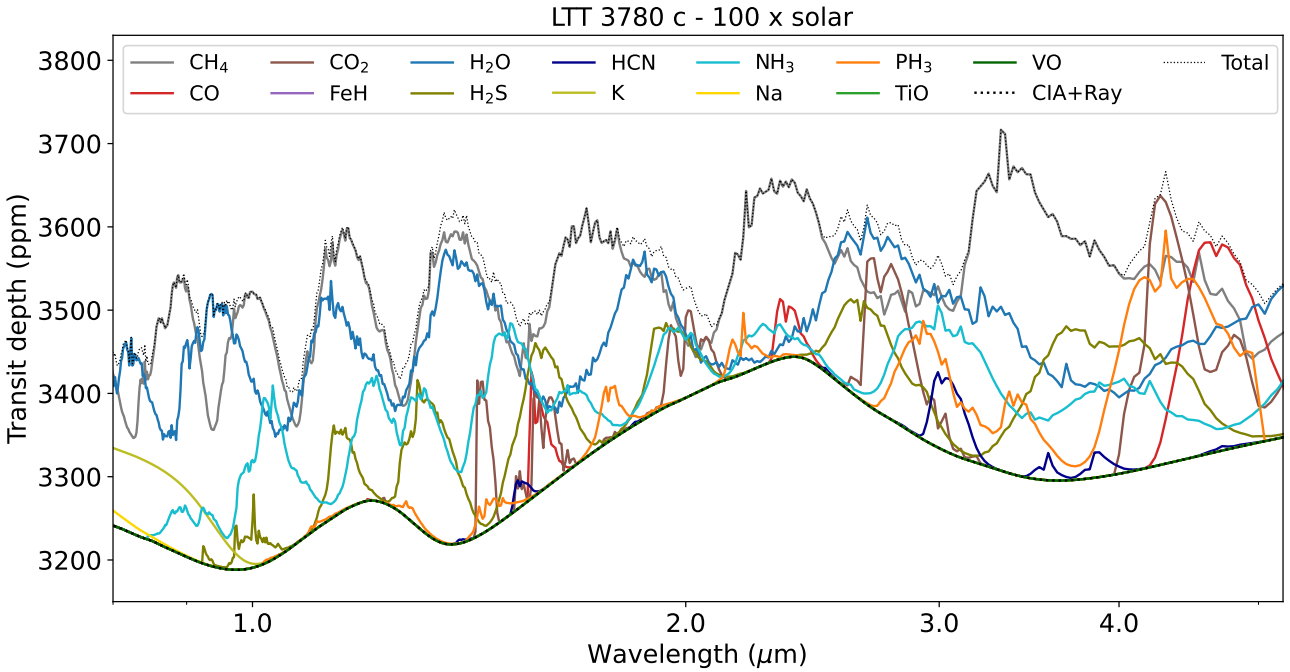

Figure 9.8: Opacity contributions to the transmission spectrum of LTT 3780 c in the wavelength range covered by a combination of JWST NIRISS and NIRSPec. The simulation is from `Exo-REM` computations for a cloud-free atmosphere with a 100 × solar atmospheric composition. CH_4 spectral features dominate the transmission spectrum above 1 µm with the strongest line around 3.5 µm.

profiles from `Exo-REM`. We separate the plot in two for the cloudy retrieval analysis for clarity. The abundances are over-estimated by the retrieval analysis for clear atmospheric scenarios (see top panels). Only the abundance of NH_3, CO_2 and CH_4 is in the uncertainty ranges for the cloudy retrieval analysis. Last, we represent in Figure 9.11 a comparison of the posterior retrieval distributions for the HST WFC3 G141 simulated transmission spectrum with five observations (blue) and the JWST transmission spectrum using NIRISS and NIRSpec (green). We indicate retrieved values for the retrieval of JWST data. As expected, the quantities are better constrained with JWST simulation than for HST. We scattered the HST spectrum by adding Gaussian noise, reinforcing the difference with the unscattered JWST spectrum. The abundance of CH_4 is constrained to both cases, which is the main goal of this study. We find $\log(CH_4) = -2.02^{+0.24}_{-0.64}$ with JWST simulation, which is not the ground truth. We binned down the spectrum to a lower resolution than the instrumental one, which might cause the difference. Keeping the instrumental resolution is probably a better strategy. We recognise that using only one transit of NIRISS and one transit NIRSpec is less costly than five observations with HST. By probing a wider wavelength range, the JWST can identify the main spectral contributor and distinguish H_2O from CH_4 absorption. However, we note that HST is also capable of such observations and must not be forgotten for the benefit of the JWST, which will only ever experience an increase in pressure for observation time.

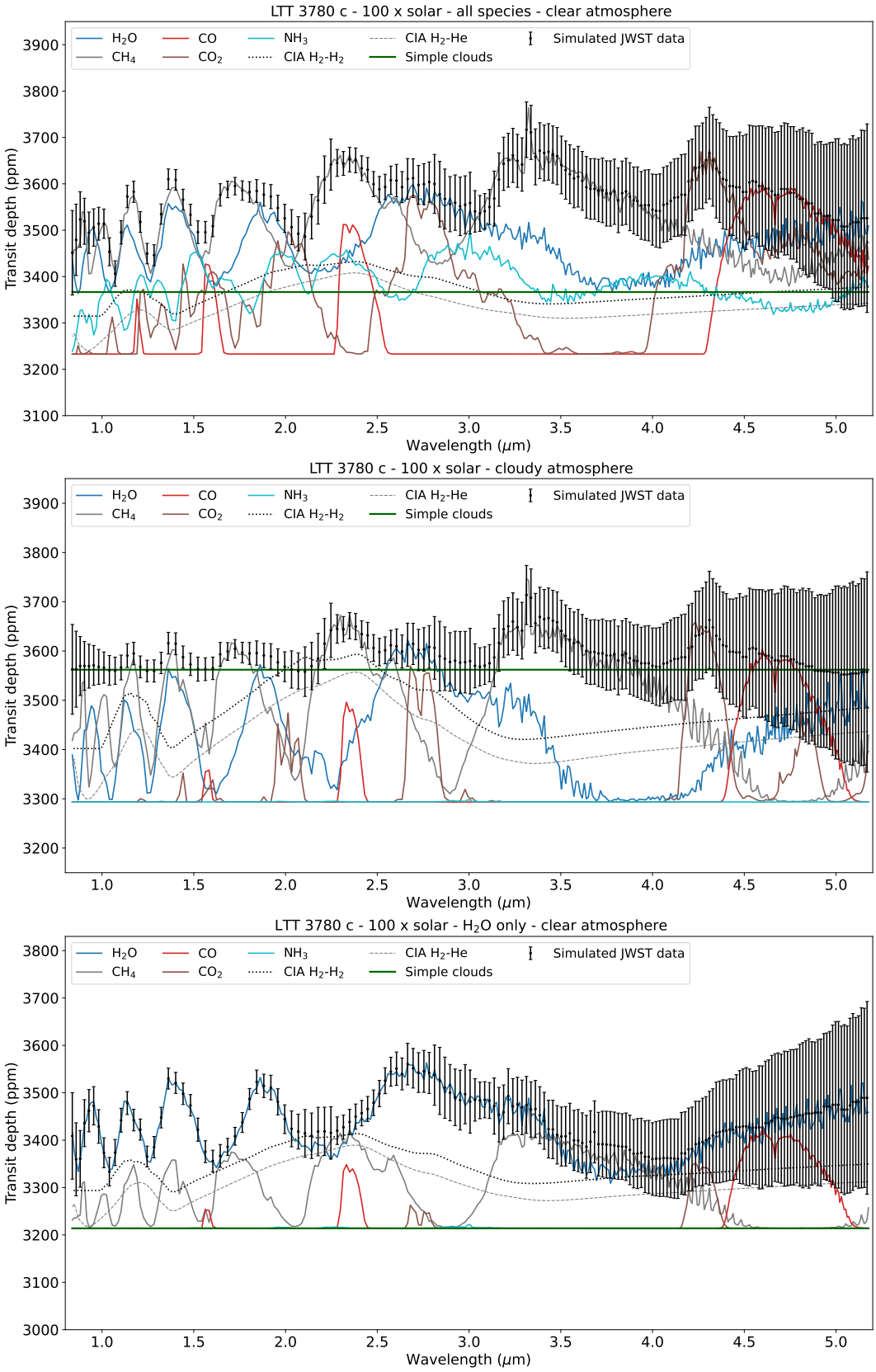

Figure 9.9: Best-fit opacity contributions to the JWST simulated transmission spectra of LTT 3780 c. We use `Pandexo` for the JWST observations based on `Exo-REM` simulations assuming a 100 × solar atmospheric composition for a clear atmosphere (top), a cloudy atmosphere (middle) and a H_2O only atmosphere (bottom). The mock retrieval analysis is performed with `Tau-REX 3`.

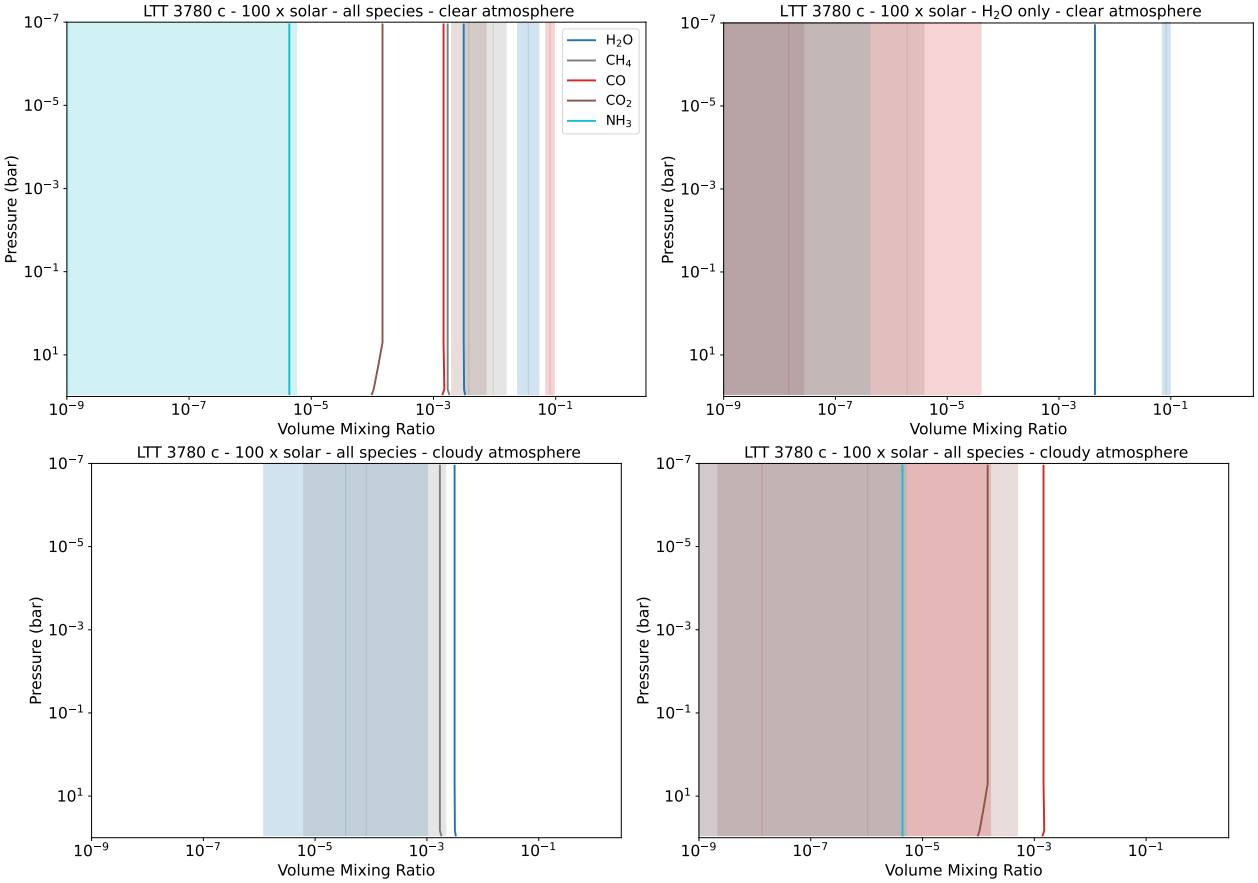

Figure 9.10: Best-fit retrieved molecular abundances profiles (shaded) and simulated profiles from the 100 × solar atmospheric composition LTT 3780 c simulations from `Exo-REM` (thick solid line). We separate the plot in two for the cloudy retrieval analysis for clarity.

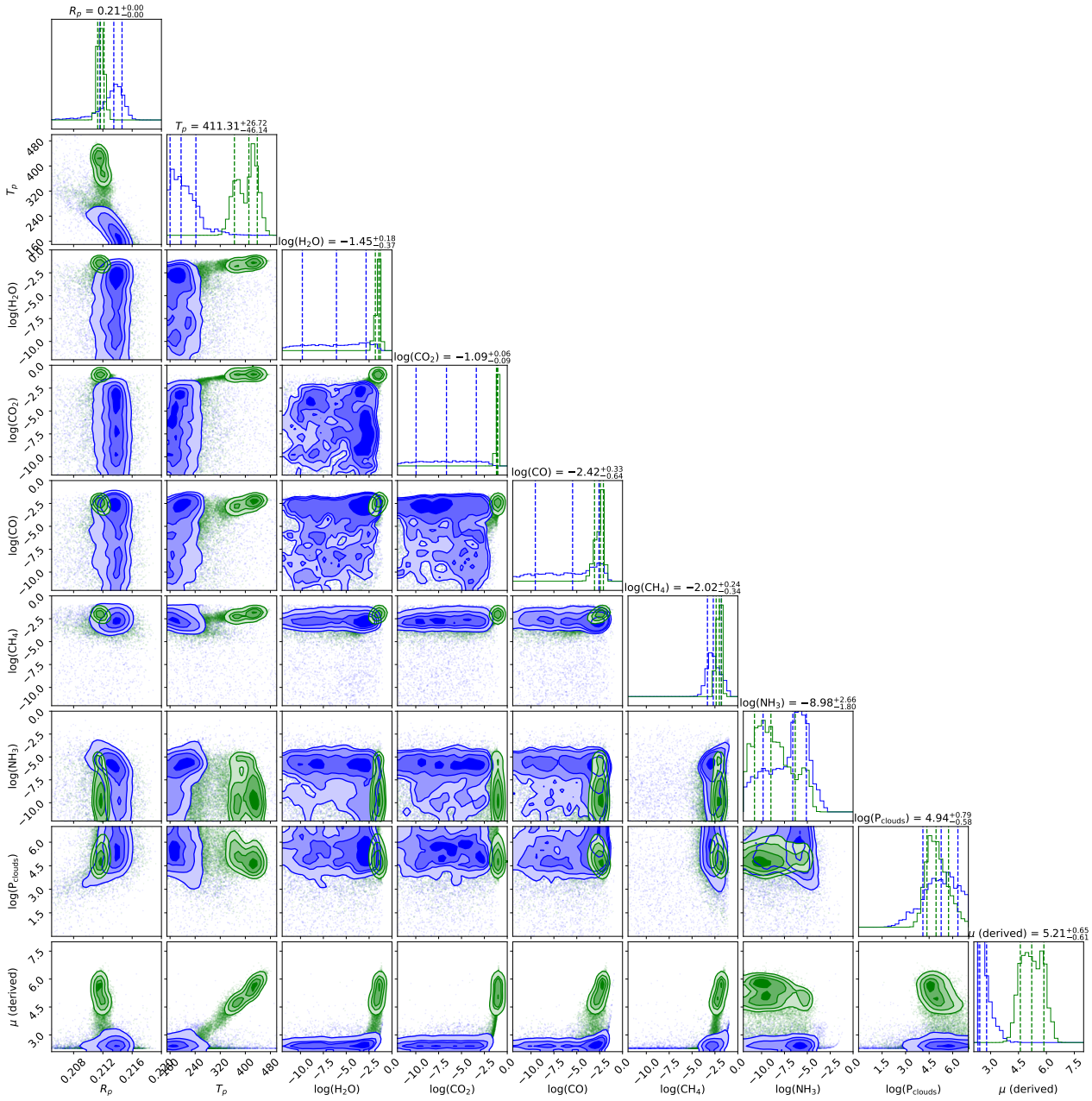

Figure 9.11: Posteriors distributions for the HST simulations with five transits of the WFC3 G141 (blue) and the JWST simulation with one transit of NIRISS and one transit of NIRSpec (green). The spectra are created based on the `Exo-REM` simulation of LTT 3780 c for 100 × solar clear atmosphere.

9.4 Conclusion

With no equivalent in the Solar-System, Sub-Neptunes and Super-Earths are the most numerous categories of planets discovered so far. However, our understanding of their composition remains incomplete, particularly clouds and hazes condensations. The unexpected depletion of methane in close-in atmospheres is still challenging to explain. Temperate to warm Sub-Neptunes, with an extended atmosphere orbiting nearby bright stars, are excellent targets for transmission spectroscopy. In anticipation of JWST observations of these targets, it is essential to perform atmospheric reconnaissance with the HST and discriminate between a clear primary atmosphere and a cloudy or hazy one, for which no molecular absorbers can be detected. In the case of a clear atmosphere, it is also crucial to determine which molecule is causing the detected feature to constrain formation and evolution models better. It is still unclear whether water or methane should dominate the spectrum around 1.4 µm in the HST WFC3 G141 wavelength range (1.1-1.65 µm) for cool planets.

We simulated JWST and ARIEL observations on HAT-P-11 b using three models based on the best-fit retrieval analysis. We combined one transit of NIRISS and one transit of NIRSpec, providing a 0.8 to 5 µm wavelength coverage, and simulated one, five and ten ARIEL transits observations for coverage of 0.5 to 8 µm. Using five transits observation of ARIEL, we can differentiate a primary cloudy atmosphere from heavier atmospheric scenarios. One transit of NIRISS combined with one transit of NIRSpec (0.8 to 5 µm) will allow us to reach the same conclusion. In-depth atmospheric characterisation using the JWST and ARIEL will dispel ambiguities for Sub-Neptunes and Super-Earths.

We address the question of the detectability of CH_4 and its differentiation with H_2O in a transmission spectrum using the example of the warm Sub-Neptune LTT 3780 c. This planet has not been observed yet, but it orbits a bright cool star and is perfect for transmission spectroscopy. We compared HST and JWST abilities to observe the atmosphere and distinguish H_2O from CH_4 absorption. We simulated its atmosphere using `Exo-REM` and chose to fix the solar atmospheric composition to 100 × solar so that CH_4 features dominate the transmission spectrum. We included 13 absorbing species and allowed for out-of-equilibrium chemistry. We simulated a cloudy configuration using KCl condensation. Using three and five observations of HST WFC3, we can differentiate CH_4 from H_2O with 3 and 5-σ. Only one transit of NIRISS combined with one transit of NIRSpec is enough to reach a similar goal. An interesting test would be to use only one mode of the JWST. This study is the first step in addressing JWST's abilities to observe warm to temperate Sub-Neptune atmospheres. Many areas for improvement in modelling and adjustment have to be taken into account. We acknowledge that we simulated the atmosphere of this planet, making critical assumptions that, if false, change the result. We list them below.

- **Atmospheric composition**: we assumed a 100 × solar metallicity to prove that we can detect CH_4 in a Sub-Neptune atmosphere. However, we note that Sub-Neptunes might possess a heavier atmosphere (300 × solar); in that case, H_2O features dominate the transmission spectrum. We did not explore the C/O ratio dimension, which could greatly impact the abundance of H_2O, CO, CO_2 and CH_4.
- **Photochemistry**: close-in Sub-Neptunes are irradiated by the host star causing CH_4 photodissociation. Photochemistry was not considered in our simulation and might change the predicted abundances. The layers probed by HST and JWST might not be impacted by photodissociation. However, 10^{-1} bar is the radiative-convective limit that UV radiation could reach.
- **Stellar activity**: if the host star is active, this can impact our abilities to identify spectral features. This was not modelled nor retrieved.
- **Binning**: We binned down NIRISS and NIRSpec simulated observations to obtain an R∼100

transmission spectrum similar to JWST NIRSpec PRISM resolution. Binning down JWST data turns out not to be the best strategy. We lose information on species transitions, which might provide us from retrieving accurate abundance values.

- **Noise**: We need to model and add scattering noise to JWST spectra. We performed the retrieval analysis without scattering noise to compare ARIEL and JWST performances. However, additional noise will alter the retrieval results.
- **Temperature-pressure profile**: we use an isothermal temperature-pressure profile in the retrieval analysis; our simulations do not. Whilst not an issue for HST observations because we probe a narrow region of the atmosphere, this might become important for JWST observations. We could implement a 4 points T/P profile in the retrieval analysis.
- **Line-lists**: In order to correctly retrieve species opacity contribution, we need to have updated line-lists, especially if we use JWST instrumental resolution.

Conclusion and Perspectives

In August 2022, the JWST Transiting Exoplanet Community Early Release Science Team revealed carbon dioxide detection in the atmosphere of the gas giant WASP-39 b (The JWST Transiting Exoplanet Community Early Release Science Team et al., 2022), proving the outstanding capabilities of the James Webb Space Telescope in characterising exoplanets atmosphere. JWST provides spectroscopy from optical to infrared (0.6 to 28 µm) with an unprecedented signal-to-noise and wavelength coverage. As we explore this new range of possibilities with JWST, and as new data become available in the coming years, we have presented in this manuscript what Hubble's transit spectroscopy observations tell us about the atmosphere of exoplanets. It focuses on developing methods to move from the study of a single dataset to the statistical study of a population of planets. We want to take stock of what Hubble taught us on atmospheric results and data processing before embarking on JWST and ARIEL data analysis. We hold a special focus on intermediate-size planets (1 to 4 $R_\oplus$), having no equivalent in our Solar-System, they remain challenging to characterise. Their occurrence rate forms a bimodal, with a noticeable gap in the number of planets around $1.7R_\oplus$ (Fulton et al., 2017), suggesting that dominant planetary formation or evolution processes shape the nature of this population.

We first analysed hot-Jupiters' upper atmosphere and their possible photo-evaporation using Hubble observations in the near ultra-violet (NUV). As a result, we have developed a tool to correct and fit transits light curves observed with the Space Telescope Imaging Spectrograph (STIS). This tool is not only intended for the analysis of data from hot-Jupiters, but also for investigating data from smaller planets such as the Super-Earth 55 Cnc e, for which we present the results of a preliminary analysis. Furthermore, we found an increase in the short-wavelength transit depth in the observations of the planets WASP-121 b and WASP-79 b. While the data for WASP-121 b have already been published, the analysis of the two transiting observations of WASP-79 b is an unprecedented study. We confirmed the photo-evaporation of WASP-121 b first seen in Sing et al. (2019). Additionally, we find a 4.5-σ difference in the planet-to-star radius ratio between optical and NUV in WASP-79 b data. This apparent rise of the planetary radius reaches 75% of the Roche lobe equivalent radius; however, this NUV's excess of absorption corresponds to 20 scale height, making it one of the largest spectral features observed in an exoplanet at this temperature.

Comparing this absorption, in terms of scale height, with three hot-Jupiters led to the discovery that the transmission spectrum reaches a similar level of absorption to SiO in WASP-178 b's atmosphere (Lothringer et al., 2022). None of the known metallic absorption lines matches our NUV transmission spectrum, but SiO's condensation could explain our observations. This result challenges (Lothringer et al., 2022)'s conclusion on SiO's condensation temperature range: 1950 to 2450 K. Further observations of WASP-79 b atmosphere in UV are required to understand this absorption better and rule out possible remaining untreated systematics. Combining the present HST STIS measurements with WFC3 UVIS observations could be an excellent strategy to confirm the rise of transit depth and SiO absorption.

The analysis of the 55 Cnc e data is an extension of the precedent work in a different regime (i.e. small planets) and, therefore, subject to unexpected difficulties. 55 Cnc e, is poorly understood, with variability in its IR and visible occultations and phase curves. There are also hints of variations in visible spectroscopic signatures. UV transit variations would thus not be surprising. However, our first analysis of 55 Cnc e STIS led to unexpected large transit depths in the NUV that is not yet confirmed nor interpreted. Follow-up analysis and tests are planned to understand this preliminary result better.

Observing in the optical and UV, below 0.6 µm, is only possible from space with Hubble. What will happen when Hubble is no longer operating? Ground-based observations at high resolution are a solution. However, they will have to be improved, as until now, it is still hard to estimate the uncertainties in the presence of residual correlated noise (Jordán et al., 2013; Beatty et al., 2017a).

We then study hot Sub-Neptune to temperate terrestrial planets, focusing on deeper regions of the atmosphere using Hubble near-infrared observations. We detailed three projects going from single target analysis to studying a population of planets with Hubble Wide Field Camera 3 grism 141 (HST WFC3 G141). For consistency, we used two softwares : `iraclis` (Tsiaras et al., 2016a,b, 2018) for the extraction, reduction and fitting of the white and spectral light curves, and `Tau-REx 3` (Waldmann et al., 2015b,a; Al-Refaie et al., 2021), a Bayesian code, for the atmospheric retrieval interpretations of the transmission spectra.

We first characterise the atmosphere of two Neptune-like planets, HD 106315 c and HD 3167 c. The near-infrared spectrum centred around 1.4 µm of these planets is fitted with water vapour. Hints of ammonia are revealed for the first planet, while carbon dioxide is also found in the atmosphere of the second planet. The latter is unexpected, but similar features are found in an independent study (Mikal-Evans et al., 2020). The most striking result is not the molecular detection, proving hard to interpret, but the size of the spectral features. We introduced in this chapter the Bayes factor (difference of Bayesian logarithm evidence) $\Delta\log(E)$ between the atmospheric model and a flat line. This quantity is used to assess the significance of atmospheric detection. We prove an atmosphere around these planets with more than 3-σ for HD 3167 c and 5-σ for HD 106315 c, as high as for hot-Jupiters. At the time of publication, only a handful of similar Sub-Neptune atmospheres have been analysed using HST WFC3 G141, leading to flat transmission spectra in some cases. These two detections were thus promising for Sub-Neptune atmospheric characterisation and motivated the Hubble transmission survey carried out later.

The second project is the individual analysis of the last planet of the well-known TRAPPIST-1 system. We provide the first constraint on the atmosphere of TRAPPIST-1 h by analysing three transits observations made with the HST WFC3. Analysing a smaller planet observation requires meticulous care in the reduction and fitting process. We found an increase of transit depth around 1.3 µm for all three observations. This was not explained by atmospheric modelling nor by stellar activity models. However, TRAPPIST-1 is a very cold M-dwarf, and many unknowns remain concerning its activity. Only a consistent photometric monitoring of the star throughout the planetary transits could help disentangle an atmospheric signal from stellar activity. While it remains difficult to prove the presence of an atmosphere around this planet, we can already state that it is not made up of hydrogen and helium. We compared atmospheric models and ruled out a clear primary atmosphere hypothesis. Similar conclusions were reached in an independent analysis of the same dataset by Garcia et al. (2022).

Last, we performed a large sample study. This work is the first small planets survey using Hubble observations. Twenty-six HST transmission spectra are consistently analysed to explore the transition from Super-Earth to Sub-Neptune. We confirm the detection of an atmosphere for 13 planets whose

radius is larger than $1.7 R_{\oplus}$, the limit set to distinguish rocky from gaseous planets. We used `Tau-REx 3` to design retrieval models and infer atmospheric properties. Our main goals are :

- prove the presence of an atmosphere through the identification of molecular spectral features
- distinguish a primary atmosphere (1× solar, 2.33 g/mol) from higher metallicities atmospheres
- assess the cloudiness of the atmosphere

Bayesian retrieval analysis converges towards a model of a hydrogen-dominated atmosphere without clouds for four planets: 55 Cnc e, HAT-P-26 b, LHS 1140 b and LTT 9779 b. We provide the first catalogue of molecular detection for Super-Earths and Sub-Neptunes in the near-infrared. To do that, we proposed a model comparison method. We remove species from the model and examine whether the loss of fit quality is significant. We confirmed the detection of water vapour for nine planets. However, once a molecule is detected, its abundance is poorly constrained, leading to degeneracies in the molecular abundances and the pressure level of the cloud layer. Eight of 13 transmission spectra with significant spectral signatures have a degenerate solution. The fit requires either an opaque cloud layer to cut off the molecular spectral signatures or heavy elements to adjust the size of the observed atmospheric signatures.

In this study, we spanned a large parameter space. We consistently analysed planets with very different characteristics (density, temperature, stellar environment). We wanted to use all the available Hubble data before James Webb's first observations to acknowledge what could be done and improve observation strategies. We acknowledge that the diversity of planets observed in this sample is a weakness of our study. Each planet has its complexity. For example, TOI-674 b and LTT 9779 b are planets located in the desert of hot Neptunes, making them very particular planets. We were looking to set up methods to analyse a larger sample of planets and answer basic questions about their atmosphere, like their cloudiness or the presence of water vapour.

Following Hubble observations results on warm Sub-Neptune atmospheres, we model and simulate observations for this type of planet. Although HST observations give us valuable initial information about their atmosphere, the limits of interpretation are quickly reached. Our study has revealed numerous degeneracies in the Bayesian analysis of the transmission spectra. The last part of the thesis attempts to break these degeneracies using self-consistent computations (first chapter) and JWST and ARIEL simulations (second chapter). We focus our modelling on two main points: the impact of cloud sedimentation on the transmission spectrum and the nature of carbon and oxygen-bearing species using a self-consistent radiative-convective model `Exo-REM`. We built a grid of models with three main dimensions: the temperature, the atmospheric metallicity and the cloudiness of the atmosphere.

First, we explored the atmospheric composition depending on the metallicity of the atmosphere. Even though H_2O is the most abundant species, CH_4 remains the main contributor for temperate to warm Sub-Neptunes with low atmospheric metallicity atmosphere. However, the retrieval analysis of the warm Sub-Neptune transmission spectra suggested the presence of H_2O at 1.4 µm in different atmospheric configurations. The apparent lack of methane is striking in particular for K2-18 b, TOI-270 d and LHS-1140 b whose retrieved and equilibrium temperatures are below 400 K and the retrieval analysis suggests a 1 to 10 × solar atmospheric metallicity. HD 3167 c transmission spectrum analysis includes H_2O and CO_2 absorption at 500 K for a 10 × solar metallicity. Both of these detections are unexpected in this configuration. Taking into account the uncertainties on the retrieved parameters, H_2O is easily formed at slightly higher temperatures and metallicity while CO_2 detection remains challenging to interpret in this Sub-Neptune atmosphere.

Then, we tested the presence and the impact of radiative clouds in the atmosphere of Sub-Neptunes using self-consistent computations of KCl and Na_2S condensations. We used the size of the water feature, around 1.4 µm, as a metric to compare observations and simulations. Using a more accurate parameterisation of clouds, we refined their nature in Sub-Neptune atmospheres. In particular, we proved that KCl clouds could be present in the atmosphere of HAT-P-11 b and HD 97658 b while Na_2S could condensate in HD 219666 b atmosphere. Photochemical hazes, not included in `Exo-REM`, are probably present in the atmosphere of GJ 1214 b, K2-24 b, TOI-270 c, GJ 436 b and GJ 1132 b and thus would explain the very low observed amplitudes.

While the modelling grid reproduces some of the results of the retrieval analysis and gives more information on the cloud coverage for Sub-Neptunes, there are some inconsistencies between HST observations and the models. We noted the absence of CH_4 spectral contributions and very low spectral features for warm Sub-Neptune not explained by clouds condensation. These discrepancies might be explained by the variety of planets chosen in the sample and the presence of a rocky surface not considered in the grid. The lack of methane detection is surprising and could be explained by a low C/O ratio or a strong chemical disequilibrium with high temperatures deep in the atmosphere. We did not explore the C/O ratio dimension in our modelling grid, and its likely strong impact on the main molecules' abundances will have to be investigated. The C/O ratio and the metallicity can not be constrained using HST WFC3 wavelength coverage as we are trying to fit several parameters with only the 1.4 µm atmospheric features size. Thus, we focused only on the weight of the atmosphere to build the grid and compare observations and modelling.

The CH_4 molecule, along with NH_3, is highly sensitive to photochemistry and could also be destroyed in the upper layers of irradiated atmospheres. They are easily photodissociated to form haze precursors, but this chain of reactions is not yet implemented in `Exo-REM`. The presence of clouds and hazes in Sub-Neptune modify the transmission spectra in a way we did not reproduce here and could explain some unexpected results, particularly warm Sub-Neptune flat transmission spectra. 2D and 3D effects are also important parameters in the formation of clouds. We showed that the condensation of H_2O on the night side and the evaporation on the day side could happen for a warm Sub-Neptune (500 K). Last, we build a grid using HD 3167 c stellar and planetary parameters; thus, the gravity is fixed to 10 m/s^2. This parameter should be varied in an improved version of the grid.

To determine the impact of optical observations on the distinction between the clear and cloudy atmosphere, we proposed and obtained CHEOPS observations during the AO-3 campaign. We showed that it is possible to use the CHEOPS photometric data point to improve the characterisation of the atmosphere. The early analysis of CHEOPS observations on HD 219666 b are combined with HST observations, and we refine this planet's parameters and atmospheric characteristics. We concluded in a cloud-free light (1 to 100 × solar) atmospheric composition. Moving from the study of a target to a planet population, we could use CHEOPS archive data to perform a large sample atmospheric reconnaissance. HD 219666 b could be included in a broader study, using previous measurements of CHEOPS on other Sub-Neptunes that populate the Radius Valley (Fulton et al., 2017) and span a more comprehensive temperature range to assess the cloudiness of these planets. We could then test the first hypothesis of (Crossfield & Kreidberg, 2017) on the apparition of hazes with temperature.

Finally, we simulate JWST and ARIEL observations for Sub-Neptune atmospheres to address two questions: Can we distinguish a clear from a cloudy atmosphere? Can we detect CH_4 in a Sub-Neptune with HST? What about JWST? We used HAT-P-11 b as an example to address the first question. Using HST transmission spectrum best-fit results, we simulated the atmosphere with `Tau-REX 3` in forward

mode. We combined one transit of NIRISS SOSS and one transit of NIRSpec G395H, providing a 0.8 to 5 µm wavelength coverage, and simulated one, five and ten ARIEL transits observations for coverage of 0.5 to 8 µm. Using five transits observation of ARIEL, we can differentiate a primary cloudy atmosphere from heavier atmospheric scenarios. One transit of NIRISS SOSS combined with one transit of NIRSpec G395H will allow us to reach the same conclusion. This simulation was done for a single target. It should be extended to a carefully chosen sample of planets to test the impact of the planetary size, density, temperature, and stellar parameters.

We address the question of the detectability of CH_4 and its differentiation with H_2O in a transmission spectrum using the example of the Sub-Neptune LTT 3780 c. This planet is a "warm K2-18 b" and perfect for detecting atmospheric features while avoiding H_2O condensation. We showed that three to five transits of HST WFC3 G141 are enough to differentiate CH_4 with H_2O. On the other hand, JWST is perfectly designed to distinguish among carbon-bearing species in the NIR and could reveal the first methane detection. Combining NIRISS SOSS and NIRSpec G395H seems to be the most appropriate strategy.

The correct use and interpretation of the JWST data are the next prescient challenges for characterising the atmosphere of exoplanets. We have shown the limitations of Hubble (1.1-1.7 µm), particularly in analysing intermediate-sized planet's atmospheres, are ubiquitous in the galaxy, yet so poorly understood. However, the results of this thesis show that synergy between the instruments is possible and crucial. JWST will not be able to observe all exoplanets. HST, in this sense, is crucial. It allows a first atmospheric reconnaissance and determines whether the planet has an atmosphere, whether a cloud cover blocks the signal, and whether there is water vapour (or methane!). HST has also taught us about systematic effects in the raw data and how to deal with them. This point is essential in dealing with unexpected noise sources in JWST raw data.

The exceptional quality of the JWST data is a boon for atmospheric characterisation, but it is also a source of immense motivation to improve the models. Rocky planets, water worlds, and planets dominated by carbon dioxide vapour are being observed with the JWST. Analysis of the transmission and emission spectra will require using spectral opacities and line-lists calculated for atmospheres not dominated by hydrogen and helium, particularly with the use of NIRISS SOSS and NIRSpec at high resolution. Besides, planets are in 3 dimensions, often tidally-locked, and we can no longer singularly rely on a 1D retrieval analysis and modelling. 3D effects are prominent for hot-Jupiter (Caldas et al., 2019; Pluriel et al., 2020a), but we also showed that clouds could condense on the night-side of a warm Sub-Neptune and evaporate on the day-side. In a broader view, clouds and hazes remain challenging to model and retrieve. Yet, condensation is predicted and strongly impacts the optical and the NIR transmission spectrum. Photochemical reactions and the production of hazes precursors are major processes to be addressed in predicting observables. NIRISS SOSS observations (0.83-2.81 µm) will be more impacted by condensation than NIRSpec (2.87-5.18 µm), and this has to be kept in mind while preparing observations. To identify carbon-bearing species and constrain the C/O ratio, NIRSpec is a brilliant option. NIRISS might be even better suited to study the cloud cover or identify water features in transmission. Whether or not we can probe and identify 3D effects with the JWST is a pending question. In this matter, the choice of the temperature-pressure profile in the retrieval analysis is essential.

An important point to address is the sampling of data. Binning down JWST high-resolution data (i.e. NIRISS SOSS or NIRSpec G235H/G395H) is probably not the best strategy. We lose information on species transitions, which might prevent us from retrieving accurate abundance.

If asked about the first essential matters regarding exoplanet atmospheres with the JWST, I will focus on the nature of intermediate-sized planets and water worlds' existence. The study of multi-planetary systems with several Sub-Neptunes and Super-Earth spanning a wide temperature range is of interest. This could be done using NIRSpec PRISM (J>10.5), which covers 0.6 to 5 µm at low-resolution R$\sim$ 100. Combining NIRISS SOSS and NIRSpec G395H is an alternative at high-resolution R$\sim$ 1000, providing even more information. Both of these strategies could break ambiguities: H_2O or CH_4? Cloudy or not cloudy? However, more importantly, it could constrain the atmosphere's C/O ratio and molecular weight and be directly linked to the formation process. These observation strategies are proposed through a prism of transit spectroscopy knowledge, but thermal emission and phase curves will also be valuable in answering these questions. Mainly, these two methods could prove the presence of an atmosphere for small rocky planets and better understand the atmosphere of planets in the hot-Neptunian desert. Additionally, the infrared detector MIRI is a good instrument for performing phase curves and thermal emission measurements of temperate planets.

Getting closer to the nature of Sub-Neptune might require observational surveys, which is possible with the JWST as the information can be obtained with a single transit. However, we must remember that ARIEL's purpose is to observe 1000 exoplanets and perform surveys. The JWST will surely transform the ARIEL mission, and synergies must, as of now, be considered.

List of Publications

1. **Near-infrared transmission spectrum of TRAPPIST-1 h using Hubble WFC3 G141 observations**
   A. Gressier, M. Mori, Q. Changeat, B. Edwards, J.P. Beaulieu, E. Marcq and B. Charnay
   Article published in Astronomy & Astrophysics Volume 658, id.A133, in February 2022
   DOI : https://doi.org/10.1051/0004-6361/202142140

2. **The Hubble PanCET Program: The near-UV transmission spectrum of WASP-79 b**
   A. Gressier et al.
   Article submitted in Astronomy & Astrophysics in July 2022

3. **Exploring the transition from Super-Earth to Sub-Neptune with a Hubble transmission survey**
   A. Gressier, Q. Changeat, B. Edwards, J.P. Beaulieu, B. Charnay and E. Marcq
   Article submitted in Astronomy & Astrophysics in August 2022

Published or Submitted paper as second author

1. **ARES IV: Probing the atmospheres of two warm small planets HD 106315 c and HD 3167 c with the HST/WFC3 Camera**
   G. Guilluy, A. Gressier et al.
   Article published in The Astronomical Journal Volume 161, Issue 1, id.19, in January 2021
   DOI : https://doi.org/10.3847/1538-3881/abc3c8

Published or Submitted paper as co-author

1. **ARES I: WASP-76 b, A Tale of Two HST Spectra**
   B. Edwards et al.
   Article published in the Astronomical Journal, Volume 160, Issue 1, id.8. in July 2020
   DOI : https://doi.org/10.3847/1538-3881/ab9225

2. **Characterizing the Hot Jupiters WASP-127 b, WASP-79 b, and WASP-62 b with the Hubble Space Telescope**
   N. Skaf et al.
   Article published in the Astronomical Journal, Volume 160, Issue 3, id.109 in September 2020
   DOI : https://doi.org/10.3847/1538-3881/ab94a3

3. **Unveiling the Two Faces of KELT-7 b with HST WFC3**
   W. Pluriel et al.
   Article published in Astronomical Journal, Volume 160, Issue 3, id.112 in September 2020
   DOI : https://doi.org/10.3847/1538-3881/aba000

4. **ARES V: No evidence for molecular absorption in HST WFC3 spectrum of GJ 1132 b**
   Mugnai et al.
   Article published in the Astronomical Journal, Volume 161, Issue 6, id.284, in June 2021
   DOI : https://doi.org/10.3847/1538-3881/abf3c3

List of Proposals

Accepted proposal as Principal Investigator

1. **The cloudiness of three warm sub-Neptunes**
   A. Gressier (PI), S. Ma, B. Edwards, K. H. Yip, Q. Changeat
   CHEOPS A-O3 observation program accepted proposal.

Accepted proposal as Co-Investigator

1. **Atmospheric Characterisation of A Disintegrating Planet in the hot-Neptune Desert**
   B. Edwards (PI) et al.
   HST Mid-Cycle 28 GO accepted proposal.

Rejected proposal

1. **Atmospheric charcaterisation of the warm Sub-Neptune LTT 3780 c** A. Gressier (PI), J.P. Beaulieu, B. Charnay, E. Marcq
   HST cycle 30 rejected proposal.

Appendix A

55-Cnc e correction contributions

This appendix presents the white light curve correction contributions of 55-Cnc e observations. Each figure corresponds to the EDPS jitter parameter polynomials (in dotted lines) included in the correction model for an observation. The normalised raw flux represented in colour data points is divided by other contributions: other parameters polynomials, transit model, and stellar baseline flux.

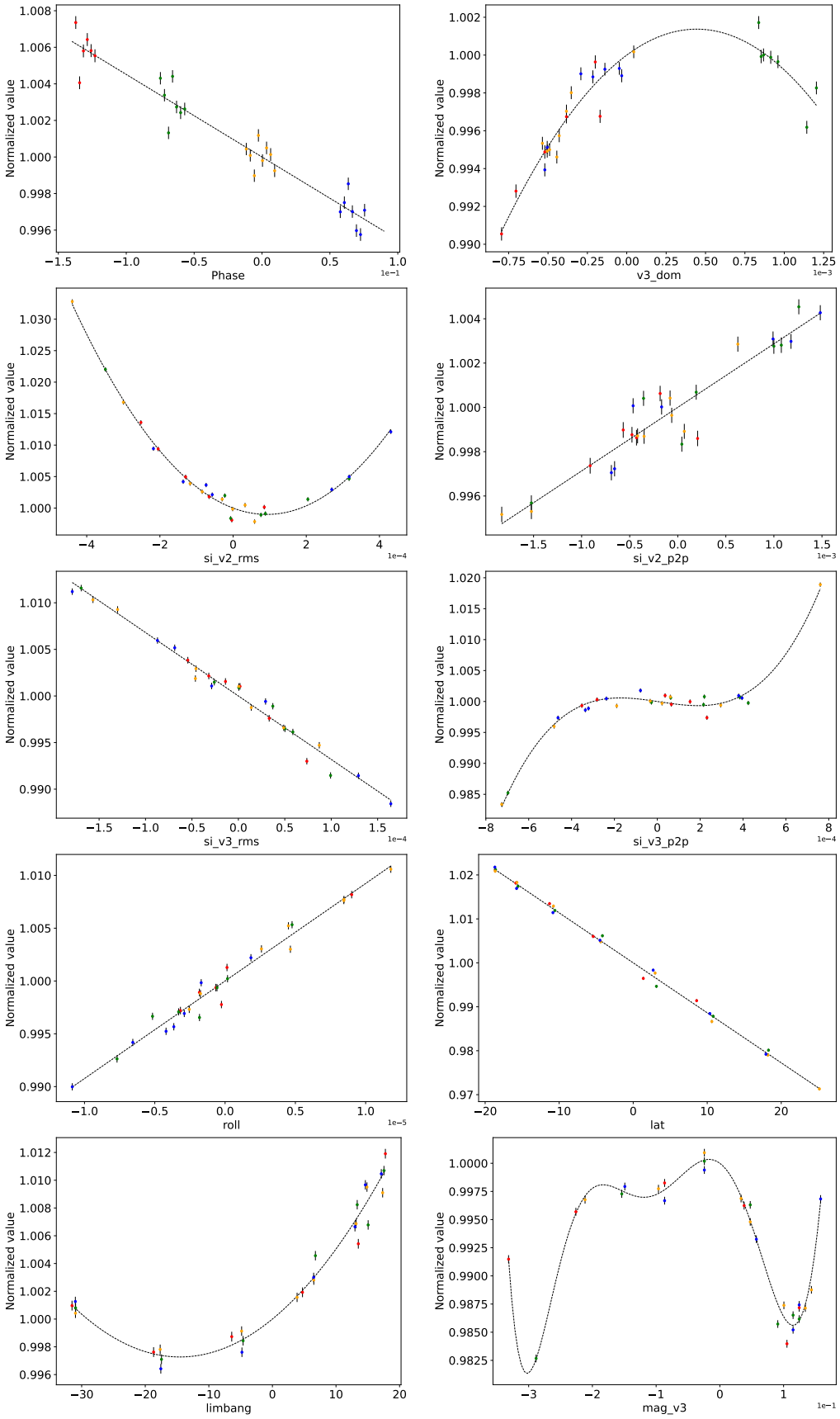

Figure A.1: Engineering jitter parameters polynomials included in the white light curve fitting of 55-Cnc e's first observations. We represent the normalised raw flux with respect to the jitter parameter. The raw flux is deprived of all other parameters.

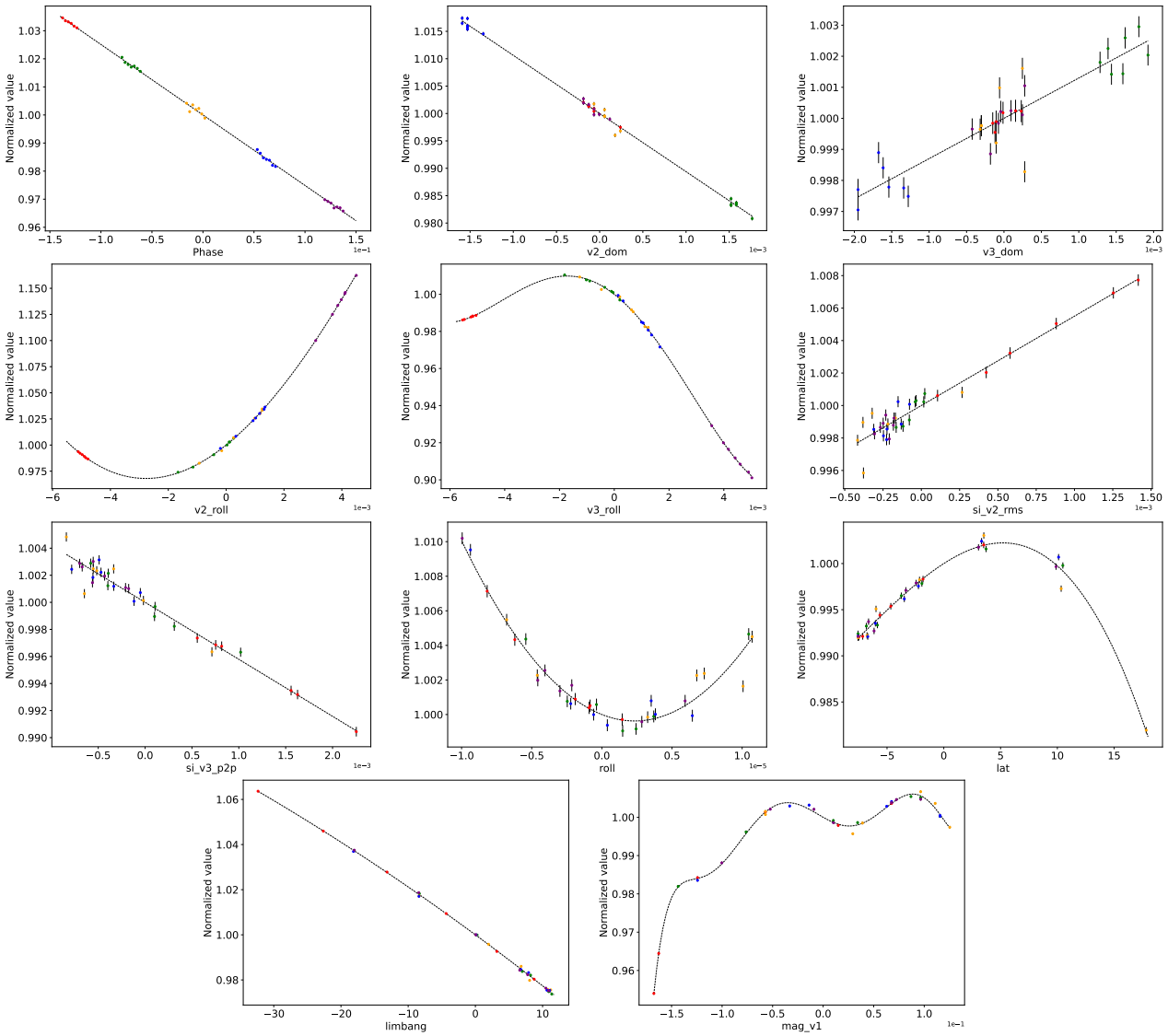

Figure A.2: Same as Figure A.1 for 55-Cnc e's second observation.

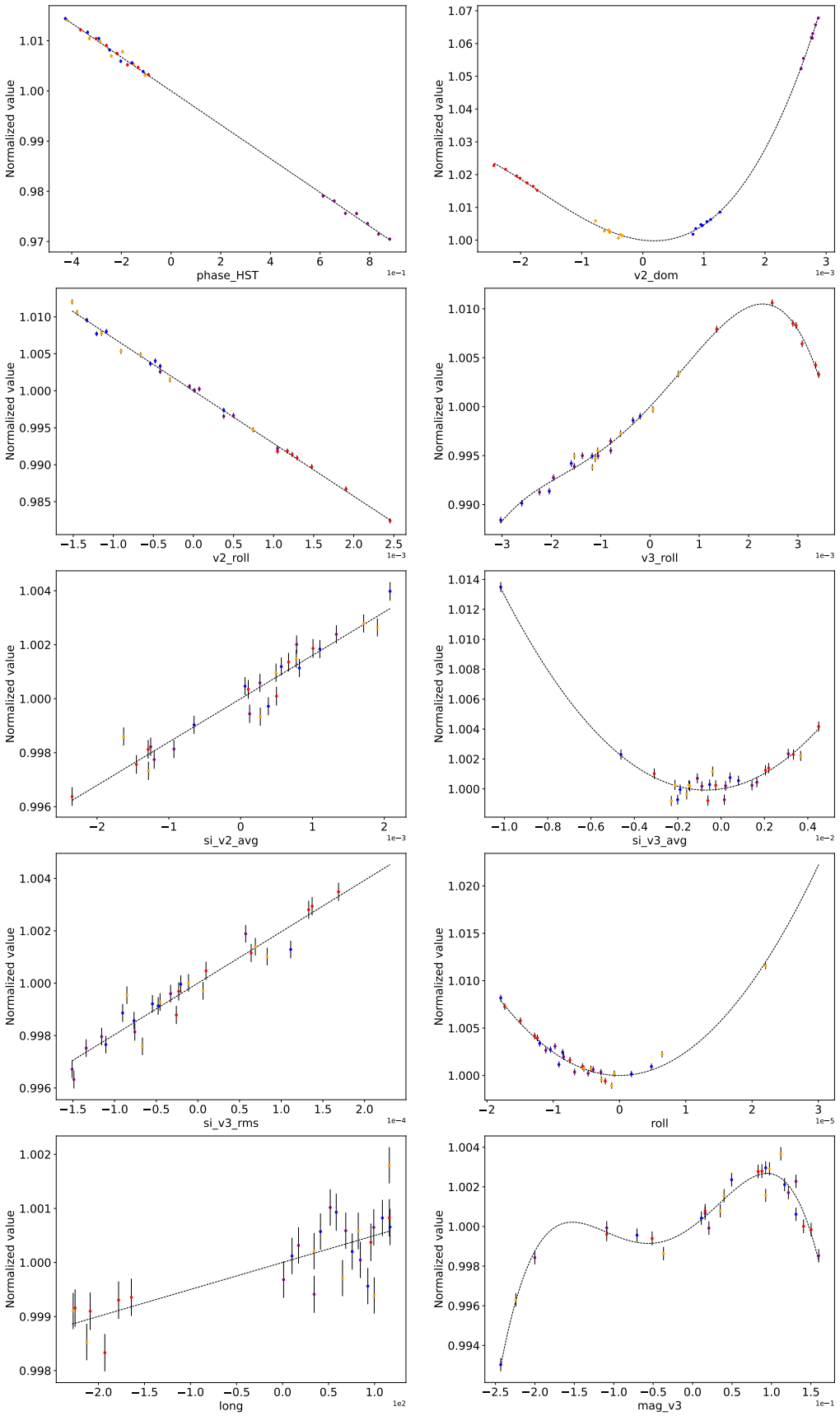

Figure A.3: Same as Figure A.1 for 55-Cnc e's third observation.

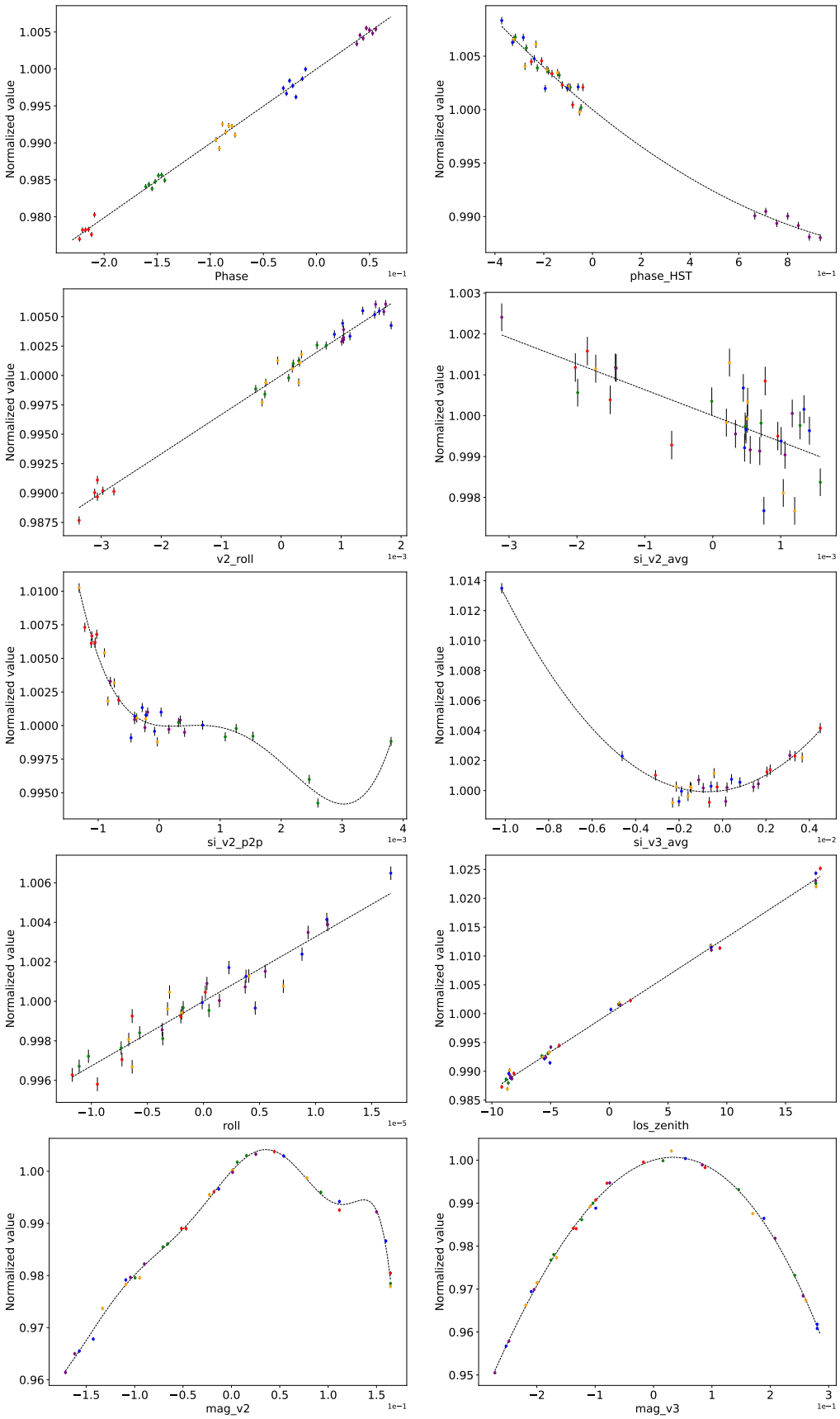

Figure A.4: Same as Figure A.1 for 55-Cnc e's fourth observation.

Appendix B

HD 106315 c and HD 3167 c supplementary materials

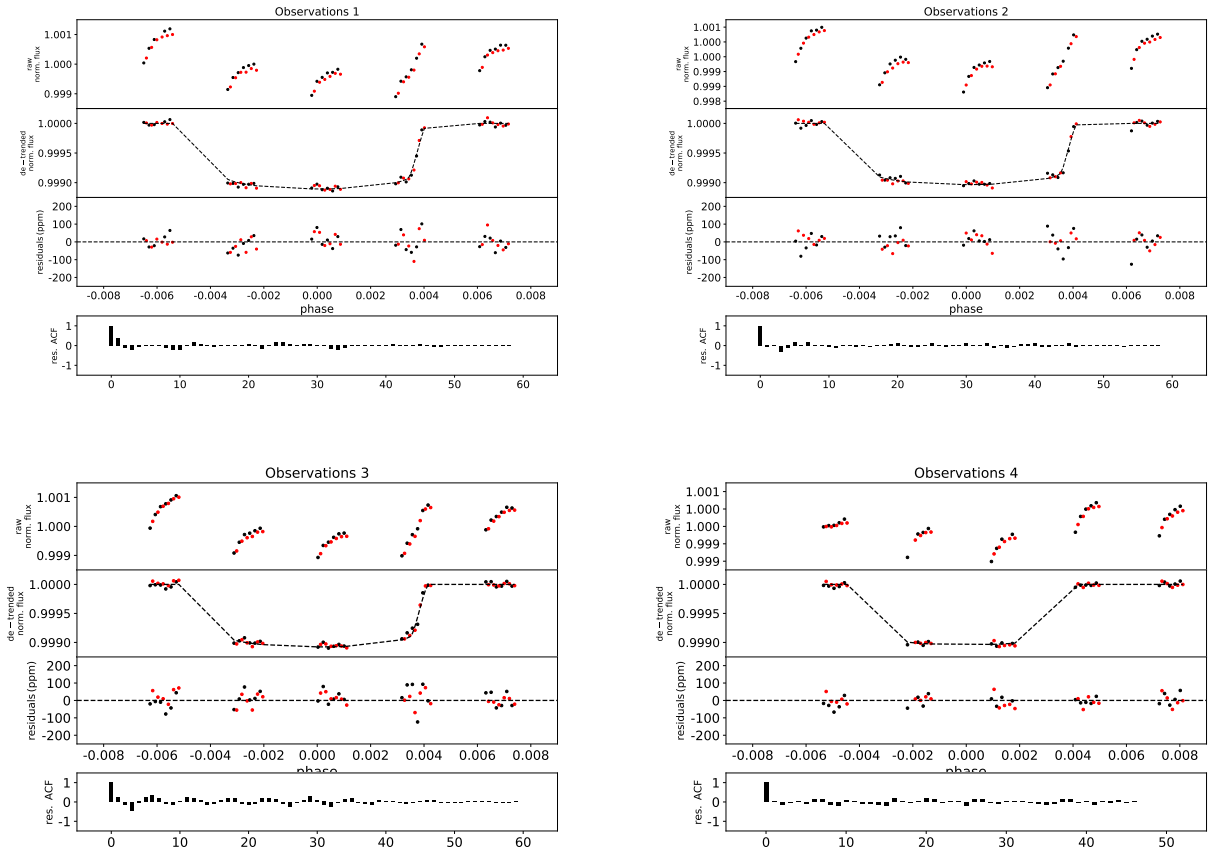

Figure B.1: White light curve fits for the four observations on HD 106315 c. For every observations we show similar plot. Top: normalised raw light-curve for the forward (black) and reverse (red) scans. Second pannels: de-trended flux (light-curves divided by the best-fit systematic effects model) (middle) and the best-fit model (dotted lines). Third pannel: fitting residuals from the best-fit model. Bottom: auto-correlation function of residuals.

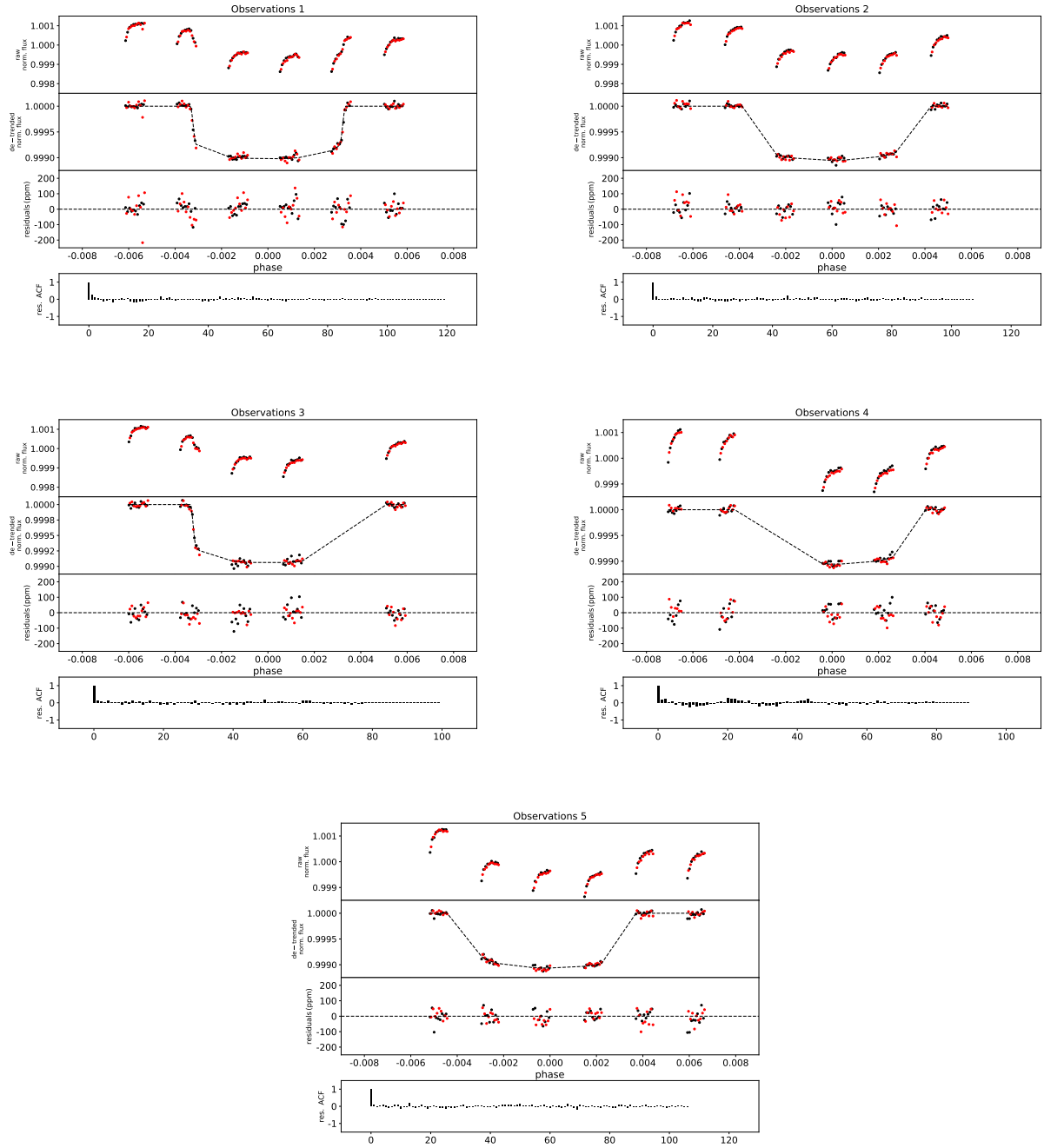

Figure B.2: Same as Figure 5.1 for the five observations on HD 3167 c

.

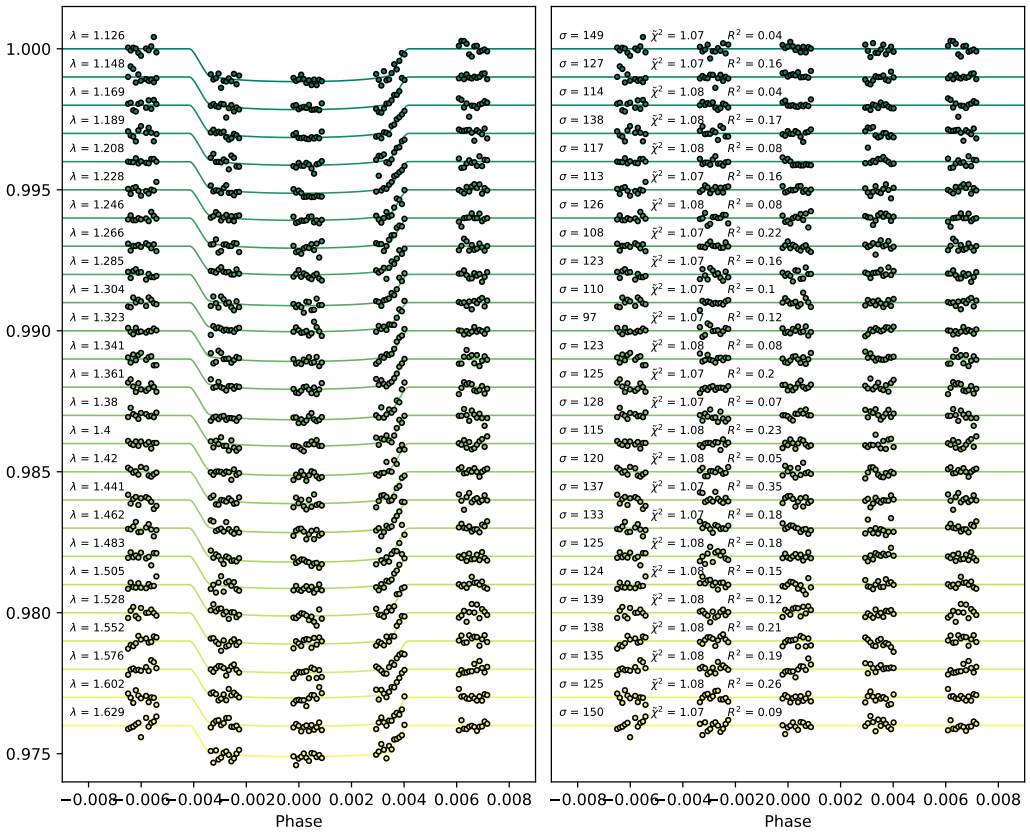
λ = 1.126
λ = 1.148
λ = 1.169
λ = 1.189
λ = 1.208
λ = 1.228
λ = 1.246
λ = 1.266
λ = 1.285
λ = 1.304
λ = 1.323
λ = 1.341
λ = 1.361
λ = 1.38
λ = 1.4
λ = 1.42
λ = 1.441
λ = 1.462
λ = 1.483
λ = 1.505
λ = 1.528
λ = 1.552
λ = 1.576
λ = 1.602
λ = 1.629
1.000
0.995
0.990
0.985
0.980
0.975
−0.008 −0.006 −0.004 −0.002 0.000 0.002 0.004 0.006 0.008
Phase
σ = 149 χ̃² = 1.07 R² = 0.04
σ = 127 χ̃² = 1.07 R² = 0.16
σ = 114 χ̃² = 1.08 R² = 0.04
σ = 138 χ̃² = 1.08 R² = 0.17
σ = 117 χ̃² = 1.08 R² = 0.08
σ = 113 χ̃² = 1.07 R² = 0.16
σ = 126 χ̃² = 1.08 R² = 0.08
σ = 108 χ̃² = 1.07 R² = 0.22
σ = 123 χ̃² = 1.07 R² = 0.16
σ = 110 χ̃² = 1.07 R² = 0.1
σ = 97 χ̃² = 1.07 R² = 0.12
σ = 123 χ̃² = 1.08 R² = 0.08
σ = 125 χ̃² = 1.07 R² = 0.2
σ = 128 χ̃² = 1.07 R² = 0.07
σ = 115 χ̃² = 1.08 R² = 0.23
σ = 120 χ̃² = 1.08 R² = 0.05
σ = 137 χ̃² = 1.07 R² = 0.35
σ = 133 χ̃² = 1.07 R² = 0.18
σ = 125 χ̃² = 1.08 R² = 0.18
σ = 124 χ̃² = 1.08 R² = 0.15
σ = 139 χ̃² = 1.08 R² = 0.12
σ = 138 χ̃² = 1.08 R² = 0.21
σ = 135 χ̃² = 1.08 R² = 0.19
σ = 125 χ̃² = 1.08 R² = 0.26
σ = 150 χ̃² = 1.07 R² = 0.09
−0.008 −0.006 −0.004 −0.002 0.000 0.002 0.004 0.006 0.008
Phase
λ = 1.126
λ = 1.148
λ = 1.169
λ = 1.189
λ = 1.208
λ = 1.228
λ = 1.246
λ = 1.266
λ = 1.285
λ = 1.304
λ = 1.323
λ = 1.341
λ = 1.361
λ = 1.38
λ = 1.4
λ = 1.42
λ = 1.441
λ = 1.462
λ = 1.483
λ = 1.505
λ = 1.528
λ = 1.552
λ = 1.576
λ = 1.602
λ = 1.629
1.000
0.995
0.990
0.985
0.980
0.975
−0.008 −0.006 −0.004 −0.002 0.000 0.002 0.004 0.006 0.008
Phase
σ = 145 χ̃² = 1.07 R² = 0.26
σ = 146 χ̃² = 1.07 R² = 0.2
σ = 126 χ̃² = 1.08 R² = 0.03
σ = 112 χ̃² = 1.07 R² = 0.2
σ = 120 χ̃² = 1.08 R² = 0.06
σ = 142 χ̃² = 1.08 R² = 0.12
σ = 112 χ̃² = 1.08 R² = 0.17
σ = 120 χ̃² = 1.08 R² = 0.21
σ = 128 χ̃² = 1.08 R² = 0.22
σ = 113 χ̃² = 1.08 R² = 0.15
σ = 117 χ̃² = 1.08 R² = 0.06
σ = 117 χ̃² = 1.07 R² = 0.07
σ = 117 χ̃² = 1.08 R² = 0.23
σ = 111 χ̃² = 1.08 R² = 0.15
σ = 110 χ̃² = 1.07 R² = 0.26
σ = 94 χ̃² = 1.08 R² = 0.18
σ = 98 χ̃² = 1.07 R² = 0.07
σ = 124 χ̃² = 1.08 R² = 0.14
σ = 136 χ̃² = 1.08 R² = 0.08
σ = 123 χ̃² = 1.07 R² = 0.01
σ = 134 χ̃² = 1.08 R² = 0.05
σ = 137 χ̃² = 1.08 R² = 0.26
σ = 118 χ̃² = 1.08 R² = 0.19
σ = 133 χ̃² = 1.08 R² = 0.2
σ = 129 χ̃² = 1.07 R² = 0.04
−0.008 −0.006 −0.004 −0.002 0.000 0.002 0.004 0.006 0.008
Phase

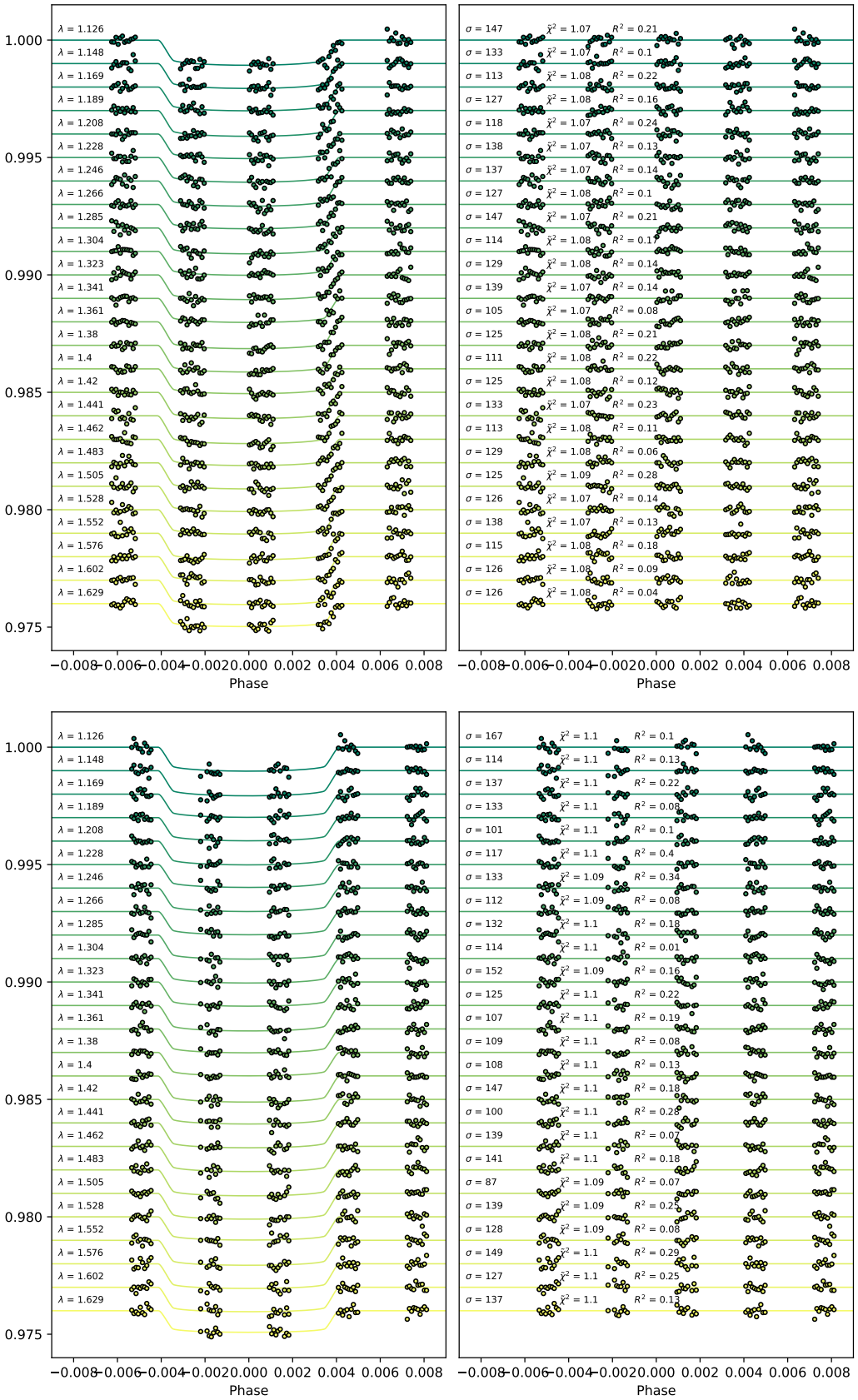

Figure B.3: Spectral light curve fits for the four observations on HD 106315 c. An artificial offset in the y-axis was applied for clarity. For each light curve, the left panel shows the de-trended spectral light curves with the best-fit model in dotted lines with the centred wavelength and the right panel shows the residuals and values for the standard deviation (σ) in ppm, the reduced Chi-squared ($\tilde{\chi}^2$), and the auto-correlation (R^2).

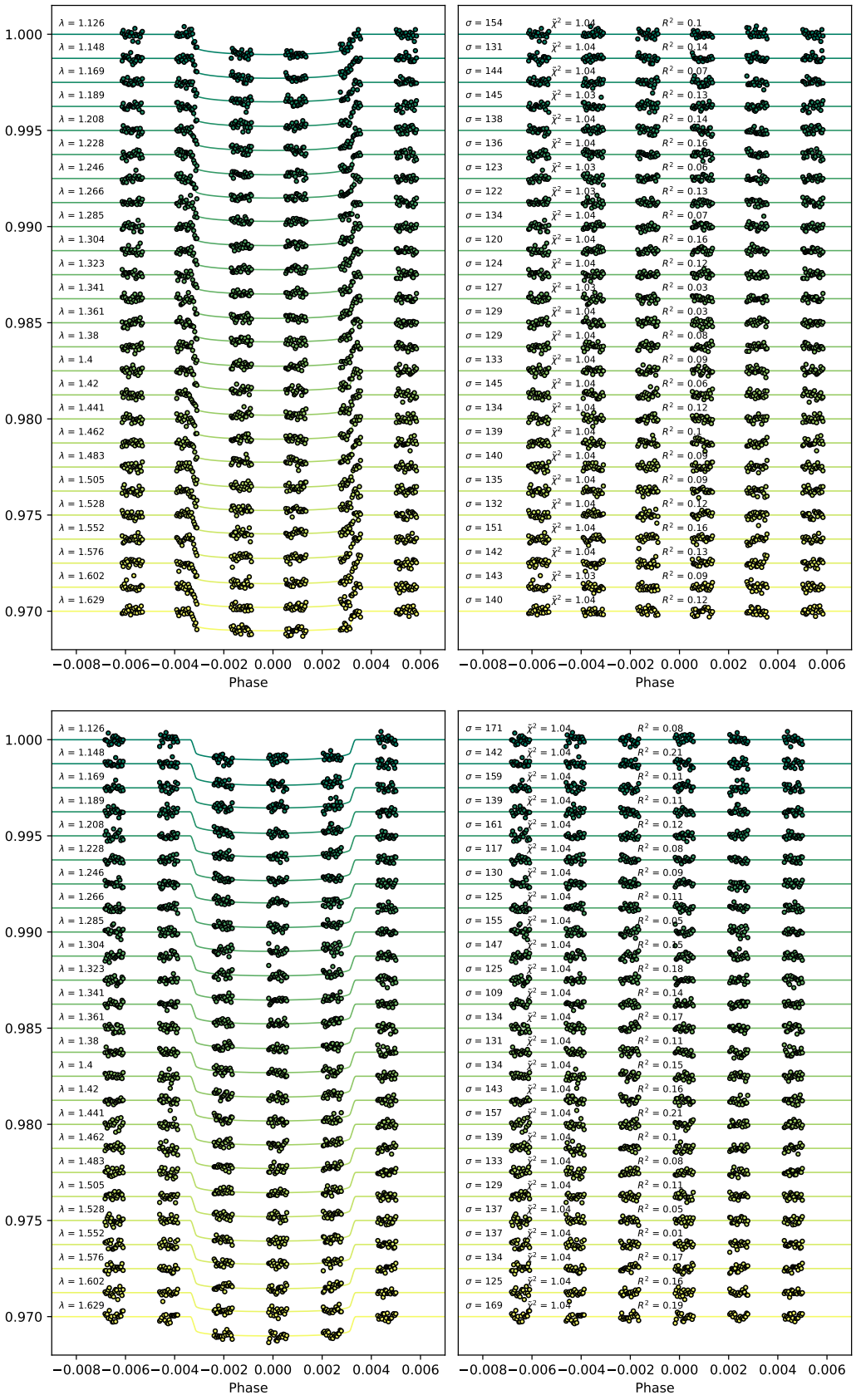
λ = 1.126
λ = 1.148
λ = 1.169
λ = 1.189
λ = 1.208
λ = 1.228
λ = 1.246
λ = 1.266
λ = 1.285
λ = 1.304
λ = 1.323
λ = 1.341
λ = 1.361
λ = 1.38
λ = 1.4
λ = 1.42
λ = 1.441
λ = 1.462
λ = 1.483
λ = 1.505
λ = 1.528
λ = 1.552
λ = 1.576
λ = 1.602
λ = 1.629
1.000
0.995
0.990
0.985
0.980
0.975
0.970
−0.008 −0.006 −0.004 −0.002 0.000 0.002 0.004 0.006
Phase
σ = 154 χ̃² = 1.04 R² = 0.1
σ = 131 χ̃² = 1.04 R² = 0.14
σ = 144 χ̃² = 1.04 R² = 0.07
σ = 145 χ̃² = 1.03 R² = 0.13
σ = 138 χ̃² = 1.04 R² = 0.14
σ = 136 χ̃² = 1.04 R² = 0.16
σ = 123 χ̃² = 1.03 R² = 0.06
σ = 122 χ̃² = 1.03 R² = 0.13
σ = 134 χ̃² = 1.04 R² = 0.07
σ = 120 χ̃² = 1.04 R² = 0.16
σ = 124 χ̃² = 1.04 R² = 0.12
σ = 127 χ̃² = 1.03 R² = 0.03
σ = 129 χ̃² = 1.04 R² = 0.03
σ = 129 χ̃² = 1.04 R² = 0.08
σ = 133 χ̃² = 1.04 R² = 0.09
σ = 145 χ̃² = 1.04 R² = 0.06
σ = 134 χ̃² = 1.04 R² = 0.12
σ = 139 χ̃² = 1.04 R² = 0.1
σ = 140 χ̃² = 1.04 R² = 0.08
σ = 135 χ̃² = 1.04 R² = 0.09
σ = 132 χ̃² = 1.04 R² = 0.12
σ = 151 χ̃² = 1.04 R² = 0.16
σ = 142 χ̃² = 1.04 R² = 0.13
σ = 143 χ̃² = 1.03 R² = 0.09
σ = 140 χ̃² = 1.04 R² = 0.12
−0.008 −0.006 −0.004 −0.002 0.000 0.002 0.004 0.006
Phase
λ = 1.126
λ = 1.148
λ = 1.169
λ = 1.189
λ = 1.208
λ = 1.228
λ = 1.246
λ = 1.266
λ = 1.285
λ = 1.304
λ = 1.323
λ = 1.341
λ = 1.361
λ = 1.38
λ = 1.4
λ = 1.42
λ = 1.441
λ = 1.462
λ = 1.483
λ = 1.505
λ = 1.528
λ = 1.552
λ = 1.576
λ = 1.602
λ = 1.629
1.000
0.995
0.990
0.985
0.980
0.975
0.970
−0.008 −0.006 −0.004 −0.002 0.000 0.002 0.004 0.006
Phase
σ = 171 χ̃² = 1.04 R² = 0.08
σ = 142 χ̃² = 1.04 R² = 0.21
σ = 159 χ̃² = 1.04 R² = 0.11
σ = 139 χ̃² = 1.04 R² = 0.11
σ = 161 χ̃² = 1.04 R² = 0.12
σ = 117 χ̃² = 1.04 R² = 0.08
σ = 130 χ̃² = 1.04 R² = 0.09
σ = 125 χ̃² = 1.04 R² = 0.11
σ = 155 χ̃² = 1.04 R² = 0.05
σ = 147 χ̃² = 1.04 R² = 0.15
σ = 125 χ̃² = 1.04 R² = 0.18
σ = 109 χ̃² = 1.04 R² = 0.14
σ = 134 χ̃² = 1.04 R² = 0.17
σ = 131 χ̃² = 1.04 R² = 0.11
σ = 134 χ̃² = 1.04 R² = 0.15
σ = 143 χ̃² = 1.04 R² = 0.16
σ = 157 χ̃² = 1.04 R² = 0.21
σ = 139 χ̃² = 1.04 R² = 0.1
σ = 133 χ̃² = 1.04 R² = 0.08
σ = 129 χ̃² = 1.04 R² = 0.11
σ = 137 χ̃² = 1.04 R² = 0.05
σ = 137 χ̃² = 1.04 R² = 0.01
σ = 134 χ̃² = 1.04 R² = 0.17
σ = 125 χ̃² = 1.04 R² = 0.16
σ = 169 χ̃² = 1.04 R² = 0.19
−0.008 −0.006 −0.004 −0.002 0.000 0.002 0.004 0.006
Phase

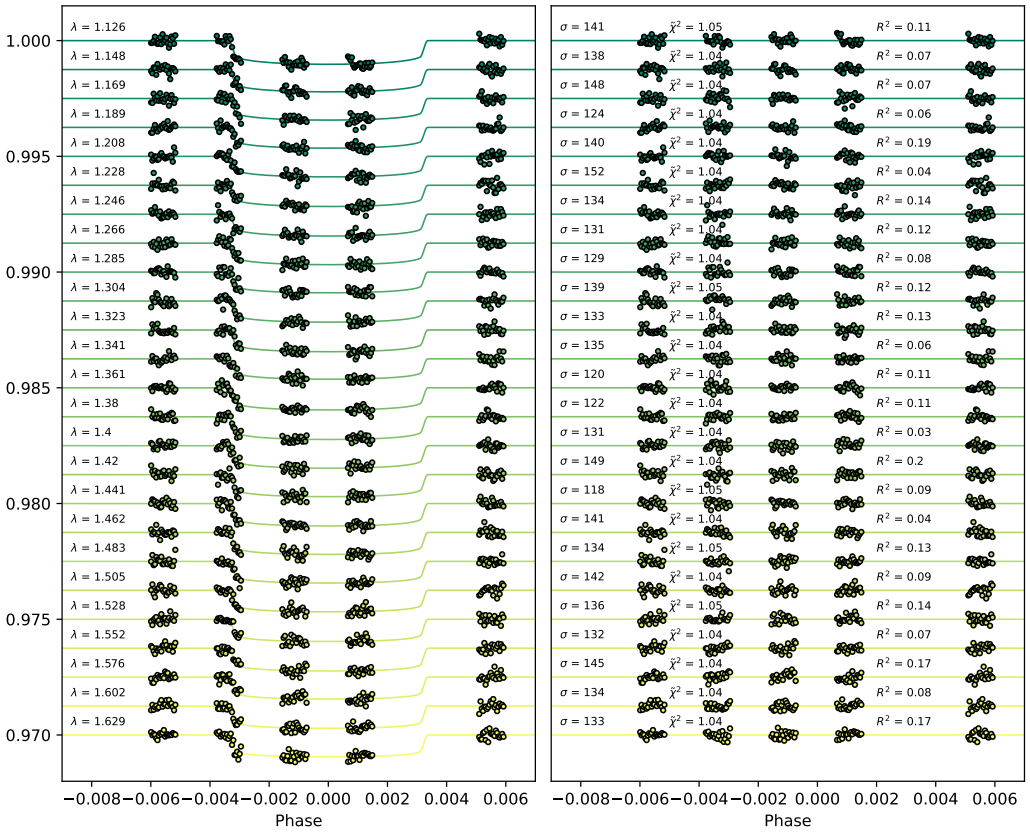
λ = 1.126
λ = 1.148
λ = 1.169
λ = 1.189
λ = 1.208
λ = 1.228
λ = 1.246
λ = 1.266
λ = 1.285
λ = 1.304
λ = 1.323
λ = 1.341
λ = 1.361
λ = 1.38
λ = 1.4
λ = 1.42
λ = 1.441
λ = 1.462
λ = 1.483
λ = 1.505
λ = 1.528
λ = 1.552
λ = 1.576
λ = 1.602
λ = 1.629
σ = 141 χ̃² = 1.05 R² = 0.11
σ = 138 χ̃² = 1.04 R² = 0.07
σ = 148 χ̃² = 1.04 R² = 0.07
σ = 124 χ̃² = 1.04 R² = 0.06
σ = 140 χ̃² = 1.04 R² = 0.19
σ = 152 χ̃² = 1.04 R² = 0.04
σ = 134 χ̃² = 1.04 R² = 0.14
σ = 131 χ̃² = 1.04 R² = 0.12
σ = 129 χ̃² = 1.04 R² = 0.08
σ = 139 χ̃² = 1.05 R² = 0.12
σ = 133 χ̃² = 1.04 R² = 0.13
σ = 135 χ̃² = 1.04 R² = 0.06
σ = 120 χ̃² = 1.04 R² = 0.11
σ = 122 χ̃² = 1.04 R² = 0.11
σ = 131 χ̃² = 1.04 R² = 0.03
σ = 149 χ̃² = 1.04 R² = 0.2
σ = 118 χ̃² = 1.05 R² = 0.09
σ = 141 χ̃² = 1.04 R² = 0.04
σ = 134 χ̃² = 1.05 R² = 0.13
σ = 142 χ̃² = 1.04 R² = 0.09
σ = 136 χ̃² = 1.05 R² = 0.14
σ = 132 χ̃² = 1.04 R² = 0.07
σ = 145 χ̃² = 1.04 R² = 0.17
σ = 134 χ̃² = 1.04 R² = 0.08
σ = 133 χ̃² = 1.04 R² = 0.17
1.000
0.995
0.990
0.985
0.980
0.975
0.970
−0.008 −0.006 −0.004 −0.002 0.000 0.002 0.004 0.006
Phase
−0.008 −0.006 −0.004 −0.002 0.000 0.002 0.004 0.006
Phase

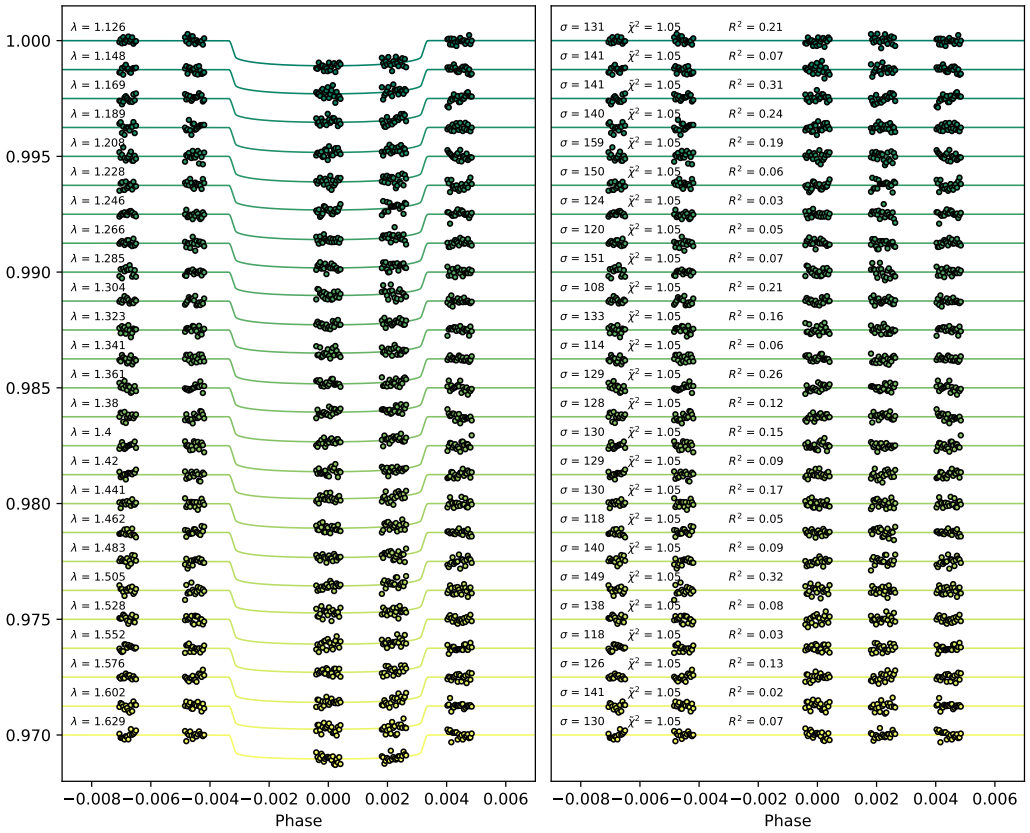
λ = 1.126
λ = 1.148
λ = 1.169
λ = 1.189
λ = 1.208
λ = 1.228
λ = 1.246
λ = 1.266
λ = 1.285
λ = 1.304
λ = 1.323
λ = 1.341
λ = 1.361
λ = 1.38
λ = 1.4
λ = 1.42
λ = 1.441
λ = 1.462
λ = 1.483
λ = 1.505
λ = 1.528
λ = 1.552
λ = 1.576
λ = 1.602
λ = 1.629
σ = 131 χ̃² = 1.05 R² = 0.21
σ = 141 χ̃² = 1.05 R² = 0.07
σ = 141 χ̃² = 1.05 R² = 0.31
σ = 140 χ̃² = 1.05 R² = 0.24
σ = 159 χ̃² = 1.05 R² = 0.19
σ = 150 χ̃² = 1.05 R² = 0.06
σ = 124 χ̃² = 1.05 R² = 0.03
σ = 120 χ̃² = 1.05 R² = 0.05
σ = 151 χ̃² = 1.05 R² = 0.07
σ = 108 χ̃² = 1.05 R² = 0.21
σ = 133 χ̃² = 1.05 R² = 0.16
σ = 114 χ̃² = 1.05 R² = 0.06
σ = 129 χ̃² = 1.05 R² = 0.26
σ = 128 χ̃² = 1.05 R² = 0.12
σ = 130 χ̃² = 1.05 R² = 0.15
σ = 129 χ̃² = 1.05 R² = 0.09
σ = 130 χ̃² = 1.05 R² = 0.17
σ = 118 χ̃² = 1.05 R² = 0.05
σ = 140 χ̃² = 1.05 R² = 0.09
σ = 149 χ̃² = 1.05 R² = 0.32
σ = 138 χ̃² = 1.05 R² = 0.08
σ = 118 χ̃² = 1.05 R² = 0.03
σ = 126 χ̃² = 1.05 R² = 0.13
σ = 141 χ̃² = 1.05 R² = 0.02
σ = 130 χ̃² = 1.05 R² = 0.07
1.000
0.995
0.990
0.985
0.980
0.975
0.970
−0.008 −0.006 −0.004 −0.002 0.000 0.002 0.004 0.006
Phase
−0.008 −0.006 −0.004 −0.002 0.000 0.002 0.004 0.006
Phase

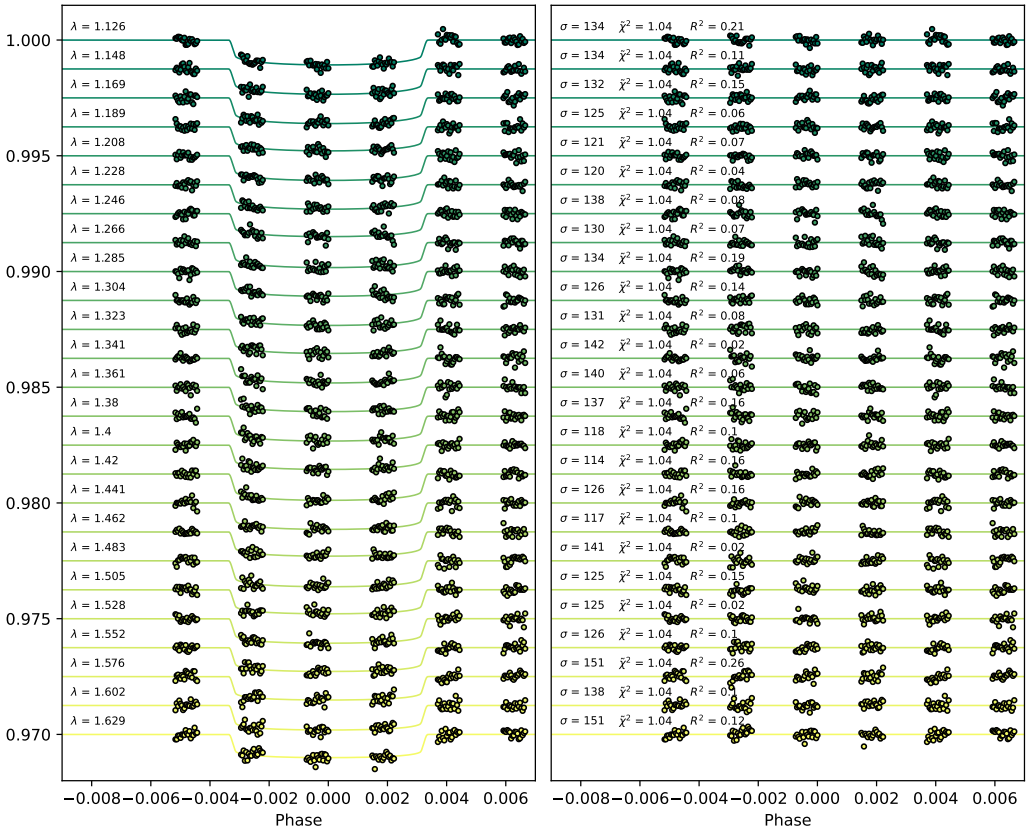

Figure B.4: Spectral light curve fits for the four observations on HD 3167 c. An artificial offset in the y-axis was applied for clarity. For each light curve, the left panel shows the de-trended spectral light curves with the best-fit model in dotted lines with the centred wavelength and the right panel shows the residuals and values for the standard deviation (σ) in ppm, the reduced Chi-squared ($\tilde{\chi}^2$), and the auto-correlation (R^2).

Appendix C

TRAPPIST-1 h supplementary materials

Table C.1: Statistical results of the stellar contamination modelling on combined TRAPPIST-1h HST WFC3 G141 data and the K2 photometry value from Luger et al. (2017a). Chi-squared (χ^2) and reduced chi-squared ($\tilde{\chi}^2 2$) were computed using the result of the stellar contamination models.

Model	χ^2	$\tilde{\chi}^2$
Flat-line	72.14	3.80
Stellar Zhang et al. (2018)	73.74	3.81
Stellar Wakeford et al. (2019)	197.75	10.15
Stellar Morris et al. (2018)	99.37	5.23

Table C.2: Best-fit logarithm evidence of a flat-line and a primary clear model for the seven planets of the TRAPPIST-1 system. The primary clear atmospheric scenario was simulated including H_2O with a volume mixing ratio fixed to 10^{-3} in a H-dominated atmosphere for all seven planets of the TRAPPIST-1 system.

Model	Flat-line	Primary clear
TRAPPIST-1 b	76.54	45.37
TRAPPIST-1 c	77.42	68.28
TRAPPIST-1 d	71.92	37.84
TRAPPIST-1 e	82.16	58.06
TRAPPIST-1 f	79.58	65.72
TRAPPIST-1 g	79.73	75.73
TRAPPIST-1 h	110.55	74.78

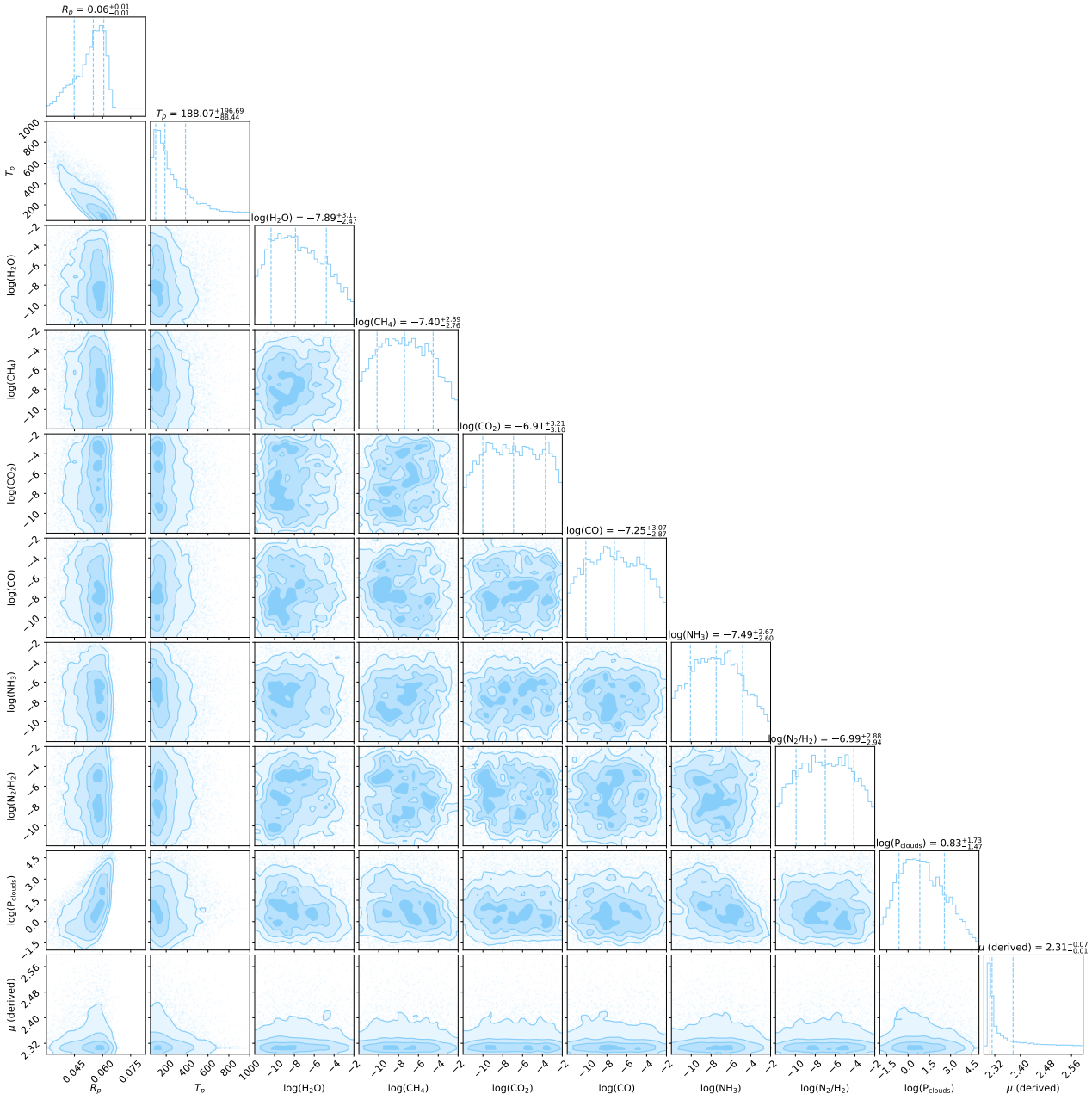

Figure C.1: Posterior distributions for the primary atmospheric retrieval on the extracted TRAPPIST-1 h spectrum.

Table C.3: Best-fit atmospheric results and derived parameters for secondary retrieval analysis. Secondary atmospheric scenarios were simulated including molecular absorption with a fixed volume mixing ratio increasing progressively from 0.01 to 0.8.

Model	$R_P(R_\oplus)$	T(K)	μ(g/mol)	H(km)	met (x solar)	χ^2	$\tilde{\chi}^2$	log(E)	Δlog(E)
Flat-line	0.61±0.11	296±225	2.30	71.28	1	64.95	3.61	110.55	N/A
VMR(H_2O)									
0.01	0.69±0.003	139±2	2.46	69.09	20	150.67	8.37	63.55	-47.00
0.2	0.71±0.003	142±6	5.45	32.98	350	97.25	5.40	91.46	-19.09
0.5	0.72±0.003	147±15	10.16	18.78	900	78.43	4.35	101.89	-8.66
0.8	0.72±0.003	153±24	14.87	13.50	1400	72.92	4.05	105.07	-5.48
VMR(CO_2)									
0.01	0.71±0.003	155±22	2.72	73.68	50	64.22	3.57	109.55	-1.00
0.2	0.72±0.003	173±24	10.65	21.48	950	63.69	3.54	111.35	0.80
0.5	0.72±0.003	174±24	23.16	10.03	2400	63.93	3.55	111.26	0.71
0.8	0.73±0.003	174±25	35.67	6.54	3800	64.30	3.57	110.98	0.43
VMR(CO)									
0.01	0.72±0.003	159±27	2.56	81.36	30	68.36	3.80	109.28	-1.27
0.2	0.72±0.003	174±24	7.45	31.19	600	63.23	3.51	111.56	1.01
0.5	0.73±0.003	175±26	15.16	15.45	1500	63.64	3.54	111.38	0.83
0.8	0.73±0.003	174±24	22.87	10.21	2300	63.97	3.55	111.15	0.60
VMR(CH_4)									
0.01	0.68±0.003	139±3	2.44	66.32	20	170.07	9.45	63.39	-47.16
0.2	0.69±0.003	141±5	5.05	33.60	300	104.28	5.79	87.53	-23.02
0.5	0.70±0.003	145±12	9.17	19.87	800	81.64	4.54	99.81	-10.74
0.8	0.71±0.004	150±18	13.30	14.43	1300	74.92	4.16	103.72	-6.83
VMR(NH_3)									
0.01	0.66±0.003	140±3	2.45	63.82	20	112.31	6.24	82.99	-27.56
0.2	0.69±0.004	145±11	5.25	33.95	350	72.48	4.03	104.48	-6.07
0.5	0.70±0.005	158±26	9.67	20.39	850	67.57	3.75	109.48	-1.07
0.8	0.71±0.004	168±26	14.09	15.11	1500	65.14	3.62	110.59	0.04
VMR(N_2)									
0.01	0.72±0.003	159±27	2.56	81.54	30	71.67	3.98	107.73	-2.82
0.2	0.73±0.003	171±25	7.45	30.78	600	65.33	3.63	110.47	-0.08
0.5	0.73±0.003	174±24	15.16	15.36	1500	64.96	3.61	110.67	0.12
0.8	0.73±0.003	171±25	22.87	10.05	2300	64.72	3.59	110.72	0.17

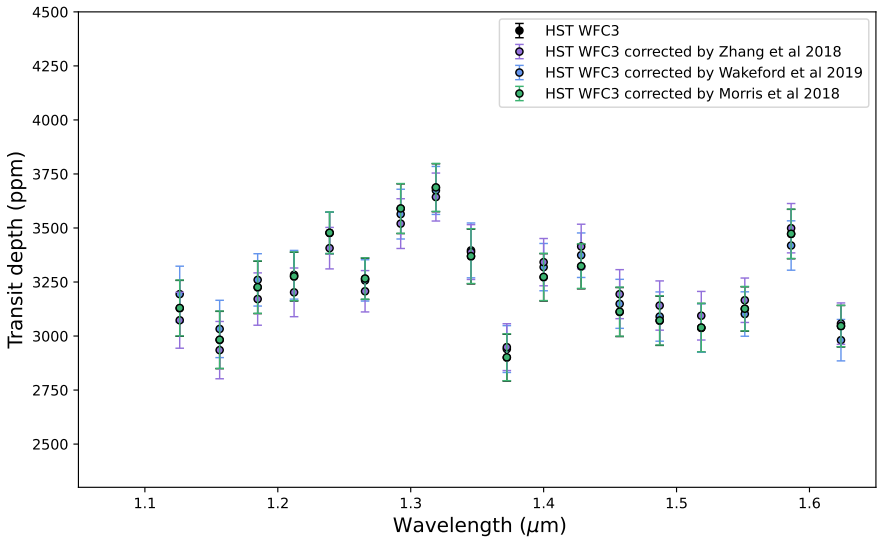

Figure C.2: Combined transit depth in ppm using the three HST/WFC3 G141 transit observations and corrected transit depth using stellar contamination models from Zhang et al. (2018) (purple), Wakeford et al. (2019) (blue) , and Morris et al. (2018) (green). The latter (in green) and the raw extracted spectrum (in black) are almost similar because the stellar contribution of Morris et al. (2018) is flat in the HST/WFC3 NIR wavelength range.

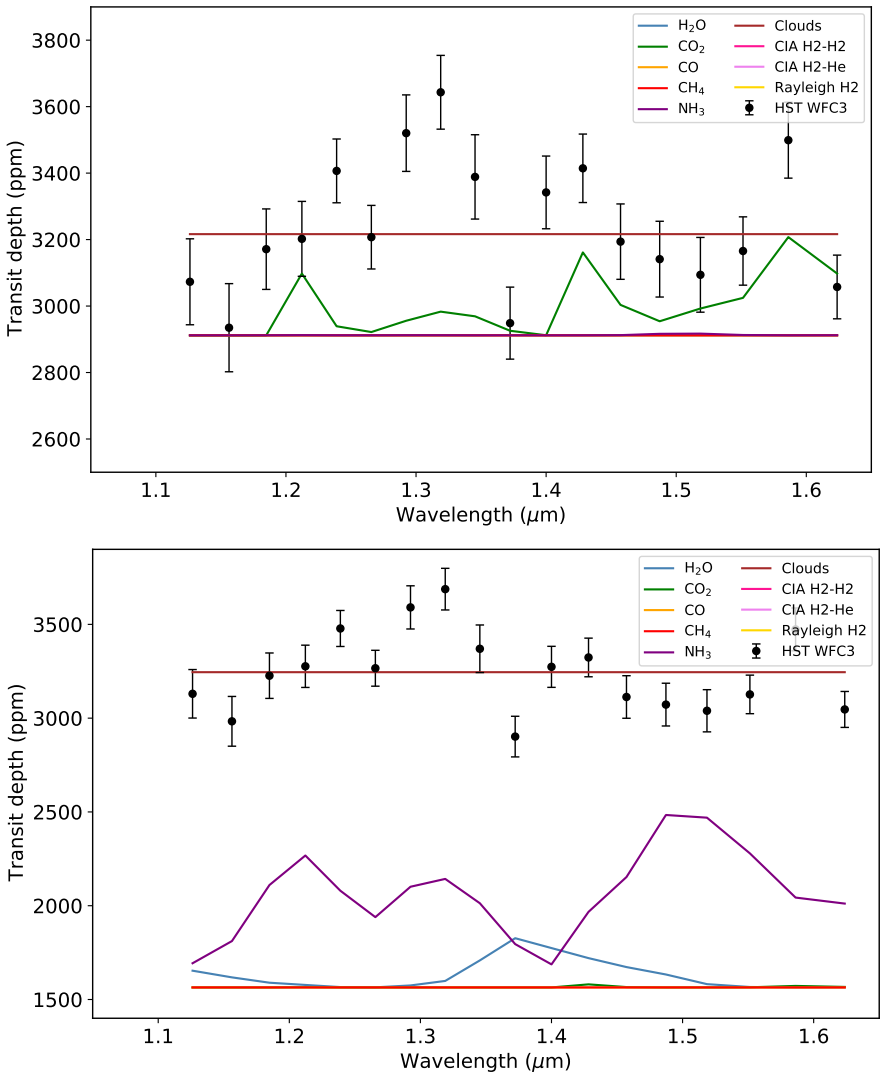

Figure C.3: Opacity contributions from the primary best-fit retrieval model on the TRAPPIST-1h spectrum corrected by Zhang et al. (2018) (top) and by Morris et al. (2018) (bottom). We omitted Rayleigh scattering opacity contributions from others species than H_2 for clarity.

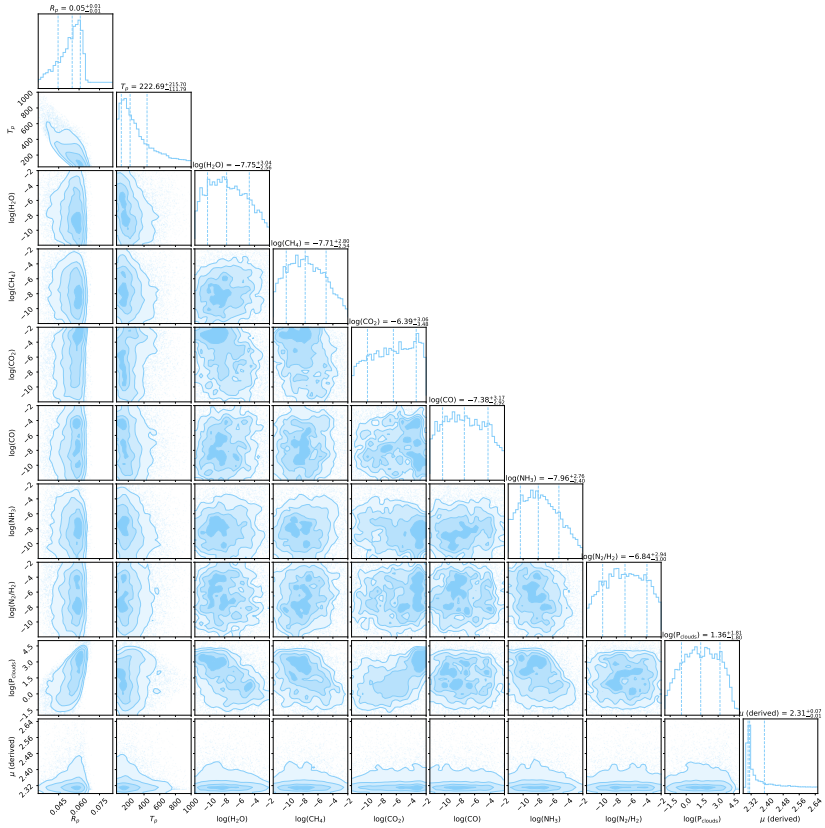
$R_p = 0.05^{+0.01}_{-0.01}$
$T_p = 222.69^{+215.70}_{-113.70}$
log(H$_2$O) = $-7.75^{+1.04}_{-1.4}$
log(CH$_4$) = $-7.71^{+2.60}_{-2.4}$
log(CO$_2$) = $-6.39^{+3.06}_{-1.48}$
log(CO) = $-7.38^{+3.17}_{-2.16}$
log(NH$_3$) = $-7.96^{+2.76}_{-2.25}$
log(N$_2$/H$_2$) = $-6.84^{+2.94}_{-1.74}$
log(P$_{clouds}$) = $1.36^{+1.61}_{-1.61}$
μ (derived) = $2.31^{+0.07}_{-0.07}$
R_p
T_p
log(H$_2$O)
log(CH$_4$)
log(CO$_2$)
log(CO)
log(NH$_3$)
log(N$_2$/H$_2$)
log(P$_{clouds}$)
μ (derived)

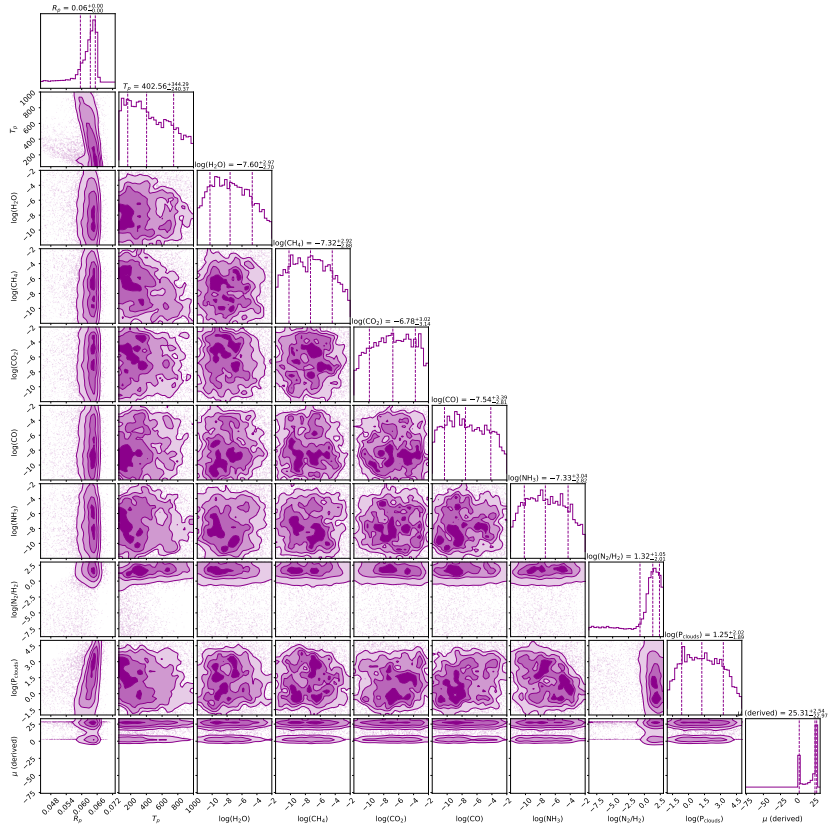
$R_p = 0.06^{+0.00}_{-0.00}$
$T_p = 402.56^{+344.29}_{-241.37}$
log(H$_2$O) = $-7.60^{+2.97}_{-2.71}$
log(CH$_4$) = $-7.32^{+2.92}_{-2.80}$
log(CO$_2$) = $-6.78^{+3.02}_{-2.13}$
log(CO) = $-7.54^{+2.29}_{-2.87}$
log(NH$_3$) = $-7.33^{+2.94}_{-2.62}$
log(N$_2$/H$_2$) = $1.32^{+1.35}_{-2.47}$
log(P$_{clouds}$) = $1.25^{+2.02}_{-1.80}$
μ (derived) = $25.31^{+2.74}_{-2.97}$
R_p
T_p
log(H$_2$O)
log(CH$_4$)
log(CO$_2$)
log(CO)
log(NH$_3$)
log(N$_2$/H$_2$)
log(P$_{clouds}$)
μ (derived)

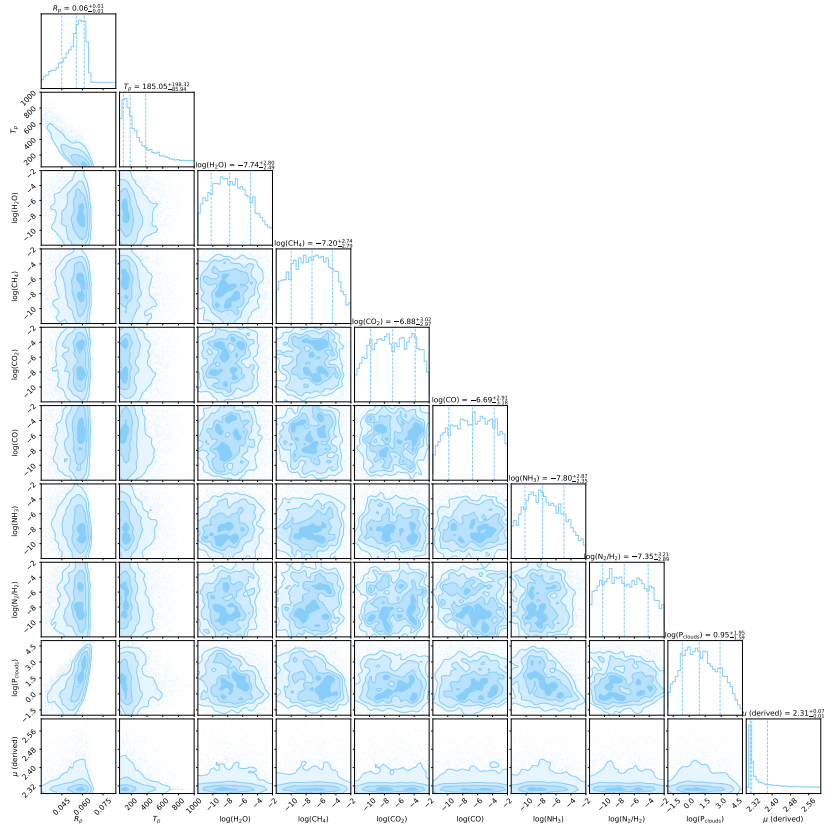
$R_p = 0.06^{+0.01}_{-0.01}$
$T_p = 185.05^{+198.32}_{-85.47}$
log(H2O) = −7.74+2.80−2.24
log(CH4) = −7.20+2.74−2.24
log(CO2) = −6.88+3.02−2.87
log(CO) = −6.69+3.91−3.16
log(NH3) = −7.80+2.87−2.47
log(N2/H2) = −7.35+3.21−2.66
log(Pcloud) = 0.95+1.55−1.70
μ (derived) = 2.31+0.07−0.07
R_p
T_p
log(H2O)
log(CH4)
log(CO2)
log(CO)
log(NH3)
log(N2/H2)
log(Pcloud)
μ (derived)

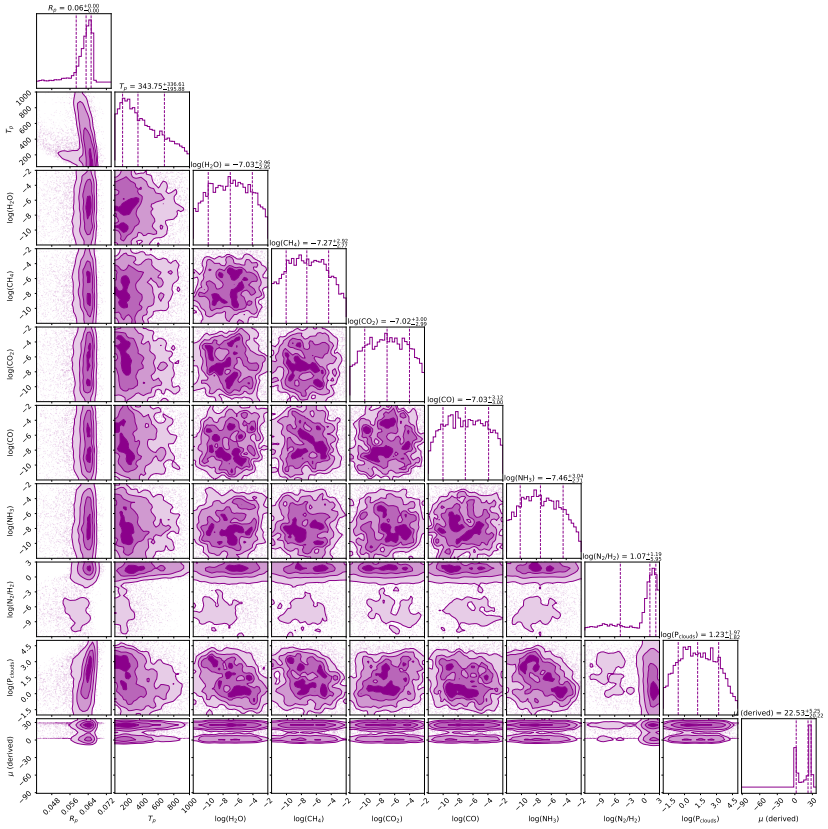
$R_p = 0.06^{+0.00}_{-0.00}$
$T_p = 343.75^{+334.61}_{-213.88}$
log(H2O) = −7.03+2.99−2.58
log(CH4) = −7.27+2.92−2.71
log(CO2) = −7.02+3.00−2.89
log(CO) = −7.03+3.12−3.00
log(NH3) = −7.46+2.94−2.47
log(N2/H2) = 1.07+1.13−3.24
log(Pcloud) = 1.23+1.97−1.82
μ (derived) = 22.53+5.23−20.73
R_p
T_p
log(H2O)
log(CH4)
log(CO2)
log(CO)
log(NH3)
log(N2/H2)
log(Pcloud)
μ (derived)

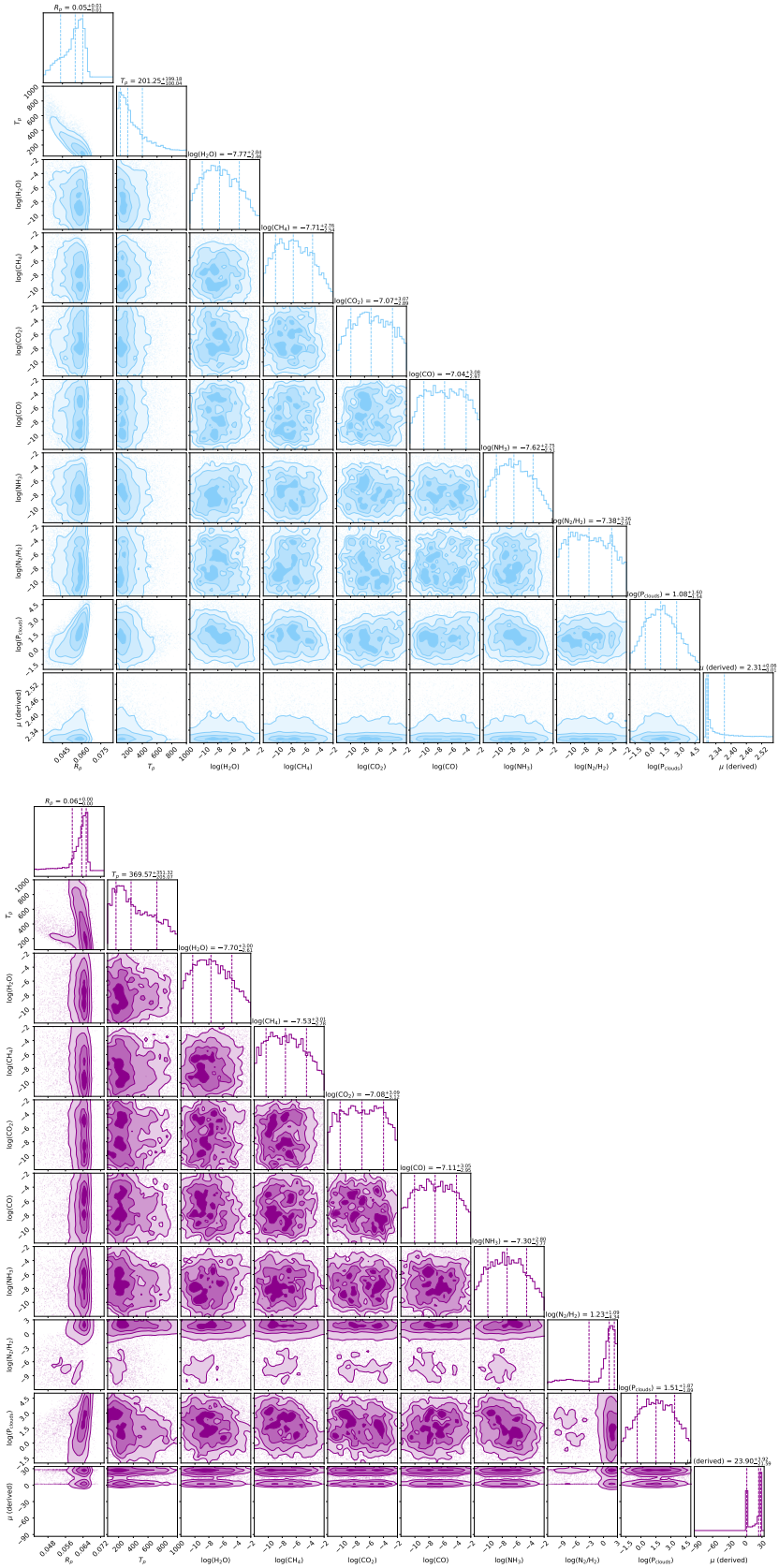

Figure C.4: Posterior distributions for the primary (blue) atmospheric retrieval and the secondary (purple) retrieval on TRAPPIST-1h spectra corrected by the stellar contamination model of Zhang et al. (2018)(top) ,Wakeford et al. (2019) (middle) and Morris et al. (2018) (bottom).

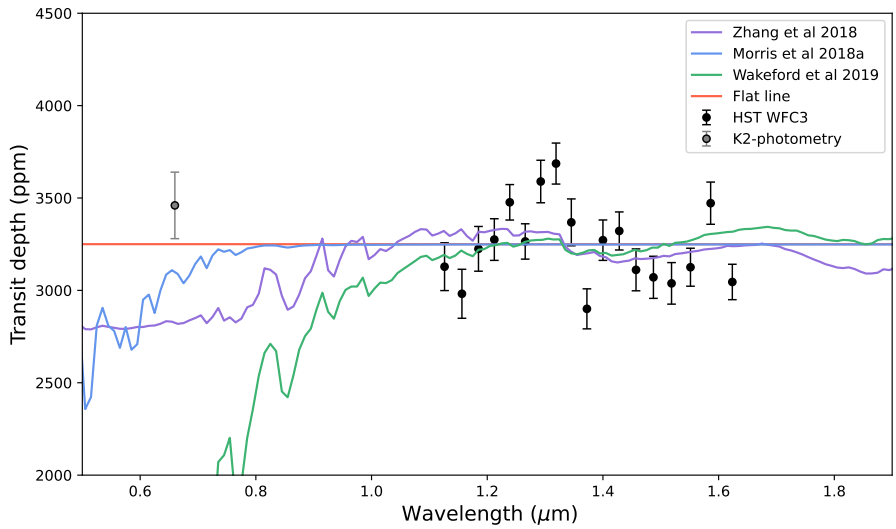

Figure C.5: Best fit models to TRAPPIST-1 h HST/WFC3 G141 data (black) and K2 optical value (Luger et al., 2017a) (grey) from stellar contamination models based on Zhang et al. (2018),Wakeford et al. (2019), and Morris et al. (2018) .

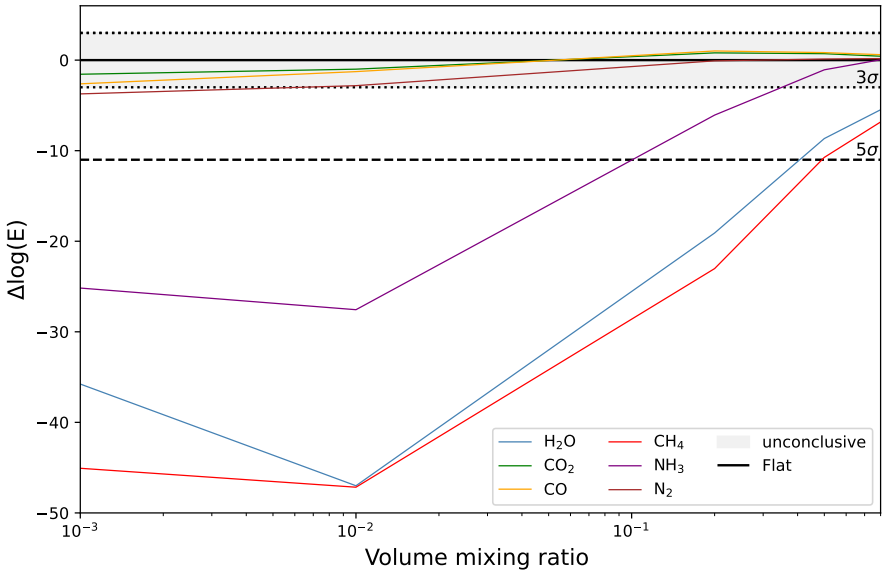

Figure C.6: Comparison of the log evidence for a flat line to that of single molecule retrievals where the abundance of the molecule is fixed and no clouds were included. The shaded region represents the set of Bayes factor values for which it is not possible to conclude compared to a flat line, that is with absolute $\Delta\log(E)$ below 3. Models below the dashed lines are strongly disfavoured compared to the flat line.

Appendix D

Hubble transmission survey retrieval results

Table D.1: Results of the **1-Primary** retrieval analysis. For the molecular contribution, we indicate the main spectral contributor and its abundance.

Name	R_P ($R_\oplus$)	T_P (K)	Main absorber X	$\log_{10}$(X) [10^{-12}-10^{-2}]	$\log_{10}(P_{clouds})$ (Pa)	μ (g/mol)	$\Delta\log(E)$
55-Cnc e	$1.65^{+0.01}_{-0.11}$	$1657.97^{+423.29}_{-286.66}$	HCN	$-2.92^{+0.63}_{-1.03}$	$4.38^{+1.0}_{-0.94}$	$2.34^{+0.1}_{-0.04}$	29.43
GJ 436 b	$3.73^{+0.11}_{-0.11}$	$548.36^{+233.43}_{-146.67}$	H_2O	$-7.32^{+2.93}_{-2.84}$	$-0.32^{+1.9}_{-1.48}$	$2.31^{+0.04}_{-0.01}$	0.04
GJ 1132 b	$0.88^{+0.11}_{-0.11}$	$464.23^{+210.61}_{-100.55}$	-	-	$0.35^{+1.97}_{-1.73}$	$2.31^{+0.02}_{-0.01}$	-0.49
GJ 1214 b	$2.41^{+0.11}_{-0.11}$	$417.42^{+129.16}_{-80.05}$	H_2O	$-4.95^{+1.82}_{-1.61}$	$2.01^{+2.03}_{-1.66}$	$2.31^{+0.02}_{-0.01}$	1.3
GJ 3470 b	$3.62^{+0.11}_{-0.22}$	$642.14^{+230.53}_{-177.1}$	H_2O	$-3.48^{+1.02}_{-1.31}$	$1.88^{+1.18}_{-1.06}$	$2.32^{+0.05}_{-0.01}$	1.73
HAT-P-11 b	$4.5^{+0.11}_{-0.11}$	$742.36^{+241.9}_{-196.61}$	H_2O	$-3.01^{+0.68}_{-1.08}$	$3.2^{+1.2}_{-0.95}$	$2.33^{+0.07}_{-0.02}$	8.78
HAT-P-26 b	$5.49^{+0.11}_{-0.22}$	$705.06^{+212.48}_{-135.94}$	H_2O	$-2.99^{+0.64}_{-0.81}$	$3.46^{+0.83}_{-0.95}$	$2.32^{+0.06}_{-0.02}$	42.48
HD 3167 c	$2.63^{+0.01}_{-0.01}$	$433.18^{+101.87}_{-74.06}$	H_2O [1]	$-4.37^{+0.64}_{-0.63}$	$5.29^{+0.45}_{-0.5}$	$2.41^{+0.16}_{-0.08}$	9.48
HD 97658 b	$2.08^{+0.01}_{-0.01}$	$1072.93^{+19.0}_{-34.03}$	H_2O [2]	$5.15^{+0.54}_{-0.62}$	$-4.0^{+0.54}_{-0.37}$	$2.60^{+0.11}_{-0.13}$	101.36
HD 106315 c	$4.17^{+0.22}_{-0.22}$	$809.0^{+338.56}_{-239.85}$	H_2O [3]	$-2.82^{+0.53}_{-0.87}$	$-2.92^{+0.59}_{-0.9}$	$2.33^{+0.06}_{-0.02}$	15.18
HD 219666 b	$4.17^{+0.11}_{-0.22}$	$961.27^{+323.21}_{-239.94}$	H_2O	$-3.19^{+0.8}_{-1.31}$	$3.19^{+1.43}_{-1.12}$	$2.32^{+0.07}_{-0.02}$	4.28
HIP 41378 b	$2.85^{+0.11}_{-0.11}$	$860.51^{+293.88}_{-214.42}$	H_2O	$-4.14^{+1.46}_{-4.55}$	$3.78^{+1.37}_{-3.64}$	$2.32^{+0.08}_{-0.02}$	1.09
K2-18 b	$2.3^{+0.01}_{-0.01}$	$284.94^{+83.58}_{-84.21}$	H_2O	$-4.01^{+1.13}_{-2.46}$	$4.14^{+0.91}_{-1.08}$	$2.33^{+0.1}_{-0.03}$	2.96
K2-24 b	$4.94^{+0.22}_{-0.33}$	$616.73^{+291.52}_{-174.48}$	NH_3	$-6.49^{+3.09}_{-3.47}$	$0.89^{+2.41}_{-2.16}$	$2.31^{+0.06}_{-0.01}$	0.16
LHS 1140 b	$1.65^{+0.01}_{-0.01}$	$255.55^{+60.34}_{-77.26}$	H_2O	$-3.22^{+0.8}_{-1.31}$	$4.3^{+0.92}_{-0.97}$	$2.33^{+0.08}_{-0.02}$	1.94
LTT 9779 b	$4.28^{+0.11}_{-0.22}$	$2339.96^{+398.34}_{-633.59}$	CIA + CO_2	$-7.04^{+2.86}_{-3.09}$	$5.19^{+0.5}_{-1.9}$	$2.31^{+0.03}_{-0.01}$	4.06
TOI-270 c	$2.3^{+0.11}_{-0.11}$	$485.91^{+146.16}_{-152.11}$	H_2O	$-4.13^{+1.34}_{-3.68}$	$1.57^{+1.26}_{-2.17}$	$2.31^{+0.04}_{-0.01}$	0.67
TOI-270 d	$1.98^{+0.01}_{-0.01}$	$393.28^{+108.92}_{-101.54}$	H_2O	$-3.26^{+0.76}_{-0.92}$	$4.06^{+0.72}_{-0.69}$	$2.33^{+0.09}_{-0.03}$	4.97
TOI-674 b	$4.72^{+0.11}_{-0.11}$	$681.91^{+235.85}_{-167.82}$	H_2O [4]	$-2.92^{+0.59}_{-0.97}$	$2.63^{+0.81}_{-0.91}$	$2.34^{+0.08}_{-0.03}$	15.64
TRAPPIST-1 b	$0.99^{+0.11}_{-0.11}$	$369.61^{+129.62}_{-109.23}$	-	-	$1.9^{+3.28}_{-2.77}$	$2.31^{+0.06}_{-0.01}$	0.58
TRAPPIST-1 c	$0.88^{+0.11}_{-0.11}$	$300.99^{+115.35}_{-81.59}$	-	-	$0.95^{+2.25}_{-2.26}$	$2.31^{+0.06}_{-0.01}$	-0.28
TRAPPIST-1 d	$0.66^{+0.11}_{-0.11}$	$221.4^{+94.9}_{-52.73}$	H_2O	$-6.51^{+1.6}_{-3.02}$	$2.62^{+2.73}_{-3.3}$	$2.31^{+0.03}_{-0.01}$	-0.07
TRAPPIST-1 e	$0.77^{+0.11}_{-0.11}$	$244.41^{+79.04}_{-75.42}$	NH_3	$-5.14^{+1.96}_{-4.35}$	$1.83^{+1.89}_{-2.56}$	$2.32^{+0.07}_{-0.01}$	0.49
TRAPPIST-1 f	$0.88^{+0.01}_{-0.11}$	$201.64^{+76.1}_{-61.12}$	-	-	$0.87^{+2.43}_{-2.01}$	$2.31^{+0.06}_{-0.01}$	0.1
TRAPPIST-1 g	$0.99^{+0.01}_{-0.11}$	$183.83^{+63.79}_{-56.58}$	-	-	$0.68^{+2.33}_{-2.12}$	$2.31^{+0.06}_{-0.01}$	-0.17
TRAPPIST-1 h	$0.55^{+0.01}_{-0.11}$	$151.64^{+61.0}_{-42.82}$	-	-	$-0.27^{+2.08}_{-1.77}$	$2.31^{+0.04}_{-0.01}$	-0.44

[1] CO_2 is also constrained with a $\log_{10}(CO_2) = -2.66^{+0.44}_{-0.66}$

[2] The best fit contribution is actually a combination of H_2O, CO_2, NH_3 and HCN. $\log_{10}(CO_2) = -2.21^{+0.15}_{-0.82}$, $\log_{10}(HCN) = -3.04^{+0.64}_{-0.49}$, $\log_{10}(NH_3) = -4.05^{+0.59}_{-0.4}$

[3] NH_3 is also constrained with a $\log_{10}(NH_3) = -5.2^{+1.01}_{-3.88}$

[4] NH_3 is also constrained with a $\log_{10}(NH_3) = -4.24^{+0.68}_{-0.91}$

Table D.2: Same as Table D.1 for the 2-Active clear retrieval analysis.

Name	R_P ($R_\oplus$)	T_P (K)	Main absorbers X	$\log_{10}$(X) [10^{-12}-1]	μ (g/mol)	Δlog(E)
55-Cnc e	$1.76^{+0.01}_{-0.01}$	$1571.53^{+387.68}_{-255.51}$	HCN	$-3.22^{+1.54}_{-1.12}$	$2.34^{+0.6}_{-0.03}$	29.94
GJ 436 b	$4.06^{+0.01}_{-0.11}$	$424.98^{+141.57}_{-75.42}$	CO_2	$-0.36^{+0.25}_{-7.27}$	$24.99^{+10.79}_{-9.08}$	-3.75
GJ 1132 b	$1.10^{+0.01}_{-0.01}$	$390.22^{+128.97}_{-68.6}$	NH_3, CO_2	$-1.88^{+0.98}_{-1.46}$, $-0.48^{+0.33}_{-7.47}$	$23.26^{+9.37}_{-6.73}$	-2.66
GJ 1214 b	$2.63^{+0.01}_{-0.01}$	$298.93^{+21.02}_{-9.83}$	H_2O, CO_2	$-1.51^{+0.59}_{-1.26}$, $-0.06^{+0.04}_{-0.06}$	$39.26^{+2.75}_{-3.86}$	-12.42
GJ 3470 b	$3.95^{+0.01}_{-0.11}$	$583.47^{+220.13}_{-151.89}$	H_2O, CO	$-2.79^{+1.51}_{-1.28}$, $-0.43^{+0.28}_{-7.29}$	$17.24^{+7.15}_{-5.96}$	0.89
HAT-P-11 b	$4.61^{+0.01}_{-0.01}$	$578.72^{+159.47}_{-98.61}$	H_2O	$-0.93^{+0.26}_{-2.19}$	$4.43^{+1.53}_{-2.01}$	9.99
HAT-P-26 b	$5.71^{+0.11}_{-0.11}$	$561.2^{+80.66}_{-45.03}$	H_2O	$-3.51^{+2.42}_{-0.58}$	$2.31^{+1.29}_{-0.01}$	41.75
HD 3167 c	$2.63^{+0.01}_{-0.01}$	$474.55^{+229.39}_{-98.48}$	H_2O, CO_2 [5]	$-3.9^{+2.19}_{-1.0}$, $-2.85^{+0.96}_{-4.16}$	$2.84^{+5.65}_{-0.48}$	11.13
HD 97658 b	$2.08^{+0.01}_{-0.01}$	$1076.39^{+16.98}_{-31.82}$	H_2O, CO_2 [6]	$-3.99^{+0.51}_{-0.35}$, $-1.95^{+0.22}_{-0.5}$	$2.85^{+0.29}_{-0.23}$	103.34
HD 106315 c	$4.28^{+0.11}_{-0.11}$	$883.98^{+215.16}_{-287.65}$	H_2O, NH_3	$-0.64^{+0.15}_{-1.08}$, $-6.29^{+2.35}_{-3.75}$	$5.94^{+1.46}_{-3.17}$	16.63
HD 219666 b	$4.28^{+0.11}_{-0.11}$	$752.27^{+246.8}_{-157.11}$	H_2O	$-2.45^{+1.61}_{-2.41}$	$2.6^{+2.14}_{-0.3}$	5.02
HIP 41378 b	$2.85^{+0.01}_{-0.11}$	$752.27^{+246.8}_{-157.11}$	H_2O, HCN	$-3.11^{+1.45}_{-4.04}$, $-4.73^{+2.41}_{-4.47}$	$2.47^{+1.35}_{-0.15}$	1.87
K2-18 b	$2.3^{+0.01}_{-0.01}$	$236.29^{+89.27}_{-62.39}$	H_2O, CO_2	$-3.84^{+1.65}_{-1.01}$, $-3.41^{+1.31}_{-4.99}$	$2.43^{+1.43}_{-0.12}$	3.47
K2-24 b	$5.38^{+0.11}_{-0.11}$	$484.06^{+207.79}_{-78.66}$	NH_3, H_2O	$-2.6^{+1.73}_{-3.7}$, $-6.86^{+3.75}_{-3.07}$	$4.71^{+8.31}_{-2.39}$	0.39
LHS 1140 b	$1.65^{+0.01}_{-0.01}$	$210.65^{+77.61}_{-55.66}$	H_2O	$-3.25^{+1.46}_{-1.11}$	$2.34^{+0.73}_{-0.03}$	2.19
LTT 9779 b	$4.39^{+0.11}_{-0.01}$	$2402.92^{+372.2}_{-597.53}$	CO_2, CH_4	$-6.37^{+5.21}_{-3.88}$, $-8.21^{+2.61}_{-2.42}$	$2.31^{+3.98}_{-0.01}$	5.71
TOI-270 c	$2.52^{+0.01}_{-0.01}$	$663.28^{+52.43}_{-145.06}$	CO_2	$-0.22^{+0.13}_{-0.16}$	$27.51^{+8.68}_{-7.55}$	1.36
TOI-270 d	$2.08^{+0.01}_{-0.01}$	$333.27^{+119.72}_{-77.9}$	H_2O, CO_2	$-3.53^{+1.42}_{-1.1}$, $-3.93^{+1.71}_{-5.02}$	$2.44^{+0.95}_{-0.13}$	5.19
TOI-674 b	$4.94^{+0.01}_{-0.01}$	$762.22^{+164.71}_{-179.85}$	H_2O, NH_3	$-0.44^{+0.23}_{-0.33}$, $-3.01^{+0.66}_{-3.12}$	$8.87^{+3.51}_{-3.28}$	16.70
TRAPPIST-1 b	$1.1^{+0.01}_{-0.11}$	$370.52^{+128.37}_{-109.14}$	CIA+ NH_3	$-7.99^{+2.21}_{-2.49}$	$2.39^{+4.38}_{-0.09}$	1.05
TRAPPIST-1 c	$1.1^{+0.01}_{-0.01}$	$278.09^{+126.02}_{-73.87}$	CIA	-	$3.45^{+12.96}_{-1.14}$	-0.99
TRAPPIST-1 d	$0.77^{+0.01}_{-0.01}$	$190.39^{+69.48}_{-32.85}$	H_2O +CIA	$-6.18^{+0.57}_{-1.14}$	$2.31^{+0.19}_{-0.0}$	0.28
TRAPPIST-1 e	$0.88^{+0.01}_{-0.01}$	$247.81^{+77.85}_{-80.96}$	CO_2, NH_3	$-2.14^{+1.35}_{-6.52}$, $-5.65^{+1.86}_{-3.87}$	$6.54^{+8.39}_{-3.47}$	0.43
TRAPPIST-1 f	$0.99^{+0.01}_{-0.01}$	$180.58^{+77.9}_{-48.39}$	CH_4 +CIA	$-6.51^{+3.49}_{-3.41}$	$4.82^{+10.64}_{-2.51}$	-0.31
TRAPPIST-1 g	$1.1^{+0.01}_{-0.01}$	$161.39^{+65.36}_{-42.05}$	H_2O, CO_2	$-6.69^{+3.59}_{-3.23}$, $-3.65^{+2.97}_{-5.57}$	$7.28^{+11.02}_{-4.9}$	-1.15
TRAPPIST-1 h	$0.77^{+0.01}_{-0.01}$	$141.86^{+59.64}_{-39.33}$	CO_2+CIA	$-0.91^{+0.66}_{-6.38}$	$14.81^{+12.28}_{-8.46}$	-1.72

Table D.3: Same as Table D.1 for 3-Hidden absorber retrieval analysis.

Name	R_P ($R_\oplus$)	T_P (K)	Main absorber X	$\log_{10}$(X) [10^{-12}-10^{-2}]	$\log_{10}(N_2/H_2)$ [10^{-12}-10^{4}]	μ (g/mol)	$\Delta\log$(E)
55-Cnc e	$1.76^{+0.01}_{-0.01}$	$1560.36^{+343.98}_{-241.61}$	HCN	$-3.49^{+0.96}_{-0.83}$	$-7.25^{+3.51}_{-2.95}$	$2.33^{+0.11}_{-0.02}$	29.88
GJ 436 b	$4.06^{+0.0}_{-0.0}$	$531.58^{+222.09}_{-143.28}$	-	-	$2.02^{+1.18}_{-1.24}$	$27.73^{+0.27}_{-3.89}$	-1.26
GJ 1132 b	$1.1^{+0.01}_{-0.01}$	$460.14^{+183.63}_{-111.9}$	NH_3	$-3.63^{+1.05}_{-3.47}$	$2.14^{+1.16}_{-1.12}$	$27.78^{+0.21}_{-2.37}$	-1.0
GJ 1214 b	$2.63^{+0.01}_{-0.01}$	$655.36^{+138.26}_{-203.5}$	H_2O	$-6.68^{+0.55}_{-0.72}$	$2.43^{+1.03}_{-1.07}$	$27.9^{+0.1}_{-1.15}$	3.53
GJ 3470 b	$3.95^{+0.01}_{-0.01}$	$784.57^{+158.32}_{-220.18}$	H_2O	$-3.44^{+0.9}_{-1.45}$	$2.16^{+1.14}_{-1.29}$	$27.79^{+0.2}_{-3.31}$	1.59
HAT-P-11 b	$4.61^{+0.01}_{-0.01}$	$651.83^{+228.45}_{-156.49}$	H_2O	$-3.84^{+0.94}_{-0.91}$	$-3.8^{+3.07}_{-5.35}$	$2.34^{+3.46}_{-0.04}$	8.41
HAT-P-26 b	$5.71^{+0.01}_{-0.01}$	$561.41^{+77.63}_{-45.35}$	H_2O	$-3.73^{+0.41}_{-0.44}$	$-7.4^{+3.53}_{-3.02}$	$2.31^{+0.01}_{-0.01}$	41.66
HD 3167 c	$2.63^{+0.01}_{-0.01}$	$430.31^{+92.56}_{-70.01}$	H_2O [7]	$-4.44^{+0.58}_{-0.59}$	$-7.18^{+3.3}_{-3.08}$	$2.41^{+0.16}_{-0.08}$	10.79
HD 97658 b	$2.08^{+0.01}_{-0.01}$	$1071.61^{+19.89}_{-35.11}$	H_2O[8]	$-4.07^{+0.44}_{-0.35}$	$-7.34^{+3.3}_{-3.06}$	$2.61^{+0.11}_{-0.13}$	102.79
HD 106315 c	$4.39^{+0.11}_{-0.11}$	$578.93^{+364.37}_{-79.39}$	H_2O[9]	$0.28^{+1.86}_{-0.21}$	$-5.79^{+5.07}_{-3.98}$	$2.36^{+3.62}_{-0.05}$	15.12
HD 219666 b	$4.39^{+0.01}_{-0.11}$	$785.79^{+245.76}_{-158.23}$	H_2O	$-4.48^{+0.96}_{-0.69}$	$-7.11^{+3.76}_{-3.15}$	$2.31^{+0.06}_{-0.01}$	4.43
HIP 41378 b	$2.85^{+0.01}_{-0.01}$	$796.26^{+297.72}_{-179.91}$	H_2O	$-4.07^{+1.34}_{-3.95}$	$-5.97^{+4.2}_{-3.71}$	$2.35^{+0.39}_{-0.04}$	1.66
K2-18 b	$2.3^{+0.01}_{-0.01}$	$258.73^{+85.28}_{-72.59}$	H_2O	$-4.22^{+0.89}_{-0.76}$	$-6.43^{+4.14}_{-3.55}$	$2.35^{+0.27}_{-0.04}$	3.13
K2-24 b	$5.49^{+0.01}_{-0.01}$	$571.84^{+289.39}_{-155.3}$	NH_3	$-4.88^{+1.89}_{-3.94}$	$0.44^{+2.1}_{-8.03}$	$20.35^{+7.56}_{-18.04}$	0.05
LHS 1140 b	$1.65^{+0.01}_{-0.01}$	$218.61^{+74.9}_{-59.67}$	H_2O	$-3.61^{+0.95}_{-0.96}$	$-6.57^{+3.85}_{-3.4}$	$2.33^{+0.14}_{-0.02}$	2.23
LTT 9779 b	$4.28^{+0.11}_{-0.01}$	$2438.08^{+342.79}_{-530.59}$	CIA	-	$-7.05^{+3.69}_{-3.1}$	$2.31^{+0.02}_{-0.01}$	5.54
TOI-270 c	$2.52^{+0.01}_{-0.01}$	$600.98^{+89.05}_{-172.77}$	NH_3	$-2.89^{+0.57}_{-0.93}$	$2.08^{+1.2}_{-1.24}$	$27.74^{+0.23}_{-3.44}$	0.74
TOI-270 d	$2.08^{+0.01}_{-0.01}$	$339.77^{+102.97}_{-74.55}$	H_2O	$-3.89^{+0.86}_{-0.8}$	$-7.13^{+3.61}_{-3.06}$	$2.35^{+0.18}_{-0.04}$	4.87
TOI-674 b	$5.05^{+0.01}_{-0.01}$	$811.28^{+159.06}_{-381.66}$	H_2O	$-3.17^{+0.73}_{-1.01}$	$-0.37^{+0.3}_{-6.42}$	$9.14^{+3.95}_{-6.83}$	14.49
TRAPPIST-1 b	$1.1^{+0.01}_{-0.01}$	$400.91^{+117.39}_{-118.05}$	-	-	$-3.53^{+4.77}_{-5.2}$	$2.41^{+23.97}_{-0.11}$	0.82
TRAPPIST-1 c	$1.1^{+0.01}_{-0.01}$	$318.22^{+112.1}_{-99.48}$	-	-	$0.63^{+2.07}_{-6.79}$	$22.49^{+5.45}_{-20.19}$	-0.43
TRAPPIST-1 d	$0.77^{+0.01}_{-0.01}$	$271.61^{+94.89}_{-83.51}$	H_2O +CIA	$-6.24^{+0.62}_{-1.98}$	$-5.73^{+6.3}_{-4.11}$	$2.32^{+19.61}_{-0.01}$	0.59
TRAPPIST-1 e	$0.88^{+0.01}_{-0.01}$	$255.64^{+72.86}_{-80.18}$	NH_3	$-5.2^{+1.5}_{-3.3}$	$0.41^{+2.21}_{-8.0}$	$19.98^{+7.95}_{-17.63}$	0.03
TRAPPIST-1 f	$0.99^{+0.01}_{-0.01}$	$213.23^{+67.74}_{-68.74}$	-	-	$0.5^{+2.11}_{-7.22}$	$21.07^{+6.86}_{-18.75}$	-0.17
TRAPPIST-1 g	$1.1^{+0.01}_{-0.01}$	$208.99^{+55.14}_{-70.88}$	-	-	$1.17^{+1.73}_{-4.33}$	$26.11^{+1.85}_{-23.64}$	-0.63
TRAPPIST-1 h	$0.77^{+0.01}_{-0.01}$	$161.69^{+60.68}_{-52.79}$	-	-	$1.87^{+1.32}_{-1.34}$	$27.61^{+0.38}_{-6.19}$	-1.19

[5] HCN is also constrained with a $\log_{10}(HCN) = -4.6^{+3.9}_{-3.6}$

[6] NH_3 and HCN are also constrained with a $\log_{10}(NH_3) = -4.08^{+0.61}_{-0.38}$ and $\log_{10}(HCN) = -2.86^{+0.61}_{-0.44}$

[7] CO_2 and HCN are also constrained with a $\log_{10}(CO_2) = -2.72^{+0.47}_{-0.64}$ and $\log_{10}(HCN) = -5.27^{+1.17}_{-3.35}$

[8] The best fit contribution is actually a combination of H_2O, CO_2, NH_3 and HCN. $\log_{10}(CO_2) = -2.2^{+0.14}_{-0.48}$, $\log_{10}(HCN) = -3.12^{+0.54}_{-0.47}$, $\log_{10}(NH_3) = -4.13^{+0.47}_{-0.37}$

[9] NH_3 is also constrained with a $\log_{10}(NH_3) = -5.1^{+0.84}_{-3.08}$

Table D.4: Same as Table D.1 for 4-Primary clear with trace of H_2O retrieval analysis. The abundance of H_2O is fixed to 10^{-3}.

Name	R_P ($R_\oplus$)	T_P (K)	μ (g/mol)	Δlog(E)
55-Cnc e	$1.43^{+0.01}_{-0.01}$	$2802.54^{+104.31}_{-177.75}$	2.32	8.8
GJ 436 b	$3.95^{+0.01}_{-0.01}$	$313.57^{+5.88}_{-2.69}$	2.32	-28.53
GJ 1132 b	$0.99^{+0.01}_{-0.01}$	$291.15^{+1.94}_{-0.87}$	2.32	-112.49
GJ 1214 b	$2.63^{+0.01}_{-0.01}$	$280.08^{+0.14}_{-0.06}$	2.32	-1410.62
GJ 3470 b	$3.84^{+0.01}_{-0.01}$	$341.51^{+2.65}_{-1.12}$	2.32	-56.39
HAT-P-11 b	$4.61^{+0.01}_{-0.01}$	$456.8^{+32.46}_{-20.27}$	2.32	8.42
HAT-P-26 b	$5.71^{+0.01}_{-0.01}$	$514.05^{+17.73}_{-10.35}$	2.32	43.12
HD 3167 c	$2.63^{+0.01}_{-0.01}$	$283.6^{+15.82}_{-9.98}$	2.32	-1.68
HD 97658 b	$2.19^{+0.01}_{-0.01}$	$368.79^{+13.17}_{-6.22}$	2.32	-25.42
HD 106315 c	$4.39^{+0.01}_{-0.01}$	$461.7^{+33.86}_{-15.59}$	2.32	10.97
HD 219666 b	$4.39^{+0.01}_{-0.01}$	$611.62^{+101.02}_{-59.88}$	2.32	4.22
HIP 41378 b	$2.85^{+0.01}_{-0.11}$	$839.76^{+256.66}_{-206.42}$	2.32	2.44
K2-18 b	$2.3^{+0.01}_{-0.01}$	$165.52^{+27.91}_{-16.83}$	2.32	2.9
K2-24 b	$5.38^{+0.01}_{-0.01}$	$387.12^{+26.45}_{-12.55}$	2.32	-9.9
LHS 1140 b	$1.65^{+0.01}_{-0.01}$	$194.39^{+55.41}_{-47.57}$	2.32	3.7
LTT 9779 b	$4.28^{+0.11}_{-0.22}$	$1206.93^{+456.26}_{-177.36}$	2.32	-5.55
TOI-270 c	$2.52^{+0.01}_{-0.01}$	$241.93^{+3.4}_{-1.44}$	2.32	-47.82
TOI-270 d	$2.08^{+0.01}_{-0.01}$	$245.51^{+51.07}_{-37.48}$	2.32	3.47
TOI-674 b	$4.94^{+0.01}_{-0.01}$	$343.41^{+5.78}_{-2.59}$	2.32	-9.49
TRAPPIST-1 b	$1.1^{+0.01}_{-0.01}$	$203.27^{+20.34}_{-9.12}$	2.32	-8.87
TRAPPIST-1 c	$1.1^{+0.01}_{-0.01}$	$185.11^{+25.75}_{-11.36}$	2.32	- 7.03
TRAPPIST-1 d	$0.77^{+0.01}_{-0.01}$	$142.81^{+4.3}_{-2.17}$	2.32	-13.3
TRAPPIST-1 e	$0.88^{+0.01}_{-0.01}$	$125.43^{+9.0}_{-4.27}$	2.32	-12.45
TRAPPIST-1 f	$0.99^{+0.01}_{-0.01}$	$111.93^{+17.6}_{-8.96}$	2.32	-4.2
TRAPPIST-1 g	$1.1^{+0.01}_{-0.01}$	$109.3^{+27.02}_{-14.25}$	2.32	-2.6
TRAPPIST-1 h	$0.66^{+0.01}_{-0.01}$	$82.63^{+3.85}_{-1.94}$	2.32	-16.91

Table D.5: Same as Table D.1 for 5-Water world retrieval analysis. The atmosphere is pure water.

Name	R_P ($R_\oplus$)	T_P (K)	μ (g/mol)	Δlog(E)
55-Cnc e	$1.76^{+0.01}_{-0.01}$	$2663.26^{+203.89}_{-468.92}$	18.02	5.06
GJ 436 b	$4.06^{+0.01}_{-0.01}$	$389.0^{+112.55}_{-57.29}$	18.02	-1.94
GJ 1132 b	$1.1^{+0.01}_{-0.01}$	$310.98^{+33.75}_{-15.81}$	18.02	-7.72
GJ 1214 b	$2.63^{+0.01}_{-0.01}$	$282.27^{+3.93}_{-1.72}$	18.02	-37.51
GJ 3470 b	$3.95^{+0.01}_{-0.01}$	$511.72^{+180.57}_{-120.59}$	18.02	2.15
HAT-P-11 b	$4.72^{+0.01}_{-0.01}$	$1049.4^{+180.23}_{-278.33}$	18.02	7.24
HAT-P-26 b	$5.82^{+0.01}_{-0.01}$	$1190.06^{+201.74}_{-213.19}$	18.02	21.5
HD 3167 c	$2.63^{+0.01}_{-0.01}$	$764.48^{+48.79}_{-103.65}$	18.02	9.14
HD 97658 b	$2.19^{+0.01}_{-0.01}$	$1072.71^{+20.26}_{-37.63}$	18.02	12.63
HD 106315 c	$4.39^{+0.11}_{-0.11}$	$1152.9^{+117.73}_{-180.46}$	18.02	12.22
HD 219666 b	$4.39^{+0.11}_{-0.01}$	$1308.38^{+280.38}_{-383.62}$	18.02	3.78
HIP 41378 b	$2.96^{+0.01}_{-0.01}$	$1067.08^{+293.2}_{-360.87}$	18.02	1.0
K2-18 b	$2.41^{+0.01}_{-0.01}$	$338.43^{+67.91}_{-104.27}$	18.02	2.77
K2-24 b	$5.49^{+0.01}_{-0.01}$	$817.25^{+248.3}_{-271.08}$	18.02	0.14
LHS 1140 b	$1.65^{+0.01}_{-0.01}$	$273.49^{+62.92}_{-92.96}$	18.02	1.45
LTT 9779 b	$4.39^{+0.11}_{-0.01}$	$2425.1^{+395.32}_{-652.72}$	18.02	2.16
TOI-270 c	$2.52^{+0.01}_{-0.01}$	$291.22^{+73.0}_{-37.41}$	18.02	-3.08
TOI-270 d	$2.08^{+0.01}_{-0.01}$	$483.2^{+77.95}_{-136.29}$	18.02	3.22
TOI-674 b	$5.05^{+0.01}_{-0.01}$	$962.08^{+61.41}_{-118.63}$	18.02	17.86
TRAPPIST-1 b	$1.1^{+0.01}_{-0.01}$	$309.52^{+147.0}_{-87.96}$	18.02	-1.54
TRAPPIST-1 c	$1.1^{+0.01}_{-0.01}$	$293.21^{+119.76}_{-89.55}$	18.02	-1.11
TRAPPIST-1 d	$0.77^{+0.01}_{-0.01}$	$176.68^{+54.28}_{-27.38}$	18.02	-2.26
TRAPPIST-1 e	$0.88^{+0.01}_{-0.01}$	$181.98^{+86.47}_{-46.2}$	18.02	-1.7
TRAPPIST-1 f	$0.99^{+0.01}_{-0.01}$	$178.04^{+83.7}_{-56.78}$	18.02	-0.64
TRAPPIST-1 g	$1.1^{+0.01}_{-0.01}$	$173.62^{+79.57}_{-59.15}$	18.02	-0.44
TRAPPIST-1 h	$0.77^{+0.01}_{-0.01}$	$99.81^{+34.43}_{-14.62}$	18.02	-3.71

Table D.6: Logarithm evidence results for six atmospheric retrievals analysis on the 26 HST WFC3 G141 transmission spectra.

Name	flat line	Primary	Active clear	Hidden absorber	Primary clear	Water World
55-Cnc e	203.88	233.31	233.82	233.76	212.76	208.94
GJ 436 b	211.86	211.90	208.11	210.60	183.33	209.92
GJ 1132 b	216.77	216.28	214.11	215.77	104.28	209.05
GJ 1214 b	180.62	181.92	168.20	184.15	-1230	143.11
GJ 3470 b	209.76	211.49	210.65	211.35	153.37	211.91
HAT-P-11 b	198.25	207.30	208.24	206.66	206.67	205.49
HAT-P-26 b	153.44	195.92	195.19	195.10	196.59	174.94
HD 3167 c	225.83	235.31	236.96	236.62	224.15	232.97
HD 97658 b	82.60	183.96	185.94	185.39	57.18	95.23
HD 106315 c	210.89	226.07	227.52	226.01	221.86	223.11
HD 219666 b	192.74	197.02	197.76	197.17	196.96	196.52
HIP 41378 b	228.14	229.23	230.01	229.80	230.58	229.14
K2-18 b	146.31	149.27	149.78	149.44	149.21	149.08
K2-24 b	200.53	200.69	200.92	200.58	190.63	200.67
LHS 1140 b	191.56	193.50	193.75	193.79	195.26	193.01
LTT-9779 b	192.10	196.16	197.81	197.64	186.55	194.26
TOI-270 c	167.22	167.89	168.58	167.96	119.40	164.14
TOI-270 d	193.27	198.24	198.46	198.14	196.74	196.49
TOI-674 b	172.15	187.79	188.85	186.64	162.66	190.01
TRAPPIST-1 b	76.04	76.62	77.09	76.86	67.17	74.50
TRAPPIST-1 c	77.53	77.25	76.54	77.10	70.50	76.42
TRAPPIST-1 d	71.91	71.84	72.19	72.50	58.61	69.65
TRAPPIST-1 e	81.97	82.46	82.40	82.00	69.52	80.27
TRAPPIST-1 f	79.51	79.61	79.20	79.34	75.31	78.87
TRAPPIST-1 g	79.53	79.36	78.38	78.90	76.93	79.09
TRAPPIST-1 h	110.44	110.00	108.72	109.25	93.53	106.73

Appendix E

Exo-REM model grid

Table E.1: Best-fit retrieval results comparison with self-consistent computations grid. The best-fit results are from the survey atmospheric retrieval analysis with `Tau-REX 3` (see Chapter 7). The temperature is set to the irradiation temperature.

	Retrieval analysis			Model grid		
Planet	Spectral contributors	μ (g/mol)	T_P (K)	metallicity (x solar)	T (K)	Expected
HAT-P-11 b	H_2O	$4.4^{+1.5}_{-2.0}$	867	300	900	H_2O
HAT-P-26 b	H_2O	$2.3^{+0.1}_{-0.1}$	993	1	1000	H_2O
HD 3167 c	H_2O, CO_2	$2.8^{+5.6}_{-0.3}$	548	10	500	CH_4
HD 97658 b	H_2O, CO_2, HCN, NH_3	$2.9^{+0.3}_{-0.2}$	733	10	700	H_2O, NH_3, CH_4
HD 106315 c	H_2O, NH_3	$5.9^{+1.5}_{-3.1}$	883	300	900	H_2O
HD 219666 b	H_2O	$2.6^{+2.1}_{-0.3}$	1073	10	1100	H_2O
K2-18 b	H_2O	$2.4^{+1.4}_{-0.1}$	283	10	300	CH_4, NH_3
LHS 1140 b	H_2O	$2.3^{+0.1}_{-0.1}$	234	1	200	CH_4, NH_3
TOI-270 d	H_2O, CO_2	$2.4^{+1.0}_{-0.1}$	387	10	400	CH_4, NH_3
TOI-674 b	H_2O, NH_3	$8.8^{+3.5}_{-3.3}$	674	1000	700	H_2O

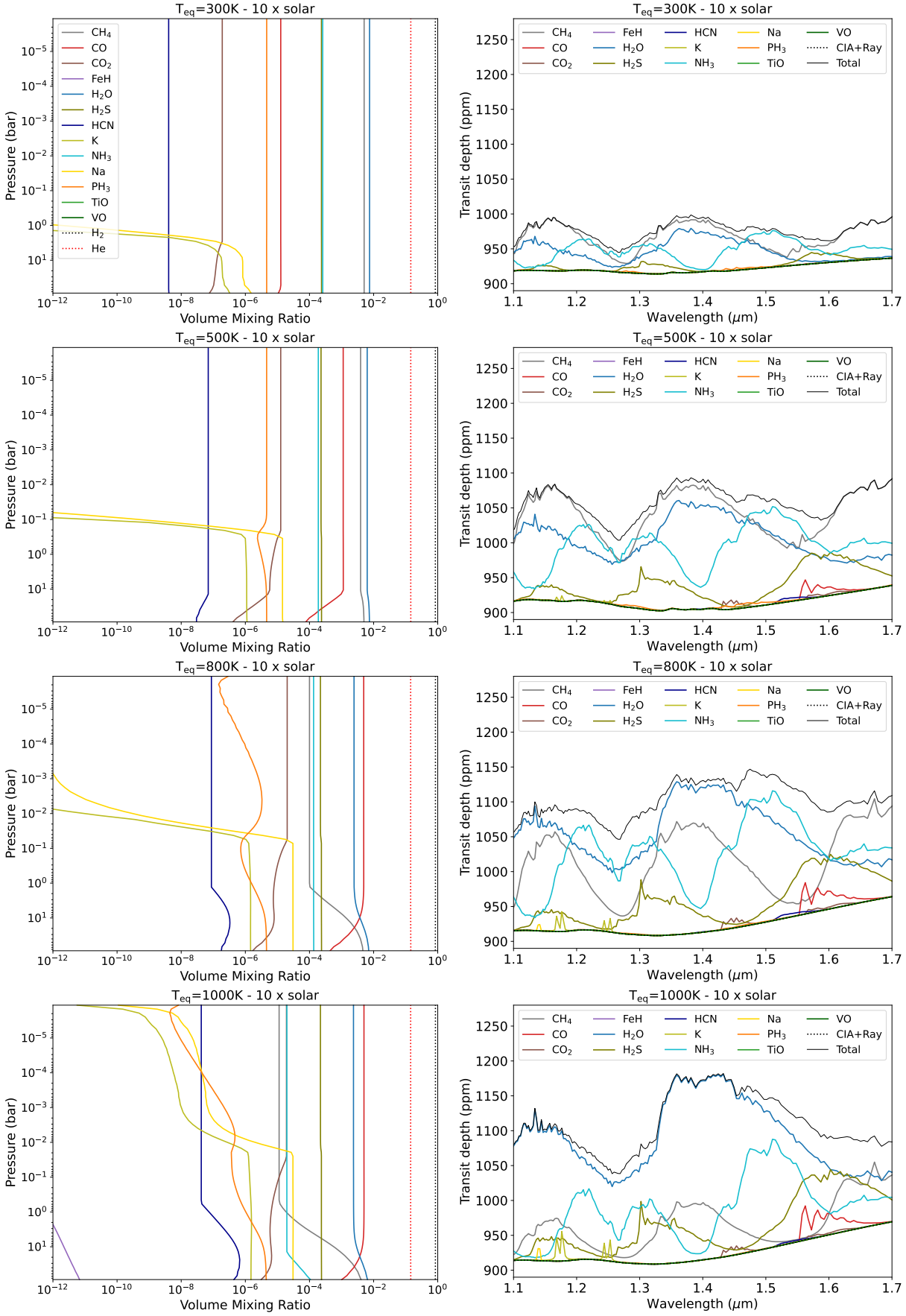

Figure E.1: Volume mixing ratios and NIR spectral opacity contributions for a 10 × solar atmospheric composition at 300, 500, 800 and 1000 K.

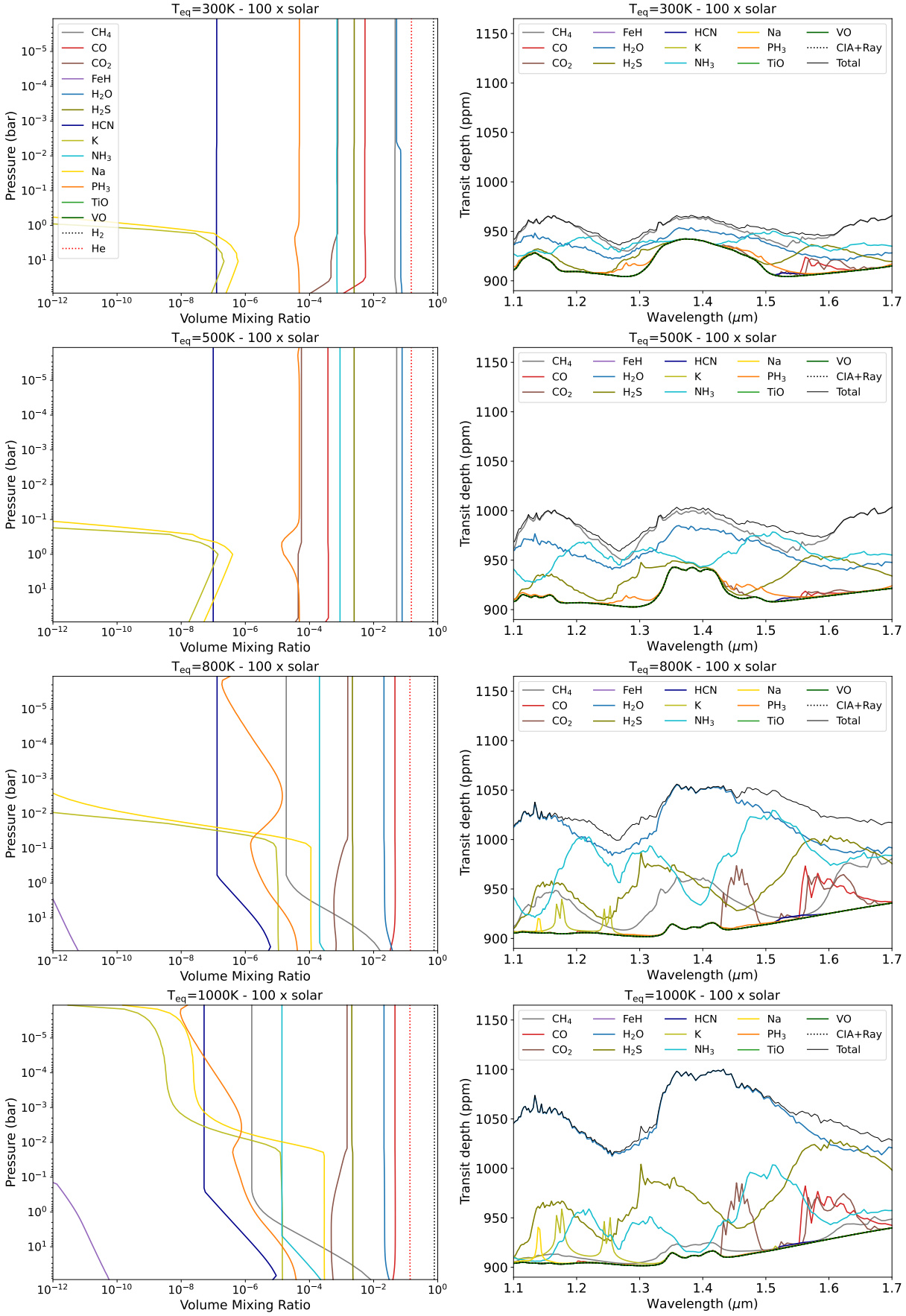

Figure E.2: Volume mixing ratios and NIR spectral opacity contributions for a 100 × solar atmospheric composition at 300, 500, 800 and 1000 K.

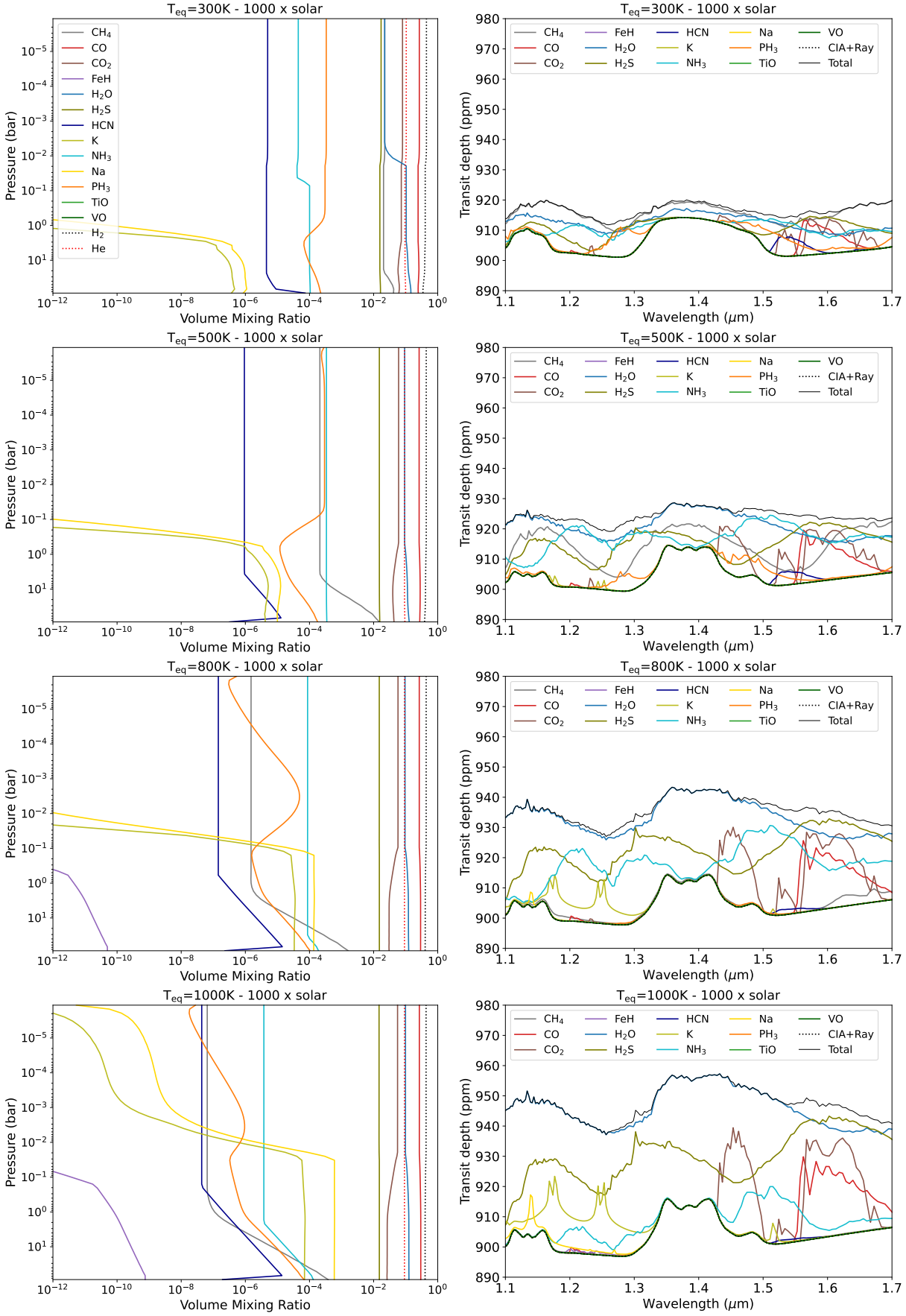

Figure E.3: Volume mixing ratios and NIR spectral opacity contributions for a 1000 × solar atmospheric composition at 300, 500, 800 and 1000 K.

Appendix F

HD 219666 b observations and modelling

Model	Cloud-free	Na_2S condensation			ZnS condensation		
1 × solar	88.7	624.2	654.5	588.1	88.8	88.8	88.8
10 × solar	34.7	151.5	200.0	183.8	34.5	34.5	34.5
100 × solar	31.2	61.8	96.9	96.2	40.5	66.4	66.2
300 × solar	35.4	54.5	88.6	88.8	37.2	59.6	61.5

Table F.1: Chi-squared (χ^2) computed using `Exo-REM` simulations and the CHEOPS/HST combined transmission spectrum.

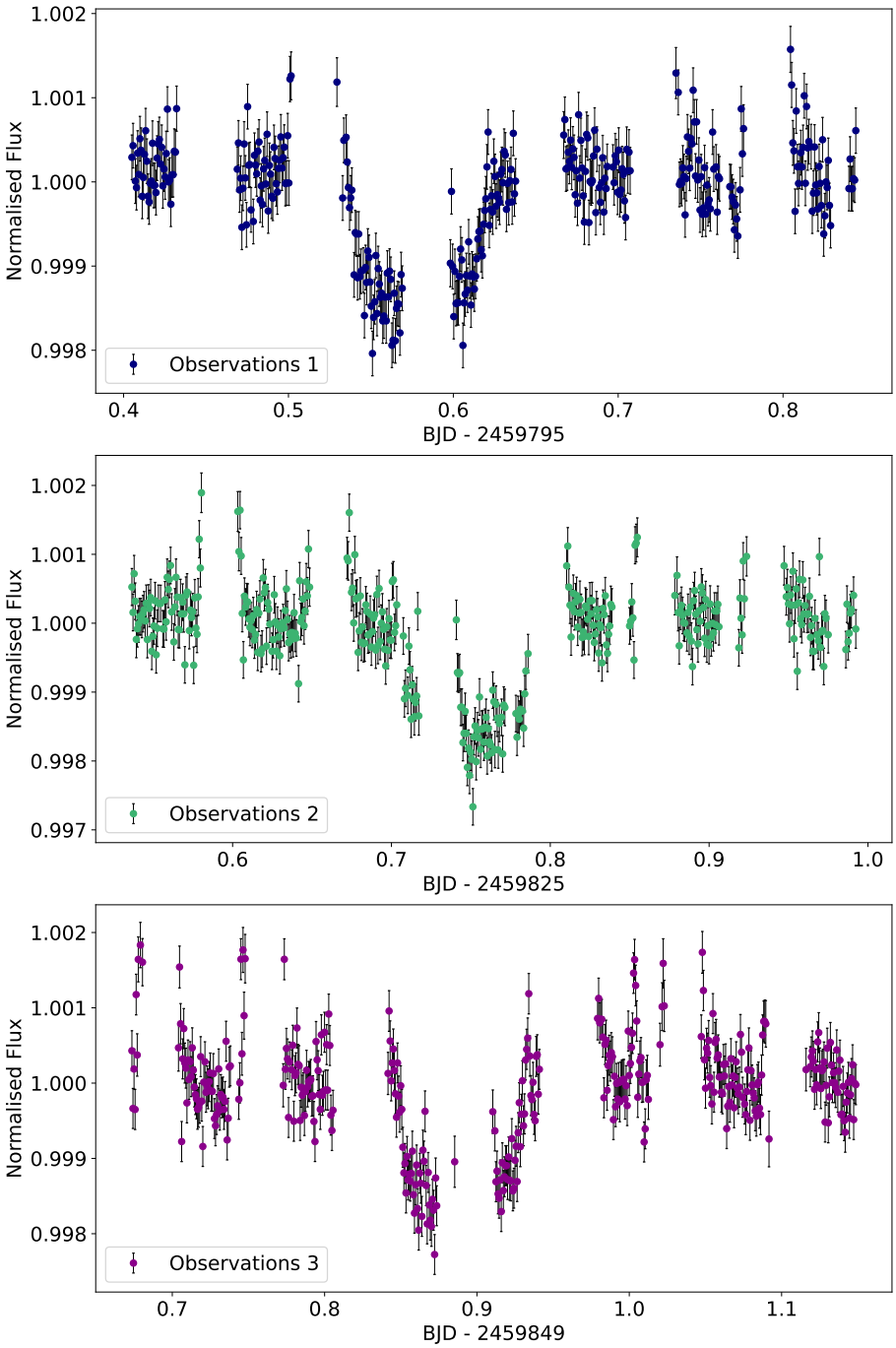

Figure F.1: CHEOPS individual raw transit light curves of HD 219666 b.

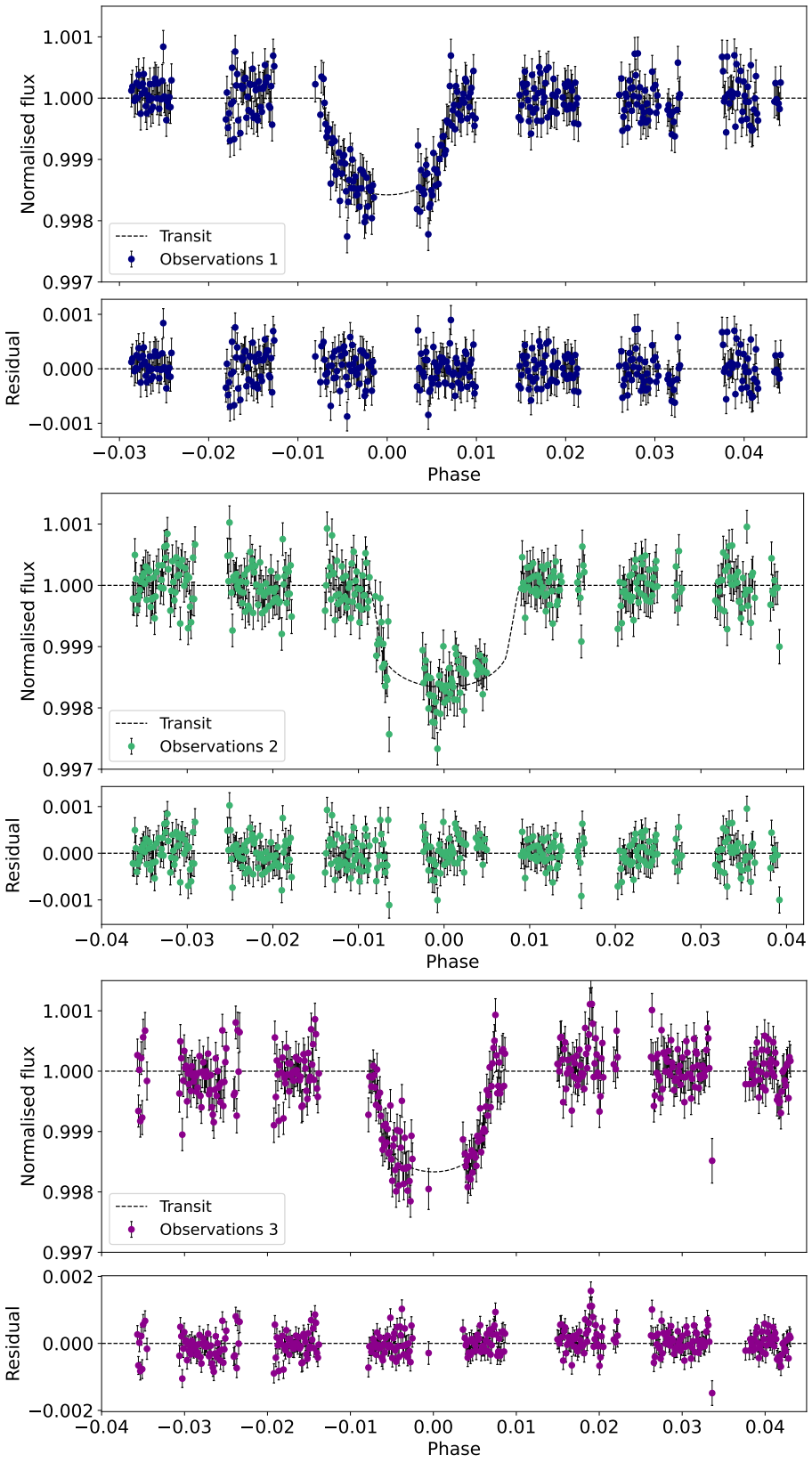

Figure F.2: CHEOPS individual corrected transit light curves of HD 219666 b.

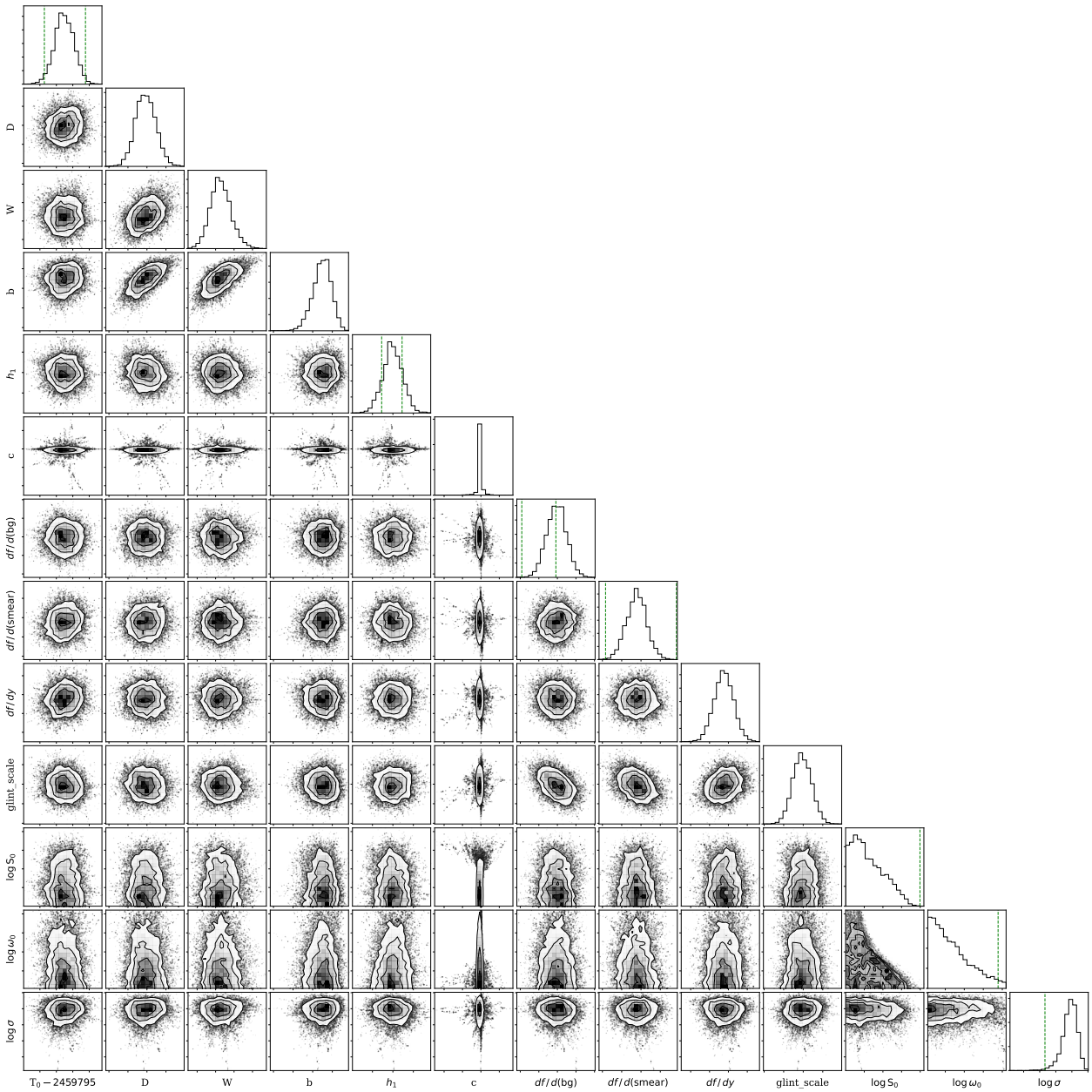

Figure F.3: Posterior distributions to CHEOPS Observations 1 transit light curve analysis of HD 219666 b.

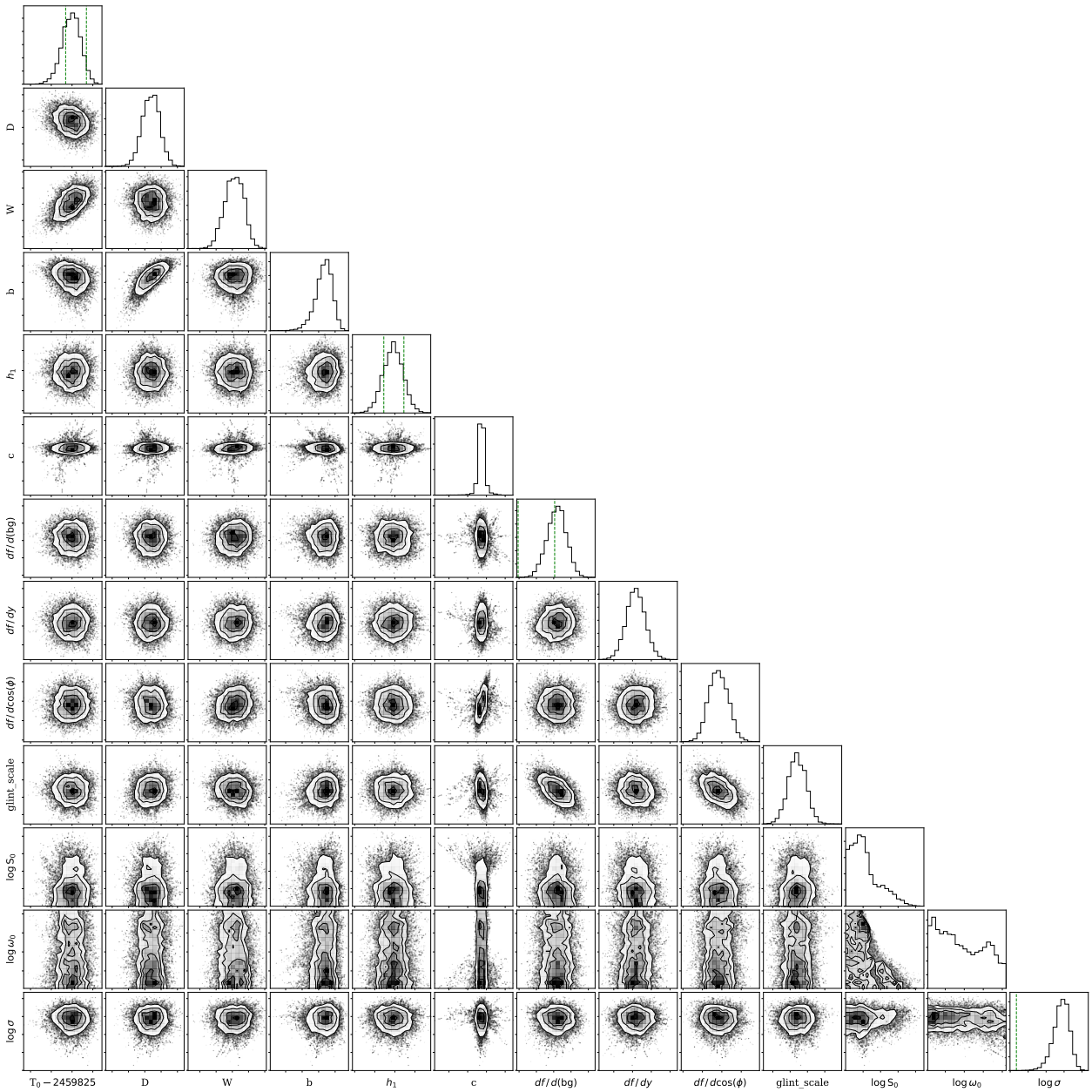

Figure F.4: Posterior distributions to CHEOPS Observations 2 transit light curve analysis of HD 219666 b.

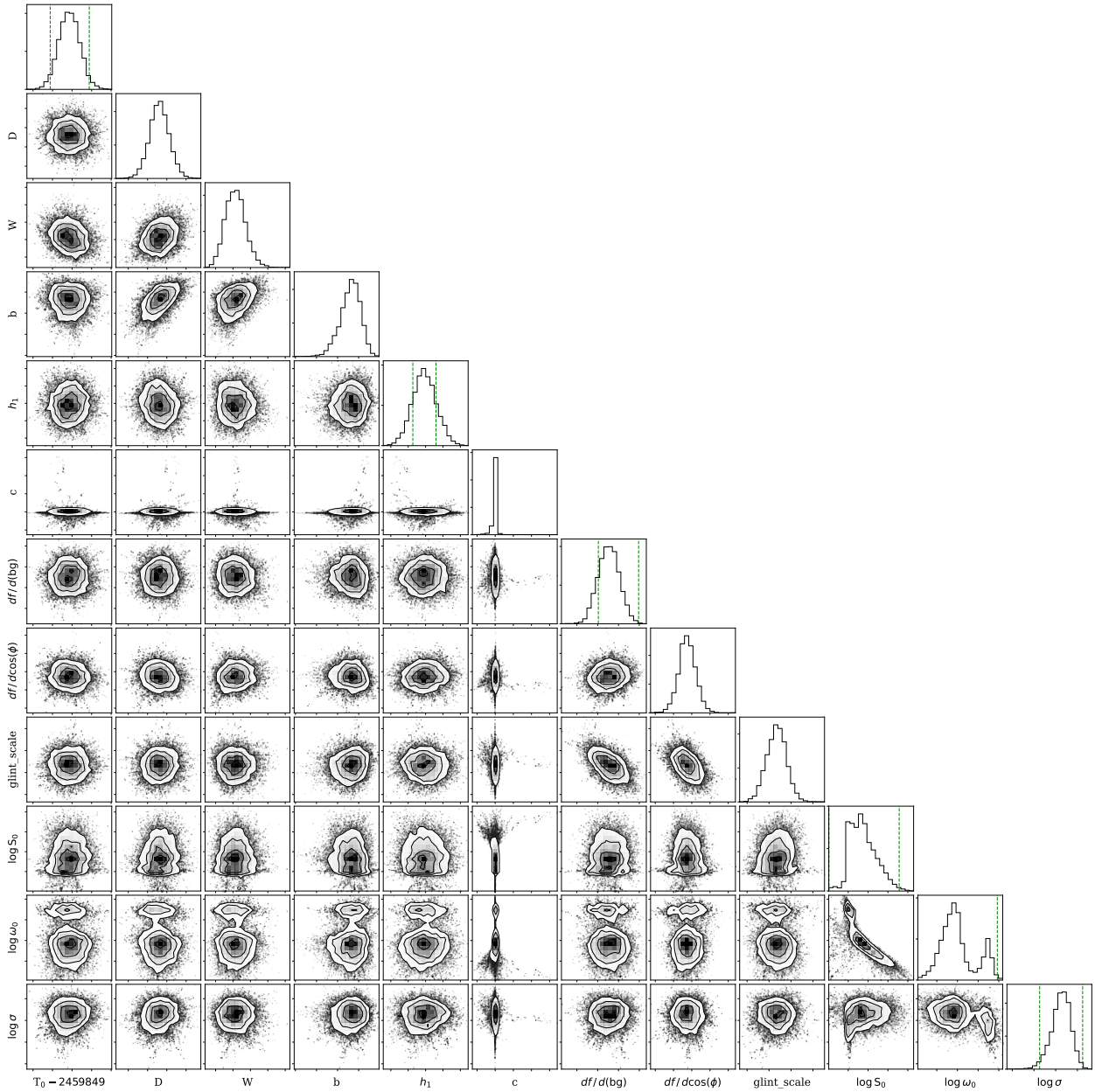

Figure F.5: Posterior distribution to CHEOPS Observations 3 transit light curve analysis of HD 219666 b.

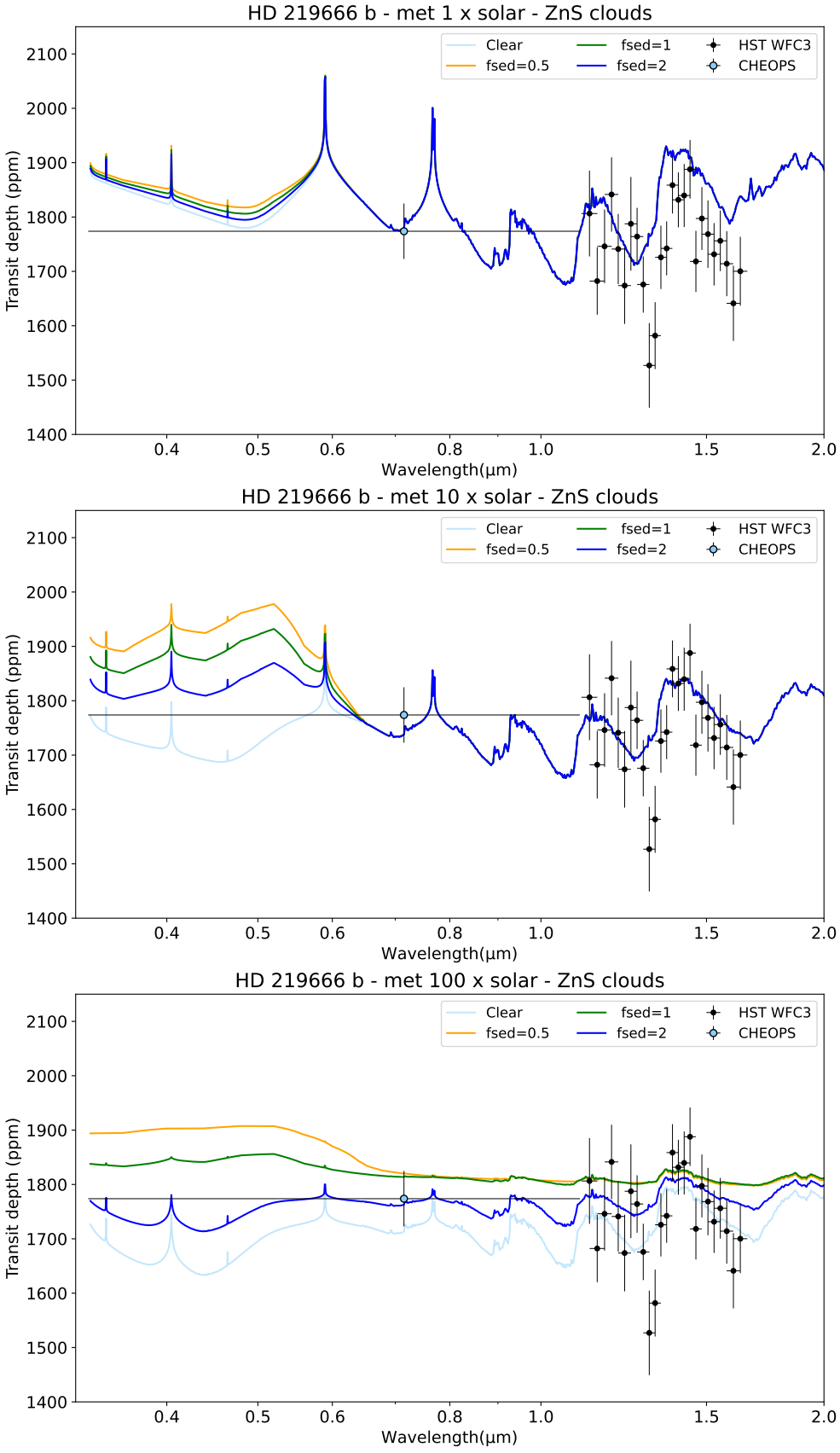

Figure F.6: CHEOPS (blue) and HST (black data points) transit observations of HD 219666 b and simulated transmission spectra for a cloudy atmosphere. The simulations are from `Exo-REM` self-consistent computations for 1 (top), 10 (middle), 100 (bottom) × solar atmospheric composition. We include ZnS clouds with three different sedimentation parameters.

Appendix G

ARIEL simulations supplementary materials

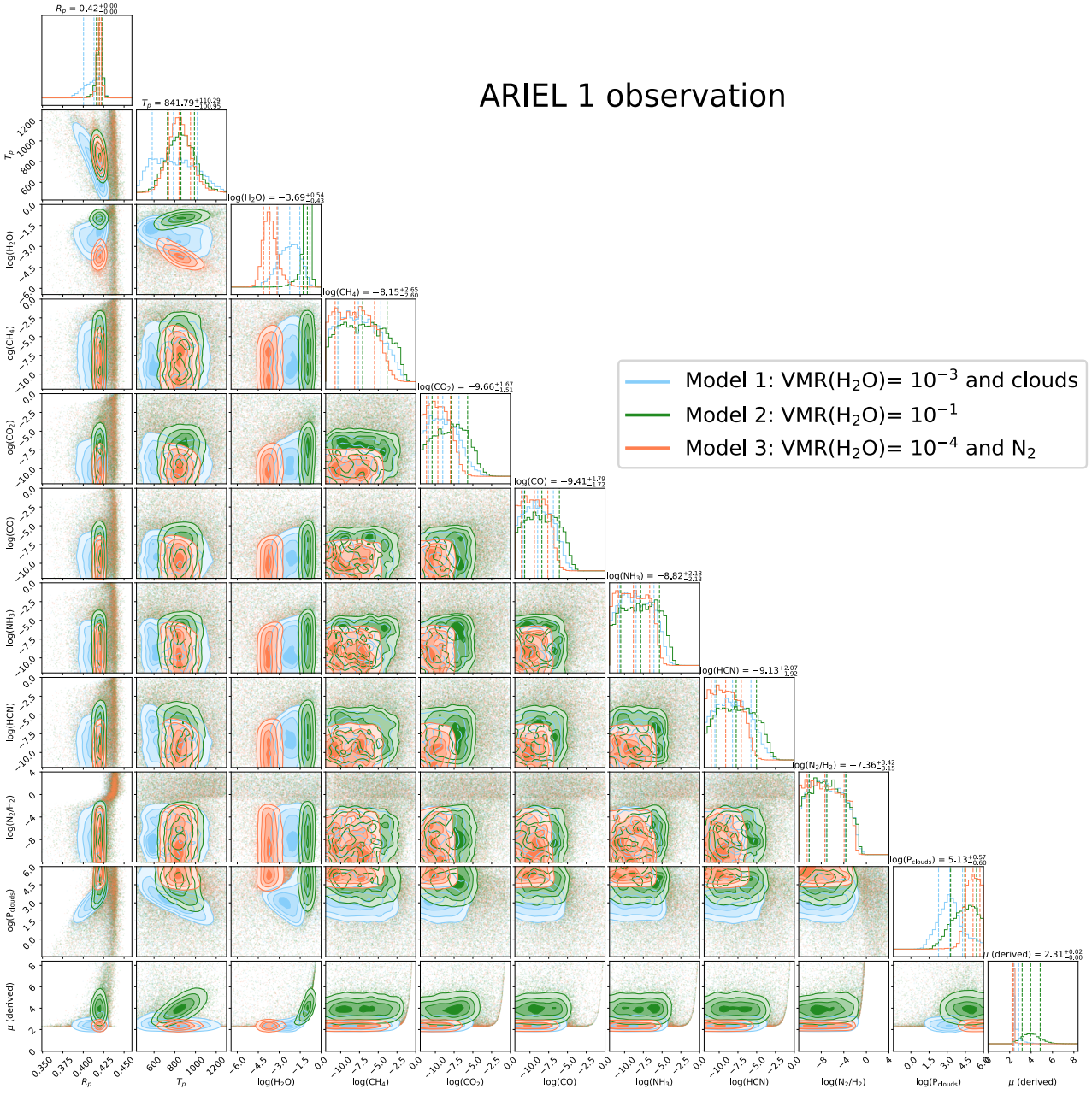

Figure G.1: Posteriors distributions for the three models of HAT-P-11 b obtained with one simulated transit of ARIEL. Model 1, in blue, is representative of a primary cloudy atmosphere, Model 2 in green, is a water-rich atmosphere and Model 3 in orange is a nitrogen-rich atmosphere.

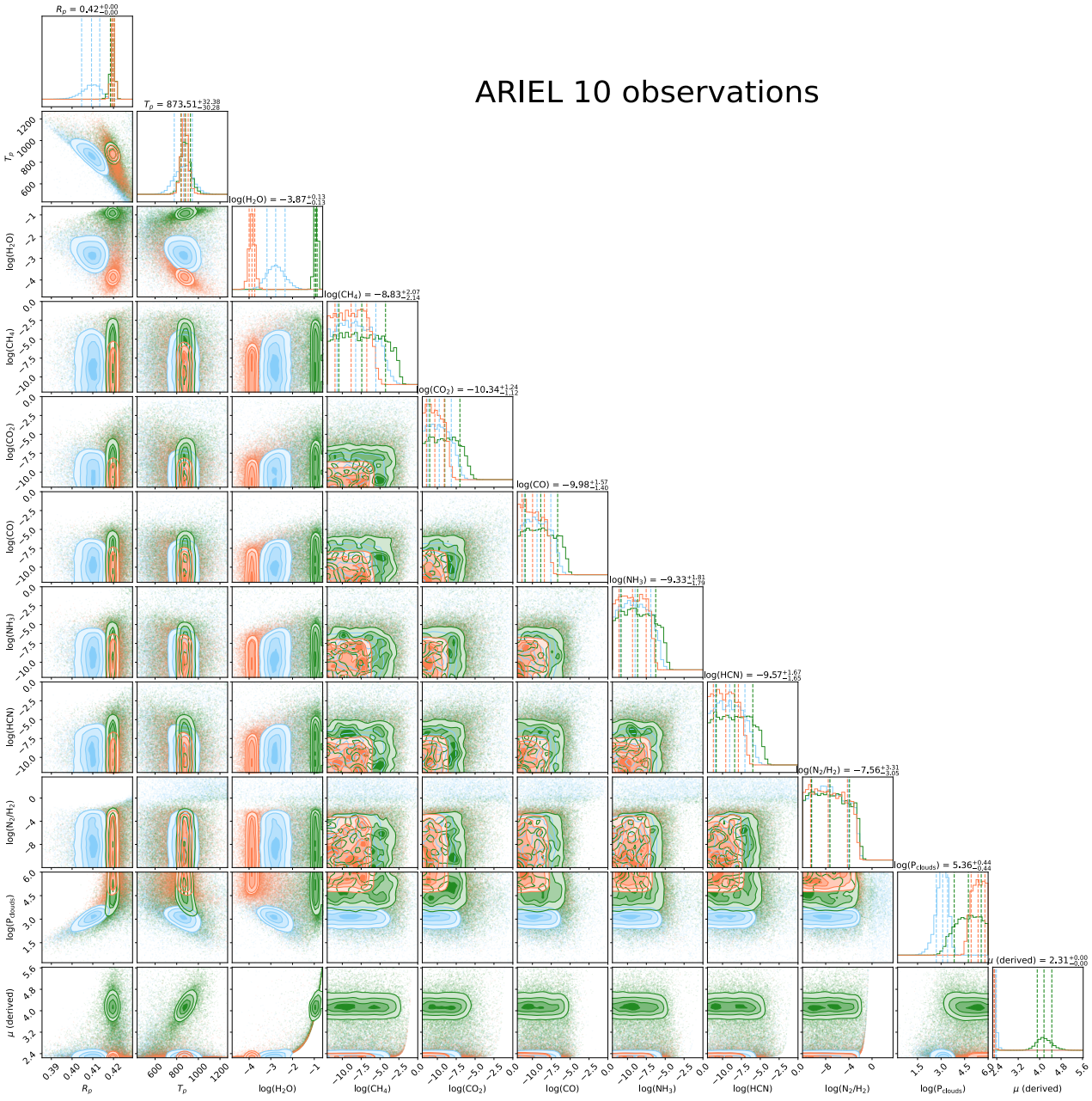

Figure G.2: Same as Figure G.1 for ten simulated transits of ARIEL.

Table G.1: Comparison of the retrieval results on HAT-P-11 b simulated spectra with ARIEL.

Number of transits	1 ARIEL			5 ARIEL			10 ARIEL		
Model	1	2	3	1	2	3	1	2	3
R_P ($R_\oplus$)	$4.50^{+0.11}_{-0.11}$	$4.61^{+0.01}_{-0.01}$	$4.61^{+0.01}_{-0.01}$	$4.50^{+0.01}_{-0.01}$	$4.61^{+0.01}_{-0.01}$	$4.61^{+0.01}_{-0.01}$	$4.50^{+0.01}_{-0.01}$	$4.61^{+0.01}_{-0.01}$	$4.61^{+0.01}_{-0.01}$
T (K)	786^{+230}_{-205}	859^{+130}_{-130}	842^{+110}_{-101}	866^{+117}_{-120}	878^{+62}_{-57}	871^{+45}_{-46}	863^{+81}_{-86}	881^{+46}_{-41}	874^{+32}_{-30}
$\log_{10}(N_2/H_2)$	$-7.14^{+3.40}_{-3.03}$	$-7.01^{+3.38}_{-3.14}$	$-7.36^{+3.42}_{-3.15}$	$-7.58^{+3.32}_{-2.93}$	$-7.27^{+3.55}_{-3.12}$	$-7.59^{+3.38}_{-3.03}$	$-7.39^{+3.29}_{-3.01}$	$-7.26^{+3.37}_{-3.18}$	$-7.56^{+3.31}_{-3.05}$
$\log_{10}(P_{clouds})$	$3.22^{+1.05}_{-0.93}$	$4.45^{+1.17}_{-0.97}$	$5.13^{+0.57}_{-0.60}$	$3.04^{+0.42}_{-0.57}$	$4.64^{+0.89}_{-0.92}$	$5.30^{+0.47}_{-0.47}$	$3.10^{+0.31}_{-0.41}$	$4.74^{+0.82}_{-0.90}$	$5.36^{+0.44}_{-0.44}$
$\log_{10}(H_2O)$	$-2.25^{+0.84}_{-0.72}$	$-0.99^{+0.19}_{-0.30}$	$-3.69^{+0.54}_{-0.43}$	$-2.65^{+0.51}_{-0.53}$	$-0.93^{+0.09}_{-0.10}$	$-3.85^{+0.20}_{-0.18}$	$-2.78^{+0.43}_{-0.40}$	$-0.93^{+0.06}_{-0.06}$	$-3.87^{+0.13}_{-0.13}$
μ (g/mol)	$2.41^{+0.43}_{-0.09}$	$3.96^{+0.89}_{-0.80}$	$2.31^{+0.02}_{-0.01}$	$2.34^{+0.08}_{-0.03}$	$4.15^{+0.39}_{-0.37}$	$2.31^{+0.01}_{-0.01}$	$2.33^{+0.05}_{-0.02}$	$4.16^{+0.29}_{-0.25}$	$2.31^{+0.01}_{-0.01}$

Bibliography

Abel, M., Frommhold, L., Li, X., & Hunt, K. L. 2011, The Journal of Physical Chemistry A, 115, 6805

Abel, M., Frommhold, L., Li, X., & Hunt, K. L. 2012, The Journal of chemical physics, 136, 044319

Ackerman, A. S. & Marley, M. S. 2001, The Astrophysical Journal, 556, 872

Addison, B. C., Tinney, C. G., Wright, D. J., et al. 2013, The Astrophysical Journal, 774, L9

Agol, E., Dorn, C., Grimm, S. L., et al. 2021, Refining the transit timing and photometric analysis of TRAPPIST-1: Masses, radii, densities, dynamics, and ephemerides

Al-Refaie, A. F., Changeat, Q., Waldmann, I. P., & Tinetti, G. 2021, The Astrophysical Journal, 917, 37

Allard, F., Homeier, D., & Freytag, B. 2012, Philosophical Transactions of the Royal Society A: Mathematical, Physical and Engineering Sciences, 370, 2765–2777

Allart, R., Bourrier, V., Lovis, C., et al. 2018, Science, 362, 1384

Arcangeli, J., Désert, J.-M., Line, M. R., et al. 2018, The Astrophysical Journal, 855, L30

Arney, G., Domagal-Goldman, S. D., Meadows, V. S., et al. 2016, Astrobiology, 16, 873–899

Bakos, G. A., Torres, G., Pal, A., et al. 2010, The Astrophysical Journal, 710, 1724

Barber, R. J., Strange, J. K., Hill, C., et al. 2014, Monthly Notices of the Royal Astronomical Society, 437, 1828

Barclay, T., Pepper, J., & Quintana, E. V. 2018, The Astrophysical Journal Supplement Series, 239, 2

Barros, S. C. C., Gosselin, H., Lillo-Box, J., et al. 2017, Astronomy & Astrophysics, 608, A25

Barstow, J. K., Aigrain, S., Irwin, P. G. J., & Sing, D. K. 2016, The Astrophysical Journal, 834, 50

Batalha, N. E., Lewis, N. K., Line, M. R., Valenti, J., & Stevenson, K. 2018, The Astrophysical Journal, 856, L34

Batalha, N. E., Mandell, A., Pontoppidan, K., et al. 2017, Publications of the Astronomical Society of the Pacific, 129, 064501

Batalha, N. M. 2014, Proceedings of the National Academy of Sciences, 111, 12647

Batista, V. 2018, 659

Baudino, J.-L., Bézard, B., Boccaletti, A., et al. 2015, Astronomy & Astrophysics, 582, A83

Bean, J. L., Kempton, E. M.-R., & Homeier, D. 2010, Nature, 468, 669–672

Beatty, T. G., Madhusudhan, N., Pogge, R., et al. 2017a, The Astronomical Journal, 154, 242

Beatty, T. G., Madhusudhan, N., Tsiaras, A., et al. 2017b, The Astronomical Journal, 154, 158

Beaulieu, J. P., Carey, S., Ribas, I., & Tinetti, G. 2008, The Astrophysical Journal, 677, 1343

Beaulieu, J. P., Kipping, D. M., Batista, V., et al. 2010, Monthly Notices of the Royal Astronomical Society, 409, 963

Beaulieu, J.-P., Tinetti, G., Kipping, D. M., et al. 2011, The Astrophysical Journal, 731, 16

Ben-Jaffel, L. & Ballester, G. E. 2013, Astronomy & Astrophysics, 553, A52

Ben-Jaffel, L., Ballester, G. E., Muñoz, A. G., et al. 2022, Nature Astronomy, 6, 141

Benneke, B., Knutson, H. A., Lothringer, J., et al. 2019, Nature Astronomy, 3, 813

Benneke, B. & Seager, S. 2012, The Astrophysical Journal, 753, 100

Benneke, B. & Seager, S. 2013, The Astrophysical Journal, 778, 153

Benneke, B., Werner, M., Petigura, E., et al. 2017, The Astrophysical Journal, 834, 10

Benneke, B., Wong, I., Piaulet, C., et al. 2019, The Astrophysical Journal Letters, 887, 9

Berta-Thompson, Z. K., Irwin, J., Charbonneau, D., et al. 2015, Nature, 527, 204

Bézard, B., Charnay, B., & Blain, D. 2022, Nature Astronomy, 6, 537

Biddle, L. I., Pearson, K. A., Crossfield, I. J. M., et al. 2014, MNRAS, 443, 1810

Blain, D., Charnay, B., & Bézard, B. 2021, Astronomy & Astrophysics, 646, A15

Boccaletti, A., Chauvin, G., Mouillet, D., et al. 2020

Bolmont, E., Selsis, F., Owen, J. E., et al. 2017, Monthly Notices of the Royal Astronomical Society, 464, 3728–3741

Bonfils, X., Almenara, J. M., Cloutier, R., et al. 2018, A&A, 618, 12

Borucki, W. J. 2016, Reports on Progress in Physics, 79, 036901

Bourrier, V., Ehrenreich, D., des Etangs, A. L., et al. 2018, Astronomy & Astrophysics, 615, A117

Bourrier, V., Ehrenreich, D., Wheatley, P. J., et al. 2017a, Astronomy & Astrophysics, 599, L3

Bourrier, V. & Lecavelier des Etangs, A. 2013, Astronomy & Astrophysics, 557, A124

Bourrier, V., Lecavelier des Etangs, A., Dupuy, H., et al. 2013, Astronomy & Astrophysics, 551, A63

Bourrier, V., Lecavelier des Etangs, A., Ehrenreich, D., et al. 2018, Astronomy & Astrophysics, 620, A147

Bourrier, V., Lecavelier des Etangs, A., & Vidal-Madjar, A. 2014a, Astronomy & Astrophysics, 573, A11

Bourrier, V., Lecavelier des Etangs, A., & Vidal-Madjar, A. 2014b, Astronomy & Astrophysics, 565, A105

Bourrier, V., Wit, J. d., Bolmont, E., et al. 2017b, The Astronomical Journal, 154, 121

Brande, J., Crossfield, I. J. M., Kreidberg, L., et al. 2022, A Mirage or an Oasis? Water Vapor in the Atmosphere of the Warm Neptune TOI-674 b

Brandl, B. R., Absil, O., Agócs, T., et al. 2018, Proceedings of the SPIE, 10702, 107021U

Brown, D. J. A., Triaud, A. H. M. J., Doyle, A. P., et al. 2017, Monthly Notices of the Royal Astronomical Society, 464, 810–839

Brown, T. M., Charbonneau, D., Gilliland, R. L., Noyes, R. W., & Burrows, A. 2001, The Astrophysical Journal, 552, 699

Buchner, J., Georgakakis, A., Nandra, K., et al. 2014, Astronomy & Astrophysics, 564, A125

Burdanov, A. Y., Lederer, S. M., Gillon, M., et al. 2019, Monthly Notices of the Royal Astronomical Society, 487, 1634–1652

Burgasser, A. J. & Mamajek, E. E. 2017, The Astrophysical Journal, 845, 110

Caldas, A., Leconte, J., Selsis, F., et al. 2019, Astronomy & Astrophysics, 623, A161

Carter, A. L., Nikolov, N., Sing, D. K., et al. 2020, Monthly Notices of the Royal Astronomical Society, 494, 5449

Cassan, A., Kubas, D., Beaulieu, J.-P., et al. 2012, Nature, 481, 167

Changeat, Q., Edwards, B., Al-Refaie, A. F., et al. 2020a, The Astronomical Journal, 160, 260

Changeat, Q., Edwards, B., Al-Refaie, A. F., et al. 2022, The Astrophysical Journal Supplement Series, 260, 3

Changeat, Q., Edwards, B., Al-Refaie, A. F., et al. 2021, Experimental Astronomy

Changeat, Q., Edwards, B., Waldmann, I. P., & Tinetti, G. 2019, The Astrophysical Journal, 886, 39

Changeat, Q., Keyte, L., Waldmann, I. P., & Tinetti, G. 2020b, The Astrophysical Journal, 896, 107

Charbonneau, D., Brown, T. M., Noyes, R. W., & Gilliland, R. L. 2002, The Astrophysical Journal, 568, 377

Charnay, B., Bézard, B., Baudino, J.-L., et al. 2018, The Astrophysical Journal, 854, 172

Chen, J. & Kipping, D. 2016, The Astrophysical Journal, 834, 17

Christiansen, J. L., Vanderburg, A., Burt, J., et al. 2017, The Astronomical Journal, 154, 122

Chubb, K. L., Rocchetto, M., Yurchenko, S. N., et al. 2021, Astronomy & Astrophysics, 646, A21

Claret, A. 2000, Astronomy & Astrophysics, 363

Claret, A. 2018, Astronomy & Astrophysics, 618, A20

Claret, A., Hauschildt, P. H., & Witte, S. 2012, Astronomy & Astrophysics, 546, A14

Claret, A., Hauschildt, P. H., & Witte, S. 2013, Astronomy & Astrophysics, 552, A16

Cloutier, R., Astudillo-Defru, N., Doyon, R., et al. 2017, A&A, 608, 13

Cloutier, R. & Menou, K. 2020, The Astronomical Journal, 159, 211

Coleman, G. A. L., Leleu, A., Alibert, Y., & Benz, W. 2019, Astronomy & Astrophysics, 631, A7

Cowan, N. B., Greene, T., Angerhausen, D., et al. 2015, Astrophysics - Earth and Planetary Astrophysics, 127, 311

Crossfield, I. J. M., Barman, T., & Hansen, B. M. S. 2011, The Astrophysical Journal, 736, 17

Crossfield, I. J. M., Barman, T., Hansen, B. M. S., & Howard, A. W. 2013, Astronomy & Astrophysics, 559, 18

Crossfield, I. J. M., Ciardi, D. R., Isaacson, H., et al. 2017, The Astronomical Journal, 153, 255

Crossfield, I. J. M. & Kreidberg, L. 2017, The Astronomical Journal, 154, 6

Damiano, M., Morello, G., Tsiaras, A., Zingales, T., & Tinetti, G. 2017, The Astronomical Journal, 154, 39

Davis, T. A. & Wheatley, P. J. 2009, Monthly Notices of the Royal Astronomical Society, 396, 1012

Dawson, R. I. & Fabrycky, D. C. 2010, The Astrophysical Journal, 722, 937

de Mooij, E. J. W., Brogi, M., de Kok, R. J., et al. 2013, Astronomy & Astrophysics, 550, A54

de Wit, J., Wakeford, H. R., Gillon, M., et al. 2016, Nature, 537, 69–72

de Wit, J., Wakeford, H. R., Lewis, N. K., et al. 2018, Nature Astronomy, 2, 214–219

Deibert, E. K., de Mooij, E. J. W., Jayawardhana, R., et al. 2021, The Astronomical Journal, 161, 209

Delrez, L., Gillon, M., Triaud, A. H. M. J., et al. 2018, Monthly Notices of the Royal Astronomical Society, 475, 3577–3597

Delrez, L., Santerne, A., Almenara, J.-M., et al. 2016, Monthly Notices of the Royal Astronomical Society, 458, 4025–4043

Deming, D., Knutson, H., Kammer, J., et al. 2015, The Astrophysical Journal, 805, 132

Deming, D., Wilkins, A., McCullough, P., et al. 2013, The Astrophysical Journal, 774, 17

Deming, L. D. & Seager, S. 2017, Journal of Geophysical Research: Planets, 122, 53

Demory, B.-O., de Wit, J., Lewis, N., et al. 2013, The Astrophysical Journal, 776, L25

Demory, B. O., Gillon, M., de Wit, J., et al. 2016, Nature, 532

Demory, B.-O., Gillon, M., Deming, D., et al. 2011, Astronomy & Astrophysics, 533, A114

Demory, B.-O., Gillon, M., Madhusudhan, N., & Queloz, D. 2015, Monthly Notices of the Royal Astronomical Society, 455, 2018

Demory, B.-O., Gillon, M., Seager, S., et al. 2012, The Astrophysical Journal, 751, L28

Dencs, Z. & Regály, Z. 2019, Monthly Notices of the Royal Astronomical Society, 487, 2191–2199

Désert, J.-M., des Etangs, A. L., Hébrard, G., et al. 2009, The Astrophysical Journal, 699, 478

Diamond-Lowe, H., Berta-Thompson, Z., Charbonneau, D., & Kempton, E. M. R. 2018, The Astronomical Journal, 156, 13

Diamond-Lowe, H., Stevenson, K. B., Bean, J. L., Line, M. R., & Fortney, J. J. 2014, The Astrophysical Journal, 796, 66

Dí az, R. F., Almenara, J. M., Santerne, A., et al. 2014, Monthly Notices of the Royal Astronomical Society, 441, 983

Dobos, V., Barr, A. C., & Kiss, L. L. 2019, Astronomy & Astrophysics, 624, A2

Dong, C., Huang, Z., & Lingam, M. 2019, The Astrophysical Journal, 882, L16

Dong, C., Jin, M., Lingam, M., et al. 2018, Proceedings of the National Academy of Sciences, 115, 260–265

Dong, C., Lingam, M., Ma, Y., & Cohen, O. 2017, The Astrophysical Journal, 837, L26

dos Santos, L. A., Ehrenreich, D., Bourrier, V., et al. 2019, Astronomy & Astrophysics, 629, A47

dos Santos, L. A., Vidotto, A. A., Vissapragada, S., et al. 2022, Astronomy & Astrophysics, 659, A62

Doyle, L. R., Carter, J. A., Fabrycky, D. C., et al. 2011, Science, 333, 1602

Dragomir, D., Benneke, B., Pearson, K. A., et al. 2015, The Astrophysical Journal, 814, 9

Dragomir, D., Matthews, J. M., Eastman, J. D., et al. 2013, The Astronomical Journal, 772, 6

Dressing, C. D. & Charbonneau, D. 2013, The Astrophysical Journal, 767, 95

Dressing, C. D. & Charbonneau, D. 2015

Ducrot, E., Gillon, M., Delrez, L., et al. 2020, Astronomy & Astrophysics, 640, A112

Ducrot, E., Sestovic, M., Morris, B. M., et al. 2018, The Astronomical Journal, 156, 218

Edwards, B., Changeat, Q., Baeyens, R., et al. 2020, The Astronomical Journal, 160, 8

Edwards, B., Changeat, Q., Mori, M., et al. 2021, The Astronomical Journal, 161, 44

Edwards, B., Changeat, Q., Tsiaras, A., et al. 2022, The Astrophysical Journal

Edwards, B., Mugnai, L., Tinetti, G., Pascale, E., & Sarkar, S. 2019, The Astronomical Journal, 157, 242

Edwards, B., Rice, M., Zingales, T., et al. 2019, Experimental Astronomy, 47, 29

Ehrenreich, D., Bonfils, X., Lovis, C., et al. 2014, Astronomy & Astrophysics, 570, 24

Ehrenreich, D., Bourrier, V., Bonfils, X., et al. 2012, Astronomy & Astrophysics, 547, A18

Ehrenreich, D., Bourrier, V., Wheatley, P. J., et al. 2015, Nature, 522, 459–461

Endl, M., Robertson, P., Cochran, W. D., et al. 2012, The Astrophysical Journal, 759, 19

Erkaev, N. V., Lammer, H., Odert, P., et al. 2016, Monthly Notices of the Royal Astronomical Society, 460, 1300–1309

Espinoza, N., Fortney, J. J., Miguel, Y., Thorngren, D., & Murray-Clay, R. 2017, The Astrophysical Journal, 838, L9

Esposito, M., Armstrong, D. J., Gandolfi, D., et al. 2019, Astronomy & Astrophysics, 623, A165

Evans, T. M., Sing, D. K., Goyal, J. M., et al. 2018, The Astronomical Journal, 156, 283

Evans, T. M., Sing, D. K., Kataria, T., et al. 2017, Nature, 548, 58–61

Evans, T. M., Sing, D. K., Wakeford, H. R., et al. 2016, The Astrophysical Journal, 822, L4

Eylen, V. V., Agentoft, C., Lundkvist, M. S., et al. 2018, Monthly Notices of the Royal Astronomical Society, 479, 4786

Fanson, J., McCarthy, P. J., Bernstein, R., et al. 2018, Proceedings of the SPIE, 10700, 1070012

Feroz, F., Hobson, M. P., & Bridges, M. 2009, Monthly Notices of the Royal Astronomical Society, 398, 1601–1614

Fletcher, L. N., Gustafsson, M., & Orton, G. S. 2018, The Astrophysical Journal Supplement Series, 235, 24

Folsom, C. P., Fionnagáin, D. Ó ., Fossati, L., et al. 2020, Astronomy &Astrophysics, 633, A48

Foreman-Mackey, D., Hogg, D. W., Lang, D., & Goodman, J. 2013, Publications of the Astronomical Society of the Pacific, 125, 306–312

Fortney, J. J., Lodders, K., Marley, M. S., & Freedman, R. S. 2008, The Astrophysical Journal, 678, 1419

Fortney, J. J., Mordasini, C., Nettelmann, N., et al. 2013, The Astrophysical Journal, 775, 80

Fossati, L., Haswell, C. A., Froning, C. S., et al. 2010, The Astrophysical Journal, 714, L222–L227

Fraine, J., Deming, D., Benneke, B., et al. 2014, Nature, 513, 526

Fressin, F., Torres, G., Charbonneau, D., et al. 2013, The Astrophysical Journal, 766, 81

Fu, G., Deming, D., Knutson, H., et al. 2017, The Astrophysical Journal Letters, 847, 6

Fulton, B., Petigura, E., Howard, A., et al. 2017, The Astronomical Journal, 154

Fulton, B. J. & Petigura, E. A. 2018, The Astronomical Journal, 156, 264

Gandolfi, D., Barragán, O., Hatzes, A. P., et al. 2017, The Astronomical Journal, 154, 123

Gao, P., Hu, R., Robinson, T. D., Li, C., & Yung, Y. L. 2015, The Astrophysical Journal, 806, 12

Gao, P., Marley, M. S., & Ackerman, A. S. 2018, The Astrophysical Journal, 855, 86

Gao, P., Thorngren, D. P., Lee, G. K. H., et al. 2020, Nature Astronomy

Garcia, L. J., Moran, S. E., Rackham, B. V., et al. 2022, HST/WFC3 transmission spectroscopy of the cold rocky planet TRAPPIST-1h

García Muñoz, A. 2007, Planetary and Space Science, 55, 1426

Garhart, E., Deming, D., Mandell, A., et al. 2020, The Astronomical Journal, 159, 137

Gibson, N. P., Aigrain, S., Pont, F., et al. 2012, Monthly Notices of the Royal Astronomical Society, 422, 753

Gillon, M. 2018, Nature Astronomy, 2, 344

Gillon, M., Bonfils, X., Demory, B.-O., et al. 2011, Astronomy & Astrophysics, 525, A32

Gillon, M., Jehin, E., Lederer, S. M., et al. 2016, Nature, 533, 221–224

Gillon, M., Triaud, A. H. M. J., Demory, B.-O., et al. 2017, Nature, 542, 456–460

Gillon, M., Triaud, A. H. M. J., Jehin, E., et al. 2013, Astronomy & Astrophysics, 555, L5

Ginzburg, S., Schlichting, H. E., & Sari, R. 2016, The Astrophysical Journal, 825, 29

Ginzburg, S., Schlichting, H. E., & Sari, R. 2018, Monthly Notices of the Royal Astronomical Society, 476, 759

Greene, T. P., Line, M. R., Montero, C., et al. 2016, The Astrophysical Journal, 817, 17

Gressier, A., Mori, M., Changeat, Q., et al. 2021, Astronomy & Astrophysics

Grimm, S. L., Demory, B.-O., Gillon, M., et al. 2018, Astronomy & Astrophysics, 613, A68

Guillot, T. 2010, Astronomy and Astrophysics, 520, A27

Guilluy, G., Gressier, A., Wright, S., et al. 2020, The Astronomical Journal, 161, 19

Harpsøe, K. B. W., Hardis, S., Hinse, T. C., et al. 2012, Astronomy & Astrophysics, 549, A10

Hartman, J. D., Bakos, G. A., Kipping, D. M., et al. 2011, The Astrophysical Journal, 728, 14

Haynes, K., Mandell, A. M., Madhusudhan, N., Deming, D., & Knutson, H. 2015, The Astrophysical Journal

Hori, Y. & Ogihara, M. 2020, The Astrophysical Journal, 889, 77

Howard, A. W., Marcy, G. W., Bryson, S. T., et al. 2012, The Astrophysical Journal Supplement Series, 201, 15

Howard, A. W., Marcy, G. W., Johnson, J. A., et al. 2010, Science, 330, 653

Hu, R., Peterson, L., & Wolf, E. T. 2020, The Astrophysical Journal, 888, 122

Huitson, C. M., Sing, D. K., Pont, F., et al. 2013, Monthly Notices of the Royal Astronomical Society, 434, 3252

Jenkins, J. S., Díaz, M. R., Kurtovic, N. T., et al. 2020, Nature Astronomy, 4, 1148–1157

Jordán, A., Espinoza, N., Rabus, M., et al. 2013, The Astrophysical Journal, 778, 184

Kass, R. E. & Raferty, A. E. 1995, Journal of the American Statistical Association, 90, 773

Kasting, J. F., Whitmire, D. P., & Reynolds, R. T. 1993, Icarus, 101

Kempton, E. M.-R., Bean, J. L., Louie, D. R., et al. 2018, Publications of the Astronomical Society of the Pacific, 130, 114401

Kempton, E. M.-R., Zahnle, K., & Fortney, J. J. 2011, The Astrophysical Journal, 745, 3

Kilpatrick, B. M., Cubillos, P. E., Stevenson, K. B., et al. 2018, The Astronomical Journal, 156, 103

Kimura, T. & Ikoma, M. 2020, Monthly Notices of the Royal Astronomical Society, 496, 3755

Kipping, D. M. & Tinetti, G. 2010, Monthly Notices of the Royal Astronomical Society, 407, 2589

Knutson, H. A., Benneke, B., Deming, & Homeier, D. 2014a, Nature, 505, 66

Knutson, H. A., Charbonneau, D., Allen, L. E., Burrows, A., & Megeath, S. T. 2008, The Astrophysical Journal, 673, 526

Knutson, H. A., Charbonneau, D., Allen, L. E., et al. 2007, Nature, 447, 183

Knutson, H. A., Dragomir, D., Kreidberg, L., et al. 2014b, The Astronomical Journal, 794

Knutson, H. A., Madhusudhan, N., Cowan, N. B., et al. 2011, The Astrophysical Journal, 735, 23

Koskinen, T., Yelle, R., Harris, M., & Lavvas, P. 2013, Icarus, 226, 1695

Kral, Q., Wyatt, M. C., Triaud, A. H. M. J., et al. 2018, Monthly Notices of the Royal Astronomical Society, 479, 2649–2672

Kreidberg, L. 2015, Publications of the Astronomical Society of the Pacific, 127, 1161–1165

Kreidberg, L. 2018, in Handbook of Exoplanets (Springer International Publishing), 2083–2105

Kreidberg, L., Bean, J. L., Désert, J.-M., et al. 2014a, Nature, 505, 69–72

Kreidberg, L., Bean, J. L., Désert, J.-M., et al. 2014b, The Astrophysical Journal, 793, L27

Kreidberg, L., Koll, D. D. B., Morley, C., et al. 2019, Nature, 573, 87

Kreidberg, L., Line, M. R., Bean, J. L., et al. 2015, The Astrophysical Journal

Kreidberg, L., Line, M. R., Thorngren, D., Morley, C. V., & Stevenson, K. B. 2018, The Astrophysical Journall, 858

Kreidberg, L., Mollière, P., Crossfield, I. J. M., et al. 2020, arXiv e-prints, arXiv:2006.07444

Kulow, J. R., France, K., Linsky, J., & Parke Loyd, R. O. 2014, The Astrophysical Journal, 786, 132

Kurucz, R. L. 1970, SAO Special Report #309

Lammer, H., Selsis, F., Ribas, I., et al. 2003, The Astrophysical Journal, 598, L121

Lanotte, A. A., Gillon, M., Demory, B. O., et al. 2014, A&A, 572, 24

Lavie, B., Ehrenreich, D., Bourrier, V., et al. 2017, Astronomy & Astrophysics, 605, L7

Lecavelier des Etangs, A., Bourrier, V., Wheatley, P. J., et al. 2012, Astronomy & Astrophysics, 543, L4

Lecavelier des Etangs, A., Ehrenreich, D., Vidal-Madjar, A., et al. 2010, Astronomy & Astrophysics, 514, A72

Lecavelier des Etangs, A., Pont, F., Vidal-Madjar, A., & Sing, D. 2008a, Astronomy & Astrophysics, 481, L83

Lecavelier des Etangs, A., Vidal-Madjar, A., Désert, J. M., & Sing, D. 2008b, Astronomy & Astrophysics, 485, 865

Lecavelier des Etangs, A., Vidal-Madjar, A., McConnell, J. C., & Hébrard, G. 2004, Astronomy & Astrophysics, 418, L1

Lee, E. J. & Chiang, E. 2015, The Astrophysical Journal, 811, 41

Lendl, M., Ehrenreich, D., Turner, O. D., et al. 2017, Astronomy & Astrophysics, 603, L5

Li, G., Gordon, I. E., Rothman, L. S., et al. 2015, The Astrophysical Journal Supplement Series, 216, 15

Libby-Roberts, J. E., Berta-Thompson, Z. K., Diamond-Lowe, H., et al. 2022, The Astronomical Journal, 164, 59

Libby-Roberts, J. E., Berta-Thompson, Z. K., Désert, J. M., et al. 2020, The Astronomical Journal, 159, 29

Lincowski, A. P., Lustig-Yaeger, J., & Meadows, V. S. 2019, The Astronomical Journal, 158, 26

Lincowski, A. P., Meadows, V. S., Crisp, D., et al. 2018, The Astrophysical Journal, 867, 76

Line, M. R., Knutson, H., Wolf, A. S., & Yung, Y. L. 2014, The Astrophysical Journal, 783, 70

Line, M. R., Stevenson, K. B., Bean, J., et al. 2016, The Astronomical Journal, 152, 203

Line, M. R., Wolf, A. S., Zhang, X., et al. 2013, The Astrophysical Journal, 775, 137

Linsky, J. L., Yang, H., France, K., et al. 2010, The Astrophysical Journal, 717, 1291–1299

Lodders, K. 2010, Principles and Perspectives in Cosmochemistry, 379–417

Lopez, E. D. & Fortney, J. J. 2014, The Astrophysical Journal, 792, 17

Lothringer, J. D., Fu, G., Sing, D. K., & Barman, T. S. 2020, The Astrophysical Journal, 898, L14

Lothringer, J. D., Sing, D. K., Rustamkulov, Z., et al. 2022, Nature, 604, 49

Lovis, C., Snellen, I., Mouillet, D., et al. 2017, Astronomy & Astrophysics, 599, A16

Luger, R., Lustig-Yaeger, J., & Agol, E. 2017a, The Astrophysical Journal, 851, 94

Luger, R., Sestovic, M., Kruse, E., et al. 2017b, Nature Astronomy, 1

Luque, R. & Pallé , E. 2022, Science, 377, 1211

MacDonald, M. G. & Dawson, R. I. 2018, The Astronomical Journal, 156, 228

MacDonald, R. J., Goyal, J. M., & Lewis, N. K. 2020, The Astrophysical Journal Letters, 893, L43

MacDonald, R. J. & Madhusudhan, N. 2019, Monthly Notices of the Royal Astronomical Society, 486, 1292–1315

Madhusudhan, N. 2019, Annual Review of Astronomy and Astrophysics, 57, 617

Madhusudhan, N., Amin, M. A., & Kennedy, G. M. 2014, The Astrophysical Journal, 794, L12

Madhusudhan, N., Harrington, J., Stevenson, K. B., et al. 2010, Nature, 469, 64

Madhusudhan, N. & Seager, S. 2011, The Astrophysical Journal, 729, 41

Makarov, V. V., Berghea, C. T., & Efroimsky, M. 2018, The Astrophysical Journal, 857, 142

Mandell, A. M., Haynes, K., Sinukoff, E., et al. 2013, The Astrophysical Journal, 779, 128

Markwardt, C. B. 2009, ASP, 411, 261

Marley, M. S., Ackerman, A. S., Cuzzi, J. N., & Kitzmann, D. 2013, University of Arizona Press

Maxted, P. F. L., Ehrenreich, D., Wilson, T. G., et al. 2021, Monthly Notices of the Royal Astronomical Society, 514, 77

Maxted, P. F. L. & Gill, S. 2019, Astronomy & Astrophysics, 622, A33

Mayo, A. W., Vanderburg, A., Latham, D. W., et al. 2018, The Astronomical Journal, 155, 136

Mayor, M. & Queloz, D. 1995, Nature, 378, 355

Mazeh, T., Holczer, T., & Faigler, S. 2016, Astronomy & Astrophysics, 589, A75

McArthur, B. E., Endl, M., Cochran, W. D., et al. 2004, The Astrophysical Journal, 614, L81

McCullough, P. R., Crouzet, N., Deming, D., & Madhusudhan, N. 2014, The Astrophysical Journal, 791, 55

Ment, K., Dittmann, J. A., Astudillo-Defru, N., et al. 2019, The Astronomical Journal, 157, 32

Mikal-Evans, T., Crossfield, I. J. M., Benneke, B., et al. 2020, The Astronomical Journal, 161, 18

Mollière, P., Wardenier, J. P., van Boekel, R., et al. 2019, Astronomy & Astrophysics, 627, A67

Moran, S. E., Hörst, S. M., Batalha, N. E., Lewis, N. K., & Wakeford, H. R. 2018, The Astronomical Journal, 156, 252

Mordasini, C., Alibert, Y., Benz, W., Klahr, H., & Henning, T. 2012, Astronomy & Astrophysics, 541, A97

Mordasini, C., van Boekel, R., Mollière, P., Henning, T., & Benneke, B. 2016, The Astrophysical Journal, 832, 41

Morello, G., Claret, A., Martin-Lagarde, M., et al. 2020, The Astronomical Journal, 159, 75

Morello, G., Waldmann, I. P., Tinetti, G., et al. 2015, The Astrophysical Journal, 802, 117

Morley, C. V., Fortney, J. J., Kempton, E. M.-R., et al. 2013, The Astrophysical Journal, 775, 33

Morley, C. V., Fortney, J. J., Marley, M. S., et al. 2012, The Astronomical Journal, 756

Morley, C. V., Fortney, J. J., Marley, M. S., et al. 2015, The Astrophysical Journal, 815, 110

Morley, C. V., Knutson, H., Line, M., et al. 2017, The Astronomical Journal, 153, 86

Morris, B. M., Agol, E., Davenport, J. R. A., & Hawley, S. L. 2018, The Astrophysical Journal, 857, 39

Moses, J. I. 2014, Philosophical Transactions of the Royal Society A: Mathematical, Physical and Engineering Sciences, 372, 20130073

Moses, J. I., Line, M. R., Visscher, C., et al. 2013, The Astrophysical Journal, 777, 34

Moses, J. I., Tremblin, P., Venot, O., & Miguel, Y. 2021, Experimental Astronomy

Mousis, O., Deleuil, M., Aguichine, A., et al. 2020, The Astrophysical Journal Letters, 896

Mousis, O., Fletcher, L., Lebreton, J.-P., et al. 2014, Planetary and Space Science, 104, 29

Mugnai, L. V., Modirrousta-Galian, D., Edwards, B., et al. 2021, The Astronomical Journal, 161, 284

Mugnai, L. V., Pascale, E., Edwards, B., Papageorgiou, A., & Sarkar, S. 2020, Experimental Astronomy, 50, 303–328

Murgas, F., Astudillo-Defru, N., Bonfils, X., et al. 2021, Astronomy & Astrophysics, 653, A60

Murray-Clay, R. A., Chiang, E. I., & Murray, N. 2009, The Astrophysical Journal, 693, 23–42

Nielsen, E. L., Rosa, R. J. D., Macintosh, B., et al. 2019, The Astronomical Journal, 158, 13

Nikolov, N., Sing, D. K., Burrows, A. S., et al. 2014, Monthly Notices of the Royal Astronomical Society, 447, 463

Nikolov, N., Sing, D. K., Fortney, J. J., et al. 2018, Nature, 557, 526

Nikolov, N., Sing, D. K., Pont, F., et al. 2013, Monthly Notices of the Royal Astronomical Society, 437, 46

Nikolov, N. K., Sing, D. K., Spake, J. J., et al. 2022, Monthly Notices of the Royal Astronomical Society

Nowak, G., Luque, R., Parviainen, H., et al. 2020, Astronomy & Astrophysics, 642, A173

Nugroho, S. K., Kawahara, H., Masuda, K., et al. 2017, The Astronomical Journal, 154, 221

Ormel, C. W., Liu, B., & Schoonenberg, D. 2017, Astronomy & Astrophysics, 604, A1

Owen, J. E. 2019, Annual Review of Earth and Planetary Sciences, 47, 67–90

Owen, J. E. & Wu, Y. 2013, The Astrophysical Journal, 775, 105

Papaloizou, J. C. B., Szuszkiewicz, E., & Terquem, C. 2018, Monthly Notices of the Royal Astronomical Society, 476, 5032–5056

Parmentier, V., Fortney, J. J., Showman, A. P., Morley, C., & Marley, M. S. 2016, The Astrophysical Journal, 828, 22

Parmentier, V., Guillot, T., Fortney, J. J., & Marley, M. S. 2015, Astronomy & Astrophysics, 574, A35

Patel, J. A. & Espinoza, N. 2022, The Astronomical Journal, 163, 228

Pepe, F., Bouchy, F., Mayor, M., & Udry, S. 2018, 855

Perryman, M., Hartman, J., Bakos, G. Á., & Lindegren, L. 2014, The Astrophysical Journal, 797, 14

Petigura, E. A., Benneke, B., Batygin, K., et al. 2018, The Astronomical Journal, 156, 12

Pierrehumbert, R. & Gaidos, E. 2011, The Astrophysical Journal, 734, L13

Pinhas, A., Madhusudhan, N., Gandhi, S., & MacDonald, R. 2018, Monthly Notices of the Royal Astronomical Society, 482, 1485

Pluriel, W., Leconte, J., Parmentier, V., et al. 2022, Astronomy & Astrophysics, 658, A42

Pluriel, W., Whiteford, N., Edwards, B., et al. 2020a, The Astronomical Journal, 160, 112

Pluriel, W., Zingales, T., Leconte, J., & Parmentier, V. 2020b, Astronomy & Astrophysics, 636, A66

Polyansky, O. L., Kyuberis, A. A., Zobov, N. F., et al. 2018, Monthly Notices of the Royal Astronomical Society, 480, 2597–2608

Pont, F., Knutson, H., Gilliland, R. L., Moutou, C., & Charbonneau, D. 2008, Monthly Notices of the Royal Astronomical Society, 385, 109

Pont, F., Sing, D. K., Gibson, N. P., et al. 2013, Monthly Notices of the Royal Astronomical Society, 432, 2917

Rackham, B. V., Apai, D., & Giampapa, M. S. 2018, The Astrophysical Journal, 853, 122

Raghavan, D., McAlister, H. A., Henry, T. J., et al. 2010, The Astrophysical Journal Supplement Series, 190, 1

Ramirez, R. M. & Kaltenegger, L. 2014, The Astrophysical Journal, 797, L25

Ramirez, R. M. & Kaltenegger, L. 2017, The Astrophysical Journal, 837, L4

Rathcke, A. D., MacDonald, R. J., Barstow, J. K., et al. 2021, HST PanCET Program: A Complete Near-UV to Infrared Transmission Spectrum for the Hot Jupiter WASP-79b

Redfield, S., Endl, M., Cochran, W. D., & Koesterke, L. 2008, The Astrophysical Journal, 673, L87–L90

Ricker, G. R., Vanderspek, R., Winn, J., et al. 2016, 9904, 99042B

Rocchetto, M., Waldmann, I. P., Venot, O., Lagage, P.-O., & Tinetti, G. 2016, The Astrophysical Journal, 833, 120

Rodriguez, J. E., Zhou, G., Vanderburg, A., et al. 2017, The Astronomical Journal, 153, 256

Rogers, L. A. 2015, The Astrophysical Journal, 801, 41

Rogers, L. A. & Seager, S. 2010, The Astrophysical Journal, 716, 1208

Rothman, L. S., Gamache, R. R., Goldman, A., et al. 1987, Appl. Opt., 26, 4058

Rothman, L. S., Gordon, I. E., Babikov, Y., et al. 2013, Journal of Quantitative Spectroscopy & Radiative Transfer, 130, 4

Rothman, L. S., Gordon, I. E., Barber, R. J., et al. 2010, Journal of Quantitative Spectroscopy & Radiative Transfer, 111, 2139

Rugheimer, S., Segura, A., Kaltenegger, L., & Sasselov, D. 2015, The Astrophysical Journal, 806, 137

Sagan, C. & Chyba, C. 1997, Science, 276, 1217

Salz, M., Czesla, S., Schneider, P. C., & Schmitt, J. H. M. M. 2016, Astronomy & Astrophysics, 586, A75

Schwarz, H., Brogi, M., de Kok, R., Birkby, J., & Snellen, I. 2015, Astronomy & Astrophysics, 576, A111

Seager, S. & Sasselov, D. D. 2000, The Astrophysical Journal, 537, 916

Sheppard, K. B., Mandell, A. M., Tamburo, P., et al. 2017, The Astrophysical Journal, 850, L32

Sheppard, K. B., Welbanks, L., Mandell, A. M., et al. 2021, The Astronomical Journal, 161, 51

Showman, A. P., Fortney, J. J., Lian, Y., et al. 2009, The Astrophysical Journal, 699, 564

Showman, A. P. & Ingersoll, A. P. 1998, Icarus, 132, 205

Sing, D. K. 2010, Astronomy and Astrophysics, 510, A21

Sing, D. K. 2018, arXiv

Sing, D. K., Fortney, J. J., Nikolov, N., et al. 2016, Nature, 529, 59

Sing, D. K., Lavvas, P., Ballester, G. E., et al. 2019, The Astronomical Journal, 158, 91

Sing, D. K., Lecavelier des Etangs, A., Fortney, J. J., et al. 2013, Monthly Notices of the Royal Astronomical Society, 436, 2956–2973

Sing, D. K., Pont, F., Aigrain, S., et al. 2011, Monthly Notices of the Royal Astronomical Society, 416, 1443

Sing, D. K., Wakeford, H. R., Showman, A. P., et al. 2014, Monthly Notices of the Royal Astronomical Society, 446, 2428

Skaf, N., Bieger, M. F., Edwards, B., et al. 2020, The Astronomical Journal, 160, 109

Skidmore, W., Anupama, G. C., & Srianand, R. 2018, arXiv e-prints, arXiv:1806.02481

Smalley, B., Anderson, D. R., Collier-Cameron, A., et al. 2012, Astronomy & Astrophysics, 547, A61

Smith, R. M., Zavodny, M., Rahmer, G., & Bonati, M. 2008, High Energy, Optical, and Infrared Detectors for Astronomy III, 7021, 70210J

Snellen, I. A. G., de Kok, R. J., de Mooij, E. J. W., & Albrecht, S. 2010, Nature, 465, 1049

Sotzen, K. S., Stevenson, K. B., Sing, D. K., et al. 2020, The Astronomical Journal, 159, 5

Southworth, J., Mancini, L., Madhusudhan, N., et al. 2017, The Astronomical Journal, 153, 14

Spake, J. J., Sing, D. K., Evans, T. M., et al. 2018, Nature, 557, 68–70

Stevenson, K. B. 2016, The Astrophysical Journal, 817, L16

Stevenson, K. B., Dé sert, J.-M., Line, M. R., et al. 2014, Science, 346, 838

Stevenson, K. B., Harrington, J., Fortney, J. J., et al. 2012, The Astrophysical Journal, 754, 136

Stevenson, K. B., Harrington, J., Nymeyer, S., et al. 2010, Nature, 464, 1161

Stevenson, K. B., Line, M. R., Bean, J. L., et al. 2017, The Astronomical Journal, 153, 68

study report, A. D. 2020, ESA

Sulis, S., Dragomir, D., Lendl, M., et al. 2019, Astronomy & Astrophysics, 631, A129

Swain, M. R., Deroo, P., Griffith, C. A., et al. 2010, Nature, 463, 637

Swain, M. R., Estrela, R., Roudier, G. M., et al. 2021, The Astronomical Journal, 161, 213

Swain, M. R., Vasisht, G., & Tinetti, G. 2008, Nature, 452, 329

Szabó , G. M. & Kiss, L. L. 2011, The Astrophysical Journal, 727, L44

Tamayo, D., Rein, H., Petrovich, C., & Murray, N. 2017, The Astrophysical Journal, 840, L19

Tamburo, P., Mandell, A., Deming, D., & Garhart, E. 2018, The Astronomical Journal, 155, 221

Tennyson, J. & Yurchenko, S. 2018, Atoms, 6, 26

Tennyson, J., Yurchenko, S. N., Al-Refaie, A. F., et al. 2016, Journal of Molecular Spectroscopy, 327, 73–94

The JWST Transiting Exoplanet Community Early Release Science Team, Ahrer, E.-M., Alderson, L., et al. 2022, Nature

Thorngren, D. & Fortney, J. J. 2019, The Astrophysical Journal Letters, 874, 6

Thorngren, D. P., Fortney, J. J., Lopez, E. D., Berger, T. A., & Huber, D. 2021, The Astrophysical Journal Letters, 909, L16

Thorngren, D. P., Fortney, J. J., Murray-Clay, R. A., & Lopez, E. D. 2016, The Astrophysical Journal, 831, 64

Tian, F. D. & Ida, S. 2015, Nature Geoscience, 8, 177

Tinetti, G., Drossart, P., Eccleston, P., et al. 2018, Experimental Astronomy, 46, 135

Tinetti, G., Vidal-Madjar, A., Liang, M.-C., et al. 2007, Nature, 448, 169

Tremblin, P., Chabrier, G., Mayne, N. J., et al. 2017, The Astrophysical Journal, 841, 30

Trotta, R. 2008, Contemporary Physics, 49, 71–104

Tsiaras, A., Rocchetto, M., Waldmann, I. P., et al. 2016a, The Astrophysical Journal, 820, 99

Tsiaras, A., Waldmann, I. P., Rocchetto, M., et al. 2016b, The Astrophysical Journal, 832, 17

Tsiaras, A., Waldmann, I. P., Tinetti, G., Tennyson, J., & Yurchenko, S. N. 2019, Nature Astronomy, 451

Tsiaras, A., Waldmann, I. P., Zingales, T., et al. 2018, The Astronomical Journal, 155, 156

Turbet, M., Bolmont, E., Bourrier, V., et al. 2020a, Space Science Reviews, 216

Turbet, M., Bolmont, E., Ehrenreich, D., et al. 2020b, Astronomy & Astrophysics, 638, A41

Turbet, M., Bolmont, E., Leconte, J., et al. 2018, Astronomy & Astrophysics, 612, A86

Turbet, M., Ehrenreich, D., Lovis, C., Bolmont, E., & Fauchez, T. 2019a, Astronomy & Astrophysics, 628, A12

Turbet, M., Tran, H., Pirali, O., et al. 2019b, Icarus, 321, 189–199

Turrini, D., Miguel, Y., Zingales, T., et al. 2018, Experimental Astronomy, 46, 45

Valencia, D., Guillot, T., Parmentier, V., & Freedman, R. S. 2013, The Astrophysical Journal, 775, 10

Valencia, D., Ikoma, M., Guillot, T., & Nettelmann, N. 2010, Astronomy and Astrophysics, 516, A20

Van Eylen, V., Astudillo-Defru, N., Bonfils, X., et al. 2021, Monthly Notices of the Royal Astronomical Society

Vanderburg, A., Becker, J. C., Kristiansen, M. H., et al. 2016a, The Astrophysical Journal Letters, 827, 11

Vanderburg, A., Bieryla, A., Duev, D. A., et al. 2016b, The Astrophysical Journal Letters, 829, L9

Vanderspek, R., Huang, C. X., Vanderburg, A., et al. 2019, The Astrophysical Journal, 871, L24

Venot, O., Cavalié, T., Bounaceur, R., et al. 2020, Astronomy & Astrophysics, 634, A78

Vida, K., Kővári, Z., Pál, A., Oláh, K., & Kriskovics, L. 2017, The Astrophysical Journal, 841, 124

Vidal-Madjar, A., Dsert, J.-M., Etangs, A. L. d., et al. 2004, The Astrophysical Journal, 604, L69–L72

Vidal-Madjar, A., Huitson, C. M., Bourrier, V., et al. 2013, Astronomy & Astrophysics, 560, A54

Vidal-Madjar, A., Lecavelier des Etangs, A., Désert, J. M., et al. 2003, Nature, 422

Vidal-Madjar, A., Lecavelier des Etangs, A., Désert, J.-M., et al. 2008, The Astrophysical Journal, 676, L57–L60

Von Braun, K., Boyajian, T. S., ten Brummelaar, T. A., et al. 2011, The Astrophysical Journal, 740, 6

Waalkes, W. C., Berta-Thompson, Z., Bourrier, V., et al. 2019, The Astronomical Journal, 158, 50

Wakeford, H. R., Lewis, N. K., Fowler, J., et al. 2019, The Astronomical Journal, 157, 11

Wakeford, H. R., Sing, D. K., Deming, D., et al. 2013, Monthly Notices of the Royal Astronomical Society, 435, 3481

Wakeford, H. R., Sing, D. K., Deming, D., et al. 2017, The Astronomical Journal, 155, 29

Wakeford, H. R., Sing, D. K., Kataria, T., et al. 2017, Science, 356, 628

Wakeford, H. R., Sing, D. K., Stevenson, K. B., et al. 2020, The Astronomical Journal, 159, 204

Waldmann, I. P., Rocchetto, M., Tinetti, G., et al. 2015a, The Astrophysical Journal, 813, 13

Waldmann, I. P., Tinetti, G., Rocchetto, M., et al. 2015b, The Astrophysical Journal, 802, 107

Watson, A. J., Donahue, T. M., & Walker, J. C. 1981, Icarus, 48, 150

Weiss, L. M. & Marcy, G. W. 2014, The Astrophysical Journal, 783, L6

Welbanks, L., Madhusudhan, N., Allard, N. F., et al. 2019, The Astrophysical Journal Letters, 887, L20

Welsh, W. F., Orosz, J. A., Carter, J. A., et al. 2012, Nature, 481, 475

Wheatley, P. J., Louden, T., Bourrier, V., Ehrenreich, D., & Gillon, M. 2017, Monthly Notices of the Royal Astronomical Society: Letters, 465, L74–L78

Winn, J. N., Matthews, J. M., Dawson, R. I., et al. 2011, The Astrophysical Journal, 737, L18

Winn, J. N., Sanchis-Ojeda, R., & Rappaport, S. 2018, New Astronomy Reviews, 83, 37

Wolf, E. T. & Toon, O. B. 2010, Science, 328, 1266

Wolfgang, A. & Lopez, E. 2014, How Rocky Are They? The Composition Distribution of Kepler's Sub-Neptune Planet Candidates within 0.15 AU

Wolszczan, A. & Frail, D. A. 1992, Nature, 355, 145

Wong, I., Benneke, B., Gao, P., et al. 2020, The Astronomical Journal, 159, 234

Wordsworth, R., Kalugina, Y., Lokshtanov, S., et al. 2017, Geophysical Research Letters, 44, 665–671

Wordsworth, R. & Kreidberg, L. 2021, Atmospheres of Rocky Exoplanets

Wordsworth, R. D., Schaefer, L. K., & Fischer, R. A. 2018, The Astronomical Journal, 155, 195

Wyttenbach, A., Ehrenreich, D., Lovis, C., Udry, S., & Pepe, F. 2015, Astronomy & Astrophysics, 577, A62

Yelle, R. V. 2004, Icarus, 170, 167

Yip, K. H., Changeat, Q., Edwards, B., et al. 2020, The Astronomical Journal, 161, 4

Yurchenko, S. N., Barber, R. J., & Tennyson, J. 2011, Monthly Notices of the Royal Astronomical Society, 413, 1828–1834

Yurchenko, S. N. & Tennyson, J. 2014, Monthly Notices of the Royal Astronomical Society, 440, 1649–1661

Zahnle, K. J. & Marley, M. S. 2014, The Astrophysical Journal, 797, 41

Zeng, L., Jacobsen, S. B., Sasselov, D. D., et al. 2019, Proceedings of the National Academy of Sciences, 116, 9723–9728

Zeng, L. & Sasselov, D. 2013, Publications of the Astronomical Society of the Pacific, 125, 227

Zeng, L., Sasselov, D. D., & Jacobsen, S. B. 2016, The Astrophysical Journal, 819, 127

Zhang, Z., Zhou, Y., Rackham, B. V., & Apai, D. 2018, The Astronomical Journal, 156, 178

Zhou, G., Rodriguez, J. E., Vanderburg, A., et al. 2018, The Astronomical Journal, 156, 93

Zhou, Y., Apai, D., Lew, B. W. P., & Schneider, G. 2017, The Astronomical Journal, 153, 243

Öberg, K. I., Murray-Clay, R., & Bergin, E. A. 2011, The Astrophysical Journal, 743, L16

Titre: Observations et modélisations de l'atmosphère des exoplanètes: de la haute atmosphère des Jupiter-chaud à la surface des planètes terrestres tempérées, étude de la transition des Super-Terre aux Sub-Neptune avec un relevé Hubble

Mots clés: exoplanètes, atmosphères, transfert radiatif, Télescope Spatial Hubble, Sub-Neptune, Super-Terre

Résumé long: Le 22 novembre dernier, le JWST Transiting Exoplanet Community Early Release Science Team a révélé des détections sans précédent de molécules et d'atomes dans l'atmosphère de la géante gazeuse WASP-39 b, démontrant les capacités exceptionnelles du Télescope spatial James Webb (JWST) pour la caractérisation de l'atmosphère des planètes extrasolaires. Alors que de nombreuses nouvelles données seront disponibles dans les années à venir, cette thèse propose d'utiliser les observations du télescope spatial Hubble (HST) en spectroscopie de transit dans le but de mieux préparer les futures analyses mais aussi de passer de l'étude d'une seule cible à l'étude statistique d'une population de planètes.

Nous nous intéressons tout particulièrement aux planètes de taille intermédiaire (1 à 4 $R_\oplus$), qui n'ont pas d'équivalent dans notre système solaire et qui restent difficiles à caractériser. Leur taux d'occurrence est bimodal, peu de planète sont trouvées autour de 1,7$R_\oplus$ (Fulton et al., 2017). Ce résultat suggère des processus de formation et d'évolution spécifiques qui façonnent cette population de planète.

Dans un premier temps, nous analysons la haute atmosphère des Jupiters-chauds avec les observations HST dans le proche ultra-violet (NUV). Nous présentons un outil pour corriger et ajuster les courbes de lumière en transits observés avec le Space Telescope Imaging Spectrograph (STIS). L'analyse de deux transits de WASP-79 b et WASP-121 b montre une augmentation du rayon de la planète entre la mesure optique et NUV. Nous confirmons la photo-évaporation de WASP-121 b observée pour la première fois dans (Sing et al., 2019) et trouvons une différence de 4,5-σ dans le rapport du rayon planétaire à l'étoile entre l'optique et le NUV dans les données WASP-79 b. Le niveau d'absorption atteint 20 hauteur d'échelle, comparable à l'absorption par le SiO dans l'atmosphère de WASP-178 b (Lothringer et al., 2022).

Nous étudions, ensuite, les couches plus profondes de l'atmosphère de planètes plus petites avec les observations en proche infrarouge. Nous produisons le premier spectre en proche IR d'une planète rocheuse froide , TRAPPIST-1 h et confirmons les prédictions de modélisation pour cette planète : il est très peu probable qu'elle possède une atmosphère primaire sans nuage. Vingt-six spectres en transmission sont analysés de manière cohérente afin d'explorer la transition entre Super-Terre et Sub-Neptune. Ce travail est la première étude de petites planètes utilisant les observations de Hubble. Nous confirmons la présence d'une atmosphère pour 13 planètes et la détection de vapeur d'eau pour neuf d'entre elles.

Cependant, de nombreuses dégénérescences subsistent dans l'analyse de ces spectres et il reste difficile de différencier une atmosphère primaire nuageuse d'une atmosphère de type terrestre. Huit des 13 spectres de transmission avec des signatures spectrales significatives ont une solution dégénérée. L'ajustement nécessite soit une couche nuageuse opaque pour couper les signatures spectrales moléculaires, soit des éléments lourds pour ajuster la taille des signatures atmosphériques observées. Nous mettons également en évidence l'absence de détection de méthane dans ces spectres, en désaccord avec les prédictions.

La dernière partie de la thèse tente de résoudre les dégénérescences en utilisant une modélisation radiative convective en 1D et des simulations JWST et ARIEL. Nous concentrons notre modélisation sur deux points principaux : l'impact de la sédimentation des nuages sur le spectre de transmission et la nature des espèces carbonées et oxygénées à l'aide d'un modèle radiatif-convectif auto-consistant `Exo-REM`. Nous avons construit une grille de modèles avec trois dimensions principales : la température, la métallicité atmosphérique et la couverture nuageuse de l'atmosphère. Afin de déterminer l'impact des observations optiques sur la distinction entre l'atmosphère claire et nuageuse, nous avons proposé et obtenu des observations CHEOPS. Nous montrons qu'il est possible d'utiliser le point de données photométriques CHEOPS pour améliorer la caractérisation de l'atmosphère. Les premières analyses des observations sur HD 219666 b sont combinées avec les observations HST, et nous affinons les paramètres et les caractéristiques atmosphériques de cette planète. Nous concluons à une composition atmosphérique légère sans nuage (1 à 100 $\times$ solaires).

Nous affinons la nature des nuages dans l'atmosphère de Sub-Neptunes et leur impact sur la taille de la signature spectrale de l'eau. Nous proposons et comparons les stratégies d'observation JWST et ARIEL pour résoudre les dégénérescences et en particulier, différencier l'absorption de l'eau de celle du méthane dans les spectres en transmission. Nous proposons d'utiliser un combinaison des instruments JWST NIRISS SOSS et NIRSpec G395H pour distinguer une atmosphère primaire nuageuse d'une atmosphère secondaire.